

Pradeep Kumar Gupta  
Rajeev Khare *Editors*

# Laser Physics and Technology

Proceedings of the School on Laser  
Physics & Technology, Indore, India,  
March 12–30, 2012

# **Springer Proceedings in Physics**

Volume 160

More information about this series at <http://www.springer.com/series/361>

Pradeep Kumar Gupta • Rajeev Khare  
Editors

# Laser Physics and Technology

Proceedings of the School on Laser  
Physics & Technology, Indore, India,  
March 12–30, 2012



Springer

*Editors*

Pradeep Kumar Gupta  
Laser Biomedical Applications &  
Instrumentation Division  
Raja Ramanna Centre for Advanced  
Technology  
Indore, Madhya Pradesh, India

Rajeev Khare  
Laser Systems Engineering Section  
Raja Ramanna Centre for Advanced  
Technology  
Indore, Madhya Pradesh, India

ISSN 0930-8989

ISBN 978-81-322-1999-6

DOI 10.1007/978-81-322-2000-8

Springer New Delhi Heidelberg New York Dordrecht London

ISSN 1867-4941 (electronic)

ISBN 978-81-322-2000-8 (eBook)

Library of Congress Control Number: 2014954797

© Springer India 2015

This work is subject to copyright. All rights are reserved by the Publisher, whether the whole or part of the material is concerned, specifically the rights of translation, reprinting, reuse of illustrations, recitation, broadcasting, reproduction on microfilms or in any other physical way, and transmission or information storage and retrieval, electronic adaptation, computer software, or by similar or dissimilar methodology now known or hereafter developed. Exempted from this legal reservation are brief excerpts in connection with reviews or scholarly analysis or material supplied specifically for the purpose of being entered and executed on a computer system, for exclusive use by the purchaser of the work. Duplication of this publication or parts thereof is permitted only under the provisions of the Copyright Law of the Publisher's location, in its current version, and permission for use must always be obtained from Springer. Permissions for use may be obtained through RightsLink at the Copyright Clearance Center. Violations are liable to prosecution under the respective Copyright Law.

The use of general descriptive names, registered names, trademarks, service marks, etc. in this publication does not imply, even in the absence of a specific statement, that such names are exempt from the relevant protective laws and regulations and therefore free for general use.

While the advice and information in this book are believed to be true and accurate at the date of publication, neither the authors nor the editors nor the publisher can accept any legal responsibility for any errors or omissions that may be made. The publisher makes no warranty, express or implied, with respect to the material contained herein.

Printed on acid-free paper

Springer is part of Springer Science+Business Media ([www.springer.com](http://www.springer.com))

# Preface

Laser is a remarkable source of light and has proved to be one of the most important inventions of the last century. Although the first laser, a Ruby laser, was operated, just about 54 years ago, on 16 May 1960, in this relatively short span of time, lasers have made their presence felt in all walks of life, be it industry, medicine, defense or in basic research. As part of its mandate to provide thrust to research in promising areas and generate qualified human resource in these areas, Science and Engineering Research Council (SERC) of the Department of Science and Technology, Government of India, funded the organization of a School on ‘Laser Physics and Technology’ at Raja Ramanna Centre for Advanced Technology (RRCAT) during March 12–30, 2012. RRCAT was requested to host the School because it is the largest laser R&D center in the country and has a comprehensive and multidimensional program on lasers and its applications. The objective of the School was to provide an in-depth knowledge of the important aspects of laser physics and technology to research scholars, post-doctoral fellows and young researchers working in this area. The topics covered included fundamentals of laser physics, techniques used to control laser parameters, non-linear optics, etc. Important laser systems such as diode-pumped solid state lasers, ultrashort pulse lasers, fiber lasers, semiconductor lasers, free electron lasers, and terahertz sources were also discussed. The School also addressed some important applications of lasers in high resolution spectroscopy, material processing, biophotonics, etc. The participants were also provided an opportunity to do hands-on experiments designed to facilitate understanding of the topics discussed during the School. Further, a few evening lectures were arranged to provide a perspective of the present status and future prospects for the physics and technology of lasers in the country.

The present volume is a collection of articles based on some of the lectures given at the School. The volume comprises of chapters which cover the fundamentals of laser physics and technology, representative laser systems and some important applications of lasers. The chapters, written by leading Indian experts of the field, provide an exposure to the fundamentals of the field and review the current status of

the field with emphasis on the work being carried out in India. It is hoped that the book should prove useful not only to doctoral students and young scientists who are embarking on a research career in this area but also to professionals who would be interested in knowing the current state of the field, particularly in Indian context.

We would like to take this opportunity to thank all the authors for their contributions and all our colleagues who have helped in bringing out this book. We are particularly indebted to our colleagues, Rama Chari, T K Sharma, G Singh, B N Upadhyaya, S K Dixit, S R Mishra, Om Prakash, K K Pant, Sendhil Raja S, C P Paul, S Verma, and C P Singh, who volunteered to read the chapters and gave comments to improve these.

Indore, Madhya Pradesh, India

Pradeep Kumar Gupta  
Rajeev Khare

# Contents

<b>1</b>	<b>Lasers: An Introduction .....</b>	1
	Pradeep Kumar Gupta and Rajeev Khare	
<b>2</b>	<b>Basics of Nonlinear Optics .....</b>	27
	Mukesh P. Joshi	
<b>3</b>	<b>Gas Lasers .....</b>	65
	S.K. Dixit	
<b>4</b>	<b>Diode-Pumped Solid-State Lasers and Intracavity Frequency Conversion .....</b>	85
	P.K. Mukhopadhyay	
<b>5</b>	<b>Semiconductor Lasers: Basics and Technology .....</b>	115
	S.K. Mehta, Alok Jain, and Deepti Jain	
<b>6</b>	<b>Fiber Lasers .....</b>	133
	K. Thyagarajan	
<b>7</b>	<b>Free Electron Lasers .....</b>	151
	K.K. Pant	
<b>8</b>	<b>Lasing in Random Amplifying Media .....</b>	165
	Hema Ramachandran	
<b>9</b>	<b>Terahertz Transients: Generation and Applications .....</b>	181
	D.S. Rana	
<b>10</b>	<b>Phase-Shifting Laser Interferometry for Measurement of Surface Form Error .....</b>	209
	Sanjib Chatterjee	
<b>11</b>	<b>High-Resolution Spectroscopy .....</b>	223
	B.M. Suri	

<b>12 Lasers in Materials Processing .....</b>	253
L.M. Kukreja, C.P. Paul, Atul Kumar, R. Kaul, P. Ganesh, and B.T. Rao	
<b>13 Biomedical Applications of Lasers .....</b>	301
Pradeep Kumar Gupta and H.S. Patel	
<b>Group Photograph .....</b>	333
<b>Index .....</b>	335

# List of Participants

Sr. no.	Names	Affiliations
1.	Manoja Kumar Biswal	CSIR-CMERI, Durgapur
2.	S. D. Meetei	Dept. of Physics, Manipur University, Cachhipur
3.	Litul Bokatiyal	Dibrugarh University, Dibrugarh, Assam
4.	Jalpa Soni	IISER, Kolkata
5.	Parvendra Kumar	IIT Guwahati, Guwahati
6.	A T T Mostako	IIT Guwahati, Guwahati
7.	Trilochan Sahu	PXE, DRDO, Balasore, Orissa
8.	Bishnu Kumar Pandey	Allahabad University, Allahabad
9.	Mahendra Kumar Maurya	BHU, Varanasi
10.	Sushil Kumar	BHU, Varanasi
11.	Manoj Mishra	Dept. of Applied Science, FET, MITS, Sikar, Rajasthan
12.	Naresh Kumar Chaudhary	Dr. R.M.L. Avadh University, Faizabad
13.	Bhupesh Kumar	IISER Mohali
14.	Vivek Kumar	IIT Delhi
15.	Bharat L Meena	IIT Kanpur, Kanpur
16.	Rashmi Negi	IRDE, Dehradun
17.	Yogesh Saxena	IRDE, Dehradun
18.	M. Ashwin Kumar	ACREHEM, University of Hyderabad, Hyderabad
19.	Anusha P.T.	ACRHEM, University of Hyderabad, Hyderabad
20.	S. Sridhar	Anna University of Technology, Tiruchirappalli
21.	Sabari Girisun	Bishop Heber College, Tiruchirappalli
22.	D. Balaji	Crystal Growth Centre, Anna University, Chennai
23.	N. Elavarasu	Dept. of Physics, Anna University, Chennai
24.	Indu Sebastian	International School of Photonics, CUSAT, Cochin

(continued)

Sr. no.	Names	Affiliations
25.	Udayabhaskar	NIT, Trichy
26.	Chitra Shaji	Pondicherry University, Puducherry
27.	Anil K Singh	BARC
28.	Asha K	RRI, Bangalore
29.	Vijay Kumar	School of Physics Univ. of Hyderabad, Hyderabad
30.	Valligatla Sreeramulu	School of Physics Univ. of Hyderabad, Hyderabad
31.	Shaiju S. Nazeer	SCTIMST, Trivandrum
32.	Nayab Rasool Shaik	Sri Venkateshwara University, Tirupati
33.	N. Karunagaran	SSN College of Engg. SSN Nagar, Kancheepuram
34.	Apurav Guleria	BARC
35.	Atul C Sahoo	BARC
36.	Bijeesh M.M.	BITS Pilani, Goa Campus
37.	S. G. Reddy	P. R. L. Navrangpura, Ahmedabad
38.	Geetanjali Sharma	School of Physics, DAVV, Indore
39.	Sami Ur Rehman	Space Applications Centre, Ahmedabad
40.	Payal Sharma	Space Applications Centre, Ahmedabad

## **Information Text About the Book**

The book, *Laser Physics and Technology*, addresses fundamentals of laser physics, representative laser systems and techniques, and some important applications of lasers. The present volume is a collection of articles based on some of the lectures delivered at the School on ‘Laser Physics and Technology’ organized at Raja Ramanna Centre for Advanced Technology during March 12–30, 2012. The objective of the School was to provide an in-depth knowledge of the important aspects of laser physics and technology to doctoral students and young researchers and motivate them for further work in this area. In keeping with this objective, the 13 chapters, written by leading Indian experts, based on the lectures delivered by them at the School, provide along with class room type coverage of the fundamentals of the field, a brief review of the current status of the field. The book will be useful for doctoral students and young scientists who are embarking on a research career in this area as well as to professionals who would be interested in knowing the current state of the field particularly in the Indian context.



## About the Editors

**Dr. Pradeep Kumar Gupta** is Associate Director at Raja Ramanna Centre for Advanced Technology, and presently heads its Laser Biomedical Applications and Instrumentation Division and the Laser Materials Development and Devices Division. Dr. Gupta is also a Senior Professor with Homi Bhabha National Institute, a deemed university. Dr. Gupta's current research interests include biomedical applications of lasers, biomedical optics and laser materials.

Dr. Gupta has over 330 research publications in peer-reviewed journals and edited volumes, over 350 conference presentations that include over 80 invited talks and holds three patents. Dr. Gupta is a Fellow of the Indian Academy of Sciences, Bangalore, and National Academy of Sciences, Allahabad. He has received the N.S. Satyamurthy memorial award of Indian Physics Association for the year 1988 for his contributions on mid-infrared coherent sources and the 1998 Homi Bhabha Science and Technology Award of the Department of Atomic Energy, for his contributions in the area of biomedical applications of lasers.

**Dr. Rajeev Khare** received his M.Sc. degree in Physics from Allahabad University. He joined the Laser Division, Bhabha Atomic Research Centre (BARC), in 1986 after graduating from the BARC Training School, and worked in the area of tunable dye lasers. Dr. Khare moved to Raja Ramanna Centre for Advanced Technology (RRCAT), Indore, in 1988, where he had set-up a laboratory to design and develop tunable dye lasers pumped by copper vapour lasers. He obtained his Ph.D. degree from Indore University in 2000 for his work on resonator schemes for dye lasers pumped by copper vapour lasers. His research interests are mainly in design and development of tunable dye lasers, copper vapour lasers, copper bromide lasers, nitrogen lasers, excimer lasers and high-resolution spectroscopy. Dr. Khare has over 40 publications in peer-reviewed journals and proceedings of conferences and he holds one patent. Dr. Khare presently heads the Dye Laser Development Laboratory at RRCAT, Indore.

# Chapter 1

## Lasers: An Introduction

Pradeep Kumar Gupta and Rajeev Khare

**Abstract** This chapter provides a brief overview of the fundamental concepts of laser physics, how lasers work, and why they differ from conventional sources of light and addresses the important factors that determine their operational characteristics.

**Keywords** Basic concepts of laser • Stable and unstable optical resonators • Frequency of operation • CW and pulsed operation • Generation of short pulses

### 1.1 Introduction

Laser is one of the most important inventions of the twentieth century. Because of their remarkable properties, lasers are finding applications in all aspects of human endeavor, unraveling mysteries of nature, medicine, industry, defense, and even home entertainment. The great diversity of the range of applications of lasers can be seen from the fact that lasers are being used for generating both the highest as well as the lowest temperature on our planet. Similarly they are being used not only to weld thick plates of metals but also the delicate layers of the retina in the eye. Of course, no single laser does all these things. The word “laser,” an acronym for light amplification by stimulated emission of radiation, is now used as a kind of family name for all devices that emit coherent light by the process of stimulated emission. The lasers differ a great deal in size, cost, wavelength, power, and other characteristics. The smallest lasers are as small as pinheads. They are mass produced and sold in large numbers at less than a hundred rupees each. One of the largest laser systems that is being used for studies on the utilization of inertially confined fusion

---

P.K. Gupta (✉)

Laser Biomedical Applications & Instrumentation Division, Raja Ramanna Centre for Advanced Technology, Indore, Madhya Pradesh 452013, India  
e-mail: [pkgupta@rrcat.gov.in](mailto:pkgupta@rrcat.gov.in)

R. Khare

Laser Systems Engineering Section, Raja Ramanna Centre for Advanced Technology, Indore, Madhya Pradesh 452013, India  
e-mail: [rkhare@rrcat.gov.in](mailto:rkhare@rrcat.gov.in)

as a source of clean energy occupies an impeccably dust-free hall as large as cricket field and costs thousands of crores of rupees. In this chapter, we provide a brief overview of the fundamental concepts of laser physics and address the important factors that determine their operational characteristics. For details, the reader is referred to the several excellent texts available [1–10].

To understand lasers it is necessary to understand the two important phrases “light amplification” and “stimulated emission.” For this let us recapitulate how light is emitted. Light emission takes place by two processes. One is spontaneous emission wherein an atom (or molecule) in excited state returns to a lower energy state, on its own, by emission of a photon with energy equal to the difference of the energies of the two atomic energy levels. In this process the atoms radiate randomly and independent of each other leading to incoherent light. The light from all conventional sources of light, which are essentially hot bodies, arises primarily by spontaneous emission of constituent atoms. In these hot bodies, atoms are continuously pumped to excited states and fall back loosing energy by spontaneous emission. It is true that in the low-pressure gas discharge like the one in fluorescent lamps, the glass walls remain cool, but the electrons and gas atoms inside the tube are accelerated to high speeds characteristic of high temperatures. In 1917, Einstein, while trying to explain the black body radiation that was receiving the attention of all the leading scientists of that time, showed that in the presence of radiation with energy resonant with the atomic transition, an atom in excited state could also be stimulated to emit a photon of the same energy. The important characteristic of stimulated emission is that the emitted photon is an exact replica of the stimulating photon, i.e., it has the same wavelength, phase, polarization, direction of propagation, etc. Thus, the process of stimulated emission provides a control on emission by independent atoms and can be used to force the atoms to emit in phase. This control on emission of individual atoms through the control on stimulating photons is the essence of laser operation.

Another important result obtained by Einstein was that a priori probability for an atom in excited state to get de-excited by stimulated emission of a photon is exactly equal to the probability for the atom to reach the excited state by the stimulated absorption of a photon. Thus, in a normal situation of thermal equilibrium where more atoms are in the lower energy state, one observes a net stimulated absorption of photons leading to light attenuation. For amplification of light, it is necessary that the upper level has more population than the lower level, a condition referred to as “population inversion.”

A schematic diagram of a laser is shown in Fig. 1.1. The laser comprises of three components: a gain medium, a pump source to achieve “population inversion,” and an optical resonator with one highly reflecting and one partially transmitting mirror to provide feedback at the frequency of operation and achieve oscillation. A part of the laser radiation that is built up in the resonator is coupled out from the partially transmitting mirror as the useful output.

It is the combination of stimulated emission process and the control on the stimulating light achieved via the optical resonator that lends lasers its striking properties

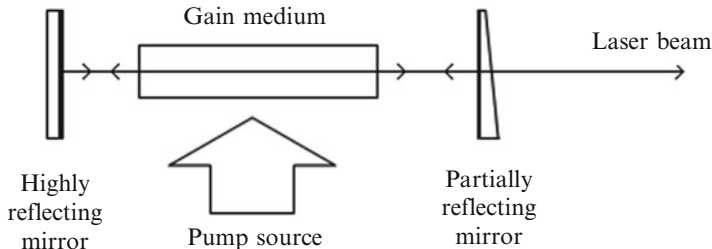


**Fig. 1.1** Schematic diagram of a laser oscillator

of directionality, monochromaticity, etc. As an example, the high directionality of lasers arises because only the radiation propagating exactly normal to the mirror surfaces will make repeated passes through the gain medium and get amplified while the radiation, propagating at any other angle, will be lost from the cavity after a few passes.

In the following we first discuss the resonant interaction of an electromagnetic radiation with an atomic gain medium to get a feel for the rather simple analysis used by Einstein to surmise the presence of stimulated emission and pave the way for the invention of lasers. Next we discuss briefly the characteristics of the gain medium, the methods used for achieving population inversion, and the control provided by the optical resonator that together determines the operational characteristics of a laser.

## 1.2 Interaction of Light with Atomic Systems

Let us begin by reviewing the interaction of an electromagnetic wave having frequency  $\nu$  with the resonant transition of a gain medium [11]. For simplicity we assume that the medium has only two energy states (Fig. 1.2), i.e., we ignore transfer of population from these states to the other states. The probability of an atom in the lower state to get excited to the upper state is given by

$$P_{12} = B_{12}\rho(\nu) \quad (1.1)$$

where  $B_{12}$  is a characteristic of the medium and is related to the transition dipole moment and  $\rho(\nu)$  is the spectral energy density at frequency  $\nu$ . An atom in the excited state has a certain probability ( $A_{21}$ ) to spontaneously decay to the lower state by emitting a photon of frequency  $\nu$ . If  $\tau_{sp}$  is the spontaneous emission lifetime of the state  $E_2$ , then

$$\tau_{sp} = \frac{1}{A_{21}} \quad (1.2)$$

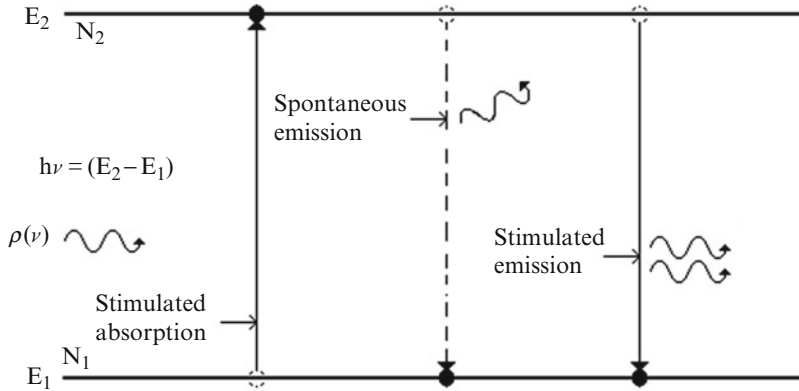


**Fig. 1.2** Interaction of radiation with a resonant two-level system

Now if it is assumed that in the presence of radiation of frequency  $\nu$ , the excited atom can be induced to emit a photon, then the total probability for an atom in the excited state to decay to the lower state is given by

$$P_{21} = A_{21} + B_{21}\rho(\nu) \quad (1.3)$$

For the atomic system to be in thermal equilibrium at the temperature  $T$  with radiation of frequency  $\nu$  and energy density  $\rho(\nu)$ ,

$$N_1 B_{12}\rho(\nu) = N_2 [A_{21} + B_{21}\rho(\nu)] \quad (1.4)$$

where  $N_1$  and  $N_2$  are the population densities in the lower and upper energy states. Thus,

$$\frac{N_2}{N_1} = \frac{B_{12}\rho(\nu)}{A_{21} + B_{21}\rho(\nu)} \quad (1.5)$$

According to Boltzmann distribution, the ratio,  $N_2/N_1$ , is given by

$$\frac{N_2}{N_1} = \exp\left(-\frac{h\nu}{kT}\right) \quad (1.6)$$

Using Eqs. (1.5) and (1.6), we get

$$\rho(\nu) = \left(\frac{A_{21}}{B_{21}}\right) \cdot \frac{1}{\left[\frac{B_{12}}{B_{21}} \exp\left(\frac{h\nu}{kT}\right) - 1\right]} \quad (1.7)$$

Equation (1.7) is a formula for the energy density of photons of frequency  $\nu$  in thermal equilibrium at a temperature  $T$  with the resonant transition of a medium. Thus, Eq. (1.7) should be consistent with the Planck's radiation formula, which is given by

$$\rho(v) dv = \left( \frac{8\pi h v^3}{c^3} \right) \frac{dv}{[\exp(\frac{hv}{kT}) - 1]} \quad (1.8)$$

A comparison of Eq. (1.7) with Eq. (1.8) leads to the following two relations:

$$B_{12} = B_{21} \quad (1.9)$$

and

$$\frac{A_{21}}{B_{21}} = \frac{8\pi h v^3}{c^3} \quad (1.10)$$

The preceding analysis, based on the analysis first carried out by Einstein in 1917 [12], not only confirms that stimulated emission occurs but also shows that the a priori probability for an atom in the excited state to get de-excited by stimulated emission of a photon is exactly equal to the probability for the atom to reach the excited state by the stimulated absorption of a photon. The constants  $A_{21}$ ,  $B_{12}$ , and  $B_{21}$  are referred to as the Einstein  $A$  and  $B$  coefficients, and the relations (1.9) and (1.10) are known as Einstein relations, which provide a connection among absorption, spontaneous emission, and stimulated emission. Using Eqs. (1.8) and (1.10), the ratio of the photons emitted by spontaneous and stimulated emissions in thermal equilibrium at temperature  $T$  can be written as

$$R = \frac{A_{21}}{B_{21}\rho(v)} = \left[ \exp\left(\frac{hv}{kT}\right) - 1 \right] \quad (1.11)$$

Thus, for  $v \ll kT/h$ , the number of photons emitted by stimulated emissions far exceeds the number by spontaneous emissions, while for  $v > kT/h$ , the number of photons emitted by spontaneous emissions far exceeds the number by stimulated emissions. At room temperature ( $T = 300$  K), in the microwave region ( $v \sim 10^{10}$  Hz),  $R \approx 1.6 \times 10^{-3}$ , and thus the stimulated emission dominates over spontaneous emission. However, for normal optical sources ( $v \sim 6 \times 10^{14}$  Hz) operating at temperature ( $T \sim 1,000$  K),  $R \approx 3.2 \times 10^{12}$ , and consequently, the emission in optical region is predominantly by spontaneous emission. This is the reason why from conventional sources of electromagnetic radiation, while the interference effects that are characteristic of coherent source can be seen at longer wavelengths, these are not seen at visible wavelengths. The dominance of spontaneous emission at shorter wavelengths also explains why it is difficult to have lasers at higher frequencies.

So far we have been considering discrete energy levels. However, due to the finite lifetime of excited states, the energy levels have certain width, and consequently the emission as well as absorption takes place over a range of frequencies  $dv$ . The distribution of emitted or absorbed intensity versus frequency is referred to as the line shape function  $g(v)$ , which is normalized according to the relation

$$\int_0^\infty g(v) dv = 1 \quad (1.12)$$

Consequently,  $g(v)dv$  gives a priori probability of emission (or absorption) of a photon due to transition from energy state  $E_2$  to energy state  $E_1$ .

Consider a beam of light traversing along  $z$  axis through an atomic system having energy levels resonant with its frequency. The change in intensity  $I_v$  of the beam during its propagation through a section lying between  $z$  and  $(z + dz)$  is given by [13]

$$dI_v(z) = -(hv) [N_1 B_{12} - N_2 B_{21}] \cdot \left( \frac{I_v(z)}{c} \right) g(v) dz \quad (1.13)$$

where all symbols have the usual meaning. From Eq. (1.13), it follows that

$$I_v(z) = I_v(0) \exp [\gamma_v z] \quad (1.14)$$

where

$$\gamma_v = B_{21} \left( N_2 - \frac{g_2}{g_1} N_1 \right) \left( \frac{hv}{c} \right) g(v) \quad (1.15)$$

Here  $g_i$  is the degeneracy of the  $i$ th level, and use has been made of the fact that  $g_1 B_{12} = g_2 B_{21}$ . For amplification  $\gamma_v$  should be positive, which requires

$$\left( N_2 - \frac{g_2}{g_1} N_1 \right) > 0 \quad (1.16)$$

The gain coefficient,  $\gamma_v$ , can be written as the product of the stimulated emission cross section,  $\sigma_{SE}(v)$ , and the population inversion density, ( $\Delta N$ ):

$$\gamma_v = \Delta N \cdot \sigma_{SE}(v) \quad (1.17)$$

The stimulated emission cross section,  $\sigma_{SE}(v)$ , is given by

$$\sigma_{SE}(v) = \left( \frac{\lambda^2}{8\pi} \right) A_{21} g(v) \quad (1.18)$$

$$= \left[ \frac{\lambda^2}{8\pi \tau_{sp}} \right] g(v) \quad (1.19)$$

### 1.3 Bandwidth of Transition

All processes like emission of radiation or atom-atom interactions, which lead to energy or phase relaxation of the oscillating dipole, limit the lifetime of the dipole and hence contribute to the width of the transition. The transition can also be broadened by processes like Doppler effect, which cause a shift in the frequency response of atoms. The line broadening mechanisms can be classified in two

types, namely, homogeneous and inhomogeneous. A line is called homogeneously broadened if the probability distribution of absorption or emission with frequency is identical for all the atoms or molecules. Examples of homogeneous broadening are natural line broadening, pressure (or collision) broadening, crystal field broadening, etc. On the other hand, if the broadening mechanism acts to shift central frequency of the response of individual atoms or molecules by different amount thereby leading to a broadened response, it is called inhomogeneous line broadening. Here the probability distribution for absorption or emission as function of frequency will not be the same for all the atoms or molecules. Examples of inhomogeneous line broadening mechanisms are Doppler broadening, broadening due to crystal imperfections and strains.

As an example, for gas lasers, the transition may be inhomogeneously broadened (Doppler broadened) at low pressures and homogeneously broadened at high pressure since collisional broadening increases linearly with pressure. The bandwidth of transition will therefore be independent of pressure at low pressures where Doppler broadening dominates but will become directly proportional to pressure in the pressure-broadened regime. Therefore, given that  $g(v)$  is inversely proportional to  $dv$ , the width of the transition, the gain (which is proportional to  $g(v) * \Delta N$ ) will increase linearly with pressure at low pressures and become independent of pressure at higher pressures as can be seen in Fig. 1.3. As an example, let us consider CO<sub>2</sub> gas. The  $\tau_{sp}$  for 10 μm transition is 3s leading to very small natural line broadening of ~50 mHz. The collisional broadening parameter is about 6 MHz per torr, and Doppler broadening at 300 K is about 60 MHz. The gain would therefore become independent of pressure ( $p$ ) for  $p \gg 10$  Torr.

It is pertinent to note here that the probability of spontaneous emission for a transition determines its minimum possible linewidth. This linewidth, called natural

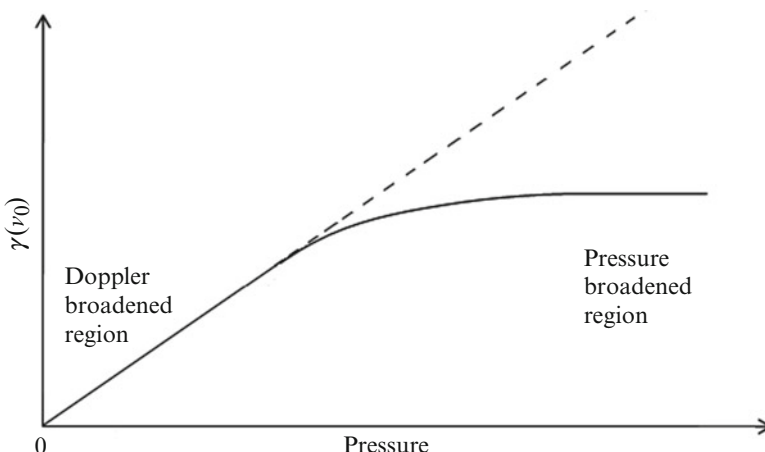


**Fig. 1.3** Typical dependence of gain for a gas laser transition on the operating pressure (Adapted from Gupta [14], p. 8)

linewidth, equals  $1/(2\pi\tau_{sp})$ . Using this fact one can see from Eq. (1.17) that the maximum possible gain on a transition equals  $\Delta N \cdot \lambda^2/2\pi$ . Thus, for a given population inversion, gain is higher for longer wavelength, and the cross section for stimulated emission  $\sigma_{SE}$  is always smaller than  $\lambda^2/2$ .

In the preceding treatment for interaction of radiation with an inverted resonant medium, we had tacitly assumed that propagating beams do not influence the population distribution in the medium. However, each stimulated emission reduces the population inversion,  $\Delta N$ , by two. Therefore, when the number of photons becomes of the same order as  $\Delta N$ , gain will reduce with increasing radiation intensity. This is the effect that determines the steady-state value of the intensity of laser radiation inside the laser oscillator. In steady state, the laser oscillates with an intracavity radiation intensity for which the radiation-induced loss of  $\Delta N$  is balanced by the rate of creation of  $\Delta N$  by the pumping mechanism.

## 1.4 Methods for Achieving Population Inversion

For achieving population inversion in different gain medium, a variety of methods are used. While optical excitation with incoherent (flashlamps) or coherent (another laser) optical sources is a generally applicable method, the other methods used include: excitation via collision with electrons using a gaseous discharge or an energetic electron beam (discussed in Chap. 3); use of chemical reactions, which leave the molecule in a excited state; and injection of current as in semiconductor diode lasers, discussed in Chap. 5.

For achieving population inversion, the rate of excitation to the upper laser level should significantly exceed the rate of decay of population from this level by all radiative and non-radiative decay processes. Gain medium in solid or liquid state has broad and strong absorption bands which can be effectively pumped by flashlamps that emit over a broad spectrum. However, for gas lasers at typical operating pressures of a few torr to tens of torr, the absorption features are characterized by a very narrow bandwidth and a much reduced absorption coefficient. Therefore, optical pumping of gases requires much higher spectral intensities, which are normally available only with lasers. Although most of the gas lasers utilize conventional electric discharge excitation, optical pumping offers the advantages of selective excitation, simple nature of pumping, and the ability to pump complex polyatomic molecules, which are too fragile to be pumped in an electrical discharge. It is also pertinent to note here that with electrical discharge excitation (or chemical excitation), one can deposit large amounts of energy and the technique can be scaled to large volumes. Thus, in situations where favorable excitation pathways exist, these techniques, in general, lead to much higher outputs. In contrast, the scalability of an optically pumped laser is constrained by the pump laser. Similar considerations also hold good for optically pumped solid and liquid lasers. Whereas optical pumping by flashlamps can provide scalability to much higher laser output, the use of lasers for optical pumping of these offers several important advantages. For example, laser diodes tuned to the absorption features of Nd:YAG result in a more

efficient excitation, and this not only improves efficiency but by reducing the heat load on the active medium also reduces the problem of the thermal lensing. These aspects are discussed in detail in Chap. 4.

## 1.5 Optical Resonator: Axial and Transverse Modes

An optical resonator consists of a pair of mirrors, aligned such that the optical radiation within the resonator makes repeated passes through the gain medium and get amplified till steady-state oscillations ensue. The simplest optical resonator comprises of two plane mirrors separated by an optical path length  $d = \sum l_i \mu_i$ , where  $l_i$  is the physical path length of the different components inside the resonator and  $\mu_i$  is the corresponding index of refraction.

For a radiation of wavelength  $\lambda$  to be contained in the resonator, i.e., be a mode of the resonator, at any arbitrary point in the resonator, the propagating beam should arrive in phase after successive round trips. This requires

$$2d = q\lambda \quad \text{or} \quad v_q = q \left( \frac{c}{2d} \right) \quad (1.20)$$

where  $q$  is an integer; thus, the resonator can support discrete frequencies  $v_q$  spaced  $\frac{c}{2d}$  apart, which are referred to as axial modes of the resonator.

The resonator is characterized by the quality factor or  $Q$  of the cavity which is defined as

$$\begin{aligned} Q &= \frac{2\pi \times \text{Energy stored in a mode}}{\text{Energy dissipated per cycle}} \\ &= 2\pi\nu \left[ \frac{\varepsilon}{-(d\varepsilon/dt)} \right] \end{aligned} \quad (1.21)$$

where  $\varepsilon$  is the energy stored in the mode. For a passive cavity (i.e., cavity without gain medium), if the fractional loss per round trip is  $L$ , then for a resonator of optical path length  $d$ , the fractional loss per unit time would be  $(\frac{cL}{2d})$ , and therefore

$$\frac{d\varepsilon}{dt} = -\varepsilon \left( \frac{cL}{2d} \right) = -\frac{\varepsilon}{t_c} \quad (1.22)$$

A comparison of Eqs. (1.21) and (1.22) gives

$$t_c = \left( \frac{2d}{cL} \right) \quad (1.23)$$

The linewidth of the cavity mode is given by

$$(\Delta\nu)_{\text{cavity}} = \frac{1}{2\pi t_c} = \frac{cL}{4\pi d} \quad (1.24)$$

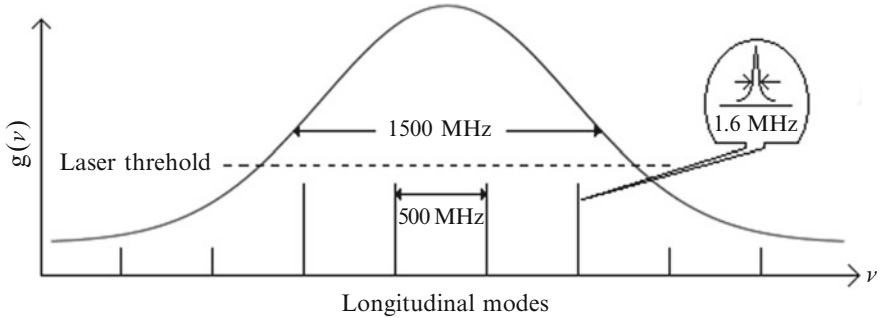


**Fig. 1.4** A schematic for the line shape function, longitudinal modes, and the passive width of the mode

This is related to cavity  $Q$  by the following expression:

$$Q = \frac{v}{(\Delta\nu)_{\text{cavity}}} \quad (1.25)$$

For a He-Ne laser with a plane-parallel resonator,  $\lambda = 632.8$  nm,  $d = 30$  cm, and  $L = 2\%$ ; thus,  $(\Delta\nu)_{\text{cavity}} = 1.6$  MHz and  $\Delta\nu_q = 500$  MHz. To put things in perspective, the Doppler-broadened line shape profile of the He-Ne laser transition, the mode spectrum, and the passive width of the cavity modes are shown in Fig. 1.4.

When steady-state oscillations are achieved at a mode,  $t_c \rightarrow \infty$ , and the linewidth of the cavity mode should become a  $\delta$  function. However, the modes retain the finite width due to the presence of spontaneous emission which is not in phase with the radiation generated by stimulated emission.

So far we have considered plane waves of infinite extent, which can be represented by a ray. Because of diffraction, beams of finite size will have curved wavefronts. The electric field associated with these will have a transverse field distribution. Only those field distributions which repeat themselves after a round trip can be a mode of the resonator. These are referred to as transverse modes, and for a typical laser resonator, these are described by [1–5]

$$\begin{aligned} E_{mn}(x, y, z) = & \left[ E_0 \frac{w_0}{w(z)} H_m \left( \frac{\sqrt{2}x}{w(z)} \right) H_n \left( \frac{\sqrt{2}y}{w(z)} \right) \times \exp \left( -\frac{(x^2 + y^2)}{w^2(z)} \right) \right] \\ & \times \left[ \exp \left( -ikz - [1 + m + n] \tan^{-1} \left( \frac{z}{z_0} \right) \right) \right] \\ & \times \left[ \exp \left( -i \frac{kr^2}{2R(z)} \right) \right] \end{aligned} \quad (1.26)$$

where

$$w^2(z) = w_0^2 \left( 1 + \frac{z^2}{z_0^2} \right) \quad (1.27)$$

$$R(z) = z \left( 1 + \frac{z_0^2}{z^2} \right) \quad (1.28)$$

$$z_0 = \frac{\pi w_0^2}{\lambda} \quad (1.29)$$

Here  $H_m(u)$  is the Hermite polynomial of order  $m$  and argument  $u$ , and it is defined by

$$H_m(u) = (-1)^m \exp(u^2) \frac{d^m}{du^m} \exp(-u^2) \quad (1.30)$$

The values for  $H_0(u)$  and  $H_1(u)$  are 1 and  $2u$ , respectively. The minimum spot size  $w_0$  and its position ( $z = 0$ ) completely characterize the beam. The first factor on the right-hand side of Eq. (1.26) describes the distribution of the field in the transverse plane and how it changes as the beam propagates along  $z$  axis. It should be noted that all the transverse modes are tightly bound to the  $z$  axis because for large values for  $x$  and  $y$ , the term  $\exp(-(x^2 + y^2)/w^2(z))$  dominates. However, for small  $x$  and  $y$ , the field is modified considerably by the polynomials being forced to zero at a finite number of points. The number of zeroes encountered, when the beam is scanned along  $x$  or  $y$  axis, represents the mode numbers  $m$  and  $n$ , respectively. Figure 1.5 shows the variation of the field for some values of  $m$  and  $n$ , and Fig. 1.5 shows the corresponding intensity pattern.

It should be noted that  $w(z)$ , referred to as the “spot size,” is the same for all the transverse modes. The quantity  $w(z)$  is a scale length for measuring the variation of field in the transverse direction. All  $\text{TEM}_{mn}$  modes have the same scale length, but the higher-order modes use a larger transverse area. A consequence of this is that all transverse modes have the same divergence (or far-field angle) and for a given physical extent of the beam, the lowest transverse mode ( $\text{TEM}_{00}$ ) has the least divergence. The  $\text{TEM}_{00}$  mode, called the fundamental mode, has Gaussian intensity profile given by

$$I = I_0 \exp \left( -\frac{2(x^2 + y^2)}{[w(z)]^2} \right) \quad (1.31)$$

where  $I_0$  is the maximum intensity and  $w(z)$  is referred to as the beam radius or the beam waist. It is the radial distance at which the intensity drops to  $1/e^2$  of its value along the axis. As the beam propagates along  $z$ , the spot size becomes larger; hence, the  $1/e^2$  points become farther from the axis. In Fig. 1.6,  $w(z)$  for the  $\text{TEM}_{00}$  beam is sketched as a function of the  $z$  coordinate. The distance  $z = z_0$ , where the beam expands from its minimum value of  $w_0$  by a factor of  $2^{1/2}$  (or the area doubles),

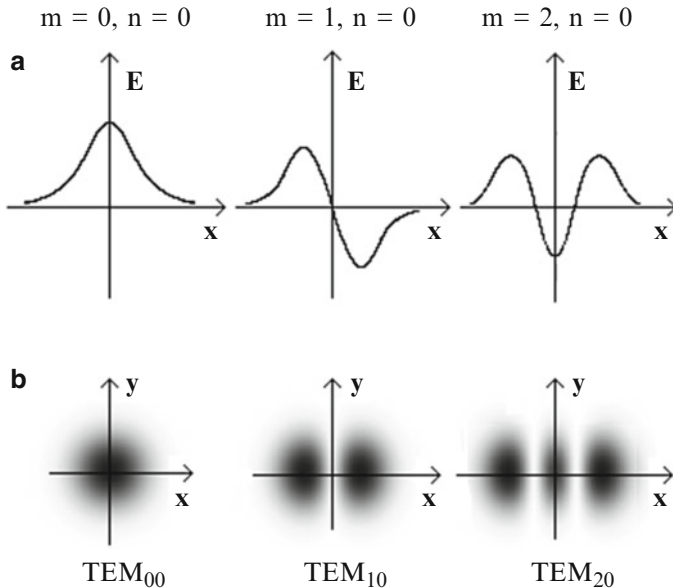


**Fig. 1.5** (a) Variation of the field of some transverse modes and (b) corresponding intensity patterns

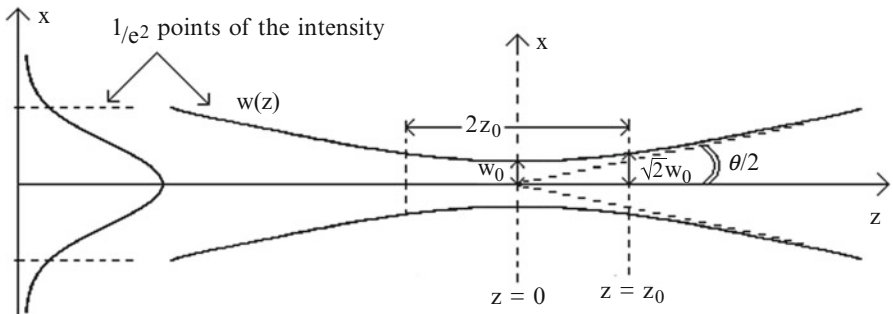


**Fig. 1.6** The locus of points in the  $Zx$  plane where the intensity of the  $\text{TEM}_{00}$  beam falls to  $1/e^2$  of its intensity on the axis. The angle made by a tangent to the hyperbola with the axis is the half angle of divergence

is referred to as the *Rayleigh range*. The term  $2z_0$  is also referred to as *confocal parameter*. For large  $z$ , the spot size is asymptotic to the dashed lines described by

$$w(z \gg z_0) = w_0 \frac{z}{z_0} \quad (1.32)$$

Thus, the beam divergence is given by

$$\theta = 2 \frac{dw}{dz} = \frac{2\lambda}{\pi w_0} \quad (1.33)$$

The second factor on the right-hand side of Eq. (1.26), the longitudinal phase factor, determines the change in phase of the field as it propagates along  $z$  direction. For a radiation of wavelength  $\lambda$  to be a mode of the resonator, the round trip phase change should be an integral multiple of  $2\pi$ , and this condition leads to the following expression for the resonant frequencies:

$$\nu_{m,n,q} = \left( \frac{c}{2d} \right) \left[ q + \frac{(1+m+n)}{\pi} \left( \tan^{-1} \left( \frac{z_2}{z_0} \right) - \tan^{-1} \left( \frac{z_1}{z_0} \right) \right) \right] \quad (1.34)$$

It follows from (1.34) that

$$\delta\nu_q = \left( \frac{c}{2d} \right) \quad (1.35)$$

Further the frequencies depend on the sum  $(m+n)$  and not on  $m$  and  $n$  separately. The difference in frequency of modes with the same value of  $q$  but different  $(m+n)$  values is given by

$$\delta\nu_{m,n} = \left( \frac{c}{2\pi d} \right) \Delta [m+n] \cdot \left( \tan^{-1} \left( \frac{z_2}{z_0} \right) - \tan^{-1} \left( \frac{z_1}{z_0} \right) \right) \quad (1.36)$$

This factor results in difference in frequency for the transverse modes. The third factor, the radial phase factor, shows that for positive  $R(z)$ , as one moves away from the axis, local field lags from that at  $r=0$ , i.e., the wavefront (the equiphase surfaces) is curved. It can be shown that the equiphase surfaces are spherical with a curvature  $R(z)$ , which is the same for all the modes.

### 1.5.1 Stable Resonators

Let us consider a resonator formed by two mirrors  $M_1$  and  $M_2$  having radii of curvature  $R_1$  and  $R_2$  and placed a distance  $d$  apart at  $z=-z_1$  and  $z=+z_2$ , respectively. The resonator will support a propagating beam whose wavefront has the same curvature as that of the mirrors at  $z=-z_1$  and  $z=+z_2$  (Fig. 1.7). From these considerations, one can derive the parameter  $z_0$ , for the propagating beam supported by the resonator as

$$z_0^2 = \frac{d(R_1-d)(R_2-d)(R_1+R_2-d)}{(R_1+R_2-2d)^2} \quad (1.37)$$

The minimum spot size  $w_0$  is given by

$$w_0^2 = \frac{2z_0}{k} = \frac{2}{k} \times \left[ \frac{d(R_1-d)(R_2-d)(R_1+R_2-d)}{(R_1+R_2-2d)^2} \right]^{\frac{1}{2}} \quad (1.38)$$

**Fig. 1.7** A spherical mirror resonator

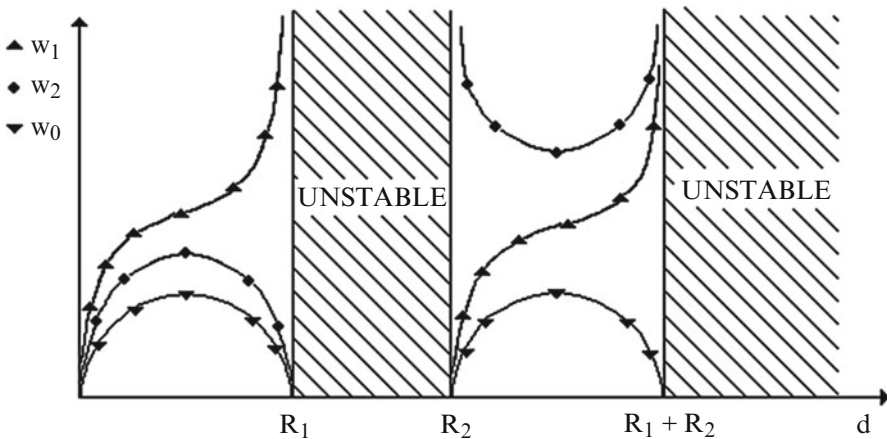
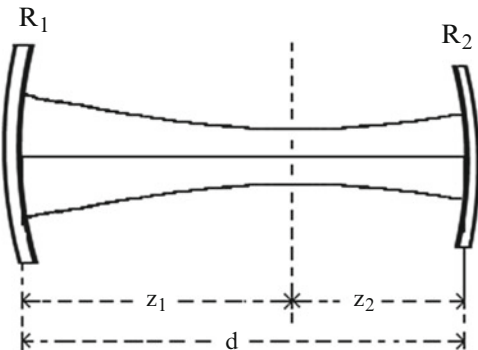


**Fig. 1.8** A schematic diagram for the variation of minimum spot size  $w_0$  and the mirror spot diameters  $w_1$  and  $w_2$  as function of resonator length  $d$  for a given radius of curvature of mirrors

The spot sizes at the two mirrors are given by

$$w_1^2 = \frac{2}{k} \times \frac{R_1[d(R_2-d)]^{\frac{1}{2}}}{[(R_1-d)(R_1+R_2-d)]^{\frac{1}{2}}} \quad (1.39)$$

$$w_2^2 = \frac{2}{k} \times \frac{R_2[d(R_1-d)]^{\frac{1}{2}}}{[(R_2-d)(R_1+R_2-d)]^{\frac{1}{2}}} \quad (1.40)$$

From Eq. (1.37), it is clear that for  $d < R_1 < R_2$  or  $(R_1 + R_2) > d > R_2$ ,  $z_0$  is real. For  $R_2 > d > R_1$  or  $d > (R_1 + R_2)$ ,  $z_0$  becomes imaginary and no stable field configuration is possible. The variation of  $w_0$ ,  $w_1$ , and  $w_2$  as a function of  $d$  is shown in Fig. 1.8. At the boundaries of stability,  $w_0$  becomes zero leading to very high divergence and infinite spot size on mirrors.

The two conditions for stable resonator can be combined to give

$$0 \leq \left[1 - \frac{d}{R_1}\right] \left[1 - \frac{d}{R_2}\right] \leq 1 \quad (1.41)$$

or

$$0 \leq g_1 g_2 \leq 1 \quad (1.42)$$

where  $g_1 = \left(1 - \frac{d}{R_1}\right)$  and  $g_2 = \left(1 - \frac{d}{R_2}\right)$ .

In order to appreciate some basic facts of stable resonators, let us consider a symmetric resonator, i.e.,  $R_1 = R_2 = R$ . From (1.37) to (1.40), we get beam parameters of this resonator as

$$z_0^2 = \frac{d (2R - d)}{4} \quad (1.43)$$

The minimum spot size  $w_0$  is given by

$$w_0^2 = \frac{[d (2R - d)]^{\frac{1}{2}}}{k} \quad (1.44)$$

The spot sizes at the two mirrors are given by

$$w^2 = w_1^2 = w_2^2 = \frac{2R}{k} \left[ \frac{d}{(2R - d)} \right]^{\frac{1}{2}} \quad (1.45)$$

From Eqs. (1.44) and (1.45), one can see that  $w_0^2$  and  $w^2$  increase with an increase in  $R$ . However, it is important to realize that even small curvatures (large values for  $R$ ) lead to narrow beams. As an example, for  $\lambda = 600$  nm,  $d = 1$  m, and  $R = 10$  m, one gets  $w \approx 0.07$  mm, and to increase  $w$  to 2 mm, one needs  $R = 876$  m. It is also pertinent to note that for  $R \gg d$ ,  $w^2 \approx \frac{1}{k}(2Rd)^{\frac{1}{2}} \approx w_0^2$ , the beam spread is very small inside the resonator. These considerations have to be taken into account to ensure that the resonator mode has good overlap with the volume of the active medium. If the resonator mode occupies a smaller volume of the active medium, the energy extraction will be poor, and if it spills over the active medium, the truncation of the beam by the aperture of the active medium will result in increased losses. While in solid state lasers, the active medium is usually in the form of rods with diameter of a few mm, in gas lasers the diameter of the active medium can be a few cm. Stable resonators may therefore not result in efficient energy extraction from large aperture active medium. For large gain lasers, where large diffraction losses can be tolerated, one can therefore use unstable resonators which provide an advantage of large mode volume.

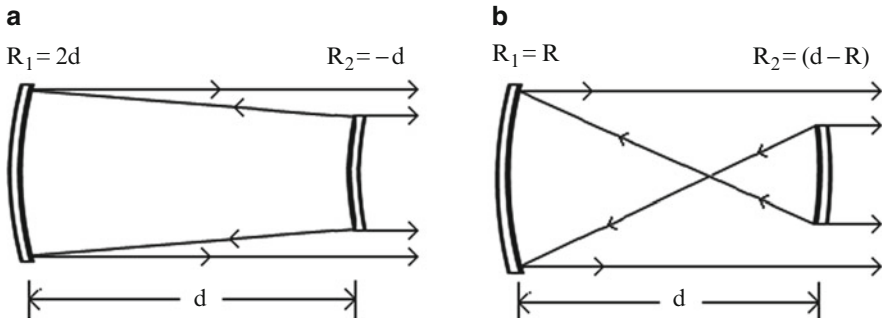


**Fig. 1.9** (a) Positive- and (b) negative-branch confocal unstable resonators

### 1.5.2 Unstable Resonators

In unstable resonators, the output coupling is through diffraction losses at the mirrors. Some examples of unstable resonators are shown in Fig. 1.9. These resonators are classified as positive-branch unstable resonators or negative-branch unstable resonators depending upon whether  $g_1 g_2 > 1$  or  $g_1 g_2 < 1$ . The most useful form of an unstable resonator is the confocal unstable resonator ( $R_1 + R_2 = 2d$ ). The advantage of this configuration is that it produces a collimated output beam.

The drawback of negative branch of unstable resonator is that it has an internal focal point which because of the resulting large focal intensity may lead to optical breakdown. The near-field pattern of the output of a confocal unstable resonator is of annular shape with an inner hole whose diameter is the same as that of the output coupler. But the far-field pattern, where the diffraction fills the central region, closely resembles that from a Gaussian beam.

## 1.6 Laser Oscillations

When active medium is pumped to have population inversion, the laser oscillations will build up from spontaneous emission that is always present when atoms are in excited state. It should be noted that an increase in the photon density on the cavity modes will cause a simultaneous reduction in the population inversion. This interplay between photon density ( $q$ ) and the population inversion ( $\Delta N$ ) [14] can be understood by referring to Fig. 1.10. Before population inversion is achieved, there is no net gain and the photon density at the cavity modes will only be because of spontaneous emission that travels at right angles to mirror surfaces and has frequency matching with the cavity modes. When the rate of pumping ( $R$ ) exceeds that required to achieve population inversion ( $R_t$ ), the population inversion  $\Delta N$  will increase with  $t$ . When  $\Delta N$  exceeds the threshold inversion ( $\Delta N_t$ ) that is required

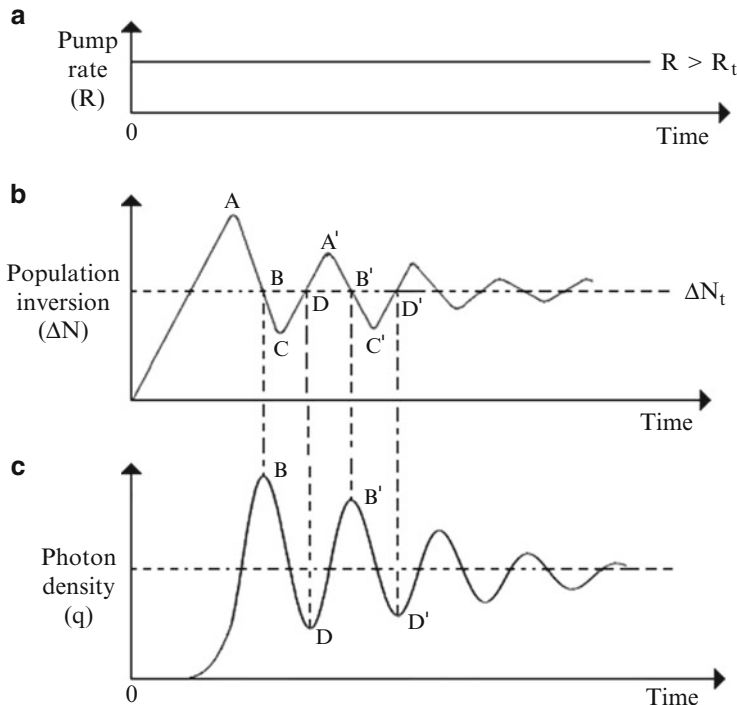


**Fig. 1.10** A schematic representation of pump rate (a) along with interplay between the population inversion (b) and photon density (c)

to ensure that the round trip gain in the active medium exceeds the losses in the resonator, the photon flux will start building up. The buildup of photon flux will result in a reduction of  $\Delta N$ , and the maximum value of the photon flux will be reached when  $\Delta N$  crosses  $\Delta N_t$ . Beyond this point, the photon flux will reduce, and the pumping will again take over causing population inversion to increase. However, since now some photon flux is already present in the cavity, for the same level of pumping, a lower maximum in population inversion is reached. Consequently, the photon density again starts building up but to a lower peak value where  $\Delta N$  again drops to  $\Delta N_t$ . This way both  $\Delta N$  and  $q$  will execute damped oscillations and slowly reach steady-state values if pumping is continued. This corresponds to continuous wave (CW) operation of a laser.

With a pulsed excitation source, the interplay between population inversion and photon density leads to relaxation oscillations with energy distributed over a number of pulses spanning the duration of the pump pulse. However, for several applications, it is desirable that all the energy is obtained in a single pulse. This can be obtained using an ingenious technique, referred to as *Q*-switching that is discussed later.

As noted above, threshold for oscillation requires that the round trip gain in the active medium of length  $\ell$  exceeds the losses in the resonator. The losses in the resonator are mainly due to diffraction loss at the mirrors or the apertures of other intracavity components, scattering losses, absorption at the mirrors, and the output coupling. If we assume that the reflectivities of the resonator mirrors are  $R_1$  and  $R_2$  and that the intensity loss factor per pass due to the distributed losses in the resonator is  $\exp(-\alpha d)$ , then the *condition for laser oscillation* becomes

$$R_1 R_2 \exp[2[\gamma(\nu) \ell - \alpha d]] \geq 1 \quad (1.46)$$

$$\gamma(\nu) \geq \frac{1}{2\ell} \ln \left( \frac{1}{R'_1 R_2} \right) \quad (1.47)$$

where  $R'_1 = R_1 \exp(-2\alpha d)$ , i.e., the distributed losses are absorbed in one of the mirror's reflectivity.

For homogeneously broadened transition,

$$\gamma(\nu) = \gamma(\nu_0) \frac{\left(\frac{\Delta\nu_h}{2}\right)^2}{[(\nu - \nu_0)^2 + \left(\frac{\Delta\nu_h}{2}\right)^2]} \quad (1.48)$$

Therefore, if the peak gain  $\gamma(\nu_0)$  is  $N$  times more than that required for threshold, then the gain will exceed loss over a frequency interval

$$2|\nu - \nu_0| \leq (N-1)^{\frac{1}{2}} \Delta\nu_h \quad (1.49)$$

For  $\Delta\nu_h = 1.5$  GHz,  $N = 5$ , the gain would exceed over a bandwidth of 3 GHz. Since the axial mode separation for  $d = 30$  cm is only 500 MHz, thus, a large number of axial modes will fall in the gain bandwidth and will experience a net gain. In steady state, will all these modes oscillate? To answer this question, let us note that the fraction of spontaneously emitted photons in the different cavity modes as well as the gain at these modes is not the same. Both are maximum for the mode which lies nearest to center frequency of  $\gamma(\nu)$  and decreases as one moves away from the line center. Thus, the mode, closest to the center frequency  $\nu_0$  of  $\gamma(\nu)$ , builds up faster than other modes.

In homogeneously broadened systems, all the atoms have the same line shape function and therefore contribute in an identical manner to the growth of all the modes. Therefore, there is a strong competition between the growing modes because if an atom gives up its energy to a field corresponding to one cavity mode, it can no longer contribute to the gain at other modes. Further, as the radiation field at the different modes builds up, the gain will reduce and in steady state the laser gain has to saturate at loss level at the frequency of oscillation. This implies that if the losses at different modes are the same, then in steady state, only the mode closest to the line center would oscillate and because for this mode gain equals loss, for all other modes, there will be a net loss (Fig. 1.11).

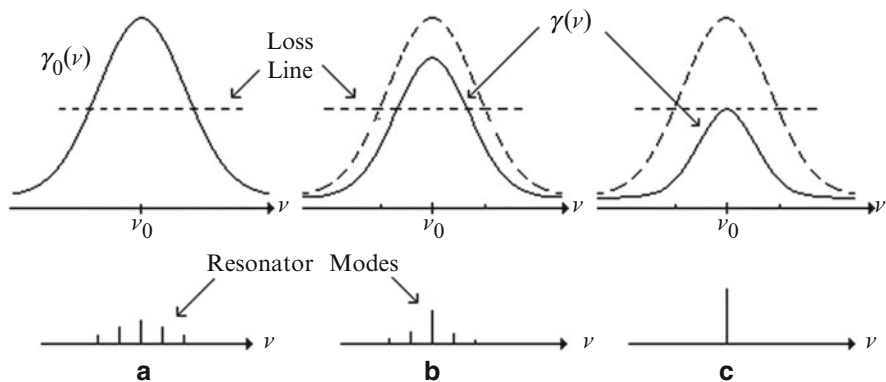


**Fig. 1.11** Growth of single mode in a homogeneously broadened medium. (a) Initially all modes, for whom gain is more than loss, begin to grow. (b) As gain saturates, the central mode grows with attenuation of side modes. (c) Finally only a single mode survives

It is pertinent to note that just as the mode with the highest gain dominates, so does the frequency corresponding to the peak of resonance will see higher gain and the bandwidth of the oscillating mode will get narrowed. This is referred to as gain narrowing.

Although from the above discussion, it follows that for a homogeneously broadened transition, the laser should always operate on a single mode that is closest to the line center frequency, this is not true because of an interesting effect. In a laser resonator, standing waves are formed at the axial mode frequencies. Therefore, the spatial distribution of the laser intensity in the resonator is not uniform. The intensity is high at antinodes and small at nodes (not zero due to losses at the resonator mirrors). As a result population inversion is depleted more at the antinodes than at nodes leading to burning of holes in the population inversion at the antinodes positions. The existence of this population inversion grating, referred to as spatial hole burning, relaxes the competition between modes. Other modes for which the antinodes fall over the nodes of the oscillating mode can also see large gain and hence oscillate resulting in multiaxial mode oscillation. A simple approach to avoid spatial hole burning and thus ensure single mode operation is the use of a ring resonator where the radiation can travel only in one direction.

For inhomogeneously broadened transition, because the frequency responses of atoms are different, different modes can interact with different group of atoms leading to multimode output.

The above discussion also tells us that if we increase the loss for modes close to the line center by putting a frequency selective element like an etalon or grating in the resonator, we can engineer higher net gain at modes away from line center. This way one can force the laser to operate away from the line center. While for inhomogeneously broadened transition, only a fraction of the inverted population will be able to contribute to the selected mode leading to poor tuning efficiency, for homogeneously broadened transition, all the inverted atoms can contribute

leading to efficient tuning. However, even for homogeneously broadened transition, a necessary consequence of tuning away from the line center will be a reduced gain and consequently reduced output power.

## 1.7 Threshold Pump Power

From the oscillation threshold condition, Eq. (1.46), we get using Eq. (1.15) the following expression for the threshold population inversion:

$$\Delta N_t = \frac{8\pi\nu^3\tau_{sp}}{g(\nu)c^3t_c} \quad (1.50)$$

where

$$t_c^{-1} = [1 - R_1 R_2 \exp(-2\alpha d)] \cdot \left(\frac{c}{2d}\right) \approx c \left[ \alpha - \left(\frac{1}{2d}\right) \cdot \ln R_1 R_2 \right] \quad (1.51)$$

For a three-level system, assuming  $g_1 = g_2$ , the optical gain  $\gamma = 0$  at a pumping level strong enough to create a population in the upper laser level,  $N_2 = N_1 = N_0/2$ . To satisfy the oscillation condition, the pumping rate has to be further increased until  $(N_2 - N_1) = \Delta N_t$ .

In contrast, for an ideal four-level laser system, the thermal population in the lower laser level can be neglected. If in addition the lifetime for this level is short, buildup of its population by the laser action can also be neglected. Under these conditions, the threshold condition reduces to  $N_2 = \Delta N_t$ .

In most laser systems,  $N_0 \gg \Delta N_t$ . The threshold pump rate for the three- and four-level system is therefore

$$[P_t]_{3\text{-level}} = \frac{N_0 h \nu}{2 t_2} V \quad (1.52)$$

$$[P_t]_{4\text{-level}} = \frac{\Delta N_t h \nu}{t_2} V \quad (1.53)$$

where  $V$  is the volume of the active medium and  $t_2$  is the lifetime of the upper laser level.

One should note that the threshold pump rate for three-level system is determined by the requirement of pumping a very large number of atoms from the ground state to the upper laser level and will therefore not show a strong dependence on mirror reflectivities. However, for a four-level system, the threshold pump rate is determined primarily by the resonator losses and will therefore have a strong dependence on mirror reflectivities.

For level of pumping beyond threshold, the intracavity power will be determined by a balance between the rate of creation of population inversion and its annihilation

because of the radiation field. For an idealized four-level system under some simplifying assumptions, it can be shown that the total power generated by stimulated emission can be expressed as [1]

$$P_e = P_t \cdot \left( \frac{R}{R_t} - 1 \right) \quad (1.54)$$

where  $P_t$  is the minimum power required to maintain the threshold inversion. This equation shows that for each increment in pumping, measured relative to the threshold value, the power increases by  $P_t$ .

### 1.7.1 Optimum Output Coupling

In stable resonators, the useful laser output is taken through transmission from one of the mirrors. If  $T$  is the useful mirror transmission and  $L_i$  the residual loss, the total loss per pass  $L$  will be

$$L = T + L_i \quad (1.55)$$

The fraction of the total power in the resonator ( $P_e$ ) that is coupled out of the laser will therefore be  $T/(T + L_i)$ . It is desirable to make  $L_i$  as small as possible since it leads to an increase in the oscillation threshold without contributing to the power output. The choice of  $T$  is more subtle. Having very low  $T$  will increase  $P_e$ , but the useful laser power coupled out will be small. On the other hand, if  $T$  is too large, losses will exceed the gain and no lasing would be possible. Thus, an optimum  $T$  exists for a given level of pumping and internal residual losses. For a high  $Q$  cavity, the optimum value for  $T$  can be shown to be [15]

$$T_{\text{opt}} = -L_i + \sqrt{g_0 L_i} \quad (1.56)$$

where  $g_0 = \gamma_0 \ell$  is the unsaturated gain per pass. As expected for a given  $L_i$ , larger value for  $g_0$  will lead to higher value for optimum transmission coupling. For a discussion of more general situations (low  $Q$  cavity), the reader is referred to [16].

## 1.8 Pulsed Operation of Lasers

With a pulsed excitation source, the interplay between population inversion and photon density leads to relaxation oscillations with energy distributed over a number of pulses spanning the duration of the pump pulse. However, for several applications, it is desirable that all the energy is obtained in a single pulse. This can be obtained using an ingenious technique, referred to as  $Q$ -switching.

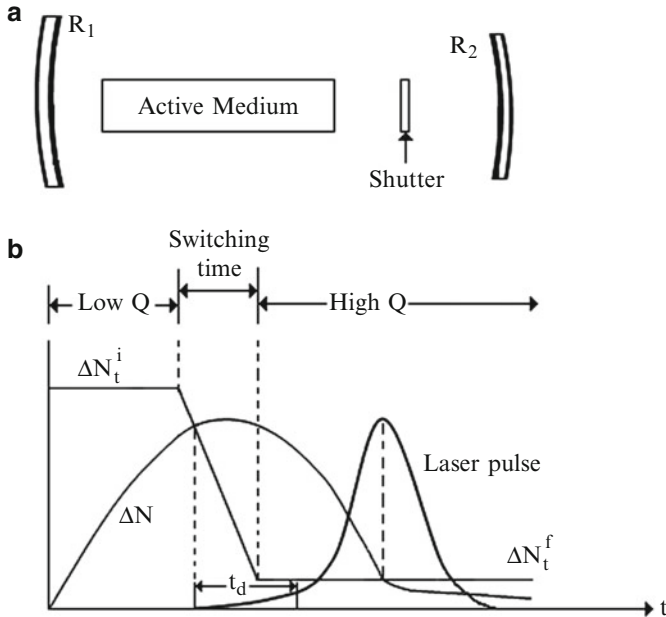


**Fig. 1.12** (a) Basic arrangement for  $Q$ -switching and (b) generation of  $Q$ -switched pulse

### 1.8.1 $Q$ -Switching

As the name suggests, the technique involves switching the  $Q$  of the cavity. First the  $Q$  of the cavity is spoiled by placing a shutter (Fig. 1.12a), so that the photon flux cannot build up and consequently the population inversion can be built to a large value. When the shutter is removed, there is a rapid buildup of oscillation because of a very large gain ( $\gamma_v \propto \Delta N$ ) and a simultaneous exhaustion of the inversion by stimulated emission. Thus, the technique allows extraction of all the stored energy in a single pulse in contrast to the relaxation oscillation associated with a constant  $Q$  cavity (Fig. 1.12b).

The switching time of the “ $Q$ -switch” should be faster than the pulse buildup time ( $t_d$ ). Otherwise the inversion falls faster than the loss and may fall below instantaneous values of threshold population inversion, which would result in multiple pulsing [14]. The falling edge of the pulse is characterized by the cavity decay time  $t_c$ . The techniques can therefore not generate pulses with duration shorter than the cavity decay time and generally lead to pulses of a few tens of ns to a few ns. For  $Q$ -switching it is desirable to have longer lifetime for the upper level as it helps storage of more population in that level. Thus, Ruby or Nd:YAG lasers with upper laser level's lifetimes of  $\sim 4$  ms and  $240\ \mu\text{s}$  are better suited for  $Q$ -switching as opposed to He-Ne or Ar-ion lasers with upper laser level's lifetimes of 100 ns and 10 ns, respectively.

### 1.8.2 Mode Locking

Pulses with duration limited by the oscillating bandwidth of the medium can be generated by the technique of mode locking. In this technique all the axial modes are locked in phase. If we assume that the amplitude of oscillating modes, spaced apart in frequency by  $\delta\nu = (c/2d)$ , is  $E_n$ , and their phases  $\phi_n$ , then the total electric field from such multimode oscillation at an arbitrary point in the resonator can be written as

$$E(t) = \sum_n E_n \exp [2\pi i \{(v_0 + n\delta\nu)t + \phi_n\}] \quad (1.57)$$

where summation is extended over the oscillating modes and  $v_0$  is chosen arbitrarily as a reference frequency. While in a typical laser,  $\phi_n$  are likely to vary randomly with time, in mode-locked laser, we lock the phases  $\phi_n$  so that these do not vary with time. If for simplicity we take the phase  $\phi_n$  to be zero and assume all modes have equal amplitude  $E_0$ , Eq. (1.57) can be shown to give [1–5]

$$E(t) = E_0 \exp (2\pi i v_0 t) \times \frac{\sin(\pi N\delta\nu t)}{\sin(\pi\delta\nu t)} \quad (1.58)$$

$$I(t) = I_0 \frac{\sin^2(\pi N\delta\nu t)}{\sin^2(\pi\delta\nu t)} \quad (1.59)$$

The peak intensity is  $N$  times the average intensity, where  $N$  is the number of modes locked together. The individual pulse width, defined as the time from the peak to the first zero, is given by

$$\tau_p = \frac{1}{N \cdot \delta\nu} \quad (1.60)$$

The duration of the mode-locked pulse is therefore approximately the inverse of the gain bandwidth. Thus, active media with larger gain bandwidths are required for the generation of shorter pulses by mode locking. As an example the gain bandwidth of the lasing transition in dyes is  $\sim 2 \cdot 10^{13}$  Hz. Therefore, the shortest pulse that can be generated is  $\sim 50$  fs.

### 1.8.3 Some Comments on the Generation of Ultrashort Laser Pulses

As discussed above using mode-locking technique, one can generate laser pulses of a few tens of fs limited by the gain bandwidth of the lasing transition. To generate still shorter duration pulses, one makes use of nonlinear optical effects like

self-phase modulation to increase the bandwidth of the pulse and then compress it in time domain to generate Fourier transform-limited pulses. One may also note at a given frequency  $\nu$ , it is not possible to generate laser pulse that has a duration of less than  $1/\nu$  (time for one cycle of oscillation at this frequency). Thus, at 500 nm ( $6 \times 10^{14}$  Hz), it is not possible to generate pulses having duration shorter than about 1.8 fs. Generation of still shorter duration pulses (attosecond) would require lasers operating at much shorter wavelengths, in X-ray region.

## 1.9 Single Frequency Laser

Lasers usually operate on a number of axial and transverse modes. Laser oscillation on a single mode can be achieved by ensuring that the losses for all the modes except the desired mode are higher than the available gain. Usually laser operation in the lowest transverse mode is desired and is achieved by placing a suitable aperture in the cavity that produces high aperture loss for the higher order transverse modes having larger spatial extent but negligible loss for the lowest transverse mode. Similarly operation on a single longitudinal mode (SLM) can be achieved by ensuring that the losses for all the axial modes except the desired one are so high that these cannot reach oscillation threshold.

### 1.9.1 Spectral Width of SLM Laser: Limiting Linewidth

As discussed earlier in Sect. 1.5, a laser oscillator, although gain equals loss for the oscillating mode, implying  $t_c = \infty$ , the oscillating modes have finite frequency width because of the random phase of the photons spontaneously emitted into the laser mode. This limiting linewidth is given by the Schawlow-Townes relation:

$$\Delta\nu_l = \frac{2\pi(\Delta\nu_c)^2 h\nu_l}{P_l} \quad (1.61)$$

where  $\nu_l$  is the laser frequency and  $P_l$  its output power. For a He-Ne laser ( $\nu_l = 4.74 \times 10^{14}$  Hz,  $P = 1$  mW,  $\Delta\nu_c = 0.5$  MHz), this gives  $\Delta\nu_l = 2 \times 10^{-3}$  Hz.

In practice the actual linewidth of the oscillating mode is considerably larger because any change in resonator optical path length  $d = \mu l$  (assuming the resonator to be completely filled by an active medium with index of refraction  $\mu$ ) will lead to a change in frequency of the oscillating mode:

$$\left| \frac{\delta\nu}{\nu} \right| = \left| \frac{\delta d}{d} \right| = \left| \frac{\delta l}{l} \right| + \left| \frac{\delta\mu}{\mu} \right| \quad (1.62)$$

Therefore, to have  $\delta\nu \sim 10^{-3}$  Hz,  $\delta d/d < 2 \times 10^{-18}$ ! i.e., the resonator length of  $d = 1$  m has to be kept constant to  $10^{-18}$  m! Therefore, in practice the laser linewidth is determined by the fluctuations in the resonator path length caused by mechanical vibrations, thermal fluctuations, and changes in refractive index of the active medium.

## 1.10 Conclusion

In this chapter, a very concise overview of the essential concepts of laser physics has been provided. This may help the reader to better assimilate the contents of the succeeding chapters. For more comprehensive discussion of Laser Physics and Technology, the reader is referred to the many excellent texts referred to in the chapter.

**Acknowledgments** The authors are thankful to Dr. K. S. Bindra, Dr. S. R. Mishra, and Dr. C. P. Paul for critical reading of the manuscript.

## References

1. A. Yariv, *Optical Electronics* (Holt, Saunders, Tokyo, 1985)
2. A. Yariv, *Quantum Electronics* (Wiley, New York, 1989)
3. J.T. Verdeyen, *Laser Electronics* (Prentice-Hall India Pvt. Ltd., New Delhi, 1993)
4. W.T. Silfvast, *Laser Fundamentals* (Foundation Books, New Delhi, 1998)
5. A.E. Siegman, *Lasers* (University Science, Mill Valley, 1986)
6. W. Koechner, *Solid State Laser Engineering* (Springer, Berlin, 2006)
7. K. Thyagarajan, A.K. Ghatak, *Lasers Theory and Applications* (Macmillan, New Delhi, 1981)
8. P.W. Milonni, J.H. Eberly, *Laser Physics* (Wiley, New Jersey, 2010)
9. O. Swelto, D.C. Hanna, *Principles of Lasers* (Plenum Press, New York, 1998)
10. A. Maitland, M.H. Dunn, *Laser Physics* (North-Holland Publishing Company, London, 1969)
11. A. Beiser, *Perspective of Modern Physics* (McGraw-Hill Kogakusha, Ltd, Tokyo, 1969), Chapter 16
12. A. Einstein, On the quantum theory of radiation. Phys. Z 18, 121–128 (1917)
13. See [3], Chapter 6
14. P.K. Gupta, Laser sources, in *Non-Linear Optics and Laser Spectroscopy*, ed. by S.C. Abbi, S.A. Ahmad (Narosa Publishing House, New Delhi, 2001)
15. See [1], Chapter 6
16. See [3], Chapter 9

# **Chapter 2**

## **Basics of Nonlinear Optics**

**Mukesh P. Joshi**

**Abstract** The fields of nonlinear optics (NLO) and laser physics and technology are intertwined. Research and development made in respective subject areas have benefited each other for their further advancement. The field of NLO therefore continues to be an active and rapidly developing research area. The aim of this chapter is to provide brief account of the basics of NLO with the description of some of the well-known NLO processes and phenomena. We consider classical treatment of light–matter interaction and restrict to dipolar polarization induced by the field in the material. We discuss various novel optical effects and phenomena due to induced second and third order nonlinear polarization in the medium. These novel effects include photon–photon interaction leading to exchange of energy among light beams and with medium excitations, generation of coherent light sources at new frequencies, modulation and control of light beam amplitude and phase, etc.

**Keywords** Anharmonic oscillator model • Nonlinear polarization and susceptibility • Sum and difference frequency generation • Nonlinear refraction and absorption • Stimulated Raman and Brillouin scattering

### **2.1 Introduction**

Nonlinear optics (NLO) involves the study of light–matter interaction incorporating nonlinear optical response of the material as a function of the optical field. The simplest response that can be considered is the dipolar polarization induced by the field in the material. As a consequence of induced nonlinear polarization in the medium and also the large field strengths available from lasers, one is able to observe novel optical effects and phenomena. These novel effects include photon–photon interaction leading to exchange of energy among light beams, generation of light at new frequencies, modulation and control of light beam properties, etc. As a result, several potential applications in the field of laser technology have emerged

---

M.P. Joshi (✉)

Laser Materials Processing Division, Raja Ramanna Centre for Advanced Technology (RRCAT),  
Laser R & D Block A, Indore 452013, India  
e-mail: [mukesh@rrcat.gov.in](mailto:mukesh@rrcat.gov.in)

out of systematic study of nonlinear optics such as frequency conversion of lasers, generation and characterization of ultrashort laser pulses, etc. Therefore, in the context of pursuing research in the areas of laser physics and technology, the field of nonlinear optics plays an important role and continues to be an active and rapidly developing research area.

The aim of this chapter is to provide brief account of topics covered in the series of lectures on NLO delivered at the Laser School. It covers basics of NLO with the description of some of the well-known NLO processes and phenomena that one often come across while pursuing research in the areas of laser physics and technology. Emphasis is on the physical understanding of various NLO processes and effects/applications rather than on detailed mathematical or analytical formulations. For details, one can refer to large number of books and review articles which cover various aspects of the subject of nonlinear optics [1–14].

## 2.2 The Nonlinear Polarization and Susceptibility

### 2.2.1 Nonlinear Polarization

The description of the interaction of light with a bulk medium can be considered within the framework of a dielectric material subjected to an electric field. When a beam of light is incident on the material, the material system is perturbed by the field associated with the beam of light. As a reaction to the external electric field, the charges in the material move so that the separation between the positive and negative charges is modified and the material gets polarized. The polarization of the material is the macroscopic manifestation of the electric dipoles induced at the microscopic level.

With the application of oscillating electric field associated with light beam, the induced polarization will follow the field and charges inside the material oscillate. As a consequence of the oscillating dipoles, light is emitted. In other words, the time-varying polarization of the material produces an electromagnetic radiation field. With thermal sources of light, i.e., bulbs, lamps, etc., the strength of oscillating electric field associated with light from these is much smaller than the atomic field in the material. The electrons of the material medium are therefore slightly perturbed from their equilibrium, and the restoring force is linear in the electronic displacement. Therefore, the restoring potential can be approximated by a harmonic potential. With linear restoring force, the system behaves like a classical forced simple harmonic oscillator, reaching a steady state where it oscillates with the same frequency as the incident beam and magnitude that is proportional to the applied electric field. Typically, the polarization of the medium ( $P$ ) defined as the electric dipole per unit volume is assumed to be directly proportional to the applied electric field ( $E$ ):

$$\vec{P} = \chi \vec{E} \quad (2.1)$$

with  $\chi$  being a constant of proportionality called the electric susceptibility of the material. The above description of linear dependence of induced polarization on applied electric field and associated electric susceptibility is sufficient to describe routinely observed optical responses like reflection, refraction, attenuation, etc. In the linear regime, none of these optical properties depend on the light intensity. When the laser sources are considered, the nature of response changes as the intensity of the optical field is of the order of atomic field. In such cases, the displacement of the electron is then no more directly proportional to the field, and higher-order nonlinear terms in the restoring force become more relevant. In the nonlinear regime, there is no direct proportionality between the polarization of the medium and the electric field. Instead, the polarization of the medium, in simplest form, can be expanded as power series in the electric field  $E$ :

$$\vec{P} = \underline{\chi}^{(1)} \vec{E} + \underline{\chi}^{(2)} (\vec{E})^2 + \underline{\chi}^{(3)} (\vec{E})^3 + \underline{\chi}^{(4)} (\vec{E})^4 + \dots \quad (2.2)$$

The  $i$ th component of  $P$  is related with the Cartesian components of the electric field:

$$P_i = \sum_j \chi_{ij}^{(1)} E_j + \sum_{j,k} \chi_{ijk}^{(2)} E_j E_k + \sum_{j,k,l} \chi_{ijkl}^{(3)} E_j E_k E_l + \dots \quad (2.3)$$

where  $i, j, k, \dots$  represent the Cartesian components of the vector  $E$  and the tensor  $\chi^{(n)}$ . The  $n$ th-order term of the expansion is proportional to the  $n$ th power of the electric field, and for the expansion to converge, each successive term must be smaller than the previous one (the perturbation expansion). As will be seen later, the ratio of each successive term with its previous term in Eq. (2.2) is of the order of  $E/E_a$ , where  $E_a$  is the internal atomic field. Therefore, for perturbation expansion of induced polarization to converge, the applied external field  $E$  must be smaller than  $E_a$ , which are typically of the order  $\sim 10^{11}$  V/m. The electric field associated with routinely employed  $Q$ -switched and mode-locked lasers is  $10^6$ – $10^8$  V/m which corresponds to an intensity  $\sim \text{GW/cm}^2$ . Much higher intensities ( $\sim \text{TW/cm}^2$  to  $\text{PW/cm}^2$  level) are now obtainable from ultrashort femtosecond laser sources, and as a subject of light–matter interaction, very interesting exotic and novel effects have been observed at fields much higher than  $E_a$ . As far as the field of laser physics and technology is concerned, these novel effects have led to the development of XUV, soft X-ray, and attosecond lasers. The description of such effects cannot be dealt based on the perturbation expansion made above for the nonlinear polarization. One then normally works in the regime of Extreme NLO [15, 16]. Therefore, our treatment of NLO in this chapter is restricted to situations for which perturbation expansion of induced nonlinear polarization is valid.

So far in the above equation, we have not made any explicit reference to the spatiotemporal or frequency dependence of induced polarization on applied electric field. Conventionally the frequency dependence of induced polarization is considered. Before going over to expressing nonlinear polarization in frequency

terms, we will make some discussion on phenomenological description of the nonlinear polarization. In general, the polarization of the material will be both a function of time,  $t$ , and the spatial coordinates,  $\vec{r}$ , of the material, that is,  $\vec{P} = \vec{P}(\vec{r}, t)$ . We will ignore the spatial dispersion of the material by adopting the “electric dipole approximation”. This approximation assumes that the wavelength of the applied light beam is much larger than the dimensions of the molecules that are responsible for the optical response. In other words, the electric field is considered to be uniform through the whole molecule, and hence, the induced polarization does not depend on the spatial coordinates on the molecular scale,  $\vec{P}(\vec{r}, t) = \vec{P}(t)$ .

Neglecting the spatial dispersion, we can express the polarization as a sum over ascending orders:

$$\vec{P} = \vec{P}^{(0)}(t) + \vec{P}^{(1)}(t) + \vec{P}^{(2)}(t) + \vec{P}^{(3)}(t) + \dots \quad (2.4)$$

where  $\vec{P}^{(0)}(t)$  is the static polarization independent of the external field  $\vec{E}(t)$ ,  $\vec{P}^{(1)}(t)$  is linear in  $\vec{E}(t)$ ,  $\vec{P}^{(2)}(t)$  is quadratic in  $\vec{E}(t)$ ,  $\vec{P}^{(3)}(t)$  is cubic in  $\vec{E}(t)$ , and so on. For each order of polarization term, one can then write the most general form of  $\vec{P}(t)$ , the  $i$ th component of the polarizations as

$$P_i^{(1)}(t) = \int_{-\infty}^{\infty} R_{ij}^{(1)}(\tau) E_j(t - \tau) d\tau \quad (2.5)$$

$$P_i^{(2)}(t) = \int_{-\infty}^{\infty} \int_{-\infty}^{\infty} R_{ijk}^{(2)}(\tau_1, \tau_2) E_j(t - \tau_1) E_k(t - \tau_2) d\tau_1 d\tau_2 \quad (2.6)$$

$$P_i^{(3)}(t) = \int_{-\infty}^{\infty} \int_{-\infty}^{\infty} \int_{-\infty}^{\infty} R_{ijkl}^{(3)}(\tau_1, \tau_2, \tau_3) E_j(\tau_1) E_k(\tau_2) E_l(\tau_3) d\tau_1 d\tau_2 d\tau_3 \quad (2.7)$$

Similar expressions can be written for other higher-order polarizations. The  $R^{(n)}$ s are polarization response function and are tensor of rank  $(n + 1)$ . Further, by invoking the condition of invariance of polarization on causality, reality, etc. [3–5], it is assumed that the polarization  $\vec{P}(t)$  depends only on  $\vec{E}(\tau < t)$ , i.e.,  $\vec{P}(t)$  depends only on past and not on future values of  $\vec{E}(t)$ , or for any  $\tau < 0$ ,  $R^{(n)}$ s are zero.

In general, this time-domain polarization response can provide complete description of the optical properties of the medium. This description is very useful particularly in case of light–matter interaction with ultrafast relaxation processes of the nonlinear medium or transient response from nonequilibrium systems. For all practical purpose, we deal with the interaction of medium with one or more monochromatic light field, and it is convenient to work in frequency dependence of induced polarization and electric susceptibility as response function.

Above expressions get simplified when we express the polarization and the electric fields in terms of its Fourier component; Eq. (2.5) reduces to

$$P_i^{(1)}(\omega) = \chi_{ij}^{(1)}(\omega; \omega) E_j(\omega) \quad (2.8)$$

where we have defined the linear dipolar susceptibility as

$$\chi_{ij}^{(1)}(\omega; \omega) = \int_{-\infty}^{\infty} R_{ij}^{(1)}(\tau) \exp(i\omega\tau) d\tau \quad (2.9)$$

Similarly from Eq. (2.6),

$$P_i^{(2)}(\omega_\sigma) = \chi_{ijk}^{(2)}(\omega_\sigma; \omega_1, \omega_2) E_j(\omega_1) E_k(\omega_2) \quad (2.10)$$

where  $\omega_\sigma = \omega_1 + \omega_2$  and  $\chi_{ijk}^{(2)}$  are the quadratic electric dipolar susceptibility:

$$\chi_{ijk}^{(2)}(\omega_\sigma; \omega_1, \omega_2) = \int_{-\infty}^{\infty} d\tau_1 \int_{-\infty}^{\infty} R_{ijk}^{(2)}(\tau_1, \tau_2) \exp[i(\omega_1\tau_1 + \omega_2\tau_2)] d\tau_2 \quad (2.11)$$

In general for  $n$ th-order electric susceptibility,

$$\begin{aligned} \chi_{i\alpha_1 \dots \alpha_n}^{(n)}(\omega_\sigma; \omega_1, \dots, \omega_n) &= \int_{-\infty}^{\infty} \dots \int_{-\infty}^{\infty} R_{i\alpha_1 \dots \alpha_n}^{(n)}(\tau_1, \dots, \tau_n) \\ &\times \exp[i(\omega_1\tau_1 + \dots + \omega_n\tau_n)] d\tau_1 \dots d\tau_n \end{aligned} \quad (2.12)$$

where

$$\omega_\sigma = \omega_1 + \dots + \omega_n$$

From Eq. (2.10), we observe that the nonlinear interaction due to  $\chi^{(2)}$  is responsible for the coupling of three beams also often referred to as three-wave interaction. Similarly, nonlinear interaction due to  $\chi^{(3)}$  will couple four waves and the process is four-wave interaction. We therefore find that nonlinear susceptibilities essentially couple the Fourier components of the light field amplitudes and produce polarization in the medium at frequency  $\omega_\sigma$ . Very often, for convenience the frequency of induced nonlinear polarization in the expressions of  $\chi^{(n)}$  is separated using a semicolon (;) from the rest. Some places in the literature, it is also separated with a negative sign from the rest. For example,  $\chi_{ijk}^{(2)}(\omega_\sigma; \omega_1, \omega_2)$  or  $\chi_{ijk}^{(2)}(-\omega_\sigma, \omega_1, \omega_2)$  will induce nonlinear polarization at  $\omega_\sigma = \omega_1 + \omega_2$ . The actual value of  $\omega_\sigma$  in each case of induced nonlinear polarization is always the sum of input frequencies. These respective nonlinear polarization terms then act like a source term in the wave equation and the related Maxwell equations.

To see the possible outcomes of induced nonlinear polarization, consider the first nonlinear polarization term,  $P^{(2)}$ . Consider a given medium is incident with two waves of frequency  $\omega_1$  and  $\omega_2$ . The input electric field then can be written as

$$E = E(\omega_1) e^{-i\omega_1 t} + E(\omega_2) e^{-i\omega_2 t} + \text{complex conjugate}$$

From Eq. (2.2), the induced second-order polarization will be

$$\begin{aligned} P^{(2)} = & \chi^{(2)}(2\omega_1; \omega_1, \omega_1) E^2(\omega_1) e^{-2i\omega_1 t} + \chi^{(2)}(2\omega_2; \omega_2, \omega_2) E^2(\omega_2) e^{-2i\omega_2 t} \\ & + 2\chi^{(2)}(\omega_1 + \omega_2; \omega_1, \omega_2) E(\omega_1) E(\omega_2) e^{-i(\omega_1 + \omega_2)t} \\ & + 2\chi^{(2)}(\omega_1 - \omega_2; \omega_1, \omega_2) E(\omega_1) E^*(\omega_2) e^{-i(\omega_1 - \omega_2)t} \\ & + \chi^{(2)}(0; \omega_1, -\omega_1) E(\omega_1) E^*(\omega_1) + \chi^{(2)}(0; \omega_2, -\omega_2) E(\omega_2) E^*(\omega_2) \\ & + \text{complex conjugate} \end{aligned} \quad (2.13)$$

From the above equation, it is clear that  $\chi^{(2)}$  in general can induce nonlinear polarizations at various frequencies like  $2\omega_1$ ,  $2\omega_2$ ,  $\omega_1 + \omega_2$ ,  $\omega_1 - \omega_2$  and also polarization at zero frequency. Each of these outcomes, due to  $P^{(2)}$ , is a well-known process such as:

- Second harmonic generation (SHG) process generating  $2\omega_1$  and  $2\omega_2$
- Sum frequency generation (SFG) process generating  $\omega_1 + \omega_2$
- Difference frequency generation (DFG) process generating  $\omega_1 - \omega_2$
- Optical rectification (OR) process generating zero frequency

In optical rectification, the polarization at zero frequency implies the generation of DC voltage in the material. In case of single input beam of frequency  $\omega$ , the SHG and SFG process will lead to the same output, and similarly DFG and OR will produce zero frequency. There are several practical applications of the above-mentioned processes in laser technology particularly with respect to the generation of coherent radiation at new (higher and lower than the input) frequencies. Details of these processes will be discussed later. There is another well-known  $\chi^{(2)}$  effect which is left out in the above list, i.e., Pockels or linear electro-optic effect. Its origin does not come out naturally in the above expression of nonlinear polarization where we initially assumed all the interacting fields are optical. If we assume one the field of zero frequency (the applied DC voltage), then  $\chi^{(2)}(\omega; 0, \omega)$  will describe the Pockels effect. Further discussion on electro-optic effect is made in the next section on properties of susceptibilities.

Similarly, the third-order susceptibility  $\chi^{(3)}$  can couple three input beams, and the most general form of polarization is

$$P_i^{(3)}(\omega_\sigma) = K \chi_{ijkl}^{(3)}(\omega_\sigma; \omega_1, \omega_2, \omega_3) E_j(\omega_1) E_k(\omega_2) E_l(\omega_3)$$

where  $K$  is the degeneracy factor which takes care of the number of distinct permutations of the frequencies involved. This factor was explicitly considered in Eq. (2.13)

for each process due to second-order polarization. The nonlinear polarizations due to  $P^{(3)}$  will generate various combinations of frequencies, and prominent among them are  $3\omega_1$ ,  $3\omega_2$ ,  $3\omega_3$ ,  $\omega_1 + \omega_2 + \omega_3$ ,  $\omega_1 - \omega_2 + \omega_3$ ,  $\omega_1 + \omega_2 - \omega_3$ , etc. Each of these outcomes due to  $P^{(3)}$  is a well-known process such as:

- Third harmonic generation (THG) process generating  $3\omega$
- Sum frequency generation (SFG) process generating  $\omega_1 + \omega_2 + \omega_3$
- Stimulated scattering processes
- Nonlinear absorption and refraction

For a single input beam of frequency  $\omega$ , the first two processes are identical as it would produce  $3\omega$ , while the last two terms are examples of sum and difference frequency mixing which lead to output frequency the same as input. Another process mentioned in the list not only leads to the generation of new frequencies but also to self-modification of input beam in terms of its amplitude and phase.

There are still higher-order polarizations possible, but, as mentioned earlier, due to the perturbation expansion of nonlinear polarization, the strength or magnitude of higher-order polarizations decreases fast with respect to the previous one. Therefore, we will restrict our discussion to effects due to  $P^{(2)}$  and  $P^{(3)}$  only.

## 2.3 Anharmonic Oscillator Model of Optical Nonlinearity

The functional form of nonlinear optical susceptibility with respect to light frequency and other material parameters provides the useful insight into the origin of NLO response and also helps to correlate the structure–property relationship. For more rigorous description of nonlinear susceptibility and for understanding the structure–property relationship, the quantum mechanical approach is more appropriate [2–4]. But for the basic understanding of properties of susceptibilities, the classical model is sufficient. Commonly used classical model to express nonlinear optical susceptibilities is the anharmonic oscillator model. It is an extension of classical Lorentz oscillator model used to obtain the linear optical susceptibility. In the anharmonic oscillator model, we introduce additional anharmonic contributions to the restoring force experienced by an electron bound by Coulomb field of the ion cores and the other electrons. The potential seen by the electron then can be expressed as

$$V(r) = \frac{1}{2}m\omega_0^2r^2 - \frac{1}{3}mar^3 - \frac{1}{4}mbr^4 \quad (2.14)$$

The equation of motion for an electron under external force due to applied electric field is then

$$\frac{d^2r}{dt^2} + 2\gamma \frac{dr}{dt} + \omega_0^2 r - ar^2 - br^3 = -\frac{e}{m}E \quad (2.15)$$

where  $r$  is the displacement of the electron from its equilibrium position,  $m$  its mass,  $e$  the magnitude of its charge,  $\omega_0$  the natural frequency of motion,  $\gamma$  a damping parameter, and  $a$  and  $b$  are anharmonic force constants and

$$E = E(\omega) e^{-i\omega t} + \text{complex conjugate}$$

Equation (2.15) can be solved by perturbation method to obtain Fourier components of higher-order corrections to the displacement of electron due to anharmonic force terms. For second-order effects, one may consider only the first anharmonic term, while for third-order effects, both anharmonic terms may be considered. Only in case of medium with center of inversion, where only even-order restoring force terms are included, we set  $a = 0$ . Polarization density for each order is then obtained using  $P(\omega) = -Ner(\omega)$  where  $N$  is the electron density for a given atomic or molecular system. Here, for the sake of simplicity, we have not considered local field effects. In principle while dealing with macroscopic quantities like susceptibilities, the influence of atomic and molecular arrangements or material symmetry on the actual field experienced by the electrons should be considered. We instead consider set of  $N$  anharmonic oscillators contributing independently toward induced polarization. This simplification is equivalent to assuming that medium dielectric constant is close to 1. By equating these polarization terms with  $P^{(2)}$  and  $P^{(3)}$ , we obtain expressions for  $\chi^{(2)}$  and  $\chi^{(3)}$ , respectively. By considering only harmonic term, we obtain well-known linear or first-order susceptibility:

$$\chi^{(1)}(\omega) = \frac{Ne^2}{m} \frac{1}{\omega_0^2 - 2i\gamma\omega - \omega^2} = \frac{Ne^2}{m} D(\omega) \quad (2.16)$$

where we define  $D(\omega) = \frac{1}{\omega_0^2 - 2i\gamma\omega - \omega^2} = D^*(-\omega)$

Similarly, we can obtain second-order susceptibility if we consider two input beams driving the anharmonic oscillator, i.e.,

$$E = E(\omega_1) e^{-i\omega_1 t} + E(\omega_2) e^{-i\omega_2 t} + \text{complex conjugate}$$

Then,

$$\chi^{(2)}(\omega_3; \omega_1, \omega_2) = -Na \frac{e^3}{m^2} D(\omega_1) D(\omega_2) D(\omega_1 + \omega_2) \quad (2.17)$$

This susceptibility describes the SFG, i.e.,  $\omega_3 = \omega_1 + \omega_2$ . Similarly for DFG, i.e.,  $\omega_3 = \omega_1 - \omega_2$ ,

$$\chi^{(2)}(\omega_3; \omega_1, -\omega_2) = -Na \frac{e^3}{m^2} D(\omega_1) D^*(\omega_2) D(\omega_1 - \omega_2)$$

For single input beam of frequency  $\omega$ , the possible output due to  $P^{(2)}$  is SHG:

$$\chi^{(2)}(2\omega) = -Na \frac{e^3}{m^2} D^2(\omega) D(2\omega) \quad (2.18)$$

Similarly third-order susceptibility can be obtained with three input frequencies to get  $\omega_4 = \omega_1 + \omega_2 + \omega_3$

$$\begin{aligned} \chi^{(3)}(\omega_4; \omega_1, \omega_2, \omega_3) &= N \frac{e^4}{m^3} \left[ b + \frac{4}{3} a^2 \left\{ D(\omega_1 + \omega_2) + D(\omega_2 + \omega_3) \right. \right. \\ &\quad \left. \left. + D(\omega_3 + \omega_1) \right\} \right] \\ &\quad \times D(\omega_1) D(\omega_2) D(\omega_3) D(\omega_1 + \omega_2 + \omega_3) \end{aligned} \quad (2.19)$$

**Comment** *The description of nonlinearity can also be obtained using the harmonic oscillator model provided we consider higher-order terms in multipole expansion, i.e., go beyond the dipole approximation and consider quadrupole moment or include magnetic interaction. Similarly, in case of isotropic medium with center of inversion, the potential must be even function of the deviation or force can only have odd powers of r. The nonlinearity then can only be through  $1/4 mbr^4$  term or through higher-order multipole terms.*

## 2.4 Properties of Susceptibilities

To get more insight into the physical significance and structure-property relationship of optical nonlinearity, it is worthwhile to consider symmetry properties of susceptibilities. We will also discuss consequences of symmetry properties of susceptibilities.

### 2.4.1 Reality Condition

It can be observed from Eq. (2.17) and definition of  $D(\omega)$  that when  $\omega \ll \omega_0$ , the nonresonant condition, the susceptibilities are real quantity, and it also follows that

$$\chi_{ijk}^{(2)}(\omega_3; \omega_1, \omega_2) = \chi_{ijk}^{(2)*}(\omega_3; -\omega_1, -\omega_2) = \chi_{ijk}^{(2)}(\omega_3; -\omega_1, -\omega_2)$$

This is reality condition of susceptibility. This relation indicates that for nonresonant interaction, the nonlinear susceptibility elements are invariant when all the frequency arguments change their signs.

### 2.4.2 Resonance Effect

Resonance occurs when any of the frequencies involved in the interaction or their combinations are close to the electronic transitions of the medium. Under this condition  $\omega \sim \omega_0$  and  $D(\omega) \sim 1/\omega\gamma$ . In case of low damping, the susceptibility value gets enhanced by several orders compared to nonresonant condition. It is advantageous in some sense to work close to resonance condition to achieve higher nonlinear response at low power of input beam, but it can also reduce the efficiency of a given nonlinear process because of self-absorption of light intensity by the medium at the incident or generated frequencies. Another consequence of resonance condition is related to slow response time of optical nonlinearity with applied optical field and the validity of perturbation expansion of induced nonlinear polarization [9].

In our description of susceptibility, using anharmonic oscillator model, we assumed only one natural frequency of oscillation of the medium. But, in general for any atomic or molecular system, there can be more than one excitation levels. In such cases, the resonance at combination frequencies, which is other than input or generated output frequency, helps in achieving higher nonlinearity as well as phase matching. In the later section on third-order processes (e.g., THG from atomic vapors), we will see how two-photon resonance condition is used to achieve phase matching from isotropic medium.

### 2.4.3 Intrinsic and Overall Permutation Symmetry

Consider two laser beams of frequencies  $\omega_1$  and  $\omega_2$  having polarizations along  $x$  and  $y$  directions, respectively, that induce a nonlinear polarization in  $z$  direction having frequency  $\omega_3$ , i.e.,

$$P_z^{(2)}(\omega_3) = \chi_{zxy}^{(2)}(\omega_3; \omega_1, \omega_2) E_x(\omega_1) E_y(\omega_2) \quad (2.20)$$

This induced polarization should be independent of the order in which  $x\omega_1$  and  $y\omega_2$  are written. As can be seen from Eq. (2.17) as well,  $\chi^{(2)}$  has intrinsic symmetry such that  $\chi_{ijk}^{(2)}(\omega_3; \omega_1, \omega_2) = \chi_{ikj}^{(2)}(\omega_3; \omega_2, \omega_1)$  where we have interchanged  $j$  and  $k$  except  $i$ . Here  $i, j, k$  essentially represent Cartesian indices. This is intrinsic permutation symmetry of susceptibility to which susceptibility remains unchanged when the indices and frequencies of input fields are simultaneously interchanged. This is true for other higher-order susceptibilities as well.

Under nonresonant condition ( $\omega \ll \omega_0$ ) when damping factors are ignored, then susceptibility remains unchanged when all the indices and corresponding frequencies are simultaneously interchanged. This is referred to as *overall* permutation symmetry, i.e.,

$$\chi_{ijk}^{(2)}(\omega_3; \omega_1, \omega_2) = \chi_{ikj}^{(2)}(\omega_2; \omega_1, -\omega_3) = \chi_{jki}^{(2)}(\omega_1; \omega_2, -\omega_3)$$

There are interesting consequences of overall permutation symmetry. It relates two different nonlinear processes. Let us consider optical rectification process described by  $\chi^{(2)}(0; \omega, -\omega)$ . Following the overall symmetry, we can interchange frequencies such that  $\chi^{(2)}(0; \omega, -\omega) \equiv \chi^{(2)}(\omega; \omega, 0)$ . Physical significance of  $\chi^{(2)}(\omega; \omega, 0)$  can be seen easily as it will induce nonlinear polarization in the medium at frequency  $\omega$  the same as that of the input when the other input field is DC electric field (applied DC voltage). The presence of nonlinear polarization at  $\omega$  would bring change in refractive index/birefringence property of the medium, and that depends linearly on the applied DC electric field. This phenomenon is called as linear electro-optic (EO) or Pockels effect. This important second-order effect was left out in Eq. (2.13) because we initially assumed that all the input fields are optical fields. When we replace one of the input frequencies in Eq. (2.13) by DC field, then EO effect will also appear as possible outcome due to  $P^{(2)}$ . One can extend the same consideration to  $P^{(3)}$ , then we observe that one of the possible outcomes is described by  $\chi^{(3)}(\omega; \omega, 0, 0)$ . This susceptibility will bring change in medium refractive index, and that depends on the square of applied DC electric field. This effect is DC Kerr effect or quadratic EO effect.

**Note** *It is important to mention here that all the frequencies involved in higher-order nonlinearities, particularly the third order, need not be of optical range. Apart from DC field as one of the input fields, the medium excitations can also take part in the nonlinear process of exchange of energy among light beams. These third-order processes, which involve material excitations, are interesting not only in the context of physics of light–matter interaction, but they are also of practical interest in developing coherent sources at frequencies which are otherwise not obtainable directly from conventional laser gain media. Prominent processes among them are stimulated Raman and Brillouin scattering, which involves exchange of light energy with vibrational or acoustic excitations, respectively. Details of these processes are discussed in later part of lecture notes.*

If the dispersion of susceptibilities is neglected, i.e., no frequency dependence, then the permutation symmetry becomes independent of frequencies. This leads to very general permutation symmetry between elements of  $\chi$ , i.e., elements remain unchanged under all permutations of the Cartesian indices. This is Kleinman's symmetry and it reduces the number of independent elements further, e.g., it reduces the number of independent elements of  $\chi^{(2)}$  from 27 to 10. Once again this symmetry consequence is valid only at frequencies far from resonances.

#### 2.4.4 Spatial Symmetry

As mentioned earlier the  $n$ th-order susceptibilities are tensors of rank  $n + 1$ . Therefore,  $\chi^{(2)}$  will have 27 elements and  $\chi^{(3)}$  will have 81 elements. The number of nonzero elements of these tensors reduces drastically and also gets related to each other if one considers material structural or spatial symmetry. As true for any other physical property, the susceptibility tensors must also remain unchanged

upon symmetry operations allowed for the medium. This reduces the number of independent and nonzero elements. It is well tabulated in the literature about the symmetry relations for  $\chi^{(2)}$  and  $\chi^{(3)}$  for all the crystallographic point groups [3, 4, 15]. The most important conclusion from this property is that for all centrosymmetric crystals with center of inversion and for all isotropic media (gases, liquids), all elements of the even-order susceptibility tensors ( $\chi^{(2)}, \chi^{(4)}, \dots$ ) must be zero. Thus, e.g., no second harmonic generation can be observed in such media. Another way of looking at the same fact follows from Eq. (2.14). Since for centrosymmetric medium, potential is even function of  $r$ , then  $V(-r) = V(r)$ . This implies  $a = 0$  and from Eq. (2.18),  $\chi^{(2)} = 0$ . Also, by applying inversion operation, i.e.,  $r \rightarrow -r$ , the physical property of the medium should not change. Since  $P$  and  $E$  are polar vectors and will change sign under inversion operation, then from Eq. (2.10), we conclude  $\chi_{ijk}^{(2)} = -\chi_{ijk}^{(2)} = 0$ . Odd-order susceptibility in such media will of course be nonzero and will provide nonlinear effects. Using gases or metal vapors, e.g., only odd-order harmonics can be produced.

**Comment** As far as bulk of the medium is concerned, the centrosymmetric or isotropic nature of the medium does not allow all even-order nonlinearity to be present. Once again it is assumed that we are concerned only with dipole approximation for light-matter interaction. If one considers quadrupole or magnetic interaction, then  $\chi_{ijk}^{(2)} \neq 0$  [4]. Also, at the surface and interfaces of isotropic media (or for that matter the medium of any symmetry), the inversion symmetry is broken and one expects  $\chi_{ijk}^{(2)} \neq 0$ . Therefore, SHG- and SFG-based spectroscopic measurements are widely used for probing surface structure and adsorption properties, interface dipoles, etc. [8].

Another important consequence of symmetry properties can be seen as there can be no THG from isotropic medium when circularly polarized light beam is used [9]. It follows from the fact that for isotropic medium  $\chi^{(3)}$  has only three independent elements, i.e.,

$$\chi_{xxxx}^{(3)} = \chi_{yyyy}^{(3)} = \chi_{zzzz}^{(3)} = \chi_{xxyy}^{(3)} + \chi_{xyxy}^{(3)} + \chi_{xyyx}^{(3)}$$

and using  $E_x = E_y$  for circularly polarized light, it is shown that  $P^{(3)}(3\omega) = 0$ . Therefore, the property of spatial symmetry of susceptibility together with the proper choice of polarizations of interacting light beams is very useful in suppressing unwanted nonlinear effects when two or more processes are possible simultaneously.

#### 2.4.5 Miller's Constant, Magnitudes of Nonlinear Susceptibilities and d-Coefficient

A rough guideline of structure-property relation and search for better NLO materials can be obtained from Miller's rule. Using Eqs. (2.16) and (2.18), we write for SHG under nonresonant condition:

$$\frac{\chi^{(2)}(2\omega)}{[\chi^{(1)}(\omega)]^2 [\chi^{(1)}(2\omega)]} = \frac{am}{e^3 N^2} \equiv \delta \text{ (Miller constant)}$$

The value of  $\delta$  is found to be nearly constant  $\sim 10^{-6}$  esu for most of NLO active materials. In other words,

$$\chi^{(2)}(2\omega) \propto [\chi^{(1)}(\omega)]^2 [\chi^{(1)}(2\omega)] \propto n^6$$

This empirical law, the Miller' rule, suggests that second-order susceptibility of SHG depends strongly on the linear optical susceptibility at  $\omega$  and  $2\omega$ , and materials with large refractive index are likely to provide large nonlinearity. Physically large  $n$  implies that materials with easily displaceable electron cloud would lead to higher nonlinearity. This empirical law is valid for most of the condensed phase ionic solid materials (except for low-pressure gases and organic materials) for second-order nonlinearity [17]. It fails in organic materials primarily because two different types of  $\sigma$  and  $\pi$  electrons contribute toward linear and nonlinear optical properties, respectively. For third-order nonlinearity, the Miller's rule fails, but a modified Wang's rule is found to be applicable for predicting, e.g., nonlinear refractive index of various materials [17]. According to Wang's rule

$$\chi^{(3)} \propto \frac{(\chi^{(1)})^2}{N_{\text{eff}} \hbar \omega_0}$$

where  $N_{\text{eff}}$  is the product of molecular number density and the oscillator strength and  $\omega_0$  is the mean absorption frequency of the material. Therefore, according to Wang's rule, the guideline for better  $\chi^{(3)}$  material is to look for low band gap materials with strong ground state absorption.

To get the estimate of the order of magnitudes of various susceptibilities, let us first obtain the ratio of polarizations. Consider Eqs. (2.16), (2.18), and (2.19) and assume nonresonant condition,  $D(\omega) \sim \omega_0^2$ , then

$$\frac{P^{(2)}}{P^{(1)}} = \frac{\chi^{(2)} EE}{\chi^{(1)} E} = \frac{eE}{m} \frac{a}{\omega_0^4}$$

Further simplification is made by assuming the magnitude of anharmonic force equals that of harmonic force and also maximum displacement for an electron could be lattice constant ( $d$ ) of solid medium such that  $ad^2 = \omega_0^2 d$ . Then

$$\frac{P^{(2)}}{P^{(1)}} \sim \frac{eE}{m} \frac{1}{\omega_0^2 d} \sim \frac{eE_L}{eE_a} \sim \frac{E_L}{E_a}$$

Here  $E = E_L$  is the strength of applied light field and  $E_a$  is atomic field. We equated  $m\omega_0^2 d$  term to centrifugal force acting on orbiting electron and which equals cohesive force on electron due to ionic core and other electrons. Similarly, we can obtain

$$\frac{P^{(3)}}{P^{(1)}} \sim \left( \frac{E_L}{E_a} \right)^2$$

In general, we can write

$$\frac{P^{(n+1)}}{P^{(n)}} \sim \frac{E_L}{E_a} \quad (2.21)$$

This relation once again asserts that the expansion made in Eq. (2.2) is valid only when  $E_L \ll E_a$ . To observe NLO effects as efficient as linear effects, the strength of light field should be comparable to atomic field, which one can obtain from laser sources.

Based on Eq. (2.21), we estimate the magnitudes of susceptibilities. Consider

$$\chi^{(2)} \sim \chi^{(1)}/E_a \quad \text{and} \quad \chi^{(3)} \sim \chi^{(1)}/E_a^2$$

Since  $\chi^{(1)} \sim 1$  and  $E_a \sim 10^6$  statvolt/cm, then  $\chi^{(2)} \sim 10^{-8}$  esu and  $\chi^{(3)} \sim 10^{-14}$  esu. Very often these units are also expressed in MKS system. The unit of  $\chi^{(n)}$  in MKS is  $(m/V)^{n-1}$  where  $n$  is the order of nonlinearity. Two commonly used units are related as

$$\frac{\chi^{(2)}(\text{MKS})}{\chi^{(2)}(\text{esu})} = \frac{4\pi}{3 \times 10^4} \quad \frac{\chi^{(3)}(\text{MKS})}{\chi^{(3)}(\text{esu})} = \frac{4\pi}{(3 \times 10^4)^2},$$

Considering all the symmetry properties discussed and allowed for a given material medium, one can observe that there are very few nonzero elements of  $\chi^{(2)}$  and  $\chi^{(3)}$  tensors for most of crystalline materials used for practical applications in NLO. Since intrinsic permutation reduces the number of elements for  $\chi^{(2)}$  from 27 to 18 and many of them are zero because of other symmetry properties, therefore it is convenient to introduce a compact notation for  $\chi_{ijk}^{(2)}$  as d-coefficient. It is defined as  $d_{ijk} = \frac{1}{2}\chi_{ijk}^{(2)}$ . The factor of  $\frac{1}{2}$  takes care of degeneracy factor while we consider SHG or SFG. Since  $j$  and  $k$  can be interchanged, therefore it is replaced by single subscript such that various combinations of last two indices can take values 1 to 6 as

$ii = 1, jj = 2, kk = 3, jk = kj = 4, ik = ki = 5, ij = ji = 6$ , then, e.g.,  $d_{ijk} = d_{ikj} = d_{14}$  or  $d_{kji} = d_{kij} = d_{36}$ .

Equation (2.10) or (2.20) for second-order nonlinear polarization for SHG can be written in matrix form as

$$\begin{pmatrix} P_x(2\omega) \\ P_y(2\omega) \\ P_z(2\omega) \end{pmatrix} = \begin{pmatrix} d_{11} & d_{12} & d_{13} & d_{14} & d_{15} & d_{16} \\ d_{21} & d_{22} & d_{23} & d_{24} & d_{25} & d_{26} \\ d_{31} & d_{32} & d_{33} & d_{34} & d_{35} & d_{36} \end{pmatrix} \begin{pmatrix} E_x^2 \\ E_y^2 \\ E_z^2 \\ 2E_zE_y \\ 2E_zE_x \\ 2E_xE_y \end{pmatrix} \quad (2.22)$$

For most of the crystalline materials, the d-coefficients are well tabulated in the literature in the form of  $3 \times 6$  matrix; e.g., for widely used crystal of potassium dihydrogen phosphate (KDP), the d-coefficients are

$$\begin{pmatrix} 0 & 0 & 0 & d_{14} & 0 & 0 \\ 0 & 0 & 0 & 0 & d_{14} & 0 \\ 0 & 0 & 0 & 0 & 0 & d_{36} \end{pmatrix}$$

Here  $d_{14} = d_{25}$ . Then possible components of induced polarization are

$$\begin{aligned} P_x^{(2)} &= 2d_{14}E_yE_z \\ P_y^{(2)} &= 2d_{14}E_xE_z \\ P_z^{(2)} &= 2d_{36}E_xE_y \end{aligned} \quad (2.23)$$

## 2.5 Wave Equation in Nonlinear Medium-Coupled Wave Equations

Nonlinear polarization induced in the medium as a result of coupling of Fourier components of interacting light fields acts as source for new wave which can be of frequency other than the input (as in SHG, SFG, DFG, THG, etc.). To understand the growth or decay of field amplitudes of all the interacting waves including the birth of new wave, one needs to solve the wave equation in nonlinear media. We are more interested in obtaining the relationship between experimentally measurable quantities, i.e., the input and the output intensity, and how efficiency of a given process depends on various parameters of light beam and material medium.

The procedure is to first identify the nonlinear polarization source term for new radiation and incorporate the same in constitutive relations and then solve

Maxwell's wave equations for all the interacting field amplitudes. We assume nonmagnetic medium with no free charges or free current density. The Maxwell's equations are

$$\nabla \cdot D = 0$$

$$\nabla \cdot B = 0$$

$$\nabla \times E = -\frac{1}{c} \frac{\partial B}{\partial t}$$

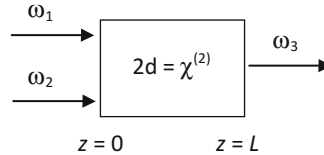
$$\nabla \times B = \frac{1}{c} \frac{\partial E}{\partial t}$$

and constitutive relation

$$D = \epsilon E = (1 + 4\pi\chi) E = E + 4\pi P \quad (2.24)$$

where  $P$  is the total polarization induced in the medium, i.e.,  $P(\omega) = P^L(\omega) + P^{NL}(\omega)$ , where  $P^L$  is linear polarization and  $P^{NL}$  is nonlinear polarization.

As a general case, we consider SFG process. Let two monochromatic waves of frequencies  $\omega_1$  and  $\omega_2$  be incident on a nonlinear medium characterized by nonlinear  $d$ -coefficient  $d = \frac{1}{2}\chi^{(2)}(\omega_3; \omega_1, \omega_2)$  and generate a new wave of frequency  $\omega_3 = \omega_1 + \omega_2$ . Let medium length be  $L$  and beams propagate in  $z$  direction as shown below.



The nonlinear polarization in this case will be

$$P^{NL} = P^{(2)}(\omega_3) = \chi^{(2)}(\omega_3; \omega_1, \omega_2) E_1(\omega_1) E_2(\omega_2)$$

For the sake of convenience, we consider scalar coupling coefficient. (Ideally an effective susceptibility or  $d$ -coefficient should be considered depending upon the directions of beam polarizations and symmetry properties of susceptibility, i.e.,  $\chi^{(2)} = \hat{e}_3 \cdot \chi^{(2)}(\omega_3; \omega_1, \omega_2) : \hat{e}_1 \hat{e}_2$ , where  $\hat{e}_i$  are polarization vectors of input fields and induced polarization, respectively). Considering degeneracy factor

$$P^{NL}(\omega_3) = 4d E_1(\omega_1) E_2(\omega_2) \quad (2.25)$$

The wave equation for each wave will be of the form

$$\nabla^2 E = \frac{\epsilon}{c^2} \frac{\partial^2 E}{\partial t^2} + \frac{4\pi}{c^2} \frac{\partial^2}{\partial t^2} P^{\text{NL}} \quad (2.26)$$

Here, linear and nonlinear polarization terms are separated out, and linear polarization is incorporated within the linear dielectric constant  $\epsilon$ . One can express wave equation explicitly for each wave propagating in nonlinear medium as

$$\begin{aligned} \nabla^2 E_1(\omega_1) &= \frac{\epsilon(\omega_1)}{c^2} \frac{\partial^2 E_1(\omega_1)}{\partial t^2} + \frac{4\pi}{c^2} \frac{\partial^2}{\partial t^2} P^{\text{NL}}(\omega_1) \\ \nabla^2 E_2(\omega_2) &= \frac{\epsilon(\omega_2)}{c^2} \frac{\partial^2 E_2(\omega_2)}{\partial t^2} + \frac{4\pi}{c^2} \frac{\partial^2}{\partial t^2} P^{\text{NL}}(\omega_2) \\ \nabla^2 E_3(\omega_3) &= \frac{\epsilon(\omega_3)}{c^2} \frac{\partial^2 E_3(\omega_3)}{\partial t^2} + \frac{4\pi}{c^2} \frac{\partial^2}{\partial t^2} P^{\text{NL}}(\omega_3) \end{aligned} \quad (2.27)$$

The above equations are known as coupled wave equations. As one can see, these equations are inhomogeneous wave equations as  $P^{\text{NL}}$  contains products of field amplitudes. Here  $P^{\text{NL}}$  is the source of wave at the corresponding frequency. Here  $P^{\text{NL}}$  at  $\omega_1$  and  $\omega_2$  is defined as

$$\begin{aligned} P^{\text{NL}}(\omega_1 = \omega_3 - \omega_2) &= 2dE_3(\omega_3) E_2^*(\omega_2) \\ P^{\text{NL}}(\omega_2 = \omega_3 - \omega_1) &= 2dE_3(\omega_3) E_1^*(\omega_1) \end{aligned} \quad (2.28)$$

It can be easily noticed that Eq. (2.28) is nothing but nonlinear polarizations of DFG process. By virtue of permutation symmetry and reality condition, the  $d$ -coefficient remains the same.

Based on the above wave equations, we will obtain, with some approximations, much simplified set of first-order differential equations relating field amplitudes. It will be helpful to understand how, as beams propagate in the medium, the growth or decay of each field amplitude depends on growth or decay of other field amplitudes and their phase. Through coupled wave equations, we can also understand how exchange of energy among light beams takes place. The formalism to be followed below remains the same for other specific processes like SHG, DFG, etc. In case of SHG, we will set  $\omega_1 = \omega_2 = \omega$  and  $\omega_3 = 2\omega$ . Similar formalism can of course be extended for third-order processes as well.

All the three interacting fields propagating in  $z$  direction can be represented as

$$E_i(z, t) = A_i e^{i(k_i z - \omega_i t)} + \text{cc} \quad \text{where } i = 1, 2, 3 \quad (2.29)$$

where  $A_i = |A_i| e^{i\varphi_i}$  are the peak amplitude of electric field and depend only on  $z$  and  $k_i$  and  $\omega_i$  are the respective wave vector and frequency of each wave. We have

introduced arbitrary phase factor  $\varphi_i$  for each field amplitude. The relation between field amplitude and intensity is taken as

$$I_i = \frac{n_i c}{2\pi} |A_i|^2 \quad i = 1, 2, 3 \quad (2.30)$$

where  $n_i = n(\omega_i)$  is the refractive index of the medium at each  $\omega_i$ . Then

$$P^{\text{NL}}(z, t) = 4dA_1 A_2 e^{i[(k_1 + k_2)z - \omega_3 t]} + cc \quad (2.31)$$

The nonlinear wave Eq. (2.27) for generated beam becomes

$$\begin{aligned} & \left[ \frac{\partial^2 A_3}{\partial z^2} + 2ik_3 \frac{\partial A_3}{\partial z} - k_3^2 A_3 + \frac{\epsilon(\omega_3) \omega_3^2 A_3}{c^2} \right] e^{i(k_3 z - \omega_3 t)} \\ &= -\frac{16\pi d\omega_3^2}{c^2} A_1 A_2 e^{i[(k_1 + k_2)z - \omega_3 t]} \end{aligned} \quad (2.32)$$

Similar equations can be written for other field amplitudes. To simplify above equations further, we make some assumption and approximations:

1. *Plane wave approximation*: This approximation is already made by assuming that amplitudes are functions of  $z$  only. In that case partial derivatives can be replaced as  $\frac{\partial}{\partial z} \Rightarrow \frac{d}{dz}$ .
2. *Slowly varying envelop approximation (SVEA)*: We assume that nonlinearity is small, and the rate at which field amplitudes grow or decay (or change in their phase) is small over the length compared to the wavelength. Equivalently one can say that energy transfer among waves is usually significant only after the waves travel over a distance much longer than the wavelengths [6]. We can therefore neglect second-order derivative in Eq. (2.32) using

$$\left| \frac{d^2 A_3}{dz^2} \right| \ll \left| k \frac{dA_3}{dz} \right|$$

With these approximations, the second-order partial differential Eq. (2.32) reduces to first-order differential equation. Then for each field amplitude,

$$\frac{dA_3}{dz} = \frac{8\pi i d\omega_3^2}{k_3 c^2} A_1 A_2 e^{i(\Delta k)z} \quad (2.33)$$

$$\frac{dA_1}{dz} = \frac{8\pi i d\omega_1^2}{k_1 c^2} A_3 A_2^* e^{-i(\Delta k)z} \quad (2.34)$$

$$\frac{dA_2}{dz} = \frac{8\pi i d\omega_2^2}{k_2 c^2} A_3 A_1^* e^{-i(\Delta k)z} \quad (2.35)$$

where  $\Delta k = k_1 + k_2 - k_3$  is the wave vector mismatch and  $\Delta k z$  is the phase mismatch between the wave being generated and its source, the nonlinear polarization. The above three equations are coupled wave equations showing the dependence of growth or decay of each field amplitude as the three-wave interaction, as in SFG, proceeds in the medium. Similarly, for higher-order process of four-wave interaction such as  $\omega_4 = \omega_1 + \omega_2 + \omega_3$ , we will have a set of four-coupled wave equations.

To obtain the relationship between measurable quantities, we solve the above equations based on initial condition. For SFG process under consideration, we integrate Eq. (2.33) to obtain  $A_3(L)$  with initial condition  $A_3(0) = 0$  and use Eq. (2.30). We consider another assumption of no pump depletion condition, i.e., small signal gain approximation such that  $\frac{dA_1}{dz} = \frac{dA_2}{dz} = 0$ , and we get

$$\begin{aligned} A_3(L) &= \frac{8\pi i d\omega_3^2}{k_3 c^2} A_1 A_2 \left( \frac{e^{i(\Delta k)L} - 1}{\Delta k} \right) \\ I_3 &= \frac{32\pi d^2 \omega_3^4}{k_3^2 c^3} |A_1|^2 |A_2|^2 n_3 \left| \frac{e^{i(\Delta k)L} - 1}{\Delta k} \right|^2 \\ &= \frac{128\pi^3 d^2 \omega_3^2 I_1 I_2 L^2}{n_1 n_2 n_3 c^3} \text{sinc}^2 \left( \frac{\Delta k L}{2} \right), \quad \text{where } \text{sinc}^2(x) = \frac{\sin^2(x)}{x^2} \end{aligned} \quad (2.36)$$

The above equation relates intensity of generated  $\omega_3$  beam with all the measurable and known quantities (the d-coefficient and refractive indices). We also notice that intensity depends on medium length in oscillatory fashion due to  $\text{sinc}^2(\frac{\Delta k L}{2})$  function. Intensity can be maximum only when  $\Delta k l/2 = 0$ . This condition is referred to as perfect phase matching condition.

## 2.6 Conservation Laws

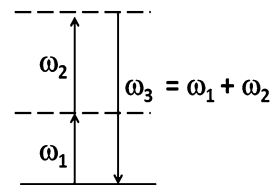
As true for any physical process, the conservation laws of energy and momentum should also be applicable to nonlinear processes as well.

### 2.6.1 Energy Conservation

In the process of SFG, we generated new beam at  $\omega_3 = \omega_1 + \omega_2$  through nonlinear interaction of two input beams of frequency  $\omega_1$  and  $\omega_2$  mediated by material susceptibility. This simple relationship is equivalent to conservation of photon energy, i.e.,

$$\hbar\omega_3 = \hbar\omega_1 + \hbar\omega_2$$

**Fig. 2.1** Electronic transition involved in SFG



In quantum picture, one photon at  $\omega_3$  is created when one photon is taken away from each wave at  $\omega_1$  and  $\omega_2$ . Energy-level diagram shown in Fig. 2.1 describes the process. The process considered is nonresonant at all the frequencies involved, which means medium energy does not take part in the energy exchange process. Except ground state, all the excited state levels are virtual levels, and the system's final state is the same as the initial state. Such processes are also termed as parametric processes. The energy conservation law is valid for other higher-order processes as well.

### 2.6.2 Manley–Rowe Relations

With respect to SFG process under discussion, it says that photon flux density in the wave at  $\omega_3$  can only be increased if photon flux densities at  $\omega_1$  and  $\omega_2$  are decreased simultaneously by the same amount. It can be shown easily with the help of coupled wave equations (2.33, 2.34, and 2.35). Consider

$$\begin{aligned} \frac{1}{\omega_1} \frac{dI(\omega_1)}{dz} &= \frac{1}{\omega_1} \frac{d}{dz} \left( \frac{n_1 c}{2\pi} A_1 A_1^* \right) = \frac{n_1 c}{2\pi \omega_1} \left( A_1 \frac{dA_1^*}{dz} + A_1^* \frac{dA_1}{dz} \right) \\ &= 4d \left[ -i A_1 A_2 A_3^* e^{i(\Delta k)z} + i A_1^* A_2^* A_3 e^{-i(\Delta k)z} \right] \end{aligned}$$

Similar expression can be written for  $\frac{1}{\omega_2} \frac{dI(\omega_2)}{dz}$  and  $\frac{1}{\omega_3} \frac{dI(\omega_3)}{dz}$   
Comparing all we get

$$\frac{1}{\omega_1} \frac{dI(\omega_1)}{dz} = \frac{1}{\omega_2} \frac{dI(\omega_2)}{dz} = -\frac{1}{\omega_3} \frac{dI(\omega_3)}{dz} \quad (2.37)$$

The above equation means that the rate of generation (loss) of photons of  $\omega_3$  beam is the same as that of loss (generation) of photons of  $\omega_1$  and  $\omega_2$  beams. These relations are helpful in understanding other parametric processes particularly the DFG process. Consider DFG process  $\omega_2 = \omega_3 - \omega_1$ . Let us assume one of the input beams  $\omega_1$  is very weak compared to other strong beams  $\omega_3$ . Then the same Manley–Rowe equation suggests that when photon of strong beam is destroyed or lost, it not only creates photon at new beam  $\omega_2$  but also amplifies the weak beam at  $\omega_1$ .

### 2.6.3 Momentum Conservation and Phase Matching

The wave vector mismatch  $\Delta k$  defined before for SFG is nothing but the conservation of photon momentum, i.e.,

$$\hbar\mathbf{k}_3 = \hbar\mathbf{k}_1 + \hbar\mathbf{k}_2 \quad (2.38)$$

It implies that coupling between three waves, as described by coupled wave equations (2.33, 2.34, and 2.35), is most efficient if the above wave vector relationship is satisfied. It also implies phase matching condition  $\Delta k_z = 0$ . It is true for each parametric photon energy transfer process. It can also be extended for other higher-order processes as well. Since Eq. (2.38) is vector relationship of propagation vectors of interacting light beams, therefore components of each wave vector should also satisfy the phase matching condition. For the case of SFG, we assumed that both the input beams travel in  $z$  direction and will generate new beam which will also travel in the same direction. Phase matching in this case is termed as collinear phase matching. When two input beams are incident on nonlinear medium making an angle  $\theta$  with each other, then it is termed as noncollinear phase matching. Vector relationship of two possible phase matching condition is shown in Fig. 2.2.

Collinear phase matching is convenient to achieve and also allows maximum interaction throughout the length of nonlinear medium. But, the generated beam also emerges in the same direction as the input. For the measurement purpose, one therefore needs filters or dispersing elements to separate them. Noncollinear phase matching is advantageous in some sense as it not only leads to spatial separation of generated beams from the input beams, but it also allows propagation angle-dependent phase matching. The disadvantage here is that nonlinear interaction takes place only in the region of beam overlap leading to low efficiency. In some situations where the choice of crystal type and the frequency ranges are such that collinear phase matching is not possible, then the only option left is noncollinear phase matching.

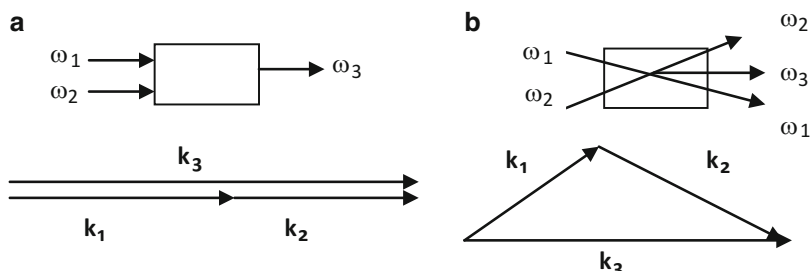


**Fig. 2.2** Two possible phase matching conditions (a) collinear phase matching and (b) noncollinear phase matching

In the situation where perfect phase matching is not achieved,  $\Delta kz \neq 0$  is also of interest. It has two immediate consequences. First, the efficiency of a given process decreases by  $\sim 1/(\Delta k)^2$ , and second, output intensity shows an oscillatory behavior with path length. This can be easily seen when  $\Delta kz$  is finite, and then as beams propagate in the medium, the relative phase of field amplitudes changes. When  $\Delta kz = \pi$ , then source polarization is out of phase with respect to the phase of radiated field. This will result in the back flow of power from  $2\omega$  beam to  $\omega$  beam. Accordingly the coherence length for a given NLO frequency mixing process is defined as  $l_c = \pi/\Delta k$ . For crystal length much larger than  $l_c$ , then for each  $l_c$ , the direction of power flow among  $\omega$  and  $2\omega$  beam keeps changing. In case crystal length is even multiple of  $l_c$ , then net output at the exit face of crystal is zero. Further details of phase matching techniques and related issues will be discussed more with specific case of SHG.

## 2.7 Crystal Anisotropy and Birefringence

This section is little digression from the main topic of NLO. Since most of device application NLO materials are anisotropic crystals, therefore it is pertinent to provide some description of wave propagation properties, particularly the birefringence property exhibited by them. It will help understand techniques of achieving phase matching and related issues.

With respect to optical properties, the crystal anisotropy refers to different dielectric permittivity for different crystallographic orientation. For non-absorbing crystals, the elements of permittivity tensor are real and can be made diagonal along the principal axes of the dielectric tensor. In general, for anisotropic crystals

$$D_i = \epsilon_{ij} E_j \quad \text{where} \quad \epsilon_{ij} = \begin{pmatrix} \epsilon_{xx} & 0 & 0 \\ 0 & \epsilon_{yy} & 0 \\ 0 & 0 & \epsilon_{zz} \end{pmatrix} \quad (2.39)$$

$$\epsilon_{ii} = \epsilon_0 (1 + \chi_{ii}^0) \equiv \epsilon_0 n_{ii}^2, \quad i = x, y, z$$

Crystals in which all the diagonal elements of  $\epsilon_{ii}$  are equal are cubic symmetry crystals. If  $\epsilon_{xx} = \epsilon_{yy} \neq \epsilon_{zz}$ , i.e., two independent components, then crystal is uniaxial. Examples are crystals with hexagonal, tetragonal, and trigonal point group symmetry. If  $\epsilon_{xx} \neq \epsilon_{yy} \neq \epsilon_{zz}$ , i.e., all the three elements are independent, then crystal is biaxial. Examples are crystals with orthorhombic, monoclinic, and triclinic point group symmetry. Then all crystals with symmetries lower than cubic will exhibit birefringence property. The axis of highest symmetry is taken as c-axis or z-axis and referred to as optic axis. For a wave propagating at an angle  $\theta$  to the optic axis, the

two orthogonal states of polarization will exhibit two different phase velocities. This difference in phase velocity is the origin of birefringence in anisotropic materials. A wave which remains polarized perpendicular to optic axis for any propagation direction is ordinary wave (o-wave) with refractive index  $n_o$ . A wave which remains polarized in the plane of optic axis and propagation vector is extraordinary wave (e-wave) with refractive index  $n_e(\theta)$ . For extraordinary wave, the polarization vector is perpendicular or parallel to the optic axis when  $\theta$  is 0 or 90°, respectively. In the case of uniaxial crystals, there is only one optic axis and we define  $n_{xx} = n_{yy} = n_0$  and  $n_{zz} = n_e$ , where  $n_e$  is the extraordinary wave refractive index when  $\theta = 90$ , i.e., its polarization vector is parallel to the optic axis. Birefringence of crystal is defined as  $\Delta n = n_e - n_0$ , when  $n_e > n_0$  crystal is positive uniaxial, and when  $n_e < n_0$ , it is negative uniaxial.

As far as how birefringence property of anisotropic crystals can help in phase matching is concerned, it is important to note that for a wave propagating in arbitrary direction, the wave vector  $\mathbf{k}$ , because of different phase velocities, can have different magnitudes for different polarizations. This allows phase matching of interacting waves at different frequencies. Also, the displacement vector ( $\mathbf{D}$ ) will remain proportional but need not be parallel to electric field vector ( $\mathbf{E}$ ), which also implies that the direction of energy flow, the Poynting vector  $\mathbf{S}$ , also need not be in the direction of wave propagation. For example, when  $\theta = 0$ , phase velocities of o- and e-wave are equal ( $c/n_0 = c/n_e$ ) and  $\mathbf{S} \parallel \mathbf{k}$ . When  $\theta = 90$ ,  $\mathbf{S} \parallel \mathbf{k}$ , but phase velocities are not equal ( $c/n_0 \neq c/n_e$ ). For all other propagation directions,  $\mathbf{S} \nparallel \mathbf{k}$  for e-wave which suggests how e-wave walks away from initial direction of wave propagation and leads to double refraction.

To determine the magnitude of wave vector for e-wave for different directions of beam propagation and also the  $n_e(\theta)$ , we first need to obtain dispersion relation for e-wave. By solving wave equation with constitutive relation as defined in Eq. (2.39), the solution of wave equation leads to two dispersion relations [14]. It suggests that anisotropic medium can support propagation of two independent waves. In k-space, one of the dispersion relations describes an equation of a sphere for o-wave and whose radius is proportional to refractive index  $n_0$ . The second dispersion relation describes an equation of an ellipsoid for e-wave whose semimajor and semiminor axes are proportional to  $n_o$  and  $n_e$ . For a given direction of propagation  $\theta$ , the value of  $n_e(\theta)$  for uniaxial crystals varies between  $n_o$  and  $n_e$  [14], as given by Eq. (2.40):

$$\frac{1}{n_e^2(\theta)} = \frac{\cos^2(\theta)}{n_0^2} + \frac{\sin^2(\theta)}{n_e^2} \quad (2.40)$$

Graphical representation of two refractive indices as a function  $\theta$  for uniaxial crystals and for a fixed frequency is shown in Fig. 2.3.

In the rest of the section, we will consider some standard NLO processes often encountered in laser technology development.

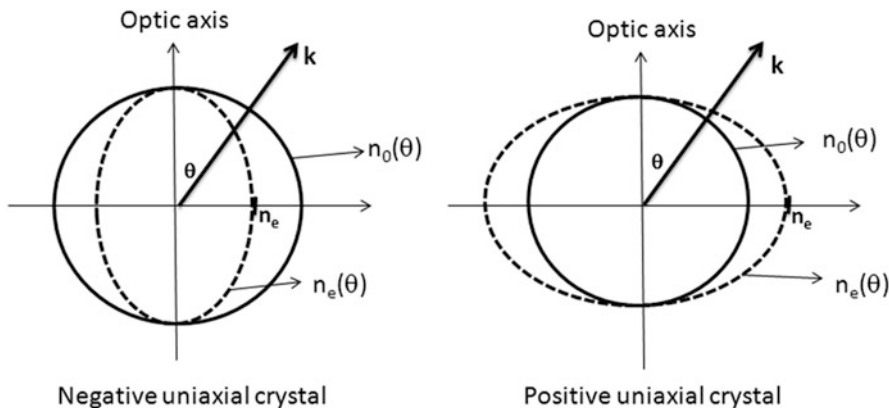


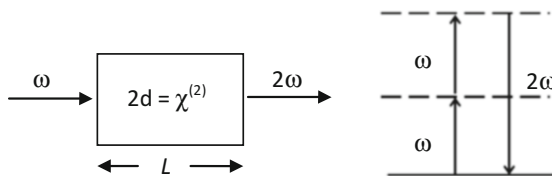
**Fig. 2.3** Graphical representation of refractive index surfaces for o-ray and e-ray in negative ( $n_e < n_o$ ) and positive ( $n_e > n_o$ ) uniaxial crystals

## 2.8 Second Harmonic Generation

This particular process is widely employed in the development of laser technology as frequency doubler. For example, one can generate coherent radiation at 532 nm when 1.06  $\mu\text{m}$  infrared beam of Nd:YAG laser is passed through suitably cut and oriented crystal of KDP. We will discuss techniques of achieving phase matching, some practical issues of SH generation, and factors affecting SHG efficiency.

We have already derived coupled wave equations for SFG in the previous section. Those equations can be easily converted for SHG when we replace  $k_1 = k_2 = k(\omega)$ ,  $k_3 = k(2\omega)$  and  $\omega_1 = \omega_2 = \omega$  and  $\omega_3 = 2\omega$ . Then from Eq. (2.36)

$$I(2\omega) = \frac{512\pi^3 d^2 \omega^2 I^2(\omega) L^2}{n^2(\omega) n(2\omega) c^3} \operatorname{sinc}^2\left(\frac{\Delta k L}{2}\right) \quad (2.41)$$



The efficiency  $\eta = I(2\omega)/I(\omega)$  of SHG process will be maximum when perfect phase matching condition  $\Delta k L/2 = 0$  is achieved.

### 2.8.1 Phase Matching and Related Issues

$\Delta k = 0$  condition also implies  $k(2\omega) = 2k(\omega)$ , i.e., the phase of generated  $2\omega$  wave follows exactly with the phase of its source, the induced nonlinear polarization. In terms of material aspect, it demands that the chosen NLO material must satisfy the condition  $n(2\omega) = n(\omega)$ , i.e., refractive index for both the frequencies  $\omega$  and  $2\omega$  should be the same. This is difficult to achieve in normal dispersive crystals, and one therefore exploits the birefringence property of anisotropic crystals to compensate for dispersion. As discussed in the previous section on crystal anisotropy, for e-ray, refractive index depends upon beam propagation direction. Therefore, for a given crystal type and beam propagation angle, appropriate polarizations of  $\omega$  and  $2\omega$  beam can be chosen such that  $n(2\omega) = n(\omega)$ . As an example, we consider negative uniaxial KDP crystal such that  $n_e(2\omega, \theta_m) = n_0(\omega)$ . The graphical representation of refractive index surfaces for  $\omega$  and  $2\omega$  beam is shown in Fig. 2.4a. The phase matching angle in this case is  $\theta_m$  where two refractive index surfaces of o-ray and e-ray for  $\omega$  and  $2\omega$  beam, respectively, intersect each other. In case of positive uniaxial crystal, the choice of beam polarization will reverse for  $\omega$  and  $2\omega$  such that  $n_e(\omega, \theta_m) = n_0(2\omega)$ . The graphical representation of intersecting refractive index surfaces of positive uniaxial crystal is shown in Fig. 2.4b. Therefore, based on the choice of beam polarizations, there are type I and type II phase matching situations. In type I, as described above,  $\omega$  beam will have single polarization and  $2\omega$  beam will be of orthogonal polarization, while in type II phase matching, the  $\omega$  beam is chosen to have both ordinary and extraordinary components and  $2\omega$  beam can be o-ray or e-ray for positive or negative uniaxial crystal, respectively.

The above-described angle-tuning phase matching is also termed as critical phase matching because the useful crystal length and SHG efficiency is limited due to beam walk-off and less tolerance over beam divergence (acceptance angle). Since for e-ray when  $0 < \theta < 90^\circ$ ,  $S \nparallel k$ , therefore after traveling some distance, the

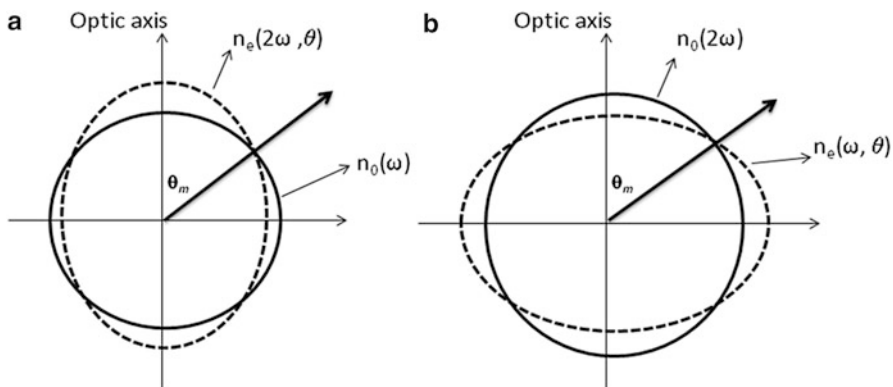


**Fig. 2.4** Angle-tuning type I phase matching of SHG in (a) negative and (b) positive uniaxial crystal

interacting  $\omega$  and  $2\omega$  beam (whichever is chosen as e-ray) will walk away from propagation direction and get spatially separated with o-ray. To avoid spatial beam walk-off, one may choose  $\theta = 90^\circ$  (where  $S \parallel k$  for e-ray), but still due to finite birefringence, the condition of  $n(2\omega) = n(\omega)$  is yet to be achieved. To compensate the difference in refractive index of  $\omega$  and  $2\omega$  beam, the temperature of crystal is adjusted to achieve  $n_e(\omega, T) = n_o(2\omega, T)$ . This is possible due to unequal temperature dependence of  $n_e$  and  $n_o$ . Phase matching achieved at  $\theta = 90^\circ$  is also termed as noncritical phase matching because it not only allows nonlinear interaction over large crystal length due to no beam walk-off effect but also offers larger tolerance over acceptance angle.

In some situations where d-coefficients of a crystal are large, it cannot be exploited for efficient SHG either due to very low or no birefringence. In such cases, phase matching is not possible and useful crystal length is limited to one coherence length  $l_c = \pi/|\Delta k|$ . To exploit large nonlinearity, one therefore adopts the technique of quasi phase matching (QPM) [4, 13, 17].

### 2.8.2 Some Practical Considerations of SHG

Equation (2.41) suggests that SHG efficiency would continue to increase with crystal length (as  $L^2$ ) and with input laser intensity without any saturation. This is unphysical because while deriving Eq. (2.41), we ignored pump beam depletion and assumed plane wave approximation. In practice, for efficient systems, pump depletion cannot be ignored and coupled wave equations should be solved with pump depletion. The SHG efficiency when pump depletion is taken into account is [1, 4, 6]

$$\eta = \tanh^2 \left( \frac{512 \pi^2 \omega^2 d^2 I(\omega) L^2}{n^2(\omega) n(2\omega) c^3} \operatorname{sinc}^2 \left( \frac{\Delta k L}{2} \right) \right)^{\frac{1}{2}}$$

Under perfect phase matching condition,

$$\eta = \tanh^2 \left( \frac{L}{L_{\text{SH}}} \right)$$

where  $L_{\text{SH}} = \left( \frac{n^2(\omega) n(2\omega) c^3}{512 \pi^2 \omega^2 d^2 I(\omega)} \right)^{\frac{1}{2}}$  is defined as interaction length for SHG, i.e., the length over which  $\sim 70\%$  conversion takes place and which depends inversely on the fundamental input beam field amplitude.

In addition, SHG efficiency is limited further by the fact that laser beam intensity profile of practical lasers is primarily Gaussian in nature. Suitable focusing geometries with respect to laser beam Rayleigh range and crystal length are optimized to maximize the efficiency [4, 8]. These practical issues then decide an optimum

**Table 2.1** Phase matching properties of few widely used crystals for 1,064 to 532 nm conversion

	Crystal				
	KDP	KTP <sup>a</sup>	BBO	LBO <sup>a</sup>	LiNbO <sub>3</sub> <sup>b</sup>
Phase matching parameters					
Type	I	II	I	I	I
Angle [°]	41.2	24.3	22.8	11	90
Temperature [°C]	25	25	25	25	107
Efficiency parameters					
Eff. nonlinear coefficient	0.37	3.18	1.94	1.16	4.7
$d_{\text{eff}}$ [pm/V]					
External angular sensitivity	1.73	0.35	6.6	0.65	0.12
$\beta_{\theta}/n_0[(\text{mrad cm})^{-1}]$					
Walk-off angle[°]	1.60	0.26	3.19	0.35	0
Bandwidth (FWHM)					
Angular $L\Delta\theta$ [mr cm]	3.2	15.9	0.84	8.5	46.3
Thermal $L\Delta T$ [°C cm]	6.7	25	55	8.4	0.7
Spectral $L\Delta\lambda$ [nm cm]	0.66	0.56	0.66	0.75	0.23
Material parameters					
Refractive index $n_o$	1.49	1.74, 1.75	1.65	1.56, 1.56	2.23
$n_e$	1.46	1.84	1.54	1.61	2.15
Absorption [%/cm]	0.5	0.5	0.5	0.5	0.2
Damage threshold [GW/cm <sup>2</sup> ]	8	1	1.5	2.5	0.2

From Ref. [18]

<sup>a</sup>Biaxial crystal<sup>b</sup>Doped with 5 % MgO

crystal length and SHG efficiency. Several NLO crystals are routinely used for SHG which provide single pass efficiency as high as 70–80 %. The choice of crystals and SHG efficiency also depends on other considerations like transparency range at chosen  $\omega$  and  $2\omega$ , damage threshold, high nonlinearity together with phase matching possibility, mechanical hardness, chemical and thermal stability, etc. Properties of few widely used crystals for generating SH of Nd:YAG laser output are shown in Table 2.1.

When dealing with SHG of ultrashort picoseconds and femtosecond duration laser pulses, some additional propagation effects that set limit on the useful crystal length need special attention. Due to large spectral bandwidth associated with these pulses, two major effects which set limit on the useful crystal length are spectral acceptance bandwidth and temporal beam walk-off. Due to frequency dependence of phase matching angle, the complete spectrum of ultrashort pulses cannot be simultaneously phase matched. This results in broadening of SH pulse width in time which is proportional to the crystal length. In addition, the peak power of the SH that can be generated by a fixed incident intensity is also limited. Temporal beam walk-off arises from the mismatch in the group velocity of interacting  $\omega$  and  $2\omega$  pulses. It is quantified as pulse-splitting length which, for two collinearly

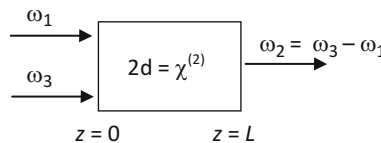
propagating pulses, is defined as the distance after which they separate by a path equal to their pulse width. It is given by

$$l^* = \Delta\tau \left( \frac{1}{v_g(\omega)} - \frac{1}{v_g(2\omega)} \right)^{-1}$$

where  $\Delta\tau$  is the full width at half maximum pulse width and  $v_g = \frac{d\omega}{dk}$  is the group velocity. From above equation, it is clear that the effects of temporal beam walk-off are more pronounced with shorter pulse and larger mismatch in the group velocities. For example, when 100 fs pulses from Ti:sapphire laser are used for SHG in KTP, the pulse-splitting length is  $\sim 2$  mm. Therefore, to avoid effects due to spectral acceptance bandwidth and temporal beam walk-off, the useful crystal length is kept small to  $\sim$ few mm or less [17].

## 2.9 Difference Frequency Generation and Optical Parametric Amplifier/Oscillator

Apart from generating higher frequency coherent radiations using SFG or SHG, the second-order nonlinear polarization can also generate coherent radiations at much lower frequency range via difference frequency generation process,  $\omega_3 = \omega_1 - \omega_2$ . From the applications point of view, the DFG process is responsible not only for generating FIR or THz radiation source but it can also be used for generating widely tunable radiation sources. To understand the same, we will first show how a weak input signal (as one of the input beams) can be amplified when coupled in a nonlinear medium with strong beam of higher frequency.



Let  $\omega_3$  be a strong beam (i.e., undepleted pump beam) and  $\omega_1$  as weak signal beam interacting in nonlinear medium to produce output at  $\omega_2$ . The coupled wave equation formalism for DFG process is identical to what we derived for SFG. We consider coupled wave equation as in Eqs. (2.34) and (2.35)

$\frac{dA_3}{dz} = 0$ , since  $A_3$  is assumed constant (undepleted pump beam):

$$\frac{dA_1}{dz} = \frac{8\pi i d\omega_1^2}{k_1 c^2} A_3 A_2^* e^{-i(\Delta k)z}$$

$$\frac{dA_2}{dz} = \frac{8\pi i d\omega_2^2}{k_2 c^2} A_3 A_1^* e^{-i(\Delta k)z}$$

We solve for perfect phase matching condition,  $\Delta k = 0$ :

$$\frac{d^2 A_2}{dz^2} = \frac{64 \pi^2 \omega_1^2 \omega_2^2 d^2}{k_1 k_2 c^4} A_3 A_3^* A_2 = \beta^2 A_2 \quad (2.42)$$

where

$$\beta^2 = \frac{64 \pi^2 \omega_1^2 \omega_2^2 d^2 |A_3|^2}{k_1 k_2 c^4} \quad (2.43)$$

General solution for Eq. (2.42) is

$$A_1(z) = A \sinh \beta z + B \cosh \beta z$$

Similarly

$$A_2(z) = C \sinh \beta z + D \cosh \beta z$$

Using initial conditions,  $A_2(0) = 0$  and  $A_1(0) = A_1$  are arbitrary

$$A_1(z) = A_1(0) \cosh \beta z$$

$$A_2(z) = i \left( \frac{n_1 \omega_2}{n_2 \omega_1} \right)^{\frac{1}{2}} \frac{A_3}{|A_3|} A_1^*(0) \sinh \beta z$$

The graphical representation field amplitude at  $\omega_1$  and  $\omega_2$  as a function of  $z$  is shown in Fig. 2.5. It shows how these field amplitudes grow with  $z$ . We also note that  $A_1(z)$  is amplified whose phase remains the same, while  $\omega_2$  beam is generated and whose phase depends on the phase of  $\omega_3$  and  $\omega_1$ .

This process of amplification of weak signal beam via DFG process is known as optical parametric amplification (OPA) process. The gain coefficient for amplification is  $\beta$ , as defined in Eq. (2.43), and is proportional to nonlinear d-coefficient and field strength of pump beam. In the context of parametric amplification, the strong  $\omega_3$  beam is referred to as pump beam ( $\omega_p$ ), weak  $\omega_1$  beam as signal beam

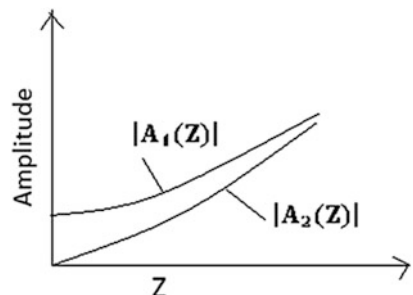


**Fig. 2.5** Spatial evolution of field amplitudes  $A_1$  and  $A_2$  for difference frequency generation for the case  $\Delta k = 0$  in the no pump depletion approximation

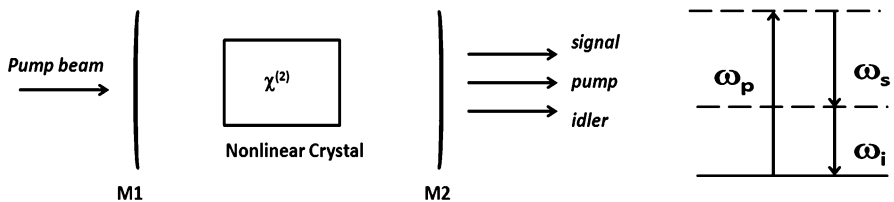


**Fig. 2.6** Schematic of an optical parametric oscillator (OPO) and electronic transitions leading to generation of signal and idler beam

( $\omega_s$ ), and the generated  $\omega_2$  as idler beam ( $\omega_i$ ). It is interesting to compare OPA with conventional laser amplifier. The major difference lies in the fact that OPA is purely a parametric process, and the amplification is by means of energy transfer from strong pump beam to signal beam mediated by medium's nonlinearity, while in laser amplifier, the amplification is via the extraction of stored energy in the gain media.

The frequency relationship of interacting beams in DFG or OPA process can be rewritten as  $\omega_p = \omega_s + \omega_i$ . This suggests that a single beam of high photon energy can be split into two low-energy photon beams of variable frequency. The combination of  $\omega_s$  and  $\omega_i$  can be anything as long as their sum equals  $\omega_p$ . This process is equivalent to OPA except that there is no externally supplied weak signal beam. With single input beam to initiate DFG process, and to convert OPA into an optical parametric oscillator (OPO), we place nonlinear crystal inside a resonator cavity as shown in Fig. 2.6. Inside the resonator, the weak signal beam is created from noise as in conventional laser oscillator. The source of noise in this case is spontaneous parametric fluorescence due to  $\omega_p$  beam. Resonator mirrors are dichroic cavity mirrors which transmit at the pump frequency and reflect at the signal frequency or at the signal and idler frequencies. In the former case, the OPO is a singly resonant OPO (SRO), and in the latter case, it is a doubly resonant OPO (DRO). The threshold for the SRO is much higher than that for the DRO.

The possible pair of frequencies as signal or idler beam that can be amplified is decided by phase matching condition  $n_p\omega_p = n_s\omega_s + n_i\omega_i$  together with the condition that feedback is provided by the cavity. Tuning of the oscillator can be achieved either by simply rotating the crystal relative to the direction of propagation of the pump beam or by setting appropriate temperature of the crystal. Once the angle or temperature is changed, a new pair of  $\omega_s$  and  $\omega_i$  from the noise gets amplified. The range over which  $\omega_s$  and  $\omega_i$  can be tuned is limited by transparency range of crystals and phase matching condition. As an example of the spectral range that can be covered by the OPO, Fig. 2.7 shows typical wavelength coverage using some widely used crystals. The OPO-based system therefore provides a truly continuously tunable powerful solid-state source of coherent radiation over wide spectral range.

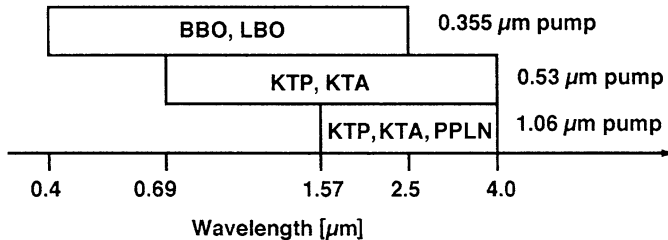


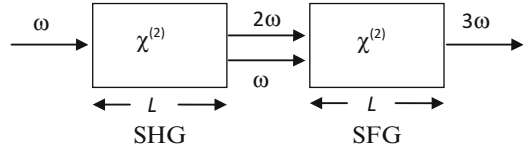
**Fig. 2.7** Typical wavelength tuning range obtainable from Nd:YAG laser-pumped OPO systems (From Ref. [18])

## 2.10 Third Harmonic Generation (THG) in Crystals and Atomic Vapors

Similar to second order, the third-order nonlinear process can be exploited for the frequency conversion. For example, one can generate coherent radiation at 355 nm when 1.06  $\mu\text{m}$  infrared beam of Nd:YAG laser is passed through suitably cut and oriented crystal of BBO. The third-order susceptibility responsible for THG is  $\chi^{(3)}(3\omega; \omega, \omega, \omega)$ . Since  $\chi^{(3)} \ll \chi^{(2)} \ll \chi^{(1)}$ , the third-order effects are generally very weak leading to low efficiency of THG. In addition, stringent phase matching condition (large birefringence needed to compensate difference of  $n(3\omega)$  and  $n(\omega)$ ), optical damage, and desirable transparency range narrow down the choice of crystals which can be used for direct THG. Therefore, in practice, direct  $\omega$  to  $3\omega$  frequency conversion is rarely employed. Instead one utilizes stronger second-order effects to generate  $3\omega$  from  $\omega$ . As shown in Fig. 2.8, how two-stage THG is achieved using two second-order processes, namely, SHG ( $\omega + \omega = 2\omega$ ) followed by SFG ( $\omega + 2\omega = 3\omega$ ). The input to second stage of SFG is provided from the output of SHG, the generated  $2\omega$  and unused  $\omega$  beam. To have sufficient intensity of  $\omega$  beam for SFG process and for nearly 100 % overall conversion of  $\omega$  to  $3\omega$ , the efficiency of SHG process is intentionally kept  $\sim 67\%$ . In practical devices based on two-stage second-order effects, nearly 70–80 % conversion efficiencies are routinely obtained.

However, the third-order susceptibility is not sensitive to inversion symmetry and can be observed in gases and atomic vapors as well. In particular, in the vacuum uv spectral region where transparent crystals are not available, atomic nonlinear media (e.g., alkali metal vapor) play an important part for producing coherent radiation sources. Phase matching for  $\omega$  to  $3\omega$  conversion in isotropic atomic vapors is still an issue, and it is achieved with the help of resonance effect. Since atoms have sharp resonances, one can approach quite close to the resonance without encountering significant absorption [5]. It is therefore possible to enhance the third-order nonlinearity by resonance enhancement and also achieve phase matching. Sharpness of atomic absorption lines also means that one has large windows of

**Fig. 2.8** Two-step second-order processes to generate third harmonic of  $\omega$



transparency in which the dispersion can be either positive or negative. For some frequencies, e.g., when atomic levels are close to, e.g.,  $\sim 2\hbar\omega$ , the anomalous dispersion allows to compensate normal dispersion between  $\omega$  and  $3\omega$  beams [5, 6]. Very often, for fine tuning, atomic vapors are mixed with a buffer gas (mostly noble gases which are transparent over frequencies of interest) to modify the refractive index [5, 6].

## 2.11 Nonlinear Refraction and Absorption

These are third-order processes described in terms of an intensity-dependent modification of the dielectric function. For example, consider nonlinear source polarization at frequency  $\omega_a$  created by the interaction of two waves with frequencies  $\omega_a$  and  $\omega_b$ :

$$\begin{aligned} P_i^{(3)}(\omega_a) &= \chi_{ijjl}^{(3)}(\omega_a; \omega_b, -\omega_b, \omega_a) E_j(\omega_b) E_j^*(\omega_b) E_l(\omega_a) \\ &= \chi_{ijjl}^{(3)}(\omega_a; \omega_b, -\omega_b, \omega_a) |E_j(\omega_b)|^2 E_l(\omega_a) \end{aligned} \quad (2.44)$$

By solving wave equation for  $E(\omega_a)$  with this source polarization, the effect is equivalent to an intensity-dependent contribution  $\Delta\varepsilon$  to the dielectric constant  $\varepsilon$ :

$$\Delta\varepsilon \propto \chi_{ijjl}^{(3)}(\omega_a; \omega_b, -\omega_b, \omega_a) I(\omega_b) \quad (2.45)$$

where  $I(\omega_b)$  is the intensity of the wave at  $\omega_b$ . Thus we find that beam propagation property of  $\omega_a$  is modified by the presence of the laser beam at  $\omega_b$  and the modification is proportional to the intensity at  $\omega_b$ . Even if only one beam is incident such that  $\omega_a = \omega_b = \omega$ , then it will experience self-action effect in terms of refraction and absorption.

### 2.11.1 Nonlinear Refraction

To understand refraction effect, consider

$$n = \sqrt{\epsilon} = \sqrt{\epsilon_r + \Delta\varepsilon} \quad (2.46)$$

where  $\epsilon_r = n^2_0$  is the real part of dielectric constant of the medium at low intensity. Assuming  $\Delta\epsilon \ll \epsilon_r$ , we obtain

$$\begin{aligned} n &\approx \sqrt{\epsilon_r} + \frac{\Delta\epsilon}{2\sqrt{\epsilon_r}} = n_0 + \Delta n \\ n &= n_0 + \frac{12\pi^2\chi^{(3)}}{n_0^2 c} I, \\ n &= n_0 + n_2 I \end{aligned} \quad (2.47)$$

where we define  $n_2 = 12\pi^2\chi^{(3)}/n_0^2 c$  (in CGS units) as nonlinear refractive index. Equation (2.47) provides direct relationship between the modified refractive index of the medium and incident laser intensity. This effect of change of refractive index with intensity is known as optical Kerr effect, and the susceptibility causing this effect is the real part of  $\chi^{(3)}(\omega; \omega, -\omega, \omega)$ . One very important consequence of intensity-dependent refractive index is that depending upon the spatial profile, an intense laser beam may self-focus or defocus in a homogeneous medium. Consider a real laser beam of finite diameter whose intensity profile can be taken as Gaussian,  $I(r) = I_{\max} \exp(-r^2/2a^2)$ . The medium refractive index, due to the intensity-dependent part as in Eq. (2.47), would also resemble the same Gaussian profile, i.e., the index of refraction is highest on the beam axis. The laser beam therefore has produced its own lens-like medium, and as a consequence, the laser beam may get self-focused (when  $n_2 > 0$ ) or defocused (when  $n_2 < 0$ ). When self-focusing effect is just compensated by the natural defocusing effect due to diffraction, the result is self-trapping of light beam with constant beam diameter throughout the nonlinear medium. This occurs for a critical power in the beam [1, 4, 6]. When intensity profile is inhomogeneous, such as random occurrence of intense spikes overriding on the Gaussian intensity profile, the generation of trapped filaments of light beam is observed [6]. Very often, due to large nonlinearity of optical components and other medium and laser power being more than the critical power, the laser beam gets focused at a very short focal length. The sudden increase in laser intensity in the medium would then allow multitude of NLO effects to occur simultaneously in the medium. Sudden rise in intensity is also the cause of catastrophic material damage. Therefore, the self-focusing effect and subsequent filamentation of intense laser beams play an important role in the propagation of high-power laser beam in materials [4, 7, 18].

One of the important applications of optical Kerr effect in laser development is Kerr lens mode locking (KLM). This has led to the generation of ultrashort mode-locked laser pulses from Ti:sapphire laser gain medium. This can be understood as follows [17, 18]. For a Gaussian beam profile, the intensity-dependent modification of refractive index produces an index profile in the gain medium causing the beam to self-focus. Inside a laser, this intensity-dependent self-focusing produces an intensity-dependent modification to the beam propagation as it passes around the cavity. By introducing an aperture or slit at another intracavity focus to select the

self-focused cavity mode, it is possible to force the laser into a short pulse mode. The role of aperture or slit in the cavity is to filter out or suppress low-intensity modes and allow intense self-focused light to get amplified in the oscillator cavity.

Another useful consequence of Kerr effect is self-phase modulation (SPM) of laser beam and related spectral broadening. Kerr effect in general would introduce space as well as time-dependent changes in the refractive index, i.e.,

$$n(r, t) = n_0 + n_2 I(r, t)$$

If laser pulse intensity is nonuniform in time domain, such as Gaussian, then different parts of the pulse would experience different additional nonlinear phase shifts:

$$\phi_{nl}(t) = \frac{2\pi}{\lambda} n_2 I(t) L$$

where  $L$  is the length of the medium. A change of phase in time means a carrier frequency deviation:

$$\delta\omega(t) = \frac{\partial\phi}{\partial t} = -\frac{2\pi}{\lambda} n_2 \frac{\partial I(t)}{\partial t} L$$

The above equation suggests that pulse has acquired a frequency modulation, i.e., *chirp*. Since pulse leading and trailing edges have opposite  $\partial I(t)/\partial t$  slope, the leading edge will redshift and trailing edge will blueshift, while the peak of the pulse will experience no shift (since slope is zero). The spectral bandwidth of incident laser pulse then undergoes spectral broadening. This effect is very dominant with ultrashort laser pulses (where  $\partial I(t)/\partial t$  slope is very large) and also in optical fiber media due to long interaction length and sufficient power confinement. An application of SPM is in developing super-continuum laser sources [20].

### 2.11.2 Nonlinear Absorption

The other well-known effect described by nonlinear source polarization, defined in Eq. (2.44), is two-photon absorption (TPA). The TPA process is simultaneous absorption of two photons of either the same or different energies. The process is a resonant excitation process such that the sum of photon energies is equal to medium excitation energy. Schematic diagram of TPA process is shown in Fig. 2.9a. The third-order nonlinearity causing TPA is positive imaginary part of  $\chi^{(3)}(\omega; \omega, -\omega, \omega)$ . The selection rule for transition involved in TPA process is always between states of the same parity, which is opposite to that in single-photon absorption process. Hence, TPA spectroscopy complements linear absorption spectroscopy in studying the excited states of material system. The absorption in the

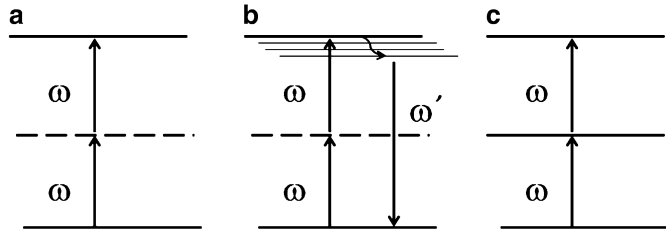


**Fig. 2.9** Schematic diagram of transition involved in (a) TPA process; the transition is between real excitation levels, while intermediate level is virtual level. (b) Two-photon-induced fluorescence process where  $\omega' > \omega$ . (c) The process of two-step resonant absorption with real intermediate level

case of TPA is nonlinear as it is proportional to the square of the instantaneous intensity. When single laser beam is used, the loss of intensity due to both linear and two-photon absorptions can be written as

$$\frac{dI}{dz} = -\alpha I - \beta I^2 \quad (2.48)$$

where  $\alpha$  and  $\beta$  are linear and two-photon absorption coefficients, respectively. By solving Eq. (2.48) for medium transmittance with the assumption that  $\alpha$  is very small (negligible linear absorption by the medium at the laser wavelength), we get

$$T = \frac{1}{1 + \beta I_{in} L}$$

where  $I_{in}$  is the input laser intensity and  $L$  is the medium length. The above equation suggests that transmittance of the medium will continue to decrease with increase of laser intensity. Several applications of materials exhibiting strong TPA in laser and laser component development have been demonstrated, and these include pulse shaping, optical limiting, pulse compression, etc. [7, 19]. Several materials also exhibit TPA-induced light emission. Basic idea here is that after transition to excited state via TPA, the excited state may relax to ground state via radiative transition as shown in Fig. 2.9b. This is up-conversion of light frequency where photon energy of emitted light is higher than the input laser used for excitation. The nature of emitted light is the same as what one would observe with linear one-photon absorption. The intensity of emitted light, due to TPA, will depend nonlinearly on excitation light intensity. Since there is no linear absorption at exciting laser wavelength, long interaction length like optical waveguide, optical fibers, etc., can be utilized for low-threshold up-conversion lasers [7, 19].

The process of TPA should be distinguished from two-step nonlinear absorption process as described in Fig. 2.9c. Here two consecutive single-photon resonant transitions are involved. The effect due to excited state absorption would occur only with some finite linear absorption in the ground state. Depending upon the

strength of absorption cross sections of ground and excited states (let us define them as  $\sigma_1$  and  $\sigma_2$ , respectively), two different nonlinear absorption effects can occur. When  $\sigma_2/\sigma_1 < 1$ , the effect is saturable absorption (SA). Due to strong ground state absorption, material may be almost opaque at low intensity and has become transparent as light intensity is increased. Applications of SA are well known in laser technology as passive elements for  $Q$ -switching and mode locking [18, 19]. When  $\sigma_2/\sigma_1 > 1$ , the effect is reverse saturable absorption (RSA) leading to decreasing transmittance of the material system as light intensity is increased. Applications of RSA are well known in optical limiting, pulse shaping, etc. [7, 19].

## 2.12 Stimulated Raman and Brillouin Scattering

### 2.12.1 *Stimulated Raman Scattering*

Raman scattering is an inelastic scattering of light with vibrational phonon modes of the medium. Scattered light frequency can be smaller (Stokes frequency) or larger (anti-Stokes frequency) than the excitation light frequency. The difference between frequencies of Stokes or anti-Stokes light and excitation light is the excitation frequency (often vibrational or rotational modes but could be electronic as well) of the medium. This scattering process is spontaneous with very small scattering cross section. The process can be stimulated when a strong (pump) wave with frequency  $\omega_p$  and a weak Stokes-shifted (redshifted) wave with frequency  $\omega_s = \omega_p - \Delta\omega$  propagate in the nonlinear medium. The Stokes wave can experience exponential gain if the frequency difference  $\Delta\omega$  corresponds to, e.g., the frequency of medium molecular vibrations. The gain in stimulated Raman scattering (SRS) process can in fact be described on the basis of parametric amplification as discussed earlier in DFG, the only difference being that the idler wave now is a material wave (i.e., molecular vibrational mode), while signal is Stokes frequency. The Stokes beam is amplified by the pump beam via idler beam:

$$I_s(z) = I_s(0) \exp[G(\omega_s)z]$$

where  $I_s$  is Stokes wave intensity,  $z$  is the distance, and  $G(\omega_s)$  is the Raman gain coefficient which is proportional to Raman susceptibility and the pump laser intensity. Raman susceptibility is negative imaginary part of  $\chi^{(3)}(\omega_s; \omega_s, -\omega_L, \omega_L)$ . The phase matching condition is automatically satisfied. The scattered output is in the form of a narrow cone in forward and backward directions.

Due to coupling of Stokes and anti-Stokes components of scattered light in the nonlinear medium, it is possible that both the components experience gain at the expense of power of the pump beam. In that case, several higher orders of Stokes and anti-Stokes components are generated, which leads to spectral broadening of incident laser beam. Depending upon the material chosen (with specific frequency of vibrational mode and high-gain coefficient), coherent radiation source

at Raman-shifted frequencies can be obtained with the help of suitable resonator (Raman laser). Typical values of pump intensities needed for SRS gain are normally small and can be easily estimated, e.g., for benzene (with vibrational frequency  $992\text{ cm}^{-1}$ ),  $G = 2.8 \times 10^{-3}\text{ cm/MW}$ . Thus, to generate  $e^{30}$  Raman photons from one noise photon in a 10 cm benzene cell requires a laser beam of  $1\text{ GW/cm}^2$  intensity. This can easily be achieved by focusing the high-peak-power pulses into Raman medium. Pump beam has to have good spectral coherence, so that it can be focused into a very small spot leading to high intensities.

### 2.12.2 Stimulated Brillouin Scattering

Brillouin scattering represents the scattering of light by acoustic phonons. In this process, a very small part of photon energy is transferred to the phonon which leads to very small frequency shift of pump wave. The main distinction with SRS is the difference in dispersion characteristics of acoustical and optical phonon branch. When the relationship  $\omega_{\text{ac}} = k_{\text{ac}} v_{\text{ac}}$  is used for acoustic phonon, the energy and momentum conservation conditions  $k_B = k_L - k_{\text{ac}}$ ,  $\omega_B = \omega_L - \omega_{\text{ac}}$  require that the frequency of Brillouin-scattered light varies with the angle of scattering  $\theta$ , i.e.,

$$\omega_B = 2\omega_L \left( \frac{n v_{\text{ac}}}{c} \right) \sin(\theta/2)$$

Due to  $\omega_{\text{ac}} \ll \omega_L$  and  $\omega_B$ , we made assumption that  $\omega_B \approx \omega_L$ . When  $\theta = \pi$ , the directions of scattered light and pump laser are opposite, and frequency shift  $\omega_B$  will be maximum, while for forward scattering the frequency shift approaches zero. Therefore, in most materials, the SBS-scattered light always emerges in direction opposite to the pump direction (the backward direction). The threshold for SBS is also minimum when  $\theta = \pi$ .

Apart from SBS as amplifying medium, the prominent application of SBS is in optical phase conjugation, pulse compression, etc. [4, 11, 18].

When laser intensity is sufficiently high and/or nonlinearity of the medium is large, several nonlinear processes can operate at the same time in the medium. As mentioned earlier, the influence of unavoidable self-focusing may increase the laser intensity in the medium and initiate, e.g., SRS at much lower threshold than expected. The influence of self-focusing in SRS and SBS is well known [1, 2, 4, 18, 19].

## 2.13 Conclusion

In this chapter, a brief account of the basics of NLO is provided along with an introduction to some important NLO process/effects that one often come across while pursuing research on laser physics and technology. For further details on these

topics and for the discussion of several other topics not covered in this chapter, the interested researcher may refer to a large number of excellent reviews and books on NLO provided as references.

**Acknowledgment** I wish to thank Dr. P. K. Gupta, Director of Laser School, for giving me opportunity to deliver lectures at Laser School and for valuable suggestions. I also thank Dr. S. C. Mehendale and Dr. S. K. Dixit for valuable suggestions and critical reading of the manuscript.

## References

1. N. Bloembergen, *Nonlinear Optics* (Benjamin, New York, 1964)
2. N. Bloembergen, *Encounters in Nonlinear Optics: Selected Papers of Nicolaas Bloembergen, with Commentary*. World Scientific Series, vol. 16 (World Scientific Publishing Co Pte Ltd, Singapore, 1996)
3. P.N. Butcher, D. Cotter, *Elements of Nonlinear Optics* (Cambridge University Press, Cambridge, MA, 1991)
4. R.W. Boyd, *Nonlinear Optics*, 3rd edn. (Academic, New York, 2008)
5. D.C. Hannah, M.A. Yuratich, D. Cotter, *Nonlinear Optics of Free Atoms and Molecules* (Springer, Berlin, 1979)
6. Y.R. Shen, *The Principles of Nonlinear Optics* (Wiley, New York, 1984)
7. R.L. Sutherland, *Handbook of Nonlinear Optics*, 2nd edn. (Marcel Dekker, Inc., New York, 2003)
8. A. Yariv, *Quantum Electronics* (Wiley, New York, 1975)
9. J.F. Reintjes, *Nonlinear Optical Parametric Processes in Liquids and Gases* (Academic, New York, 1984)
10. C. Flytzanis, V. Degiorgio, *Nonlinear Optical Materials: Principles and Applications, Proceedings of the International School of Physics "Enrico Fermi" Course 126* (Ios Press, Amsterdam, 1995)
11. G.P. Agrawal, *Nonlinear Fiber Optics* (Academic, Boston, 1989)
12. T.P. McLean, "Linear and nonlinear optics of condensed matter," in *Interaction of Radiation with Condensed Matter*, lectures presented at Winter College Trieste, January 14-March 26, 1976 (International Atomic Energy Agency, Vienna, 1977), pp. 3-92
13. S.S. Jha, *Perspectives in Optoelectronics* (World Scientific, Singapore, 1995)
14. A. Yariv, P. Yeh, *Optical Waves in Crystals* (Wiley, New York, 1984)
15. M. Wegener, *Extreme Nonlinear Optics: An Introduction* (Springer, Berlin, 2005)
16. H.C. Kapteyn, M.M. Murnane, I.P. Christov, *Phys. Today*, 39 (2005)
17. A. Miller, D.M. Finlayson, *Laser Sources and Applications* (IOP Publishing, London, 1997)
18. W. Koechner, *Solid State Laser Engineering*, 6th edn. (Springer, Berlin, 2006)
19. G.S. He, S.H. Liu, *Physics of Nonlinear Optics* (World Scientific, Singapore, 1999)
20. R.R. Alfano, *The Super-Continuum Laser Sources* (Springer, New York, 1989)

# Chapter 3

## Gas Lasers

S.K. Dixit

**Abstract** The field of gas lasers, started with the invention of He–Ne laser in 1961, has witnessed tremendous growth in terms of technology development, research into gaseous gain medium, resonator physics and application in widely diverse arenas. This was possible due to high versatility of gas lasers in terms of operating wavelengths, power, beam quality and mode of operation. In recent years, there is a definite trend to replace the gas lasers, wherever possible, by more efficient and compact solid-state lasers. However, for many industrial, medical and military applications, the gas lasers still rule the roost due to their high-power capabilities with good beam quality at specific wavelengths. This chapter presents a short review covering the operating principle, important technical details and application potential of all the important gas lasers such as He–Ne, CO<sub>2</sub>, argon ion, copper vapour, excimer and chemical lasers. These neutral atoms, ions and molecule gas lasers are discussed as per applicable electrical, chemical and optical excitation schemes. The optically pumped gas lasers, recently experiencing resurgence, are discussed in the context of far infrared THz molecular lasers, diode-pumped alkali lasers and optically pumped gas-filled hollow-core fibre lasers.

**Keywords** Lasers • Atomic and molecular gas lasers • Electric discharge excitation • Chemical pumping • Optical excitation

### 3.1 Introduction

The gas laser is a quantum device with the gain medium in the form of gas or vapour. In a gas laser, the lasing species may be neutral atoms, ions or molecules. The laser excitation agencies can also be different such as electron, photon, gas dynamic expansion, chemical or nuclear energy. The lasing transitions may be electronic, vibrational or rotational. Accordingly, the lasing wavelengths vary from VUV ( $\sim 100$  nm) to FIR ( $\sim 1,000$   $\mu\text{m}$ , THz radiations). The continuous wave (CW)

---

S.K. Dixit (✉)

Laser Systems Engineering Section, Raja Ramanna Centre for Advanced Technology (RRCAT), Indore, India

e-mail: [skdixit@rrcat.gov.in](mailto:skdixit@rrcat.gov.in)

laser power varies from milliwatts (mw) to megawatts (MW). In pulsed operation, the pulse energy has a wide range from  $\mu\text{J}$  to  $\text{kJ}$ . The pulse repetition rates may vary from Hz to tens of kHz. In some of the lasers, the gain is so high that superradiant operation is possible without an optical resonator. In gas lasers, tailored for optimum performance, the gas pressure varying from few mbar to multi-atmosphere and the gas flows up to supersonic speed have been employed. It is also well known that beam quality of gas lasers is very good even at the high-power levels. Such a wide choice on the output parameters is possible due to many unique properties of gas laser systems. These are ready availability of gases or gas mixtures, high optical quality, volume scalable, damage-free gas gain medium from which the heat can be removed very efficiently, well-developed electrical excitation gas discharge techniques and optical resonator geometries. It is for this reason that the number and types of gas lasers are far more than solid-state and liquid lasers. As of today, there is an intense competition among gas, solid-state and liquid lasers guided by efficiency, ease of operation, output parameters, type of applications, demand and cost. In a continuing process, many important lasers of the past are losing their sheen, and at the same time many newer ones are coming up.

This article presents the operating principle, important technical details and application potential of well-known gas lasers – a field started in 1961 with the development of CW 1.15  $\mu\text{m}$  IR He–Ne laser by Ali Javan [1]. For ease of discussion, the neutral atoms, ions and molecules gas lasers are divided by three major excitation mechanisms, i.e. electrical, chemical and optical.

## 3.2 Electrically Excited Gas Lasers

The majority of gas laser classes, i.e. He–Ne,  $\text{CO}_2$ , metal vapour, excimer and ion lasers, are based on electrical discharge through the gain medium contained in a plasma tube with proper electrodes. The population inversion is achieved by excitation/ionisation of atoms and molecules through inelastic collision with the electrons. In electrical discharge lasers, the main parameters are discharge voltage, current, rise time, electron density, electron temperature, densities of gain species and buffer gas.

### 3.2.1 Helium–Neon (*He–Ne*) Laser

The He–Ne laser, invented in 1961 at the Bell Telephone Laboratories, USA, has several firsts to its credit: the first gas laser, the first continuous wave laser and probably also the first laser to demonstrate the effectiveness of resonant excitation energy transfer for lasing action. Even after 50 years of its invention, the He–Ne laser remains the most popular, highly utilised, very low cost and most rugged with very long lifetimes (several years). It has been demonstrated to lase in more than 100

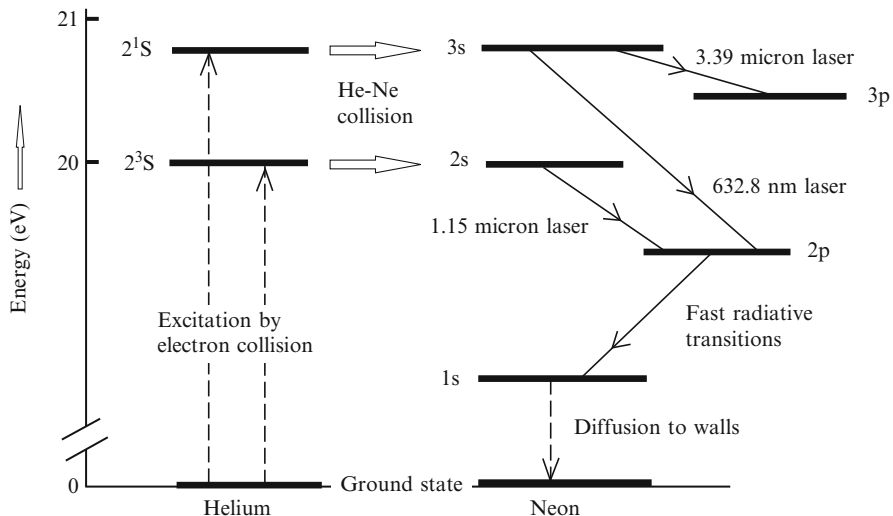


**Fig. 3.1** Energy levels of He–Ne laser

wavelengths with suitable resonator optics, though the most popular wavelengths are IR (1.15  $\mu\text{m}$ ), red (633 nm), orange (612 nm), yellow (594 nm) and green (543 nm).

From the physics point of view, a He–Ne laser is a four-level laser in neon atomic transitions as shown in Fig. 3.1. Though the laser is an electrical discharge one, the mechanism of population inversion in neon is through the resonant excitation energy transfer from the far more abundant (90 % of total mixture) helium atoms.

The helium atoms are excited (e-atom collision) to metastable levels (lifetime  $\sim$ a few seconds) 2<sup>3</sup>S and 2<sup>1</sup>S which cannot decay to ground state due to forbidden optical transition. These metastable He atoms resonantly transfer their energy to Ne atoms (atom–atom collision) due to their close matching with Ne 3s and 2s levels. These excited Ne levels function as upper laser levels for population inversion. The 3s-3p, 3s-2p and 2s-2p are the Ne lasing transitions for IR and visible radiations. The lower laser level 2p fast decays to level 1s by spontaneous emission. The 1s level is depopulated to ground state by collision with the glass walls of discharge tube, thus completing the four-level lasing process.

Technically, a He–Ne laser is based on a glass capillary of diameter 1–2 mm and length 20–50 cm. Such small diameter tubes lead to effective collision-induced depopulation of 1 s level, thereby ensuring higher laser gains and also favours TEM<sub>00</sub> mode operation. However, the small diameter tube also leads to low power. The discharge tube is sealed with resonator mirrors itself with a glass to metal seal. The total gas fill pressure is in range 2–5 Torr to attain the optimum electron temperature for efficient excitations. The operation is based on the DC discharge (2–20 mA) in the plasma tube. The initial voltage to switch on the discharge is in range 8–10 kV. After switching the discharge on, the operation voltage drops to 1–1.5 kV. Due to small gain of He–Ne laser, low loss, stable resonator optics is used. This

consisted of mirrors of 100 and 99 % reflectivity with radii of curvature designed to obtain TEM<sub>00</sub> Gaussian mode operation. The typical output parameters of a He–Ne laser are TEM<sub>00</sub> mode, Gaussian intensity profile, 1 mm beam diameter (at 1/e<sup>2</sup>), 1 mrad divergence, 10 mW CW laser power and 1–1,000 MHz line-width, depending on whether the operation is single or multiaxial modes.

The He–Ne lasers are extensively used in laser demonstration, basic optics experiments, alignment, interferometry, holography and as laser gyroscope.

### 3.2.2 Ion Lasers

An ion laser is based on lasing between the energy levels of an ion present in ionised gas. The first ion laser, operated by William Bridges [2] in 1964, was an argon ion (Ar<sup>+</sup>) laser. Still today, the Ar<sup>+</sup> laser remains one of the most powerful CW visible (488 and 514 nm) lasers. Another important ion laser is krypton ion (Kr<sup>+</sup>) laser producing a host of visible radiations. A combo model of Ar–Kr ion laser is called a white light laser as they produce three basic colours – blue, green and red – lasing in a suitable power ratio.

Figure 3.2 shows the energy levels of an Ar<sup>+</sup> laser. A high-current intense electric discharge pumps the argon ions to the upper laser level (4p) located at about 36 eV above the neutral argon atom ground state. The 4p – 4s, ionic transitions produce green and blue visible laser lines.

The lower laser level (4s) swiftly decays to the ion ground state (3p) emitting very high photon energy 72 nm radiations. The ion ground state decays to the atom

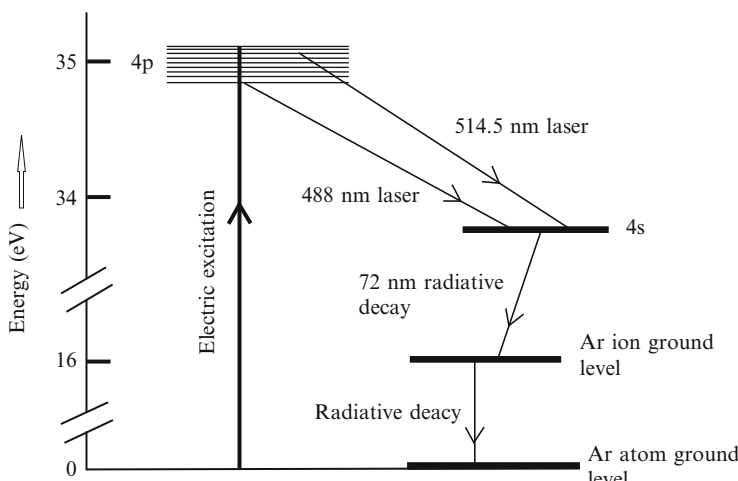


**Fig. 3.2** Energy levels of Ar<sup>+</sup> laser

ground state radiatively completing the lasing loop. The lasing transition is also observed in doubly ionised argon ions ( $\text{Ar}^{++}$ ) producing UV (351 nm) radiations.

The technical issues in an  $\text{Ar}^+$  ion laser are much more complex than those of a He–Ne laser. A very high-current (10–50 A) DC discharge is needed to produce sufficient number of excited ions for efficient lasing. This generates a huge amount of heat in the laser tube which needs to be removed by water cooling. A special laser discharge tube is to be used which can withstand high temperature and also intense 72 nm UV radiations. One such choice is the beryllium oxide (BeO) tube as it has low vapour pressure, high chemical purity and high thermal conductivity. A high-current (10s of A), low-voltage (100s of V) power supply with a provision to provide initial (a few kV) trigger pulse to initiate discharge is used. In some of higher power devices, an axial magnetic field (500–1,000 G) is applied to concentrate the discharge thereby increasing the current density for more efficient lasing action. The optical resonator is designed to produce  $\text{TEM}_{00}$  mode. In general, the laser output is multiline (many wavelengths). Single wavelength is selectable by rotating the prism placed within the optical resonator. The  $\text{Ar}^+$  laser is a sealed device with gas pressure of about 1 Torr in discharge tube of bore diameter 0.5–2 mm and length 50–100 cm. The typical output parameters of an argon ion laser are  $\text{TEM}_{00}$  mode, Gaussian intensity profile, 1–2 mm beam diameter (at  $1/e^2$ ), 0.5 mrad divergence, 5–30 W CW laser power and 3–5 GHz line-width (multiaxial modes). Single axial mode is possible with a special resonator scheme with an intra-cavity etalon; however, the laser power is substantially reduced.

Ion lasers find applications in optical metrology, Doppler velocimetry, laser interferometry, Raman spectroscopy, fibre grating fabrication, laser entertainment shows and pump sources for CW dye and Ti:sapphire laser. Currently, there is an increasing trend to replace the  $\text{Ar}^+$  laser with a CW diode-pumped solid-state laser source operating at 532 nm, obtained from the second harmonic of 1.06  $\mu\text{m}$  Nd:YAG laser.

### 3.2.3 Metal Vapour Lasers

This category of lasers is based on lasing transitions in atoms of metal vapour produced either by heating the metal or by chemical reaction of metal with a suitable reagent. The ace representative of this category is the copper vapour laser (CVL), invented by W. Walter [3] in 1966. The CVL is the most powerful and the most efficient, high repetition rate, pulsed laser in the visible (510, 578 nm) part of a spectrum. An average power of level of 0.5 and 2 kW is available from a CVL oscillator and oscillator amplifier system, respectively. Another important laser in the class is gold vapour laser operating at red (628 nm) and UV (312 nm) spectrum. In Indian context, a mature technology development programme of high beam quality, high-power CVL exists [4–10] at RRCAT, Indore, for generation of high repetition rate UV and tunable visible laser radiations and their applications.

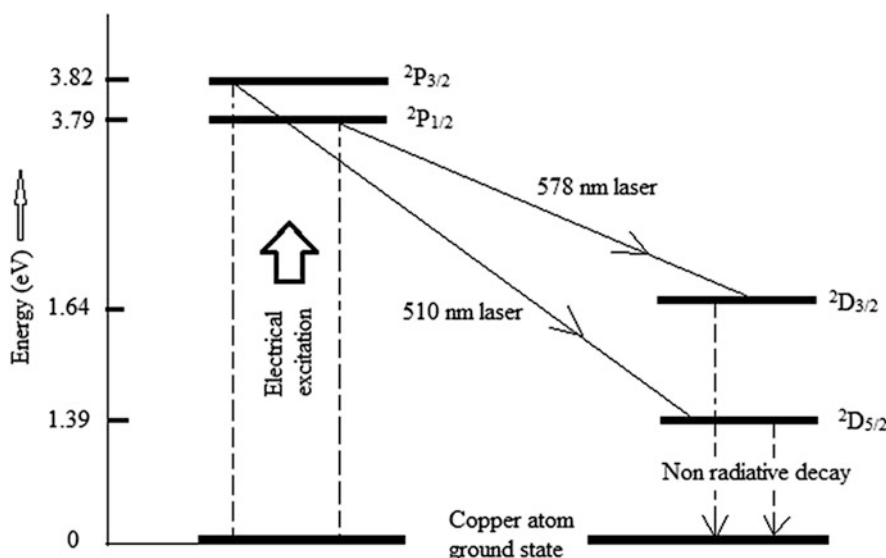


Fig. 3.3 Energy levels of copper vapour laser

From the physics point of view, a CVL is a three-level system with lasing transition of a self-terminating nature. Figure 3.3 shows the energy level diagram. The upper laser levels ( $^2P$ ) are resonantly connected with ground state ( $^2S$ ), thereby leading to strong trapping of radiations. With this constraint, the upper laser level can only decay to metastable level ( $^2D$ ) which is the lower laser level. Due to optical forbidden  $^2D$ - $^2S$  transition, the lower level decays to ground state only by collision with electrons or walls of the discharge tube.

Since this depopulation process is slow, CVL operation is only pulsed albeit at high repetition rates. Also due to large lifetime difference of the upper and lower laser levels, the lasing self terminates in 10s of ns. The  $^2P_{3/2} - ^2D_{5/2}$  (510 nm) and  $^2P_{1/2} - ^2D_{3/2}$  (578 nm) are the strong lasing transitions of a CVL. The gain of a CVL is so high that it can lase without a resonator, although for optimum extraction of stored optical power and for good beam quality, an optical resonator is a must.

As of today, several successful versions of CVLs are available with different technical details. These are conventional CVL, copper bromide (CuBr) laser and CVL with HCl/HBr gas additives. These are broadly classified into low temperature (500–600 °C), e.g. CuBr and CVL/HBr systems, and high temperature (1,500–1,600 °C), e.g. CVL and CVL/HCl systems. The higher temperature versions are based on an alumina ( $Al_2O_3$ ) discharge tube, wrapped in a thick insulating layer of alumina fibre to retain the temperature. Water cooling of the discharge tube is a must. The buffer gas (neon) or the mixture of buffer gas and HCl gas flows through the discharge tube at an optimum flow rate, controlled by gas/vacuum handling unit. The lower temperature versions are mostly based on fused silica tube, with or without thermal insulation. They may operate both in sealed and flowing gas operation, with

or without the water cooling arrangement depending on the laser power levels. The electrical excitation scheme for all the versions of CVL is almost same. A storage capacitor is charged to nearly twice the supply voltage, through a resonant charging circuit. The charging time for the storage capacitor should be less than the laser inter-pulse period. The voltage is transferred to the discharge electrode via a peaking capacitor to sharpen the voltage pulse. The electrical discharge resulting in self-breakdown of the gas in the discharge tube serves the dual purpose of heating the tube and excitation of copper atom levels for lasing. A high repetition rate, high-voltage switch is required in the modulator circuit for generating a fast rise time voltage pulse. A hydrogen-filled gas discharge device, namely, a thyratron, is widely used for this purpose though solid-state switches are now also used. A high-voltage pulse of 10–20 kV with rise time less than 100 ns and peak current of 100 s of ampere is required for efficient excitation in CVLs. The laser operation is in 5–30 kHz pulse repetition rates. The CVL discharge tubes of bore diameter 10–80 mm, length 50–300 cm and gas pressure of 20–50 mbar are most commonly used.

Copper vapour laser is a large aperture, high gain device where both the plane-plane and unstable resonators can be used. The plane–plane resonator consisted of a 100 % reflecting mirror and an uncoated glass window (reflectivity  $\sim 8\%$ ) as output coupler. The unstable resonator uses both 100 % mirror with laser beam coupled out by a fully reflecting scraper mirror with a central hole, located in the resonator at  $45^\circ$  to the optical axis. The unstable resonator has the advantage of lowering the beam divergence while at the same time extracting from the whole gain medium. The typical output parameters of CVLs are 10–80 mm beam diameter (at  $1/e^2$ ), top-hat beam profile, 0.2–5 mrad divergence, 5–200 W laser power, 5–20 kHz repetition rate, 10 GHz line-width (multiaxial modes) and 20–70 ns pulse width.

The copper vapour lasers find applications in precision processing of different materials, pump source for tunable dye and Ti:sapphire lasers, separation of isotopes, medicine, high-speed photography, underwater applications and fibre grating writing. Recently, diode-pumped solid-state lasers with equivalent performance of CVL in power range of 10s of W are available. They have replaced CVLs in many applications. The CVL still holds good position in view of its direct amplification of visible radiation to very high powers without resorting to frequency conversion, good beam quality and lower cost.

### 3.2.4 *Carbon Dioxide (CO<sub>2</sub>) Laser*

The infrared (9.6, 10.6  $\mu\text{m}$ ) CO<sub>2</sub> laser invented by Kumar Patel [11] in 1964 is one of the most powerful, efficient and versatile of all the lasers. Different modes of operation (CW, pulsed, *Q*-switched, mode locked and wavelength tunable), different excitation schemes (DC, RF, microwave, pulsed, e-beam pumped, gas dynamic expansion) and different gas flow modes (sealed, slow flow and fast axial flow) as well as transverse excited atmosphere (TEA), waveguide and gas dynamic geometries make the CO<sub>2</sub> laser a truly versatile. The CW laser power of 10s of kW,

pulse energy of 100 s of J, electro-optic efficiency of 30 % and an excellent beam quality established this laser as the workhorse of laser-based industrial applications. In Indian context, a mature technology development programme of high-power pulsed and CW CO<sub>2</sub> laser exists [12–15] at RRCAT/BARC for applications in laser-matter interaction.

The CO<sub>2</sub> laser is based on lasing transitions in the quantised vibrational energy levels of CO<sub>2</sub> molecule. A CO<sub>2</sub> molecule has two oxygen atoms covalently bonded to a central carbon atom leading to three fundamental modes of vibration – symmetric, bending and asymmetric stretching. In the symmetric mode, the two oxygen atoms oscillate symmetrically along the axis of the molecule in unison, either towards or away from each other. In the bending stretch mode, the oscillation of the molecules is in perpendicular direction to the axis. In the asymmetric mode, if one oxygen atom moves towards the carbon atom, the other moves away with alternating movements. These three vibrational states are referred to by quantum numbers n<sub>1</sub>, n<sub>2</sub> and n<sub>3</sub> related number of quanta to the symmetric, bend and asymmetric stretch modes, respectively. For example, (001) means that the CO<sub>2</sub> molecule has a single vibrational quantum in asymmetric stretch mode. Figure 3.4 shows the energy level diagram of a CO<sub>2</sub> laser. The upper metastable laser level (001) is resonantly excited by a very efficient energy transfer from the electrically excited long-lived N<sub>2</sub> molecule. The (001) to (100) and (001) to (020) are the transitions corresponding to the central lasing wavelengths of 10.6 μm and 9.6 μm, respectively. De-excitation of CO<sub>2</sub> from (100) level to (010) level is very efficient; however, the relaxation from (010) level to ground state (000) is very inefficient hampering the population inversion. This situation is tackled by adding a large proportion of helium gas in CO<sub>2</sub>/N<sub>2</sub> active medium.

Addition of helium greatly helps in de-excitation of CO<sub>2</sub> molecules to ground state, thereby completing the lasing process. Helium also cools the gain medium due to high thermal conductivity leading to high laser powers. Thus, the CO<sub>2</sub> laser

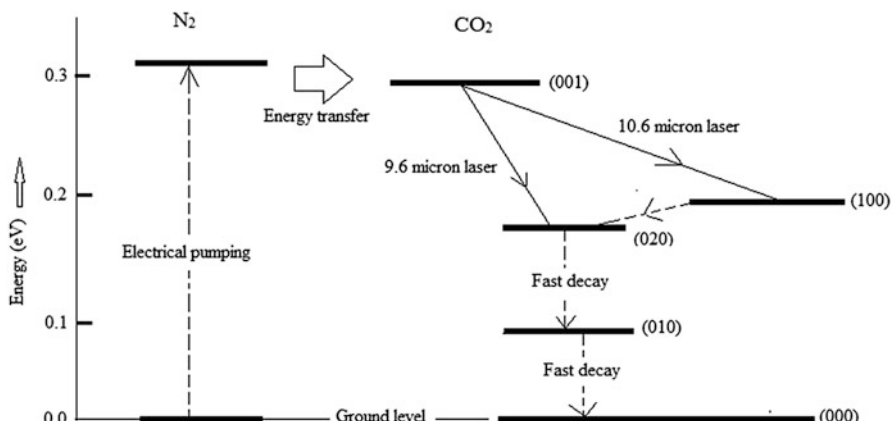


**Fig. 3.4** Energy levels of CO<sub>2</sub> laser

always consist of N<sub>2</sub> and He gases in the optimised ratio (CO<sub>2</sub>: N<sub>2</sub>: He) of 1:1:3 to 1:1:8 depending on the laser model. The rotational lines associated with each vibrational energy level also take part in lasing giving a feature of multiline/tunable CO<sub>2</sub> laser.

The technical details of the CO<sub>2</sub> laser differ with different models. In sealed off version, both the longitudinal DC discharge-based cylindrical tube laser and the transverse RF excitation-based waveguide (cylindrical or rectangular tube) laser are a mature technology. The waveguide laser has some advantage in terms of much compact size for the same power level as that of the longitudinal laser. The laser power up to 100 W can be easily achieved in sealed off laser. However, in sealed off mode, special efforts are needed to control temperature rise, contamination, material erosion and CO<sub>2</sub> molecule dissociation to lengthen the laser lifetime. Contamination and thermal aspects can be overcome to a great extent by flowing the laser gases. It was observed that in a CO<sub>2</sub> laser, the laser output power scales up in direct proportion to mass flow rate and gas pressure as long as electrical input power is scaled in direct proportion and the gas temperate is kept below a limit by efficient cooling. Accordingly, many versions of CO<sub>2</sub> with different gas mixture flow speeds and power, namely, slow axial flow (flow speed – 10s of lit/min) laser of power of a few hundreds of Watt, fast axial flow laser (flow speed – 100s lit/s) of power of a few kW and fast transverse flow laser with a power of 10s of kW, are available. The CO<sub>2</sub> laser power of 100 kW or more is available from a gas dynamic excitation mechanism. In such a case, the hot CO<sub>2</sub> at high pressure is expanded through a small nozzle into a near vacuum, a process that produces population inversion as the expanding gas cools. The TEA CO<sub>2</sub> laser operates for the pulsed mode at gas pressure of 1 atm. or more with electric excitation transverse to laser axis. The laser pulse width from 10s of ns to a few  $\mu$ s, the pulse repetition rate of 100s of Hz and the pulse energy in 100s of J are routinely achieved. The CO<sub>2</sub> pulse energy can be substantially scaled up by pulsed e-beam pumping of discharge medium with a pressure of 10s of atm. and with no fundamental limit on the volume scaling.

The IR CO<sub>2</sub> laser needs special optics. The gold-coated metal mirrors and zinc selenide windows and lenses are used. Both stable and unstable resonators are used. A stable resonator is formed with a curved mirror of 100 % reflectivity and an output coupler with reflectivity of 10–20 % (usually, a semi-reflective coated zinc selenide mirror). TEM<sub>00</sub> mode is routinely achieved in low power operations. For line selection, one of the resonator mirrors is replaced with a grating. Single axial mode operation is achieved with an intra-cavity etalon.

The CO<sub>2</sub> laser wavelengths are strongly absorbed in organics, plastics, ceramics, tissues and water. In metals, they have weak absorption at room temperature. However, the absorption increases considerably in heated metal due to plasma formation. Accordingly, the CO<sub>2</sub> lasers are being extensively used in cutting and welding of metals, cutting of non-metals, plastics, heat treatment of metal surfaces, engraving, marking and in the medical field such as surgery to cut skin, stop minor bleeding during surgery, remove or vaporise abnormalities and to perform skin resurfacing. These lasers also find applications in range finding, spectroscopy

and photochemistry. Raman shifted pulsed CO<sub>2</sub> laser source ( $\sim 16 \mu\text{m}$ ) is well recognised to selectively excite uranium (U-235) isotope in a molecular approach – a recently focussed area for laser-based isotope separation. The kW class fibre and disc lasers are emerging as alternative to CO<sub>2</sub> laser for many applications. However, low cost, easily repairable and better power scalable CO<sub>2</sub> lasers are still the most widely used in industrial applications such as cutting, welding, cladding, alloying and rapid manufacturing.

### **3.2.5 The Pulsed UV Excimer and Nitrogen Lasers**

The pulsed UV laser sources are currently the cornerstone of high-resolution photolithography and eye vision correction where no other wavelength band can compete. The nitrogen (N<sub>2</sub>) laser was the first UV laser discovered in 1963 by Heard [16] followed by excimer laser in 1970 by Basov [17]. As of today, the excimer or exciplex lasers have a large variety of lasing medium (UV wavelength) such as Ar<sub>2</sub> laser (126 nm), F<sub>2</sub> laser (157 nm), ArF laser (193 nm), KrF laser (248 nm), XeCl laser (308 nm) and XeF laser (351 nm) as well as large range in laser pulse energy, power and repetition rate as compared to a low energy, low repetition rate N<sub>2</sub> laser (337 nm). The excimer lasers are the most powerful lasers in the UV region with KrF laser leading the pack. The average laser power of up to 1,000 W, pulse repetition rate of 1000s of Hz, pulse energy of several kJ and pulse width of 10–100 ns is available. In Indian context, excimer lasers are developed [18, 19] at RRCAT. A compact sealed off nitrogen laser is developed [20] at RRCAT for fluorescence-based measurement of the concentration of uranium salts in ground water to an accuracy of 0.1 ppb.

The name excimer/exciplex refers to excited species such as dimers (diatomic noble gas or halogen molecule) or other complexes (molecule consisting of one atom each of rare gas and halogen) which exist only in electronically excited state. In ground state, the molecule dissociates into separate atoms. Figure 3.5 shows the energy levels of an excimer and N<sub>2</sub> laser. Both the lasers are based on electronic UV transitions of the molecule with the difference that lasing transition in an excimer is bound to free whereas it is bound to bound in N<sub>2</sub> laser.

Effectively, as soon as the excimer molecules are formed in the excited state, the population inversion is on as the ground state population is always nil. In contrast, in N<sub>2</sub> laser, the ground state accumulates the population due to metastable nature, i.e. the lasing is self-terminating. Both the lasers are inherently pulsed, however, due to different reasons. The N<sub>2</sub> laser is pulsed because of self-terminating lasing transition. In an excimer laser, the excited lasing molecules are predominantly formed due to a three-body recombination process, e.g. (Kr<sup>+</sup> + F<sup>-</sup> + third body He  $\rightarrow$  KrF\* + He). This process requires a large amount of buffer gas He or Ne at the pressure of 1 bar or more. At such a high-pressure active medium, the continuous discharge cannot sustain due to arc or spark formation. In addition, following the

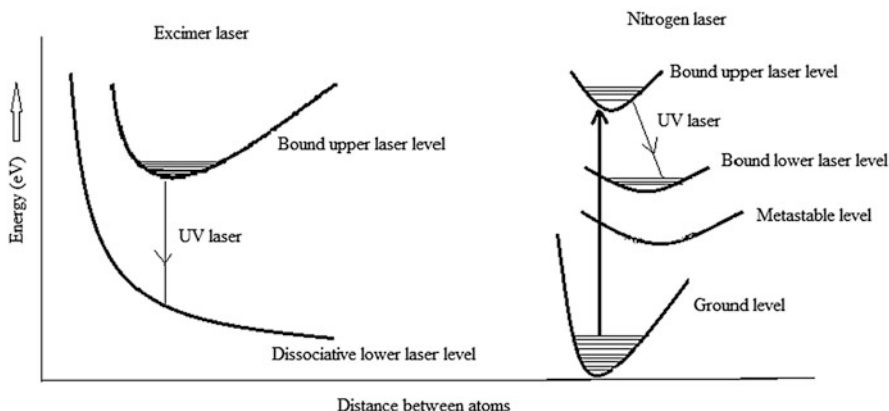


**Fig. 3.5** Representative energy levels of excimer and nitrogen lasers

laser action, the highly reacting disintegration products and heat need to be removed before the lasing action can resume. Consequently, the excimer laser can only be operated in the pulsed mode.

The technical issues of an excimer laser are more complex than a  $N_2$  laser. First, high-pressure (several bars) gas mixture of halogen (<0.5 %), rare gas (5–10 %) and rest buffer gas need special handling. Second, the material choice used for laser construction is also special in view of corrosive nature of halogen component. Also, the threshold value of population inversion in excimer laser is high in view of the significant line-width of the lasing transition. Both the excimer and  $N_2$  laser require fast electrical excitation and employ transverse excitation geometry. The pulsed voltage of 10s of kV is switched very fast in less than 100 ns, by fast high-voltage thyratron or solid-state switch, in storage to peaking capacitor energy transfer-based circuit. Suitable pre-ionisation of discharge is also necessary. The excimer laser also employed e-beam pumping. Both the lasers produce lasing even in the absence of a resonator due to very high laser gains. The laser beams have rectangular shape in view of transverse discharge geometry. Both the stable and unstable resonators are employed with such high gain lasers. The laser beam divergence is significantly lower with unstable resonator. For many applications, e.g. photolithography, the line narrowing of excimer laser is required and achieved with intra-cavity etalon. The typical parameters of  $N_2$  lasers are 10s of  $\mu J$  to mJ pulse energy, 3–10 ns pulse width and up to 200 Hz pulse repetition rate. The typical parameters of excimer lasers are, pulse energy – 10s of mJ to 100s of J, pulse width – 10–100 ns, pulse repetition rate – up to kHz and average power – 10–100s of Watts.

The excimer lasers are being extensively used in the fabrication of large-scale integrated circuits with a feature as small as 10s of nm by lithographic technique. The vision correction by direction ablation of corneal tissues (LASIK); the precision processing of polymers, plastics, ceramics, semiconductor, glass, Teflon and diamond; fibre grating fabrication; pulsed laser ablation; and dye laser

pumping are the current and very relevant applications of excimer lasers. The low pulse energy N<sub>2</sub> is also used in niche applications where a compact and low cost UV system is needed.

### 3.3 Chemically Excited Gas Lasers

In this category, also known as chemical lasers, the population inversion results due to chemical reaction. The chemical lasers have potential to provide huge laser power as already been demonstrated by development of MW average power systems. In addition, these lasers are easily mobile. Huge investment is being made in this field due to military applications of these lasers. The most successfully developed chemical lasers are hydrogen fluoride (HF)/deuterium fluoride (DF) lasers and iodine lasers.

#### 3.3.1 Hydrogen/Deuterium Fluoride (HF/DF) Lasers

The lasers based on vibrationally excited products of a chemical reaction were first conceived by Penner and Polyani [21] in 1961 and first demonstrated by Kasper and Pimental [22] in 1965. The CW mid-infrared hydrogen fluoride (2.6–3.0 μm) and deuterium fluoride (3.6–4.0 μm) lasers are the leading examples. The DF laser beam propagation is much better than HF laser due to its much reduced attenuation in atmospheric water content. The MW average powers achieved from HF/DF lasers is the highest continuous power from any known laser.

The lasing in HF/DF laser is based on the molecular transition between the vibrational ( $\nu$ ) energy levels with fine-tuning by rotational ( $J$ ) levels. Figure 3.6 shows the lasing diagram of HF and DF molecules. The upper laser levels are populated by the fundamental chemical reaction involving molecules and free atoms, e.g.  $H_2/D_2 + F \rightarrow HF^*/DF^* + H$ . The allowed molecular transitions ( $\Delta\nu = \pm 1$ ,  $\Delta J = \pm 1$ ) are multiple and lase simultaneously, leading to multiline operations. The excited molecules are deactivated by collisions with molecules with same or other types.

Technically, the HF/DF lasers are very complex involving several stages. The first stage is the creation of high-density free fluorine atoms. This is carried out in a combustion process with reactants, e.g. NF<sub>3</sub> and D<sub>2</sub> or C<sub>3</sub>H<sub>4</sub> are mixed in a high-pressure combustor. The heat evolved in combustion breaks NF<sub>3</sub> into N<sub>2</sub> and fluorine atoms. Next, this atomic fluorine is injected together with He into the lasing cavity where it is mixed with H<sub>2</sub>/D<sub>2</sub> to produce excited HF<sup>\*</sup>/DF<sup>\*</sup>. The mixing of fuels in the laser cavity is by low pressure supersonic expansion through fine nozzles. The lasing ensues in an optical resonator placed normal to gas flow. Usually an unstable optical resonator is employed which extracts the laser beam out by reflection from a scraper mirror. The beam quality is the generated laser beam closely connected with

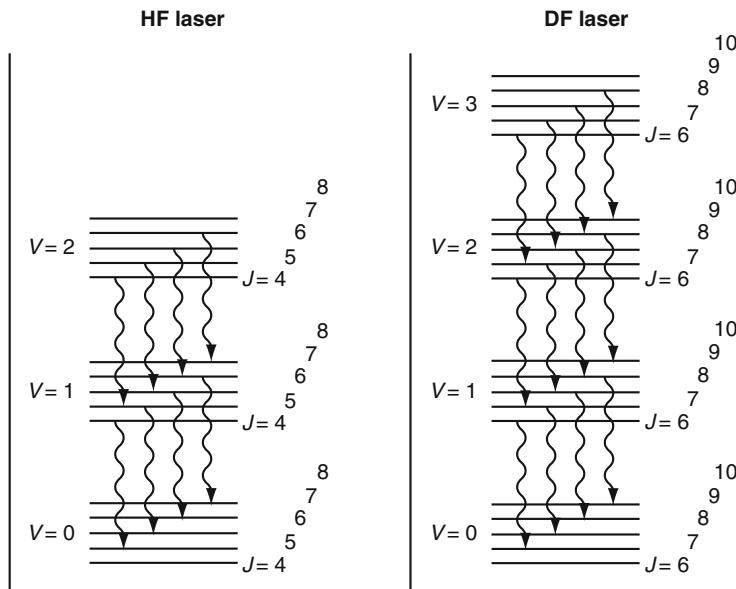


**Fig. 3.6** Vibrational-rotational levels of HF and DF chemical lasers

the homogeneity of a supersonic mixing process. The HF and DF gases are very toxic and corrosive and need special handling. The other necessities of the laser system are pressure recovery, heat exchanger, exhaust systems, high-pressure gas handling and cooling arrangements. These lasers have been used as fielded weapons against rockets and artilleries.

### 3.3.2 Chemical Oxygen Iodine Laser (COIL)

A CW COIL is based on electronic lasing transition ( $1.315 \mu\text{m}$ ) in resonantly excited iodine atoms by singlet oxygen produced chemically. This laser was first conceived by Derwent and Thrush [23] in 1970 and first demonstrated by McDermott [24] in 1978. This work followed the earlier work in 1964 of Kasper and Pimental [25] on flash lamp-pumped pulse iodine laser based on photodissociation of alkyl iodide molecules. An iodine laser has many advantages over HF/DF laser in terms of lower wavelength and single line operation implying better focusability and better transmission through atmosphere/optical fibres. 100s of kW of CW laser power and 100s of J pulse energy in 1 ns pulse width are available. The COIL has been chosen for airborne laser weapon programmes for operation in aeroplanes for military applications. Recently, the research in all gas phase iodine laser (AGIL) is being vigorously pursued.

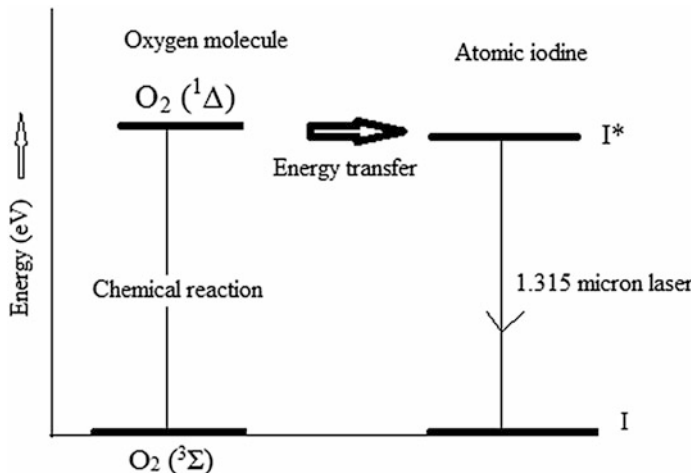
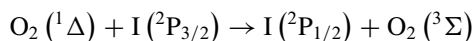


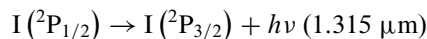
**Fig. 3.7** Lasing scheme of atomic iodine chemical laser

The iodine laser is based on  $5^2P_{1/2} - 5^2P_{3/2}$  electronic transition in atomic iodine. This lasing transition is a magnetic dipole type as electric dipole transition is forbidden. The lasing is in between the selected hyperfine states of upper and lower laser levels. The excitation of upper metastable laser level (lifetime  $\sim 125$  ms) is by resonant energy transfer from singlet oxygen  $O_2 (^1\Delta)$  molecule as shown in Fig. 3.7. The singlet oxygen, generated by a special chemical process, has a lifetime of about an hour, very reactive and in close resonance ( $<300\text{ cm}^{-1}$ ) with  $P_{1/2}$  levels of iodine. The singlet oxygen serves the dual purpose of dissociating the iodine molecules and exciting the iodine atoms.

The pumping reaction is given by



The lasing process is governed by



The technical details and complexities of a COIL are almost the same as that of other members of chemical laser family, i.e. HF/DF lasers. The first stage is the creation of singlet oxygen. This is carried out in a chemical reaction of chlorine gas with liquid solution of  $H_2O_2$  and  $NaOH$ . Next, this singlet oxygen is injected into the lasing cavity where it is mixed with  $I_2$  and He mixture. The mixing of fuels in the laser cavity is by supersonic expansion through fine nozzles. The lasing ensues in an optical resonator placed normal to gas flow. The other necessities of the laser system are pressure recovery, heat exchanger, exhaust systems, high-pressure gas handling and cooling arrangements.

An active research is on to develop a new class of COIL dispensing off with a complicated gas–liquid reaction system to generate singlet oxygen. One way is to generate the singlet oxygen by electric discharge. Another process is all gas phase iodine laser (AGIL). AGIL uses a reaction of chlorine atoms with gaseous hydrazoic acid ( $\text{HN}_3$ ) to produce excited molecules of nitrogen chloride ( $\text{NCl}_3$ ) which passes their energy to the iodine atoms much like singlet oxygen does in COIL. The iodine atoms then emit the laser radiation. The iodine laser ( $1.315\ \mu\text{m}$ ) has been demonstrated in both the novel systems and further studies are being carried out.

### 3.4 Optically Pumped Gas Lasers

The optical pump sources (laser diode, flash lamp and laser) have been the engine of solid-state/liquid laser technology but never found favour with gas lasers. This is in view of a very poor energy transfer from pump to the gas active medium. However, for certain niche areas such as achieving laser in narrowly spaced rotational energy levels of molecules and pumping of very high quantum efficiency ( $\sim 98\%$ ) alkali laser, the narrow line-width optical pumping has been very effectively utilised. In optically pumped gas lasers, the most successfully developed are far infrared (FIR) molecular lasers and near IR diode-pumped alkali lasers. Recently, optically pumped gas-filled hollow-core IR fibre lasers have been demonstrated.

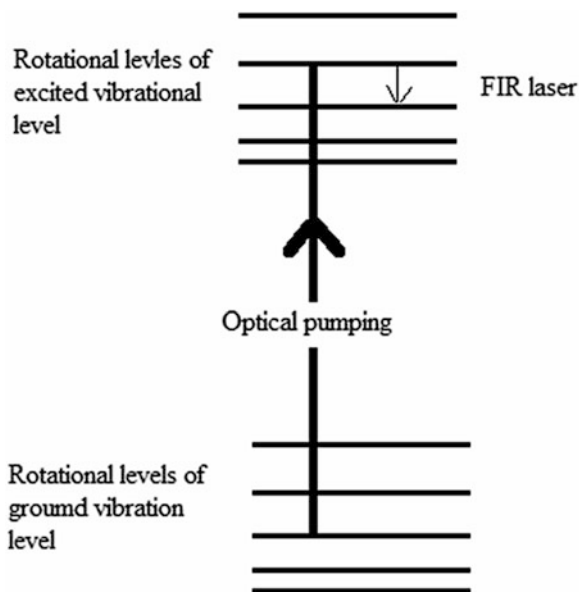
#### 3.4.1 *Optically Pumped FIR (THz) Lasers*

The laser sources with wavelength range  $100\ \mu\text{m}$  to  $1\ \text{mm}$  ( $3\ \text{THz}$  to  $0.3\ \text{THz}$ ) are classified as THz radiation which are recently gaining importance due to huge application potential in terahertz spectroscopy and terahertz imaging. The molecular laser operating on rotational energy levels can produce this wavelength range. However, due to very small rotational energy difference ( $\sim 10\text{s of meV}$ ), the broad energy distribution electric discharge excitation is not selective enough to pump upper laser level alone without excitation of lower level. The very selective optical pumping from a narrow line-width laser can however produce population inversion in rotation lines of molecules. Such a class is optically pumped FIR (THz) laser – a field started in 1970 by Chang and Bridges [26]. The representative laser of this class is methanol ( $\text{CH}_3\text{OH}$ ) laser operating at  $118.8\ \mu\text{m}$  ( $2.5\ \text{THz}$ ) pumped by single line  $\text{CO}_2$  laser.

Figure 3.8 shows vibrational–rotational energy level diagram of  $\text{CH}_3\text{OH}$  laser. The pump source is a selected line of  $9.6\ \mu\text{m}$  band of  $\text{CO}_2$  laser.

The rotational laser line ( $118.8\ \mu\text{m}$ ) is as per the selection rules ( $\Delta\nu = 0$ ,  $\Delta J = \pm 1$ ) for the molecule possessing permanent electric dipole moment such as methanol. By switching to a different pump laser line of  $\text{CO}_2$  laser, a different type of rotational modes of the methanol molecule can be excited, thereby producing different laser lines.

**Fig. 3.8** Representation of FIR (THz) lasing



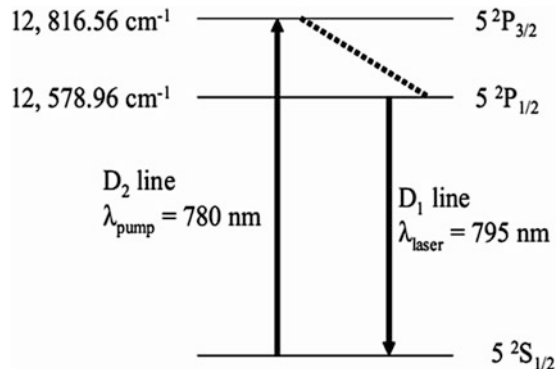
Technically, the THz laser mainly consists of the IR pump laser and the FIR laser cavity: the usual pump source DC/RF excited, line tunable, sealed off and CW CO<sub>2</sub> laser with a line-width of about 100 MHz. The FIR laser cavity is a stable resonator or a waveguide resonator with a hole in one of the resonator metal mirrors to allow the entry of the pump beam. The output coupler is very special which reflects the pump beam but transmits the laser beam. The optical efficiency of a THz laser is quite low. Typical output power of a few milliwatts is obtained with a pump power of 10s of Watts. The THz wavelengths can be tuned by tuning the pump laser wavelengths. The methanol laser wavelength can be tuned from 70 to 700 μm. The ethanol (C<sub>2</sub>H<sub>5</sub>OH) laser wavelength can be tuned discretely from 70 to 1,300 μm. Recent research are directed to employ the quantum cascade laser (easy tunability and line-width of MHz) as the pump source for THz lasers. However, the power of these semiconductor lasers is low and needs improvement.

Another very useful optically pumped laser is CO<sub>2</sub> laser-pumped CF<sub>4</sub> laser for generating step tunable coherent radiation over 15.3–16.3 μm. This laser was developed [27] in BARC. This spectral range is very useful for selective excitation of <sup>235</sup>UF<sub>6</sub> molecule for isotope separation process.

### 3.4.2 Diode-Pumped Alkali Laser

The diode-pumped alkali laser (DPAL) – proposed by Krupke [28] in 2003 – combines the attractive properties of high beam quality, heat handling and power

**Fig. 3.9** Lasing scheme of diode-pumped rubidium vapour laser



scalability of gas lasers and efficient pumping by diode lasers. The DPAL is based on very high quantum efficiency, atomic transition of alkali elements such as cesium (95 %) and rubidium (98 %). The atomic vapour of these alkalis can be efficiently pumped with commercially available high-power laser diode arrays. It is envisaged that high-power alkali laser may emerge as an alternative to diode-pumped solid-state and chemical laser. Currently, the best DPAL performance [29] is from rubidium laser with CW laser power of 145 W at 795 nm at a slope efficiency of 28 %.

The DPAL are three-level lasers as shown representatively for rubidium in Fig. 3.9. This is based on three lowest lying electronic levels of alkali atom. The optically allowed pump transition ( $S_{1/2}$  –  $P_{3/2}$ ) is well matched with diode laser wavelength of 780 nm.

The excited atoms of  $P_{3/2}$  level relax to the upper laser level  $P_{1/2}$  by collisions with the high-pressure buffer gas and a molecular gas mixture. The buffer gas also broadens the atomic transitions sufficiently to render them spectrally homogeneous for enhanced absorption of the pump radiation. The  $P_{1/2}$  to  $S_{1/2}$  is the lasing transition. The pump diode laser spectral width (2–3 nm) greatly exceeds the collisionally broadened laser levels width (0.05–0.1 nm). Despite this, due to large alkali atom pump transition peak cross section, a substantial pump laser absorption takes place in the Lorentzian wings of the pump transition.

The technical designs of DPALs are still evolving. A DPAL essentially consists of a vapour cell made of metal, a provision to heat this cell (100–200 °C) to generate the required alkali vapour pressure, a high-pressure buffer gas filling system, an optical resonator and laser diode to pump the gain medium. The buffer is a mixture of helium (3–5 atm. pressure) and ethane (70–100 Torr). Both sealed off and flowing gas versions are in operation. The optical pumping is either axial or transverse. The optical pumping is now facilitated by availability of high-power, volume Bragg grating coupled laser diode arrays with the line-width less than 0.3 nm. The optical pump radiation can be introduced to gain medium by several ways. It may be either through one of the resonator mirrors or by polarisers or in a transverse scheme where the gas flow, pump beam and laser axis are orthogonal. The optical to optical

conversion efficiencies of rubidium laser have reached 50 and 80 % with laser diode pump (2 nm line-width) and Ti:sapphire laser pump (10s of MHz line-width), respectively. The CW laser powers of 145 W from rubidium and 10 W from cesium laser are available. These lasers are projected to be capable of producing 100 s of kW of laser power.

### **3.4.3 *Hollow-Core Optical Fibre Gas Laser***

The hollow-core optical fibre gas laser (HOFGLAS) – proposed and demonstrated by Jones/Nampoothiri [30, 31] – combines the attractive properties of compactness, long interaction length and low lasing threshold of fibre laser and potential for high power and narrow line-width of gas laser. The lasing medium is optically pumped gas molecules filled in hollow-core (HC) photonic crystal fibre. The pulsed lasing in  $C_2H_2$  and HCN at  $\sim 3 \mu m$  wavelength is demonstrated when pumped with pulsed OPO source at  $\sim 1.5 \mu m$ . The CW operation seems to be possible with right combination of active gas and the pump laser. Currently, the lasing wavelength in HOFGLAS is limited to  $\sim 3.5 \mu m$  by the material absorption for silica glass. The lasing wavelength may be pushed to  $\sim 10 \mu m$  by employing HC chalcogenide glass fibres.

For the gas molecules, employed so far in HOFGLAS, i.e.  $C_2H_2$  and HCN, the laser action is based on optical pumping from ground rotational–vibrational states and lasing transition from the pumped rotational levels of an upper vibrational state to that of lower vibrational state. The damage threshold due to SBS, SRS, thermal lens and material damage is much higher for a HOFGLAS as compared to a solid core fibre laser. This is due to the fact that in a HOFGLAS, the electromagnetic wave interacts only through an evanescent field with fibre (cladding). This is an order of magnitude lower than the peak field in the core which are gas molecules with much higher damage threshold for the mentioned processes.

The technical designs of HOFGLASs are still in infancy. The reported  $C_2H_2$  HOFGLAS consisted on a  $40 \mu m$  core diameter and  $1.46 \text{ m}$  length hollow-core photonics crystal fibre (HC-PCF). This was terminated in small vacuum chambers filled with active gas for filling into fibre. The optical pump source was 1 ns pulses OPO operating at  $1.521 \mu m$ . The pump beam is coupled (by suitable optics) to one end gas-filled fibre, and the laser output is observed at other end. The  $C_2H_2$  gas pressure was about 2 Torr. The laser was observed in single pass regime without any optical resonator. Suitable filter separated the transmitted pump light from laser pulse exiting the fibre. The lasing was observed at  $3.114$  and  $3.172 \mu m$  wavelengths. The pump laser threshold was as low as 200 nJ. The maximum laser conversion efficiency was 27 % at pump laser energy of 1  $\mu J$  while 500 nJ of laser pulse energy was obtained at pump of 5  $\mu J$ . Similar experiment with HCN-filled laser demonstrated a much poorer performance as compared to  $C_2H_2$ . Further work is needed in the field.

### 3.5 Summary

To summarise the chapter, the gas lasers have been one of the most widely researched, manufactured and utilised. Their versatility has fuelled intense research activity in optical physics, resonator cavities, gas discharge and laser–matter interaction. Their applications in research, medical, industrial and military fields continue. However, due to recent advances in diode laser technology, there is a definite trend to replace the gas lasers, wherever possible, by more efficient and compact solid-state laser of equivalent or better performance, though at the expense of much higher cost. However, for very high average power of tens of kW, the beam quality and the material damage of solid-state lasers are still the issues needing more attention. It is envisaged at the level of 10s of MW of average laser power, many exotic applications such as ground-based launch of small satellite into space, space debris removal and energy transmission through space may become feasible. Such a power source will most likely be a gas laser. The hybrid solid-state–gas lasers provide avenues for newer laser research.

## References

1. A. Javan, W.R. Bennett, D.R. Herriott, Population inversion and continuous optical maser oscillation in a gas discharge containing a He-Ne mixture. *Phys. Rev. Lett.* **6**, 106 (1961)
2. W.B. Bridges, Laser oscillation in singly ionized argon in the visible spectrum. *Appl. Phys. Lett.* **4**, 128 (1964)
3. W.T. Walter, M. Piltch, N. Solimene, G. Gould, Pulsed laser action in atomic copper vapor laser. *Bull. Am. Phys. Soc.* **11**, 113 (1966)
4. J.K. Mittal, P.K. Bhadani, B. Singh, L. Abhinandan, R. Bhatnagar, Design and performance of a 20W copper vapour laser. *J. Phys. E* **21**, 388 (1988)
5. S.K. Dixit, B. Singh, S.V. Nakhe, J.K. Mittal, R. Bhatnagar, Negative branch unstable resonator copper vapor laser. *Opt. Lett.* **15**, 428 (1990)
6. S.K. Dixit, J.K. Mittal, B. Singh, P. Saxena, R. Bhatnagar, A generalized diffraction filtered resonator with a copper vapor laser. *Opt. Commun.* **98**, 91 (1993)
7. S.K. Dixit, B. Singh, J.K. Mittal, R. Choube, R. Bhatnagar, Analysis of the temporal and spatial characteristics of the output from short inversion time self-terminating lasers with various resonators. *Opt. Eng.* **33**, 1908 (1994)
8. B. Singh, V.V. Subramaniam, S.R. Daultabad, A. Chakraborty, 100 W kinetically enhanced copper vapor laser at 10 kHz repetition-rate, high ( $\sim 1.5\%$ ) efficiency with low ( $\sim 1.6\text{ kW/l}$ ) specific input power and performance of new resonator configurations. *Opt. Commun.* **281**, 4415 (2008)
9. R. Biswal, P.K. Agrawal, G.K. Mishra, S.V. Nakhe, S.K. Dixit, J.K. Mittal, Development of a 16 kHz repetition rate, 110 W average power Copper HyBrID laser. *Pramana* **75**, 953 (2010)
10. R. Biswal, P.K. Agarwal, S.K. Dixit, S.V. Nakhe, A study on the purification of HBr gas by fractional distillation technique and its effect on improvement of Copper-HBr laser performance. *Opt. Eng.* **51**, 114203 (2012)
11. C.K.N. Patel, Continuous-wave laser action on vibrational-rotational transitions of CO<sub>2</sub>. *Phys. Rev. A* **136**, 1187 (1964)
12. D.J. Biswas, A.K. Nath, U. Nundy, U.K. Chatterjee, Multiline CO<sub>2</sub> lasers and their uses. *Prog. Quantum Electron.* **14**, 1 (1990)

13. A.K. Nath, A. Lala, P. Choudhary, M. Kumar, Design and operation characteristics of a high power transverse flow pulser sustained cw CO<sub>2</sub> laser. *Pramana J. Phys.* **38**, 379 (1992)
14. D.J. Biswas, J.P. Nilaya, M.B.S. Prasad, P. Raote, Switch-less operation of a TEA CO<sub>2</sub> laser. *Opt. Express* **13**, 9636 (2005)
15. G.C. Patil, P.N. Jonnalagadda, D.J. Biswas, Performance of a self-switched TEA CO<sub>2</sub> laser with multi/two/single spark channel preioniser. *Opt. Commun.* **284**, 5177 (2011)
16. H. Heard, Ultraviolet gas laser at room temperature. *Nature* **200**, 67 (1963)
17. N.G. Basov, V.A. Danilychev, Y.M. Popov, D.D. Khodkevich, The quantum generator in vacuum area of a spectrum at excitation liquid xenon by electronic beam". *JETP Lett.* **12**, 329 (1970)
18. P. Bhatnagar, B. Singh, U. Nundy, Low pressure 50 mJ KrF Laser. *Opt. Eng.* **33**, 1905 (1994)
19. N.S. Banerjee, N.K. Varshnay, K.M. Krishnan, D.V. Ghodke, *Development of 150 mJ, 150 Hz Xenon Chloride Laser with two stage Magnetic Pulse Compression circuit*, National Laser Symposium NLS-09, BARC, Mumbai, January, 13–16, 2010
20. R.S. Sendhil, P.K. Gupta, Laser based instruments for the nuclear fuel cycle. *RRCAT Newslet.* **20**, 25 (2007)
21. J.C. Polanyi, Proposal for an infrared maser dependent on vibrational excitation. *J. Chem. Phys.* **34**, 347 (1961)
22. J.V.V. Kasper, G.C. Pimentel, HCl chemical laser. *Phys. Rev. Lett.* **14**, 352 (1965)
23. R.G. Derwent, D.R. Kearns, B.A. Thrush, The excitation of iodine by singlet molecular oxygen. *Chem. Phys. Lett.* **6**, 115 (1970)
24. W.E. McDermott, D. Pchelkin, D.J. Benard, R.R. Bouske, An electronic transition chemical laser. *Appl. Phys. Lett.* **32**, 469 (1978)
25. J.V.V. Kasper, G.C. Pimentel, Atomic iodine photo dissociation laser. *Appl. Phys. Lett.* **5**, 231 (1964)
26. T.Y. Chang, T.J. Bridges, Laser action at 482, 496, and 541 μm in optically pumped CH<sub>3</sub>F. *Opt. Commun.* **1**, 423 (1970)
27. P.K. Gupta, V.P. Singhal, N.S. Shikarkhane, S. Sasikumar, U. Nundy, U.K. Chatterjee, Design and operational characteristics of a 16 μm CF<sub>4</sub> laser. *Pramana J. Phys.* **34**, 249 (1990)
28. W.F. Krupke, R.J. Beach, V.K. Kanz, S.A. Payne, Resonance transition 795 nm rubidium laser. *Opt. Lett.* **28**, 2336 (2003)
29. J. Zweibaum, A. Komashko, W.F. Krupke, Alkali vapour lasers. *Proc. SPIE* **7581**(75810G) (2010)
30. A.M. Jones, A.V.V. Nampoothiri, A. Ratanavis, T. Fiedler, N.V. Wheeler, F. Couyn, R. Kadel, F. Benabid, B.R. Washburn, K.L. Corwin, W. Rudolph, Mid-infrared gas filled photonic crystal fiber laser based on population inversion. *Opt. Express* **19**, 2309 (2011)
31. A.V.V. Nampoothiri, A.M. Jones, C. Fourcade-Dutin, C. Mao, N. Dadashzadeh, B. Baumgart, Y.Y. Wang, M. Alharbi, T. Bradley, N. Campbell, F. Benabid, B.R. Washburn, K.L. Corwin, W. Rudolph, Hollow-core Optical Fiber Gas Lasers (HOFGLAS): a review. *Opt. Mat. Express* **2**, 948 (2012)

# Chapter 4

## Diode-Pumped Solid-State Lasers and Intracavity Frequency Conversion

P.K. Mukhopadhyay

**Abstract** In this article the physics and technology of DPSS lasers with intracavity frequency conversion and the challenges faced in the thermal issues, opto-mechanical design, power scaling, pulse compression, beam quality, short-term and long-term stability, etc., are discussed. The details of some of the systems like ophthalmic laser, multicolor laser, and 100 W-class green laser developed at Solid State Laser Division at RRCAT, Indore, are presented.

**Keywords** Solid-state lasers • Diode lasers • Intracavity frequency conversion • Multicolor laser • High-power green laser

### 4.1 Introduction

LASER, in its simplest form, mainly consists of three parts: an active medium, an excitation mechanism, and a resonator. As the name suggests, a solid-state laser employs an active medium which is solid state in nature. Solid-state lasers are an important class of lasers. The large density of active ions and ease of handling of the solid-state active media facilitate efficient, compact, and reliable operation of the laser systems.

Solid-state lasers require optical sources to excite the gain medium. For a long time, flash lamps were the only option for this purpose. The drawback with this technique is the very poor overlap of their emission spectrum with the absorption spectrum of the active ions which leads to a poor efficiency of the laser system. On the other hand, the emission spectra of laser diodes are concentrated in a narrow spectral region and can be tuned to the peak absorption band of many solid-state gain media by adjusting the diode-junction temperature or by changing the composition of semiconductor material. This not only leads to efficient absorption but also avoids unnecessary heating of the gain medium resulting from the absorption at nonuseful spectral components like what happens under flash-lamp pumping. In addition to

---

P.K. Mukhopadhyay (✉)  
Solid State Laser Division, Raja Ramanna Centre for Advanced  
Technology (RRCAT), Indore, India  
e-mail: [pkm@rrcat.gov.in](mailto:pkm@rrcat.gov.in)

these unique advantages of diode pumping over the flash lamps, it also enables compactness, reliability, higher lifetime, and better beam quality of the solid-state laser system.

Indeed, the use of diode lasers for efficient pumping of laser gain medium was demonstrated in the early stage of laser development. The first report on the use of semiconductor sources to pump a solid-state laser was by Newman [1] who found that radiation near 880 nm from recombination in GaAs diodes, essentially an LED, could excite fluorescence near 1.06  $\mu\text{m}$  in Nd:CaWO<sub>4</sub>. Next, Keyes and Quist [2] demonstrated the first diode laser-pumped solid-state laser shortly after the development of the first GaAs diode lasers [3–6]. The solid-state laser was CaF<sub>2</sub>:U<sup>3+</sup> at 2.613  $\mu\text{m}$ . Ross [7] demonstrated the first diode laser-pumped Nd:YAG laser. This was pumped by a single GaAs diode laser in a transverse geometry. The YAG rod was at room temperature, but the diode laser was at 170 K for reliable operation. Most of this initial work in diode pumping concentrated in designing and demonstrating simple Nd-doped devices because the gain was too low for the insertion of intracavity elements. Chinn [8] demonstrated a longitudinal geometry, intracavity frequency-doubled NPP laser pumped by a dye laser. Thresholds of 5 mW and outputs of 1 mW single-ended output are achieved; the author noted that with simple optimization, semiconductor pumping of this source should be possible. Actual demonstration of such a device was made by Kuratev [9] by using BaNbNb<sub>5</sub>O<sub>15</sub> crystal for intracavity frequency doubling of an LED-array-pumped Nd:YAG laser. *Q*-switching was demonstrated in LED-pumped Nd:YAG and Nd-doped potassium-gadolinium tungstate (KGW) [10].

However, the need to operate at cryogenic temperature and short life prevented the use of diode lasers as pump sources for any serious applications until the mid-1980s. With the significant progress in diode laser fabrication technology during the last two decades, high-power laser diodes that can be operated reliably at the room temperature with more than 10,000 h of continuous operation are now available. The availability of such laser diodes led to a surge of interest in using them to pump solid-state laser gain media. Since then, research in the field has flourished and led to a significant maturity. The literature shows intensive investigation of a vast amount of diode-pumped solid-state (DPSS) laser configurations. An output power of 10 kW at 1.06  $\mu\text{m}$  has recently been obtained from a diode-pumped Nd:YAG laser [11].

The importance of DPSS lasers is increasing by the day as they find widespread applications in our society like in optical communications, navigation, laser medicine and diagnostics, metallurgy and material processing, geodesy and cartography, and so on. Modern DPSS lasers are fast emerging as a replacement for other laser systems based on gas or liquid active medium and enabling new technologies to generate wavelengths where the laser sources are not available.

In this article the physics and technology of DPSS lasers with intracavity frequency conversion and the challenges faced in the thermal issues, optomechanical design, power scaling, pulse compression, beam quality, short-term and long-term stability, etc., are discussed. The details of some of the systems made at Solid State Laser Division at RRCAT, Indore, for some specific applications like ophthalmic laser, the multicolor laser, and 100 W-class green laser are presented.

## 4.2 The Gain Medium

Neodymium ( $\text{Nd}^{3+}$ )-doped crystals are the most important solid-state material for diode pumping as the emission wavelength of AlGaAs-based laser diodes at  $\sim 800 \text{ nm}$  matches excellently with one of the strong absorption band of these gain media. In fact,  $\text{Nd}^{3+}$  was the first of the trivalent rare earth ions to be used in a laser, and it remains by far the most important element in this group. Stimulated emission has been obtained with this ion incorporated in at least 100 different host materials. Higher power levels have been obtained from Nd lasers compared to any other four-level material. In this article we focus on the principal host materials which are of importance for diode pumping like YAG and vanadate crystals ( $\text{YVO}_4$  and  $\text{GdVO}_4$ ). The energy-level diagram of these crystals is shown in Fig. 4.1. In these hosts, the stimulated emission is obtained at a number of frequencies within three different groups of transitions centered at  $\sim 0.9$ ,  $\sim 1.06$ , and  $\sim 1.3 \mu\text{m}$ . Radiation at these wavelengths result due to transitions from the metastable level  ${}^4\text{F}_{3/2}$  to the lower-lying Stark sublevels  ${}^4\text{I}_{9/2}$ ,  ${}^4\text{I}_{11/2}$ , and  ${}^4\text{I}_{13/2}$ , respectively [11]. Above the upper laser level are located the pump bands starting with the manifold  ${}^4\text{F}_{5/2}$ , which is responsible for absorption around 808 nm. The branching ratios for room temperature fluorescence from the upper laser level to the various manifolds are as follows:  ${}^4\text{F}_{3/2} \rightarrow {}^4\text{I}_{9/2} \approx 0.30$ ,  ${}^4\text{F}_{3/2} \rightarrow {}^4\text{I}_{11/2} \approx 0.6$ ,  ${}^4\text{F}_{3/2} \rightarrow {}^4\text{I}_{13/2} \approx 0.15$ , and  ${}^4\text{F}_{3/2} \rightarrow {}^4\text{I}_{15/2} < 0.01$ . Table 4.1 lists some of the important laser parameters for  $\text{Nd}^{3+}$  ion-doped YAG and vanadate crystals. The  ${}^4\text{F}_{3/2} \rightarrow {}^4\text{I}_{11/2}$  transition producing radiation at  $\sim 1.06 \mu\text{m}$  has the highest emission cross section in all the Nd-doped laser materials.

The stimulated-emission cross sections for transitions, at  $0.9 \mu\text{m}$  and at  $1.3 \mu\text{m}$ , are about an order of magnitude lower than that for  $1.06 \mu\text{m}$ . To obtain output at

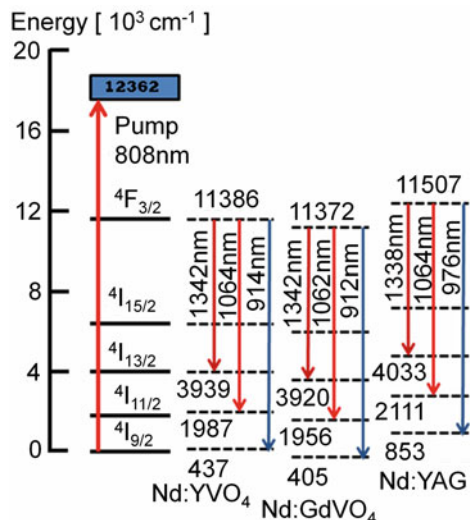


**Fig. 4.1** Energy-level diagram of  $\text{Nd}^{3+}$ -doped crystal. The downward arrows represent the major transitions at  $1.06 \mu\text{m}$ ,  $1.3 \mu\text{m}$ , and  $0.9 \mu\text{m}$ . The upward arrow represents the pump transition under diode pumping

**Table 4.1** Properties of Nd<sup>3+</sup>-doped crystal<sup>1</sup>;  $\sigma_{\text{em}}$ : stimulated-emission cross section,  $\tau_f$ : fluorescence lifetime,  $K$ : thermal conductivity

Crystal	Nd:YAG	Nd:YVO <sub>4</sub>	Nd:GdVO <sub>4</sub>
$^4F_{3/2} \rightarrow ^4I_{11/2}$	1,064 nm	1,064 nm	1,062 nm
$\sigma_{\text{em}} (\times 10^{-19} \text{ cm}^2)$	2.8	15.6	7.8
$^4F_{3/2} \rightarrow ^4I_{9/2}$	946 nm	914 nm	912 nm
$\sigma_{\text{em}} (\times 10^{-19} \text{ cm}^2)$	0.37	0.48	0.66
$^4F_{3/2} \rightarrow ^4I_{13/2}$	1,338 nm	1,342 nm	1,342 nm
$\sigma_{\text{em}} (\times 10^{-19} \text{ cm}^2)$	1.0	0.60	0.60
Fluorescence lifetime ( $\tau_f$ )	230 $\mu\text{s}$	90 $\mu\text{s}$	90 $\mu\text{s}$
K (Wm <sup>-1</sup> K <sup>-1</sup> )	11.1	5.1	11.7

these wavelengths, parasitic oscillations at the higher-gain transitions are typically suppressed by dichroic mirrors and intracavity dispersive prisms. The  $\sim 0.9 \mu\text{m}$  emission originates from the  $^4F_{3/2}$  manifold and terminates at the highest Stark level of the ground manifold  $^4I_{9/2}$ . Because the lower laser level is close to the ground state, there is a significant thermal population in this level at room temperature. This residual population induces a partial reabsorption of the laser radiation which increases the threshold. Therefore, the lasers operating at  $0.9 \mu\text{m}$  emission wavelength are quasi-three-level lasers.

### 4.3 The Pumping Scheme

Laser diodes can be used to pump the gain medium either in the end-pumping or side-pumping geometry. In the end-pumping configuration, the pump beam is introduced along the axis of the resonator, whereas in side-pumping, it enters the active medium transverse to the resonator axis as shown in Fig. 4.2a, b, respectively. Both the pumping schemes have their own merits and demerits. End pumping leads to highly efficient operation with excellent beam quality due to the good geometrical overlap of the pump beam with the cavity modes, but it suffers from poor power scaling due to the thermal fracture of the laser crystal. On the other hand, side-pumping configuration has excellent power-scaling capability but suffers from lower efficiency and poor quality of the output beam. For end-pumping purpose a fiber-coupled laser diode (FCLD) is used and the tip of the fiber is reimaged on the gain medium with a couple of lenses. The focal lengths of the imaging lenses are chosen to maximize the overlap of the pump-beam spot size and the cavity mode size at the gain medium. In side-pumping configuration a number of linear array laser diode bars are employed. The diode bars are placed close to the laser rod for threefold symmetric pumping of the gain medium. For uniform distribution of the pump beam inside the gain medium and to increase the pump-beam absorption by the gain medium, the laser rod is enclosed by a cylindrical chamber formed by diffusive

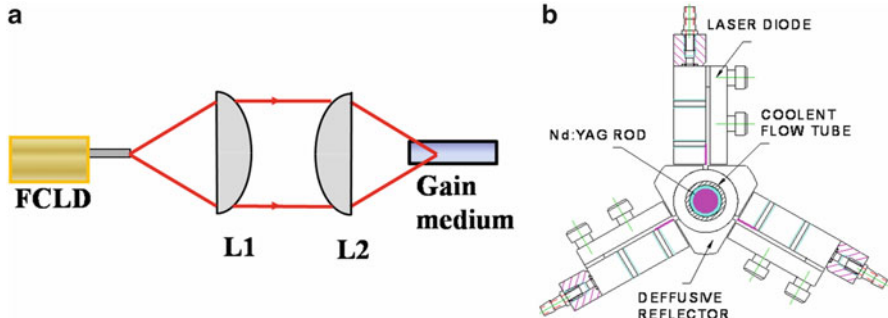


**Fig. 4.2** Pumping schemes: (a) end-pumping configuration (b) transverse-pumping configurations

reflectors as shown in Fig. 4.2b. The diffuse reflectors reflect back the unabsorbed pump beam toward the gain medium in random directions improving the uniformity of the pump-beam distribution and the absorption efficiency at the pump wavelength by the gain medium.

#### 4.4 Input Output Relation in DPSS Laser at Fundamental Wavelength

From the rate equation analysis, the output power versus the input pump power can be obtained as [12]:

$$P_{\text{out}} = \sigma_s [P_{\text{in}} - P_{\text{th}}], \quad (4.1)$$

where  $P_{\text{out}}$  is the output power,  $\sigma_s$  is the slope efficiency,  $P_{\text{th}}$  is the threshold pump power, and  $P_{\text{in}}$  is the pump power emitted from the laser diode. The slope efficiency and the threshold pump power are given by

$$\sigma_s = \frac{T}{T + L_i} \eta_p \eta_o, \quad (4.2)$$

$$P_{\text{th}} = \frac{I_{\text{sat}}}{\eta_p l} V_{\text{eff}} \frac{(L_i + T)}{2}, \quad (4.3)$$

where,  $I_{\text{sat}}$  is the saturation intensity for the gain medium ( $I_{\text{sat}} = h\nu_L/\sigma_{\text{em}}\tau_f$ ),  $h\nu_L$  is the laser photon energy,  $\eta_p$  is the pumping efficiency,  $l$  is the length of the gain medium,  $L_i$  is the roundtrip intrinsic losses,  $T$  is the transmission of the output mirror at the lasing wavelength,  $\eta_o$  is the spatial overlap efficiency of the pump beam with the cavity mode, and  $V_{\text{eff}}$  is the effective volume of the pump beam and the cavity

mode inside the gain medium. The pumping efficiency  $\eta_p$  when multiplied to  $P_{\text{in}}$  gives the population at the upper laser level. It is the product of various fractions involved in the process:  $\eta_p = \eta_t \eta_a \eta_q \eta_s$ , where  $\eta_t$  is the ratio of the power incident on the crystal to  $P_{\text{in}}$ ,  $\eta_t$  is the fraction of the pump power absorbed by the gain medium,  $\eta_q$  is the fraction of the population at the upper laser level to population at the pump band created by the absorption of the beam, and  $\eta_s$  is the ratio of the pump wavelength to the laser wavelength to account for the quantum defect. Assuming the spatial intensity distribution of the pump and cavity mode is TEM<sub>00</sub> Gaussian in shape, then the overlap efficiency and the effective mode volume can be obtained as

$$\eta_o = w_{L0}^2 \frac{\left(w_{L0}^2 + 2w_p^2\right)}{\left(w_{L0}^2 + w_p^2\right)^2}, \quad (4.4)$$

$$V_{\text{eff}} = \frac{\pi}{2} \left(w_p^2 + w_{L0}^2\right) l, \quad (4.5)$$

where  $w_p$  and  $w_{L0}$  are the pump and cavity mode size at the gain medium, respectively. It follows from Eqs. (4.1), (4.2), (4.3), (4.4), and (4.5) that the pumping arrangement and the resonator configuration should be designed in such a way that the pump spot size as well as the cavity mode size should be as small as possible to minimize the threshold pump power and the mode size should be larger than the pump spot size to maximize the slope efficiency. In fact,  $\alpha$ , the ratio of the cavity mode area to the pump-beam area at the gain medium ( $\alpha = w_{L0}^2/w_p^2$ ) is an important parameter that influences strongly the output power. Writing the output power in terms of  $\alpha$ , we get

$$P_{\text{out}} = \frac{T \eta_p}{T + L_i} \cdot \frac{\alpha (2 + \alpha)}{(1 + \alpha)^2} [P_{\text{in}} - P_{\text{tho}} (1 + \alpha)/2] \quad (4.6)$$

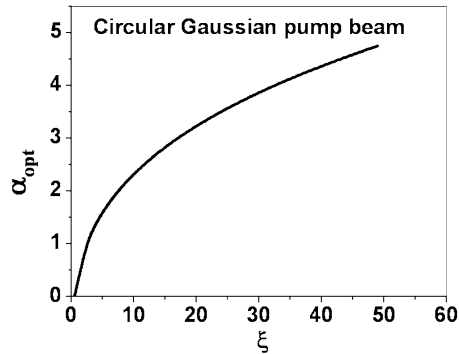
where  $P_{\text{tho}} = \pi(T + L_i)I_{\text{sat}} w_p^2/2\eta_p$ . Let us define  $\xi = P_{\text{in}}/P_{\text{tho}}$  as the normalized pump power, and differentiating (4.6) with respect to  $\alpha$  yields the condition for the optimum output power

$$\frac{d}{d\alpha} \left\{ \frac{\alpha (2 + \alpha)}{(1 + \alpha)^2} [\xi - (1 + \alpha)/2] \right\} = 0. \quad (4.7)$$

Solving for  $\xi$ , we get the relation between the input power and the optimum value of  $\alpha$

$$\xi = \frac{\left(2 + 4\alpha_{\text{opt}} + 3\alpha_{\text{opt}}^2 + \alpha_{\text{opt}}^3\right)}{4}. \quad (4.8)$$

**Fig. 4.3** The variation of  $\alpha_{\text{opt}}$  as a function of normalized input pump power  $\xi$  for circular Gaussian pump beam



This equation states that an optimum value of the mode to pump spot size ratio exists and this optimum value is an increasing function of the pump power. The behavior of  $\alpha_{\text{opt}}$  with the normalized input power  $\xi$  is shown in Fig. 4.3. It can be seen from this plotting that a larger pump power requires a larger mode to pump spot size ratio for maximum output power.

Now the output power depends on the transmission of the output coupler mirror. Differentiating Eq. (4.1) with respect to the transmission of the coupler mirror and equating it to zero, one can find the optimum coupler transmission ( $T_{\text{opt}}$ ) as a function of the pump power as

$$T_{\text{opt}} = \left( \sqrt{2 \frac{\eta_p L_i}{I_{\text{sat}} V_{\text{eff}} / l} P_{\text{in}}} - L_i \right). \quad (4.9)$$

It can be seen from Eq. (4.9) that the optimum transmission of the output coupler mirror varies as the square root of the pump power. Thus, for a given pump power, one can design the pumping and resonator geometry to obtain an optimum value for the mode to pump spot size ratio and optimum reflectivity for the output coupler mirror. Under this optimum condition, the maximum output power can be obtained as

$$P_{\text{out,opt}} = \frac{\eta_p \alpha_{\text{opt}} (2 + \alpha_{\text{opt}})}{(1 + \alpha_{\text{opt}})^2} \left[ \sqrt{P_{\text{in}}} - \sqrt{\frac{L_i I_{\text{sat}}}{4 \eta_p} w_p^2 (1 + \alpha_{\text{opt}})} \right]^2. \quad (4.10)$$

## 4.5 Intracavity Frequency Conversion in DPSS Laser

Coherent CW light sources in the visible region are of great importance for a number of scientific and technical applications such as in metrology, remote sensing, medicine, material processing, glass annealing, pumping of other laser systems, and optical parametric oscillators, etc. Intracavity frequency mixing (ICFM) in

diode-pumped solid-state lasers is an efficient method to generate high-power visible laser radiation. Neodymium ( $\text{Nd}^{3+}$ )-doped gain media are particularly suited for diode pumping and also have a large number of lasing transitions ranging from 900 to 1,400 nm. Hence, laser beams in the wavelength range from blue to red can be generated by the process of intracavity or external to cavity frequency mixing.

The efficiency of frequency conversion, in the small-signal approximation, is proportional to the intensity of the fundamental wavelength(s). As the intensity of laser radiation inside the laser resonator is considerably higher compared to the intensity of the radiation which is taken out of the cavity, in general, the intracavity frequency mixing (ICFM) process can be far more efficient compared to the frequency mixing outside the resonator. However, the ICFM poses several challenges: such as the perturbation in the dynamics of lasing process due to the ICFM, back conversion, problems related to the intensity-dependent losses, thermal issues, and damage problems, etc. In this article we will consider several physical and technological issues related to ICFM in laser systems in Nd:doped host materials like YAG,  $\text{YVO}_4$ , etc., which are pumped by semiconductor diodes. We will be primarily describing the intracavity frequency doubling (ICFD) or intracavity second harmonic generation (ISHG) process to obtain strong and efficient generation of radiation in the blue, green, and red wavelength regions with one example of intracavity frequency mixing for generation of yellow radiation.

Table 4.2 lists the nonlinear crystals used for the intracavity frequency doubling and frequency mixing. The KTP or LBO crystals were used for the generation of green and yellow beams whereas the LBO crystal was used for the generation of blue and red beams. The crystal and the plane of interaction were chosen considering the phase-matching requirements and the effective nonlinearity for the respective frequency conversion process.

In the intracavity second harmonic generation, the nonlinear crystal for frequency conversion is placed inside the cavity in order to exploit the high intracavity intensity at the fundamental wavelength as shown in Fig. 4.4a. The laser resonator is a high-finesse cavity at the fundamental wavelength and a low-finesse cavity at the second harmonic wavelength. The output coupling at the fundamental wavelength occurs in the form of second harmonic beam through the frequency conversion at the nonlinear crystal. Hence, the transmission of the coupler mirror at the fundamental wavelength can be written as

$$T = K_m I_\omega, \quad (4.11)$$

**Table 4.2** Parameters of the nonlinear crystals used for frequency conversion

Interacting wavelengths (nm), phase-matching type	Crystal, plane	Phase-matching angle	Effective nonlinearity, $d_{\text{eff}}$ (pm/V)
914 → 457, type I	LBO, XY	$\theta = 90^\circ, \phi = 21.7^\circ$	0.8
1,064 → 532, type II	KTP, XY	$\theta = 90^\circ, \phi = 23.5^\circ$	3.58
1,342 → 671, type I	LBO, XZ	$\theta = 86.1^\circ, \phi = 0^\circ$	0.82
1,064 + 1,342 → 593.5, type II	KTP, XZ	$\theta = 78^\circ, \phi = 0^\circ$	3.69

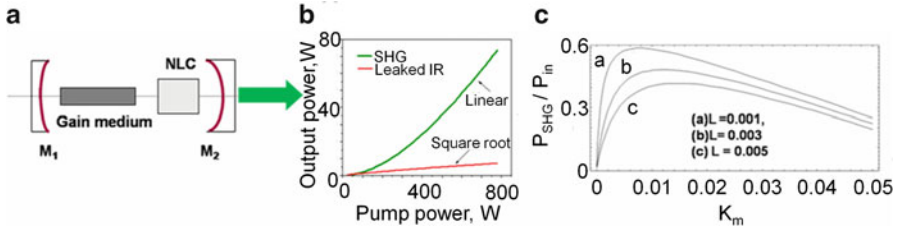


**Fig. 4.4** (a) Schematic of intracavity frequency conversion configuration. (b) Input-output relation for the frequency-converted power. (c) Optimum nonlinearity to obtain maximum frequency-converted power

where  $I_\omega$  is the intracavity intensity at the fundamental wavelength and  $K_m$  is the nonlinear coupling coefficient given by  $K_m = f l_{nl}^2 C^2$ , where  $f$  is the ratio of the mode area at the gain medium to that at the nonlinear crystal,  $l_{nl}$  is the length of the nonlinear crystal, and  $C$  is the nonlinear drive parameter given by  $C^2 = (8\pi^2 d_{eff}^2 / \epsilon_0 c \lambda_\omega^2 n_0^3) \text{Sin}^2(\Delta K l / 2) / (\Delta K l / 2)^2$ , where  $d_{eff}$  is the effective nonlinearity,  $\lambda_\omega$  is the fundamental wavelength, and  $\Delta K$  is the phase mismatch associated with the frequency conversion process. Substituting  $T$  from (4.11) in (4.2) and (4.3) and using Eq. (4.1), the second harmonic power can be obtained as

$$P_{\text{SHG}} = \frac{K_m I_\omega}{K_m I_\omega + L_i} \eta_p \eta_o \left[ P_{\text{in}} - \frac{I_{\text{sat}} V_{\text{eff}}}{\eta_p l} \frac{(L_i + K_m I_\omega)}{2} \right]. \quad (4.12)$$

In Fig. 4.4b we plot the numerically obtained second harmonic power as a function of the input diode-pump power for Nd:YAG/KTP-based system. It can be seen that the output second harmonic power represented by the green line in Fig. 4.4b increases almost linearly with the pump power. The residual power at the fundamental wavelength that is leaking through the output mirror is also plotted (red line) in the same figure. It can be seen from Fig. 4.4b that due to the intensity-dependent loss in the form of the second harmonic beam generation, the fundamental power varies as the square root of the incident pump power. The maximum intracavity frequency-converted power at a given pump power depends on the value of  $K_m$  and on the total roundtrip intracavity loss as shown in Fig. 4.4c. Hence, to obtain maximum second harmonic (SH) power, the resonator should be designed with a ratio of mode size at the gain medium to that at the nonlinear crystal such that the value of  $K_m$  is close to the optimum value and the intracavity losses should be bare minimum. In order to maximize the output power, care must be taken to avoid the back conversion of the SH beam to the fundamental beam by keeping the SHG crystal close to the harmonic mirror (to reduce the dispersion in air) and temperature stabilization as well as optimization of beam focusing (or collimation) to ensure good phase matching at all power levels.

## 4.6 Pump Power-Induced Thermal Effects

One may conclude from Eq. (4.10) that the output power from a DPSS laser can be scaled up just by increasing the pump power and the maximum output power is limited by the available pump power. However, in practice, the pump power-induced thermal effects in the gain medium impose a limitation on the power scalability from a DPSS laser. Efficient management of these thermals effects is the key for the development of high-power DPSS laser with high efficiency and good beam quality. So, let us first look at the pump power-induced thermal effects in DPSS lasers.

In solid-state laser gain medium, a fraction of the absorbed pump power is deposited in the form of heat inside the gain medium. The primary mechanism for this is the quantum defect arising from the difference in the pump and laser photon energy. Further, the nonradiative transitions associated with the excited state absorption, cross-relaxation, and up-conversion processes also lead to heat deposition.

The integrated effect of geometries of heat deposition (pumping profile) and cooling leads to an inhomogeneous temperature distribution across the gain medium which in turn leads to an inhomogeneous refractive index variation due to thermo-optic and photoelastic effects. For a Gaussian-type pump profile, the temperature distribution is nearly parabolic inside the pumped region and non-parabolic outside the pumped region of the gain medium as shown in Fig. 4.5a. Thus, the thermally loaded gain medium acts like a highly aberrated lens. The expression for thermal lens focal length,  $f_{\text{th}}$ , as function of the pump power is given by

$$f_{\text{th}} = \frac{KA}{\eta_h P_{\text{abs}}} \left( \frac{1}{2} \frac{dn}{dT} + \alpha_t C_{r,\varphi} n_o^3 + \frac{\alpha r_o (n_o - 1)}{l} \right)^{-1} \quad (4.13)$$

where  $K$  is the thermal conductivity,  $A$  is pumped area,  $\eta_h$  is the fractional thermal loading,  $P_{\text{abs}}$  is the absorbed pump power,  $dn/dT$  is the thermo-optic coefficient,  $\alpha_t$  is the thermal expansion coefficient,  $n_o$  is the refractive index of the gain medium,

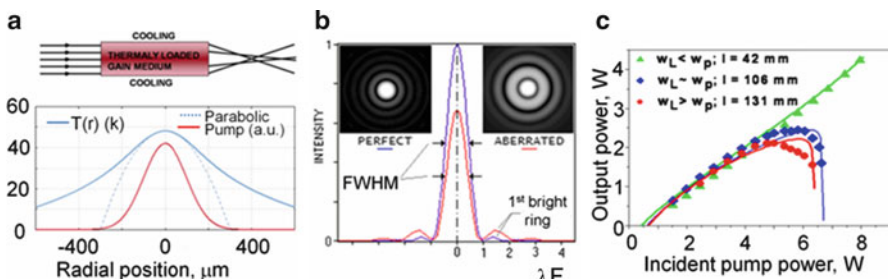


**Fig. 4.5** Thermal effects in solid-state gain medium, (a) temperature distribution and thermal lens formation, (b) loss due to thermal aberration, (c) the effect of aberrated thermal lens on the performance of the laser

and  $C_{r,\phi}$  is the photoelastic coefficient for the radial and azimuthal configuration, respectively. The first term in the parenthesis is due to the dependence of refractive index of the gain medium on the temperature and accounts for the 70 % of the thermal focal power. The second and third term arises due to the mechanical stress and thermal expansion of the crystal [11]. It can be seen from Eq. (4.13) that the thermal focal length is inversely proportional to the absorbed pump power. Further, the thermal focal length increases with the average pumped area in end-pumped system and increases with the cross-sectional area of the rod in side-pumping configuration. Due to the thermal lensing, the cavity parameters vary dynamically with the pump power and ultimately the cavity becomes unstable as the pump power approaches some critical value. In addition, the thermal aberration reduces the on-axis intensity for a paraxial beam as shown in Fig. 4.5b. This reduction in the on-axis intensity is a loss for the laser beam, and it can be shown that this loss increases with the square of the absorbed pump power and depends critically on the ratio [13] of cavity mode size to pump spot size. Hence, the threshold of the laser increases dynamically with the pump power leading to saturation and rolling over of the output power. The effect of aberrated thermal lens on the performance of the laser is shown in Fig. 4.5c. We plot the measured output power as a function of the pump power (points) along with the simulation results (solid lines) for three different configurations. It can be seen from Fig. 4.5c that when the mode size is smaller than the pump spot size, the output power increases almost linearly with the pump power, but as the cavity mode size becomes comparable or larger than the pump spot size, it leads to saturation and rolling over of the output power as the pump power is increased. Further, the thermal aberration not only reduces the laser efficiency but also degrades the quality of the output beam. The deterioration of the beam quality due to the thermal aberrations scales up with the pump power as well as increases with the mode to pump spot size ratio [14]. Thus, the successful development of high-power DPSS laser system and with intracavity frequency conversion strongly depends on the choice of the laser crystal, thermal management, and resonator design.

## 4.7 Operation at $\sim 900$ nm and Generation of Deep Blue Beam Radiation

The 914-nm emission originates from the  $^4F_{3/2}$  manifold and terminates at the highest Stark level of the ground manifold  $^4I_{9/2}$  in Nd:YVO<sub>4</sub> crystal. Because the lower laser level is only  $437\text{ cm}^{-1}$  above the ground state, there is a significant thermal population in this level at room temperature. This residual population induces a partial reabsorption of the laser radiation which increases the threshold. To achieve a low absorbed pump power at threshold,  $P_{a,\text{th}}$ , one must choose the optimum length  $L$  of the active material so the reabsorption losses will be minimal

with a significant absorption at the pump beam; these losses are described by the last term in parentheses on the right-hand side of Eq. (4.14):

$$P_{\text{a.th}} = \frac{h\nu_p (w_p^2 + w_{L0}^2)}{4\sigma\eta_q (f_l + f_u)\tau} (T + 2L_i L + \delta_{\text{reab}}), \quad (4.14)$$

where  $h\nu_p$  is the energy of a pump photon;  $w_p$  and  $w_{L0}$  are the radii of the pump beam and the cavity mode, respectively;  $\sigma$  is the stimulated-emission cross section;  $\eta_q$  is the pump quantum efficiency;  $f_l$  and  $f_u$  are the fractional populations of the lower and the upper laser levels, respectively;  $\tau$  is the fluorescence decay time;  $T$  is the transmission of the resonator out-coupling mirror;  $L_i$  describes the residual intrinsic internal resonator losses; and  $\delta_{\text{reab}}$  is the loss term due to the reabsorption of the laser beam arising from the residual population in the lower laser level. The loss term due to the reabsorption of the laser beam can be obtained as [13]

$$\delta_{\text{reab}} = \frac{\sigma f_l N_{\text{ion}} L I_{\text{sat}}}{I} \ln \left( 1 + \frac{2I}{I_{\text{sat}}} \right), \quad (4.15)$$

where,  $N_{\text{ion}}$  is the concentration of doping ions,  $I_{\text{sat}}$  is the saturation intensity given by  $I_{\text{sat}} = h\nu_L / [(f_l + f_u)\sigma\tau]$  with an energy  $h\nu_L$  of a laser photon,  $I$  is the intracavity intensity at the gain medium, and  $L$  is the length of the gain medium. It can be seen from Eq. (4.15) that the reabsorption loss is saturable with the intracavity laser intensity at the gain medium. Hence, the pump intensity must be scalable for high gain for laser operation well above the threshold, as the term for  $\delta_{\text{reab}}$  that describes the saturation of the reabsorption loss approaches zero for high circulating intensities ( $I$ ).

The layout of the compact intracavity-doubled Nd:YVO<sub>4</sub>/LBO blue laser at 457 nm is shown in Fig. 4.6. The pump source is a 30 W 808-nm-fiber-coupled laser diode array (LDA) with a core diameter of 400 μm with 0.22 numerical aperture. The output fiber-tip is reimaged on the gain medium to a spot radius of 200 μm. We used a 5-mm-long a-cut Nd:YVO<sub>4</sub> crystal with 0.1 at.% doping concentration as the gain medium. The gain medium was wrapped in Indium foil and placed in a water-cooled copper mount. The crystal cooling water temperature was maintained at 10 °C to reduce the thermal population at the lower laser level. The resonator is a simple three-mirror V-shaped cavity designed to obtain a tight spot size at the frequency doubling crystal and a large mode area at the gain medium to obtain a good overlap with the pump beam. The input flat mirror (M1) is highly reflecting

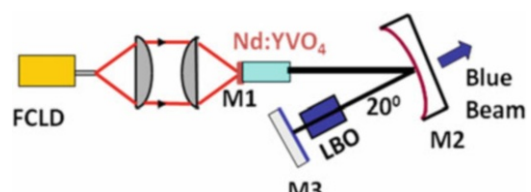


**Fig. 4.6** Schematic of the experimental setup for blue beam generation

(>99.8 %) at the lasing wavelength at 914 nm but highly transmitting (>95 %) at the pump wavelength at 808 nm. The mirror M1 was directly coated on the front-end surface of the crystal.

The cavity was folded by a curved mirror (M2) with 50 mm radius of curvature. The end mirror (M3) is again a flat mirror with a dual-wavelength high-reflection coating at 914 and 457 nm to retroreflect the backward-generated blue beam. The frequency doubling crystal is kept close to M3. The intracavity-generated blue beam is taken out through the mirror M2. All the three mirrors are coated for high transmission at 1,064 and 1,342 nm to avoid the parasitic oscillation at these wavelengths due to their high gain. For intracavity frequency doubling to generate deep blue radiation at 457 nm, type I critical phase-matched LBO crystal (4 mm × 4 mm × 10 mm) is used. The LBO crystal is placed near the mirror M3 to exploit the high intracavity intensity for efficient second harmonic generation.

As the pump power is increased beyond 11 W, the laser crosses the threshold and intense blue beam is readily observed. A photograph of the blue laser under operation is shown in Fig. 4.7. In Fig. 4.8 the slope efficiency curve for the blue

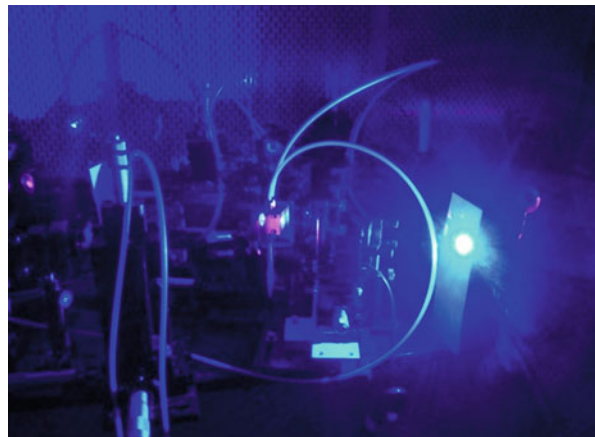


**Fig. 4.7** A photograph of the blue laser under operation

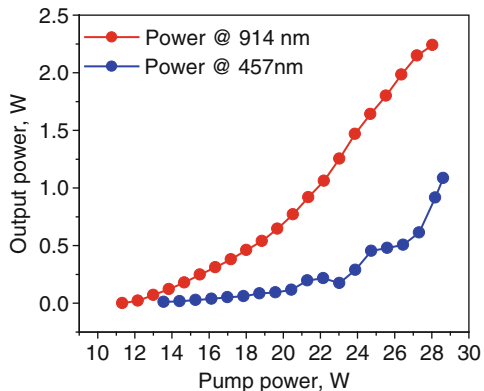
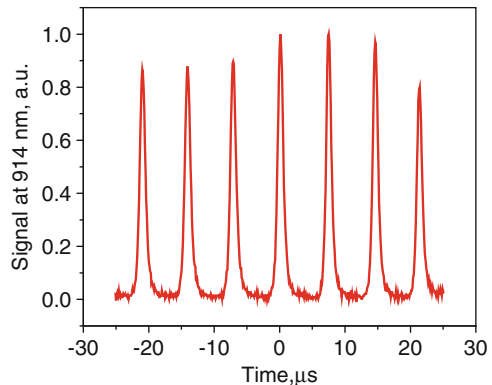


**Fig. 4.8** Slope efficiency curve at 914 nm and intracavity frequency-doubled wavelength at 457 nm

**Fig. 4.9** Self-pulsing behavior at 914 nm with 0.3 at.% doped Nd:YVO<sub>4</sub> crystal



beam as well as at the fundamental wavelength is shown. The operation at 914 nm is obtained in compact plano-concave linear cavity with a curved (100 mm ROC) output mirror with 2 % transmission at the lasing wavelength. There are two main characteristics about the output power as a function of input pump power. The first is high lasing threshold (~11 W) and the second is that there is a turning point (~21 W) where the fundamental and 457 nm output power rises rapidly from tens of milliwatts to hundreds of milliwatts. The reasons for these characteristics are all attributed to the saturation of reabsorption loss of the quasi-three-level for fundamental wave 914 nm. At lower pump power, lower circulating intensity exists in the cavity and the corresponding high reabsorption loss leads to high threshold. As the pump power increases, the circulating intensity becomes so high that it bleaches the reabsorption loss and the output power increases suddenly at this point. The laser will operate like four-level system after this turning point for the reabsorption loss is approaching zero [13]. At the maximum emitted diode pump power of 29 W, the CW power at 914 nm and at 457 nm was measured to be 2.3 W in fundamental laser configuration and 1.1 W in blue laser configuration, respectively. The output blue beam power is ~50 % of the IR beam obtained from the laser.

It is worth to mention here that the doping concentration in the Nd:YVO<sub>4</sub> crystal is an important parameter for CW operation at 914 nm. We observed strong self-pulsing operation with a higher doping concentration such as 0.3 at.% doped Nd:YVO<sub>4</sub> crystal as plotted in Fig. 4.9 due to the saturable reabsorption process. A train of pulses with 150 kHz repetition rate was observed with nearly 100 % depth of modulation. The individual pulse duration (FWHM) was ~1 μs.

## 4.8 Operation at 1,064 nm and Green Beam Generation

Due to the high-emission cross section and four-level nature of  $^4F_{3/2}$  to  $^4I_{11/2}$  transition for lasing at 1,064 nm and large effective nonlinearity of the KTP crystal for SHG at 1,064 nm, we used a compact linear cavity for efficient green beam generation by intracavity frequency doubling as shown in Fig. 4.10.

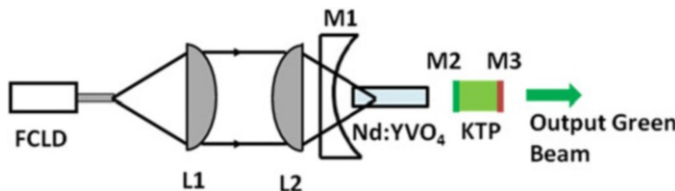
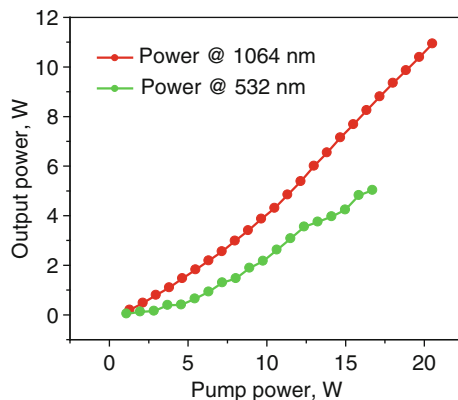


**Fig. 4.10** Schematic of the green laser setup

**Fig. 4.11** Slope efficiency curves of the laser for 1,064 nm and 532 nm operation



The input curved mirror M1 (ROC 1 m) was having HR coatings at 1,064 nm and HT coating at the pump wavelength at 808 nm. The end mirror M3 is highly reflecting at 1,064 nm but highly transmitting at 532 nm and was coated directly on end face of the KTP crystal. The other face of the KTP crystal was coated HR at 532 nm for retroreflecting the intracavity-generated green beam. The KTP crystal was cut for type II phase matching. In Fig. 4.11 we plot the slope efficiency curve for the green laser along with the measured power at the fundamental wavelength at 1,064 nm obtained by replacing the KTP crystal with a flat coupler mirror with 10 % transmission at 1,064 nm. It can be seen from Fig. 4.11 that 11 W of IR power at 1,064 nm was obtain at a pump power of 20 W corresponding to 55 % optical-to-optical conversion efficiency and more than 5 W of CW green beam at 532 nm was obtained at a pump power of ~15 W corresponding ~30 % optical-to-optical conversion efficiency. The output beam is circular in shape with a nearly diffraction-limited beam quality ( $M^2 < 1.2$ ). A photograph of the green laser system under operation is shown in Fig. 4.12.

#### 4.8.1 Green Laser Photocoagulator

Green laser beam with good beam quality is extremely useful for medical treatment particularly for the treatment of diabetic retinopathy. Patients who are suffering from

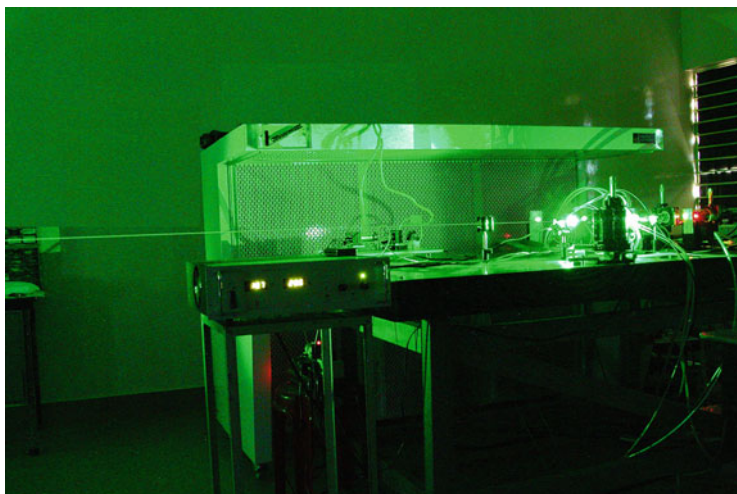


**Fig. 4.12** Photograph of the green laser under operation

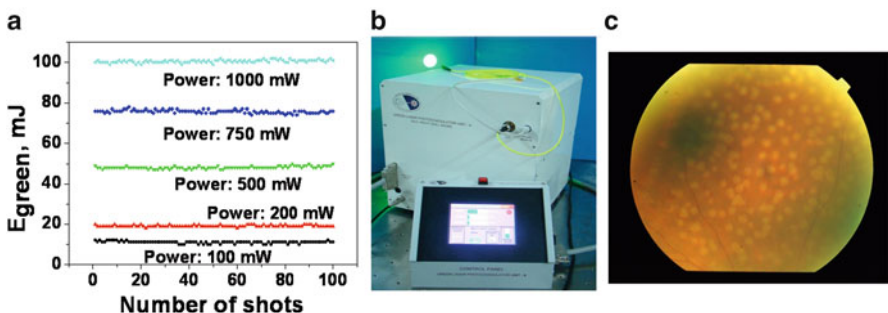


**Fig. 4.13** (a) Power stability of the green beam. (b) Green laser photocoagulator. (c) Treated portion of the retina of the patient suffering from diabetic retinopathy

prolonged diabetics develop excess blood vessels in the retina of the eye. Growth of excess blood vessels and the bursting of blood vessels can lead to blindness in such patients. Green laser beam can reach the retina of the eye without much absorption in the intermediate ocular media and can get absorbed at the blood vessels in the retina of the patients enabling controlled cutting and sealing of blood vessels. The work on green laser has been culminated in the development of a green laser photocoagulator for the treatment of diabetic retinopathy as shown in Fig. 4.13. For this application in ophthalmology, the laser diode was operated in rectangular pulsed current mode with the pulse duration varying from 50 ms to 1,000 ms, pulse energy from 50 mW to 1.2 W, and repetition rate from single shot to burst mode of 100 pulses. Figure 4.13a shows the shot-to-shot power stability in the green beam for different settings of the output power. It can be seen that the shot-to-shot pulse energy is highly stable with less than ±1.5 % energy fluctuation.

A photograph of the complete green laser photocoagulator system is shown in Fig. 4.13b. All necessary features for a medical system like foot switch operation, safety interlocks, power monitoring and display, power and exposure control, etc., are incorporated in the system. This system was given to Aravind Eye Care System, Madurai, and more than 35 patients were successfully treated in about one month. Figure 4.13c shows the photograph of a small part of the treated portion of the retina of a patient suffering from diabetic retinopathy after irradiation by the green laser photocoagulator developed in SSLD.

#### 4.8.2 High-Power CW Green Beam Generation

To generate high-power CW green beam, the diode-side-pumping configuration is employed in a Z-shaped cavity configuration. This cavity configuration has two advantages. The rod face is imaged on the KTP crystal with required demagnification; hence, the spot size does not change with pump power. In addition the focused spot size in KTP is now independent of beam size in the gain medium. Further for ICFD a high gray track resistant KTP crystal cut for type II phase matching at room temperature was used. The room temperature operation made the system very stable as the thermal problems associated with the heating of KTP were easier to resolve. The laser arrangement is shown schematically in Fig. 4.14a. The laser consists of a pump head to couple the diode laser beam to the Nd:YAG rod and the KTP crystal in a Z-shaped laser cavity which consists of four dielectric mirrors. The end mirrors, M1 and M4, are flat mirrors and the resonator is folded by two plano-concave mirrors, M2 and M3, with radii of curvatures (ROC) 50 cm and 25 cm, respectively. The pump head is placed in the arm formed by the mirrors M1 and M2 and the KTP crystal is placed in the arm formed by the mirrors M3 and M4. In Fig. 4.14b we plot the minimum and maximum limit of the pump power within which the cavity remains stable as a function of the distance d1, obtained by ABCD matrix analysis of the cavity with the pump power-induced thermal lensing

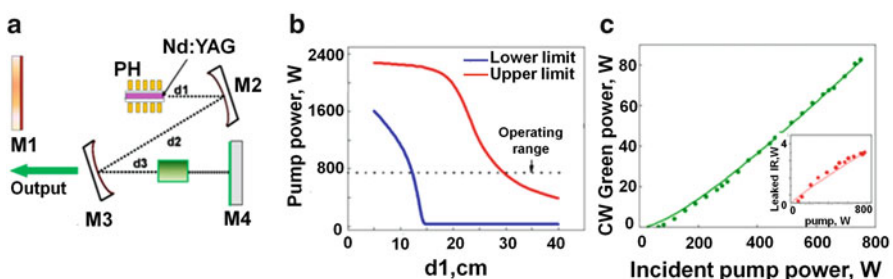


**Fig. 4.14** (a) Schematic of laser setup. (b) Upper and lower limit of the pump power for stable cavity operation as a function of  $d_1$ . (c) Variation of output green power as a function of the pump power. *Inset:* variation of leaked IR power through M3 as function of pump power

in the gain medium. Based on this analysis the distance  $d_1$  is adjusted to 25 cm to obtain stable operation throughout the operating range of the pump power as well as appropriate spot size at the various intracavity locations for efficient operation. The points in Fig. 4.14c show the CW green output power as a function of the total diode pump power. The laser has a threshold of 60 W, and at the maximum pump power of 750 W, the CW green power obtained is 82.5 W corresponding to 11 % optical-to-optical conversion efficiency [15]. The inset shows the residual IR power (maximum 2.8 W) leaking out through the output mirror. The solid lines in Fig. 4.14c are the estimated variation of the green power as well as the residual IR power which are in excellent agreement with the experiment.

#### 4.8.3 High Average Power Green Beam Generation

To generate high average power green beam, we repetitively  $Q$ -switched the laser using a dual acousto-optic modulator in a highly compact linear cavity configuration [16]. The dual acousto-optic modulator was required to increase the hold off, i.e., to suppress spontaneous CW oscillations at high pump power. The schematic of the laser setup and the corresponding slope efficiency curve is shown in Fig. 4.15a and b, respectively. The gain medium is a 100-mm-long Nd:YAG rod side-pumped by 15-nos of laser diodes, and the frequency doubling crystal is a type II phase-matched LBO crystal, which had higher damage threshold compared to KTP crystal. The laser was operated at 30 kHz repetition rate. Maximum 146 W of average green power was obtained at a total diode pumping power of 750 W corresponding to more than 19 % optical-to-optical conversion efficiency. The minimum pulse duration obtained was 90 ns. In the Z-cavity configuration due to the longer cavity length, the pulse duration was  $\sim$ 200 ns and the power was limited to 130 W. One of the major applications of high average power green laser is to pump a tunable dye laser system required in some strategic program of DAE.

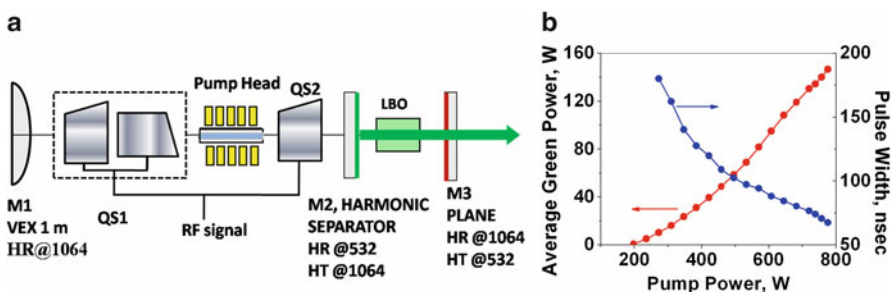


**Fig. 4.15** (a) Schematic of the laser setup. (b) Variation of average green power and pulse width with pump power

However, for efficient pumping of a dye laser, it is necessary to generate high average power green beam of pulse duration  $<50$  ns with short rise and fall time. This is difficult to achieve in intracavity frequency-doubled system due to the high finesse of the laser resonator for the fundamental wavelength. To reduce the fall time and hence the pulse duration, we replaced the plane mirror M2 in Fig. 4.15a which was having high reflection at 532 nm and high transmission at 1,064 nm. The new M2 mirror was highly reflecting at 532 nm and was partially transmitting ( $T = 30\%$ ) at the fundamental wavelength leading to reduction in photon lifetime and the resultant reduction in pulse duration at the cost of output power. The coupled-cavity analysis also shows that substantial reduction in pulse duration is expected. With this configuration the fall time of the green pulses reduced by a factor  $\sim 3$  and the generated pulse duration (FWHM) was  $\sim 37$  ns [17]. Around 55 W of average green power at 6 kHz, repetition rate was obtained at a pump power of  $\sim 400$  W. Further the timing jitter of the green pulses was reduced considerably with this configuration, making it suitable for pumping dye lasers in a MOPA type of configuration. The work culminated in the development of a complete portable green laser system as shown in Fig. 4.16a. The laser was used to pump a Rh6G-based tunable dye laser in Littrow mode cavity configuration (in collaboration with LSED, RRCAT). The photograph of dye laser pumping setup is shown in Fig. 4.16b. Figure 4.16c shows the results of the dye laser pumped by this, in-house built, green laser. More than 2 W of dye laser output was obtained at a green pump power of  $\sim 16$  W. The dye laser output was tunable from 570 to 610 nm.

Though we have generated  $\sim 80$  W of CW and  $>140$  W of average power at 532 nm by intracavity frequency doubling of diode-pumped Nd:YAG rod laser, the quality of the output beam was quite poor with a measured  $M^2$ -parameter of  $>40$ . Some applications like processing of metals, long-distance dazzling applications and pumping of Ti:sapphire-based amplifier require high average power green beam with  $M^2$ -parameter  $<20$  [16]. The reason for poor beam quality from the diode-side-pumped system is mainly due the large pumped volume which can support large numbers of higher-order modes [11]. Apart from this, the thermal birefringence which is particularly significant in Nd:YAG rod also leads to degradation of the beam quality. In order improve the beam quality, we have developed a thermal

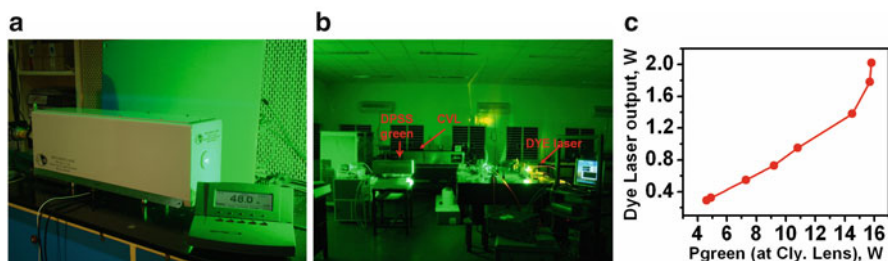


**Fig. 4.16** (a) Portable green laser system. (b) Dye laser pumping setup. (c) Dye laser output power versus incident green laser power

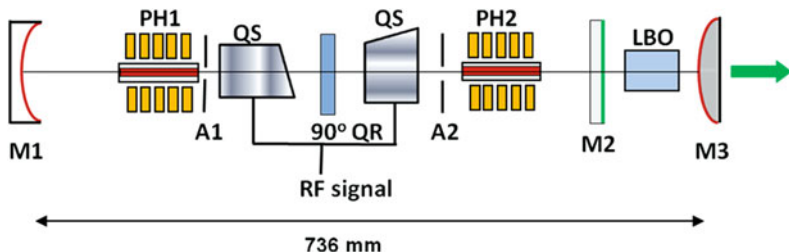


**Fig. 4.17** Schematic of the thermal birefringence-compensated DPSS green laser setup

birefringence-compensated laser arrangement with a resonator design to obtain a large  $\text{TEM}_{00}$  mode volume in order to reduce the number of oscillating higher-order transverse modes.

The laser setup is shown schematically in Fig. 4.17. It is comprised of two pump head modules (PH1 and PH2) to couple the diode laser beam to the Nd:YAG rod, a LBO crystal for intracavity frequency doubling, two acousto-optic modulators (QS) for repetitive *Q*-switching, a 90° quartz rotator for birefringence compensation, and a linear resonator. Two diode-pumped Nd:YAG pump modules have the same geometry and separated by a distance. The distance between two pump heads was adjusted based on the prior simulation results. Each laser head consists of a Nd:YAG rod (diameter: 4 mm; length 100 mm, orientation [111]) with 0.6 at.%  $\text{Nd}^{3+}$  doping concentration, a cooling sleeve, a diffusive optical reflector, and three diode array modules. The pump beam from the linear diode arrays was coupled to the laser rod through three slits (1.5 mm width) of the diffusive optical cavity in threefold symmetry. The total pumping power from the laser diodes from these two pump heads is estimated to be  $\sim 1.5$  kW. Two water-cooled apertures A1 and A2 of diameter 3.8 mm were also placed close to outer faces of the both laser rods.

For second harmonic generation (SHG), an 18-mm-long LBO crystal cut for type II phase matching at room temperature was used. For repetitive *Q*-switching (20 kHz), two orthogonally oriented AO modulators (carrier frequency 24 MHz) were used as shown in the schematic. The laser resonator was a concave-convex linear cavity to obtain a large mode area at the gain medium in order to obtain good beam quality. The rear mirror M1 is a plano-concave (radius of curvature of 2 m) with high-reflection coating at the fundamental wavelength at 1,064 nm ( $R > 99.7\%$ ) and second harmonic wavelength 532 nm ( $R > 99.5\%$ ). Mirror M2 is a plane harmonic mirror with antireflection coating at 1,064 nm ( $R < 2\%$ ) and high reflection at 532 nm ( $R > 99.5\%$ ) in order to retroreflect the backward-generated green beam. The output mirror M3 is a plano-convex mirror with high-reflection coating at the fundamental wavelength ( $R > 99.7\%$ ) and high-transmission coating ( $T > 95\%$ ) at the SHG wavelength to couple out the green beam. The pump head will be placed between the two mirrors M1 and M2 and the LBO crystal were kept between the mirrors M2 and M3. A 90° quartz rotator will be placed in between the two pump head for the compensation of the thermally induced birefringence in the laser rod. The quartz rotator rotates the state of polarization of a beam

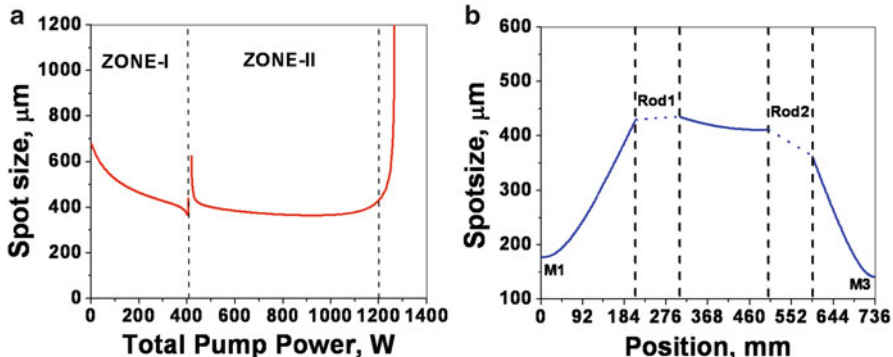
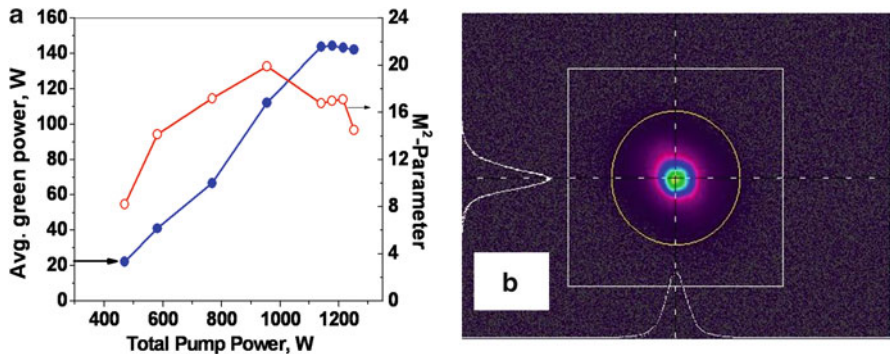


**Fig. 4.18** (a) Variation of the TEM<sub>00</sub> beam radius at PH1 as a function of the pump power. (b) Variation of TEM<sub>00</sub> spot radius as function of position from M1 at the maximum pump power

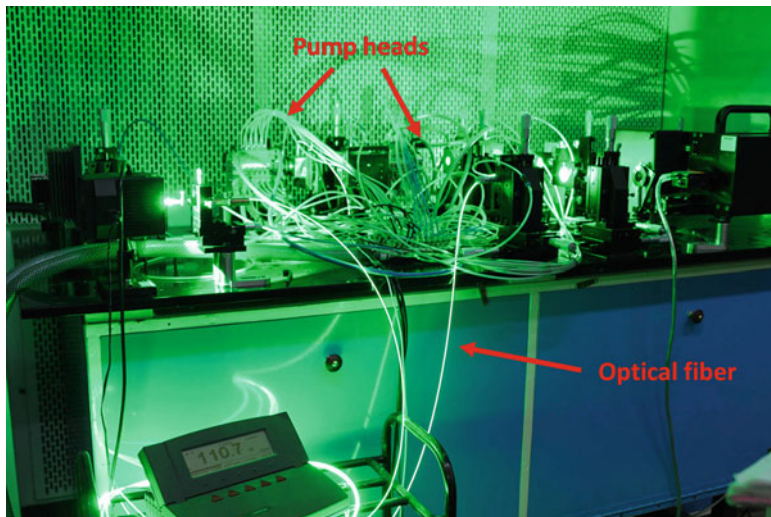
passing through it by 90°. Hence the radially and azimuthally polarized beam in one Nd:YAG rod become azimuthally and radially polarized beam in the other Nd:YAG rod respectively, and in this way both the polarizations experience the same path difference as the beam makes roundtrip through the cavity leading to a compensation of thermally induced birefringence.

Figure 4.18a shows the simulated variation of TEM<sub>00</sub> mode spot radius at the location of the PH1 as a function of the total pump power. It can be seen that the resonator has two stable operating zones (zone-I and zone-II) due to the pump power-induced thermal lensing effect. In order to obtain high output power, the laser was operated in zone-II; however, the total pump power was restricted below 1.25 kW to have the resonator stability. In Fig. 4.18b the estimated variation of the TEM<sub>00</sub> mode size as function of position from the end mirror M1 along the length of the cavity at a pump power of 1.2 kW is shown. It can be seen that the mode radius is nearly same at both the pump heads whereas it has reduced considerably at the location of the LBO crystal which is useful for efficient intracavity frequency conversion. Further, the average mode radius at the gain medium is around 0.5 mm which gives an estimated [11]  $M^2$  value of  $\sim 14.4$ . Thus, the simulation results show that the above resonator design can potentially deliver high-power average green beam with an  $M^2$  value less than 15.

The performance of the laser is shown in Fig. 4.19. The solid circles in blue of Fig. 4.19a show the variation of the average green power and the red open circles show the corresponding measured  $M^2$  parameter of the beam as a function of the pump power. It can be seen that as the resonator approaches to the unstable zone with increasing the pump power, the average green power nearly saturates to  $\sim 140$  W; however, the  $M^2$  parameter of the beam is improved considerably. At the maximum operating pump power of  $\sim 1.2$  kW, the  $M^2$  parameter is measured to be 14.6 which is close to the estimated value. Figure 4.19b shows the recorded beam profile from the laser. It can be seen that the beam is circular in shape with a smooth Gaussian-type intensity variation across it. In Fig. 4.20 we show a photograph of the laser setup under operation. The excellent quality of the green beam enables



**Fig. 4.19** Performance of the laser (a) blue solid circles, variation of average green power, and red open circles,  $M^2$ -parameter with the pump power. (b) Recorded spectral profile of the output green beam (Color figure online)



**Fig. 4.20** Photograph of thermal birefringence-compensated green laser with fiber coupling

to couple the beam in thin optical fiber of 200  $\mu\text{m}$  core diameter with more than 80 % coupling efficient. At the maximum operating pump power, around 110 W of average green power was measured at the exit tip of the fiber.

## 4.9 Operation at 1,342 nm and Red Beam Generation

The laser set up for efficient operation at 1,342 nm and intracavity frequency doubling for intense red beam generation at 671 nm is same as shown in Fig. 4.6; only the HR coatings at 914 nm is replaced with that at 1,342 nm. For intracavity

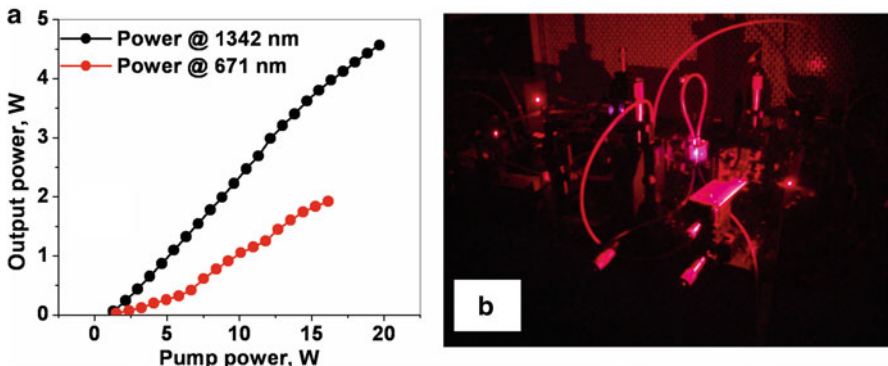


**Fig. 4.21** (a) Laser slope efficiency curves for the fundamental wavelength operation at 1,342 nm and intracavity frequency-doubled configuration at 671 nm. (b) A photograph of the red laser under operation

frequency doubling, a LBO crystal was used for type I phase matching in the x-z plane. First we operated the laser at the fundamental wavelength at 1,342 nm in a linear plano-concave cavity with a concave (ROC 100 mm) coupler mirror with 5 % transmission at 1,342 nm. The CW output power as a function of the diode pump power is shown by the black points in Fig. 4.21a. It can be seen that the laser had a threshold of  $\sim 1$  W and a maximum 4.5 W of CW power at 1,342 nm was obtained at diode pump power of  $\sim 20$  W corresponding to 22.5 % optical-to-optical conversion efficiency. The performance of the laser in intracavity frequency-doubled configuration is shown by the red circles in Fig. 4.21a. More than 2 W of CW red beam at 671 nm was obtained at a pump power of  $\sim 16$  W corresponding  $\sim 12.5$  % optical-to-optical conversion efficiency. However, further increase in the pump power leads to a rollover of the output red power at 671 nm due to the strong thermal lensing effect arising from the large quantum defect for 1,342 nm operation and longer length of the resonator in intracavity frequency-doubled configuration. A photograph of the red laser at 671 nm under operation is shown in Fig. 4.21b.

## 4.10 Dual-Wavelength Operation

Lasers emitting simultaneously at multiple wavelengths can find wide applications in many fields such as environmental monitoring, laser radar, spectral analysis and THz research, etc. In traditional laser systems, however, only one wavelength (or line) operation can normally be obtained if no special measure is taken. The emission lines with weak gain are usually depressed by the line with strong gain because of the gain competition between the laser emission lines, and this competition generally results in only the laser line with the strongest gain being generated. To meet the requirement of simultaneously multiple laser line oscillation,

special design of the laser oscillation cavity is necessary to control and to reduce the gain competition among the multiple wavelength lines of the gain medium. The first report about the multiple wavelength laser was presented by Bethea in 1973 by using a Nd:YAG as the gain medium [18]. After that, multiple wavelength lasers based on Nd:YAG [19], Nd:YLF [20], Nd:YVO<sub>4</sub> [21], and Nd:CNGG [22] have been reported, by means of designing a typical coating for the output coupler, generating in spatially shifted regions of the gain medium and using two quarter-wave plates (QWP) to make the intrinsic frequency split, etc. However, these are complex systems not only requiring precise control of the laser and cavity parameters but also suffering from wavelength and power instability due to strong gain competition. Further, the power at the individual wavelength cannot be independently controlled due to the fixed relative gain. We have demonstrated a simple laser construction for oscillation at two closely spaced wavelengths by combining Nd:YVO<sub>4</sub> and Nd:GdVO<sub>4</sub> crystals in a single cavity. We have earlier seen that for certain transitions these two crystals oscillate with slightly different wavelengths. Hence, by pumping both the crystals simultaneously in a single cavity, dual-wavelength operation with controllable individual power can easily be obtained. Further, Nd:YVO<sub>4</sub> and Nd:GdVO<sub>4</sub> being anisotropic crystals with polarized emission, the polarization state of the individual wavelength can be varied by changing the relative orientation of the c-axis of these two crystals.

The experimental setup for dual-wavelength generation at 912 and 914 nm is shown schematically in Fig. 4.22. A 5-mm-long Nd:YVO<sub>4</sub> crystal with 0.3 at.% doping and a 3-mm-long Nd:GdVO<sub>4</sub> crystal with 0.2 at.% doping concentration is inserted in a plane-parallel cavity made with two flat mirrors M1 and M2 coated suitably for oscillation at  $\sim 900$  nm. The crystals are pumped independently by two fiber-coupled laser diodes. Both the crystals are placed inside a single water-cooled

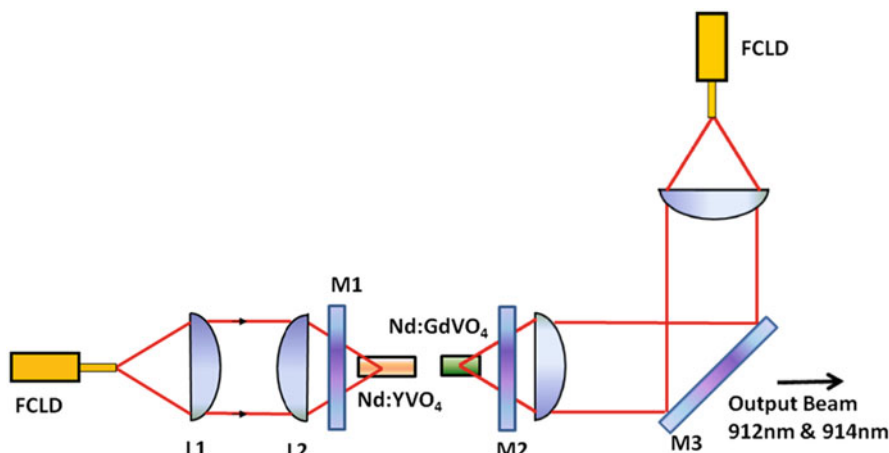


**Fig. 4.22** Schematic of the laser setup for dual-wavelength operation at 914 and 912 nm

**Fig. 4.23** Recorded spectra from the dual-wavelength laser setup. Inset is the oscilloscope trace to show the low-noise continuous wave operation

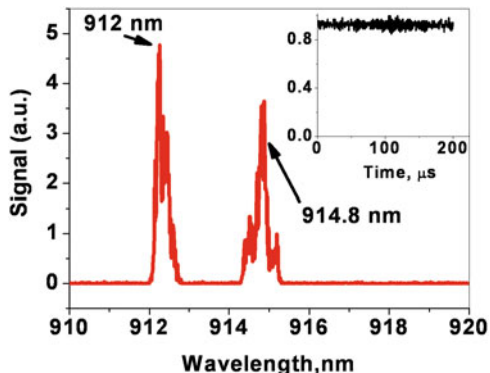
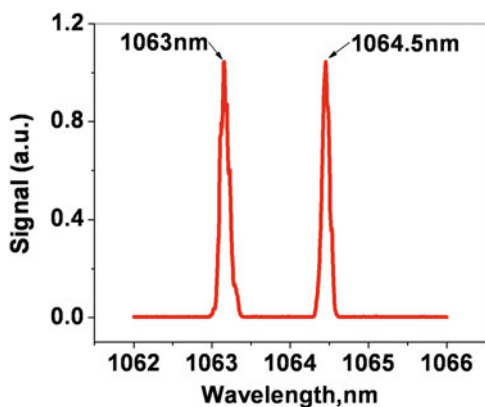


**Fig. 4.24** Dual-wavelength operation at 1,063 and 1,064.5 nm



copper block and the temperature of the copper block was maintained at 10 °C. The output is taken through the mirror M2.

The recorded spectrum of the combined output is shown in Fig. 4.23. It can be seen that the output is oscillating with two distinct wavelengths at 912 and 914.8 nm. The difference of frequency corresponds to 0.7 THz. The inset of the figure shows the oscilloscope trace of the output power which shows very little temporal modulation though we have used 0.3 at.% doped Nd:YVO<sub>4</sub> crystal. This is due to the high intracavity intensity which leads to the bleaching of the population at the lower laser level.

In a similar cavity configuration as shown in Fig. 4.22, dual-wavelength operation at 1,063 nm and at 1,064.5 nm is obtained (Fig. 4.24) by choosing mirrors with suitable reflectivity. The difference frequency corresponds to 0.3 THz. The total power obtained from this hybrid laser is in excess of 10 W which is divided almost equally in each of the wavelength component.

The polarization and power at the individual wavelength can be varied independently by changing the orientation of the crystal and by changing the corresponding diode-pumping power. The flexibility in controlling the parameters of each of the wavelengths makes these sources useful for THz frequency generation.

## 4.11 Yellow Beam Generation by Intracavity Sum-Frequency Mixing

To generate yellow beam by intracavity sum-frequency mixing, a simultaneous dual-wavelength operation at 1,064 nm and 1,342 nm is obtained in a combined dual-gain dual-cavity configuration as shown in Fig. 4.25. The resonator for oscillation at 1,064 nm is made of the mirrors M4, M5, M2, and M3, whereas the mirrors M1, M2, and M3 constitute the resonator for oscillation at 1,342 nm. These two resonators are combined to a V-shaped common arm formed by the mirrors M5, M2, and M3, with the help of the mirror M5 which has a high-reflection coating at 1,064 nm but high-transmission coating at 1,342 nm. The mirror M3 and M2 are coated highly reflecting for both 1,064 nm and 1,342 nm and highly transmitting at 593 nm for coupling out the generated yellow beam. Two Nd:YVO<sub>4</sub> crystals are used as the gain media for each of the wavelengths and placed in the respective cavity and pumped separately by laser diodes. Figure 4.26a shows the dual-wavelength operation at 1,064 and 1,342 nm under this configuration. For intracavity frequency mixing, a type II phase-matched KTP crystal is placed near the mirror M3 of the common arm. As the two wavelengths start oscillating simultaneously, yellow beam is readily observed. Figure 4.26b shows the recorded spectra of the output yellow-orange beam at 593.5 nm.

In Fig. 4.27a we plot the variation of the CW power of the yellow beam as a function of the total pump power. The maximum CW yellow power obtained was  $\sim 100$  mW. The reason for the low yellow power is due to the increased intracavity losses as large numbers of intracavity components are used. Further, the generated yellow power becomes unstable at higher pumping power and starts rolling over

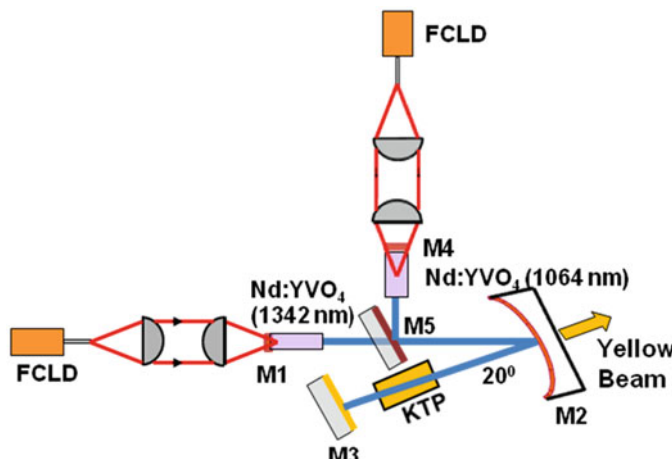


**Fig. 4.25** Schematic of the laser setup for simultaneous lasing at 1,064 and 1,342 nm and intracavity sum-frequency mixing to generate yellow wavelength at 593.5 nm

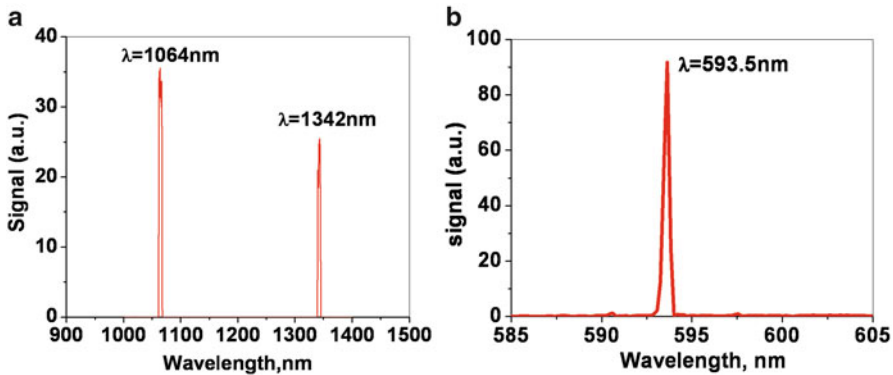


**Fig. 4.26** (a) Dual-wavelength operation at 1,064 and 1,342 nm. (b) Recorded spectra of the yellow laser beam

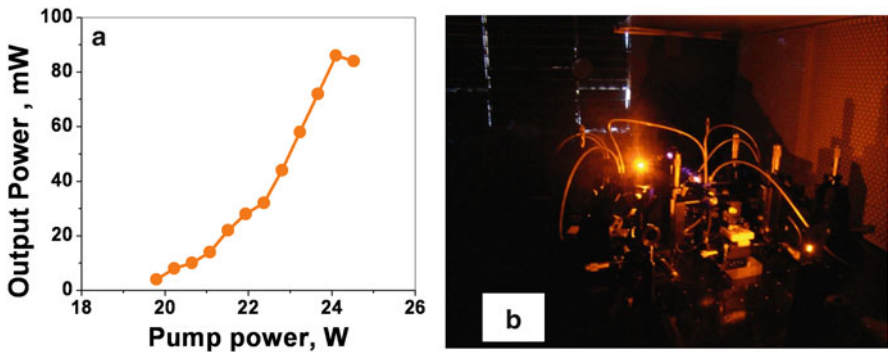


**Fig. 4.27** (a) Variation of generated yellow power as a function of the total pump power. (b) A photograph of the yellow laser under operation

as the pump power is increased. This could be due to the strong injection of 1,064 nm laser beam to the cavity for 1,342 nm which disrupts the oscillation at this wavelength. A photograph of the yellow laser under operation is shown in Fig. 4.27b.

## 4.12 Multicolor Laser and Incoherent Color Mixing to Generate White Light

Some applications like laser display, laser show, laser animation, and laser TV require simultaneous red (671 nm), green (532 nm), blue (457 nm), and yellow (593 nm) beam and their incoherent color mixing in a compact configuration [23]. All the work on intracavity frequency conversion processes as described above has

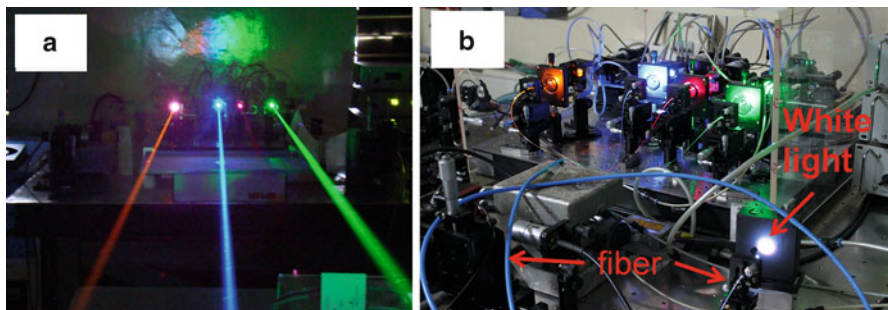


**Fig. 4.28** (a) Photograph of compact RGYB laser system. (b) White beam generation by incoherent color mixing from the RGYB laser using a multiport fiber combiner

been culminated in the development of the compact red-green-yellow-blue (RGYB) laser as shown in Fig. 4.28a. To make a compact system, all the color lasers are configured in a compact linear cavity configuration. The individual power of the colors is in the range of 50–200 mW. For incoherent mixing of the color laser beams a fiber-based multiple pump combiner (7X1) (commonly used in fiber laser) was employed. The input fiber port had a core diameter of 200  $\mu\text{m}$  which are combined to a single output port of 400  $\mu\text{m}$  core diameter. The four laser beams were coupled to four of the seven input ports of the fiber-optic beam combiner which delivers the beam in a single output. By adjusting the power of the individual lasers, intense continuous white light beam of  $\sim 300$  mW of power was obtained (Fig. 4.28b).

### 4.13 Summary

In summary diode-pumped solid-state lasers are rapidly emerging as the replacement for many gas-ion lasers and flash-lamp-pumped solid-state lasers. In this article we discussed several issues related with the DPSS lasers at the fundamental as well as intracavity frequency-doubled configuration under different pumping schemes and in CW and pulsed mode of operation. We have outlined the experimental procedures to generate laser beam at various near infrared as well as in the visible spectral regions by exploiting all the possible transitions in Nd:doped laser material under diode pumping and given experimental demonstrations using Nd:doped crystals. These studies have culminated in the development of several systems like green laser photocoagulator, multicolor (red-green-blue-yellow) laser, coupled-cavity green laser for dye laser pumping, dual-wavelength laser for THz frequency generation, high-power CW green laser, and high average power high brightness green laser system. The design issues and experimental results of these systems are discussed in detail.

## References

1. R. Newmann, J. Appl. Phys. **34**, 437 (1963)
2. R.J. Keyes, T.M. Quist, Appl. Phys. Lett. **4**, 50–52 (1965)
3. R.N. Hall, G.E. Fenner, J.D. Kingsley, T.J. Soltis, R.O. Carlson, Phys. Rev. Lett. **9**, 366–368 (1962)
4. M.I. Nathan, W.P. Dumke, G. Burns, F.H. Dill, G.J. Lasher, Appl. Phys. Lett. **1**, 62–64 (1962)
5. N. Holonyak, S.F. Bevacqua, Appl. Phys. Lett. **1**, 82–83 (1962)
6. T.M. Quist, R.H. Rediker, R.J. Keyes, W.E. Krag, B. Lax, A.L. McWhorter, H.J. Zeiger, Appl. Phys. Lett. **1**, 91–92 (1962)
7. M. Ross, Proc. IEEE **56**, 196–197 (1968)
8. S.R. Chinn, Appl. Phys. Lett. **29**, 176–179 (1976)
9. L.I. Kuratev, Bull. Acad. Sci. USSR. Phys. Ser. **48**, 104–112 (1984)
10. A. Akiyama, H. Takada, H. Yuasa, N. Nishida, in *24th Annual Meeting of the Laser Society of Japan*, Tokyo, 50–53 (2004)
11. W. Koechner, *Solid State Laser Engineering* (Springer, New York, 2006)
12. P.K. Mukhopadhyay, K. Ranganathan, J. George, S.K. Sharma, T.P.S. Nathan, Opt. Laser Technol. **35**, 173–180 (2003)
13. T.Y. Fan, R.L. Byer, IEEE J. Quantum Electron **QE-23**, 605 (1987)
14. P.K. Mukhopadhyay, K. Ranganathan, J. George, S.K. Sharma, T.P.S. Nathan, Pramana J. Phys. **58**(4), 657–668 (2002)
15. A.J. Singh, P.K. Mukhopadhyay, S.K. Sharma, K. Ranganathan, S.M. Oak, IEEE J Quantum Electron **47**(3), 398–405 (2011)
16. S.K. Sharma, P.K. Mukhopadhyay, A.J. Singh, K. Ranganathan, S.M. Oak, Rev. Sci. Inst. **81**, 73104 (2010)
17. P.K. Mukhopadhyay, S.K. Sharma, A. Singh, S.M. Oak, Rev. Sci. Instrum. **82**, 046113 (2011)
18. C.G. Bethea, IEEE J. Quantum Electron **9**, 254 (1973)
19. H.Y. Shen, R.R. Zeng, Y.P. Zhou, G.F. Yu, C.H. Huang, Z.D. Zeng, W.J. Zhang, Q.J. Ye, IEEE J. Quantum Electron **27**, 2315–2318 (1991)
20. H.Y. Zhu, G. Zhang, C.H. Huang, Y. Wei, L.X. Huang, A.H. Li, Z.Q. Chen, Appl. Phys. B **90**, 451–454 (2008)
21. Y.Y. Lin, S.Y. Chen, A.C. Chiang, R.Y. Tu, Y.C. Huang, Opt. Express **14**, 5329–5334 (2006)
22. H.H. Yu, H.J. Zhang, Z.P. Wang, J.Y. Wang, Y.G. Yu, Z.B. Shi, X.Y. Zhang, M.H. Jiang, Opt. Lett. **34**, 151–153 (2009)
23. E. Innerhofer, F. Brunner, S.V. Marchese, R. Paschotta, U. Keller, RGB source powers up - laser projection displays. Photonics Spectra **38**, 50–54 (2004)

# Chapter 5

## Semiconductor Lasers: Basics and Technology

S.K. Mehta, Alok Jain, and Deepti Jain

**Abstract** Laser diodes have become the essential part of electro-optical systems used in different areas of human activity. To learn about the laser diodes, it is essential to know the basics of their principle of operation, the different kinds of diode lasers, their applications in different systems etc. The present chapter describes mainly the aspect related to basics of laser diodes and their development technology. In Sect. 5.2, the basics of laser diodes covering fundamentals of semiconductors, their principle of operation and various configurations of emission from laser diodes are given. In Sect. 5.3 the technology of development of material structures and fabrication of laser diode is described. The characterisation of laser diodes is also included in the same section. The various applications of laser diodes and arrays are described in Sect. 5.4.

**Keywords** Basics of semiconductor lasers • Diode laser configurations • Fabrication of laser diodes • Packaging and characterisation of laser diode • Applications of laser diodes

### 5.1 Introduction

Laser diodes and arrays have become increasingly important due to the fact that they can deliver reasonably high light power with high electrical to optical efficiency, cover large range of wavelength spectrum ( $\sim 0.350\text{--}300\text{ }\mu\text{m}$ ), have smaller size and longer operating life and are more reliable in comparison to other lasers. These properties of laser diodes have made them very useful for direct use and as an optical pump source for solid-state and fibre lasers. Laser diodes are semiconductor-based p-n junction light source using the electroluminescence due to the radiative recombination of electrons and holes injected across the junction in a resonant cavity. In this chapter we consider mainly the aspect related to basics of laser diodes and their development technology. In Sect. 5.2, the basics of laser diodes

---

S.K. Mehta (✉) • A. Jain • D. Jain  
Solid State Physics Laboratory, Timarpur, Delhi 110054, India  
e-mail: [sk.mehta123@gmail.com](mailto:sk.mehta123@gmail.com)

covering fundamentals of semiconductors, their principle of operation and various configurations of emission from laser diodes are given. In Sect. 5.3 the technology of development of material structures and fabrication of laser diode is described. The characterisation of laser diodes is also included in the same section. The various applications of laser diodes and arrays are described in Sect. 5.4. There exist a large number of books and review articles, some of which are given in the reference section at the end for further studies [1–8]. This article will serve as a useful guide for beginners in the area of laser diodes.

## 5.2 Semiconductor Laser Basics

In this section, first the basics of semiconductors and then of laser diodes are described.

### 5.2.1 Basics of Semiconductors

Before discussing the laser diodes, the basics of semiconductors are described briefly with emphasis on the physical concepts which are particularly useful for semiconductor light sources. In semiconductors, there exist groups of energy levels (available for electrons) which are very close to one another and such groups are called bands. The upper group of levels is called conduction band. The lower group of levels is called valence band. These two bands are separated by a forbidden energy gap or energy bandgap  $E_g$ . Figure 5.1 shows an idealised energy-band representation of insulators, semiconductors and metals. In insulators bandgap is

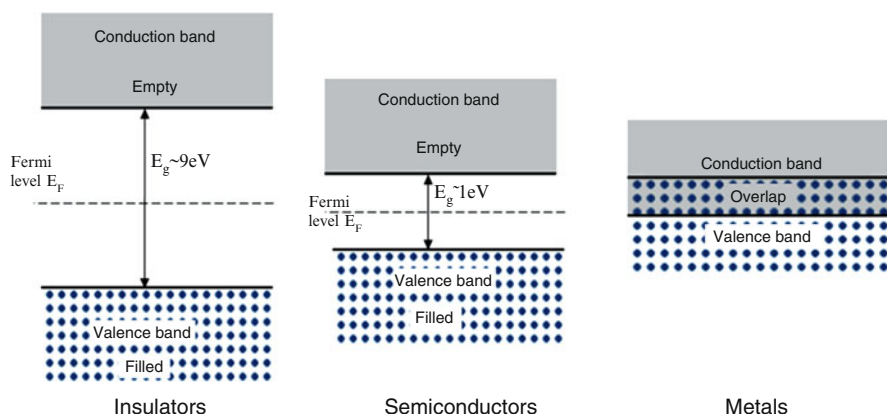


**Fig. 5.1** Schematic energy-band representation of insulator, semiconductor and metals

very large (6–10 eV) and consequently there are no free electrons to participate in current conduction. In metals, the conduction band is partially filled as conduction and valence band overlap, so there is no bandgap and conduction can readily occur. In semiconductors the bandgap (<3 eV) is not as large as in insulator. At room temperature due to thermal agitation, some electrons are raised from valence band to conduction band and free electron-hole pairs are generated. A vacancy produced in valence band, also called a hole, is equivalent to positively charged particle. These electrons and holes are mobile under application of electric field and produce electrical current [6].

The distribution of electrons in energy levels in a band of semiconductor is described by the Fermi function [6] given below

$$f(E_c) = \frac{1}{1 + e^{(E_c - E_F)/kT}} \quad (5.1)$$

where  $k$  is Boltzmann constant,  $T$  is absolute temperature,  $E_C$  is conduction band edge and  $E_F$  is Fermi level. The  $E_F$  is the energy level at which the probability of occupation by an electron is exactly half.

An important characteristic of semiconductor is that its conduction properties can be tailored by doping them by impurities. These impurities result in n-type (excess electrons) or p-type (excess holes) semiconductors. A semiconductor can be prepared with one part as p-type and the other as n-type to form a p-n junction [6, 9]. When the p-region of semiconductor is biased positively, holes from p-region and electrons from n-region are injected across the junction. They recombine with carriers of opposite charge and in process release excess energy mostly as heat in indirect gap materials like Si or mostly as light in direct gap materials like GaAs.

The semiconductors used for laser diodes have a direct bandgap. These materials have the minimum of conduction band energy exactly coinciding (at the same momentum) with maximum of valence band energy on energy-momentum ( $E$ - $k$ ) diagram as shown in Fig. 5.2. In indirect band semiconductors, the minimum of conduction band energy does not coincide with maximum of valence band energy [6]. The absorption or emission of photon from such semiconductors has to be accompanied by emission or absorption of phonon to conserve the momentum. The radiative transitions probability is much higher in direct gap semiconductors because no phonon participation is required for this direct transition. The energy of the emitted photon is equal to the bandgap energy of the semiconductor.

### 5.2.2 Basics of Operation of Laser Diodes

To describe the basic principle of operation of laser diodes, one needs to understand the interaction of light with matter. During interaction with light, a semiconductor, similar to an isolated atom, may undergo three processes [7], namely, absorption, spontaneous emission or stimulated emission. The necessary condition for the laser

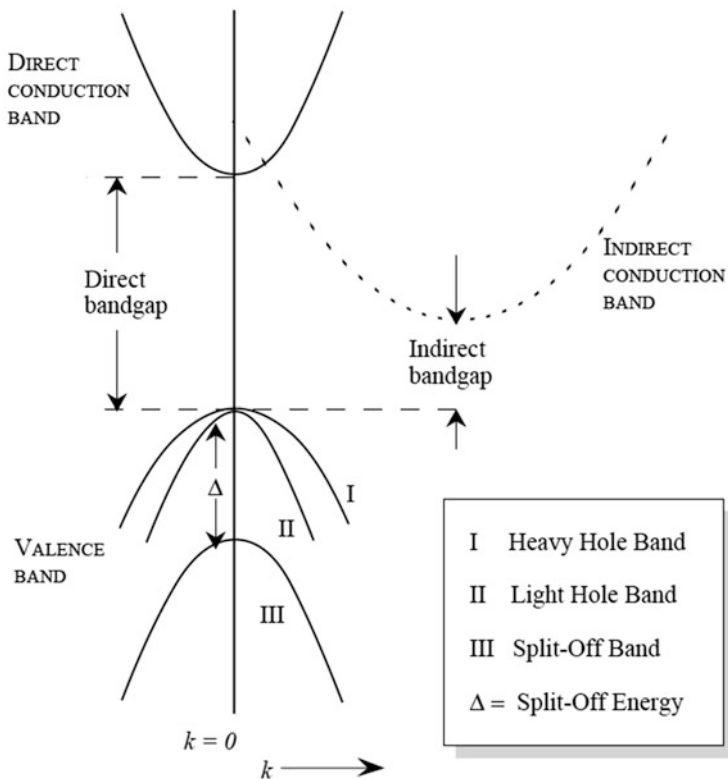


**Fig. 5.2** Schematic of valence, direct and indirect bandgap conduction bands. The conduction band of the direct gap semiconductor is shown in the *solid line*, while the conduction band of the indirect semiconductor is shown in the *dashed line*

action to take place is that stimulated emission should dominate among the three processes listed above. Three main conditions required for operation of any kind of laser are

- A pumping mechanism for creating population inversion
- A gain medium that can amplify the electromagnetic radiation propagating in it
- A feedback mechanism to obtain resonant condition

The lasing action in semiconductor lasers is achieved by forward biasing a heavily doped p-n junction [1]. Energy-band representation of heavily doped unbiased p-n junction is shown in Fig. 5.3a.  $E_{fn}$  and  $E_{fp}$  are quasi-Fermi levels for electrons and holes, respectively [10]. When a forward voltage is applied, the built-in electric field across the junction is reduced, and it allows injection of carriers. As shown in Fig. 5.3b, electrons and holes in the vicinity of junction can recombine radiatively and emit photons. The frequency  $\nu$  of photon emitted is given by Eq. (5.2)

$$h\nu = E_g \quad (5.2)$$

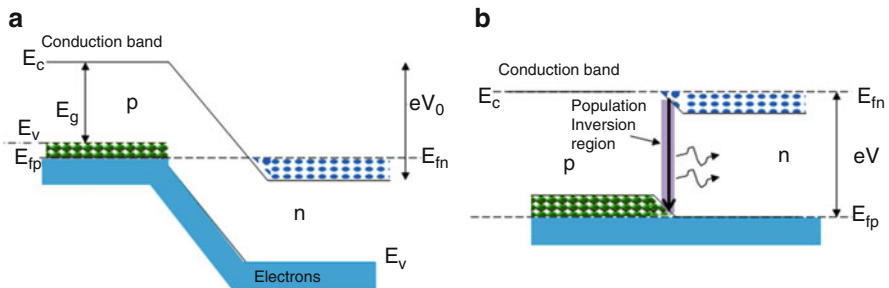


**Fig. 5.3** Schematic representation of (a) unbiased p-n junction and (b) forward-biased p-n junction

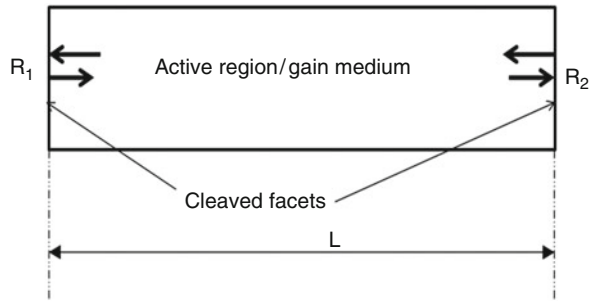
where  $h$  is the Planck's constant and  $E_g$  is the energy bandgap of the semiconductor material. When the applied bias exceeds a certain value, a large density of electrons and holes are injected to the opposite sides and population inversion is achieved in the narrow region (called active region) near the junction shown as inversion region in Fig. 5.3b. In this region the rate of photon emission exceeds that of absorption. Now the spontaneously emitted photons can stimulate a downward transition of electrons, thereby emitting photons of the same phase and frequency as the original photon. If the rate of such stimulated emission is made sufficiently high, the material exhibits gain. The frequency of emitted radiation must satisfy the condition [1, 10]

$$E_g \leq h\nu < (E_{fn} - E_{fp}) \quad (5.3)$$

The values of  $E_{fn}$  and  $E_{fp}$  depend on number of electrons/holes raised to conduction/valence band by the pumping process, respectively. Necessary condition for the lasing can be obtained in terms of quasi-Fermi levels, i.e. the separation of the quasi-Fermi levels should at least be equal to the energy bandgap.

To achieve lasing, the gain region needs to have an optical cavity to provide the necessary feedback. The semiconductor lasers have great advantage of forming optical resonant cavity by using the natural cleavage plane [1, 4, 6], which are the crystallographic plane along which atomic bonding is weakest and therefore easily broken to form mirrors. The cleaving process is used to form the resonant cavity with perfectly smooth, opposite parallel mirrors forming a Fabry-Perot (FP) resonator. The two reflector of the resonator are formed by cleaving the III-V semiconductor (GaAs/AlGaAs-based laser diodes) along one of the {011} natural cleavage planes. Photons emitted in the active region will travel along the waveguide and are reflected back and forth several times from each end face before they are partially emitted out from front facet. As the light wave passes through the cavity, it is not only amplified by stimulated emission but also lost due to free-carrier absorption, scattering at defects and inhomogeneities, other non-radiative transitions and end mirror losses. Finally, if there is more amplification than loss, the lasing is

**Fig. 5.4** Schematic of gain region within a Fabry-Perot cavity



achieved. The threshold condition can be derived by considering Fig. 5.4. The net absorption within the cavity can be given by [4]

$$\alpha = -\Gamma g + \alpha_{\text{int}} \quad (5.4)$$

where  $\Gamma$  is the confinement factor and represents the fraction of the light contained within the active region,  $g$  is the optical gain and  $\alpha_{\text{int}}$  represents internal losses of the cavity.

If  $R_1$  and  $R_2$  are the facet reflectivities of the two end facets and  $L$  is the length of the cavity, the net change in the amplitude after one round trip is set to unity at the laser threshold. This leads to the condition

$$(R_1 R_2)^{\frac{1}{2}} \exp(-\alpha L) = 1 \quad (5.5)$$

The Eq. (5.4) can be written in the form

$$\Gamma g = \alpha_m + \alpha_{\text{int}} \quad (5.6)$$

where  $\alpha_m = \frac{1}{2L} \ln \left( \frac{1}{R_1 R_2} \right)$  is the mirror loss and accounts for the radiation emitted from the FP cavity because of the finite facet reflectivities.

The above equation indicates that the gain due to the external pumping must balance the total losses to achieve lasing. The pumping current at which this condition is achieved is called threshold current. Approximate expression for threshold current can be derived as follows.

The optical gain in a semiconductor at injected carrier density  $n$  can be given by [4]

$$g(n) = a(n - n_0) \quad (5.7)$$

where  $a$  is gain coefficient and  $n_0$  is the carrier density required to achieve population inversion and is referred to as transparency carrier density. Using Eq. (5.6), the threshold carrier density can be given by

$$n_{\text{th}} = n_0 + (\alpha_m + \alpha_{\text{int}}) / a\Gamma \quad (5.8)$$

The threshold current density can be obtained by considering the carrier density rate equation

$$\frac{\partial n}{\partial t} = D (\nabla^2 n) + \frac{J}{qd} - R(n) \quad (5.9)$$

where first term accounts for the carrier diffusion,  $D$  is the diffusion coefficient,  $J$  is the current density,  $q$  is the magnitude of electron charge,  $d$  is active layer thickness and  $R(n)$  is the carrier loss due to various recombination processes.

In the steady-state  $\partial n/\partial t = 0$  and the diffusion term can be neglected. So the above equation reduces to

$$J = qdR(n) \quad (5.10)$$

Considering the various radiative and non-radiative recombination processes,  $R(n)$  can be written as

$$R(n) = A_{\text{nr}}n + Bn^2 + Cn^3 + R_{\text{st}}N_{\text{ph}} \quad (5.11)$$

$A_{\text{nr}}n$  term is due to non-radiative recombinations,  $Bn^2$  is due to spontaneous recombinations,  $Cn^3$  due to auger recombinations and the last term due to stimulated recombinations. Near-threshold stimulated emission can be neglected, and using above equations we get

$$J_{\text{th}} = qd n_{\text{th}} / \tau_e(n_{\text{th}}) \quad (5.12)$$

where  $\tau_e(n) = (A_{\text{nr}} + Bn + Cn^2)^{-1}$  is the carrier recombination time. The above expression can also be written as [1]

$$J_{\text{th}} = \frac{J_0 d}{\eta_i} + \frac{d}{\eta_i \beta \Gamma} \left[ \alpha_{\text{int}} + \frac{1}{L} \ln \frac{1}{R} \right] \quad (5.13)$$

where  $J_0$  is transparency current density,  $\eta$  is internal quantum efficiency and  $\beta$  is the gain coefficient. This equation indicates that to reduce the threshold current density of a laser diode, we need to increase the value of  $\eta_i$ ,  $\Gamma$ ,  $L$ ,  $\beta$ ,  $R = R_1 R_2$  and reduce  $d$  and internal loss  $\alpha_{\text{int}}$ .

### 5.2.2.1 Different Configurations of Laser Diodes

The laser diodes can have two major configurations: edge-emitting and surface-emitting lasers (Fig. 5.5). The edge-emitting lasers, also referred to as Fabry-Perot laser, use a waveguide to confine the light in the plane of the semiconductor chip

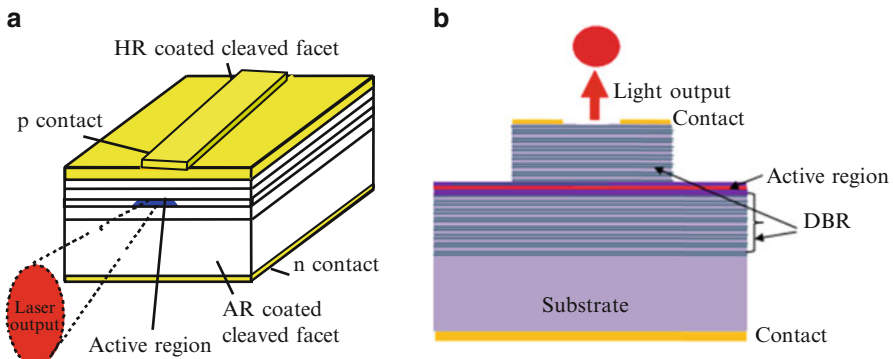


**Fig. 5.5** Schematic of (a) edge-emitting and (b) vertical-cavity surface-emitting laser diode

and emit light from the edge of the chip. The resonant cavity in these laser diodes is formed by end mirrors. In certain cases in place of end mirrors, the cavity is formed by periodic variation in refractive index within the optical waveguide by corrugating the interface between two dielectric layers providing feedback in distributed manner. These are called distributed feedback laser diodes. This configuration acts as internal grating leading to narrower spectral output. The Fabry-Perot lasers are not wavelength selective. This leads to lasing of higher modes and allows for mode jumps [1, 4].

The other – surface-emitting – configuration also referred to as vertical-cavity surface-emitting lasers (VCSELs, pronounced as vixels) has laser cavity axis and emits light perpendicular to the plane of the laser chip. The VCSELs have good fundamental mode circular beams, but at powers of only a few milliwatts, while single-stripe edge-emitting lasers can emit up to several watts [11].

### 5.2.2.2 High-Power Laser Diodes Arrays and Stacks

For still higher optical power, one needs to monolithically combine several of single emitters together in a bar. The bars are generally of 10 mm length containing as many as 25–100 monolithic single emitters depending upon the fill factor. These bars can give light output power in 100–200 W range. These bars usually have multimode emission. With special design of phase-locked bars, narrower spectral width can be achieved [12]. For still higher powers several of these bars are stacked either horizontally or vertically and output power in kilowatt range can be achieved. These high-power stacks can be used either for direct diode applications or pumping of solid-state lasers. They are continuously making inroads in the industrial and military applications [13, 14]. Schematics of typical linear array and a vertical stack are shown in Fig. 5.6.

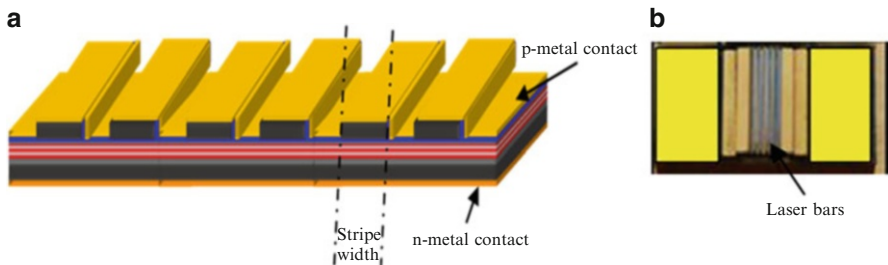


**Fig. 5.6** Schematic of (a) laser diode linear array and (b) vertical stack

### 5.3 Technology of Laser Diodes

In this section, the technology of growth of material structure and fabrication of laser diode is described.

#### 5.3.1 Material Structures and Their Growth Technology

We will first describe the progressive improvement in the material structure of laser diodes, their growth method and materials for different wavelength.

##### 5.3.1.1 Advent of Heterostructure Material Structure for Laser Diodes

The lasers described in Sect. 5.2.2 are called homojunction as the material on both n and p side of the junction is same. These kind of lasers exhibit very large threshold current density ( $\sim 5 \text{ kAcm}^{-2}$ ) and are not suitable for any practical use. In homojunction lasers, the carriers cannot be confined efficiently in the active region. These homojunctions laser diodes do not operate at room temperature. A breakthrough came in the progress of laser diode with the advent of semiconductor heterostructures [1, 15, 16]. Z. Alferov and H. Kroemer were awarded Nobel Prize in the year 2000 for pioneering work in the development of heterostructures. The carrier and photon confinement was improved by the use of a heterojunction, where unlike homojunction two materials like GaAs/GaAlAs having different bandgaps and refractive index are used. To achieve a good-quality heterostructure, the lattices between two semiconductors should be matched closely. When GaAs (lattice constant  $a = 5.6533 \text{ \AA}$ ) is used as the substrate, the ternary compound AlGaAs can

have a lattice mismatch of less than 0.1 %. For InGaAsP quaternary compound, InP ( $a = 5.8687 \text{ \AA}$ ) as substrate gives a very good lattice match. Now strained-layer (where the lattice constants do not match) heterostructures with thickness less than the critical thickness have been employed for laser diodes. The strain in the active layer provides additional degree of freedom to improve the performance of laser diodes [17, 18].

The present heterostructures for laser diodes evolved over a time from single heterostructure (SH) to double heterostructure (DH) and then low-dimensional heterostructures [1]. We briefly describe each one of them. In SH lasers, the waveguide consists of a central p-GaAs active layer bounded on one side by n-GaAs and p-AlGaAs on the other. The interface between p-GaAs and AlGaAs provides abrupt bandgap and refractive index step that is considerably higher than homojunction types of lasers, which improves carrier and optical confinement. These SH lasers provide confinement on one side of active layer only, although the threshold current density is reduced in comparison to homojunction lasers but is still considerably high to be operated at room temperature in continuous mode.

Further improvement in performance is obtained by using double-heterostructure lasers. Figure 5.7 shows energy-band diagram of a typical double-heterostructure (DH) laser where the active region having a lower bandgap (GaAs) is sandwiched between the two n and p type layers of higher bandgap material (AlGaAs). The AlGaAs layers are called the cladding layers as they provide confinement for carriers and optical field. On application of forward bias, electrons from the n-type and holes from the p-type are injected into the active region. Once inside the active region, carriers cannot cross over to other side because of the potential barrier resulting from the bandgap difference. These types of structures can confine the carriers efficiently within the active region. The generated optical field inside the optical layer should remain confined in the vicinity of the gain region for lasing action. In DH structures the optical confinement occurs by fortunate coincidence. The higher bandgap AlGaAs has a lower refractive index as compared to lower bandgap GaAs. This helps in the optical confinement of the radiation inside the active region by the total internal reflection at the interface of GaAs-AlGaAs layers. This results in substantial reduction in threshold current of laser diodes.

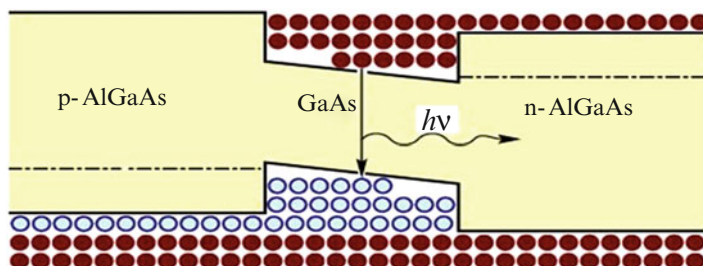


**Fig. 5.7** Energy-band diagram of heterojunction under forward bias

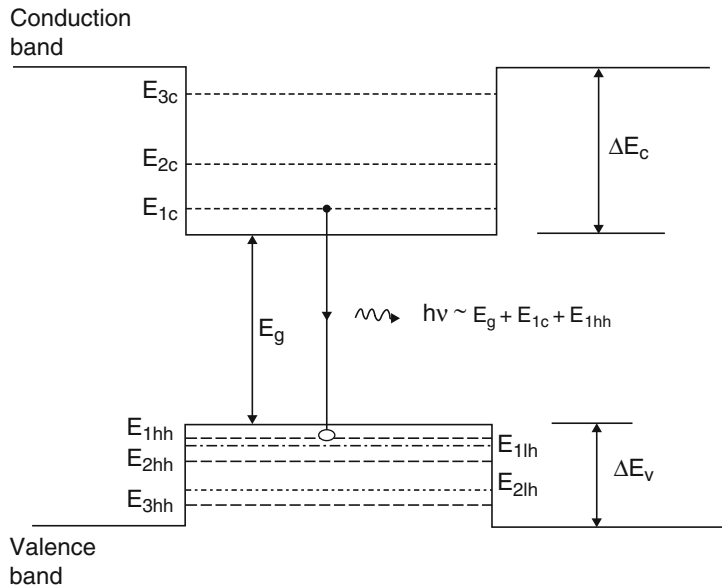


**Fig. 5.8** Schematic diagram of confined-particle energy levels of electrons ( $E_{1c}$ ,  $E_{2c}$ ,  $E_{3c}$ ) heavy holes ( $E_{1hh}$ ,  $E_{2hh}$ ,  $E_{3hh}$ ) and light holes ( $E_{1lh}$ ,  $E_{2lh}$ ) in a quantum well

In DH lasers the active layer thickness is around 0.1–0.3  $\mu\text{m}$ . The threshold current of the laser diodes can be further reduced by using quantum-well structures (QW) where the active region is a thin layer of around 10 nm thickness. This thickness value is comparable to the de Broglie wavelength of carriers and leads to quantum-mechanical effects [19, 20] due to quantisation effect. In these structures the motion of the carriers normal to the active layer is restricted. As a result the energy of the carriers moving in that direction is quantised into discrete energy levels (Fig. 5.8), instead of the continuous energy band. This effect results in an order of magnitude lower threshold current density in QW lasers than conventional DH lasers. Another important advantage of these lasers is the ability to vary the lasing wavelength only by changing the thickness of the quantum well. Other major attractions of QW lasers are low-frequency chirp, narrow spectral line width and lower sensitivity to temperature. Nowadays laser diodes are mostly fabricated with QW structures.

The active layer in QW structure is very thin and simply too small to confine the light effectively. So to exploit the properties of quantum well, laser structures are grown utilising multiple layers. Such structures are called separate confinement heterostructures (SCH) where separate layers are optimised for carrier confinement and optical confinement. A typical symmetric SCH is shown in Fig. 5.9. In this figure the active layer is quantum well of thickness  $d$  and the layers on both sides of the active layer act as carrier confining layers ( $\text{Al}_y\text{Ga}_{1-y}\text{As}$ ). The Al fraction in these confining layers is chosen in such a way that it confines most of the injected

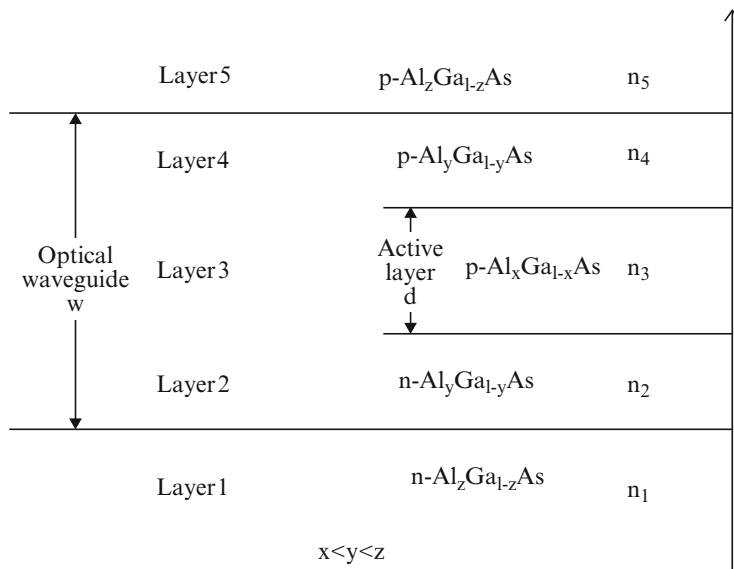


**Fig. 5.9** A typical symmetric SCH structure as five-layer dielectric waveguide

carriers within the active quantum-well layer. But the refractive index difference does not confine the light for small  $d$ . The larger step in the refractive index between  $\text{Al}_z\text{Ga}_{1-z}\text{As}$  and  $\text{Al}_y\text{Ga}_{1-y}\text{As}$  ( $z > y$ ) serves to confine the light and thereby provides the optical confinement. The quantum-well and confining layers form the optical waveguide, shown as  $w$  in Fig. 5.9. The SCH structures are useful for achieving low threshold current density and small beam divergence at large emission power. Most of the commercial laser diodes since the 1990s have been SCH quantum-well diodes. Further improvement in threshold current density is obtained by grading the alloy ( $\text{Al}_y\text{Ga}_{1-y}\text{As}$ ) composition of confining layer. Such structure is called graded-index separate confinement heterostructure (GRINSCH) [13].

Apart from quantum-well structures, material structures containing quantum wires – one-dimensional – or quantum dots – zero-dimensional – have as well been employed to further [20] improve laser diode characteristics. The technology of development of such laser diodes is still being perfected.

### 5.3.1.2 Epitaxial Growth of Material Structure

The fabrication of laser diodes and arrays involves the growth of quantum-well material structure which in simplest form is as shown in Fig. 5.9. The layer structure according to the requirement is grown by either molecular beam epitaxy (MBE) [17] or molecular organic chemical vapour deposition (MOCVD) technique [21, 22]. These are much more advanced epitaxial techniques in comparison to liquid- and vapour-phase epitaxy used in earlier times. A very precise control of thickness and

composition through two-dimensional growth methods is possible with MOCVD and MBE. For growth of high-quality material structure, one needs to optimise various growth conditions (like growth temperature, group III to V ratio) to obtain smooth interfaces of quantum well and low oxygen content in aluminium-containing layers. Low oxygen content provides higher radiative efficiency of the AlGaAs layer. MOCVD method is more suitable for high-scale production. However, these epitaxial methods require very expensive equipments and elaborate operational and maintenance infrastructure.

### 5.3.1.3 Semiconductor Materials for Different Wavelengths of Laser Diodes

The wavelength of emission of laser diode is the key parameter as the interaction of light is strongly dependent on the wavelength for both solid-state and biological systems. New materials and structures for semiconductor lasers is a topic of intense research and development. The laser emission wavelengths from different material systems cover the range from 0.3 to 3  $\mu\text{m}$  at room temperature. With the advent of quantum-cascade lasers [13, 23] which exploits intersub-band transitions, the wavelength range can be extended to over 300  $\mu\text{m}$ .

The first semiconductor lasers were demonstrated using *p-n* junctions in GaAs [1, 2]. GaAs-based devices are used for 630–1,060 nm wavelength range. InGaAsP/InP system can cover a wavelength range of 1,100–1,900 nm and is most widely used in lasers, used for fibre-optic communication systems. The spectral range covered by III–V compound and alloys is shown in Fig. 5.10 [3, 4].

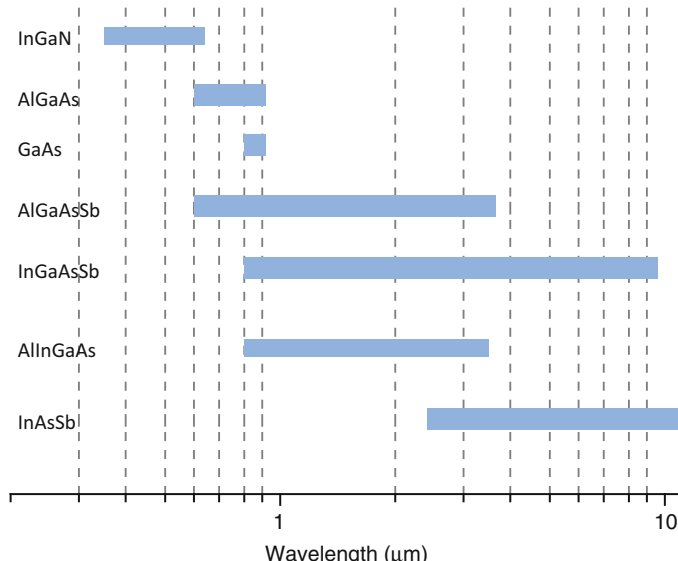


**Fig. 5.10** Spectral coverage of lasers based on III–V semiconductors alloys and compound

For long wavelengths in IR, as required in pollution diagnostics, antimonide-based alloys or quantum-cascade lasers are used. Blue-green laser diodes were earlier fabricated using II-VI materials, where lattice matching to GaAs substrates can be achieved using the ZnMgSSe-based system [3, 4]. Now nitride-based alloys (GaN-AlN-InN) have overtaken this wide gap area and significant progress has been made using these materials. The InAlGaN system has direct bandgap over the whole composition range. This material system can cover wavelength range from around 350 to 620 nm [3].

### 5.3.2 Technology of Fabrication of Laser Diodes

The laser diode chip fabrication involves the stripe formation, metallisation for ohmic contact formation, cleaving and scribing of laser structure for resonant cavity formation, multilayer dielectric coatings (high-reflective HR and antireflection AR) of laser facets for obtaining optical power from one end and for protection of facets from degradations, packaging of laser diodes and arrays on packages capable of providing good heat sinking. These steps are described below.

#### 5.3.2.1 Fabrication of Laser Diode Chip

The laser diodes are fabricated in stripe-geometry configuration as shown in Fig. 5.5a. In stripe-geometry devices the current flow is confined essentially to the stripe region only. Stripe-geometry formation helps in the reduction of operating current, reduces filamentation (localised emission from narrow regions) and improves degradation properties in comparison to broad-area laser diodes [1]. Stripe geometry with small width (5–10  $\mu\text{m}$ ) helps in realising single-mode emission. Stripe geometry can be realised by formation of mesa, proton bombardment or buried heterostructure [4]. These structures can be classified into two groups: gain guided or index guided. In gain-guided structures the lateral confinement of optical mode is provided by lateral variation of optical gain, whereas in index guided, lateral confinement is by virtue of change in refractive index. The proton-bombarded stripe is a gain-guided structure and buried heterostructure is strongly index guided, whereas mesa-stripe devices are considered weakly index guided.

Mesa-stripe structures are fabricated by masking the stripe using photolithography and etching the epitaxial layers outside the stripe. A dielectric is then deposited outside the stripe region. In proton-bombarded devices stripes are formed by masking the stripe and irradiating the material with high-energy particles like protons to create regions of high resistivity, which confines the current in stripe region. There are number of other schemes of stripe formation and a detailed description can be found in [4].

After stripe formation metallisation on epitaxy side is carried out for ohmic contact formation. The wafer, typically 350–500  $\mu\text{m}$  thick, is then thinned down to 100–120  $\mu\text{m}$ . The thinning of the wafer is necessary to reduce the series resistance

and facilitate cleaving to form the laser mirrors. Metallic contacts are then deposited on thinned substrate side. A detailed description of stripe-geometry fabrication and VCSEL can be found in reference [1, 11]. The wafer with metallic contacts is cleaved along crystallographic planes – to form laser mirrors – into bars having typical length of one cm. The cavity length is determined by the width of these bars [13]. After cleaving, the facets must be immediately coated to protect the mirrors against oxidation and to modify the reflectivity of the facets. The facet coating may be carried out using electron beam or sputtering techniques. For antireflection coating, single layer of quarter-wavelength thickness of material like  $\text{Al}_2\text{O}_3$  or  $\text{SiO}_2$  is used. For high-reflection, dielectric stack of quarter-wavelength thickness of alternate low ( $\text{Al}_2\text{O}_3$ ) and high refractive index material ( $\text{TiO}_2/\text{Si}$ ) is used.

### 5.3.2.2 Packaging of Laser Diode

After facet coating these laser diode bars are scribed to form single-stripe laser diodes. Then these laser diodes are packaged on suitable packages. Packaging is one of the most important steps in the development of laser diode because it provides heat dissipation, mechanical support and electrical connections and makes device usable outside the laboratory [13, 24].

Laser diode packaging is a three-step process. The first step is die bonding of laser diode chip to a heat sink using a suitable solder. These solders can be categorised into two types: hard solder like AuSn or soft solder like indium. The choice of solder is dependent on number of parameters [14]. The standard heat sink material in nearly all commercially available laser diode packages is copper owing to its excellent thermal conductivity, good mechanical machining properties and comparably low price. The copper package acts as mechanical support, provides heat sinking and acts as p electrode. One important issue in the die bonding is the placement of the laser diode chip with respect to the edge of the seat of mounting. The emitting front of the laser diode chip needs to be precisely aligned with respect to front edge of package. In case a part of the front facet of the chip hangs out, hot spots may appear there, resulting in possible facet damage and reduction of lifetime. If the front facet is behind the edge of package, the shape of the emitted light beam will be distorted due to reflections from the package surface. In the second step, on the topside of laser chip gold wire bonding is carried out for making n electrode, which is insulated from the copper package. Finally the package is hermetically sealed using optical window to protect the laser from environmental degradation.

### 5.3.2.3 Characterisation of Laser Diodes

The most important parameters of laser diode are threshold current, output power and slope efficiency. Figure 5.11a shows typical light-current characteristics of a laser diode. On increasing the injected current, initially output optical power increases slowly and this corresponds to spontaneous emission. At certain current

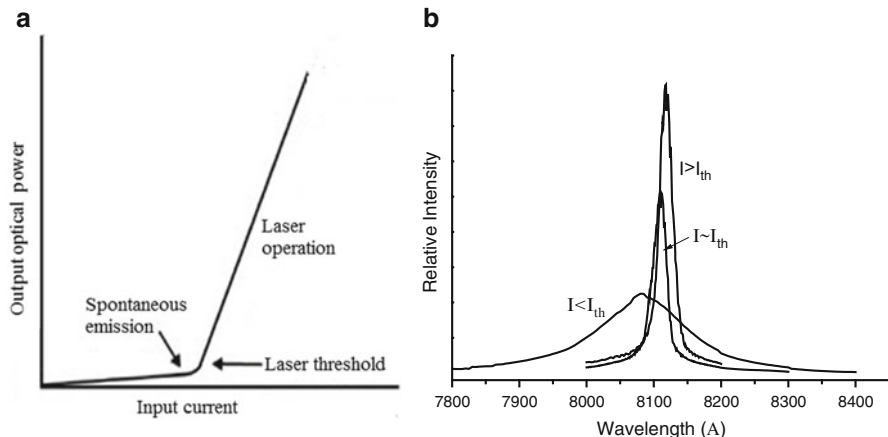


**Fig. 5.11** Typical (a) light-current characteristics and (b) emission spectrum at different current levels of laser diodes

value there is a sharp increase in output power. This current value is called threshold current of laser diode and corresponds to onset of lasing. Beyond this current value, the curve is linear and slope of this part of the plot gives slope efficiency, which is defined as power per unit current. The slope efficiency is also an indicator of differential quantum efficiency.

Figure 5.11b shows emission spectrum of laser diode at different injection current. At current lower than the threshold value, the spectra is broad and full width at half maxima (FWHM) lies in 100–400 Å range. As the current is increased, the light output increases sharply and spectrum narrows down considerably. Above the threshold current FWHM reduces to 10–20 Å. This narrowing of the spectral width is an indicator of lasing action.

The near-field image of laser emission can be seen by Si CCD detector. It shows the variation of intensity on the facet from several elements. The image of emission as on the facet can be used for analysis of non-uniformity and other defects [1]. The beam profile and divergence in free space of laser light is obtained by far-field pattern of laser diode. The pattern gives intensity variation in both perpendicular and parallel direction to the plane of junction. The output beam of diode laser is highly elliptical because of the rectangular shape of the emitting aperture. Typically, full angle at half maxima is  $\sim 40^\circ$  and  $\sim 10^\circ$  in perpendicular and parallel directions, respectively [13].

## 5.4 Applications

Laser diodes find applications in all spheres of human activity – be it in defence, atomic energy, space, medical, industry, telecommunication, data storage, entertainment or cosmetics, etc. In defence, space and atomic energy, they are extensively

used in optical pumping of solid-state laser in range finder, target designators, proximity fuse bomb, directed energy weaponry, remote sensing, spectroscopy, field imaging, etc. In medical they are being used for pain relieving, wound healing, photodynamical treatment of cancer lesions and noninvasive diagnostics. In industry the high-power laser diodes are used for material processing, cutting, welding, laser-assisted machining, soldering of contacts on PCB boards, etc. [14]. In cosmetics they are used for skin treatment and hair reduction [25]. The single-mode laser diodes are used in long-haul communication [26]. Laser diodes are also used in compact discs drives for reading and writing purposes, laser printers, barcode readers, image scanning, combustion ignition and laser pointers. In combination with solid-state lasers, they are used for laser shows etc. Long-wavelength laser diodes are used for environmental monitoring [23].

## References

1. H.C. Casey, M.B. Panish, *Heterostructure Lasers* (Academic, New York, 1978)
2. H. Kressel, J.K. Butler, *Semiconductor Lasers and Heterojunction LEDs* (New Academic Press, London, 1977)
3. E. Kapon, *Semiconductor Lasers: Materials and Structures* (Academic, London, 1999)
4. G.P. Agarwal, N.K. Dutta, *Long-Wavelength Semiconductor Lasers* (Van Nostrand Reinhold Company, New York, 1986)
5. C.H. Gooch, *Gallium Arsenide Lasers* (Wiley-Interscience, New York, 1969)
6. S.M. Sze, *Physics of Semiconductor devices*, 3rd edn. (Wiley, New Jersey, 2007)
7. N.G. Basov, *Semiconductor Lasers Nobel Lecture* (Elsevier, Amsterdam, 1972)
8. W.T. Tsang, *Semiconductor Injection Lasers, I Semiconductors and Semimetals: Lightwave Communications Technology, Part B* (Academic, London, 1985)
9. C. Kittel, *Introduction to Solid State Physics* (John Wiley & Sons, 8th edn, 2004)
10. B.G. Streetman, *Solid State Electronic Devices* (Prentice Hall of India, Englewood Cliffs, NJ, 2006)
11. H. Li, K. Iga, *Vertical Cavity Surface Emitting Laser Devices* (Springer, Berlin Heidelberg, 2003)
12. D. Botez, D.R. Scifres, *Diode Laser Arrays* (Cambridge University Press, Cambridge, 1994)
13. R. Diehl, *High-Power Diode Lasers: Fundamentals, Technology, Applications*. Topics in Applied Physics, vol. 78 (Springer, Heidelberg, 2000)
14. F. Bachmann, P. Loosen, R. Poprave, *High Power Diode Lasers: Technology and Applications* (Springer Series in Optical Sciences, 2007)
15. H. Kroemer, Quasi electric fields and band offsets: teaching electrons new tricks Nobel lecture. Rev. Mod. Phys. **73**, 783–793 (2001)
16. Z.I. Alferov, The double heterostructure: concept and its applications in physics, electronics and technology Nobel lecture. Rev. Mod. Phys. **73**, 767–782 (2001)
17. E.H.C. Parker, *Technology and Physics of Molecular Beam Epitaxy* (Plenum Press, New York, 1985)
18. W.T. Tsang, Quantum confinement heterostructure semiconductor lasers, in *Semiconductor and Semimetals*, vol. 24 (Academic, New York, 1987), pp. 397–458
19. R. Dingle, *Festkorperprobleme/Advances in Solid-State Physics*, vol. 15 (Pergamon/Vieweg, Braunschweig, 1975)
20. P. Zory, *Quantum Well Lasers* (Academic, New York, 1993)
21. A.Y. Cho, J.R. Arthur, in *Progress in Solid State Chemistry*, ed. by G. Somorjai, J. McCaldin (Pergamon, New York, 1975)

22. G. Stringfellow, *Organometallic Vapor-Phase Epitaxy: Theory and Practice* (Academic, San Diego, California, 1998)
23. H.C. Liu, F. Capasso, *Intersubband Transitions in Quantum Wells: Physics and Device Applications II*. Semiconductor and Semimetals, vol. 86 (Academic, San Diego, 2000)
24. J.W. Tomm, J. Jimenez, *Quantum-Well Laser Array Packaging: Nanoscale Packaging Techniques* (McGraw Hill, 2007)
25. C. Raulis, S. Karsai, *Lasers and IPL Technology in Dermatology and Aesthetic Medicine* (Springer-Verlag, Berlin Heidelberg, 2011)
26. K. Thyagarajan, A. Ghatak, *Fibre Optic Essentials* (Wiley, Hoboken, New Jersey, 2007)

# Chapter 6

## Fiber Lasers

K. Thyagarajan

**Abstract** Optical fiber lasers in which the lasing takes place within the core of an optical fiber have assumed tremendous importance in recent years. Using components developed specifically for fiber telecommunication applications, fiber lasers have seen an explosive growth in terms of high output powers, ultrashort pulses, and extensive wavelength region. After a very brief introduction to optical fibers and their characteristics specific to fiber laser applications, using the laser rate equations, the chapter provides the fundamentals of fiber lasers and their operating characteristics.

**Keywords** Single-mode fiber • Fiber lasers • Erbium-doped fiber laser • Fiber laser analysis

### 6.1 Introduction

Optical fiber lasers in which an appropriately doped optical fiber forms the gain medium is revolutionizing the field of lasers. Fiber lasers possess many interesting advantages vis-à-vis other laser systems. In particular, since the laser beam is confined to a very small cross-sectional area within the core of the fiber, large pump intensities can be achieved even with small pump powers and thus leading to lower pump power thresholds. Since both the pump and the laser beam are propagating within the fiber, they overlap very well and this also adds to increased efficiency of the laser and efficiencies of 80 % are possible. Since the fiber guides the pump beam, one can use very long-length cavities without bothering about the divergence of the pump laser beam. As the ratio of surface area to volume of fiber laser is very large, it does not suffer from thermal problems and heat dissipation is much easier. The output beam is of very good quality since it emerges as the fundamental mode of the fiber. Also since the components in the laser are made up of fibers which are all spliced, there are no mechanical perturbation problems such as in

---

K. Thyagarajan (✉)  
Physics Department, IIT Delhi, New Delhi, India  
e-mail: [ktrajan@physics.iitd.ac.in](mailto:ktrajan@physics.iitd.ac.in)

bulk lasers with separate mirrors. Using components developed specifically for the telecommunication applications, fiber lasers have seen an explosive growth in terms of high output powers, ultrashort pulses, and extensive wavelength region. With developments in large-mode area optical fibers, photonic crystal fibers, etc., the field is continuing to grow [8, 10].

There are many important fiber lasers such as erbium-doped fiber laser (for operation at 1,550 nm), ytterbium-doped fiber laser (for operation at 1,060 nm), bismuth-doped fibers (for operation in the region of 1,150 to 1,550 nm [2], etc. In this chapter we will discuss the theory behind erbium-doped fiber lasers. The analysis given here closely follows the book on lasers [12] where more details can be found.

## 6.2 Single-Mode Optical Fiber

In this section we will present an overview of single-mode optical fibers and their characteristics specific for fiber laser applications. For further details on optical fiber properties, readers are referred to books on fiber optics [see e.g., [3]].

An optical fiber is a cylindrical structure consisting of a central core of radius  $a$  and refractive index  $n_1$  surrounded by a cladding of refractive index  $n_2$  with  $n_2 < n_1$  (Fig. 6.1). Light guidance takes place through the phenomenon of total internal reflection at the core-cladding interface. In order to understand light propagation through the optical fiber, we need to solve Maxwell's equations in the different regions and apply appropriate boundary conditions [3]. Practical fibers have a small fractional index difference between the core and cladding [ $(n_1 - n_2)/n_1 \ll 1$ ], and under such a weakly guiding situation, we can approximate the modes to be linearly polarized. The solution of the eigenvalue problem leads to what are referred to as linearly polarized modes (LP modes). Each mode at a frequency  $\omega$  is characterized by a transverse field distribution of the form

$$E(x, y, z, t) = A\psi(x, y) e^{i(\omega t - \beta z)} \quad (6.1)$$

where  $\psi(x, y)$  represents the transverse field distribution of the mode and  $\beta$  is the propagation constant of the mode. As evident from Eq. (6.1), the mode field

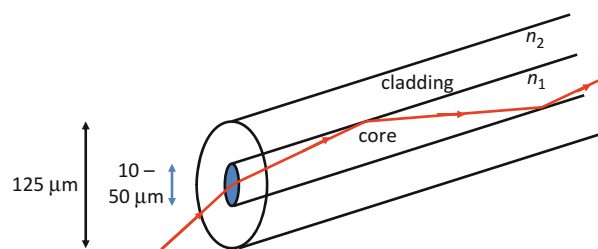


**Fig. 6.1** A step-index optical fiber in which light guidance takes place through the phenomenon of total internal reflection

propagates along the fiber axis ( $z$ -direction) without any change in the transverse field pattern with a propagation constant  $\beta$ . We can define an effective index  $n_{\text{eff}}$  of the mode by the following equation:

$$n_{\text{eff}} = \frac{\beta}{k_0} \quad (6.2)$$

where  $k_0 (= \omega/c)$  is the propagation constant in free space. The phase velocity of the mode will be given by

$$v_p = \frac{c}{n_{\text{eff}}} \quad (6.3)$$

and the group velocity of the mode is given by

$$v_g = \frac{c}{N_{\text{eff}}} \quad (6.4)$$

where

$$N_{\text{eff}} = n_{\text{eff}} - \lambda_0 \frac{dn_{\text{eff}}}{d\lambda_0} \quad (6.5)$$

is referred to as the group effective index; here  $\lambda_0$  is the free space wavelength.

In view of cylindrical symmetry of the fiber, the mode solutions are in terms of Bessel functions. The field distribution of the  $\text{LP}_{lm}$  guided mode is given by

$$\begin{aligned} \psi(r, \phi) &= A \frac{J_l(\frac{Ur}{a})}{J_l(U)} \begin{bmatrix} \cos l\phi \\ \sin l\phi \end{bmatrix}; \quad r < a \\ &= A \frac{K_l(\frac{Wr}{a})}{K_l(W)} \begin{bmatrix} \cos l\phi \\ \sin l\phi \end{bmatrix}; \quad r > a \end{aligned} \quad (6.6)$$

where

$$U^2 = a^2 (k_0^2 n_1^2 - \beta^2) \quad (6.7)$$

$$W^2 = a^2 (\beta^2 - k_0^2 n_2^2) \quad (6.8)$$

and

$$V^2 = U^2 + W^2 \quad (6.9)$$

with  $V$  representing the normalized  $V$ -parameter of the fiber. The eigenvalue equation that determines the propagation constant  $\beta_{lm}$  of the  $\text{LP}_{lm}$  mode is given by

$$U \frac{J'_l(U)}{J_l(U)} = W \frac{K'_l(W)}{K_l(W)} \quad (6.10)$$

where primes denote differentiation with respect to the argument. The  $m$ th solution of the above equation gives the propagation constant of the  $\text{LP}_{lm}$  mode. The modal field of the  $\text{LP}_{lm}$  mode is characterized by  $2l$  zeroes in the azimuthal direction and by  $(m - 1)$  zeroes along the radial direction (excluding the zero at  $r = 0$ ). Thus, an observation of the transverse modal distribution can tell us about the  $l$  and  $m$  values of the mode. It may be mentioned that for each  $\text{LP}_{lm}$  mode, there are two independent orthogonal linear polarizations that are possible. Thus, one can have an  $x$ -polarized  $\text{LP}_{01}$  and a  $y$ -polarized  $\text{LP}_{01}$  mode. Thus, the  $\text{LP}_{01}$  mode is doubly degenerate.

An optical fiber is characterized by a normalized parameter referred to as  $V$ -number defined by the following equation (see Eq. (6.9)):

$$V = \frac{2\pi}{\lambda_0} a \sqrt{(n_1^2 - n_2^2)} \quad (6.11)$$

Each fiber supports a certain number of discrete guided modes and a continuum of radiation modes. The larger the value of  $V$ , the larger the number of guided modes supported by the fiber.

A single-mode fiber is one which supports only a single guided mode corresponding to  $l = 0$  and  $m = 1$ . The fundamental mode is referred to as the  $\text{LP}_{01}$  mode. This mode has no  $\phi$  dependence. A step-index fiber behaves as a single-mode fiber if  $V < 2.4048$ . Thus, a given fiber will behave as a single-mode fiber for wavelengths larger than a specific wavelength referred to as the cutoff wavelength.

Although analytical expressions for the modal field distribution exist for step-index fibers, in general graded-index fibers, one cannot obtain analytical solutions to the modal fields. At the same time, in most fibers, the fundamental field distribution resembles a Gaussian distribution and can be approximated by the following transverse field profile:

$$E(r) = A e^{-r^2/w^2} \quad (6.12)$$

where  $w$  is referred to as the spot size.

For step-index fibers an empirical expression for the spot size is given by the following approximate formula [6]:

$$\frac{w}{a} \approx \left( 0.65 + \frac{1.619}{V^{1.5}} + \frac{2.879}{V^6} \right); \quad 0.8 < V < 2.5 \quad (6.13)$$

The spot size determines various characteristics of the fiber such as losses across joints, coupling efficiency from a source, etc. It also determines the fraction of the power contained within the core of the fiber which in turn determines the effective gain of a fiber that is doped only within the core.

One of the important characteristics of an optical fiber is referred to as pulse dispersion. Pulse dispersion refers to the phenomenon of change in the temporal variation of an optical pulse as it propagates through an optical fiber. Using Fourier

transform, any pulse of light can be considered to be a superposition of various frequencies. Since the propagation constant of the mode depends on the frequency, different frequency components suffer different phase shifts as they travel through the fiber. This leads to a modification of the temporal variation of the pulse.

For an input Gaussian pulse as given

$$\Psi(z = 0, t) = Ce^{-t^2/\tau_0^2} e^{i\omega_0 t} \quad (6.14)$$

the output pulse can be obtained to be of the form [3]

$$\Psi(z, t) = \frac{C}{(1 + \sigma^2)^{1/4}} \exp\left[-\frac{T^2}{\tau^2(z)}\right] \exp\left[i\left(\Phi(z, t) - \beta(\omega_0)z\right)\right] \quad (6.15)$$

where

$$\begin{aligned} \Phi(z, t) &= \omega_0 t + \kappa\left(t - \frac{z}{v_g}\right)^2 - \frac{1}{2}\tan^{-1}(\sigma), \\ T &= t - \frac{z}{v_g}, \quad \kappa = \frac{\sigma}{(1 + \sigma^2)\tau_0^2}, \quad \sigma = \frac{2\alpha z}{\tau_0^2}, \\ \tau^2(z) &= \tau_0^2(1 + \sigma^2), \quad \alpha = \left.\frac{d^2\beta}{d\omega^2}\right|_{\omega=\omega_0} \end{aligned} \quad (6.16)$$

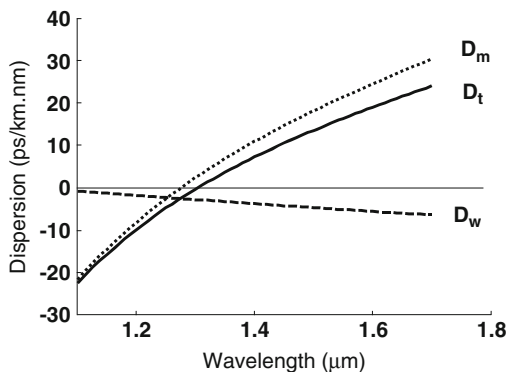
Equation (6.15) shows that as the pulse propagates through the fiber, it retains the Gaussian shape but the temporal duration  $\tau(z)$  increases leading to what is referred to as pulse broadening. Pulse broadening leads to limitations on the maximum bit rate of information that can be sent through an optical fiber. Note also that the temporal variation of the phase of the output pulse does not depend linearly on  $t$  and hence the output pulse is chirped. In fact, since the spectrum of the input and the output pulses are the same and the output pulse is broader, the output pulse must be chirped.

Pulse broadening is characterized by the parameter  $\alpha$  which is nothing but the second derivative of the propagation constant with frequency (Eq. 6.16). Now, the frequency dependence of the propagation constant is due to two primary reasons:

- (a) Dependence of the refractive indices of the core and cladding on frequency which leads to what is referred to as material dispersion.
- (b) Explicit dependence of  $\beta$  on the frequency, which leads to what is referred to as waveguide dispersion.

The total dispersion is almost equal to the sum of material and waveguide dispersions. Figure 6.2 shows a plot of the material, waveguide, and total dispersions in a standard single-mode fiber. One can see that the total dispersion passes through zero around 1,300 nm; this wavelength is referred to as zero dispersion wavelength. Since waveguide dispersion can be controlled by the design of the optical fiber, the

**Fig. 6.2** Variation of material dispersion ( $D_m$ ), waveguide dispersion ( $D_w$ ), and total dispersion ( $D_t$ ) of a step-index single-mode fiber. Notice that the total dispersion becomes zero at a specific wavelength



wavelength of zero dispersion can also be controlled by appropriate fiber design. Fibers with zero dispersion at 1,550 nm are referred to as dispersion-shifted fibers (DSF), while fibers with zero dispersion away but close to the low-loss region around 1,550 nm are referred to as nonzero dispersion-shifted fibers (NZ-DSF).

For continuous wave fiber lasers, dispersion does not play any significant role. On the other hand, dispersion is important in short-pulse lasers. For example, if we consider a pulse width of 200 fs at 1,550 nm, then its bandwidth is approximately 6.4 nm. If the fiber dispersion is 5 ps/km-nm and if the fiber length is 20 m, then the total accumulated dispersion is 640 fs which is indeed very large. Thus, dispersion effects become very important in short-pulse fiber lasers and it is important to control the dispersion of the pulses within the fiber laser. This can be achieved by using a combination of fibers with different dispersion profiles, such as having fibers with positive and negative dispersion coefficients, or by employing fibers having a proper dispersion variation at the operating wavelength.

In deriving Eq. (6.15) we have expanded the propagation constant about the center frequency of the pulse via the following equation:

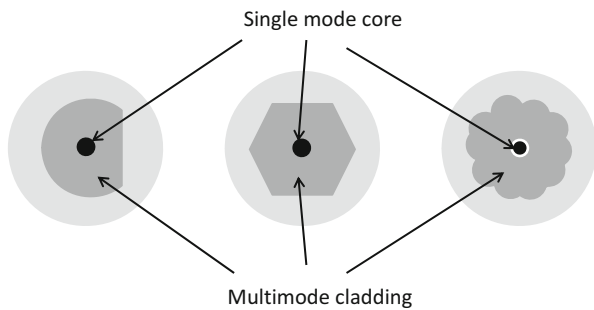
$$\beta(\omega) = \beta(\omega_0) + (\omega - \omega_0) \frac{d\beta}{d\omega} + \frac{1}{2}(\omega - \omega_0)^2 \frac{d^2\beta}{d\omega^2} + \frac{1}{6}(\omega - \omega_0)^3 \frac{d^3\beta}{d\omega^3} + \dots$$

and have retained terms up to the second derivative only. This is a reasonable approximation in the case of pulses of picoseconds duration; however, when the pulse width is of the order of tens of femtoseconds, the higher-order terms cannot be neglected and these need to be considered in the analysis.

### 6.2.1 Double-Clad Fibers

Using conventional fibers with doped single-mode core and a cladding, the laser power is restricted to about 1 W. To achieve higher output powers, fiber lasers use

**Fig. 6.3** Examples of double-clad fiber designs with noncircular outer cladding to ensure that the pump light is absorbed more efficiently



double-clad fibers as the amplifying medium (Fig. 6.3). In this fiber, the central core guides the laser wavelength and is single moded at this wavelength. The inner cladding is surrounded by an outer cladding and this region acts as a multimoded guide for the pump wavelength. The radius of the inner cladding is large and so is the refractive index difference between the inner cladding and the outer cladding. This ensures that power from large area diode lasers can be launched into the inner cladding of the fiber efficiently. At the same time since light at the laser wavelength is propagating as a fundamental mode in the inner core, the laser output would be single moded. The pump power propagating in the inner cladding propagates in the form of different rays (or modes). If the cladding is of circular cross section, then it is possible that some of the rays (skew rays) propagating in the cladding never have an opportunity to cross the core and this portion of the pump would never be used in creating inversion (since the doping is in the core of the fiber) and thus leading to reduced conversion efficiencies. In order that all the rays corresponding to the pump power propagating in the inner cladding of the fiber cross the core, the inner cladding is made noncircular. In such designs all rays cross the fiber core and thus take part in creating population inversion in the fiber. Such a design results in much increased pumping efficiency and can lead to very much increased pump conversion efficiencies.

### 6.3 Fiber Laser Analysis

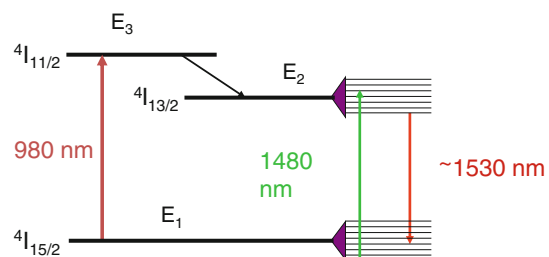
Figure 6.4 shows a schematic of a fiber laser. A pump laser is used to create population inversion in a short piece of fiber with its core doped with appropriate dopants. On providing optical feedback using mirrors at the end of the amplifying fiber, it is possible to achieve laser oscillation. The feedback can be either provided by reflections from the ends of the fiber or by external mirrors or by using fiber Bragg grating which is a highly wavelength selective mirror integrated into the core of the fiber.

We will now derive expressions describing an erbium-doped fiber laser (EDFL). We will consider the EDFL to be a three-level laser and assume that ions pumped



**Fig. 6.4** Schematic of a fiber laser

**Fig. 6.5** Energy levels of erbium in silica matrix



into level  $E_3$  by a 980 nm pump laser jump rapidly to level  $E_2$ , which is the upper laser level (Fig. 6.5) and assume that ions pumped from level  $E_1$  to level  $E_3$  by a 980 nm pump laser jump rapidly to level  $E_2$ , the upper laser level. Let  $N_1$ ,  $N_2$ , and  $N_t$  represent, respectively, the erbium ion density (number of erbium ions per unit volume) in energy levels  $E_1$  and  $E_2$  and the total erbium ion density. Since we are assuming that ions relax rapidly from level  $E_3$ , we have  $N_3 \sim 0$  and

$$N_t = N_1 + N_2 \quad (6.17)$$

We assume that the entire fiber core of radius  $a$  is uniformly doped with erbium ions. Although the pump is assumed to propagate only in one direction, light waves corresponding to the lasing wavelength will form a standing wave in the laser cavity. Hence, there would be waves at the laser wavelength propagating along both the  $+z$  as well as the  $-z$  direction. We will assume the pump to be traveling along the  $+z$  direction.

The rate equation describing the time rate of change of erbium ion population density  $N_2$  in level  $E_2$  is given as

$$\frac{dN_2}{dt} = -\frac{N_2}{\tau_{sp}} + \frac{\sigma_p I_p}{h\nu_p} N_1 - \frac{\sigma_{se} I_s^+}{h\nu_s} N_2 + \frac{\sigma_{sa} I_s^+}{h\nu_s} N_1 - \frac{\sigma_{se} I_s^-}{h\nu_s} N_2 + \frac{\sigma_{sa} I_s^-}{h\nu_s} N_1 \quad (6.18)$$

where the terms on the right-hand side correspond respectively to spontaneous emission per unit time per unit volume with  $\tau_{sp}$  representing the spontaneous lifetime of the level  $E_2$ , the induced absorption per unit time per unit volume due to the pump with  $I_p$  representing the pump intensity and  $\sigma_p$ , the absorption cross section at the pump frequency  $\nu_p$ , the stimulated emission per unit time per unit volume induced by the signal of intensity  $I_s^+$  traveling along the  $+z$  direction,  $\sigma_{se}$  represents the emission cross section at the signal frequency  $\nu_s$ , the induced

absorption per unit time per unit volume due to the signal frequency  $\nu_s$  induced by signal of intensity  $I_s^+$  traveling along the  $+z$  direction,  $\sigma_{\text{sa}}$  represents the absorption cross section at signal frequency  $\nu_s$ , and the stimulated emission and absorption per unit time per unit volume induced by the signal of intensity  $I_s^-$  traveling along the  $-z$  direction.

Unlike conventional lasers, in the case of fiber lasers, the pump and signal waves travel as modes in the fiber. These modes are characterized by specific intensity distributions along the transverse cross section of the fiber. Due to the guidance mechanism, unlike in the case of conventional lasers when the laser light within the cavity will diffract, in the case of fibers, there would be no diffraction of the waves. In view of this we should describe the propagation of pump and signal along the fiber length in terms of powers rather than in terms of intensities. In order to do so, we introduce two new functions  $f_p(r)$  and  $f_s(r)$  at the pump and signal frequencies as

$$I_p(r) = P_p(z) f_p(r) \quad (6.19)$$

and

$$I_s^\pm(r) = P_s^\pm(z) f_s(r) \quad (6.20)$$

Here  $P_p(z)$  and  $P_s^\pm(z)$  represent the powers carried by the pump propagating along the  $+z$  direction and signal propagating along the  $+z$  and  $-z$  directions, respectively, and  $f_p(r)$  and  $f_s(r)$  represent the transverse dependence of the modal intensity patterns at the pump and signal frequencies. Usually the pump and signal beams travel as the fundamental modes of the fiber, and thus we assume that the intensity distributions at the pump and signal are dependent only on the cylindrical radial coordinate  $r$  and are independent of the azimuthal coordinate  $\phi$ . By integrating Eqs. (6.19) and (6.20) along the entire transverse cross section, we note that the functions  $f_p(r)$  and  $f_s(r)$  satisfy the following normalization conditions:

$$2\pi \int_0^\infty f_{p,s}(r) r dr = 1 \quad (6.21)$$

Since the population of a level depends on the intensity of the interacting light wave and the intensities at the pump and signal frequencies depend on the coordinate  $r$ , in general the populations  $N_1$  and  $N_2$  also depend on  $r$ . In order to simplify the analysis, we shall neglect this dependence and assume that  $N_1$  and  $N_2$  are independent of  $r$  and depend only on the longitudinal coordinate  $z$ .

The actual transverse intensity patterns  $f_p(r)$  and  $f_s(r)$  of a step-index single-mode fiber are described in terms of Bessel functions (Eq. (6.6)). A very good approximation for the transverse intensity variation is the Gaussian approximation as given by Eq. (6.12).

Combining Eqs. (6.17), (6.18), (6.19), (6.20), and (6.21), we obtain the following coupled equations [12]

$$\frac{d\tilde{N}_2}{dt} = -\frac{\tilde{N}_2}{\tau_{sp}} + \frac{\sigma_p \Gamma_p}{h\nu_p A} P_p \tilde{N}_1 - \frac{(\sigma_{se} \tilde{N}_2 - \sigma_{sa} \tilde{N}_1) \Gamma_s}{h\nu_s A} (P_s^+ + P_s^-) \quad (6.22)$$

$$\frac{dn_p}{dz} = -\sigma_p N_t \Gamma_p \tilde{N}_1 n_p \quad (6.23)$$

$$\frac{dn_s^\pm}{dz} = \pm [(\sigma_{se} + \sigma_{sa}) \tilde{N}_2 - \sigma_{sa}] N_t \Gamma_s n_s^\pm \quad (6.24)$$

where  $A (= \pi a^2)$  represents the area of cross section of the doped region of the fiber. In the above equations the normalized population densities are defined by

$$\tilde{N}_1 = \frac{N_1}{N_t}; \quad \tilde{N}_2 = \frac{N_2}{N_t} \quad (6.25)$$

and the photon flux (i.e., the total number of photons crossing per unit time across a plane perpendicular to the fiber axis) at pump and signal wavelengths is defined by

$$n_p = \frac{P_p}{h\nu_p}; \quad n_s^\pm = \frac{P_s^\pm}{h\nu_s} \quad (6.26)$$

We now define

$$\Gamma_p = 2\pi \int_0^a f_p(r) r dr; \quad \Gamma_s = 2\pi \int_0^a f_s(r) r dr \quad (6.27)$$

which represent the fractional powers inside the core at the pump and signal wavelengths, respectively. Using Eqs. (6.25), (6.26), and (6.27) in Eq. (6.22), we obtain

$$\frac{d\tilde{N}_2}{dt} = -\frac{\tilde{N}_2}{\tau_{sp}} - \frac{1}{N_t A} \frac{dn_p}{dz} - \frac{1}{N_t A} \left( \frac{dn_s^+}{dz} - \frac{dn_s^-}{dz} \right) \quad (6.28)$$

Equations (6.23), (6.24), and (6.28) describe the evolution of pump and signal powers and population along the length of the doped fiber. These equations can be solved to obtain various parameters of the erbium-doped fiber amplifier and laser.

### 6.3.1 Solutions Under Steady State

Under steady state, assuming the time derivative to be zero in Eq. (6.28) and using the resulting value of  $\tilde{N}_2$  in Eq. (6.24), we obtain

$$\frac{dn_s^\pm}{n_s^\pm} = \mp \left[ \alpha_s + \frac{1}{n_{ss}} \left( \frac{dn_p}{dz} + \frac{dn_s^+}{dz} - \frac{dn_s^-}{dz} \right) \right] dz \quad (6.29)$$

where the signal absorption coefficient  $\alpha_s = \Gamma_s N_t \sigma_{sa}$  and the intrinsic signal saturation photon number  $n_{ss} = \frac{A}{\Gamma_s \tau_{sp} (\sigma_{se} + \sigma_{sa})}$

Similarly we have

$$\frac{dn_p}{n_p} = - \left[ \alpha_p + \frac{1}{n_{ps}} \left( \frac{dn_p}{dz} + \frac{dn_s^+}{dz} - \frac{dn_s^-}{dz} \right) \right] dz \quad (6.30)$$

where  $\alpha_p = \sigma_p N_t \Gamma_p$  and  $n_{ps} = \frac{A}{\Gamma_p \tau_{sp} \sigma_p}$  represent the pump absorption coefficient and the intrinsic pump saturation photon number.

Equations (6.29) and (6.30) can be integrated from  $z = 0$  to  $z = L$  to get

$$n_s^+(L) = n_s^+(0) e^{-\alpha_s L} e^{(n_{pa} + n_{sa}^+ + n_{sa}^-)/n_{ss}} \quad (6.31)$$

$$n_s^-(0) = n_s^-(L) e^{-\alpha_s L} e^{(n_{pa} + n_{sa}^+ + n_{sa}^-)/n_{ss}} \quad (6.32)$$

$$n_p(L) = n_p(0) e^{-\alpha_p L} e^{(n_{pa} + n_{sa}^+ + n_{sa}^-)/n_{ps}} \quad (6.33)$$

where

$$\begin{aligned} n_{pa} &= n_p(0) - n_p(L); \\ n_{sa}^+ &= n_s^+(0) - n_s^+(L); \\ n_{sa}^- &= n_s^-(L) - n_s^-(0) \end{aligned} \quad (6.34)$$

Equations (6.31), (6.32), and (6.33) represent, respectively, the number of photons at pump and signal wavelengths propagating in the forward and backward direction, respectively, that have been absorbed by the doped fiber (negative value of the quantity would imply net emission rather than absorption).

### 6.3.2 Fiber Laser Characteristics

We will now use the equations derived above to analyze the characteristics of erbium-doped fiber lasers. In a fiber laser, the pump creates population inversion in the doped fiber and a pair of reflectors on either end of the doped fiber provide for optical feedback. If the cavity losses are compensated by the gain provided by the doped fiber, then lasing begins. For steady-state lasing, we require that the signal photon flux be the same after one round trip, i.e., the losses suffered by the signal photon flux in one round trip be compensated exactly by the gain from the inversion.

Let  $R_1$  and  $R_2$  represent the reflectivities of the two mirrors. Then the condition of gain compensating loss in one roundtrip implies

$$\frac{(n_{pa} + n_{sa}^+ + n_{sa}^-)}{n_{ss}} = \alpha_s L - \frac{1}{2} \ln(R_1 R_2) \quad (6.35)$$

We shall now discuss some general features of erbium-doped fiber laser.

### 6.3.3 Threshold

We can estimate the threshold pump power required to start laser oscillation. We first note that at threshold since the laser power is still small, we can put  $n_{sa}^+ \approx n_{sa}^- \approx 0$ . Thus, from Eq. (6.35) we get

$$n_{pa} \approx \left( \alpha_s L - \frac{1}{2} \ln R_1 R_2 \right) n_{ss} \quad (6.36)$$

Using this value in Eqs. (6.33) and (6.34), we get

$$n_{p,th} = n_{p,th}(0) = \frac{n_{ss} \left( \alpha_s L - \frac{1}{2} \ln R_1 R_2 \right)}{\left[ 1 - e^{-\alpha_p L} e^{(\alpha_s L - \frac{1}{2} \ln R_1 R_2) n_{ss} / n_{ps}} \right]} \quad (6.37)$$

and the threshold pump power would be

$$P_{p,th} = h\nu_p n_{p,th} \quad (6.38)$$

If most of the incident pump power is absorbed by the doped fiber, then  $n_p(L) \ll n_p(0)$  and  $n_{pa} \approx n_p(0)$ . In such a case, we obtain a simplified expression for  $P_{p,th}$ :

$$P_{p,th} = h\nu_p n_p(0) = \frac{h\nu_p A}{\Gamma_s \tau_{sp} (\sigma_{se} + \sigma_{sa})} \left( \alpha_s L - \frac{1}{2} \ln R_1 R_2 \right) \quad (6.39)$$

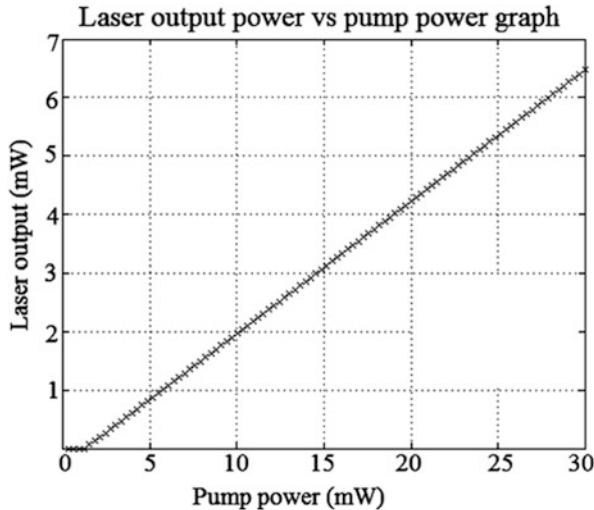
### 6.3.4 Laser Output Power

The laser power exiting the fiber laser from mirror with reflectivity  $R_2$  is

$$P_{laser} = n_s^+(L) (1 - R_2) h\nu_s \quad (6.40)$$

Using the expression for  $n_s^+(L)$  and simplifying, we obtain [12]

**Fig. 6.6** Simulated variation of output laser power with the input pump power

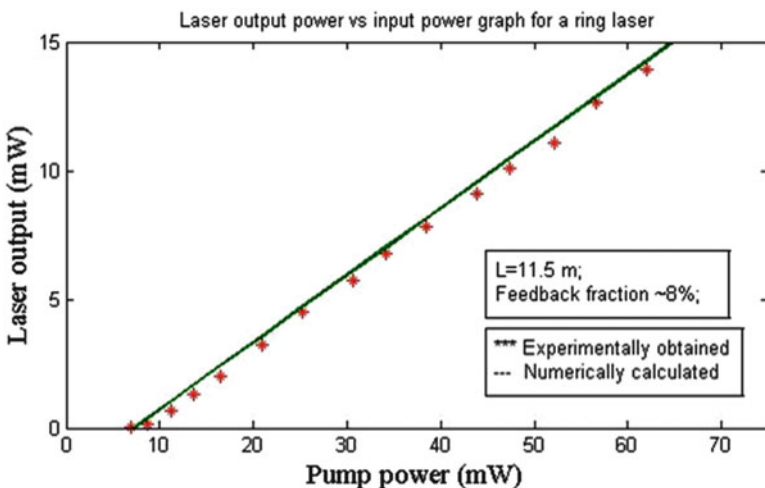


$$\begin{aligned}
 n_s^+(0) = & \left[ \left( \frac{1}{\sqrt{R_1 R_2}} - 1 \right) + \frac{(1 - \sqrt{R_1 R_2})}{R_1} \right]^{-1} \\
 & \times \left[ n_p(0) \left\{ 1 - e^{-\alpha_p L} e^{(\alpha_s L - \frac{1}{2} \ln R_1 R_2) n_{ss} / n_{ps}} \right\} - n_{ss} \left\{ \alpha_s L - \frac{1}{2} \ln (R_1 R_2) \right\} \right]
 \end{aligned} \quad (6.41)$$

Using this value we can obtain the output power from the laser.

Figure 6.6 shows the variation of output laser power as a function of the input pump power for a typical erbium-doped fiber laser. For low input pump powers, there is no output. After reaching threshold the output laser power monotonically increases with the input pump power. Figure 6.7 shows a comparison of measured and simulated output laser power with input pump power. Figure 6.8 shows a typical measured output laser spectrum.

It is indeed possible to generate extremely high powers from fiber lasers. Figure 6.9a shows the fiber laser configuration using Yb-doped cladding-pumped fiber and Fig. 6.9b shows the output power variation with input pump power; the corresponding slope efficiency is about 71.7 %. The measured output power is about 40 W for a pump power of about 60 W. Fiber lasers giving output powers of 1.36 kW have been demonstrated, and there are efforts to achieve even larger powers from fiber lasers and such high-power fiber lasers are expected to revolutionize the area of applications of lasers in industries. With such high optical powers, optical fibers start to exhibit nonlinear effects which tend to degrade the performance of the fiber laser. Since the nonlinear effects are proportional to the intensity of the propagating radiation, one way to reduce the nonlinear effects is to increase the mode area so that for a given power the intensity would be less. Using photonic microstructure



$$P_{th} = 0.81 \text{ mW(exp)}; 0.71 \text{ mW (theo)}$$

$$\text{Slope efficiency} = 25\%$$

**Fig. 6.7** Comparison of simulated and experimentally measured variation of laser power with input pump power (Ref. [7])

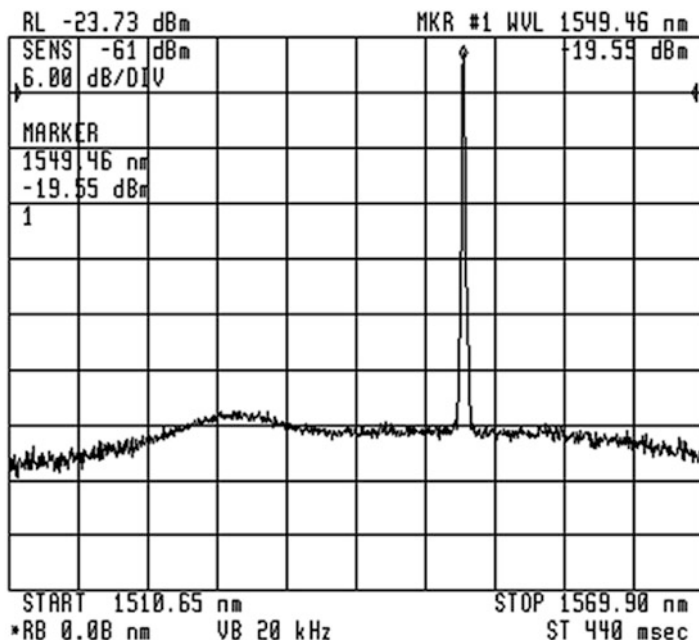


**Fig. 6.8** A typical laser spectrum of erbium-doped fiber laser (Ref. [7])

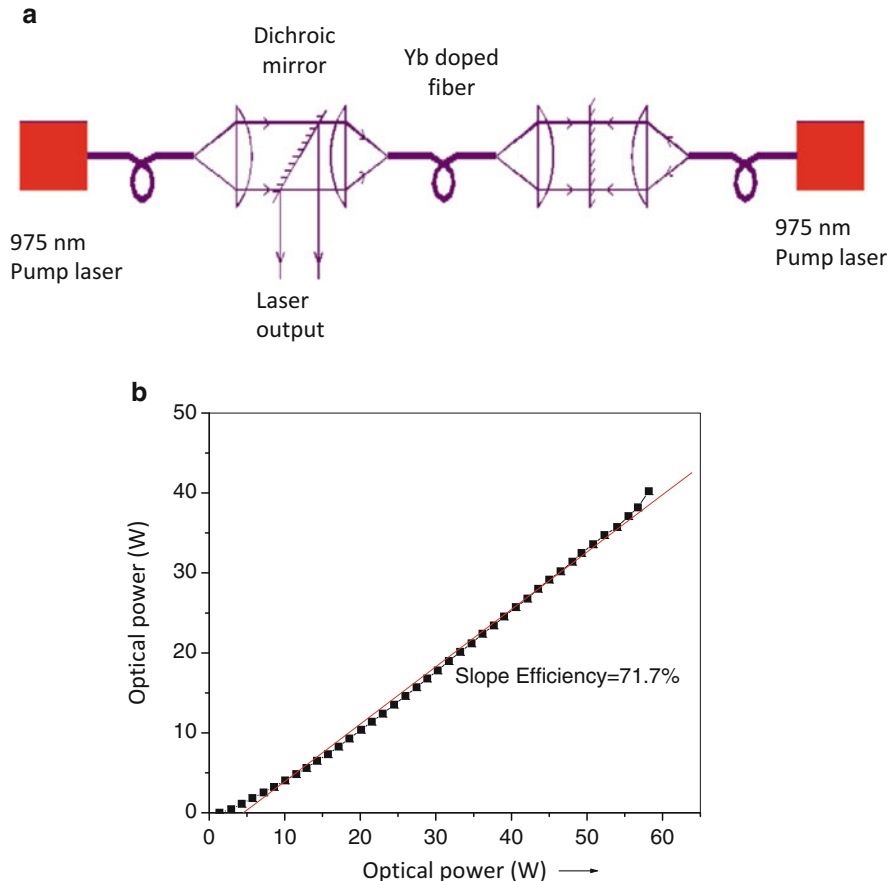


**Fig. 6.9** (a) Schematic of high-power Yb-doped fiber laser. (b) Variation of laser output with input pump power (Ref. [13])

fibers, it is possible to achieve single-mode operation over a large wavelength range and also achieve large-mode areas. Fibers have a very small numerical aperture of less than 0.03 and core diameters larger than  $60 \mu\text{m}$  leading to mode field diameters of about  $50 \mu\text{m}$  and are very interesting for fiber laser applications.

## 6.4 Pulsed Fiber Lasers

Q-switching and mode locking are two standard techniques for realizing pulsed lasers. In the case of Q-switching, the Q of the cavity is kept low so that the pumping can enhance the population inversion to values much higher than threshold,

and with an optical switch, the Q is restored to large values. Since the losses in the cavity have reduced, the gain in the cavity is much more than the loss resulting in the generation of an intense pulse of light. Q-switching can lead to high energy pulses in the nanosecond regime. There are many techniques for Q-switching including active and passive Q-switching. Novel techniques have been used for fiber laser Q-switching. For example, an electronically driven variable optical attenuator (VOA) is made a part of the fiber laser cavity, and with an external electrical signal, the Q of the cavity can be switched by using the VOA [1]. Saturable absorbers are very good candidates for Q-switching. This could be using other doped fibers or using semiconducting media as saturable absorbers.

In the case of mode locking, the various longitudinal modes of the cavity are locked in phase, and this results in a periodic train of ultrashort-pulses; the repetition frequency of the pulses is the transit time through the cavity and the pulse width is inversely proportional to the gain bandwidth of the laser. Figure 6.10a

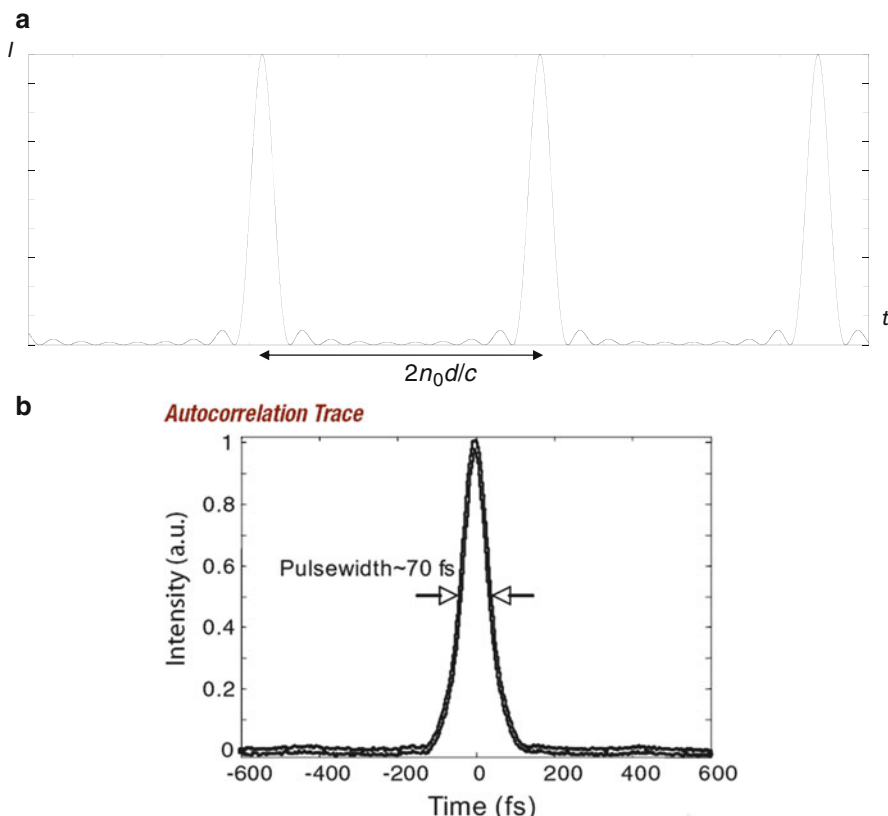


**Fig. 6.10** (a) Simulated train of mode-locked pulses (b) A typical output pulse from a mode-locked fiber laser

shows simulation results of a typical train of mode-locked pulses and Fig. 6.10b shows a typical mode-locked pulse from a commercially available erbium-doped mode-locked laser. Recently carbon nanotubes and graphene are finding widespread applications in mode locking of fiber lasers [9, 14].

Nonlinear polarization rotation is a very interesting technique for mode locking of fiber lasers. In the presence of nonlinear effects, an elliptically polarized light undergoes rotation of its polarization state as it propagates through an optical fiber. By using appropriate all fiber components such as polarizers and polarization controllers, it is possible to use this phenomenon to achieve mode locking [12].

## 6.5 Novel Fiber Designs

The amplifying characteristics of an optical fiber depend on the dopants as well as on the fiber geometry through the overlap integrals. For a given rare earth dopant, some modification of the characteristics of the amplifying fiber can be achieved by a proper design of the fiber refractive index profile which in turn modifies the modal intensity patterns. For example, by using segmented claddings in optical fibers, it is possible to shift the effective amplification band to lower wavelengths in the range of 1,480–1,525 nm. Figure 6.11 shows the gain characteristics of a segmented-clad fiber design wherein by appropriately modifying the fiber transverse refractive index profile, it is possible to shift the gain to the lower wavelength region [4]. With a proper feedback such an amplifying fiber can lead to lasing even in the short wavelength region of erbium [11]. Such designs can also be applied for other dopants such as thulium [5]. Such fiber designs can lead to extending the band of operation of fiber amplifiers as well as fiber lasers.

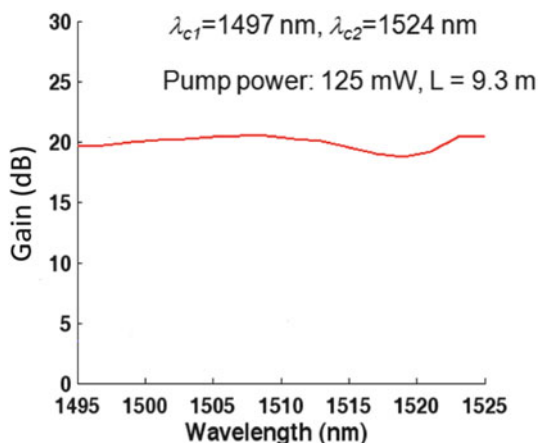


**Fig. 6.11** Gain spectrum of a segmented-clad fiber with erbium doping in the core

## References

1. You Min Chang, Junsu Lee, Young Min Jhon, Ju Han Lee, Active Q-switching in an erbium-doped fiber laser using an ultrafast silicon-based variable optical attenuator. Opt. Express **19**, 26911 (2011)
2. E.M. Dianov, Bismuth-doped optical fibers: a challenging active medium for near-IR lasers and optical amplifiers. Light: Sci. Appl. **1**, e12 (2012). doi:[10.1038/lسا.2012.12](https://doi.org/10.1038/lسا.2012.12)
3. A. Ghatak, K. Thyagarajan, Introduction to Fiber Optics, (Cambridge University Press, Cambridge, MA, 1998), Reprinted by Foundation Books, India, 1999
4. C. Kakkar, K. Thyagarajan, Segmented clad fiber design for tunable leakage loss. J. Lightwave Technol.-Spec. Issue Opt. Fiber Des. **23**, 3444–3453 (2005)
5. C. Kakkar, G. Monnom, K. Thyagarajan, B. Dussardier, Inherently gain flattened L+ band TDFA based on W-fiber design. Optics Commun. **262**, 193–199 (2006)
6. D. Marcuse, Loss analysis of single mode fiber splices. Bell Syst. Tech. J. **56**(1977), 703 (1977)
7. S. Mukherjee, S. Sahoo, *Studies on Fiber Lasers*, M Sc thesis, Physics Department IIT Delhi, 2012
8. J. Nilsson, D.N. Payne, High-power fiber lasers. Science **332**, 921 (2011)
9. D. Popa, Z. Sun, T. Hasan, F. Torrisi, F. Wang, A.C. Ferrari, *Sub-100 fs Pulse Generation from a Fiber Oscillator Mode-Locked by Nanotubes* (University of Cambridge, Cambridge, MA, 2011). CMK6, CLEO-2011
10. D.J. Richardson, J. Nilsson, W.A. Clarkson, High power fiber lasers: current status and future perspectives [Invited]. J. Opt. Soc. Am. B **27**, B63 (2010)
11. K. Thyagarajan, C. Kakkar, S-Band single stage EDFA with 25 dB gain using distributed ASE suppression. IEEE Photonics Tech. Lett. **16**, 2448–2450 (2004)
12. K. Thyagarajan, A. Ghatak, *Lasers: Fundamentals and Applications* (Springer, New York, 2010). Macmillan India, 2011
13. B.N. Upadhyaya, A. Usha Chakravarty, S.M. Kuruvilla, M.R.S. Oak, K. Thyagarajan, Self-pulsing characteristics of a high power single transverse mode Yb-doped cw fiber laser. Opt. Commun. **283**, 2206–2213 (2010)
14. F. Wang, A.G. Rozhini, V. Scardaci, Z. Sun, F. Hennrech, I.H. White, W.I. Milne, A.C. Ferrari, Wideband-tunable, nanotube mode-locked, fibre laser. Nat. Nanotechnol. **3**, 738 (2008)

# Chapter 7

## Free Electron Lasers

K.K. Pant

**Abstract** Free electron lasers are electron beam-based sources of coherent, high-power tunable radiation which can, in principle, be designed to operate at any wavelength ranging from mm waves to X-rays. In recent years, these devices have successfully been operated at THz and hard X-ray wavelengths where conventional sources of radiation are either not available or are not very efficient. This chapter briefly discusses the principle of operation and important subsystems of FELs, their special features, and the typical characteristics of some operational FELs. A review of the present status of activity in India and abroad is also discussed briefly.

**Keywords** Basics of free electron laser (FEL) • Components of FEL • FEL radiation characteristics • Terahertz sources • Present status of FELs in world

### 7.1 Introduction

A free electron laser (FEL) is a source of high-power coherent electromagnetic (EM) radiation in which “free electrons” in a relativistic electron beam from an accelerator are propagated through a spatially periodic arrangement of magnets, called an undulator. A fraction of the kinetic energy of the relativistic electrons is converted to electromagnetic waves of wavelength ( $\lambda_L$ ), which depends upon the wavelength, or period, of the spatially periodic magnetic field ( $\lambda_U$ ), the relativistic gamma factor ( $\gamma$ ) of the electrons, and the undulator parameter ( $K_U = eB_U\lambda_U/2\pi mc$ ) as given by the expression

$$\lambda_L = \frac{\lambda_U}{2\gamma^2} (1 + K_U^2). \quad (7.1)$$

---

K.K. Pant (✉)

Free Electron Laser Laboratory, Materials and Advanced Accelerator Sciences Division,  
Raja Ramanna Centre for Advanced Technology (RRCAT), Indore 452 013, India  
e-mail: [kkpant@rrcat.gov.in](mailto:kkpant@rrcat.gov.in)

As seen from Eq. (7.1), the wavelength  $\lambda_L$  of radiation from an FEL can be tuned over a large range of wavelengths by varying the energy of the electron beam,  $\gamma$ , or the undulator parameter,  $K_U$ .

The basic principle of operation of an FEL is similar to that of microwave sources like klystrons and traveling wave tubes, which also employ an electron beam for the generation of electromagnetic radiation. However, these devices employ a nonrelativistic electron beam propagating through a slow-wave structure supporting transverse magnetic (TM) modes. Since the transverse dimensions of slow-wave structures and waveguides scale inversely with wavelength of the radiation to be generated, these devices face problems of beam purity and power-handling capacity for operation at submillimeter and shorter wavelengths. In an FEL, the interaction inside the undulator is between a beam of relativistic electrons and a freely propagating transverse electromagnetic (TEM) mode. Hence, there is neither an adverse scaling of transverse dimensions of the device with the wavelength of operation nor a limit on power-handling capacity for the device since the electron beam itself is a broken-down medium. Successful lasing in an FEL critically depends upon the quality of the electron beam as well as on the quality of undulator magnetic field, and both requirements become more stringent for operation at shorter wavelengths.

Since the principle of operation of an FEL is uniform for all wavelengths, an FEL can in principle be tuned over a wide-wavelength range provided the requirement of qualities of electron beam and undulator field are fulfilled. For example, the FEL at the Free Electron Laser Institute (FELI) in Japan operates from 0.23 to 100  $\mu\text{m}$  using five undulators. The pulse structure of EM radiation from an FEL mimics the pulse structure of the electron beam and has no dependence upon the wavelength of operation. Since most operating FELs employ radio-frequency (RF) linear accelerators (linacs), the electron beam from these devices has pulse widths that are typically a few percent of the time period of RF employed in the accelerator. For example, FELs operating with S-band linacs at 2856 MHz usually generate trains of pulses 5–10 picosecond long for a macro-pulse duration of a few microseconds repeating at few Hz to few tens of Hz. With the recent progress in pulse compression techniques for electron beams from accelerators, FELs have also been operated at pulse widths as short as a few tens of femtosecond.

The size of an FEL is large as compared to that of conventional lasers and microwave sources since they employ a long undulator and an accelerator to generate the relativistic electron beam. FEL facilities also require a radiation shielded area since the electron beam produces significant amount of harmful Bremsstrahlung X-rays when it is dumped after emerging out from the undulator. FELs therefore do not compare favorably with conventional lasers and microwave sources at wavelengths where these sources operate efficiently but are preferred at wavelengths where these conventional sources do not operate, for example, in the terahertz (THz) and X-rays wavelength regimes.

The next section discusses a standard configuration of an FEL and salient features of some of its important subsystems. The basic principle of operation of an FEL is discussed in detail in Sect. 7.3 where the method of buildup of coherence in an

FEL, which makes it different from a synchrotron radiation source, is also discussed. Section 7.4 discusses some important advantages FELs have over other conventional radiation sources, which have made FELs popular, particularly in certain wavelength regions where conventional radiation sources are either not available or are not very efficient. This is followed by a brief review of the current status of FEL activity across the world and in India in Sect. 7.5 followed by a concluding paragraph in Sect. 7.6.

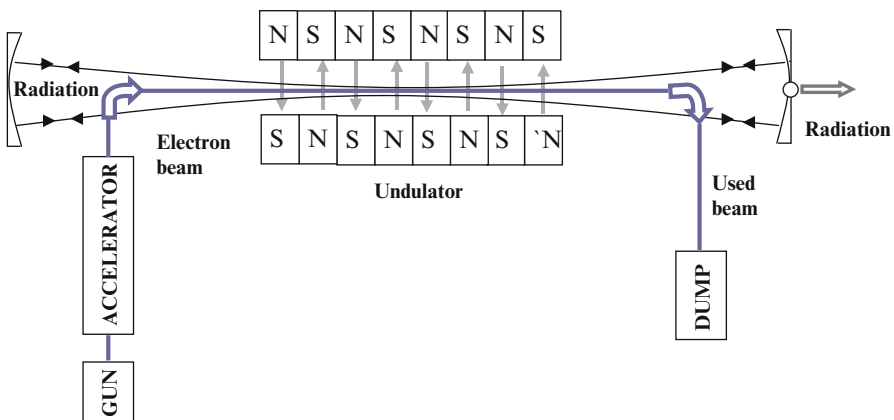
## 7.2 Important Subsystems

Figure 7.1 shows a typical schematic of an FEL with its three important subsystems – an electron accelerator, an undulator, and the optical cavity formed using two mirrors on either side of the undulator.

### 7.2.1 Electron Accelerator

Most present-day FELs use radio-frequency linear accelerators (RF linacs) that range in energies from a few MeVs for long-wavelength FELs to few tens of GeVs for hard X-ray FELs. Though there are FELs operating with other kinds of accelerators too like DC accelerators, induction linacs, storage rings, etc., the discussion in this chapter is limited mainly to RF linac-based FELs.

The parameters qualifying an accelerator are electron beam energy  $W$ , electron beam current  $I_b$ , relative energy spread in the electron beam  $dW/W$ , and emittance



**Fig. 7.1** Schematic of an FEL showing its important subsystems and method of out-coupling of radiation from its optical cavity

$\varepsilon$  of the electron beam. In its simplest form, emittance of an electron beam from an accelerator can be defined as a product of its radius at waist and asymptotic divergence. In addition to these, another critical parameter is the pulse-to-pulse mean energy jitter, which depends mainly upon the stability of the RF system powering the RF linac. While energy of the electron beam determines the wavelength of operation of the FEL and peak current determines the gain, the relative energy spread and emittance of the electron beam critically affect the process of lasing. Long-wavelength FELs are more tolerant to large values of emittance and relative energy spread. For short-wavelength FELs, these parameters become the limiting factors and present-day X-ray FELs like the Linac Coherent Light Source (LCLS) at Stanford operate with an accelerator that is state of the art for the electron beam delivered by it.

The choice of the accelerator for an FEL is dictated by its operating parameters. The most popular choice of electron linacs for FELs are the conventional normal conducting (NC) disk-loaded traveling wave (TW) RF linacs, which have been used in FELs with wavelength ranging from hundreds of microns (THz FELs) to X-rays (X-ray FELs). FELs designed to operate at very high average power are also built using superconducting radio-frequency (SCRF) cavities to reduce power loss in the RF cavities. The length of the accelerator is dictated by the beam energy required. For THz FELs requiring a few MeV energy electron beam, the accelerator length could be of the order of a meter, while for hard X-ray FELs which need close to 15 GeV electron beams, the length of the accelerator is hundreds of meters.

Since electrons from an RF linac need to be propagated through an undulator in an FEL, the accelerator here includes a magnetic transport line to focus and transport the electron beam from the exit of the RF linac to the entry of the undulator. The principle of the transport line, which comprises focusing, defocusing, and bending magnets, is similar to that of an optical beam transport system with lenses and mirrors. Electron beam diagnostic elements, required to monitor the electron beam at different locations, are included in the beam transport line.

### 7.2.2 *Undulator*

An undulator is a spatially periodic arrangement of magnets that generates a magnetic field of amplitude  $B_U$  and periodicity  $\lambda_U$  with a field distribution that is static in time but varies sinusoidally in space. Undulators can be built using pure permanent magnets, pure electromagnets, or a combination of permanent magnets and electromagnets as in hybrid undulators. Permanent magnets are preferred where operation with short undulator period is desired. Since the polarization of radiation from an undulator is identical to that of the undulator magnetic field itself, various configurations of magnets have been proposed to obtain different polarizations of the undulator magnetic field varying from linear to elliptical to variable polarizations. The most popular undulator configurations employed worldwide are the Halbach configuration for linearly polarized undulators and the APPLE-II configuration for variable-polarization undulators.

**Fig. 7.2** Typical arrangement of permanent magnets in an undulator employing the Halbach configuration. Each rectangle refers to one magnet with the arrow within showing the direction of magnetization

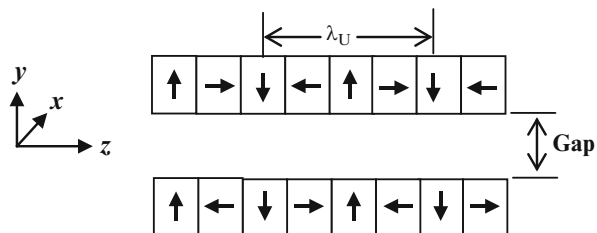


Figure 7.2 shows a typical arrangement of permanent magnets first proposed by Halbach for the generation of a sinusoidally varying linearly polarized undulator magnetic field along the undulator axis given by

$$\mathbf{B}_U = B_U \sin(k_U z) \mathbf{y}, \quad (7.2)$$

where  $k_U = 2\pi/\lambda_U$ . This desired sinusoidal on-axis field distribution is obtained by arranging two rows of magnets equidistant from the axis with the orientation of individual magnets in each row as shown in Fig. 7.2. The electrons propagate along the  $z$  direction and the magnetic field is along the  $y$  direction. The length of the bar magnets along the  $x$  direction is chosen such that there is uniform  $B_y$  field over the full size of the beam along this direction. In other words, the “good field region” along the  $x$  direction should be larger than the size of beam in this direction. The field strength of an undulator is characterized by the undulator parameter  $K_U = eB_U\lambda_U/2\pi mc$ . For FELs,  $K_U$  is typically of the order of 1 or slightly less than 1 and the magnetic arrangement is called as an undulator. When  $K_U \gg 1$ , as in synchrotron radiation sources (SRS), the device is called as a wiggler.

### 7.2.3 Optical Cavity

In an oscillator configuration of an FEL, the undulator is located between two mirrors which form an optical cavity like a Fabry-Perot resonator as shown in Fig. 7.1. Radiation emitted by the first bunch of electrons propagating through the undulator is reflected back and forth inside the optical cavity for repeated interaction with subsequent bunches of electrons ultimately leading to lasing as discussed in the next section. Out-coupling of FEL radiation from the optical cavity is accomplished either by making the downstream mirror partially transmitting or by making a small hole in the downstream mirror to out-couple a fraction of power at every reflection. In an FEL, it is important to align the axis of the optical cavity with that of the undulator for maintaining overlap between the electron and the optical beams for efficient energy exchange between the two.

Except for FELs at X-ray wavelength where operation in oscillator configuration is not possible for want of mirrors, FELs at other wavelengths can be operated in both oscillator and amplifier configurations.

### 7.3 Principle of Operation

The principle of operation of an FEL is presented in many books and articles using different approaches. In this section, we discuss the operating principle using the approach followed in references [1] and [2] with some discussions based on [3]. Consider a beam of relativistic electrons propagating in the  $z$  direction along the axis of an undulator supporting a spatially periodic magnetic field given by Eq. (7.2). The magnetic field here is in the  $y$  direction and the electrons experience a Lorentz force in the  $x$  direction. Since the magnetic field of the undulator is static in time but spatially periodic along the  $z$  direction, the direction of the Lorentz force also changes with the same periodicity causing the electrons to execute a snakelike “wiggly” motion in the  $x$ - $z$  plane as they propagate along the axis of the undulator. Since the magnetic field of the undulator along the  $y$  direction has a phase dependence of  $\sin(k_U z)$ , as shown in Eq. (7.2), the electrons propagating through the undulator acquire an  $x$  component of velocity with a phase dependence given by

$$v_x = v_x \sin(k_U z) x. \quad (7.3)$$

As a consequence of this wiggly motion, the electrons initially moving with a constant velocity along  $z$  direction now become accelerated charged particles which emit radiation as dictated by laws of electrodynamics, with the wavelength of radiation given by Eq. (7.1). An electron beam from an RF linac comprises a large number of electrons in each bunch, which we assume are distributed uniformly along the length of each bunch. All electrons radiate randomly as they propagate through the undulator with no definite phase relationship between radiation emitted by different electrons. The net radiation coming out of the undulator is essentially this “spontaneous emission” with a pulse length equal to the bunch length of electrons from the RF linac. From the principle of superposition, the power in the radiation  $P_R$  is proportional to  $N_e$ , the number of particles in the bunch. The phenomenology of this process is the same as that of radiation from synchrotron radiation sources.

The amplitude of transverse oscillations executed by an electron inside the undulator is given by  $K_u/\gamma$ . For  $K_u \sim 1$ , which is the case for most FELs, the amplitude of transverse oscillations of the electrons is  $\sim 1/\gamma$ . A charged relativistic particle emits radiation in a direction perpendicular to the oscillation of the particles with the intensity of radiation peaking at  $90^\circ$  to the oscillatory motion and concentrated in a narrow cone with a semi-angle  $1/\gamma$ . Since the amplitude of the electron’s transverse oscillations is also  $1/\gamma$ , an observer at the end of the undulator receives radiation from the full transverse oscillation executed by the electron. This overlap between transverse oscillations and the radiation cone of semi-angle  $1/\gamma$  also helps in the buildup of coherence in an FEL, as discussed later in this section.

The electrons undergo transverse oscillations and radiate as per laws of electrodynamics only when they propagate through the length of the undulator  $L_u = N_u \lambda_u$ , where  $N_u$  is the number of undulator periods. Consequently, the electrons radiate only for a finite time and the Fourier transform of this radiation gives the spectral

width of undulator radiation, which is equal to  $I/2N_u$ . Typically, the undulator for an IR or terahertz (THz) FEL has about 50 periods, which means that the line width of radiation is of the order of 1 %.

A synchrotron radiation source (SRS) with a wiggler, which is similar in construction to an undulator, also works on the same principle discussed above for the generation of spontaneous, or incoherent, radiation. However, the buildup of coherence in an FEL results in high brightness of radiation that is greater by orders of magnitude as compared to that from SRS. As discussed earlier, the electron excursion in the transverse direction in an FEL is of the order of  $K_u/\gamma = I/\gamma$ , which is the same as the semi-angle of the cone in which spontaneous radiation is emitted. As the electrons propagate through the undulator, they stay within the radiation cone and there is a second-order interaction between the radiation field and the transverse oscillations of the electrons due to the undulator, leading to the buildup of coherence. In a SRS with a wiggler,  $K_u \gg I$  and the transverse electron excursion is much greater than the semi-angle of the cone in which spontaneous radiation is emitted. Hence, there is poor overlap between the radiation and electrons as they propagate through the wiggler resulting in no buildup of coherence.

In order to understand the buildup of coherence in an FEL, consider a configuration where in addition to the undulator magnetic field discussed earlier, the electron beam also sees an electromagnetic wave whose field components can be represented as

$$\begin{aligned} \mathbf{E}_R &= x E_R \cos(k_R z - \omega_R t + \phi_R), \\ \mathbf{B}_R &= y B_R \cos(k_R z - \omega_R t + \phi_R). \end{aligned} \quad (7.4)$$

Here,  $E_R$  and  $B_R$  are the electric and magnetic fields, respectively, of the radiation generated at a frequency  $f_R = 2\pi/\omega_R$  with a wave vector  $k_R = 2\pi/\lambda_R$ ,  $\lambda_R$  being the wavelength of radiation emitted, and  $\phi_R$  is an initial phase. This electromagnetic field could be present in the undulator either due to the incoherent spontaneous radiation emitted by electrons as discussed earlier or due to a seed radiation in an amplifier configuration. The amplitudes ( $E_R$  and  $B_R$ ) and phase  $\phi_R$  are slowly varying down the undulator.

The first-order Lorentz force experienced by an electron due to the undulator magnetic field imparts to it a velocity  $v_x$  given by Eq. (7.3). Since this “wiggling” electron and the spontaneous radiation emitted by it co-propagate down the undulator with overlap maintained between the two as discussed earlier, exchange of energy between the electric field  $xE_R$  of the radiation and the  $v_x$  motion of the electrons in the undulator is given by

$$mc^2 \frac{d\gamma}{dt} = e \mathbf{E}_R \cdot \mathbf{v}_x. \quad (7.5)$$

From Eqs. (7.3), (7.4), and (7.5), one obtains

$$\frac{d\gamma}{dt} \propto -\cos(k_R z - \omega_R t + \phi_R) \sin(k_U z). \quad (7.6)$$

The right-hand side of this equation can also be written as  $\{\sin(k_R z - k_u z - \omega_R t + \phi_R) - \sin(k_R z + k_u z - \omega_R t + \phi_R)\}$ , where both the sine terms oscillate between +1 and -1 averaging out to zero as the electron moves down the undulator. By suitably choosing an electron velocity  $v_{z0} = \omega_R/(k_R + k_U)$ , the second term in the phase dependence above is almost constant or slowly varying and does not average out to zero. Hence, a net energy exchange between radiation and the electron is possible in this case.

This is better understood if we look at the interaction of an electron moving with a constant velocity along the “ $z$ ” direction with a co-propagating wave having a component of electric field along the  $z$  direction and a phase velocity  $v_\phi$ . If the electron velocity is very different from the phase velocity of the wave, it sees random fluctuating phases of the electric field of the co-propagating wave. Hence, the net effect on the electron due to the electric field of the co-propagating wave averages out to zero. On the other hand, if the electron has a velocity equal to the phase velocity of the co-propagating wave, it sees the same phase of the electric field as they co-propagate, and depending upon the value of phase of the field, it can gain energy from the wave, lose energy to the wave, or remain unaffected. The interaction between the electrons and the ponderomotive wave is similar to the above analogy, and it is possible for the electron to lose energy to the ponderomotive wave, which ultimately results in growth of radiation.

The quantity  $\psi = (k_R z + k_u z - \omega_R t)$  is called as the phase of a ponderomotive wave driven in the electron beam due to the second-order interaction between the  $v_x$  component of velocity acquired by the electrons in the undulator and the electric field of the radiation wave. Depending upon the quantity  $\psi + \phi_R$ , an electron can either gain or lose energy to the radiation. The electron beam from the accelerator initially has electrons distributed uniformly in phase. Hence, as this beam propagates down the undulator with a velocity  $v_{z0} = \omega_R/(k_R + k_U)$ , electrons lying in a phase  $0$  ( $\pm 2n\pi$ , where  $n$  is an integer) to  $\pi$  ( $\pm 2n\pi$ ) lose energy, while the others lying between  $\pi$  ( $\pm 2n\pi$ ) and  $2\pi$  ( $\pm 2n\pi$ ) are accelerated, resulting in no net energy exchange. If the electron distribution can be modified to have electrons only between phases  $0$  to  $\pi$ ,  $2\pi$  to  $3\pi$ , and so on, all electrons will lose energy to the ponderomotive wave, which in turn will result in growth of radiation.

In an FEL, this desired redistribution of electrons within each bunch from the accelerator occurs as the bunch travels through the undulator. The first-order Lorentz force experienced by the electrons due to the undulator magnetic field causes them to experience a force in the  $x$  direction, and they acquire a velocity  $v_x$  in that direction. As these “wiggling” electrons and the spontaneous radiation emitted by them co-propagate down the undulator, they experience a second-order Lorentz Force due to an interaction of their  $v_x$  motion with the  $B_y$  magnetic field of the electromagnetic wave given by Eq. (7.4). This results in a “ponderomotive” force along the  $z$  direction with a time and space dependence given by  $\sin(k_u z) \cos(k_R z - \omega_R t + \phi_R)$ . If the initial electron velocity is chosen appropriately as discussed above, there is a net force along the  $z$  direction causing a redistribution of the initially uniform distribution of electrons in each bunch leading to micro-bunching around the phases  $0, 2\pi, 4\pi$ , etc., with the separation between bunches given by  $2\pi/(k_U + k_R)$ .



**Fig. 7.3** Bunching of electrons by the ponderomotive wave. “A” shows an un-bunched electron beam with uniform distribution of electrons (gray) over all phases of the ponderomotive wave and “B” shows electrons bunched around phases 0,  $\pi$ ,  $2\pi$ , etc.

Figure 7.3 shows the redistribution of charge leading to micro-bunching. Since  $k_R \gg k_U$ , the bunch spacing  $\sim \lambda_R$  and radiation from the micro-bunches are in phase leading to coherence. From the principle of superposition, the radiated power  $P_R$  in this case is proportional to  $N_e^2$ , which gives orders of higher brightness for the radiation emitted by the FEL as compared to synchrotron radiation sources. For example, an electron bunch with 0.1 nC charge propagating through an undulator contains  $\sim 10^8$  electrons and spontaneous emission power from this electron bunch is proportional to this number of electrons. Development of micro-bunching in an FEL as discussed above ideally results in development of full coherence in the output radiation giving a gain of  $10^8$  as compared to the spontaneous emission output from the same bunch.

From the laws of electrodynamics, growth of electromagnetic radiation at a given angular frequency  $\omega$  and wave number  $k$  requires a driving current having the same Fourier components ( $\omega, k$ ). Hence, the initially uniform distribution of electrons in each bunch from an accelerator in an FEL has to be modified by micro-bunching to obtain a current density with the required Fourier components ( $\omega_R, k_R$ ). For example, consider an FEL operating in the infrared region with a wavelength of 30  $\mu\text{m}$  or a frequency of 10 THz corresponding to a time period of 0.1 picosecond(ps). At this time scale, the 10 ps long beam from the accelerator is like a uniform distribution without any component of current at the desired frequency. Micro-bunching is required in each bunch from the accelerator on a time scale shorter than 0.1 ps to generate a current density at the radiation frequency to drive this electromagnetic radiation. The ponderomotive wave driven in the electron beam due to the interaction of the electrons with the undulator and radiation fields generates the required micro-bunching leading to growth of radiation in an FEL.

In order to study the growth of radiation in an FEL, one needs to solve the electromagnetic wave equation with the driving terms on the right-hand side as shown in Eq. (7.7).

$$\nabla^2 \mathbf{A}_R - \frac{1}{c^2} \frac{d^2 \mathbf{A}_R}{dt^2} = -\mathbf{J}. \quad (7.7)$$

Here,  $\mathbf{A}_R (\omega_R, k_R)$  is the vector potential associated with the electromagnetic wave, or the FEL radiation, and  $\mathbf{J}(\omega_R, k_R)$  is the current density having the same Fourier components as that of the electromagnetic wave in order to drive it. Determination of this current requires the study of electron motion in the FEL, which again

depends upon the evolution of the electric and magnetic fields of the electromagnetic radiation in the FEL. Hence, analytical treatment of an FEL involves the solution of coupled equations governing the motion of particles and the growth of radiation in the device, which is presented very lucidly in references [2, 3]. Many numerical codes have been developed to study FEL interaction considering the contribution due to three-dimensional space and time-dependent effects in the device, and contemporary FELs are designed using one or many of these codes.

## 7.4 Why Are FELs Attractive?

### 7.4.1 Tunability

The most attractive feature of an FEL is its tunability. It is evident from Eq. (7.1) that the wavelength of radiation, ( $\lambda_L$ ), can be tuned either by varying the  $\gamma$  (energy) of the electron beam coming from the accelerator or by varying the undulator parameter  $K_U$ . While the former is easier and can be achieved by varying the RF power fed to the linac, the latter involves changing the gap between undulator jaws to vary the undulator field strength, thereby changing the undulator parameter. A classic example of this tunability is the FEL at the Institute for FEL at Osaka in Japan where radiation from  $0.23\text{ }\mu\text{m}$  to  $100\text{ }\mu\text{m}$  wavelength is generated using five undulators. Tunability is very important for experiments where very fine lines are to be discriminated.

### 7.4.2 Choice of Pulse Structure

The pulse structure of the radiation generated by an FEL mimics the pulse structure of the electron beam propagating through the undulator. Consequently, FELs can operate with any desired pulse structure independent of the wavelength of operation. This is achieved by tailoring the pulse structure of the electron beam from the accelerator for the intended application.

### 7.4.3 High-Power Operation

Ideally, there is no upper limit on the power output that can be obtained from an FEL. This is due to the fact that the active medium in an FEL is the electron beam, which itself is an ionized medium which cannot be broken down further as in atomic and molecular systems subjected to high electric fields during operation at high powers. Further, the electron beam transfers only a small fraction of its energy to

the FEL radiation with the remaining energy in the beam being brought out of the interaction region and dumped in a suitably designed beam dump. Consequently, there is no problem of heat removal from the machine since all energy is removed at the speed of light. X-ray FELs have demonstrated GW of peak power in fs pulses while a long-wavelength FEL has been successfully operated at 10 kW CW average power. Progress on the power output from FELs is dependent upon the progress in accelerator technology.

#### ***7.4.4 Mirror-Less Operation at X-Ray Wavelengths***

As one moves to wavelengths shorter than 100 nm, it is difficult to have mirrors that can be used to make the optical cavity of an oscillator. With FELs, there is a regime of operation called as the high gain regime where, in a single pass through the device, a high-intensity bunch of electrons can drive an FEL to reach saturation over an undulator length of few 10s of meters. This regime of operation is very popular in X-ray FELs operating in the self-amplified spontaneous emission (SASE) mode where an intense (kA of peak current), energetic (few GeV for X-rays) electron bunch is propagated through an undulator that is 30–40 m long. The initial spontaneous emission from the electron bunch is amplified as it propagates through the undulator with continuous interaction between the radiation and electron bunches resulting in saturation of lasing action after which very high-peak-power, coherent X-ray radiation with intensities that are orders of magnitude higher than those possible from present-day synchrotron radiation sources are obtained. Many versions of this mode of operation, including those employing a seed laser with harmonic generation, have been proposed and are being tried out to improve the performance of these X-ray FELs. It may be noted that SASE mode of operation has been successfully demonstrated at longer wavelengths also. However, due to the availability of mirrors at these wavelengths, the oscillator configuration is more popular at these wavelengths.

### **7.5 Present Status of FELs**

After the first successful operation of an FEL in 1976 by John Madey and his group at Stanford University, where they demonstrated operation of an FEL in an amplifier configuration at infrared wavelength, the same group also demonstrated operation in an oscillator configuration at the same wavelength using an optical cavity. The first operation of an FEL in the optical regime was at Orsay in France where a storage ring FEL on the ACO storage ring produced red color light. While the undulator used in this FEL is similar to that used in other FELs, the electron accelerator here is a synchrotron instead of a linear accelerator (linac), which is the most popularly employed injector for FELs. FELs have subsequently been operated at practically all

wavelengths with major emphasis being wavelengths where conventional lasers and microwave sources are not very efficient [4]. Current trends on FEL development are therefore focused mainly on two wavelength regimes – IR/terahertz (THz) and V-UV/X-ray wavelengths.

With a lot of interest focusing around THz radiation for scientific as well as for security-related applications, many FELs have been built or proposed in the last decade at these long wavelengths. Depending upon the application, these FELs operate either with short pulse and high-peak powers required for scientific applications or at high CW average powers for imaging or homeland security-related applications. A THz FEL has been successfully operated at Novosibirsk in Russia at a CW average power level of 400 W in what is called as an energy recovery linac (ERL) configuration using normal conducting linacs. Similarly, an FEL using a similar ERL configuration but with superconducting cavities has been successfully operated at the Jefferson Lab in the United States at CW average power levels of more than 10 kW.

Recently, with growing interest in high brightness sources of hard X-rays, many short-wavelength FELs have been built/proposed. The first such X-ray FEL is the Linac Coherent Light Source (LCLS) at the Stanford Linear Accelerator Center in the United States which has successfully demonstrated lasing at  $1.5 \text{ \AA}$  with bright femtosecond (fs) pulses of X-ray radiation which have been used for a variety of research applications. The SACLA X-ray FEL in Japan has also lased recently producing bright beams of hard X-rays. Similar X-ray FELs are also being built in Europe (X-FEL), Paul Scherer Institute in Switzerland, Pohang Light Source in Korea, etc. and greater details about these FELs can be obtained from their respective websites. These FELs are the state of the art in FEL research since successful building and commissioning of these devices involves many cutting-edge technologies like advanced electron beam generation and manipulation techniques, beam diagnostics, very stable RF and control systems, etc. The operating parameters of LCLS are typical of such X-ray FELs:  $\lambda \sim 1.5 \text{ \AA}$ , pulse width  $\sim 100 \text{ fs}$ , peak brightness  $\sim 12 \times 10^{32} \text{ photons/s/mm}^2/\text{mrad}^2/0.1\% \text{ BW}$ , and peak coherent power  $\sim 9 \text{ GW}$ .

Significant work has also been done on new and improved configurations of FELs to tap the progress made in science and technology of accelerators. While LCLS utilizes conventional normal conducting linacs, the X-FEL project proposes to use superconducting RF technology for the injector linac which will enable them to operate with a higher duty cycle. Superconducting RF technology is also being exploited to build energy recovery linacs that operate at close to 99 % efficiency. Such a configuration has already demonstrated 10 kW CW average power at IR wavelength, which is very useful for homeland security applications. On the X-ray FEL front, various schemes like high-gain harmonic generation (HGHG), high harmonic generation (HHG), and FEL oscillator configuration using an optical cavity with Bragg crystal mirrors are being tried out, or have been proposed in projects like the FERMI and SPARC FELs in Italy, Dalian and SDUV FELs in China etc.

In India, experimental activity related to FELs was initiated at the Institute for Plasma Research (IPR), Ahmedabad, and at the University of Pune in the 1990s.

While activity at Pune University initially focused on building an undulator for use in an FEL, the activity at IPR, Ahmedabad, was on propagation of a sheet electron beam generated by their injector through a planar, five-period undulator to generate mm waves. This was successfully accomplished by them in 1996 [5]. Significant theoretical studies on FELs have been performed at the Indian Institute of Technology (IIT), Delhi, University of Lucknow, and at the Devi Ahilya Vishwavidyalaya (DAVV), Indore. DAVV, Indore, has recently initiated experimental activity related to development and characterization of prototype undulators for FELs.

The Raja Ramanna Centre for Advanced Technology (RRCAT), Indore, initiated activities on FELs in late 1990s, beginning with theoretical studies on different types of FEL configurations and for the design of an FEL at far-infrared wavelengths. Subsequently, the first project to build a far-infrared FEL was taken up in the year 2002 which envisaged the setting up of a THz FEL designed to lase at  $80\text{--}150\text{ }\mu\text{m}$  wavelength using an electron beam of energy 7–10 MeV and a 2.5 m long pure permanent magnet undulator (NdFeB) with a period of 5 cm. This effort involved the in-house development of all important subsystems – the injector linac [6], the undulator [7], the optical cavity, the electron beam transport line, and the RF system. This FEL, called as the compact ultrafast terahertz FEL (CUTE-FEL), was commissioned in 2010 and the first spontaneous THz radiation from the device was observed in 2011. Subsequently, with improvements in the injector system of the FEL, first signature of nonlinear dependence of radiated power on the electron beam current has been observed in 2012 [8]. Efforts are underway to further increase the nonlinearity and move toward saturation with the commissioning of a crucial RF power amplifier for the pre-buncher cavity.

Efforts are also presently underway on building an infrared FEL (IR-FEL) designed to lase at  $15\text{--}30\text{ }\mu\text{m}$  wavelength using an injector linac of 15–25 MeV energy and a 2.5 m long pure permanent magnet undulator with 5 cm period. This IR-FEL is proposed to be used for materials science research by an in-house group for which a user facility is presently being developed.

## 7.6 Conclusions

FELs are electron beam-based sources of intense, coherent, tunable electromagnetic radiation which can, in principle, operate over a wide-wavelength region from THz to hard X-rays. On account of being coherent, the radiation power output from an FEL is many orders of magnitude higher than that possible using a synchrotron radiation source operating at the same wavelength. Though they are operationally not as simple and compact as conventional lasers or microwave sources, they have certain unique characteristics like tunability, uniformity of operation principle over all wavelengths, high-power-handling capacity, etc., that make them very popular at wavelengths where the conventional sources are either not available or not very efficient. Many user facilities based on FELs are in operation today at wavelengths ranging from far-infrared to soft and hard X-rays.

## References

1. C.A. Brau, *Free Electron Lasers* (Academic, San Diego, 1990)
2. V. Kumar, *Some Studies on Free Electron Laser Oscillators*, Ph.D. thesis, 2003.
3. T.C. Marshall, *Free Electron Lasers* (Macmillan, New York, 1985)
4. W.B. Colson et al., *Free Electron Lasers in 2011*, Proceedings of the 2011 FEL Conference (FEL 2009), Liverpool, UK, p. 591, 2009
5. A.V. Ravi Kumar, K.K. Jain, Propagation of a sheet electron beam through a planar five-period electromagnetic undulator. *Appl. Phys. Lett.* **69**, 290 (1996)
6. B. Biswas, S.K. Gupta, U. Kale, M. Khursheed, A. Kumar, V. Kumar, S. Lal, P. Nerpagar, K.K. Pant, A. Patel, A.K. Sarkar, *Development and Commissioning of the CUTE-FEL Injector*, Proceedings of the International Particle Accelerator Conference (IPAC'10), Kyoto, Japan, 1716, 2010
7. B. Biswas, Vinit Kumar, S. Chouksey, S. Krishnagopal, Design, construction and characterization of the compact ultrafast terahertz free electron laser undulator. *Pramana* **7**(6), 1321 (2008)
8. B. Biswa, U. Kale, M. Khursheed, A. Kumar, V. Kumar, S. Lal, P. Nerpagar, A. Patel, K.K. Pant, Signature of build-up of coherence in an indigenously built Compact Ultrafast Terahertz free electron laser. *Curr. Sci.* **105**(1), 26 (2013)

# Chapter 8

## Lasing in Random Amplifying Media

Hema Ramachandran

**Abstract** The transport of light in certain media is diffusive – this happens due to repeated scattering off refractive index inhomogeneities. This chapter begins with a discussion of the factors that bring about and control the diffusion of light in random media. Thereafter, the transport of light through random amplifying media is discussed. This has given rise to many interesting phenomena like the “mirrorless random lasing” and the observation of Lévy statistics. These will be elaborated upon.

**Keywords** Random lasers • Light scattering • Lévy statistics • Diffusive photon propagation • Monte Carlo simulations of light amplification

### 8.1 Introduction

A stone, when dropped into water, sinks to the bottom in a straight line path. A drop of ink, on the other hand, diffuses and spreads outward while also gradually falling down. Photons, when sent into a turbid medium, do likewise – some of them travel in ballistic paths, undeviated from their initial direction of travel. Others adopt diffusive trajectories, being scattered in random directions. What governs these trajectories? Where does one encounter such strong scattering of photons? Is strong scattering of any relevance? These and similar questions form the subject matter of the initial part of the lecture. Thereafter, I will discuss how strong multiple scattering has led to the concept of “random lasers,” how such mirrorless lasers are realized practically, and how one may simulate the emission characteristics of such random active media. Finally, I will describe how an unusual characteristic can be seen in very strongly scattering scatterings – that of Lévy statistics.

Light travels in a straight line path until it encounters an inhomogeneity in the refractive index. If “ $a$ ,” the linear dimension of the inhomogeneity, far exceeds “ $\lambda$ ,” the wavelength of light, i.e.,  $a \gg \lambda$ , then the situation is one of geometrical

---

H. Ramachandran (✉)  
Raman Research Institute, Sadashiv Nagar, Bangalore 560080, India  
e-mail: [hema@rri.res.in](mailto:hema@rri.res.in)

optics – one that we are most familiar with. Snell's laws of reflection and refraction hold. The reflection that one sees in a mirror, the correction to eyesight using spectacles, and the glitter of a diamond due to total internal reflection are all phenomena that belong to this regime.

The case of  $a \sim \lambda$  corresponds to Mie scattering, encountered, for example, in scattering by water droplets in clouds. The scattering is anisotropic and often is strongly peaked in the forward direction and could have several intensity maxima and minima as a function of the scattering angle. The scattering in this regime is very sensitive to the shape of the scatterer.

The regime that we will dwell upon at length in this lecture is the Rayleigh scattering regime, where  $\lambda/10 < a < \lambda$ . The scattering is almost isotropic. Such a situation is seen, for example, in mist, where the very tiny droplets of water suspended in air cause light to scatter randomly in all directions. Thus, a source of light cannot be seen through mist as a localized region from which the light is emanating; rather one sees diffuse illumination spread in all directions, making it difficult to locate the source.

The blue of the sky is also a result of Rayleigh scattering – here, the sunlight is scattered by molecules in the air. As Rayleigh scattering is proportional to the inverse fourth power of the wavelength of light, the shorter wavelengths are scattered more. While sunlight has the full visible spectrum present, the blue component is scattered much more than the red. Thus, when viewed from the ground, the sky appears blue (Fig. 8.1).

For the extreme case of  $a \ll \lambda$ , individual particles cannot be discerned by light. Thus, individual particles cannot scatter light; the medium offers a mean refractive index.

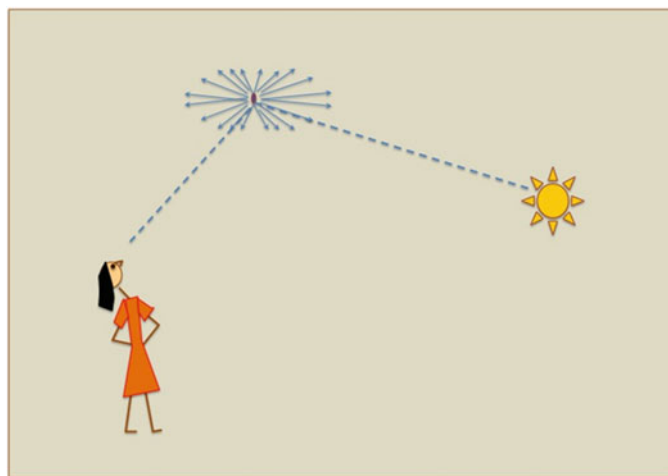


**Fig. 8.1** Schematic showing the light from the sun being scattered by molecules in the air. As shorter wavelengths are scattered most, the sky appears blue

## 8.2 Some Definitions

Let us now examine the above qualitative scenarios in a more quantitative fashion. We define the following parameters:

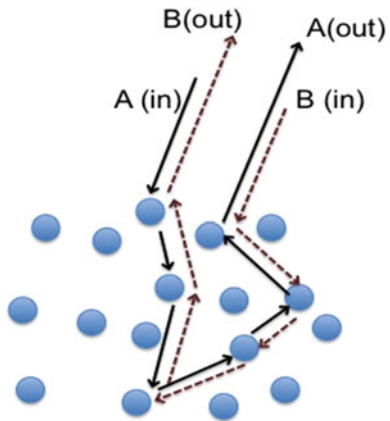
- The size parameter,  $x = a/\lambda$ ,  
i.e., the ratio of the diameter of a spherical scatterer to the wavelength of light.
- The refractive index contrast,  $R = n_s/n_m$ ,  
i.e., the ratio of the refractive index of the scatterer to that of the surrounding medium.
- The scattering efficiency,  $Q$ , which is proportional to  $R$ .
- The scattering cross section,  $\sigma = \pi (a/2)^2 Q$ .
- The scattering mean free path,  $l_s = (n_s \sigma)^{-1}$ , that is, the mean distance a photon travels within the medium before it encounters a scatterer.
- The anisotropy parameter,  $g = \langle \cos \theta \rangle$ , that is, the average of the cosine of the scattering angle,  $\theta$ . For isotropic scattering,  $g = 0$ ; for forward scattering,  $g = 1$ .
- The transport mean free path,  $l^* = l_s/(1 - g)$ , that is, the mean distance a photon travels within the medium before the direction of its travel is randomized.
- The gain length,  $l_g$ , that is, the length of the amplifying medium, over which light intensity is amplified by a factor  $e$ .
- The amplification length,  $l_a$ , the average distance between the beginning and the ending points for which the actual path length traversed by the photon is  $l_g$ . In a homogeneous amplifying medium (without scattering), light travels in a straight line; thus,  $l_{\text{amp}} = l_g$ . In a RAM, owing to multiple scattering and the consequent random paths of the photons, the actual arc length of travel of a photon is much greater than the chord distance between the beginning and the ending points. This gives rise to the concept of  $l_{\text{amp}}$ . In the diffusive sample,  $l_{\text{amp}} = \sqrt{D \tau_{\text{amp}}}$ , where  $D$  is the diffusion coefficient,  $\tau_{\text{amp}} = l_g/v$ , and  $v$  is the transport velocity of light in the medium. In a three-dimensional system,  $D = v l^*/3$ ; thus,  $l_{\text{amp}} = \sqrt{l^* l_g / 3}$ .
- In an absorbing medium, the analogue of the gain length is the inelastic mean free path  $l_i$ , defined as the path length over which light intensity is reduced to  $1/e$  of its initial value, due to absorption. Hence, the amplification length  $l_{\text{amp}}$  is analogous to the absorption mean free path  $l_{\text{abs}} = \sqrt{l^* l_i / 3}$ .

## 8.3 Different Regimes of Scattering

For the rest of the lecture, we will deal only with Rayleigh scatterers. Let us consider a collection of monodisperse spherical particles suspended randomly (positions are random) in fluid, e.g., water. Three regimes of light transport can be distinguished depending on the strength of scattering:

1. The ballistic regime: This is the weak scattering regime, where the system size  $L$  is smaller than the transport mean free path. Photons travel essentially in the forward direction.

**Fig. 8.2** Depiction of a scattering path ( $A$ , solid line) and its time-reversed counterpart ( $B$ , dashed line) contributing to coherent backscattering



2. The localization regime: This is the other extreme – that of strong scattering. The system size  $L$ , in this case, far exceeds the transport mean free path. Further, the mean free path is of the order of the wavelength of light, and thus, interference effects play a significant role. One such effect, the coherent backscattering, seen in the weak localization regime, arises as follows. Consider a path where light enters the medium and, after a few scatterings, emerges out of the medium, back toward the source. For every path that light could have taken to enter the medium and emerge from it at the same point, another path can be defined that follows identically the segments of the first path, but in the reverse order (Fig. 8.2). Both paths are equally probable. Thus, light traveling in the two paths undergoes the same amount of phase shifts and interferes constructively on emerging. This happens only when the entry and exit points are identical or are very slightly separated ( $\sim l^*$ ). This constructive interference manifests itself as a narrow cone of bright light in the exact backscattered direction, with an intensity twice that of the background.

Another interesting effect is that of localization. When the scattering is very strong, such that  $2\pi l^* \leq \lambda$  – the Ioffe-Regel criterion [1, 2] – the system is in the Anderson or strong localization regime. Light is trapped within the medium, due to strong recurrent scattering. The rigorous analysis invokes interference effects that are dominant when the scattering mean free path is smaller than the wavelength of light. One may picture this as the light field being scattered even before a single oscillation is complete. Due to such strong scattering, the return probability of the intensity to closed-loop paths is very high, thereby reducing the diffusion constant. The diffusion constant can, thus, become zero at large scatterer strength, implying that the wave can no longer escape from its original region in space or the light propagation ceases and hence the name localization. Weak localization is said to be the precursor of the strong (Anderson) localization. Localization of light waves in strongly scattering media was theoretically predicted [3–5] in the 1980s which was then demonstrated experimentally (in both the microwave [6, 7] and the visible regime [8]).

Interestingly, a medium where the localization condition has been achieved is strongly reflecting. This is because if light cannot come out of a medium, it cannot enter the medium either.

3. Diffusive regime: This is intermediate to the two cases discussed above. Here  $\lambda \ll l^* \ll L$ .

While the first inequality ensures that localization effects are small, the second inequality implies multiple scattering of the wave traversing the system.

The propagation of light in the diffusive regime can be described as a random walk of photons with the direction of each succeeding step determined probabilistically and can be described by the particle diffusion equation in a gain medium:

$$\frac{\partial I(r, t)}{\partial t} = D \nabla^2 I(r, t) + \frac{v}{l_g} I(r, t)$$

where,  $I(r, t)$  is the optical intensity at a position  $r$  inside the medium at time  $t$ ,  $D$  is the diffusion coefficient,  $v$  is the transport velocity of light in the medium. The last term in the above equation is the gain term. The diffusion equation is a classical equation that completely neglects interference effects between multiply scattered waves and describes only the average intensity.

## 8.4 Random Amplifying Media (RAM)

We now turn our attention to a novel type of light source that is based on the principle of random multiple scattering – the random laser, also known as the mirrorless laser. A typical laser has an active medium contained between two mirrors that form an optical cavity (Fig. 8.3a).

The active medium is pumped and spontaneously emitted photons are amplified as they travel through the active medium. The light traveling along the cavity axis is

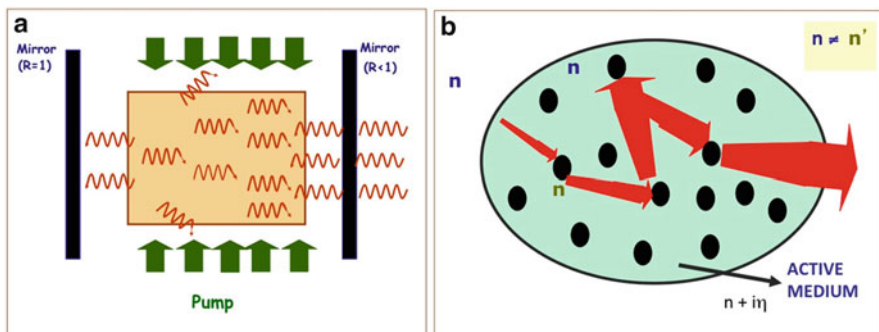
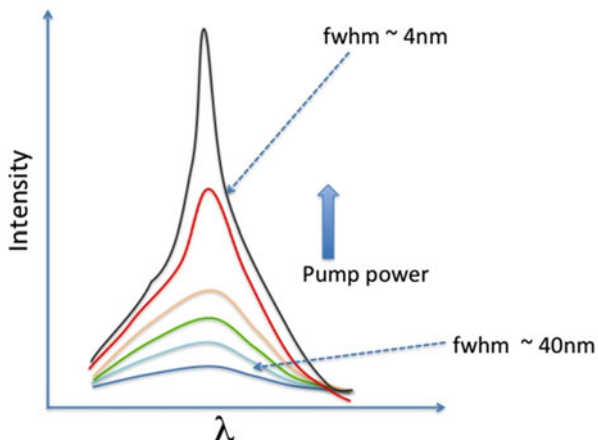


**Fig. 8.3** Schematic of (a) a conventional laser and (b) a random laser

**Fig. 8.4** Schematic of emission from a diffusive random laser showing linewidth collapse



repeatedly reflected back and forth between the mirrors (provided its wavelength is resonant with the cavity length). Each transit through the active medium amplifies the light, leading to coherent, narrowband, directional laser emission.

Let us now examine a system made of a liquid active medium in which scatterers are randomly suspended; there is no external cavity (end mirrors). An example of such a medium is a suspension of polystyrene microspheres in a solution of rhodamine dye in ethanol (Fig. 8.3b). This medium can be pumped with green light, say from a frequency-doubled Nd-YAG laser, so that the dye molecules are excited. The spontaneously emitted light from the dye is amplified as it travels through the dye. The presence of the scatterers causes the light to be repeatedly scattered within the active medium, thereby enhancing amplification. As the intensity builds up, gain narrowing occurs (Fig. 8.4). This is the essence of a random amplifying medium (RAM). The light emitted is not directional, nor coherent, nor is monochromatic like that of a conventional laser. Thus, the RAM, as described above, is an “incoherent random laser” or a “diffusive random laser.”

In 1966, Ambartsumyan et al. realized a laser cavity in which one mirror of the Fabry-Pérot cavity was replaced by a scattering surface which results in the multiple scattering of light in the cavity [9, 10]. However, as it lacked spectral purity, directionality, and coherence, it did not generate much interest in the scientific community.

In 1968, Letokhov [11] theoretically proposed self-generation of light in a RAM, in the diffusive regime. By solving the diffusion equation for the photon energy density in the presence of uniform and linear gain, he showed that as the volume of the scattering medium exceeds the critical volume  $V_{cr}$  ( $\approx (l \cdot l_g / 3)^{3/2}$ ), the photon energy density increases exponentially with time. Because this process of photon generation is analogous to the multiplication of neutrons in an atomic bomb [12], this device is sometimes called a “photonic bomb.” In reality the light intensity will not diverge (there is no explosion) because gain depletion quickly sets in and  $l_g$  increases.

For a long time, Letokhov's theoretical work was not followed by experiments. However, in the late 1980s, several reports of laser-like emission in powdered luminophosphors appeared [13–20], opening up the field of random lasing. In a powder laser, it is hard to tell whether the feedback is provided by multiple scattering or internal reflection, because the gain medium and scattering elements are not separated in the powder. In 1994, Lawandy et al. [21] demonstrated isotropic laser-like emission from an optically pumped laser dye solution (rhodamine 640 perchlorate in methanol), in which point-like scatterers ( $\text{TiO}_2$  microspheres of mean diameter  $< 1 \mu\text{m}$ ) were randomly suspended. A collapse of the linewidth of emission was observed above a threshold pump power and was interpreted as the onset of lasing when the gain due to the enhanced path lengths within the active medium, brought about by multiple scattering, exceeded the intensity loss from the system. Linewidth collapse is a well-known phenomenon which occurs even in homogeneous amplifying media due to amplified spontaneous emission (ASE). The remarkable fact in these experiments was that the threshold of the pump power at which the emission spectrum collapsed drastically was almost two orders of magnitude smaller in the case of microsphere-laser dye suspension, compared to the case of ASE in the neat dye solution. Further, the peak emission intensity was shown to increase by more than three orders of magnitude upon the addition of scatterers [22]. As opposed to the crushed laser crystal RAM, the dye-scatterer RAM separated the scattering and amplifying media, thereby allowing the scattering strength to be varied independent of the optical gain via scatterer density and dye concentration, respectively. This in turn facilitated a systematic study of the scattering effect on feedback. Since this observation, many experiments were carried out to examine the origin and various features of the narrow-linewidth emission reported by them. Simultaneously, several theoretical studies [23–27] have been conducted to provide models that will efficiently describe the behavior of these materials and help in an understanding of the underlying mechanisms that are responsible for their laser-like characteristics.

Clearly, in all the above cases, the phase condition within the scattering medium is ignored because of the nonresonant diffusive nature of feedback provided by the weak scatterers – it only returns light into the gain volume, instead of to its original position. In fact, the probability of emitted light returning to its original position is so low in the diffusive regime that the interference effect on the feedback is negligible. Therefore, this kind of laser is called a random laser with nonresonant or incoherent feedback, or a diffusive random laser. Incoherent random lasing is similar to amplified spontaneous emission (ASE) in that it drastically narrows the emission spectrum (from a few tens of nanometers to a few nanometers) and transforms the usual linear excitation-emission intensity relation to a highly nonlinear one, above the pump threshold.

In the case of strong scattering and high optical gain, coherent feedback can be obtained due to recurrent scattering over closed-loop paths, where light returns to a scatterer from which it was scattered before. This is most probable for large scattering strengths (strong scattering), when the transport mean free path becomes comparable to the emission wavelength that is approaching the photon

localization regime. If the amplification along such a loop path exceeds the loss (due to escape from the loop), laser oscillation should occur in the loop, which then serves as a laser resonator. The requirement of the phase shift along the loop being a multiple of  $2\pi$  (condition for constructive interference) determines the oscillation frequencies. Random lasing with coherent feedback is characterized by the appearance of discrete, narrow lasing peaks (of linewidths  $<1$  nm, being limited by the spectrometer resolution) in the emission spectrum above the pump threshold in addition to a drastic increase of emission intensity.

Cao et al. demonstrated coherent random lasing with coherent feedback in ZnO/GaN nanoparticles [28] and in a suspension of ZnO particles in rhodamine [29]. At low pumping power, the spectrum consists of a single broad spontaneous emission band (linewidth  $\sim$ a few tens of nanometers). When the pump power exceeded a threshold, discrete, narrow peaks (widths  $<0.1$  nm) emerged in the emission spectra in systems that were close to localization threshold. The number of these discrete, spectral peaks increased with further increase in the pump power. Recurrent scattering and interference was invoked to explain the observed effects in these systems. However, subsequent experiments and Monte Carlo simulations [30] have shown that such spiked emission can be seen even in moderate scattering regimes, where interference effects are not important. As the medium is random, there is shot-to-shot variation in the position and intensities of the spikes (Fig. 8.5).

The quantum statistical property of laser emission from the ZnO powder was also probed in a photon counting experiment [28]. It was observed that the photon number distribution in a single mode changes continuously from the Bose-Einstein distribution near the threshold to the Poisson distribution well above the threshold. Later, three-dimensional, spatial confinement of laser light in a micron-size ZnO cluster (called a “micro random laser”) was demonstrated, through multiple scattering and interference [31, 32]. The interference effect being wavelength sensitive, light at only certain frequencies could be confined in a given cluster.

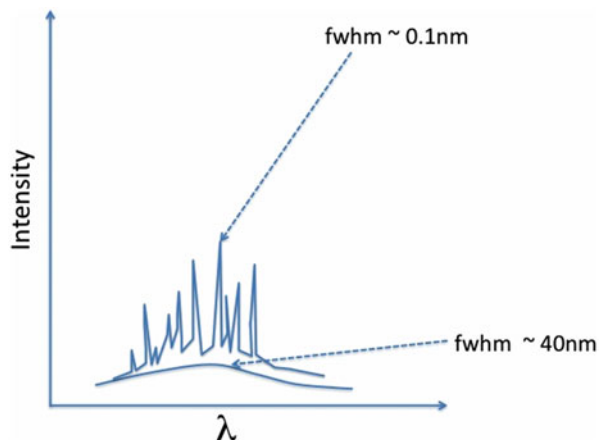


**Fig. 8.5** Schematic of emission from coherent random laser, showing spiked emission. Also shown, for comparison, is the typical broadband, featureless emission at low pump powers

## 8.5 Monte Carlo Simulations of Random Amplifying Media

Can one predict the emission from a dye-scatterer system? The answer is yes: the features can be predicted, while the actual single shot spectrum cannot. Typical emission spectra can be simulated by the Monte Carlo technique where the diffusive motion is viewed as a random walk of the photon, with the step lengths and the step directions uncorrelated but following a prescribed probability distribution. The stimulated amplification (in the active medium) can be introduced through an exponential number growth (multiplicative amplification) of the initial seed photon.

In a typical simulation, a spontaneous (seed) photon is assumed emitted at some position  $(x, y, z)$  in the active medium with  $0 < x/L, y/L, z/L < 1$  picked randomly from a uniform distribution. Its wavelength is picked from a weighted random distribution that mimics the dye's emission spectrum. This photon is allowed to propagate along some random direction over a distance  $l_s$  in the active medium before it undergoes a scattering event, upon which the direction of its propagation (scattering angle  $\theta$  and azimuthal angle  $\phi$ ) is randomly altered (with a distribution weighted by the scattering anisotropy function). The cumulative length of travel within the active bulk medium before its exit and its wavelength are kept track of. The total emitted intensity  $I(l)$  associated with this photon in then  $I(l) = \exp(l/l_g)$ , where  $l = \sum_i l_i$  is the total length of travel of the photon in the active medium. This process of tracing the path of a spontaneously emitted photon within the RAM till it exits was termed as a “simulation run” and is repeated for about a million seed photons. Each run, thus, corresponded to a different probabilistic photon path. Note that the seed photons have random wavelengths, but all photons simulated by a given seed photon have the same wavelength as the seed. One can thus build up the spectrum by keeping track of the number of photons emitted and amplified at the different wavelengths (see, e.g., [33]). As the photons may exit from any face, the calculated intensity constitutes the total emission from the sample.

## 8.6 Mirrorless Lasers and Random Walks

The path of a photon in a random medium is random. Thus, the process can be understood using the same formalism as for random walks. A random walk, defined as a path composed of many independent random steps, is observed in a broad spectrum of systems ranging from watching winnings fluctuate in games of chance to completely erratic motion of a drunkard wandering from one lamppost to another to modern studies of nonlinear dynamics. The Brownian motion, which describes the completely erratic motion of very small particles undergoing unending collisions with the surrounding particles, which hit them from all sides, is the simplest of random walks (Fig. 8.6). Fundamental dynamical processes such as molecular transport in liquids, atomic and molecular diffusion on surfaces, motion

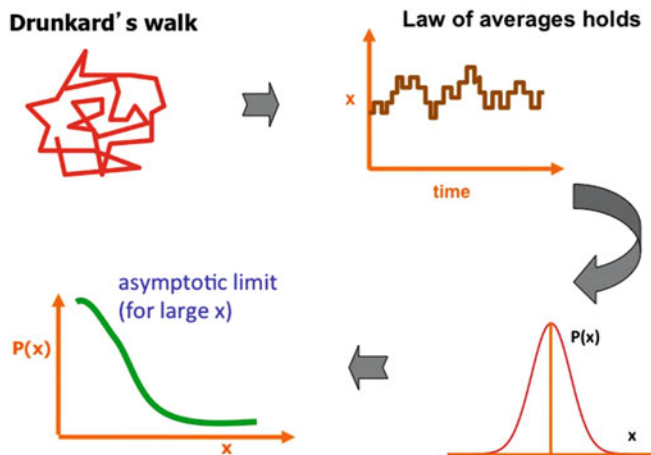


**Fig. 8.6** A random walk; the displacements are of more or less uniform length and the law of averages holds, giving a Gaussian distribution of step sizes

of microorganisms, and many other examples have all been described in terms of Brownian motion. Einstein showed that the mean-squared displacement of the random walk of the Brownian particle grows linearly with time, i.e.,  $\langle x^2(t) \rangle \sim t$ ; i.e., the root-mean-squared displacement of the Brownian particle from its starting point increases with the square root of time ( $\sqrt{t}$ ) and not linearly. The probability of a Brownian particle being at distance  $d$  from its starting point after time  $t$  is represented by a “Gaussian” – a bell-shaped curve centered at the origin (Fig. 8.6) which very rapidly drops to zero. The width is proportional to  $(\sqrt{t})$  and is a measure of the distance beyond which there is little probability of finding the particle, i.e., as the particle goes far from the mean value, the probability rapidly drops to zero. A striking aspect of this result is its universality. Irrespective of the microscopic details, like nature of the particle, its surroundings, temperature, etc., the probability distribution of the particle’s displacement (after a sufficient lapse of time) follows the Gaussian law of width  $\sqrt{t}$ . This is often described by the central limit theorem (CLT) [34] which states that the sum of a large number of independent, identically distributed random variables with finite variance converges to a Gaussian distribution with the variance linearly proportional to the number of terms in the sum. The CLT is valid under very general conditions. Irrespective of the law of probability followed by  $x_i$  ( $i = 1, 2, \dots, N$ ) and irrespective of their mutual correlations (provided these are weak), the probability distribution of  $X_N$  always remains a Gaussian curve, whose width increases as  $\sqrt{N}$ .

The Gaussian distribution is so ubiquitous that the central limit theorem is often accepted as universal. However, in rare situations, physical phenomena can exhibit statistical properties where CLT is violated and a non-Gaussian distribution is obtained – where the mean may or may not exist and the variance always diverges.

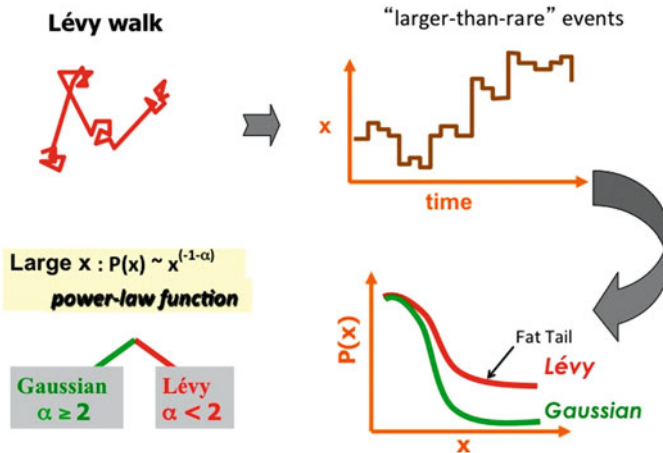


**Fig. 8.7** A Lévy walk showing a large number of nearly uniform small steps and a few large steps. The total displacement is dominated by the few large steps

These occur in random walks termed as Lévy flights [35] that have infinite mean-squared step size and arise for such random series of events where the rare or atypical events are so large in magnitude that they dominate the numerous small events. This results in a finite probability of observing improbable events [36] and thus gives the distribution a “fat” or “heavy” tail in the asymptotic limit (Fig. 8.7). Thus, in Lévy distributions, the determinant even is the rare event, and the sum reflects mainly the value of the largest terms. On the other hand, Gaussian sums are “democratic,” with each term contributing to a similar extent to the final result.

The probability density  $f(x)$  of a random variable  $x$ , may, in general be written as a power law, with the tail being given by

$$f(x) \approx \frac{1}{x^{1+\alpha}} : \text{for } x \rightarrow \infty$$

If  $\alpha \geq 2$ , the variance  $\langle x^2 \rangle$  is finite and the usual or classical CLT holds and the probability distribution is Gaussian. If  $\alpha < 2$ , i.e., the probability  $f(x)$  of obtaining a given value of  $x$  decreases less rapidly than  $1/x^3$  for large  $x$ , the variance diverges,  $x$  is said to have a fat tail or a broad probability density, and the usual CLT does not apply. If  $\alpha \leq 1$ , even the mean,  $\langle x \rangle$ , diverges. The sum (total displacements) for the case  $\alpha < 2$  is thus dominated by the rare but large steps – the Lévy flight.

Lévy flights have been used by physicists to explain certain experimental observations like photoconductivity in amorphous materials [37, 38], anomalous diffusion in living polymers [39], strange kinetics [40], rotating fluid flow [41], subrecoil laser cooling [42], interstellar scintillations [43], current fluctuations in narrow metal-insulator-metal tunnel junction [44, 45], and even in share prices in

the financial markets. In nature, the flight of birds and movements of insects looking for food are found to be Lévy walks – they move a long distance and then forage in a small local area before moving off again.

I will now discuss the observation Lévy statistics in random amplifying media. The fluctuations in the intensity of emission from dye-scatterer RAMs, over different realizations of its randomness, show Lévy statistics. The random realizations can originate due to different reasons. For example, there is randomness inherent in the diffusive motion of the photon through the RAM – the origin of the spontaneous photon, the wavelength of emission, the distance traveled between two scatterings, the direction of scatter are all random. Further, the configuration of the scatterers that are suspended in the liquid dye solution is also changing constantly due to the Brownian motion. This configurational change occurs over time scales smaller than the interval between successive pump pulses (shots) in experiments, and thus, each shot samples a different random realization of the RAM, giving rise to the “sample-to-sample” fluctuation. It can be theoretically shown [46] that the probability distribution  $p_g$  for gain  $g$  is given by

$$p_g(g) \cong \left( \frac{8\pi a p_o l^* l_g}{3} \right) \frac{1}{g^{1+a_1}}$$

where

$$a_1 = \frac{\pi^2 l^* l_g}{3a^2} \equiv \text{the first Lévy exponent}$$

Clearly,  $p_g(g)$  shows a power law behavior. This can describe either the Gaussian ( $a_1 \geq 2$ ) or the Lévy ( $a_1 < 2$ ) statistics. Thus, we can readily see that the divergence of the gain variance, that is, the crossover from the Gaussian to the Lévy statistics, can occur by strong gain or strong scattering. Increasing pumping and increasing dye concentration both serve to decrease  $l_g$ , the exponent  $a_1$  decreases, the tail becomes fatter (rare events become more probable), and the variance of  $g$  diverges for  $a_1 < 2$ . This suggests a means of controlling the crossover from a finite variance (Gaussian) to a divergent variance (Lévy) limit. Similar controlled crossover can also be achieved either by increasing the number density of scatterers or by enhancing the refractive index mismatch between the active bulk and the passive scatterers, both of which reduce  $l_g$ . Such tailoring of the exponent has indeed been realized experimentally [46, 47] and these will be discussed now (Fig. 8.8).

Light from a pulsed laser (532 nm,  $\sim 30$  ps) was incident on the sample (dye-scatterer system) contained in a cuvette. The emission from the sample is collected by a fiber and is analyzed on a spectrometer. Typically,  $\sim 1,000$  spectra are collected, and the intensity at a given wavelength is monitored. Strong shot-to-shot variation in intensity was observed. A histogram of the intensity at a given wavelength was constructed.

As the power law exponent  $\alpha \sim l^* l_g$ , we see that the transition from the Gaussian to the Lévy may be effected by decreasing either  $l^*$  or  $l_g$ . The former can be achieved

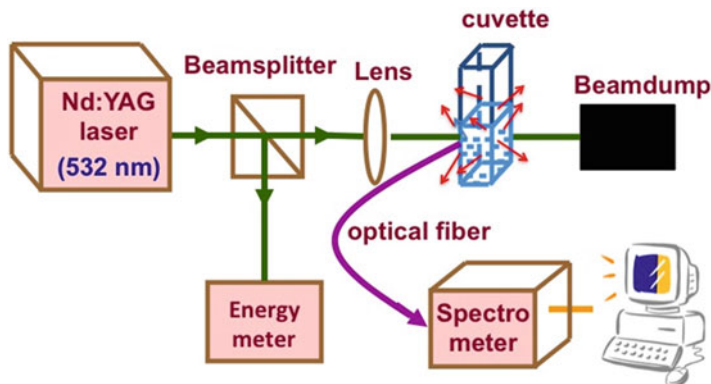


**Fig. 8.8** Schematic of a typical experiment to record emission from a RAM

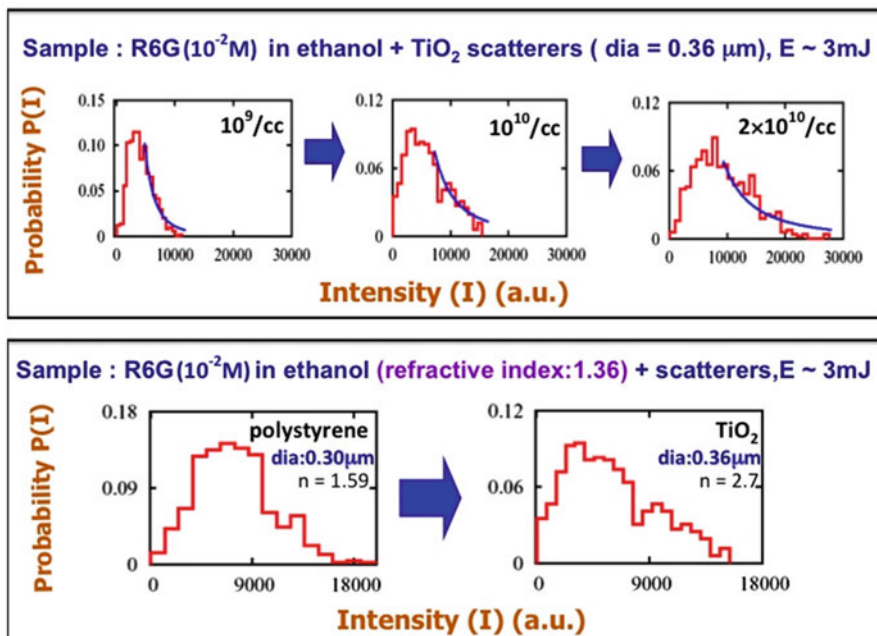


**Fig. 8.9** Histograms of the intensity fluctuation at 570 nm from a RAM, showing the Gaussian to Lévy transition effected by decreasing the transport mean free path

by increasing scattering either by increasing the number density of scatterers or by increasing the refractive index contrast. The latter can be achieved by increasing the pump power or the concentration of the dye. Figure 8.9 shows the Gaussian to Lévy transition effected by a decrease of  $l^*$  and Fig. 8.10 by a decrease in  $l_g$ .

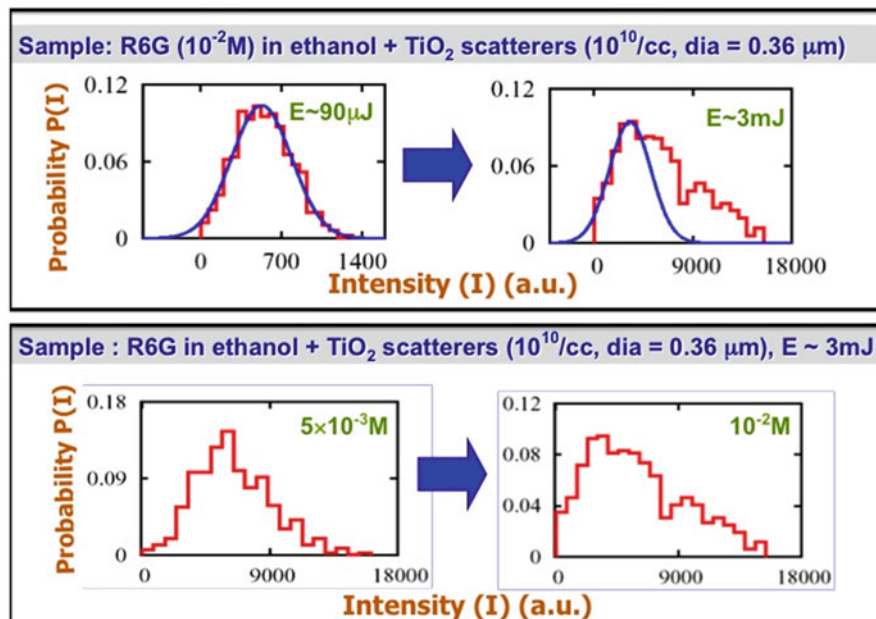


**Fig. 8.10** Histograms of the intensity fluctuation at 570 nm from a RAM, showing the Gaussian to Lévy transition effected by decreasing the gain length

## 8.7 Conclusion

We see that the random amplifying medium, once dismissed as uninteresting, has proved to be quite the opposite. It has shown many unexpected features and is now becoming a very rich field of investigation.

**Acknowledgments** It is a pleasure to acknowledge Dr. Divya Sharma and Dr. Sushil Mujumdar, my former students, who worked very diligently on much of the work presented here.

## References

1. A.F. Ioffe, A.R. Regel, Prog. Semicond. **4**, 237 (1960)
2. N.F. Mott, *Metal-Insulator Transitions* (Taylor & Francis, London, 1974)
3. S. John, Phys. Rev. Lett. **53**, 2169 (1984)
4. P.W. Anderson, Philos. Mag. B **52**, 505 (1985)
5. S. John, Phys. Today **44**, 32 (1991)
6. N. Garcia, A.Z. Genack, Phys. Rev. Lett. **66**, 1850 (1991)
7. A.Z. Genack, N. Garcia, Phys. Rev. Lett. **66**, 2064 (1991)
8. D.S. Wiersma, P. Bartolini, A. Lagendijk, R. Righini, Nature **390**, 671 (1997)

9. R.V. Ambartsumyan, N.G. Basov, P.G. Kryukov, V.S. Letokhov, IEEE J. Quantum Electron. **2**, 442 (1966)
10. R.V. Ambartsumyan, P.G. Kryukov, V.S. Letokhov, Y.A. Matveets, Sov. Phys. JETP **26**, 1109 (1968)
11. V.S. Letokhov, Sov. Phys. JETP, **26**, 835 (1968) (Zh. Eksp. Teor. Fiz., **53**, 1442 (1967))
12. B. Davison, J.B. Sykes, *Neutron Transport Theory* (Oxford University Press, Oxford, 1958)
13. V.M. Markushev, V.F. Zolin, C.M. Briskina, Sov. J. Quantum Electron. **16**, 281 (1986)
14. V.M. Markushev, N.É. Ter-Gabriélyam, C.M. Briskina, V.R. Belan, V.F. Zolin, Sov. J. Quantum Electron **20**, 773 (1990)
15. N.É. Ter-Gabriélyan, V.M. Markushev, V.R. Belan, C.M. Briskina, O.V. Dimitrova, V.F. Zolin, A.V. Lavrov, Sov. J. Quantum Electron. **21**, 840 (1991)
16. M.A. Noginov, N.E. Noginova, S.U. Egarievwe, H.J. Caulfield, P. Venkateswarlu, T. Thompson, M. Mahdi, V. Ostroumov, J. Opt. Soc. Am. B **13**, 2024 (1996)
17. C. Gouédard, D. Husson, C. Sautert, F. Auzel, A. Migus, J. Opt. Soc. Am. B **10**, 2358 (1993)
18. A.Y. Zyuzin, JETP **86**, 445 (1998)
19. A.Y. Zyuzin, Europhys. Lett. **46**, 160 (1999)
20. F. Auzel, P. Goldner, J. Alloys Compd. **300**, 11 (2000)
21. N.M. Lawandy, R.M. Balachandran, A.S.L. Gomes, E. Souvain, Nature **368**, 436 (1994)
22. B.R. Prasad, H. Ramachandran, A.K. Sood, C.K. Subramanian, N. Kumar, Appl. Optics **36**, 7718 (1997)
23. A.Y. Zyuzin, Phys. Rev. E **51**, 5274 (1994)
24. S. John, G. Pang, Phys. Rev. A **54**, 3642 (1996)
25. D.S. Wiersma, A. Lagendijk, Phys. Rev. E **54**, 4256 (1996)
26. G.A. Berger, M. Kempe, A.Z. Genack, Phys. Rev. E **56**, 6118 (1997)
27. C.W.J. Beenakker, Phys. Rev. Lett. **81**, 1829 (1998)
28. H. Cao, Y.G. Zhao, S.T. Ho, E.W. Seelig, Q.H. Wang, R.P.H. Chang, Phys. Rev. Lett. **82**, 2278 (1999)
29. H. Cao, J.Y. Xu, S.-H. Chang, S.T. Ho, Phys. Rev. E **61**, 1985 (2000)
30. S. Mujumdar, R. Torre, H. Ramachandran, D.S. Wiersma, J. Nanophoton. **4**, 041550 (2010)
31. H. Cao, Y. Ling, J.Y. Xu, C.Q. Cao, Phys. Rev. Lett. **86**, 4524 (2001)
32. H. Cao, J.Y. Xu, E.W. Seelig, R.P.H. Chang, Appl. Phys. Lett. **76**, 2997 (2000)
33. S. Mujumdar, H. Ramachandran, Opt. Commun. **176**, 31 (2000); D. Sharma, H. Ramachandran, N. Kumar, Opt. Commun. **273**, 1 (2007)
34. W. Feller, *An Introduction to Probability Theory and Its Applications* (Wiley, New York, 1971)
35. M.F. Shlesinger, G.M. Zaslavsky, U. Frisch, *Lévy Flights and Related Topics in Physics, Lecture Notes in Physics*, vol. 450 (Springer, Berlin, 1995)
36. C. Tsallis, Phys. World **10**, 42 (1997)
37. H. Scher, E.W. Montroll, Phys. Rev. B **12**, 2455 (1975)
38. G. Pfister, H. Scher, Adv. Phys. **27**, 747 (1978)
39. A. Ott, J.P. Bouchaud, D. Langevin, W. Urbach, Phys. Rev. Lett. **65**, 2201 (1990)
40. M.F. Shlesinger, G.M. Zaslavsky, J. Klafter, Nature **363**, 31 (1993)
41. T.H. Solomon, E.R. Weeks, H.L. Swinney, Phys. Rev. Lett. **71**, 3975 (1993)
42. F. Bardou, J.P. Bouchaud, O. Emile, A. Aspect, C. Cohen-Tannoudji, Phys. Rev. Lett. **72**, 203 (1994)
43. S. Boldyrev, C.R. Gwinn, Phys. Rev. Lett. **91**, 131101 (2003)
44. J. Moodera, L.R. Kinder, T.M. Wong, R. Meservey, Phys. Rev. Lett. **74**, 3273 (1995)
45. T. Miyazaki, N. Tezuka, J. Magn. Magn. Mater. **151**, 403 (1995)
46. D. Sharma, H. Ramachandran, N. Kumar, Fluct. Noise Lett. **6**, L95–L101 (2006)
47. D. Sharma, H. Ramachandran, N. Kumar, Opt. Lett. **31**(1806) (2006)

# Chapter 9

## Terahertz Transients: Generation and Applications

D.S. Rana

**Abstract** The recent advances in terahertz (THz) science and technology – encompassing various spectroscopic and imaging techniques – have enriched all the disciplines of fundamental and applied sciences. In the current research scenario, most of the techniques of generation and detection of electromagnetic THz radiation are based on infrared femtosecond lasers. A rapid growth in THz technology for more than a decade emanates from a parallel development of ultrafast lasers and efficient THz emitters and detectors. In this chapter, I will briefly review some well-established tabletop techniques of THz generation and detection based on modulated current density in semiconductors, optical rectification, and electro-optic sampling in nonlinear crystals and intersubband transition-induced intense emission in semiconductor superlattices called THz quantum cascade lasers. The applications of THz technology, i.e., time-domain spectroscopy and imaging, will be discussed in particular context of condensed matter physics. The two main facets of these applications are the realization of ultrafast carrier, spin and polarization dynamics using THz emission spectroscopy and the understanding of the low-energy dynamics/excitations arising from strong correlations probed by the THz time-domain spectroscopy.

**Keywords** Terahertz (THz) generation and detection • THz time-domain spectroscopy • THz emission spectroscopy • THz imaging • Low-energy dynamics • Ultrafast optical functionality

### 9.1 Introduction

One Terahertz (THz) means  $10^{12}$  Hz, wave number of  $33.3\text{ cm}^{-1}$ , an energy equivalent of 4.1 meV, and wavelength of  $300\text{ }\mu\text{m}$ . Electromagnetic radiation with a frequency of 0.3–20 THz is generally called terahertz/THz radiation or T-ray. In electromagnetic spectrum, the THz region lies between the infrared region and the

---

D.S. Rana (✉)

Indian Institute of Science Education and Research, Bhopal, Madhya Pradesh 462023, India  
e-mail: [dsrana@iiserb.ac.in](mailto:dsrana@iiserb.ac.in)

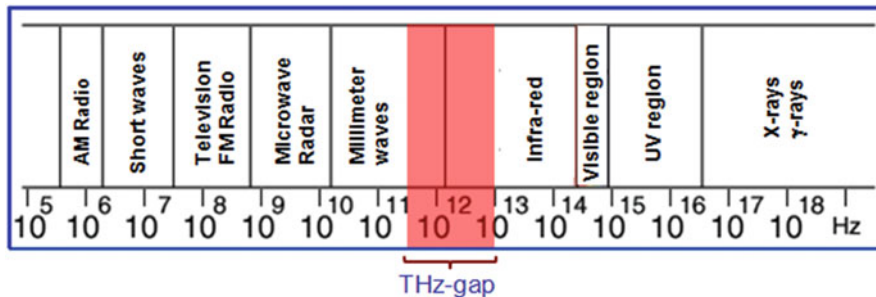


**Fig. 9.1** THz gap in the electromagnetic spectrum

microwave region. Until the advent of THz spectroscopy, there existed a gap in electromagnetic spectrum called “THz gap” (Fig. 9.1), due to the unavailability of stable femtosecond lasers and efficient THz emitters and detectors [1–8]. Now that these problems have been solved, the THz spectroscopy is maturing rapidly. In spectroscopy terms, it has closed the gap between *optical* high-frequency side and *electronic* low-frequency side of the spectrum [4].

Among the main features of THz radiation, it is reflected by metals and strongly absorbed by water and other biomolecules [1–5, 9]. Owing to the low energy of THz photon, it does not induce ionization, and, hence, T-ray imaging and scanning has emerged as the most viable option to replace biologically hazardous X-ray scanning at the airports and other public places [1–6]. The THz imaging has also proved to be a highly versatile technique for materials science, semiconductor industry, human tissue scanning, and related biomedical applications [9–24]. The advent of terahertz science is marked by the generation of electromagnetic THz radiation using ultrafast femtosecond lasers in the early 1990s. This triggered the onset of tabletop THz spectroscopic systems. The importance of femtosecond lasers is apparent in their role of ultrafast excitations of charge carriers or dipoles in THz sources. The absorption of such ultrafast pulse induces the excitations and relaxation processes in time scale of picoseconds, thus resulting in electromagnetic emission in the THz frequency region. Despite the limitation of intensity and power of such tabletop systems, their rise in diverse areas of science and materials characterization has been phenomenal [1–9, 25–54]. The THz technology has become indispensable for contemporary scientific advancements (for review, see Ref [1–9]).

The applications of THz technology in all pure and applied sciences have made it one of the most rapidly growing fields in contemporary research [1–6]. Initially, THz science was mainly restricted to study electronic processes and low-energy dynamics in semiconductors [1]. It was only recently that its potential was realized not only in other fields of physics but also in other disciplines of science such as biology and chemistry [7]. The techniques that have been developed are THz emission spectroscopy, THz-TDS, THz imaging in time-domain spectroscopy mode, laser THz emission microscopy, THz tomography, and optical-pump/THz probe time-domain spectroscopy, etc. [1–54]. These techniques are being used

to develop technology for human scanning for security purposes at the airports, medical sciences, chemical and biological species identification, data processing, decoding the heritage sites, photo-functionality of magnetic and electronic materials, monitoring of electronic intersubband processes, manipulating metamaterials, carrier dynamics in electronic materials, dielectrics, quantum wells, gases and liquids, etc. [1–9]. Recently developed laser THz emission microscopes have actually been put in industrial application for inspection of faults in semiconductor chips [1, 2, 55–58]. The list of possible applications is long and rapidly growing.

One of the major challenges in this area of technology is the quest and exploration of powerful and efficient THz sources and detectors and their applications for spectroscopic and imaging purposes. In this chapter, I will briefly review some important and useful techniques of THz generation and detection and THz technological applications, particularly in the context of correlated systems and functional materials.

## 9.2 Sources of THz Radiation

### 9.2.1 THz Emission via Ultrafast Modulation of Current Density

This is one of the easiest and most efficient ways of THz generation for several applications in contemporary technology. This exploits the classical Maxwell's equation of electromagnetic emission by the means of time-dependent modulation of current density as

$$E(r, t) = \frac{l_e}{4\pi\epsilon_0 c^2 r} \frac{\partial J(t)}{\partial t} \sin \theta \propto \frac{\partial J(t)}{\partial t} \quad (9.1)$$

where  $E(r, t)$  is the far-field THz electric field emitted by the ultrafast modulation of current density  $J$  measured at distance  $r$ . The  $l_e$  is the length of dipole antenna. The most important factor for this emission is ultrafast laser source with pulse energy greater than the band gap of the material.

### 9.2.2 THz Emission via Photoconductive Antenna Semiconductor

To realize the THz emission, an electric field-biased semiconductor is illuminated by femtosecond laser pulses with photon energy greater than the band gap. The electrons are excited to the conduction band and accelerated by the applied DC electric field. The lifetime of the accelerated carriers depends on the time duration

of the pulse. It must be noted that ultrafast stimulus provided is of the order of  $\sim 100$  femtosecond and induces a transient current density ( $J$ ) which modulates in the time scale of few picoseconds and emits electromagnetic radiation in the frequency range of few THz.

While almost every semiconductor emits THz radiation as per Eq. (9.1), the most important aspects of the emitted radiation are the spectral bandwidth and the power and efficiency of the emitted pulse. Large mobility and short lifetime of the photoexcited carriers are two essential attributes of the efficient THz generation. Among various semiconductors, the GaAs films deposited on silicon are the most suitable for THz emission. Further optimization showed that the films grown by molecular beam epitaxy at low temperature, called low-temperature-grown GaAs (LT-GaAs) films, exhibit the maximum efficiency. The LT-GaAs grown by molecular beam epitaxy at low temperatures of about  $250^{\circ}\text{C}$  results in the formation of As clusters. The resulting effects are reduced dark current, a large increase in the carrier mobility, and reduced carrier lifetime. This enhances the resistivity which results in the enhancement of power and large spectral bandwidth of THz emission from LT-GaAs vis-à-vis ordinary GaAs. All are desirable characteristics for spectroscopic applications of THz radiation [1–8].

Another important parameter that controls the bandwidth and the power of THz emission in LT-GaAs is the antenna that is formed on the film for DC bias. As shown in Fig. 9.2, various known structures are parallel line planar-type, dipole-type, bow-tie, interdigitated antenna, etc. [2].

THz emitter system based on the photoconductive (PC) antenna behaves as a Hertzian dipole. PC gap is pumped with femtosecond pulses with photon energy larger than the band gap of the semiconductor. The photo-induced free electrons are generated in the conduction band. The carriers are then accelerated in phase by the bias field and decay with a time constant determined by the carrier lifetime, resulting in a pulsed photocurrent. Current modulation occurs in the subpicosecond regime

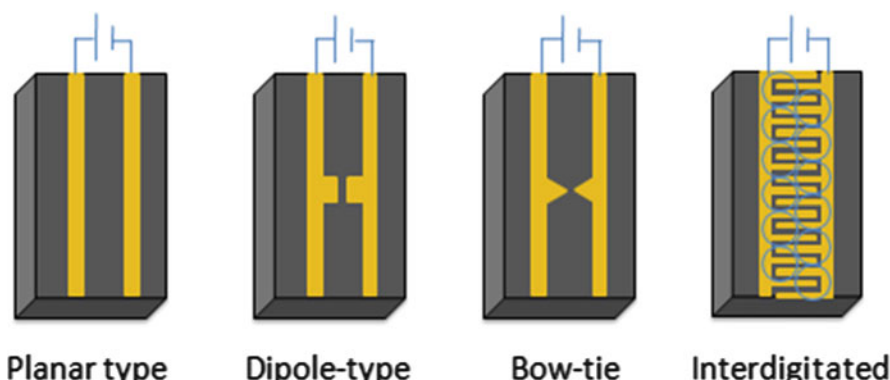


**Fig. 9.2** Illustration of parallel line planar-type, dipole-type, bow-tie, and interdigitated antenna for THz emission

that emits a subpicosecond electromagnetic transient, i.e., THz pulse. For Hertzian dipole antenna in free space, the radiated electric field  $E(r, t)$  at a distance  $r$  and time  $t$  is given by Eq. (9.1) explained in the earlier section.

### 9.2.3 THz Emission via Photo-Dember Effect

Photo-Dember effect [29] is a result of difference in diffusion current due to electrons and holes. Diffusion current due to electrons ( $J_n$ ) and holes ( $J_h$ ) is given by

$$J_n \sim -eD_e \frac{\partial n}{\partial x}, J_h \sim -eD_h \frac{\partial h}{\partial x} \quad (9.2)$$

where  $n$  and  $h$  are photo-created electrons and hole, respectively.  $D_e$  and  $D_h$  are electron and hole diffusion current, respectively. Dember current is given by  $J_D = J_n + J_h$ . The THz emission due to Dember current is proportional to the difference in mobility and temperature of electrons and holes and gradient in current density. Important properties for THz emission by photo-Dember effect are as follows: (1) low dark current enhances the photo-Dember effect; (2) the emitted THz field amplitude due to photo-Dember effect varies linearly with the laser photo-intensity, i.e.,  $E_{THz} \propto V_D \propto I$ , for lower intensity and varies logarithmically in a high-intensity regime, i.e.,  $E_{THz} \propto V_D \propto \ln(I)$ ; and (3) the  $V_D$ , if large enough, does not depend strongly on the electron–hole mobility ratio. The semiconductors emitting efficient THz radiation via photo-Dember effect are n-type InSb and p-type InSb. In both these cases, the emitted THz radiation has the same polarity. An illustration of photo-Dember effect is given in Fig. 9.3a.

### 9.2.4 Surface Depletion Layer

This originates because of the pinning of the Fermi level of the surface states which lie within the band gap [29]. The pinning of the Fermi level results in the band bending at the surface with the formation of a depletion region. The difference in energy level on the surface and in the bulk results in the formation of an in-built electric field. This in-built electric field accelerates the photo-generated carriers in the same way as the applied electric field accelerates the carriers in antenna-based LT-GaAs THz emission. Among various systems, n-type and p-type InP semiconductors are dominant sources of THz emission due to surface depletion layer formation. The in-built electric field in p-type region will drive the carriers in the opposite direction compared to that in n-type systems. This will result in THz emission of opposite polarity in these two types of semiconductors. This is contrary to the THz emission due to photo-Dember effect in which emission from

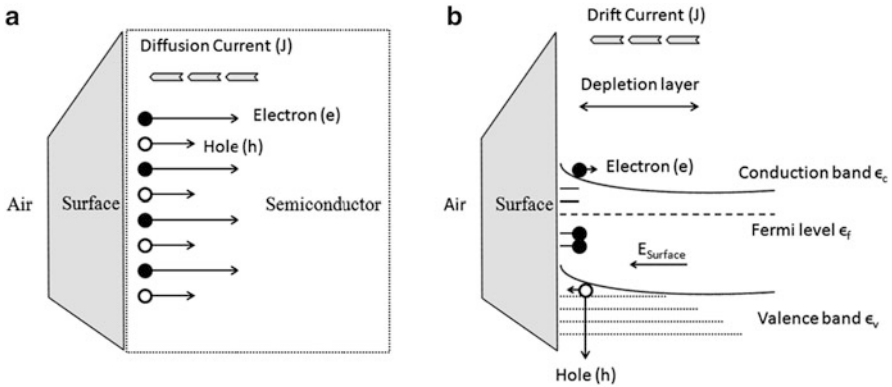


**Fig. 9.3** (a) Mechanism of photo-Dember effect: the difference in diffusion current of electrons and holes results in transient current and, hence, the THz emission. (b) Band bending at the surface and formation of depletion region. The difference in energy level on surface and in the bulk results in the formation of in-built electric field. This in-built electric field accelerates the photo-generated carriers and emits the THz emission

both p-type and n-type semiconductors is of the same polarity. An illustration of transient current resulting in THz by this mechanism is given in Fig. 9.3b.

### 9.2.5 THz Generation via Nonlinear Processes

Various nonlinear processes for THz generation include optical rectification, difference frequency generation, and optical parametric amplification [1, 2, 6, 7]. Overall, these techniques exploit the principle of difference frequency generation which can be explained by considering two optical fields oscillating at frequencies  $E_1 = E_0 \cos \omega_1 t$  and  $E_2 = E_0 \cos \omega_2 t$ . When these fields interact with a material, a DC polarization is developed in the material by means of a second-order nonlinear electric susceptibility ( $\chi_2$ ) of the material. A DC second-order nonlinear polarization ( $P_{nl}$ ) may then be written as

$$P_{nl} = \chi_2 \left( \frac{E_0}{2} \right) [\cos(\omega_1 - \omega_2)t + \cos(\omega_1 + \omega_2)t] \quad (9.3)$$

In this equation, the nonlinear polarization is proportional to the difference frequency  $\omega_1 - \omega_2$  and the sum frequency  $\omega_1 + \omega_2$ . While the sum frequency is not relevant in the present case, the difference frequency only accounts for the THz generation and this technique is called optical rectification. Based on this principle, the THz generation using a tabletop femtosecond laser may be understood as the follows. The femtosecond laser pulse contains various frequency components in its spectrum. These frequency components by the means of optical rectification

$(\omega_1 - \omega_2)$  generate a THz pulse with spectral bandwidth depending on the frequency components of the femtosecond laser pulse or, in other words, on the duration of the femtosecond laser pulse.

### 9.2.5.1 Difference Frequency Generation

It is a second-order nonlinear optical process and special case of optical rectification. While in optical rectification, there are many frequency components and a combination of difference in these components generates a spectrum of THz beam, whereas the difference frequency generation, as such, is used for the generation of a single frequency THz wave using two single well-defined frequencies. In both the optical rectification and difference frequency generation, a non-centrosymmetric crystal which has predominant nonlinear optical effects is the fundamental requisite. The optical beams of two narrowband laser beams with slightly different frequencies copropagate and are linearly polarized in the same direction. Their interference results in a beat, which oscillates with the difference frequency or beat frequency ( $(\omega_T = \omega_1 - \omega_2, \omega_1 > \omega_2)$ ) and, hence, the generation of THz beam.

### 9.2.5.2 Optical Parametric Amplification (OPA)

Optical parametric amplification is also a second-order nonlinear optical process. In this technique, a photon of the laser pulse ( $\omega_p$ ) is converted into two photons called idler and THz photons ( $\omega_i$  and  $\omega_T$ , respectively) such that  $\omega_p = \omega_i + \omega_T$ . In this case, it is imperative that the phase-matching condition  $k_p = k_i + k_T$  is satisfied [2(b)]. Once this momentum ( $k$ ) conservation of these pump, idler, and THz wave vectors is achieved, both the idler and THz waves are amplified and a reasonably good THz output beam is achieved. The LiNbO<sub>3</sub> is the most suitable material to realize THz by OPA. It generates tunable narrowband THz waves in LiNbO<sub>3</sub> crystals. Recently, a more efficient technique has been devised, in which tilted front laser pulses were illuminated on LiNbO<sub>3</sub> to achieve high-power (up to 1 MV/cm) THz pulses [28]. Various materials which are efficient in THz emission via nonlinear technique are ZnTe, GaP, GaAs, GaSe, CdTe, LiNbO<sub>3</sub>, and organic crystal DAST (diethylaminosulfur trifluoride) and its derivatives.

Continuous THz wave can be generated by various means such as photo-mixing, difference frequency generation, parametric amplification, etc. A disadvantage of THz emission from these sources is their low average power output. In this regard, the molecular lasers, THz quantum cascade lasers (THz-QCL), and free electron lasers (FEL) have a large power output in the range of several hundred of micro- to milliwatt. Among these sources having large THz power output, the molecular laser is bulky in size and FEL is the beamline source. The THz-QCL, on the other hand, is a compact source with a temperature-dependent power output. It is in a stage of early development and is expected to be useful for imaging purposes. An exhaustive

review on these sources is given in the book titled *Principles of THz Science* (see Ref [2]). However, a brief introduction of THz-QCL is given below.

### 9.2.6 THz Quantum Cascade Lasers

A quantum cascade laser (QCL) is a semiconductor laser different from conventional lasers. It is a semiconductor heterostructure laser with superlattices of alternating layers of dissimilar semiconductors. The emission of THz radiation is realized when an applied external bias induces transitions between two quasi-two-dimensional states in the superlattice [27, 34].

The operation of QCLs essentially involves two processes, namely, (i) intersubband transitions and (ii) the cascade effect. An intersubband transition involves only electrons: it is therefore called a unipolar process. This is unlike the process of radiative recombination of electron and hole pairs in diode semiconductor lasers. The same electron which undergoes an intersubband transition in one period of the superlattice gets injected into the next period and subject to another intersubband transition. This process repeats until the electron reaches the end of the superlattice. This is called “cascading” as it describes the repetitive/cascading nature of the multiple intersubband transitions. The cascading process wins over the conventional limitation of quantum efficiency because this technique realizes the output of multiple photons by a single electron.

A period comprises an injector, an injection barrier, and an active region. Intersubband transitions in the active region, comprising multiple quantum wells, result in electromagnetic emission. For the sake of simplicity of understanding, the lasing action is a three-level QCL system and is illustrated in Fig. 9.4.

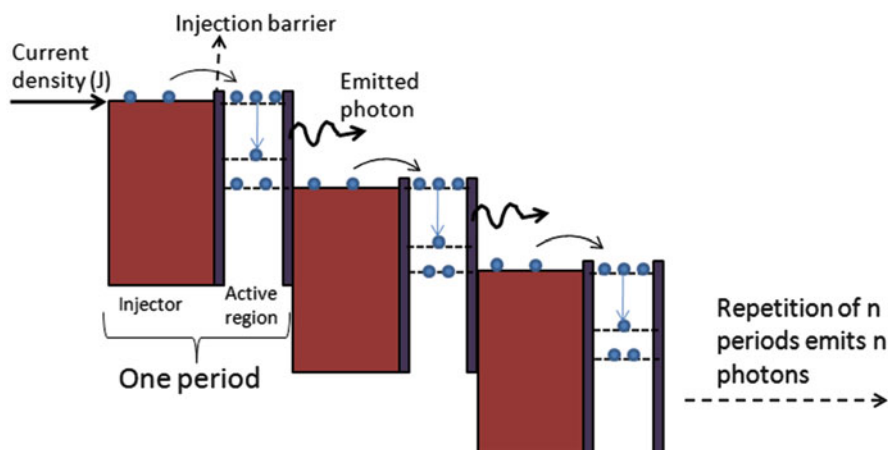


**Fig. 9.4** An illustration of the mechanism of cascading and lasing in a superlattice structure quantum cascade laser (QCL)

This superlattice structure is biased by a static electric field. A population inversion is created between levels 3 and 2. For cascading, the bias voltage is adjusted so that level 1 of an active region is aligned with level 3 of the next period. Then, the used electrons in one active region are injected into the next period for the same action [2(b), 27, 34]. As mentioned earlier, the advantage of THz-QCL is the large power of THz beam which cannot be achieved by other tabletop techniques. A very high power up to 10 mW at liquid nitrogen temperature and up to 200 mW at liquid helium (LHe) temperature has been obtained.

THz-QCL has also some inherent limitations. The energy of a 1 THz photon of about 4.1 meV is so that the thermal excitations can easily disturb the electron configuration and, hence, the population inversion required for lasing in a QCL. The output power of QCLs is very low at room temperature. However, it increases with decreasing temperature. As mentioned above, a power of about 200 mW can be obtained at liquid helium temperature of 4 K. At present, the highest operating temperature of THz QCLs is in the vicinity of 180 K. Another difficulty is limitations to confine laser modes in a small volume due to the long wavelength of THz wave. This mode confinement is important because stimulated emission efficiency is proportional to the light intensity in the gain medium. A review of THz QCLs may be found in Refs. [2(b), 27, 34].

Except p-type Ge lasers, THz QCLs are currently the only solid-state source whose coherent output power exceeds 10 mW above 1 THz. A power of up to  $\sim$ 200 mW at LHe temperature (4 K) and a frequency in the range of 1.5–4.5 THz are the two achievements of THz QCLs. However, for the simplicity of applications, it is required that efficient THz QCLs operating at room temperature are designed. In a recent development, the THz-QCL based on difference frequency generation has also been realized [2(b)].

## 9.3 Detection of THz Transients

THz detection can be done in two ways, one in which only the intensity is obtained and the other methodology provides the information about both the amplitude and phase in the time domain. Here, a brief discussion of only second kind will be given as this technique is widely used for THz detection in spectroscopic and imaging techniques.

### 9.3.1 *Detection of THz Radiation Using Photoconductive Antenna*

The emitted far-field THz radiation by the means of transient photocurrent is focused on to the detector with the help of either parabolic mirrors or THz transparent Teflon and TPX lenses. The other side of detector, which is also a

dipole-type LT-GaAs antenna, is illuminated by the femtosecond laser pulse which is synchronized with the THz pulse with the help of linear translation stage equipped with a stepper motor. The femtosecond laser pulses excite the carriers above the band gap of GaAs. These carriers are then accelerated by the electric field of THz wave which is synchronized with femtosecond pulses onto the detector. The magnitude and polarity of the photocurrent is directly proportional to the THz electric field. As the magnitude of the photocurrent is very low, a preamplifier amplifies this current by about one order of magnitude which is then detected by lock-in amplification technique.

The entire waveform is determined by a weak optical probe which optomechanically gates the THz pulse by a motorized time-delay unit. In the absence of a bias field, a THz field induces a current in the photoconductive gap when an optical probe pulse injects photocarriers. The induced photocurrent is proportional to the THz field amplitude. The THz pulse shape is mapped out in the time domain by measuring the photocurrent while varying the time delay between the THz pulse and the optical probe. Sensing with a PC antenna also measures broadband THz pulses in the time domain.

### ***9.3.2 Detection Using Electro-optic Sampling***

This technique uses the Pockels effect and measures the actual electric field of THz pulses in the time domain [7, 8]. Generally, the same nonlinear crystal such as ZnTe which is used for the THz emission by optical rectification is used for the THz detection using electro-optic sampling. The emitted THz radiation is focused on the detecting nonlinear crystal with the help of appropriate optics. The THz field induces birefringence in the ZnTe crystal, which is proportional to the amplitude of free propagating THz field. Simultaneously, the probe femtosecond pulse laser beam is also focused on the ZnTe in which birefringence is induced by the THz beam. This birefringence will split the pump beam into two beams which will be focused onto the balanced diodes. The current generated in these diodes will be amplified and then fed into the two channels of a lock-in amplifier. The difference in the current of two diodes is directly proportional to the THz field inducing birefringence. Here, the birefringence and the photocurrent are sensitive to both the amplitude and the phase. Hence, the THz waveform can be recorded in the time domain. The mechanism of THz detection by electro-optic sampling is given in Fig. 9.5.

A combined setup of broadband THz generation and detection measures changes in both the amplitude and phase of THz pulses induced by a sample, which provides enough information to determine the absorption and dispersion of the sample. This technique is named THz time-domain spectroscopy (THz-TDS).

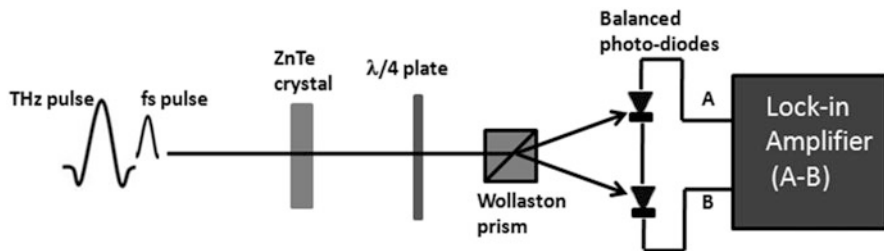


**Fig. 9.5** An illustration of the mechanism of THz detection by the electro-optic sampling

## 9.4 Applications of THz Radiation-Based Spectroscopic and Imaging Techniques

THz spectroscopy has already demonstrated a variety of applications in diverse aspects of science and technology. In chemical and pharmaceutical sciences, THz spectroscopy has been highly useful in identifying different species, their content, and their vibrational properties. In biology, the THz applications include distinction between healthy and cancerous tissues [12, 14–24]. Other security applications include THz spectroscopic identification of dangerous arms and RDX and illicit drugs [11, 12].

In pure sciences particularly physics, this is proving highly effective in unveiling several new scientific phenomena, such as THz photo-functionality showing the ultrafast dynamics of electric/magnetic fields in a material and time-domain spectroscopy probing the low-energy dynamics such as phonon modes, charge-density waves, spin waves, etc., in oxide materials [25, 26, 42–46]. Similarly, the research in THz science is expanding in chemical and biological sciences [12–24].

THz spectroscopy has also been highly effective to devise industrial applications of some popular nano-materials [59]. The far-field THz-TDS has recently demonstrated carbon nanotubes as highly efficient polarizer. Far-field THz emission spectroscopy also holds promise to tune the conductance of fullerenes for fabricating the ultrafast switches. On the other hand, the near-field THz spectroscopy has efficiently scanned the mobile currents in semiconductor nano-devices [60].

### 9.4.1 THz Imaging

Recently, one of the major thrusts in THz technology is the development of THz imaging techniques using the principle of THz time-domain and THz emission spectroscopy [61–70]. This technique is also useful for a wide range of applications comprising scanning of biological tissues, chemical substances (for instance, RDX), scanning currents in superconductors, etc. But the applications of THz emission-based imaging are mainly limited to materials such as semiconductors, oxide

materials having high-resistivity states, superconductors, etc. [1, 38, 52]. Though applications of these THz imaging cover all areas of science, the biggest challenge is to achieve nanometric resolution of these microscopes. Once this is achieved, THz imaging microscopes will not only be able to compete with but should be able to replace existing microscopic techniques.

THz science and technology holds the maximum potential probably in physical science; however, much is yet to be realized. A vast majority of scientist work on physics and related applications of materials. While reviews of applications of THz technology in various spheres can be found in several books and review articles, detailed reviews of the applications in condensed matter systems and materials science are not so common. Major THz techniques being used in condensed matter physics are THz emission spectroscopy, laser THz emission microscopy, THz time-domain spectroscopy, optical-pump/THz probe spectroscopy, etc. Though applications of these techniques in superconductors and colossal magnetoresistance materials were presented in the book *Terahertz Optoelectronics* edited by K Sakai [2], an update and extension of such applications in other class of exotic materials is required. In view of this, I am going to review some existing data from literatures and discuss further the scope of THz technology in strongly correlated systems.

#### **9.4.2 THz Technology for Condensed Matter Systems and Materials Science**

THz spectroscopy being a noncontact and noninvasive technique can probe a variety of intrinsic properties of the materials and is free from any experimental artifacts. It not only enhances our scientific knowledge of materials but also brings unseen and unexpected outcomes. In strongly correlated electron systems, the electron–electron and the electron–phonon interactions play a dominant role in defining the physical properties. Transition metal oxides present typical examples such as high-temperature superconductors (HTSC), colossal magnetoresistance (CMR) manganites, ferroelectrics, and multiferroics [71–94]. While the field of multiferroics is quite new [71–78], the research in HTSC and CMR materials has reached to some acceptable maturity.

THz spectroscopy and imaging explore a wide range of ultrafast and low-energy electronic process in the time scale of few picoseconds [41, 57]. The THz-TDS probes so far elusive low-lying excitations and creates a clear overall picture of electronic properties of materials. Materials under the purview of these studies mainly comprise superconductors, ferroelectrics, multiferroics, magnetoresistive/charge-ordered systems,  $V_2O_5$ , etc. It started with the pioneering work of Tonouchi et al. [2(a)] who realized THz emission from high-temperature superconductors by breaking of supercurrents and subsequently visualizing the vortex state by imaging based on THz emission. Another simultaneous pioneering work by Kida and Tonouchi [2(c)] was devoted to understanding low-energy dynamics in metallic manganites  $La_{0.7}Ca_{0.3}MnO_3$  and charge-ordered manganite  $Pr_{0.7}Ca_{0.3}MnO_3$ . In the

latter system, for the first time, the emergence of collective excitations of multidimensional charge-density waves (CDWs) was experimentally demonstrated by the application of THz-TDS. In a more sophisticated experiment of optical-pump/THz probe TDS, Averitt et al. were able to achieve some complex electronic and magnetic phases which were thermally inaccessible in  $\text{La}_{0.7}(\text{Ca}/\text{Sr})_{0.3}\text{MnO}_3$  metallic manganites [90]. The THz-TDS has been able to detect mostly elusive soft phonon mode in ferroelectric  $\text{SrTiO}_3$  [41]. In yet another achievement of this technique, THz emission from multifunctional  $\text{BiFeO}_3$  by both the means of ultrafast modulation of spontaneous polarization and the difference frequency generation has demonstrated application potential by ultrafast optical manipulation in such systems [40, 49–53]. In different kinds of multifunctional systems as  $\text{RMnO}_3$  ( $R = \text{Tb}, \text{Yb}, \text{Y-Eu}$ , etc.) in which spiral/conical magnetic structure induces electrical polarization, low-energy excitations such as magnons/electro-magnons were discovered by the means of THz-TDS. Recently, applications of high-power THz-TDS in  $\text{SrTiO}_3$  could elucidate the emergence of ferroelectricity in this system.

As clear from the brief review given above, the THz-TDS has still not realized the scope of its applications in a wide variety of materials. Also, the applications of THz-TDS are most effective in single crystals of the materials. A widely encountered problem by various scientists is the difficulty in either growth or obtaining large enough size of single crystal of materials which are interesting from the perspective of THz-TDS investigations. This problem can be partially sorted out by performing such studies on epitaxial thin films. This not only provides the specimens of nearly the same quality as the single crystals but also offers the flexibility of easily choosing a crystallographic orientation of the desired interest in those systems which exhibit orientational anisotropy for certain properties. Also, by growing epitaxial films of appropriate thickness, it offers added advantage to perform THz-TDS in transmission mode on metallic system. The same cannot be achieved in single crystals as the penetration depth of the THz waves in metallic systems is quite low compared to the lowest achievable thickness of single-crystal specimens. This leaves the only option of THz-TDS in reflection mode which is a relatively difficult experiment to perform. Owing to these reasons, in our recent work, we showed that THz-TDS in epitaxial thin films of correlated and functional materials is an interesting area for exploring new physics of low-energy dynamics. We will briefly introduce the technique to perform THz-TDS studies on epitaxial thin films, the mechanism to calculate the complex refractive index and extract THz dynamic conductivity and dielectric constant. Different types of low-energy dynamics and collective excitations in the epitaxial thin films of selected half-doped and charge-ordered manganites systems have also been discussed.

#### 9.4.3 Terahertz Time-Domain Spectroscopic (THz-TDS) Setup

A schematic diagram of the THz-TDS setup is shown in Fig. 9.6. The titanium-sapphire laser is  $\approx 100$  femtosecond with a repetition rate of 76 MHz (mechanically

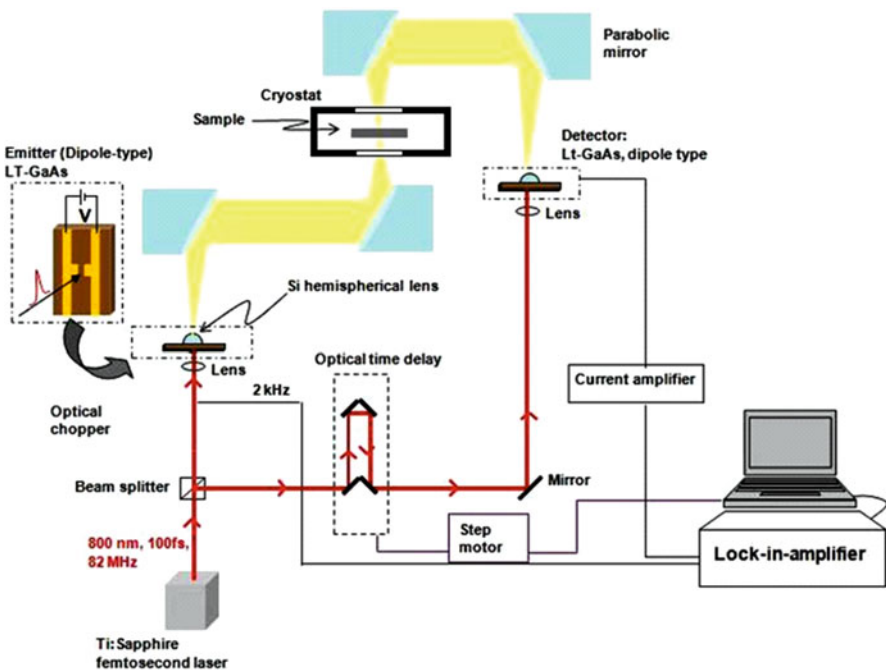


**Fig. 9.6** A THz time-domain spectroscopic system constructed using LT-GaAs dipole-type photoconductive switch as emitter and detector. For the sake of simplicity, only key components of the setup are shown. A beam of femtosecond laser pulses is split into two using a beam splitter. One part of the beam is focused in the gap of dipole-type LT-GaAs photoconductive emitter. Emitted THz radiation is collimated and focused with the help of off-axis parabolic mirror onto the backside of the LT-GaAs detector. On the other side of detector, the second part of the split femtosecond laser beam is focused which excites the carriers, which are accelerated by the THz electric field. This photocurrent is then amplified and detected using a lock-in amplifier. Here, it may be noted that the measured photocurrent at the detector is directly proportional to the emitted THz electric field

chopped at few kilohertz) with photoconductive antenna (PCA) for the generation of the THz waves. The generated THz pulse is focused by using a pair of off-axis parabolic mirrors on to the sample housed in the cryostat for temperature-dependent measurements from 320 to 20 K. The transmitted THz beam and the optical probe beam co-propagate (by suitably adjusting the delay) and focused onto a PCA. The optical femtosecond laser beam creates the photocarriers by the band gap excitations in the dipole-type PCA. The electric field of the THz beam focused on the PCA accelerates these carriers to give rise to a photo-current. This photo-current, which is directly proportional to THz electric field, is detected using a lock-in technique. Output signal from lock-in amplifier versus time-delay scanning of the probe beam reveals the THz pulse waveform (Fig. 9.5).

#### 9.4.4 THz Emission Spectroscopy for Ultrafast Optical Functionality

THz emission from materials depicts their optical functionalities, which has direct implications for cutting-edge technological applications. Some materials of contemporary technology relevance are multiferroics, ferroelectrics, CMR materials, spintronic materials, nano-materials, oxide solar cells, etc. These systems either are relevant to data storage industry or possess properties important for energy storage. The realization of scientific and technical potential of the ultrafast photo-control of systems proposed here will render THz spectroscopic applications on the remaining range of materials.

Strong electron–phonon and spin–phonon couplings in CMR manganites are indicative of several low-energy excitations (in the energy range of 1–30 meV). Reports appeared on the existence of both the charge-density waves (CDWs) in charge-ordered (CO) systems such as in half-doped and some electron-doped series of  $\text{La}_{1-x}\text{Ca}_x\text{MnO}_3$  compounds [84–86]. This has sparked interest in probing the low-lying excitations in manganites. It may be noted that the THz-TDS is the most sensitive technique to probe excitations in this low-energy region. However, the implementation of THz-TDS in various correlated systems is of considerable interest. For some simple yet useful examples, I will discuss some of our recent results of THz spectroscopic studies on charge-ordered manganites in the following section.

Epitaxial thin films of charge-ordered  $\text{Pr}_{0.5}\text{Sr}_{0.5}\text{MnO}$  (PSMO) and  $\text{Nd}_{0.5}\text{Sr}_{0.5}\text{MnO}$  (NSMO) were grown on  $(\text{LaAlO}_3)_{0.3}(\text{Sr}_2\text{AlTaO}_6)_{0.7}$  [LSAT] (100), (110), and (111) single-crystal substrates while  $\text{Eu}_{0.5}\text{Sr}_{0.5}\text{MnO}_3$  (ESMO) were grown along LSAT (100) orientation using pulsed laser deposition technique. Measurements of temperature-dependent (40–320 K) THz-TDS on all the thin films were performed by using PCA (GaAS) as THz emitter and electro-optic sample (ZnTe) was used for detecting THz wave in THz time-domain spectrometer. THz wave was focused onto the sample housed in a cryostat using a pair of off-axis parabolic mirrors (Fig. 9.4). The frequency dependence of conductivity and dielectric constant in the energy range of  $\sim 1\text{--}6$  meV were extracted from the THz-TDS data using Fresnel's equations (without resorting to Kramer–Kronig analysis) as explained below.

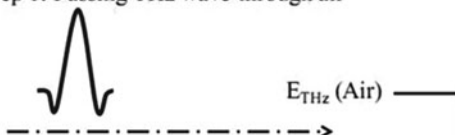
#### 9.4.5 Extraction of THz Optical Conductivity of Thin Films

Common optical spectroscopic techniques generally measure the intensity of light at specific frequencies, whereas THz-TDS technique directly measures the THz wave's temporal electric field. A schematic of THz time-domain spectroscopic studies of thin films in transmission mode is depicted in Fig. 9.6. It consists of the following steps: (1) THz wave is initially passed through the free space through the aperture size of 6 mm inside the cryostat and its temporal waveform is recorded;

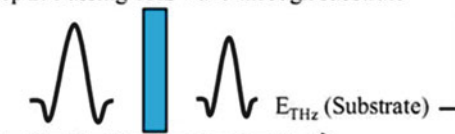
(2) now a blank substrate on which film which is deposited is mounted on aperture, THz wave is passed from the substrate, and the temporal waveform is recorded; (3) using Fresnel's equations, the complex refractive index of the substrate is calculated; (4) substrate mounted onto the aperture is replaced by the thin film + substrate, THz wave is passed through the film, and its temporal waveform is recorded; (5) now all the time-domain information is converted to frequency domain by the means of fast Fourier transformation; and (6) by solving Fresnel's equations for a bilayer systems as thin film + substrate and using the complex refractive index of the substrate, the complex refractive index of the film is calculated. Finally, having the knowledge of the film and substrate thickness, final desired quantities, i.e., THz optical conductivity and dielectric constant, are extracted. These calculations are processed as follows. Fourier transformations of this time-domain data (temporal THz waveform) give the amplitude and phase of the THz wave pulse. The ratio of the Fourier transforms of the data recorded with substrate (used as reference) and then with substrate + thin film (Fig. 9.7) yields the complex refractive index of the thin film in the frequency domain, and complex refractive index of the thin film is given as  $\tilde{n}(\omega) = n(\omega) - i\kappa(\omega)$  from where we can calculate the complex dielectric constant  $\tilde{\epsilon}(\omega) = \epsilon_1(\omega) - i\epsilon_2(\omega)$  and complex conductivity  $\tilde{\sigma}(\omega) = \sigma_1(\omega) - i\sigma_2(\omega)$  using the relations  $\epsilon_1(\omega) = n(\omega)^2 - \kappa(\omega)^2$ ,  $\epsilon_2(\omega) = 2n(\omega)\kappa(\omega)$ ,  $\sigma_1(\omega) = \epsilon_0\omega\epsilon_2(\omega)$ , and  $\sigma_2(\omega) = \epsilon_0\omega[\epsilon_\infty - \epsilon_1(\omega)]$  where  $\epsilon_\infty$  is dielectric constant for the bound electrons and  $\epsilon_0$  is the permittivity of vacuum.

Frequency (or photon energy)-dependent THz optical conductivity ( $\sigma$ ) of NSMO and ESMO films at 80 K were obtained by solving Fresnel's equations without resorting to Kramer-Kronig analysis (Fig. 9.8). We observed a finite peak-like

#### Step 1: Passing THz wave through air



#### Step 2: Passing THz wave through substrate



#### Step 3: Passing THz wave through substrate + thin-film

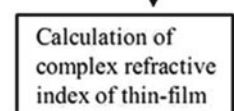
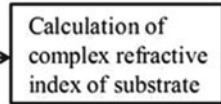
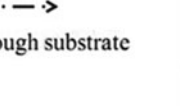
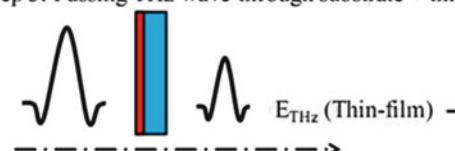
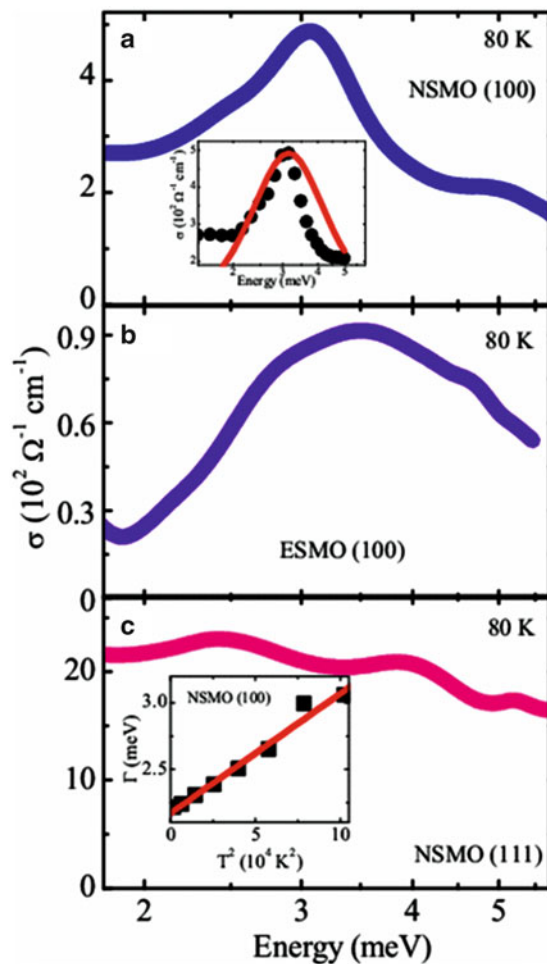


**Fig. 9.7** A schematic for extraction of complex refractive index for the thin films

**Fig. 9.8** Optical conductivity ( $\sigma$ ) as a function of photon energy at 80 K for (a) NSMO (100), (b) ESMO (100), and (c) NSMO (111). Inset shows conductivity fit at 80 K for NSMO (100)



structure in  $\sigma$  for PSMO (110), NSMO (100), and ESMO (100) films, and this peak-like feature gets totally submerged in the Drude continuum for NSMO (111) film (Fig. 9.8).

We also observed CDW collective excitations in stripe-type CO of PSMO manganite. Despite a large conductivity in CO state of this system, the CDW mode was extracted by selectively probing its anisotropic crystallographic axes. Of the (110) and (111) epitaxial PSMO films, both of which exhibit bulk-like CO, the CDW mode manifests only in (110) epitaxial film along a particular in-plane orientation. The CO (111) and phase-separated (100) films lack this CDW mode and exhibit Drude conductivity. The data are shown in Fig. 9.9. The observation of CDW along a selective axis was a consequence of the anisotropic nature of stripe CO. Overall, a variety of charge dynamics in PSMO governed by entirely different mechanisms highlights richness in low-energy phenomena induced by stripe-type CO such as in PSMO vis-à-vis those induced by CE-type CO such as in NSMO and ESMO.

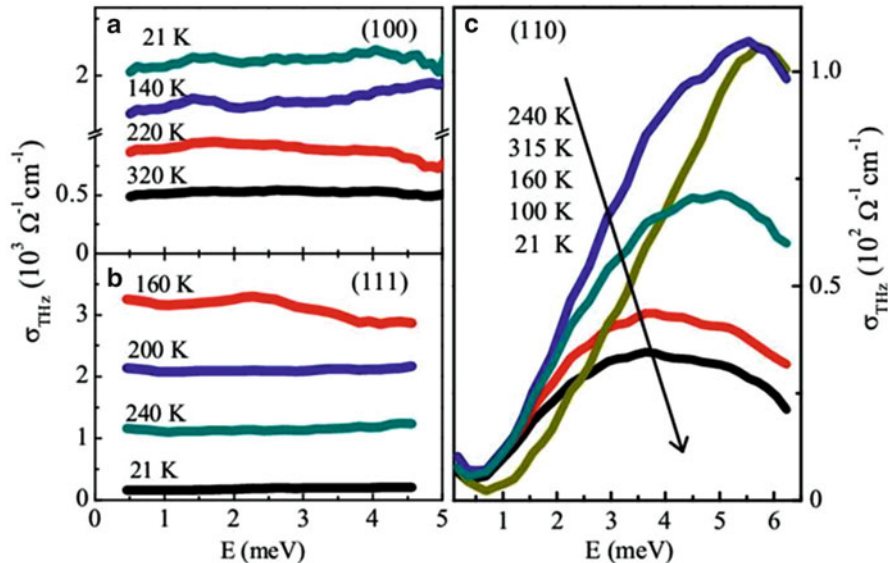


**Fig. 9.9** Optical conductivity ( $\sigma_{\text{THz}}$ ) as function of THz photon energy ( $E$ ) at various temperatures for (a) PSMO (100), (b) PSMO (111), and (c) PSMO (110) films

In the following points, we will discuss various aspects of this finite frequency peak structure for manganite (NSMO and ESMO) thin films and some salient features displayed by CDW:

1. The CDW peak generally emerges in the  $\sim$ meV region. The peak formation in  $\sigma$  at  $\sim$ 3 meV (0.9 THz) for NSMO (100) and ESMO (100) films indicates the existence of low-energy collective excitations presumably originating from the CDW. Moreover, we found a dip in dielectric constant ( $\epsilon$ ) (at  $\sim$ 3.5 meV) where  $\sigma$  shows a peak-like feature for NSMO (100) and ESMO (100) films, which can be assigned generally to the excitations due to CDW (data not shown here for the sake of brevity).
2. In simplest form, the pinning of CDW to the underlying lattice can be described by a simple harmonic oscillator response Eq. (9.4). The conductivity peak of NSMO (100) can be suitably fitted to Eq. (9.5) (inset Fig. 9.8a). The equation of motion for the CDW condensate [89] along the  $x$  axis can be given by

$$\frac{dx^2}{dt^2} + \frac{1}{\tau} + \omega_0^2 x = \frac{eE}{m^*} e^{i\omega t} \quad (9.4)$$

Then the real part of conductivity is

$$\sigma(\omega) = \frac{\sigma_0 \omega^2 / \tau^2}{(\omega_0^2 - \omega^2)^2 + \omega^2 / \tau^2} \quad (9.5)$$

Here,  $x$  denotes the center of mass coordinate of the collective mode,  $E$  is the applied field,  $\omega_0$  is average pinning frequency,  $\tau$  is the relaxation time, and  $m^*$  is the effective mass. Moreover, at the lower-frequency side, swelling of the peak structure for NSMO (100) and ESMO (100) is observed which is generally ascribed to the internal deformation of the CDW condensate. In contrast NSMO (111) does not seem to obey Eq. (9.5) and shows a Drude-like conductivity mainly owing to its larger ferromagnetic phase content.

3. The phenomenological relation for the scattering rate obeyed by some classic CDW systems like  $K_{0.3}MoO_3$  and  $(TaSe_4)_2I$  is as under:

$$\Gamma = A + BT^2 \quad (9.6)$$

where  $\Gamma = 1/\tau$  and  $A$  and  $B$  are constants and  $\Gamma$  should remain finite at  $T = 0$ . Here,  $T^2$  term arises from phason–phason scattering processes, and it was found that the ambient amplitude modes and acoustic phonons played only subsidiary roles in the scattering processes. Moreover, CDW systems obeying Eq. (9.6) rule out any thermal origin of finite frequency peak below single-particle excitation gap  $2\Delta$  because that results in an exponential dependence of the  $\Gamma$ , which was found for semiconductors like GaAs with lightly doped impurities of Si. NSMO (100) thin films were found to obey Eq. (9.6) (inset Fig. 9.8c).

Finally, we comment on the CDW peak in  $\sigma$  for ESMO (100) film ( $\sim 80\text{--}100 \Omega^{-1} \text{cm}^{-1}$ ) which is shallower and weak as compared to NSMO (100) film ( $\sim 450\text{--}550 \Omega^{-1} \text{cm}^{-1}$ ). ESMO (100) is a spin-glass system with spin-glass transition ( $T_{SG}$ )  $\sim 60$  K while NSMO (100) is a robust CO system with charge-ordering temperature ( $T_{CO}$ )  $\sim 240$  K. The peak in  $\sigma$  remained visible in the entire temperature regime from 40 to 300 K for both NSMO (100) and ESMO (100) thin films, and this may be assigned to local charge order (CO) fluctuations happening for both the systems. Moreover, CDW peak in  $\sigma$  for ESMO (100) is asymmetric in comparison to NSMO (100). This deformation of the CDW peak in ESMO (100) can be largely attributed to the size/quenched disorder due to cationic size mismatch between  $\text{Eu}^{3+}$  ( $\sim 1.12 \text{\AA}$ ) and  $\text{Sr}^{3+}$  ( $\sim 1.31 \text{\AA}$ ). The CDW peak in  $\sigma$  for ESMO (100) is 3–4 times lesser than that of NSMO (100), suggesting that ESMO (100) and NSMO (100) are a short- and long-range ordered systems with ( $q = 1/2$ ), respectively.

#### 9.4.6 THz Emission Spectroscopy

The experimental apparatus for THz emission spectroscopy is similar to that of apparatus for THz-TDS. There are two differences, namely, (1) in THz emission apparatus, only two parabolic mirrors are required as the THz beam is to be focused only onto the THz detector, and (2) the THz emitter is not the LT-GaAs but the system under investigation from which the THz emission is intended.

#### **9.4.7 THz Emission Spectroscopy of Multiferroic, Magnetic, and Electronic Materials**

The THz emission spectroscopy has immense potential for exploring both applied and fundamental aspect of correlated materials. THz emission from electronic materials takes place by ultrafast modulation of electric/magnetic field inside the material, while in non-centrosymmetric materials, the THz emission may occur as a result of optical rectification/difference frequency generation due to the nonlinear properties of the material. THz generation by various methods can be explained by the general Maxwell's wave (Eq. [7]) as

$$\Delta E(r, t) - \frac{1}{c^2} \frac{\partial^2 E(r, t)}{\partial t^2} = \frac{4\pi}{c} \frac{\partial^2 P(r, t)}{\partial t^2} + \frac{4\pi}{c} \frac{\partial J(r, t)}{\partial t}$$

In this relationship, THz emission can occur through a time-varying current density ( $J$ ) and/or modulation of polarization ( $P$ ). The former one emits THz radiation from the insulators, semiconductors, and superconductors via photo-induced time-varying current density. THz emission from CO manganites and high  $T_c$  superconductors are two such examples. Given the insulating/semiconducting state of the robust charge-ordered (CO) manganites, THz emission is a potential technique for the investigation of their less understood phenomena such as phase separation, phase transition under the external stimuli (photon in present case), photo-induced first-order transitions, etc. [81–83]. Emission from such compounds can be effected as per the second source terms ( $\partial J/\partial t$ ) in the aforementioned equation and the emitted THz radiation carries signatures of various physical properties of such materials and unveils interesting physical phenomena which cannot be probed using conventional techniques.

The second source, i.e., the polarization, can be decomposed as  $P = P_S + P_{NL}$ , which indicates that THz emission can be due to time-varying spontaneous polarization  $P_S$  (such as partial/complete depolarization) and/or optical rectification in nonlinear medium ( $P_{NL}$ ). While the latter is a widespread and well-established source of THz emission [2–6] such as emission via optical rectification and difference frequency generation from nonlinear crystals ZnTe, ZnS, DAST, etc. The latter source of emission due to spontaneous polarization,  $P_S$ , is unknown and can be potentially realized in multiferroic/ferroelectric materials [44, 50–52]. The THz emission due to  $P_S$  is of great importance as it is a direct means of probing the ultrafast polarization dynamics of ferroelectric memories, and its realization promises to provide understanding of the time scale at which the electric dipoles in the spontaneous polarized state are accessible for read or write operations. To utilize this aspect of THz science, we plan to ferroelectric/multiferroic systems having large  $P_S$ .

Multiferroic materials, defined by the coexistence of electric and magnetic orders in the same phase [71, 72], are the best suited materials for THz emission spectroscopy. Magnetoelectricity in multiferroics refers to the mutual control of

electric and magnetic orders [71]. THz emission from poled multiferroics can provide additional noncontact and nondestructive optical probe to retrieve the electrical/magnetic stored data in the following way. Using an ultrafast femtosecond laser pulse of energy, more than the band gap of the multiferroic will excite the carriers, resulting in transient depolarization of ferroelectric/magnetic order, followed by retrieval of ordered state. The emitted THz field will be directly proportional to the polarization/magnetization of the material. This not only explains the optical functionality of the materials, it also reflects the electron–phonon and spin–phonon coupling in the material. Multiferroics and ferroelectrics having non-centrosymmetric structure are also strong candidates for THz emission via difference frequency generation too.

#### 9.4.8 THz Emission from Multiferroic $\text{BiFeO}_3$

THz emission from multiferroic  $\text{BiFeO}_3$  (BFO) takes place on poled condition. The polarity of emitted THz radiation reverses on reversing the sign of poling electric field. Variations in the peak amplitude and the polarity of THz emission as a function of poling electric field spans a ferroelectric hysteresis loop. However, such hysteretic emission realizes only from (100) and (110) epitaxial films while (111) film behaves differently (Fig. 9.10). This crystallographic anisotropy in electromagnetic THz radiation from multiferroic BFO (100), (110), and (111) films suggests the ultrafast depolarization of ferroelectric order as a new mechanism of THz emission. This implies that the spontaneous polarization in ferroelectric materials can be manipulated in time scale of picoseconds, thus paving the way to ultrafast data storage devices based on nonvolatile ferroelectric memories.

Given the multiferroic character of BFO, apart from THz emission via ultrafast depolarization, one ought to consider the possibility of magnetic contribution too. However, magnetic origin of THz emission necessitates the presence of significantly large magnetic moment, such that the absorption of laser pulses results in ultrafast spin heating either close to or above the Curie temperature to effect net destruction of magnetic moment (demagnetization) [45]. Since BFO is antiferromagnetic and none of the (100), (110), and (111) films possess any ferromagnetic-like moment that can amount to THz emission by ultrafast demagnetization, hence, we rule out any contribution of magnetic origin to THz emission from BFO. However, it is obvious to compare the ultrafast polarization dynamics of ferroelectric BFO with already known spin dynamics of magnetic orders. In magnetic systems, the femtosecond excitation yields the desired knowledge of ultrafast dynamics of spin memory via demagnetization upon spin heating, spin reorientation, photomagnetization, etc. Different spectroscopic techniques fairly agree that femtosecond stimuli facilitate the manipulation of magnetic spin orders in about a picosecond [49]. We note that THz emission due to ultrafast depolarization (i.e.,  $E_{\text{ps}}$ ) is conceptually similar to emission due to ultrafast demagnetization of ferromagnetic order except that the nonthermal mechanism of the former is an advantage for its practical

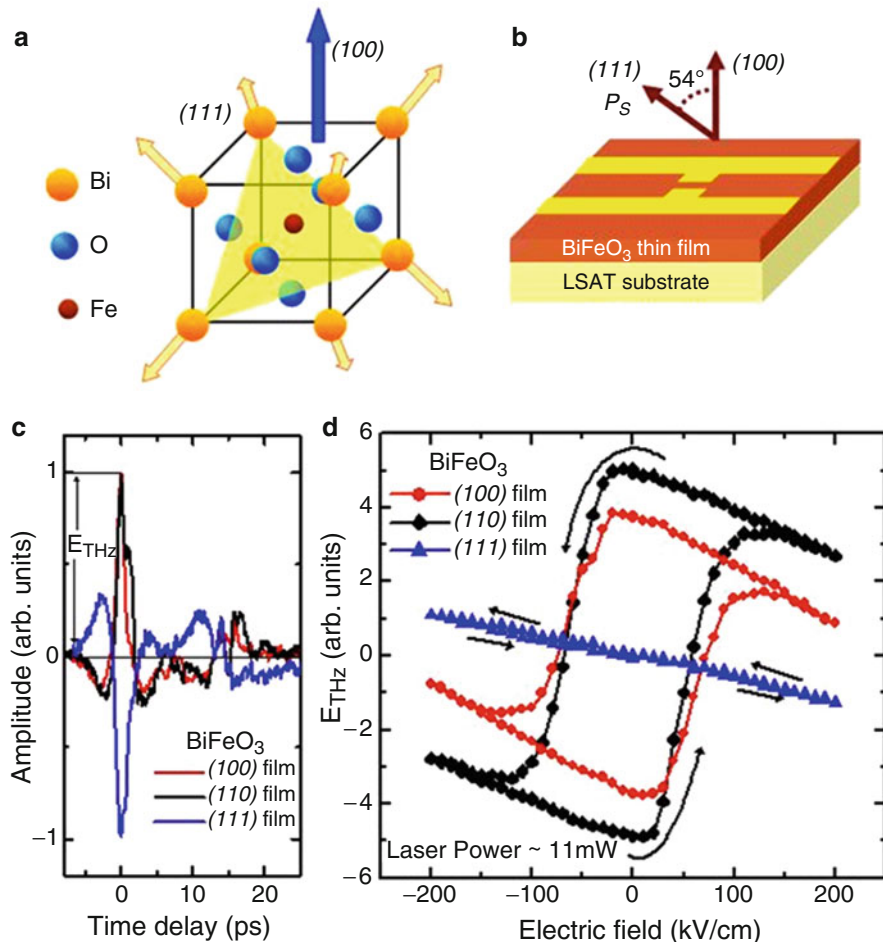
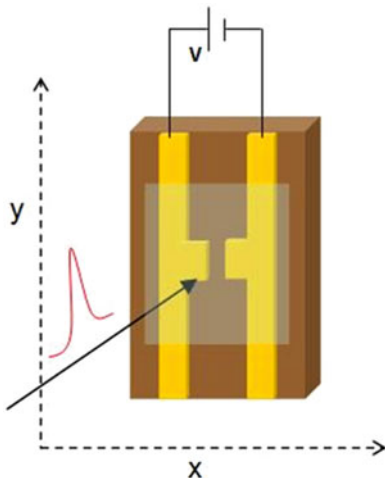


**Fig. 9.10** (a) Perovskite structure of  $\text{BiFeO}_3$  in which the possible orientations of  $\text{BiFeO}_3$  along the (111) directions are depicted. (b) The Au dipole antenna on the  $\text{BiFeO}_3/\text{LSAT}$  thin film heterostructure and relative direction of (111)-oriented polarization in (100)-oriented film on the LSAT (100) substrate. (c) THz time-domain waveforms for all of the (100), (110), and (111)  $\text{BiFeO}_3$ -oriented films. Waveforms for (100) and (110) films were obtained at zero bias after poling the sample in an electric field of  $200 \text{ kV/cm}$ , while the waveform for (111) films was obtained in an electric field of  $-200 \text{ kV/cm}$ .  $E_{\text{THz}}$  is the peak amplitude of the waveform. (d) The dependence of  $E_{\text{THz}}$  on the applied electric field generates a hysteresis loop for (100)- and (110)-oriented films and an almost linear variation with opposite polarity for (111) films

cause. For instance, a laser frequency of  $82 \text{ MHz}$  used in present experiments suggests that the spontaneous polarization retrieves in less than  $12$  nanoseconds, whereas the demagnetization experiments [45] use a laser frequency of  $\sim 1\text{--}2 \text{ kHz}$  to avail enough time for spin cooling. In this regard, the nonthermal mechanism of ultrafast depolarization is similar as of the spin reorientation dynamics of both

**Fig. 9.11** Illustration of mechanism of the raster scan around the antenna to map THz emission in a LTEM



antiferromagnetic and ferromagnetic orders. This depicts that optical manipulation of spontaneous polarization can be performed at exceptionally large speeds.

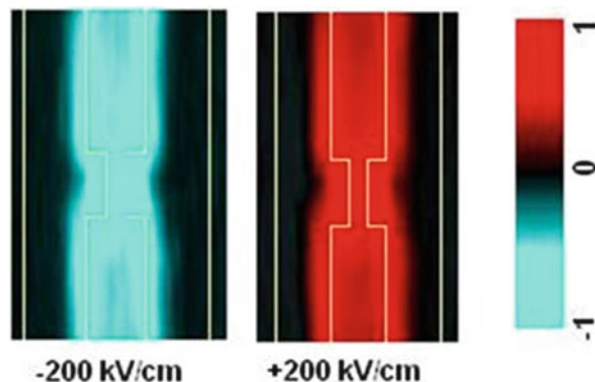
#### 9.4.9 *Laser THz Emission Imaging Microscope (LTEM)*

The LTEM exploits the principle of THz emission [56]. A raster scan is performed around the antenna and spatial distribution of THz emission is recorded (Fig. 9.11). An example of imaging of the switching of ferroelectric domains is presented here. As the ferroelectric domains are switched by  $180^\circ$ , the polarity of THz is also reversed. Using these concepts, the ferroelectric domain can be imaged at any particular point in the THz-E ferroelectric loop [51]. This implies that LTEM images of BFO poled with electric fields of opposite polarities should have domain switched by  $180^\circ$ . Figure 9.12 shows such LTEM images of BFO (100) film in which the domains of opposite polarities can be seen. This technique can be used to image various physical properties of different correlated systems such as high-temperature superconductors, charge-ordered manganites, ferroelectrics, electronic phase-separated materials, magnetic systems, etc. [71–94].

#### 9.4.10 *Technological Implications of Application of THz Emission to Multiferroic BiFeO<sub>3</sub>*

THz emission due to ultrafast depolarization promises several technological advances of ferroelectrics. THz emission can be controlled by poling conditions, such as photo-assisted poling enhances emission compared to one poled in electric

**Fig. 9.12** LTEM images of BFO (100) film in which domains of opposite polarities are shown



field alone. As a result, a better THz radiation flux is a signature of enhanced data storage densities. Furthermore, the  $E_{\text{THz}}\text{-}E$  saturated loops have a coercivity of  $\sim 70\text{--}80 \text{ kV/cm}$  (Fig. 9.8d) vis-à-vis a coercivity of  $\sim 300\text{--}400 \text{ kV/cm}$  established by ferroelectric measurements, suggesting that a remarkable suppression in coercivity by 4–5 factors can be achieved by photo-assisted poling. The photo-assisted poling seems to have strong implications to “laser-assisted data recording.” In this concept, which is limited to ferromagnetic memories, the laser-induced heating softens the lattice to enable data recording with reduced magnetic coercivity. The photo-assisted poling in  $\text{BiFeO}_3$  explicitly suggests that the concept of laser-assisted data recording is applicable to the ferroelectric memories. In addition, the nonthermal mechanism of depolarization is a huge advantage of speedy laser-assisted data recording.

#### 9.4.11 Pump-Probe THz Emission and Optical-Pump/THz-Probe Spectroscopy

These techniques are advanced forms of THz emission and TDS spectroscopy [2, 6]. A schematic for pump-probe/THz emission is depicted in Fig. 9.13. This technique is used to understand the excitation and relaxation times of the carriers/magnetic moments/electric dipole moments responsible for the THz emission. The knowledge of such time scale is important for efficient THz emission and also to understand ultrafast processes in various materials.

An advanced technique based on THz-TDS is called optical-pump/THz probe spectroscopy [6]. In this technique, depending on the system under investigation, the carriers or the magnetic moments or the electric dipole moments are excited (pumped) with the visible femtosecond laser beam with a repetition rate of few kHz and the resulting excitation and relaxation processes are probed by the THz beam (in transmission mode) having a repetition rate of about 100 MHz. This technique is helpful in generating and understanding several thermally inaccessible phases.

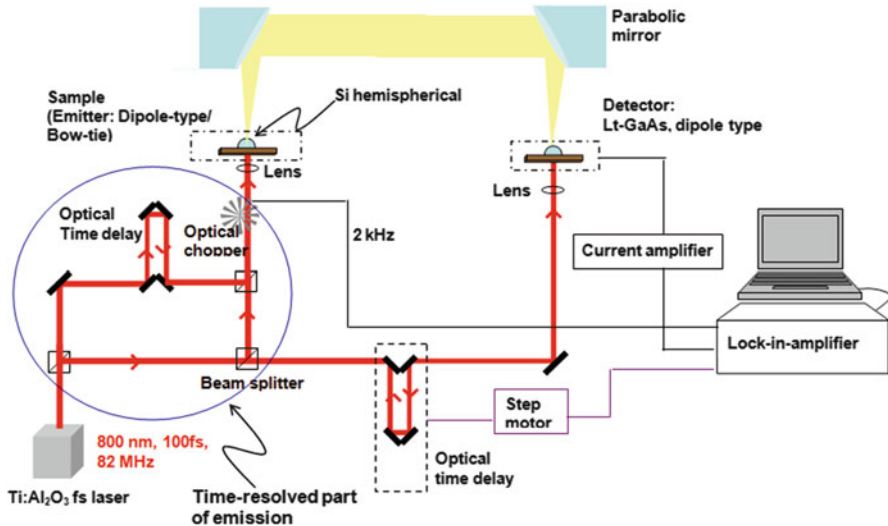


**Fig. 9.13** Schematic diagram of pump and probe THz emission spectroscopic system. For the sake of simplicity, only key components of the setup are shown. The *rounded part* is the time-resolved part of the emission spectroscopy

#### 9.4.12 Concluding Remarks

To sum up, I would like to mention that THz technology holds enormous potential for advancements in both pure and applied aspects in all disciplines of science. The last decade has seen exponential growth in this area of technology and this surge in research developments will probably continue to exist for the next two decades. The two most important factors that have contributed enormously in the development of tabletop THz spectroscopic and imaging techniques are the availability of the stable and tunable femtosecond laser sources and the efficient THz emitters and detectors. Collaborative efforts of the scientific communities working in the areas of THz science, materials sciences, biological and chemical sciences, and the industry can realize the enormous potential of this technology being transformed for the better service of mankind.

#### 9.4.13 Further Readings

Detailed reviews on techniques of THz generation and detection are available, namely, (1) *Terahertz Optoelectronics* edited by K Sakai presents in details the tabletop methods of normal and broadband THz radiation, (2) *Principles of THz Science and Technology* edited by Yun-Shik Lee not only discusses various techniques of continuous and pulsed THz generation but also gives an overview

of applications in THz spectroscopy and imaging, (3) *THz spectroscopy* edited by Susan Dexheimer in addition to the spectroscopic applications of THz radiation in various spheres of science also briefly discusses the photoconductive antenna-based and optical rectification–electro-optic sampling-based techniques of THz generation and detection, and (4) *Sensing with Terahertz Radiation* edited by D. Mittleman mainly discusses and reviews the imaging capabilities of THz radiation.

## References

1. M. Tonouchi, *Nat. Photonics* **1**, 97 (2007)
2. (a) K. Sakai (ed.), *Terahertz Optoelectronics* (Springer, Berlin, 2005); (b) Yun-Shik Lee, *Principles of Terahertz Science* (Springer, New York, 2009); (c) N. Kida, M. Tonouchi, *Phys. Rev. B* **66**, 024401 (2002)
3. D. Mittleman (ed.), *Sensing with Terahertz Radiation* (Springer, Berlin/Heidelberg, 2003)
4. J.M. Chamberlain, *Philos. Trans. R. Soc. Lond. A* **362**, 199–213 (2004)
5. A. Borak, *Science* **308**, 638 (2005)
6. T.M.C. Beard, G.M. Turner, C.A. Schmuttenmaer, *J. Phys. Chem. B* **106**, 7146 (2002)
7. G.K. Kitaeva, *Laser Phys. Lett.* **5**, 559 (2008)
8. S.L. Dexheimer (ed.), *THz Spectroscopy: Principles and Applications* (CRC Press/Taylor & Francis Group, Boca Raton, 2008)
9. J. Joo-Hiuk Son, *Appl. Phys.* **105**, 102033 (2009)
10. J. Barber et al., *J. Phys. Chem. A* **109**, 3501 (2005)
11. H.-B. Liu, Y. Chen, G.J. Bastiaans, X.-C. Zhang, *Opt. Express* **14**, 415 (2006)
12. K. Kawase, Y. Ogawa, Y. Watanabe, H. Inoue, *Opt. Express* **11**, 2549 (2003)
13. D. Clery, *Science* **297**, 763 (2002)
14. R.M. Woodward, B.E. Cole, V.P. Wallace, R.J. Pye, D.D. Arnone, E.H. Linfield, M. Pepper, *Phys. Med. Biol.* **47**, 3853 (2002)
15. B.M. Fischer et al., *Opt. Express* **13**, 5205 (2005)
16. Y.C. Shen, T. Lo, P.F. Taday, B.E. Cole, W.R. Tribe, M.C. Kemp, *Appl. Phys. Lett.* **86**, 241116 (2005)
17. H. Zhong, A. Redo-Sanchez, X.-C. Zhang, *Opt. Express* **14**, 9130 (2006)
18. E. Pickwell, V.P. Wallace, *J. Phys. D Appl. Phys.* **39**, R301 (2006)
19. E. Pickwell, B.E. Cole, A.J. Fitzgerald, M. Pepper, V.P. Wallace, *Phys. Med. Biol.* **49**, 1595 (2004)
20. A.J. Fitzgerald, V.P. Wallace, M. Jiminez-Linan, L. Bobrow, R.J. Pye, A.D. Purushotham, D.D. Arnone, *Radiology* **239**, 533 (2006)
21. D. Crawley, C. Longbottom, V.P. Wallace, B. Cole, D. Arnone, M.J. Pepper, *Biomed. Opt.* **8**, 303 (2003)
22. M.R. Stringer, D.N. Lund, A.P. Foulds, A. Uddin, E. Berry, R.E. Miles, A.G. Davies, *Phys. Med. Biol.* **50**, 3211 (2005)
23. J.-B. Masson, M.-P. Sauviat, G. Gallot, *Appl. Phys. Lett.* **89**, 153904 (2006)
24. S. Hadjiloucas, R.K.H. Galvao, J.W. Bowen, *J. Opt. Soc. Am. A* **19**, 2495 (2002)
25. B. Ferguson, Zhang Xi-Cheng, *Nat. Mater.* **1**, 26 (2002)
26. D.J. Hilton, R.P. Prasantkumar, S.A. Trugman, A.J. Taylor, R.D. Averitt, *J. Phys. Soc. Jpn.* **75**, 11006 (2006)
27. B.S. Williams, H. Callebaut, S. Kumar, Q. Hu, J.L. Reno, *Appl. Phys. Lett.* **82**, 1015 (2003)
28. J. Hebling, Yeh Ka-Lo, M.C. Hoffmann, B. Bartal, K.A. Nelson, *J. Opt. Soc. Am. B* **25** (2008)
29. G. Ping, T. Masahiko, in *Terahertz Optoelectronics*, ed. by K. Sakai (Springer, Berlin, 2005)
30. J. Han, H. Xu, Z. Zhu, X. Yu, W. Li, *Chem. Phys. Lett.* **392**, 348 (2004)

31. B. Fischer, M. Hoffmann, H. Helm, G. Modjesch, P.U. Jepsen, *Semicond. Sci. Technol.* **20**, S246 (2005)
32. C.J. Strachan et al., *J. Pharm. Sci.* **94**, 837 (2005)
33. G.M. Day, J.A. Zeitler, W. Jones, T. Rades, P.F. Taday, *J. Phys. Chem. B* **110**, 447 (2006)
34. R. Kohler et al., *Nature* **417**, 156 (2002)
35. J.B. Pendry, D. Schurig, D.R. Smith, *Science* **312**, 1780 (2006)
36. S. Zhang et al., *Phys. Rev. Lett.* **95**, 137404 (2005)
37. T.J. Yen et al., *Science* **303**, 1494 (2004)
38. W.J. Padilla, A.J. Taylor, C. Highstrete, M. Lee, R.D. Averitt, *Phys. Rev. Lett.* **96**, 107401 (2006)
39. K. Wang, D.M. Mittleman, *Nature* **432**, 376 (2004)
40. D. Grischkowsky, S. Keiding, M. van Exter, C. Fattinger, *J. Opt. Soc. Am. B* **7**, 2006 (1990)
41. K. Liu, J. Xu, T. Yuan, X.-C. Zhang, *Phys. Rev. B* **73**, 155330 (2006)
42. N. Nagai, R. Kumazawa, R. Fukasawa, *Chem. Phys. Lett.* **413**, 495 (2005)
43. N. Nagai, T. Imai, R. Fukasawa, K. Kato, K. Yamauchi, *Appl. Phys. Lett.* **85**, 4010 (2004)
44. M. Misra, K. Kotani, I. Kawayama, H. Murakami, M. Tonouchi, *Appl. Phys. Lett.* **87**, 182909 (2004)
45. J. Orenstein, J. Corson, S. Oh, J.N. Eckstein, *Ann. Phys.* **15**, 596 (2006)
46. K. Takahashi, N. Kida, M. Tonouchi, *Phys. Rev. Lett.* **96**, 117402 (2006)
47. E. Beaurepaire et al., *Appl. Phys. Lett.* **84**, 3465 (2004)
48. J. Tilborg et al., *Phys. Rev. Lett.* **96**, 014801 (2006)
49. D.S. Rana et al., *Adv. Mater.* **20**, 29 (2009)
50. K. Takahashi, M. Tonouchi, *Appl. Phys. Lett.* **90**, 052908 (2007)
51. D.S. Rana, K. Takahashi, K.R. Mavani, I. Kawayama, H. Murakami, M. Tonouchi, *Appl. Phys. Lett.* **91**, 031909 (2007)
52. D.S. Rana, K. Takahashi, K.R. Mavani, I. Kawayama, H. Murakami, M. Tonouchi, *Phys. Rev. B* **77**, 024105 (2008)
53. D.S. Rana, K. Takahashi, K.R. Mavani, I. Kawayama, H. Murakami, M. Tonouchi, T. Yanagida, H. Tanaka, T. Kawai, *Europhys. Lett.* **84**, 76016 (2008)
54. K.R. Mavani, M. Nagai, D.S. Rana, H. Yada, I. Kawayama, M. Tonouchi, K. Tanaka, *Appl. Phys. Lett.* **93**, 231908 (2008)
55. K.R. Mavani, D.S. Rana, K. Takahashi, I. Kawayama, H. Murakmai, M. Tonouchi, *Europhys. Letters* **81**, 17009 (2008)
56. T. Kiwa, M. Tonouchi, M. Yamashita, K. Kawase, *Opt. Lett.* **28**, 2058 (2003)
57. W.L. Chan et al., *Rep. Prog. Phys.* **70**, 1325 (2007)
58. K. Takahashi et al., *Appl. Phys. Lett.* **83**, 4303 (2003)
59. Lei Ren et al., *Nano Lett.* **9**, 2610 (2009)
60. A.J. Huber, F. Keilmann, J. Wittborn, J. Aizpurua, R. Hillenbrand, *Nano Lett.* (2008). doi:[10.1021/nl802086x](https://doi.org/10.1021/nl802086x)
61. K.L. Nguyen et al., *Opt. Express* **14**, 2123 (2006)
62. S. Ariyoshi, *Appl. Phys. Lett.* **88**, 203503 (2006)
63. D.M. Mittleman, R.H. Jacobsen, M.C. Nuss, *IEEE J. Sel. Top. Quantum. Electron.* **2**, 679 (1996)
64. S.M. Kim et al., *Appl. Phys. Lett.* **88**, 153903 (2006)
65. H.-T. Chen, R. Kersting, G. Cho, *Appl. Phys. Lett.* **83**, 3009 (2003)
66. A.W.M. Lee, Q. Hu, *Opt. Lett.* **30**, 2563 (2005)
67. M. Herrmann, M. Tani, K. Sakai, *Japan J. Appl. Phys. Part 1* **39**, 6254 (2000)
68. K.J. Siebert, H. Quast, R. Leonhardt, T. Loffler, M. Thomson, T. Bauer, H.G. Roskos, S. Czasch, *Appl. Phys. Lett.* **80**, 3003 (2002)
69. A. Dobroiu, M. Yamashita, Y.N. Ohshima, Y. Morita, C. Otani, K. Kawase, *Appl. Opt.* **43**, 5637 (2004)
70. F. Rodriguez-Morales, K.S. Yngvesson, R. Zannoni, E. Gerecht, D. Gu, X. Zhao, N. Wadefalk, J.J. Nicholson, *IEEE Trans. Microw. Theory Tech.* **54**, 2301 (2006)

71. (a) M. Fiebig, *J. Phys. D Appl. Phys.*, **38**, R123 (2005); (b) W. Eerenstein, N.D. Mathur, J.F. Scott, *Nature* **442**, 759 (2006)
72. N.A. Spaldin, *J. Phys. Chem. B* **104**, 6694 (2000)
73. J. Wang, J.B. Neaton, H. Zheng, V. Nagarajan, S.B. Ogale, B. Liu, D. Viehland, V. Vaithyanathan, D.G. Schlom, U.V. Waghmare, N.A. Spaldin, K.M. Rabe, M. Wuttig, R. Ramesh, *Science* **299**, 1719 (2003)
74. M. Dawber, K.M. Rabe, J.F. Scott, *Rev. Mod. Phys.* **77**, 1083 (2005)
75. Z.J. Huang, Y. Cao, Y.Y. Sun, Y.Y. Xue, C.W. Chu, *Phys. Rev. B* **56**, 2623 (1997)
76. T. Kimura, T. Goto, H. Shintani, K. Ishizaka, T. Arima, Y. Tokura, *Nature* **426**, 55 (2004)
77. M. Fiebig, T. Lottermoser, D. Fröhlich, A.V. Goltsev, R.V. Pisarevet, *Nature* **419**, 818 (2002)
78. T. Kimura, S. Kawamoto, I. Yamada, M. Azuma, M. Takano, Y. Tokura, *Phys. Rev. B* **67**, 180401R (2003)
79. R. Valdas Aguilar, A.B. Sushkov, C.L. Zhang, Y.J. Choi, S.-W. Cheong, H.D. Drew, *Cond-matt, arXiv:0704.3632v4*
80. J. Hemberger, F. Schrettle, A. Pimenov, P. Lunkenheimer, V.Y. Ivanov, A.A. Mukhin, A.M. Balbashov, A. Loidl, *Phys. Rev. B* **75**, 35118 (2007)
81. C.N.R. Rao, B. Raveau (eds.), *Colossal Magnetoresistance, Charge Ordering & Related Properties of Manganese Oxides* (World Scientific Publishers, Singapore, 1998)
82. Y. Tokura (ed.), *Colossal Magnetoresistive Oxides* (Gordon and Breach Science Publishers, Amsterdam, 2000)
83. E. Dagotto (ed.), *Nanoscale Phase Separation and Colossal Magnetoresistance* (Springer, Berlin, 2002)
84. R. Schmidt, *Phys. Rev. B* **77**, 205101 (2005)
85. P. Calvani, G. Marzi, P. De Dore, S. Lupi, P. Maselli, F. D'Amore, S. Gagliardi, *Phys. Rev. Lett.* **81**, 4504 (1999)
86. A. Nucara, P. Maselli, P. Calvani, R. Sopracase, M. Ortolani, G. Gruener, M.C. Guidi, U. Schade, J. García, *Phys. Rev. Lett.* **101**, 66407 (2008)
87. A. Chainani, H. Kumigashira, T. Takahashi, Y. Tomioka, H. Kuwahara, Y. Tokura, *Phys. Rev. B* **56**, R15513 (1997)
88. (a) R. Rana, D.S. Rana, K.R. Mavani, I. Kawayama, H. Murakami, M. Tonouchi, *Appl. Phys. Lett.* **101**, 252401 (2012); (b) R. Rana, N. Awari, P. Pandey, A. Singh, S.S. Prabhu, D.S. Rana, *J. Phys.: Condens. Matter* **25**, 106004 (2013); (c) P. Pandey, N. Awari, R. Rana, A. Singh, S.S. Prabhu, D.S. Rana, *Appl. Phys. Lett.* **100**, 062408 (2012)
89. G. Grüner, *Rev. Mod. Phys.* **60**, 1129 (1988)
90. R.D. Averitt, A.I. Lobad, C. Kwon, S.A. Trugman, V.K. Thorsmølle, A.J. Tayloret, *Phys. Rev. Lett.* **87**, 17401 (2001)
91. A. Moreo, S. Yunoki, E. Dagotto, *Phys. Rev. Lett.* **83**, 2773 (1999)
92. T. Saitoh, D.S. Dessau, Y. Moritomo, T. Kimura, Y. Tokura, N. Hamada, *Phys. Rev. B* **62**, 1039 (2000)
93. S. Cox, J.C. Loudon, A.J. Williams, J.P. Attfield, J. Singleton, P.A. Midgley, N.D. Mathur, *Phys. Rev. B* **78**, 35129 (2008)
94. D.S. Rana, R. Nirmala, S.K. Malik, *Europhys. Lett.* **70**, 376 (2005)

# Chapter 10

## Phase-Shifting Laser Interferometry for Measurement of Surface Form Error

Sanjib Chatterjee

**Abstract** I describe wedge phase-shifting (WPS) and polarization phase-shifting (PPS) Fizeau interferometers (FIs) for the measurement of surface form error of plane surfaces. In WPS, a pair of identical fused silica wedge plates, which together form a variable thickness parallel plate, is used in the FI cavity for introducing phase shifts. For PPS, two different methods are discussed. In the first method, a quarter-wave plate (QWP) is placed in the FI cavity for producing test and reference beams with orthogonal linear polarizations. Another QWP transforms the test and reference beams to opposite circular polarizations of which the components selected by a linear polarizer interfere. Polarization phase shifts are introduced by varying the angular orientation of the linear polarizer. In the second method, a Sagnac interferometer (SI)-based polarization phase-shifting FI is described. A polarization phase-shifting SI is used to generate laterally separated virtual point sources at the back focal plane of a telescope objective for producing tilted plane-wave components with orthogonal linear polarizations. The orthogonal linear polarization components reflected from the reference and the test surfaces are utilized for introducing polarization phase shift between the reference and test waves. The method for elimination of instrumental aberration is discussed.

**Keywords** Surface form error • Phase-shifting interferometry • Polarization phase shift • Fizeau interferometer • Sagnac interferometer

### 10.1 Introduction

Surface form error can be defined as the macroscopic departure from the desired or intended surface form such as plane, spherical, etc. It is thus related to surface height variations corresponding to long spatial wave lengths. Plane optical surfaces are extensively used in optical systems and surface form error for plane surfaces refers to macroscopic departure from flatness. Primarily, wave-front distortion is produced

---

S. Chatterjee (✉)

Raja Ramanna Centre for Advanced Technology, Indore 452013, India

e-mail: [schat@rrcat.gov.in](mailto:schat@rrcat.gov.in)

due to surface form error in the optical components. Therefore, it is important to measure surface form error of optical components during fabrication as well as for finished optical components.

Fizeau interferometers (FIs) [1] are widely used in optics laboratories for the measurements of surface forms, parallelism, homogeneity, etc., of optical components. In its simplest form, an FI is a real wedge interferometer, i.e., the optical path difference (OPD) between the reference and the test waves cannot be made zero and the configuration is most suitable with a coherent source, such as a laser, although quasi-monochromatic sources can also be used. Though FIs are not exactly common path interferometers, the interfering waves from the reference and the test surfaces travel nearly the same path through the interferometer system (from the reference surface). Due to the common path of the reference and the test waves through the interferometer system, the measurement results are least affected by aberrations of the interferometer system and the FI systems are least susceptible to external mechanical vibrations. Thus, it is relatively easy to set up FI-based system but one really needs a high-quality reference surface.

Phase-shifting interferometry (PSI) [2–4] has been regarded as the most useful and accurate method for quantitative evaluation of phase information. PSI technique is extensively used in FIs. Piezoelectric transducer (PZT)-based mechanical phase shifters are most common. The main disadvantage of PZTs is that the displacement is not always a linear function of the applied voltage. The effect of nonlinearity of PZT on PSI is discussed in Ref. [5].

The most common methods of introducing phase shifts or modulation are available in literature (Refs. [3, pp. 296–300, 4, pp. 506–510]). Accuracy of PSI technique, sources of errors, susceptibility and sensitivity of different algorithms, techniques of reduction of errors, and calibration of phase shifter have been discussed in detail in various reports (Refs. [2, pp. 373–374, 4, pp. 536–546]).

This chapter discusses the following two simple phase-shifting techniques:

1. Wedge phase shifting [6]
2. Polarization phase shifting [7, 8]

In wedge phase shifting (WPS), wedged plates, which are identical optical glass/fused quartz plates with their wedges in opposite directions, are introduced in the Fizeau cavity. Together, they form a variable thickness parallel plate, whose thickness can be varied, and hence, phase shift can be introduced by laterally translating one of the wedges.

In polarization phase shifting (PPS), generally, the reference and the test waves with linear orthogonal polarizations are transformed to opposite circular polarizations and are allowed to pass through a linear polarizer. The (geometrical) phase shift is introduced by varying the angular orientation of the pass direction of the polarizer. The PPS has been applied to different interferometric configurations. The most important advantage of PPS is that it is possible to capture all the necessary phase-shifted interferograms simultaneously, thereby reducing the vibration susceptibility to a minimum and extending the scope of the measurement to dynamic interferometry.

## 10.2 Wedge Phase-Shifting Fizeau Interferometer

Optical schematic of the FI system for the measurement of surface figure of plane optical surfaces is shown in Fig. 10.1. Light from a He-Ne laser source (not shown in Fig. 10.1) is allowed to pass through a spatial filtering arrangement consisting of a microscope objective (MO) and an appropriate pinhole (PH) placed at the front focal point of the microscope objective. PH is also situated at the back focal point of a well-corrected telescope objective (TO) and thus an expanded collimated beam is produced. FI cavity is formed between the uncoated front surface (R) of a high optical quality plane reference plate of fused silica and the test object surface (J). The plane reference plate and the test object are mounted in high-quality tip, tilt mirror mounts. The reference plate is wedged ( $0.5^\circ$ ) to eliminate the effect of unwanted Fresnel reflections from its rear surface, which is antireflection coated. Rays reflected from the reference and the test surfaces interfere to produce two beam Fizeau fringes. The beam splitter (BS) directs the interfering waves towards an imaging lens (IL) and a CCD camera. The iris diaphragm (ID) placed at the rear focal plane of the telescope objective blocks unwanted light. Fizeau fringes are grabbed by means of a CCD camera, frame grabber, and PC arrangement.

Now we discuss a case where the phase shifts are introduced by wedge-type phase shifter [6]. The FI cavity is shown in Fig. 10.2, where the reference plate, test object, and master plate surfaces are indicated by R, J, and M, respectively. In Fig. 10.2, both master plate and test object are shown but only one, either the master plate or the test object, would be present during actual measurement. The role of the master plate would be discussed later. Phase-shifting wedged plates shown by W1 and W2 in Fig. 10.2 are identical optical glass/fused quartz plates with their wedges in opposite directions. Together, they form a variable thickness parallel plate whose thickness can be varied, and hence, phase shift can be introduced by laterally translating one of the wedges (say, W2).

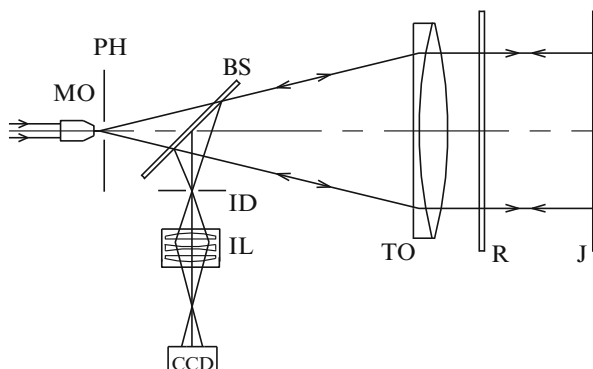
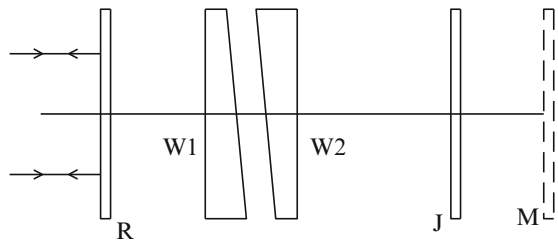


**Fig. 10.1** Optical schematic of Fizeau interferometer

**Fig. 10.2** Fizeau interferometer cavity with wedge phase shifter



The optical path difference introduced due to lateral shift of W2 is given by

$$\Delta = 2(n - 1)s \tan \theta \quad (10.1)$$

where  $n$ ,  $s$ , and  $\theta$  are refractive index, lateral displacement, and wedge angle, respectively, of the wedged plates. The factor 2 in Eq. (10.1) accounts for the double passing of the beam through the wedges. Taking partial derivatives in Eq. (10.1), it is possible to find out the effect of the small deviation of the parameters  $n$ ,  $\theta$ , and  $s$  on  $\Delta$ . We can write

$$\partial\Delta = 2s \tan \theta \partial n + 2(n - 1) \tan \theta \partial s + 2(n - 1) s \sec^2 \theta \partial \theta \quad (10.2)$$

From Eq. (10.2), one can calculate maximum inaccuracy, which may be introduced in each phase step for this type of phase shifter.

In the present technique, the phase-shifting wedged plates are placed in between the test and reference surfaces, and thus any wave-front deformation introduced due to the imperfections in the wedged shifter would be added to that due to the surface flatness deviation of the test surface. The problem can be minimized by using a wedged phase shifter of high optical quality. Final results can be made free from the effect of the system aberrations by subtracting phase values obtained by PSI technique between the high optical quality master surface and reference surface from that obtained for the test object surface with respect the same reference surface.

From Fig. 10.2, the optical path difference between master and reference surfaces (considering the Fizeau cavity with master plate) is given by

$$\Delta_1 = 2 \{ [RW1] + [W1 W2] + [W2 M] \} \quad (10.3)$$

where optical path in the right-hand side of Eq. (10.3) is indicated by square brackets.

Similarly, the optical path difference between the test object and reference surface (considering the Fizeau cavity with test object in Fig. 10.2) is given by

$$\Delta_2 = 2 \{ [RW1] + [W1 W2] + [W2 J] \} \quad (10.4)$$

Above equations yield

$$\Delta_2 - \Delta_1 = 2 \{ [W2 J] - [W2 M] \} = 2 [JM] \quad (10.5)$$

It is evident that the right-hand side of Eq. (10.5) is the optical path difference between the test object surface and the master surface. Therefore, by computing  $\Delta_2$  and  $\Delta_1$  at each point of the interference field, it is possible to determine surface form of the test surface with respect to the master surface. The master surface must be of high optical quality. Hence, it is possible to get accuracy better than that can be obtained with the reference surface. In the present technique, the lateral displacement [Eq. (10.1)] of one of the wedges, required to produce the necessary phase shift, is small. Therefore, the residual wave-front deformation due to the phase-shifting wedges remains practically constant during phase shifting and the phase values change equally for each point over the beam aperture due to the shift of the wedge.

There are standard techniques for the measurement of surface flatness of optical components using phase-shifting FI. The piezoelectric phase shifters are the most common. We have described a FI-based setup with simple, inexpensive wedge-type phase shifter. The wedge phase shifters are free from nonlinearity effect, commonly encountered in piezoelectric phase shifters, and capable of producing accurate phase steps. A technique for elimination of system aberrations has been discussed. The most important advantage of the technique described is that it is easy to implement and can achieve high accuracies.

### 10.3 Polarization Phase-Shifting Fizeau Interferometer with a Quarter-Wave Plate

Optical schematic of the FI-based setup [7] for the measurement of surface figure of plane optical surfaces is shown in Fig. 10.3. Light from a linearly polarized He-Ne (632.8 nm) laser source (not shown in Fig. 10.3) is allowed to pass through a spatial filtering arrangement consisting of a microscope objective (MO) and an appropriate pinhole (P) placed at the front focal point of the microscope objective. The pinhole is also situated at the back focal point of a well-corrected telescope objective (TO), and thus, a linearly polarized, expanded collimated beam is produced. FI cavity is formed between the uncoated front surface (R) (surface adjacent to the test surface) of a high optical quality transparent plane reference plate of fused silica and the test object surface (O). The reference plate is wedged ( $\sim 0.5$  deg) to eliminate the effect of unwanted Fresnel reflections from its rear surface, which is antireflection coated. The plane reference plate and the test object are mounted on high-quality tip-tilt mirror mounts. Beams reflected from the reference and the test surfaces interfere to form two beam Fizeau fringes. To introduce polarization phase shift between the interfering beams, the direction of polarization of the beam reflected from the

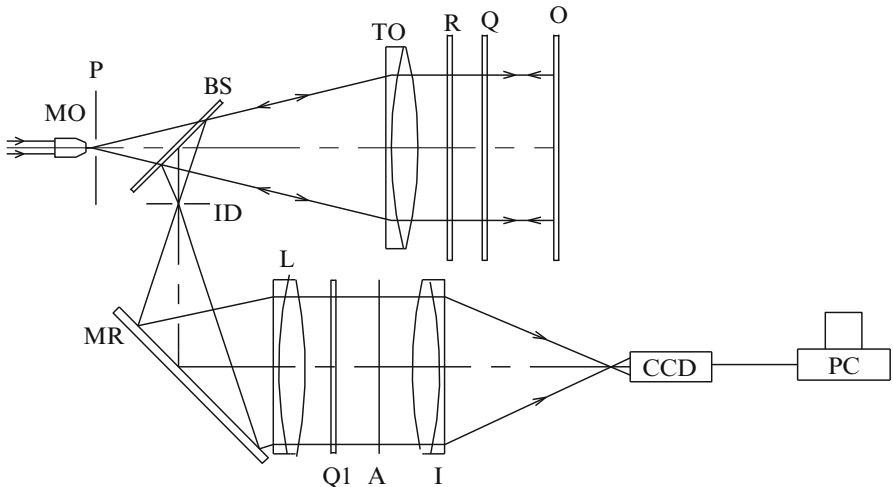


**Fig. 10.3** Optical schematic of the QWP-based polarization phase-shifting Fizeau interferometer

object surface is rotated by means of a quarter-wave plate (QWP), (Q), placed in the Fizeau cavity with its axes at  $45^\circ$  with the direction of polarization of the incident collimated beam from TO. The incident collimated beam after passing through Q becomes circularly polarized, and after reflection at the object surface and double passing through Q, the beam becomes linearly polarized in orthogonal direction with that of the beam reflected from the reference surface R. Polarization maintaining beam splitter (BS) directs these beams towards a folding mirror (MR). The iris diaphragm (ID) placed at the rear focal plane of the telescope objective blocks unwanted light. The beams are then collimated by lens L whose rear focal point coincides with that of the telescope objective (TO). These beams which are linearly polarized in orthogonal directions are made circularly polarized (left and right circular polarizations) by a quarter-wave plate (Q1) placed with its axes at  $45^\circ$  to the directions of polarizations of the linearly polarized orthogonal beams. An analyzer (A) (i.e., linear polarizer) placed after the quarter-wave plate (Q1) selects linear components from the circularly polarized beams along its pass directions. These linear components interfere to produce two beam Fizeau fringes. Fizeau fringes are grabbed by means of a CCD Camera, frame grabber, and PC arrangement. The test object plane is imaged on the CCD plane by means of the imaging lenses (I).

The following analysis [7] shows that it is possible to introduce phase shifts between the interfering components by changing the angular position of the analyzer A (in its plane).

Jones vectors for linearly polarized light with direction of polarization in the vertical and horizontal directions can be written as  $E_v = \begin{bmatrix} 0 \\ 1 \end{bmatrix}$  and  $E_h = \begin{bmatrix} 1 \\ 0 \end{bmatrix}$ , respectively.

Jones matrix for the QWP with its fast axis at an angle of  $45^\circ$  with respect to the horizontal direction is given by  $D = 1/\sqrt{2} \begin{bmatrix} 1 & i \\ i & 1 \end{bmatrix}$ .

After passing through the QWP (Q1), the vertically polarized beam will become

$$E_1 = \frac{1}{\sqrt{2}} \begin{bmatrix} 1 & i \\ i & 1 \end{bmatrix} \begin{bmatrix} 0 \\ 1 \end{bmatrix} = \frac{1}{\sqrt{2}} \begin{bmatrix} 1 \\ -i \end{bmatrix} e^{i\pi/2}$$

which is a left circularly polarized beam, and the horizontally polarized beam will become

$$E_2 = \frac{1}{\sqrt{2}} \begin{bmatrix} 1 & i \\ i & 1 \end{bmatrix} \begin{bmatrix} 1 \\ 0 \end{bmatrix} = \frac{1}{\sqrt{2}} \begin{bmatrix} 1 \\ i \end{bmatrix}$$

which is a right circularly polarized beam.

Jones matrix of an analyzer with its pass axis at an angle  $\theta$  with respect to the horizontal direction is represented by  $A(\theta) = \begin{bmatrix} \cos^2\theta & \cos\theta \cdot \sin\theta \\ \cos\theta \cdot \sin\theta & \sin^2\theta \end{bmatrix}$ .

When the circularly polarized components ( $E_1$  and  $E_2$ ) pass through the analyzer placed with its axis at an angle  $\theta$  with respect to the horizontal, the transmitted components ( $E_1^1, E_2^1$ ) through the analyzer are given by

$$\begin{aligned} E_1^1 &= A(\theta) E_1 = \frac{1}{\sqrt{2}} \begin{bmatrix} \cos^2\theta & \cos\theta \cdot \sin\theta \\ \cos\theta \cdot \sin\theta & \sin^2\theta \end{bmatrix} \begin{bmatrix} 1 \\ -i \end{bmatrix} e^{i\pi/2} \\ &= \frac{1}{\sqrt{2}} \begin{bmatrix} \cos\theta \\ \sin\theta \end{bmatrix} e^{-i(\theta-\pi/2)} \end{aligned} \quad (10.6)$$

$$E_2^1 = A(\theta) E_2 = \frac{1}{\sqrt{2}} \begin{bmatrix} \cos^2\theta & \cos\theta \cdot \sin\theta \\ \cos\theta \cdot \sin\theta & \sin^2\theta \end{bmatrix} \begin{bmatrix} 1 \\ i \end{bmatrix} = \frac{1}{\sqrt{2}} \begin{bmatrix} \cos\theta \\ \sin\theta \end{bmatrix} e^{i\theta} \quad (10.7)$$

respectively.

It is evident from Eqs. (10.6) and (10.7) that  $E_1^1$  and  $E_2^1$  are linearly polarized beams with the same state of polarization  $\begin{bmatrix} \cos\theta \\ \sin\theta \end{bmatrix}$ , hence they will interfere. The interfering components have a phase difference ( $\alpha$ ) given by

$$\alpha = \pi/2 - 2\theta \quad (10.8)$$

Therefore, depending upon the position (angular orientation of the pass axis) of the analyzer, different phase shifts can be introduced between the two interfering components.

## 10.4 Polarization Phase-Shifting Fizeau Interferometer with a Cyclic Path Optical Configuration

In the following, a polarization phase shifting (PPS)-type FI is discussed [8]. A cyclic path optical configuration (CPOC) is used to generate two coherent (virtual) point sources at the back focal plane of a corrected telescope objective (TO) for producing a pair of tilted collimated beams with linear orthogonal polarizations in the FI cavity. Orthogonal linear polarization components reflected from the reference and the test surfaces are utilized for PPS.

Optical schematic of the PPS-type FI system for the measurement of surface form of plane optical surfaces is shown in Fig. 10.4. A CPOC, shown as black box, is used to generate two coherent (virtual) point sources (P and S) at the back focal plane of a corrected telescope objective (TO) for producing a pair of tilted collimated beams with linear orthogonal polarizations in the FI cavity. The center line denotes the axis of TO. Orthogonal linear polarization components (*p* and *s*) reflected from the reference plane, (R), and the test surface, (T), are utilized for PPS. By adjusting the angular orientations of the reference and the test surfaces, it is possible to align the desired interfering beam components along nearly same direction. A thin plate beam splitter (BS1) at  $45^\circ$  orientation deflects a portion of the converging *p* and *s* components in the perpendicular direction and the real images are formed at the focal plane of the TO on the reflection side of the BS1. An appropriate pinhole (PH) allows only the superimposed central spots and blocks the rest. A lens (CL) collimates the beams passing through PH. Quarter-wave plate, (QWP1), transforms the state of polarizations of the beams to opposite circular polarizations and the linear components along the direction of pass axis of the polarizer (P) interferes. An imaging lens (IL) is used to focus the plane of the test surface (TS) and the interferogram is formed on a rotating diffuser screen (RD). A second imaging lens

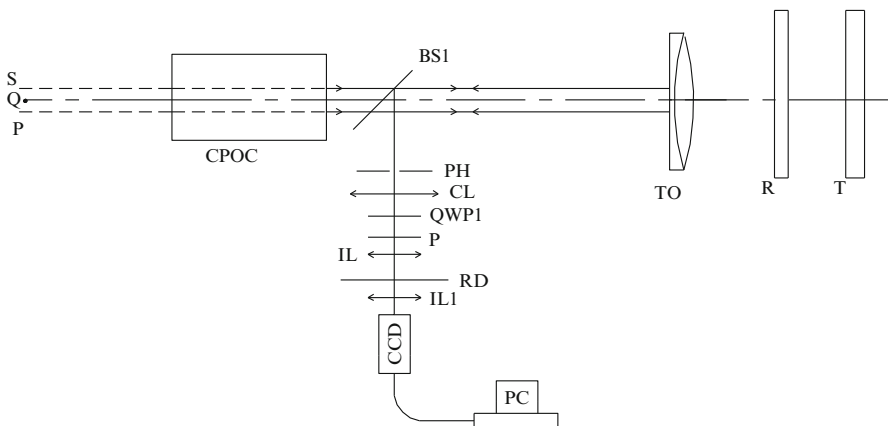


**Fig. 10.4** Schematic of polarization phase-shifting Fizeau interferometer

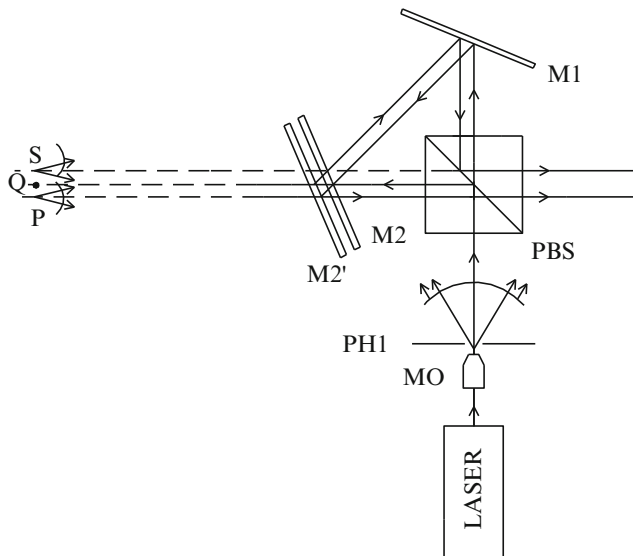
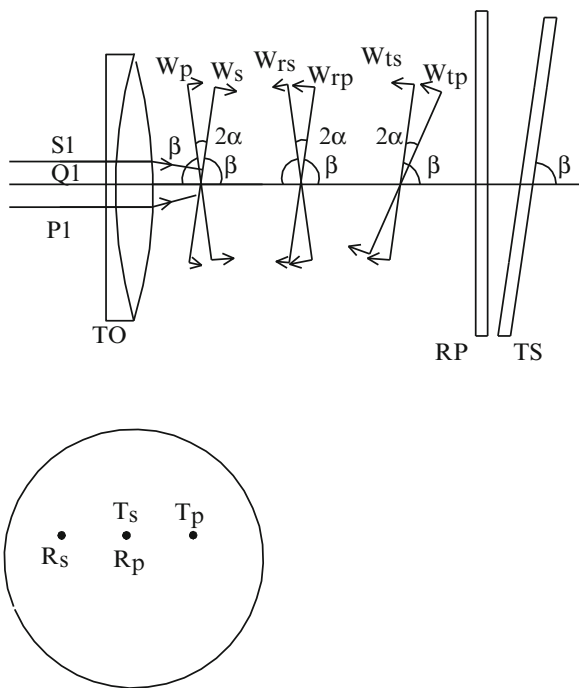


**Fig. 10.5** Schematic of a polarization CPOC for generation of coherent point sources

(IL1) transfers the fringe image on to the plane of a two-dimensional CCD detector where it is captured by means of a frame grabber and personal computer (PC).

Now, consider Fig. 10.5 for understanding the function of the CPOC. Light from a linearly polarized He-Ne (632.8 nm) laser source is allowed to pass through a spatial filtering arrangement consisting of a microscope objective, MO, and an appropriate pinhole, PH1, placed at the front focal point of the MO. The diverging beam from PH1 is split up into transmitted, p-polarized (p) and reflected, s-polarized (s) components by the beam splitting plane of a polarization beam splitter (PBS), which together with plane mirrors (M1) and (M2) forms a CPOC. For simplicity, we have shown the path of the central ray only. M1 and M2 can be adjusted to make the central rays of the p and s components traverse the same triangular path (TP) but in opposite directions. Thus, the CPOC is set for zero shear condition and the emergent beams from the exit side of PBS appear to diverge from a virtual image point Q. M2 is the position of the mirror at zero shear condition and M2 coincides with the position of virtual image of M1 at the beam splitting plane of the PBS. Lateral shear between the counter-propagating central rays in TP can be introduced by shifting one of the plane mirrors from zero shear position, as shown by M2' in Fig. 10.5. On introduction of lateral shear, the emergent p and s beam components appear to diverge from the virtual image points P and S, respectively. The lateral separation ( $d$ ) between P and S is given by  $d = \sqrt{2}s_0$ , where  $s_0$  is the separation between M2 and M2'. P and S also suffer a small longitudinal shift, equal to  $s_0$ , with respect to Q. P and S are adjusted to be at the back focal plane of a corrected TO and are kept equally separated with respect to the optical axis of the TO (Fig. 10.4).

**Fig. 10.6** Nature of the incident and Fresnel-reflected wave fronts. Relative positions of the focal spots are shown in the inset



Thus, as shown in Fig. 10.6, two sets (p and s) of expanded collimated beams denoted by plane wave fronts  $W_p$  and  $W_s$  emerge from TO. Each set of collimated beams is angularly tilted by an angle ( $\alpha$ ), with respect to the optical axis of the TO, given by  $\alpha = \tan^{-1} (d/2f)$ , where  $f$  is the focal length of the TO.  $W_p$  and  $W_s$  suffer Fresnel reflections on the surface of the reference plate (RP) placed normal to the optical axis of the TO. The reflected p and s wave fronts represented by  $W_{rp}$  and  $W_{rs}$  after passing through the TO would converge toward S and P (Fig. 10.4), respectively. The relative positions of the focal spots on the focal plane of the TO (on the reflection side of BS as shown in Fig. 10.4) is illustrated in the inset of Fig. 10.6, where the focal points for the Fresnel-reflected p and s components from the RP are shown by  $R_p$  and  $R_s$ , respectively. The test surface (TS) can be tilted to Fresnel reflect, nearly normally, one of the incident collimated beam components, either p or s. As shown in Fig. 10.6, the TS is tilted at an angle  $\beta$ , where  $\beta = (90^\circ - \alpha)$  and  $W_s$  undergoes a normal reflection on the TS. The reflected p and s wave fronts from the TS are denoted by  $W_{tp}$  and  $W_{ts}$ , respectively. Now,  $W_{ts}$  is (nearly) parallel to  $W_{rp}$  and they come to focus (almost) at the same point in the focal plane of the TO. In the inset in Fig. 10.6,  $T_p$  and  $T_s$  denote the focal points due to Fresnel-reflected p and s components from the TS. In actual practice,  $T_s$  is made to coincide with  $R_p$  by adjusting the tilt of the TS.

The optical path difference (OPD) between the interfering waves can be expressed as

$$\Delta_1 = [W_{ts}] - [W_{rp}] \quad (10.9)$$

where the quantities in the square brackets are used to indicate the OPD. As the interfering waves are nearly parallel to each other, the return path of the beams through the system would be the same for both and hence cancels out. We can write

$$[W_{ts}] = [W_s] + [2W_t] \quad (10.10)$$

$$[W_{rp}] = [W_p] + [2W_r] \quad (10.11)$$

where  $[2W_r]$  and  $[2W_t]$  are the changes in the OPDs due to the reflections on the reference and the test surfaces, respectively. Substituting Eqs. (10.10) and (10.11) in Eq. (10.9) and simplifying, we get

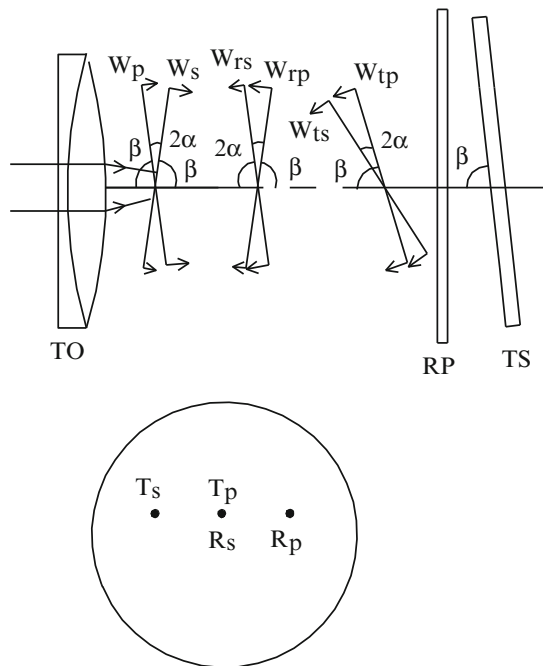
$$\Delta_1 = 2 \{ [W_t] - [W_r] \} + \{ [W_s] - [W_p] \} \quad (10.12)$$

It is necessary to reduce the effect of the off-axis aberrations to a negligible value by reducing the separation between the (virtual) source points at P and S to a minimum. The minimum separation between the (virtual) source points is restricted by the size of the focal spot of the beam reflected from the TS. It is evident that the focal spot size depends on the wave-front aberrations and diffraction. The diameter of the PH (in Fig. 10.4) should be approximately 1.8–2 times bigger than the spot size, so as to allow the passage of the superimposed central spots without any diffraction and block the other, and the minimum separation between the source points can be taken as equal to the diameter of the PH. Taking  $f = 1,000$  mm and  $d = 50 \mu\text{m}$ , we obtain  $\alpha \approx 5.0$  arc seconds. Thus, the angle of inclination  $\alpha$  is very small in comparison to the angular field of view, which is of the order of few degrees, for a well-corrected telescope objective. Hence, the effect of the off-axis aberration is practically negligible. Moreover, the virtual point sources at P and S are symmetrical about the optical axis of the TO, and except for the errors in fabrications of the TO, which may give rise to asymmetric wave-front aberrations, the nature of the incident wave fronts  $W_p$  and  $W_s$  would be same. Thus, for a good-quality TO,  $[W_p]$  is practically the same as  $[W_s]$ . Hence, the surface form measurement is not affected by the instrumental aberration and the function of the FI is similar to that of an on-axis one for all practical purposes.

Nevertheless, it is possible to eliminate the effect of any residual aberration. The test surface is tilted by  $(-\beta)$  so as to retrace back the incoming p waves as shown in Fig. 10.7.  $W_{tp}$  is made parallel to  $W_{rs}$  and the OPD between the interfering waves can be written as

$$\Delta_2 = [W_{tp}] - [W_{rs}] \quad (10.13)$$

**Fig. 10.7** Incident and Fresnel-reflected wave fronts. Relative positions of the focal spots are shown in the inset



where  $[W_{tp}] = [W_p] + [2W_t]$  and  $[W_{rs}] = [W_s] + [2W_r]$  and we get

$$\Delta_2 = 2 \{[W_t] - [W_r]\} - \{[W_s] - [W_p]\} \quad (10.14)$$

The optical path difference between test surface and reference plate is given by

$$\begin{aligned} \Delta &= [W_t] - [W_r] \\ &= \frac{(\Delta_1 + \Delta_2)}{4} \quad (\text{from Eqs. 10.12 and 10.14}) \end{aligned} \quad (10.15)$$

Thus, by measuring  $\Delta_1$  and  $\Delta_2$  and by applying PSI,  $\Delta$  can be obtained from Eq. (10.15).

## 10.5 Surface Micro-roughness

Surface micro-roughness is the topographic relief of a surface and corresponds to surface height variations relating to small spatial wavelengths. Primarily, scattering of light occurs due to surface micro-roughness. To reduce scatter the optical surface must be smooth, i.e., must have low surface micro-roughness relative to the wavelength of incident light. Interference microscopes based on Michelson, Mirau,

and Linnik configurations are commonly used. Each configuration has its useful range of magnifications. Two-dimensional CCD detector arrays are commonly used for capturing multiple interferograms, which are processed using phase-shifting interferometry to obtain surface profile and surface micro-roughness of the optical surface. Phase shifts are commonly applied by using a PZT. It is evident that the higher rate of sampling, i.e., small lateral sampling interval, which is given by the ratio of the spacing between the detector pixels and microscope objective magnification, is obtained due to magnification of the microscope objective. The diffraction-limited optical resolution is however given by  $0.61\lambda/NA$ , where NA is the numerical aperture of the microscope objective while the height resolution primarily depends on the large dynamic range of the detector.

## 10.6 Phase Calculations

To determine surface form error or surface micro-roughness by PSI [6–8], a series of interferograms are captured as the phase difference between the interfering components is changed, in steps, by a constant amount. The intensity at a point  $(x, y)$  in the interference field can be written as

$$I(x, y) = I_0(x, y) \{1 + V(x, y) \cos [\phi(x, y) + \alpha_j]\} \quad (10.16)$$

where  $I_0(x, y)$ ,  $V(x, y)$ ,  $\phi(x, y)$  are the mean intensity, fringe visibility, and original phase difference between the two interfering beams at the point  $(x, y)$ , respectively, and  $\alpha_j = (j - 1)\alpha$ , with  $j = 1, 2, 3, \dots$  and  $0 < \alpha < \pi$  represent phase shift between the adjacent frames. We have used an algorithm which uses five different values of intensity,  $I_1, I_2, I_3, I_4, I_5$  corresponding to  $j = 1, 2, 3, 4, 5$  and  $\alpha = \pi/2$  and  $\phi$  is given by

$$\phi = \text{arc tan} [2(I_4 - I_2) / (I_1 + I_5 - 2I_3)] \quad (10.17)$$

For an error  $\varepsilon$  in phase shift (so that  $\alpha = \pi/2 + \varepsilon$ , where  $\varepsilon$  is a small quantity), the error in  $\phi$  is given by

$$\Delta\phi = (\varepsilon^2/4) \sin 2\phi \quad (10.18)$$

which shows the insensitivity of this algorithm to phase shift miscalibration-type system error.

Taking absolute values of numerator and denominator of Eq. (10.17),  $\phi$  is first calculated in modulo  $\pi/2$ , and then comparing signs of  $\sin \phi$  and  $\cos \phi$  (Ref. [2], p. 366),  $\phi$  is transformed to modulo  $2\pi$ .

The calculated phases are wrapped and unwrapping/phase integration is performed by comparing the phase difference between adjacent pixels. Unwrapped phase values are least-squares fitted and deviation from a reference plane

is obtained. Phase variations are converted to optical path variations by using the following relation:

$$\delta = (\lambda/4\pi) \phi \quad (10.19)$$

where  $\delta$  and  $\lambda$  represent optical path length and wavelength of light, respectively.

**Acknowledgment** I thank Pavan Kumar for careful reading of the manuscript and Rishipal for drawing of the figures.

## References

1. M.V. Mantravadi, D. Malacara, Newton, Fizeau and Haidinger interferometers, in *Optical Shop Testing*, ed. by D. Malacara (New Jersey, USA, 2007), pp. 17–32
2. K. Creath, Phase measurement interferometry techniques, in *Progress in Optics*, ed. by E. Wolf, vol. xxviii (North-Holland, Amsterdam, 1988), pp. 349–393
3. J. Schwider, Advanced evaluation technique in interferometry, in *Progress in Optics*, ed. by E. Wolf, vol. xxviii (North-Holland, Amsterdam, 1990), pp. 271–359
4. J.E. Greivenk, J.H. Bruning, Phase shifting interferometry, in *Optical Shop Testing*, ed. by D. Malacara (New Jersey, USA, 2007), pp. 506–655
5. C. Ai, J.C. Wyant, Effect of Piezo-electric transducer non-linearity on phase shift interferometer. *Appl. Opt.* **26**, 1112–1116 (1987)
6. S. Chatterjee, Measurement of surface figure of plane optical surfaces using Fizeau interferometer with wedge phase shifter. *Opt. Laser Technol.* **37**(01), 43–49 (2005)
7. S. Chatterjee, Y. Pawan Kumar, B. Bhaduri, Measurement of surface figure of plane optical surfaces with polarization phase-shifting Fizeau interferometer. *Opt. Laser Technol.* **39**(2), 268–274 (2007)
8. S. Chatterjee, Y. Pawan Kumar, Polarization phase shifting Fizeau interferometer with a cyclic path optical configuration, *Opt. Eng.* **48**(11), 115601(1–6) (2009)

# Chapter 11

## High-Resolution Spectroscopy

B.M. Suri

**Abstract** Classical high-resolution spectroscopy had been of interest for the sake of studies related to isotope shifts and hyperfine interactions and for resolving complex spectra associated with heavy elements like lanthanides and actinides. In this chapter, some of the history of classical high-resolution spectroscopy has been described. The highest-resolution laser spectroscopy is usually performed with CW lasers which have inherent ultra-narrow linewidths. Pulsed dye lasers though have relatively large linewidth because of Fourier transform limit but can still be usefully employed for multicolor laser spectroscopy of various elements with complex spectra. We have demonstrated the utility of pulsed dye lasers for studying lanthanides and actinides by employing techniques like multicolor optogalvanic spectroscopy in hollow cathode discharges, multicolor laser-induced fluorescence, and resonance ionization spectroscopy in atomic beams. We have for the first time utilized ICCD-based spectrograph for some of the measurements. These techniques have yielded excellent new information on atomic parameters like radiative lifetimes, branching ratios, and absolute transition probabilities of singly or multiply excited atomic levels. These techniques have inherent simplicity and may offer themselves as excellent alternative to conventional techniques and have universal applications of interest to wide cross section of atomic spectroscopists.

**Keywords** Laser spectroscopy • Sub-Doppler spectroscopy • Atomic parameters • Saturation spectroscopy • Optogalvanic spectroscopy

### 11.1 Introduction

Spectroscopy is a classical subject dealing with the interaction of matter and radiation. This was born with the help of dispersive optics developed few centuries earlier. The first serious impact in this subject was made by Kirchhoff by the study of solar spectra and its relation to abundance of few elements in the Sun. This got a

---

B.M. Suri (✉)

Laser & Plasma Technology Division, BARC, Mumbai, India

e-mail: [prof.bmsuri@gmail.com](mailto:prof.bmsuri@gmail.com)

major fillip in the early part of the last century when quantum mechanics explained in greater details the linkage between atomic structure and observed spectra. Since then, it has been a parallel march of refined theories of atomic structure and interactions on the one hand and development of more sophisticated spectrographs on the other. A revolutionary change happened around the 1970s when the first tunable laser was developed. Orders of magnitude higher spectral intensity and reduction in linewidth of light source became possible, and it enabled the study of successively finer details of atomic, molecular, and nuclear interactions. More importantly, it changed the scenario with respect to applications of this subject. In its infancy the applications were mainly related to astrophysics graduating to spectrochemical analysis. Laser spectroscopy on the other hand diversified and expanded these applications on a much wider canvas making use of distinctive characteristics of tunable lasers. For example, laser isotope separation, ultra-trace analysis, remote and range resolved pollution measurements, and laser spectroscopy of short-lived isotopes in accelerators were among a new range of applications.

Classical spectroscopic techniques of emission and absorption in various atomic and molecular media require appropriate light sources, analyzing instruments like spectrographs and recording or detection instruments. Depending upon the species to be studied, these sources cover spectral region ranging from far infrared to vacuum ultraviolet. Some of these are spectral line sources or are continuum – depending upon which these are utilized for different purposes. These sources are used for studying spectra of chosen species or used as wavelength standards covering different spectral regions or used as intensity standards. These sources are characterized by their intensity, excitation width, and spectral range whether discrete or continuum and whether in equilibrium or not. For example, combustion flames with temperature around 2,000 K are used for the study of radical species, while discharge arcs with temperature around 5,000 K generate neutral as well as ionic lines. Sparks can generate higher ionization stages up to  $10^+$  states. Laser-induced plasmas are known to generate species up to  $40^+$ , while specialized plasma sources can generate much higher degree of ionization. Normal and abnormal glow discharge conditions like hollow cathode discharge lamps and electrode less discharge lamps excited by microwaves have been used for higher-resolution (because of smaller excitation width achievable) spectroscopy and spectroscopy of radioactive species (because of small amount of sample required and good containment), respectively. There are specialized light sources like Nernst glower for spectral range in infrared ( $>10 \mu\text{m}$ ). For VUV also rare gas discharges as windowless radiation sources are employed in vacuum environment covering region up to about 60 nm.

## 11.2 High-Resolution Spectroscopy

Dispersion of absorbed or emitted light, using prism-based instruments, is employed for analyzing spectra. Prism-based instruments are limited in spectral region to be covered because of limitations of transmission through the prism material.

Also resolving power attainable is quite small even with largest prisms possible. These are used nowadays very sparsely – mainly as pre-dispersers for main instruments. Most of the present-day spectrographs and monochromators use gratings as dispersive elements. Resolving power as high as few hundred thousand is achievable using specialized configurations. For modern-day high-resolution monochromators, holographic gratings are employed with attendant advantages like low costs, avoidance of ghosts etc. These grating-based instruments which, in their earlier versions, are called spectrographs employed photographic plates with smaller emulsion grains for achieving high resolution. Same instruments with photoelectric instruments like photomultiplier tubes are called monochromators. By using PMTs of different photocathodes, large spectral range can be covered. These instruments are wavelength scanning type and involve turning the grating at slow speed to cover different spectral regions at high resolution. These instruments have been supplemented, in some cases overtaken, by a new range of detectors called charge-coupled detectors. Depending upon the size of these detectors and spectrographs of matching lateral dispersion, large spectral regions can be covered in a very short time. But this is often at cost of achievable resolution for the case of conventional grating-based instruments. This is because of combined requirements of high resolution and wider spectral region to be covered which calls for a different kind of spectrograph and large-size CCD detector. Echelle grating-based spectrographs are best answers to such problems. Normally, these are operated in much higher order and several orders are detected to infer about a specific spectrum. This way, wide spectral region can be covered at moderately high resolution – as this still cannot compete with conventional spectrometer (of best attained resolving power). This problem of higher resolving power together with wider spectral region is solved in a different way by employing a kind of interferometer to be described later.

Gratings are employed in monochromators or spectrographs in different mountings depending upon the application like requiring higher resolution or wider spectral region to be covered or even type of detector (PMT or CCD or photographic plate) to be employed. There are several features which distinguish different monochromators like resolving power, linear or angular dispersion, free spectral range, diffraction order being employed, etc. Resolving power indicates the extent to which two close-by spectral lines can be distinguished from one another. This is proportional to the diffraction order employed (normally first order) and the total number of rulings illuminated:

$$\text{Resolving power : } R = nN$$

$$\text{Angular dispersion : } \frac{d\theta}{d\lambda} = \frac{n}{d \cos \theta}$$

where  $n$  is the diffraction order and  $N$  is the total number of lines and  $d$  is the groove spacing of grating of total width  $W$ . For conventional grating monochromator, resolution limit in  $\text{cm}^{-1}$  is of the order of inverse of grating width in cm ( $\sim 1/2 W$ ). But practical limits are many times dictated by how large a grating can be ruled

finely, minimum slit widths that can be employed or various aberrations in optics, etc. Typically, 1,200–2,400 lines/mm are employed and resolving power of few hundred thousand can be achieved. From the above equation, it can be seen that resolving power is the same for fine ruling and low order combination as it is for coarse ruling and higher order combination. It is this latter concept which is employed in what is called echelle grating where typical diffraction order is  $n \sim 100$  and total number of lines  $N = 10,000$  with width  $W$  of grating about 25 cm. This enables attaining in principle resolving power about  $10^6$ . This restricts the free spectral range which is inversely proportional to the diffraction order employed or grating element width. Because of this, a pre-disperser like prism spectrograph has to be employed to separate out spectral output of different orders. Also final spectrum is reconstructed from combining spectral output from several orders. This way, large spectral range can be covered with high resolution. This spectrometer is becoming popular nowadays in conjunction with CCD cameras and computers for smooth reconstruction of actual spectrum.

All types of grating spectrometers still have certain limitations in achieving resolution required for studying isotope effects like isotope shifts and hyperfine structure or study of lineshape effects. Different types of interferometers have proved very effective for attaining high resolution. For example, Fabry-Perot (FP) interferometers which employ orders 10–1,000 times that of echelle gratings are capable of resolution  $\sim 10^7$ . In this case, also free spectral range is inversely proportional to thickness of interferometer. For a 10 cm thick FP, resolving power  $10^7$  is achieved with FSR  $\sim 0.05 \text{ cm}^{-1}$ . This again requires the use of pre-dispersers like prisms. For high-resolution spectroscopy, FP interferometer is employed in different ways – either by having a fixed spacer and linearly varying pressure in airtight chamber containing FP interferometer or by changing spacer thickness using piezoelectric transducers (PZTs). In the present-day versions, mostly photoelectric recording is employed which uses a circular aperture close to central fringe system. Figure 11.1 shows an example of how FP interferometer can be

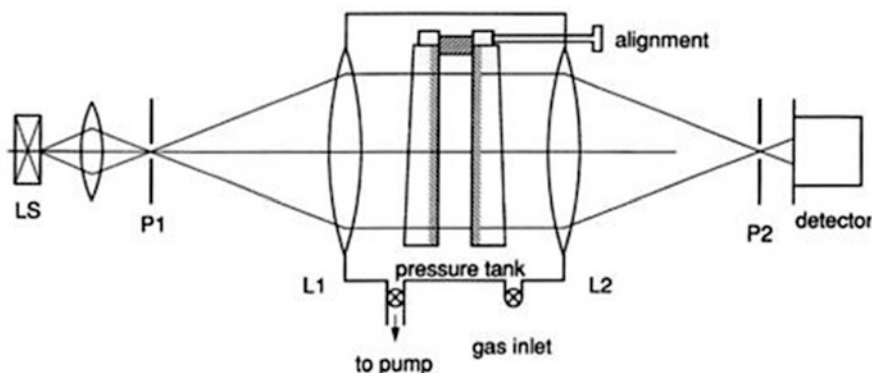


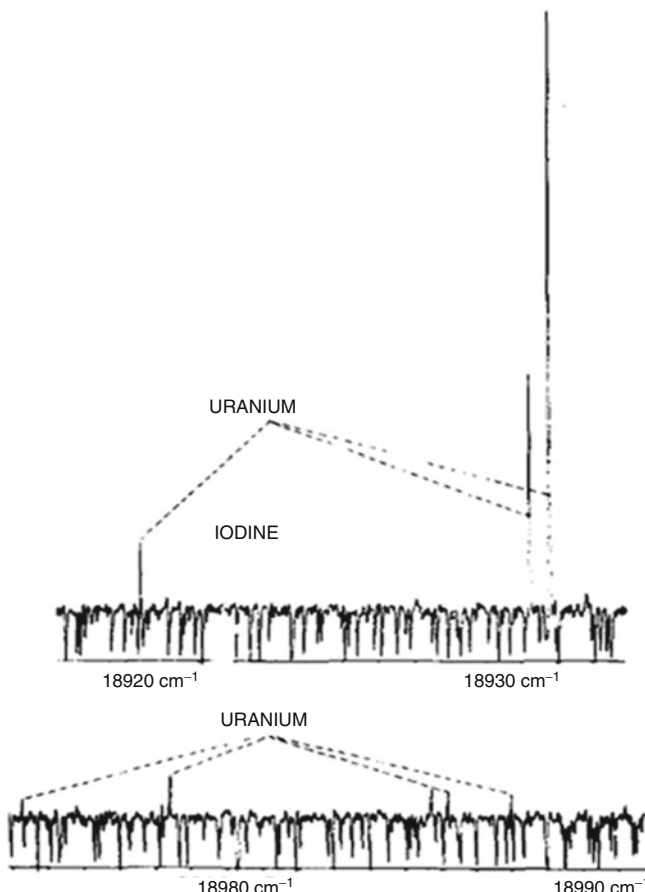
**Fig. 11.1** Use of plane FP interferometer for photoelectric recording of spectrally resolved light

used for high-resolution spectroscopy. This schematic illustrates how light from a discreet spectral light source, of linewidth smaller than free spectral range of FP interferometer, is incident on a pressure-scanned FP etalon and fringes formed yield high-resolution spectra as pressure scanning is directly related to wavelength scanning.

### 11.3 Complex Spectra and High-Resolution Spectroscopy

As one moves up the ladder of periodic table, starting from simplest case of hydrogen spectrum, complexities grow. There are various reasons for this. First of all, the interactions like spin orbit interaction and hyperfine interaction between electronic and nuclear spins increase as the atomic number Z increases. This causes mingling of features from different states and interpretation of spectra becomes difficult. Also higher orbital angular momenta shells are progressively filled with electrons. Some of them are highly degenerate and a large number of electronic states arise for these elements. Quite often an open s, p, or d shell accompanies f shell – making the spectrum even more complicated. Most of the elements have more than one isotope – some of them up to about a dozen of them; each isotope generating its own spectra. Additionally, odd isotopes have hyperfine structure. Ground states of many elements are multiplets, and thus, many close low-lying levels exist and are reasonably well populated as per Boltzmann distribution. All these reasons and some more lead to complex spectra in classical spectroscopic techniques of absorption and emission. Despite the large database existing on spectra of many of these elements, major deficit of information existed as per predictions of atomic structure calculations, particularly for highly excited states both below and above continuum. This calls for extra efforts on part of experimental spectroscopists to employ specialized techniques and generate relevant data and its analysis.

Similar to atomic spectroscopy, molecular spectra also can be quite complex. The origin of complexity is related to degrees of freedom of constituent atoms of the molecules. Electronic state of even a simplest molecule like diatomic molecule has several vibrational states, and furthermore, each vibrational state has several rotational states. These levels are populated as per Boltzmann distribution. This leads to complexity in the spectra. Some of the complexities of these atomic and molecular spectra are quite nicely illustrated in the case of uranium atom and iodine molecule. Uranium atom has  $f^3ds^2$  electrons in the outermost shell of the ground state. This gives rise to high density of spectral lines in emission spectrum. Iodine molecule is a diatomic molecule with high atomic mass of constituent atoms, large moment of inertia, and large rotational constant, and consequently it has high density of rovibrational levels. Figure 11.2 shows iodine absorption spectrum in a room temperature cell juxtaposed against uranium emission spectrum. Much higher density of lines in iodine spectrum is evident. These spectra are recorded using high-resolution Fourier transform spectrometer (FTS).



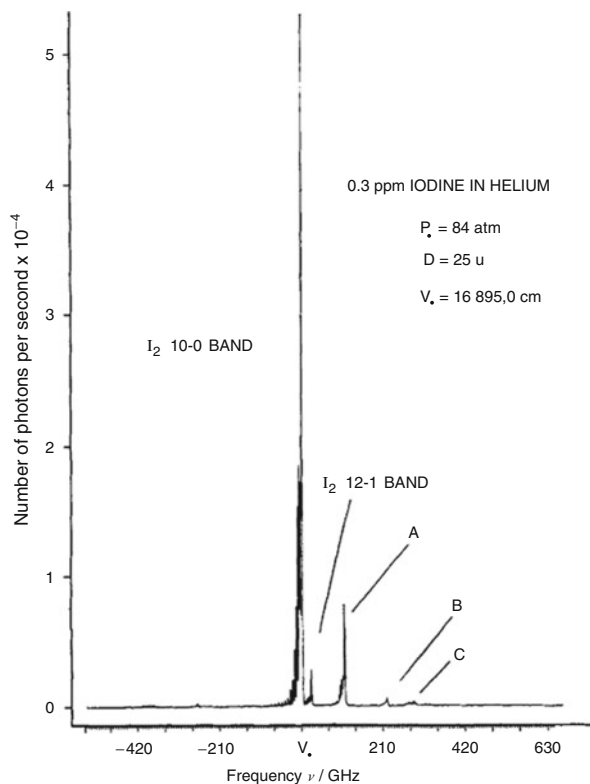
**Fig. 11.2** Portion of iodine absorption spectrum compared against uranium emission spectrum in same region (considered very dense atomic spectrum)

Figure 11.3 shows the spectra from cooled molecular beam of iodine mixed with helium; as can be seen, much higher resolution becomes possible (explained later). Figure 11.4 shows still finer resolution attained by using laser-induced fluorescence using tunable dye laser and cooled molecular beam – these spectra are able to resolve hyperfine components.

## 11.4 Laser Spectroscopy

High-resolution spectroscopy was revolutionized with the advent of tunable lasers. These light sources seemed to fulfill the dream of spectroscopists because of their certain distinctive characteristics. These lasers have much higher power, much

**Fig. 11.3** Portion of absorption spectrum of iodine and helium mixed in supersonic cooled molecular beam ( $A, B, C$  are features due to iodine helium complex)



**Fig. 11.4** Hyperfine structure of one transition  $X, v'', J''$  to  $B, v', J'$  with lower calibration spectrum with molecular beam excited by single-mode tunable dye laser

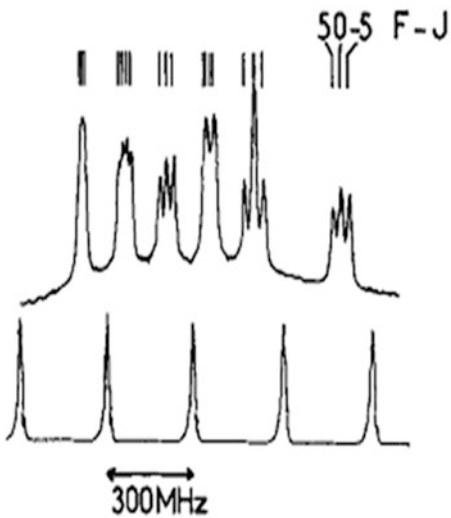


**Table 11.1** Comparison between spectroscopic uses of conventional light source and single-mode dye laser

	Conventional light source (RF discharge lamp)	Continuous single-mode dye laser
Linewidth	1,000 MHz	1 MHz
Total output of line	$10^{-1}$ W	$10^{-1}$ W
Power within a useful solid angle	$10^{-2}$ W	$10^{-1}$ W
Irradiated area (depends on focusing)	$10 \text{ cm}^2$	$10^{-4} \text{ cm}^2$
$I(v)$ power density per unit frequency	$10^{-6} \text{ W}/(\text{cm}^2 \cdot \text{MHz})$	$10^3 \text{ W}/(\text{cm}^2 \cdot \text{MHz})$

narrower linewidth, wide spectral bandwidth, low divergence, and high focusability compared to conventional spectroscopic light sources. Together, all of these features have great impact in addressing issues related to high-resolution spectroscopy among others. Table 11.1 makes comparison between conventional light source like a discharge lamp and a tunable laser of equivalent power. As can be seen, the advantages in terms of sensitivity and specificity are very high. These features have to be viewed together with additional enabling possibilities like multiphoton spectroscopy, Doppler-free spectroscopy, resonance ionization spectroscopy, and advanced spectroscopic instrumentation for deriving maximum benefits for high-resolution spectroscopy with high sensitivity.

Laser spectroscopy distinguishes itself from classical spectroscopy in many ways. One of them is the type of media which can be addressed or it can probe. Accordingly, a wide range of new possibilities have emerged yielding new information and new physics. Figure 11.5 indicates a variety of tunable lasers and sample (or media) together with the type of studies which have become possible. On the one hand, extremely high spectral resolution is enabled with CW tunable lasers, and on the other hand, superfine dynamic effects have been explored using up to femtosecond lasers. It may be worthwhile to recall comparative advantages of laser spectroscopy over that of classical – even though the latter has made some advances of its own. In classical spectroscopy, spectral resolution attainable is limited by dispersing spectrometers, but modern-day FTS are still of great value and high resolution up to about  $0.001 \text{ cm}^{-1}$  or more is achievable. In the case of laser spectroscopy, tunable lasers with narrow linewidth are available from IR to UV enabling a wide range of spectroscopic applications.

Normally, monochromators are not essential in laser spectroscopy experiments. High spectral resolution of about 1 MHZ is possible using CW tunable lasers and even more can be possible using specialized techniques. Detection sensitivity is limited by detector noise and high spectral power density takes care of the same. Because of low divergence of lasers, good collimation and long path traversal enables long path length low-pressure absorption cells facilitating higher sensitivity and spectral resolution. Combining with techniques of intracavity absorption and cavity ringdown, absorption as small as  $10^{-10}/\text{cm}$  is achievable. Pulsed tunable lasers can be employed for the study of short-lived species, radicals, etc. This school

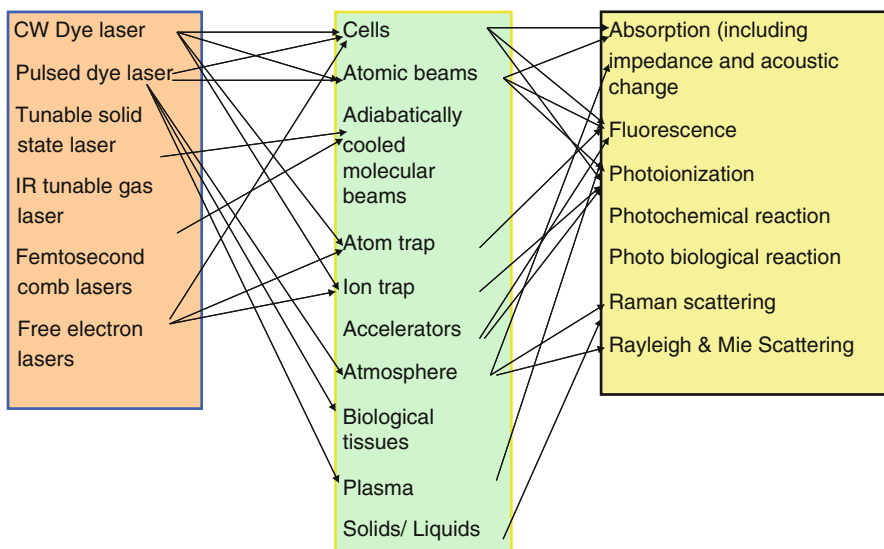


**Fig. 11.5** Different types of tunable lasers, media, and interactions possible

has addressed many such facets of laser spectroscopy. In this presentation, I briefly describe below how laser spectroscopic techniques help improve resolution and facilitate simplification and thus interpretation of complex spectra. I also illustrate the use of pulsed (nanosecond) dye lasers for generating useful spectroscopic information related to lanthanides and actinides, enabling better understanding of these complex spectra. This work has been carried out in our lab at BARC.

## 11.5 Spectral Line Broadening

From Heisenberg's uncertainty principle, the electron in an excited state is only there for a short time so energy cannot have precise value. This leads to what is called natural broadening of energy levels. Profile of naturally broadened line is given by a dispersion profile (also called damping profile or Lorentzian profile). Typical FWHM of these profiles are related as inverse of radiative lifetime and are of the order of a few MHz. But in most practical situations, one cannot do spectroscopy with this much resolution because of various line broadening mechanisms. One of the most prevalent among gaseous samples is what is called Doppler broadening. This arises because molecules in gaseous samples are in constant random motion with Maxwellian distribution of velocities. As per Doppler effect, spectral frequency absorbed by these molecules is shifted depending upon their velocities.

Combining Doppler shifts of all molecule and Maxwellian distribution of these molecules, one obtains thermal broadening line profile given by

$$\frac{I_v}{I_{\text{total}}} = \frac{c}{v} \sqrt{\frac{m}{2\pi kT}} \exp\left(-\frac{mc^2(v - v_0)^2}{2v^2kT}\right)$$

Where spectral absorption line reaches half its depth, the total spectral width FWHM  $\Delta\omega_D$  is given by

$$\begin{aligned} &= 2\sqrt{\ln 2}\omega_0 \frac{v_p}{c} \\ &= \frac{\omega_0}{c} \sqrt{\frac{8kT \ln 2}{m}} \\ &= 7.76 \times 10^{-7} v_0 \sqrt{\frac{T}{m}} \end{aligned}$$

where  $T$  is the temperature in K and  $m$  is the mass in atomic units and Doppler width in MHz. Many laser spectroscopic techniques have been developed mainly to address this particular broadening and beat this limit on resolution attained. Briefly some of these techniques are described below.

## 11.6 Saturation Spectroscopy

This is based on the principle that Doppler broadening is inhomogeneous as far as molecules of different velocities are concerned. Figure 11.6 shows excitation/absorption profile  $\alpha(\omega)$  caused by laser  $(\omega_1, k_1)$ , also called pump laser, under different excitation conditions and Lamb dip arises in inhomogenous spectral line profile. This population distribution is probed by a second weak laser  $\omega'$ . This pump laser is said to burn a hole in this population distribution. Spectral width of this hole is arising due to natural homogeneous width and width caused by saturation effect of this transition (selected velocity group). As can be seen, this width is much smaller than inhomogeneous Doppler-broadened width.

As we tune probe laser close to the peak of this Doppler profile, only homogeneous profile dip remains and this dip is called Lamb dip. Now if there are two different close-by energy levels being studied by saturated absorption spectroscopy, both broadened by Doppler broadening, then even though they were not resolvable because of their Doppler broadening in normal absorption spectroscopy, these can now be resolved when individual Lamb dips are well separated as can be seen in Fig. 11.7.

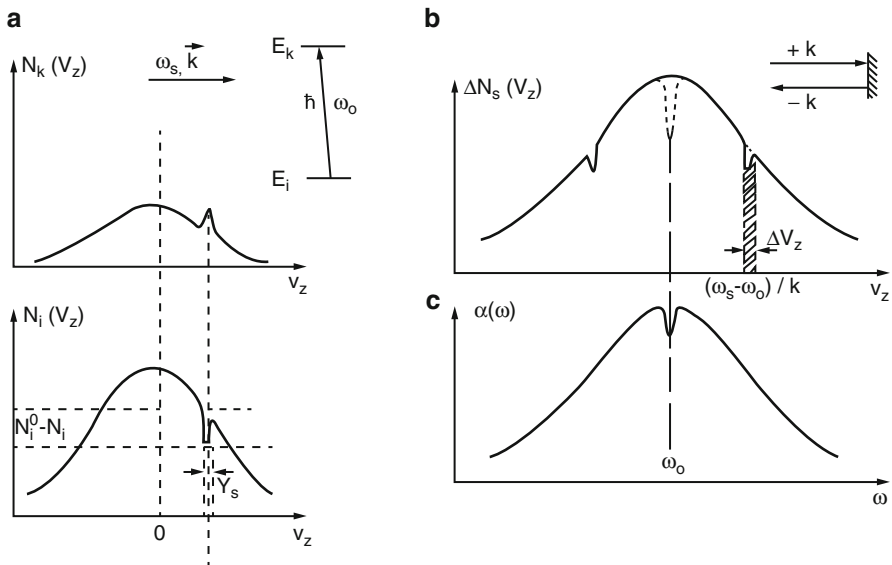


**Fig. 11.6** Saturation of an inhomogeneous line profile. (a) Bennett hole and dip produced by a monochromatic running wave with  $\omega + \omega_0$ . (b) Bennett holes caused by the two counterpropagating waves for  $\omega$  not equal to  $\omega_0$  and for  $\omega + \omega_0$ . (c) Lamb dip in the absorption profile  $\alpha(\omega)$

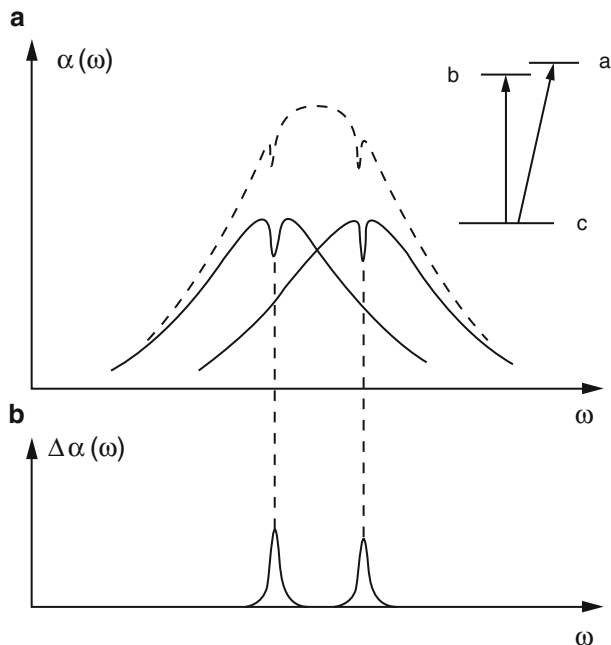


**Fig. 11.7** Spectral resolution of the Lamb dips of two transitions with overlapping Doppler profiles

## 11.7 Two-Photon Transitions

Two-photon transitions as a possibility were predicted much before lasers came on the scene but became realizable in various manifestations only using lasers, as shown in Fig. 11.8.

The first scheme shows two-photon transition with a real intermediate state, the second one is with what is called a virtual intermediate state, and the third and fourth schemes show Raman excitation schemes which are also part of family of two-photon processes. The following equation is the transition probability of two-photon transition:

$$A_{if} \propto \frac{\gamma_{if} I_1 I_2}{[\omega_{if} - \omega_1 - \omega_2 - v(k_1 + k_2)]^2 + (\gamma_{if}/2)^2} \cdot \left[ \sum_k \frac{R_{ik} \cdot e_1 \cdot R_{kf} \cdot e_2}{(\omega_{if} - \omega_1 - v k_1)} + \frac{R_{ik} \cdot e_2 \cdot R_{kf} \cdot e_1}{\omega_{if} - \omega_2 - v k_2} \right]^2$$

where  $I_s$  are the intensities,  $\omega$ 's are the frequencies, and  $k$ 's are the propagation vectors. The term outside parenthesis is related to lineshape and within parentheses is transition probability. Integration over all molecular velocities gives Voigt profile with half-width proportional to  $k_1 + k_2$ . If the beams are copropagating, then it is maximum and for counterpropagating case cancellation reduces the linewidth – it is Lorentzian with half-width ( $\gamma_{if}$ ). As per resonance condition, all molecules absorb at the sum of two-photon frequencies independent of their velocities (and absorption frequencies). This is distinctive from the case of saturation spectroscopy. Thus, resolution is improved, but sensitivity is not lost. Some of the additional features are related to the type of selection rules operative and polarization effects. Selection rules are governed by transition matrix elements between initial and

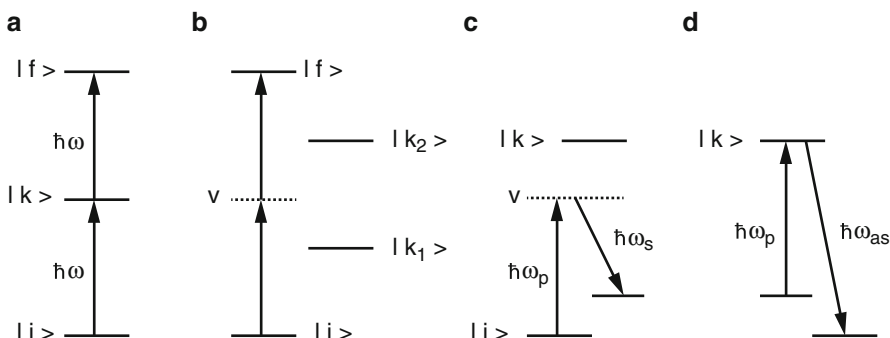


**Fig. 11.8** Level schemes of different two-photon transitions: (a) resonant two-photon absorption with real intermediate level, (b) nonresonant two-photon absorption, (c) Raman transition, and (d) resonant anti-Stokes Raman scattering

intermediate and intermediate and final states, and as a consequence, s-s and s-d transitions become allowed. Generalized absorption profile is the sum of a Doppler-broadened part and a Lorentzian part of FWHM  $\nu_{if} = \nu_i + \nu_f$ . Area under Doppler part is half of that under Lorentzian, but peaks are as per ratio  $\nu_{if}/2\Delta\nu_d$ . For a typical case, Doppler width is 2 GHz and Lorentzian is 20 MHz. Thus, the ratio of Doppler-free part to Doppler-broadened part is about 200. All these features bring out distinctive advantages of two-photon spectroscopy for high-resolution purposes, along with several other advantages like the study of different parity states, higher sensitivity, etc.

## 11.8 Collimated Molecular Beams

This method of achieving high resolution is quite often employed for the measurement of isotope shifts and also hyperfine structure. This is based on the principle that there is a selection of small directed group of molecules which are made to interact from among all the molecules present in a sample cell. In the hot zone of an oven, molecules are distributed as per Maxwellian distribution of velocities. Molecules are allowed to effuse out of a small hole toward a laser interaction zone. At some distance from this hole is a collimating aperture. Because of restricted group of velocities, FWHM of laser atom interaction linewidth is reduced by a factor proportional to the size of the aperture and inversely proportional to the distance from the aperture to collimator. This arises from the ratio of velocity components proportional to transverse and axial directions. This is depicted in Fig. 11.9. As an example case, for aperture size 1 mm and distance between aperture and collimator of 10 cm, the reduction in Doppler width is by a factor of 200. This must be remembered that because of smaller number of interacting molecules, signal strength goes down and more sensitive detection system has to be employed. These techniques have also been successfully employed for laser isotope separation as well.

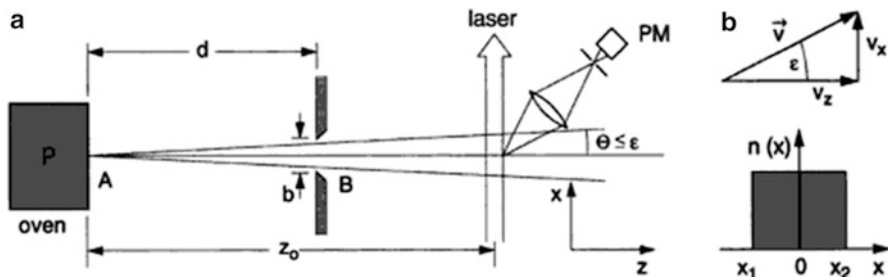


**Fig. 11.9** Laser excitation spectroscopy with reduced Doppler width in a collimated molecular beam: (a) schematic experimental arrangement and (b) collimation ratio and density profile  $n(x)$  in a collimated beam effusing from a point source A

## 11.9 Supersonic Molecular Beams

These are molecular beams where mean free path is much less than the effusive hole diameter. Supersonic molecular beam generation becomes possible by the use of high density of molecules expanding from a reservoir into a vacuum chamber. Most of the initial internal energy is converted to flow energy and final internal energy being reduced; this is called a cooled molecular beam. This expanding gas is governed by modified Maxwellian distribution which is centered around acquired flow velocity. This is shown in Fig. 11.10. This expanding gas has molecules of different velocities and their efficient collisions facilitate energy transfer and cooling process. This has great consequences for simplification of complex molecular spectra. This cooling of molecular beam reduces internal vibrational and rotational energy. Reduction of rotational temperature is achieved with noble gases, while gases like nitrogen are used for vibrational cooling. These cooled beams have only lower J and v states populated while higher J and v states are not populated; rotational temperature up to 1 K has been experimentally demonstrated. This new population distribution results in great simplification of spectra. Figure 11.11 shows an example of simplification of molecular spectra using supersonic beams. These techniques have been successfully employed for resolving complex molecular spectra like that of uranium hexafluoride. Combining cooled molecular beams with tunable single-mode lasers, best resolution results are achieved.

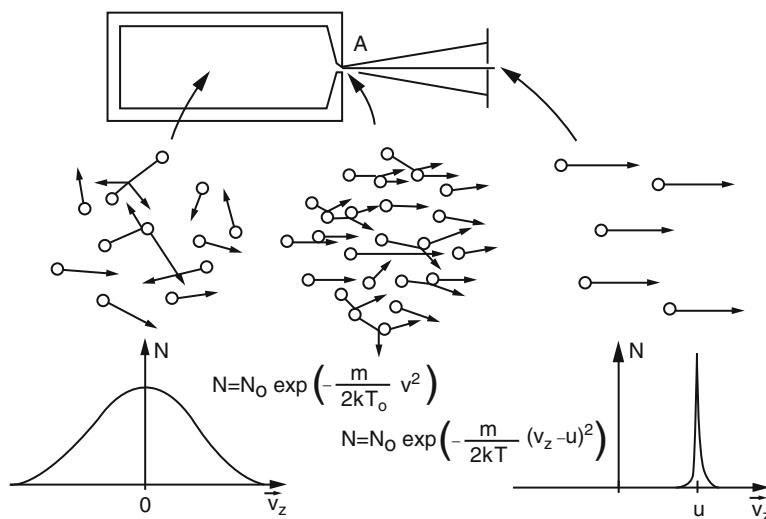
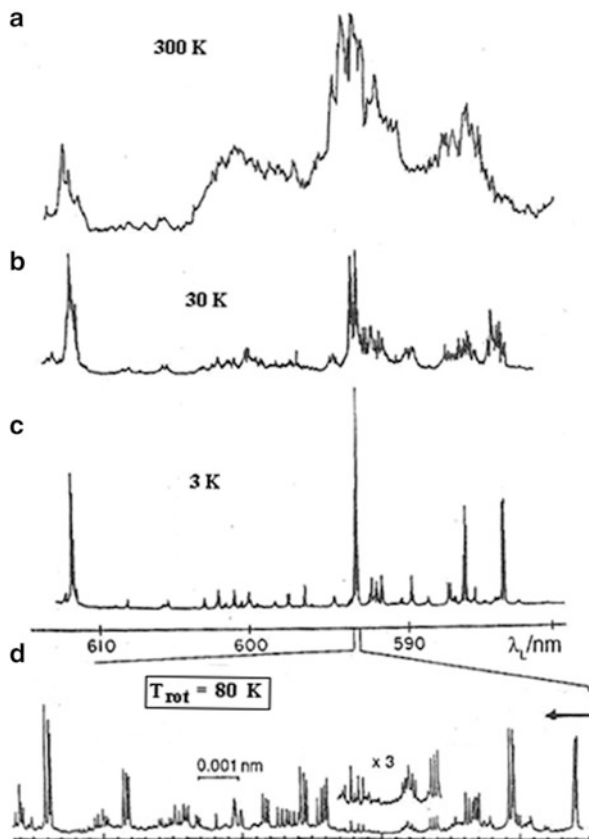


**Fig. 11.10** Molecular model of adiabatic cooling by collisions during the expansion from a reservoir with Maxwellian distribution into the directed molecular flow with a narrow distribution around the flow velocity  $u$

**Fig. 11.11** Section of excitation spectrum of NO<sub>2</sub> obtained under (a) in vapor cell at  $T = 300$  K at 0.05 mbar, (b) in pure NO<sub>2</sub> beam at  $T_{\text{rot}} = 30$  K, and (c) in a supersonic argon beam seeded with 5 % NO<sub>2</sub> at  $T_{\text{rot}} = 3$  K. (a–c) excited with dye laser of 0.05 nm bandwidth. (d) A section recorded with 1 MHz dye laser



## 11.10 High-Resolution Spectroscopy in Fast Beams

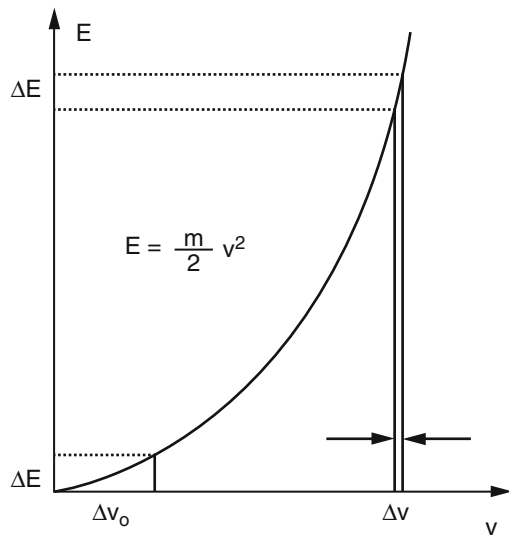
Limitation of transverse velocity components by apertures reduces Doppler width, and resolution in a laser spectroscopy experiment can be improved, as described above; this is called geometric cooling. There is another means to manipulate longitudinal velocity components, and this makes use of high accelerating field. In this case, laser beam traverses collinearly to accelerated ion beams and velocity distribution is narrowed down. This is based on the principle that thermal velocities and electric field-induced velocities do not get added but corresponding energies get added. Also thermal energy is much less than electrical energy, since ion beams are accelerated by several tens of kilovolts. This implies the final velocity spread (after acceleration) is much less than the initial velocity spread, as can be seen from the following equation, and how it comes about is also indicated in Fig. 11.12 below.

Final velocity spread  $\Delta v$  is given by

$$\Delta v = \Delta v_0 \sqrt{\frac{E_{\text{th}}}{eU}}$$

$$E_{\text{th}} \ll eU \Rightarrow \Delta v \ll \Delta v_0$$

**Fig. 11.12** Principle of acceleration cooling



where  $\Delta v_0$  is the initial velocity spread,  $E_{\text{th}}$  is the thermal energy, and  $U$  is the accelerating potential. This reduced and controllable velocity spread has consequences for high-resolution spectroscopy. First of all, accelerated ion beams are directly amenable to collinear laser spectroscopy. Additionally, by making these ion beams interact in a charge exchange cell, fast neutral beams can be generated in turn making them also amenable to similar resolution improvements. An indirect consequence is even high-power fixed wavelength lasers can be used for excitation along with voltage tuning, thus improving simplicity as well as sensitivity of the technique. This technique has been well exploited for studying isotopic effects in short-lived isotopes using accelerators [1].

## 11.11 Multiphoton Spectroscopy of Lanthanides and Actinides

Most of the atoms in periodic table have excitation/ionization potentials in the range of 2–9 eV. The present-day tunable lasers (both CW and pulsed) can cover spectral region from 2 to 4 eV. Thus, combining two- and three-photon excitation and using a variety of excitation/ionization schemes, most of the elements, or rather isotopes, can be efficiently and state selectively photoexcited (or photoionized). Figure 11.13 shows an example of different possible photoexcitation/photoionization schemes.

For the sake of experimental reasons and efficiency of photoionization scheme, copper vapor laser-pumped dye lasers are used and a large range of elements can be covered. Some of the example cases of efficient photoionization schemes optimized for several elements are shown in Fig. 11.14. Lanthanides and actinides are very

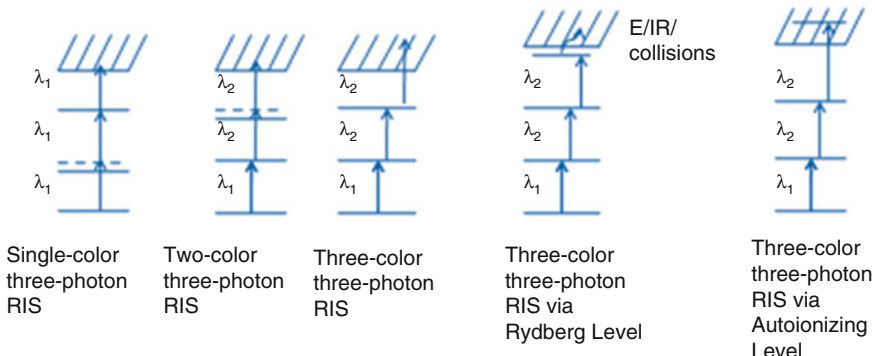


**Fig. 11.13** Different variations of resonance ionization schemes

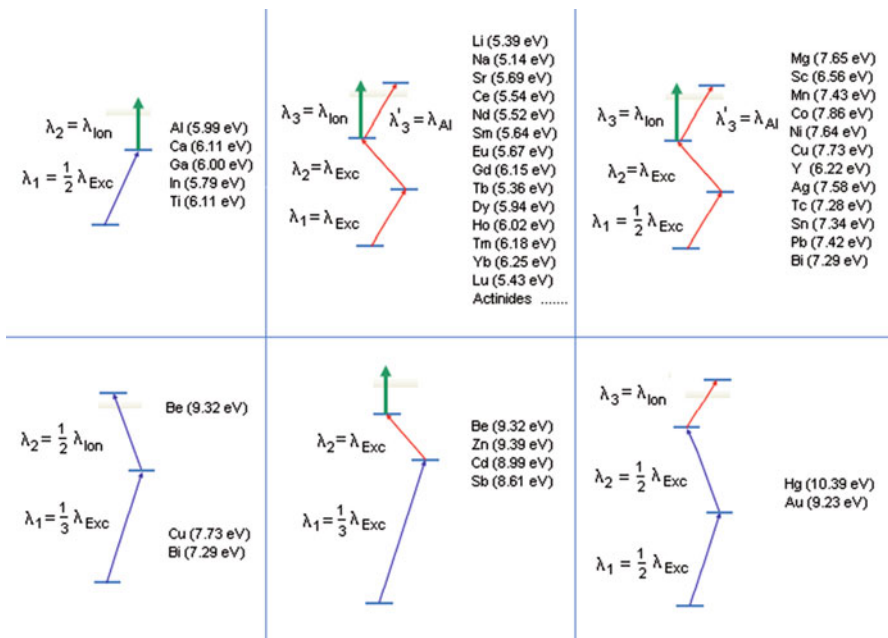


**Fig. 11.14** Possible resonance ionization schemes of different elements using copper vapor laser-pumped dye lasers

interesting cases for applying these techniques for the sake of supplementing the results obtained by classical spectroscopic studies and eliciting useful information and interpreting complex spectroscopic data. To illustrate the point, I describe three major laser spectroscopic techniques used for investigating these complex spectra by employing resonance excitation/ionization.

## 11.12 Optogalvanic Spectroscopy

This is an excellent technique of laser spectroscopy in gas discharges. In different zones of discharges, various atomic and ionic species exist with certain population distribution in ground or excited states. A laser resonant with some of the species can alter the steady-state population distribution of these species. Since probabilities of ionization of different states by means of electron impact are different, thus total ionization rate is affected. This induces change in impedance of the discharge tube detected as a voltage pulse (if pulsed laser is used), which is detected by using synchronous electronics. Many of the lanthanides and actinides are low vapor pressure elements and thus difficult to study in gaseous state by normal means. But by employing specialized glow discharges like hollow cathode discharges, these species can be generated in vapor form by means of sputtering. This enables laser spectroscopy of lanthanides and actinides in hollow cathode discharges. Most of the times, the region of discharge explored is negative glow, which is field-free, and using nanosecond lasers induces optogalvanic pulse of about microsecond duration depending upon atomic relaxation parameters and circuit constants. This technique has been employed by large number of groups [1] worldwide for various types of spectroscopic investigations. Our group has also used it extensively both in single-color and multicolor excitation spectroscopy [2, 3]. We have also developed what is called photoionization optogalvanic spectroscopy. In this technique, cathode dark space is explored using resonant laser(s) [4]. In this case, a distinctive nanosecond laser-induced photoionization signal can be observed. These two distinct signals and their features are given in Fig. 11.15. Using this technique, multiphoton ionization

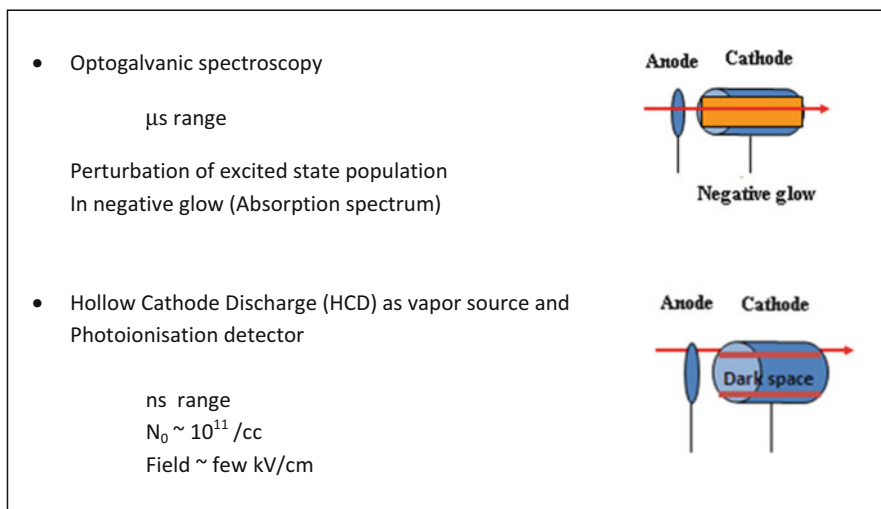


**Fig. 11.15** Optogalvanic and photoionization spectroscopy in hollow cathode discharge (HCD)

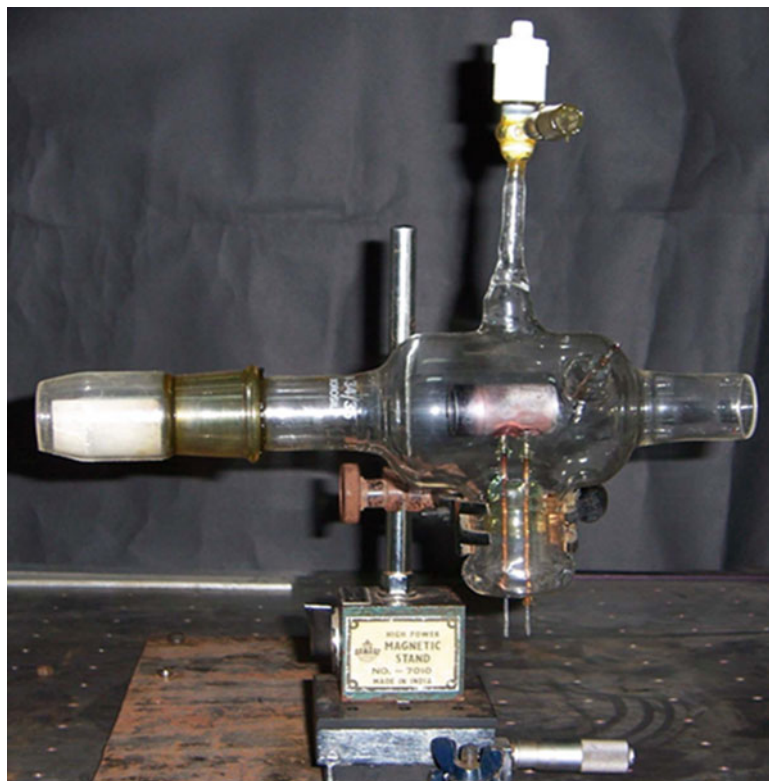
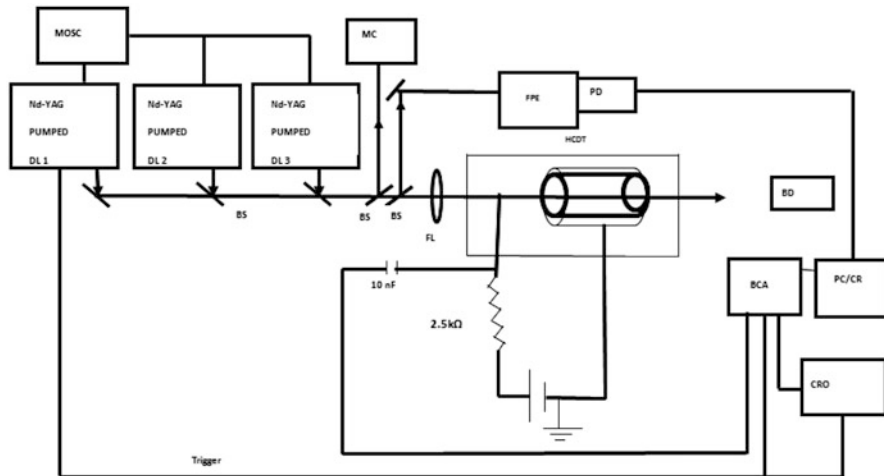


**Fig. 11.16** U-Ne hollow cathode discharge tube for optogalvanic spectroscopy

spectroscopy can be performed. We have employed this for exploring highly excited states of uranium atom [4]. All these studies have been carried out in a home-built hollow cathode discharge tube as shown in Fig. 11.16. We have also explored high-lying autoionization states of uranium using three-color optogalvanic spectroscopy. Figure 11.17 shows the experimental setup employed for single- or multistep optogalvanic spectroscopy.

Optogalvanic-based techniques have the advantage that higher metastable levels are well populated in discharges and lasers can probe these levels. This has the consequence that higher energy regions can be explored. This was made use of in our experiments by starting from  $620 \text{ cm}^{-1}$  metastable level by using Rh 6G-based dye lasers and employing a three-step optogalvanic spectroscopy to explore autoionization states in the energy region  $52,850\text{--}53,350 \text{ cm}^{-1}$  – a totally unchartered territory so far [3]. This way, by using four different excitation schemes, as given in [3], we identified 102 new even-parity autoionisation states and assigned them probable J values.



FPE- Fabry perot etalon, PD- Photodiode, MOSC- Master oscillator, MC-Monochromator, DL- Dye laser, BD- Beam dump, HCDT- Hollow cathode discharge tube, FL- Focusing lens, BCA- Box car averager, PC/CR- Personnel computer/Chart recorder

**Fig. 11.17** Schematic of experimental setup used for multicolor optogalvanic spectroscopy

### 11.13 Resonance Ionization Spectroscopy

As mentioned earlier, employing tunable lasers in the visible region, multiphoton spectroscopy of lanthanides and actinides can be carried out to study high-lying bound as well as autoionization states. We have exploited this technique for observation of new highly excited energy levels [5–7] and measurement of their isotope shifts [8] and radiative lifetimes [9]. Most of these studies employed either two-color three-photon or three-color three-photon ionization. Most of these studies employed mass spectrometers for filtering out impurities or unwanted resonances. Figure 11.18 shows the basic experimental setup.

Different types of tunable lasers pumped either by Nd:YAG or copper vapor lasers were used. Also both quadrupole and time-of-flight mass spectrometers were employed. Very high sensitivity and selectivity were achieved. Atomic beams of uranium were essential part of the mass spectrometers. The level of sensitivity achieved can be gauged from the fact that in these beams, besides ground state, metastables at  $620\text{ cm}^{-1}$ ,  $3,800\text{ cm}^{-1}$ , and even  $6,249\text{ cm}^{-1}$  were probed and large number of new resonances/highly excited energy levels could be observed. By tuning the mass spectrometer to either 238 or 235 mass, isotope shift measurements became possible and high isotope selectivity of more than 10,000 could be easily obtained. Figure 11.19 shows traces of isotope selectivity as observed by mass spectrometer with tunable lasers tuned to 235 mass and slightly detuned. Figure 11.20 shows a typical portion of two-color three-photon ionization spectrum along with calibration

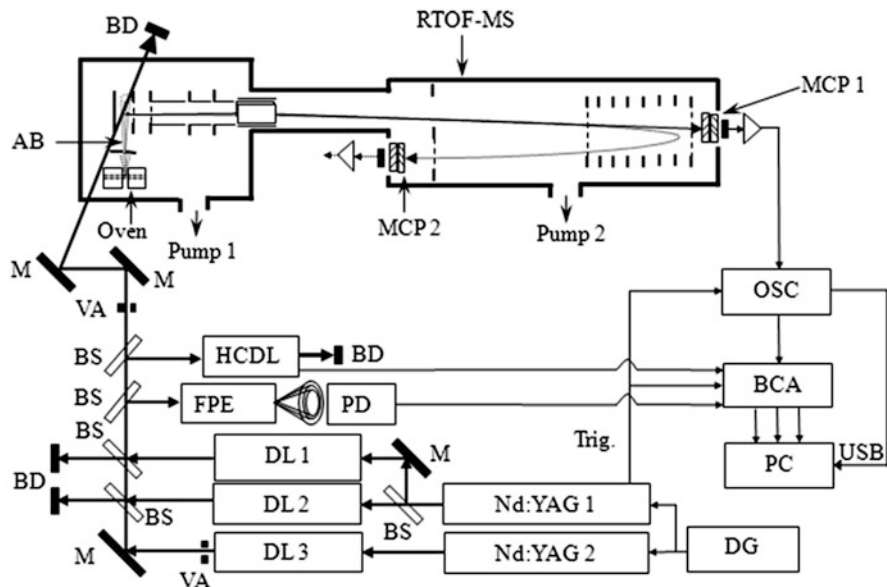


**Fig. 11.18** Schematic of experimental setup for resonance ionization mass spectrometry

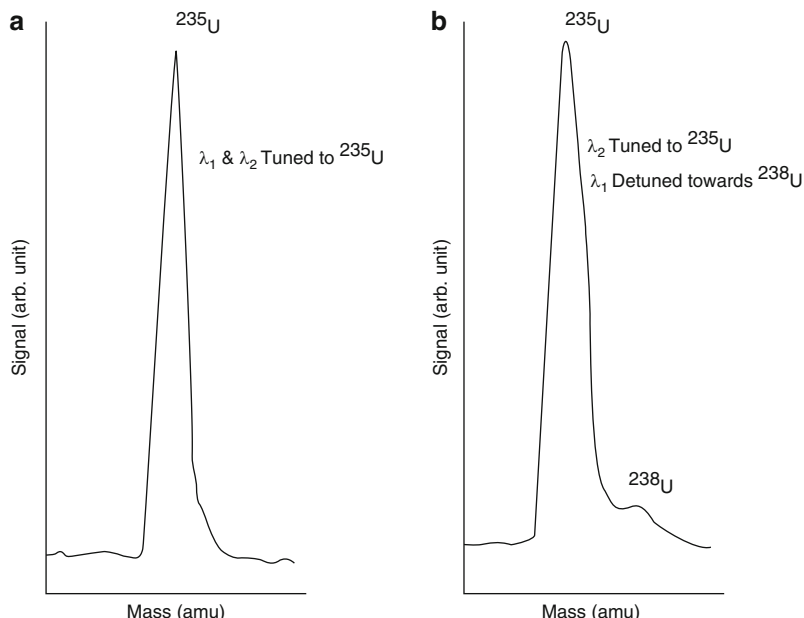


**Fig. 11.19** Typical mass spectrum of an isotope-selective two-color three-photon ionization resonance of uranium, isotope selectivity more than 10,000

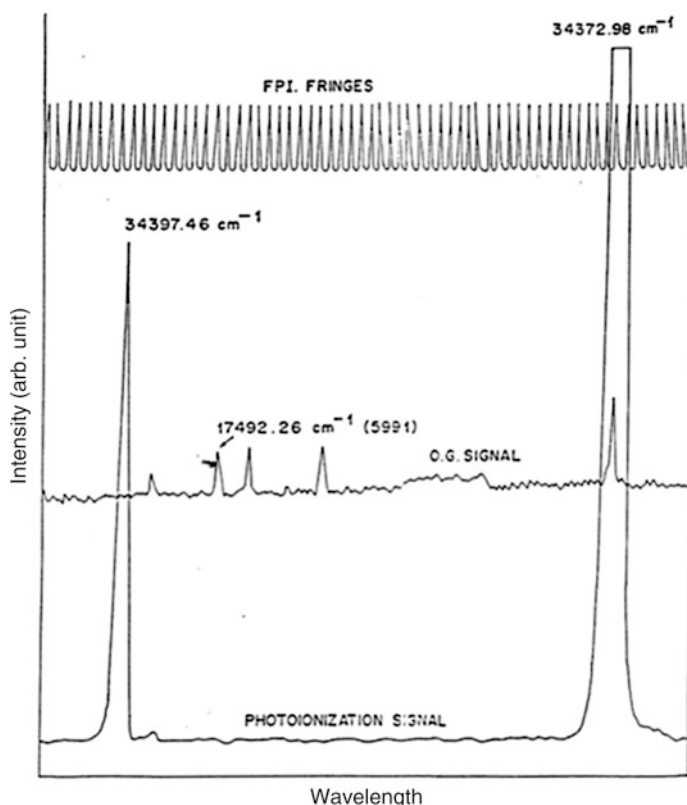
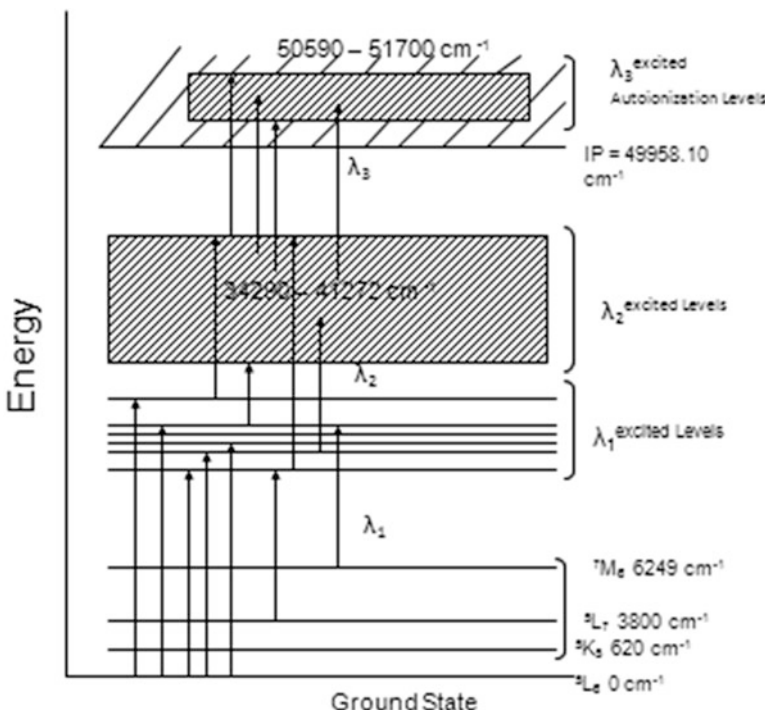


**Fig. 11.20** Typical two-color three-photon ionization spectrum of uranium

optogalvanic spectrum and Fabry-Perot fringes for dispersion scale. Figure 11.21 shows energy level diagram of uranium atom, where the shaded portion shows the region where new energy levels were explored and hundreds of new energy levels were observed and their angular momenta identified using resonance ionization mass spectrometry.

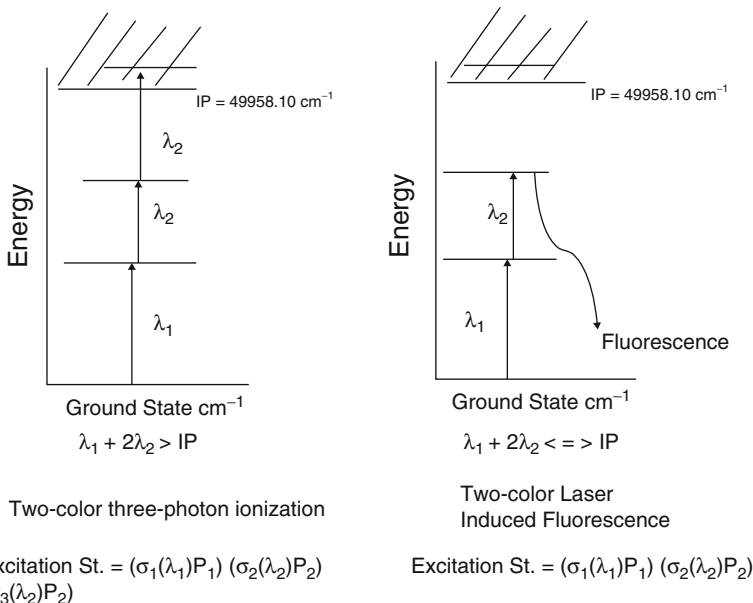
### 11.14 Multistep Laser-Induced Fluorescence

In the late 1970s or the early 1980s, multistep laser-induced fluorescence was quite often employed for deciphering complex spectra of lanthanides, actinides, and similar others, but soon with the development of much more sensitive and selective RIMS technique, the use of the earlier technique of LIF became less prevalent. On close examination of the results of the two techniques for the case of two-color fluorescence (LIF) and two-color three-photon ionization, it becomes noticeable that



**Fig. 11.21** Uranium atom energy level diagram: *shaded portion* shows the region explored by multiphoton ionization spectroscopy

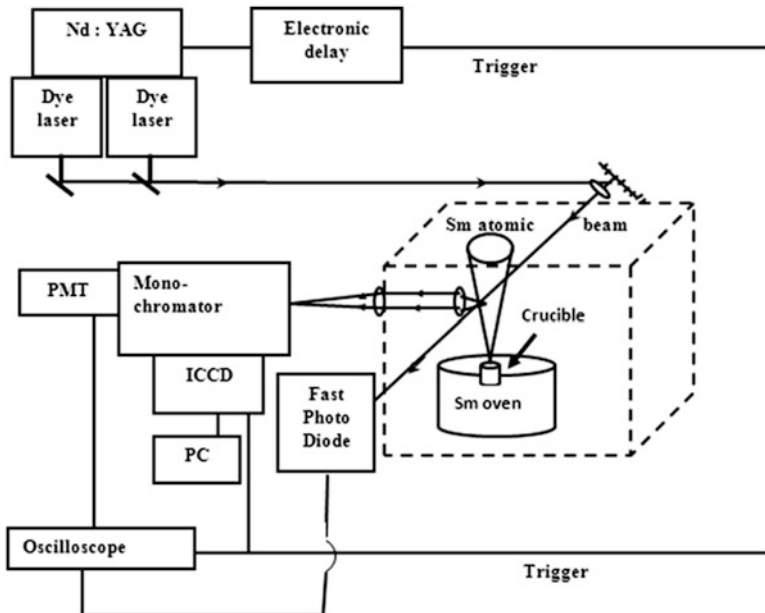
relative intensities are different in two spectra as much as some of the resonances found to be strong in one are not even observable in the other and vice versa. We investigated this “anomalous” behavior experimentally. The reasons for this can be understood as follows. As can be seen from Fig. 11.22, two-color three-photon ionization has three cross sections in picture, namely, first step excitation cross section, second step excitation cross section, and third step cross section, and due to their combined effect either continuum or an autoionization resonance state is reached – while two-color laser-induced fluorescence has only two cross sections in picture, first and second step excitation cross sections. This third step excitation cross section influences the relative intensities in two spectra to be different. Another noticeable feature is that two-color three-photon ionization is possible when the sum of single-photon energy of one- and two-photon energies of other is greater than the energy of ionization potential, but in the case of two-color LIF, it is applicable for all photon energies, provided both of them are resonant. As mentioned earlier, these observations were noticeable for two spectra of uranium in experiments of Miron et al. [10] and Carlson [11]. We further investigated this principle for the specific case of samarium experimentally. We compared our results on two-color LIF with that of two-color RIMS of Jayasekhar et al. [12]. Similar conclusions were



**Fig. 11.22** Comparison of relative intensities in two-color LIF and three-photon ionization

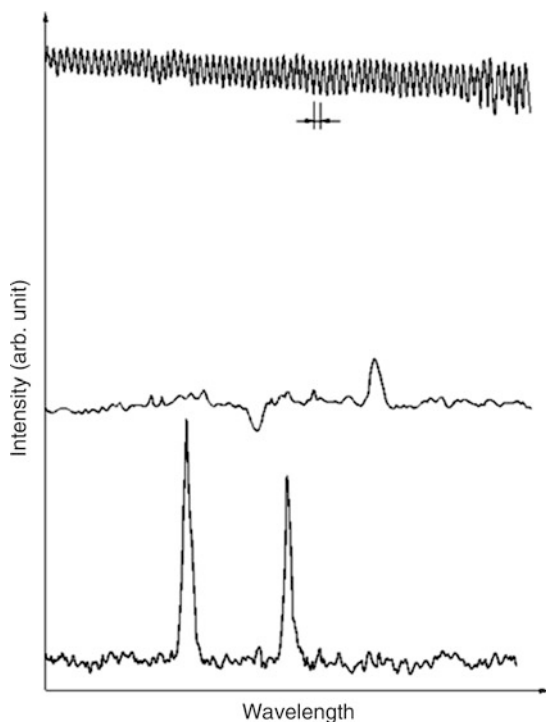
noticeable in the case of samarium also [13]. In the process despite RIMS being more sensitive technique, LIF demonstrated its utility by observing new resonances.

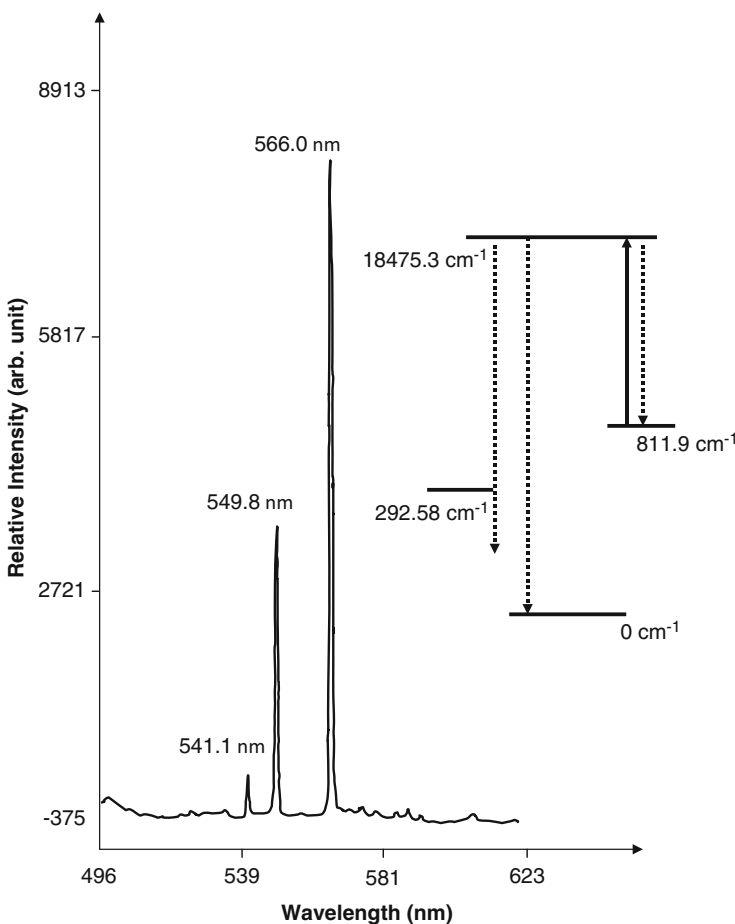
Another facet of multicolor LIF in the modern-day context is that LIF can be coupled to fast ICCD-based spectrographs. This enables simultaneous spectrally and temporally resolved fluorescence. We have exploited this for the sake of measurement of radiative lifetimes, branching ratios, and excitation cross sections of both first and second steps [14]. Figure 11.23 shows the schematic of the experimental setup for this purpose. Figure 11.24 shows a portion of two-color laser-induced fluorescence spectrum of samarium along with optogalvanic spectrum of uranium in the same region (for absolute wavelength reference) and Fabry-Perot fringes as part of dispersion scale. This LIF spectrum was recorded by using PMT as detector. By choosing a specific resonance and resolving it spectrally with the help of ICCD spectrally resolved LIF from a chosen level, all corresponding decay channels can be elucidated. This can be used for measuring branching fractions of decay from that energy level. By fixing on a particular decay channel peak and temporally monitoring its radiative decay, it is possible to measure radiative lifetime of that level. Combining the results of spectrally resolved LIF and temporally resolved LIF of a specific feature, it is possible to measure excitation cross sections of that pair of levels. This scheme can be extended to the second excitation step. Figure 11.25 shows the LIF from the first excited level. Figure 11.26 shows the radiative decay plot of a specific feature.



**Fig. 11.23** Experimental setup for temporally and spectrally resolved two-color LIF spectroscopy

**Fig. 11.24** Typical two-color laser-induced fluorescence spectrum of samarium along with uranium optogalvanic signal and Fabry-Perot etalon fringes

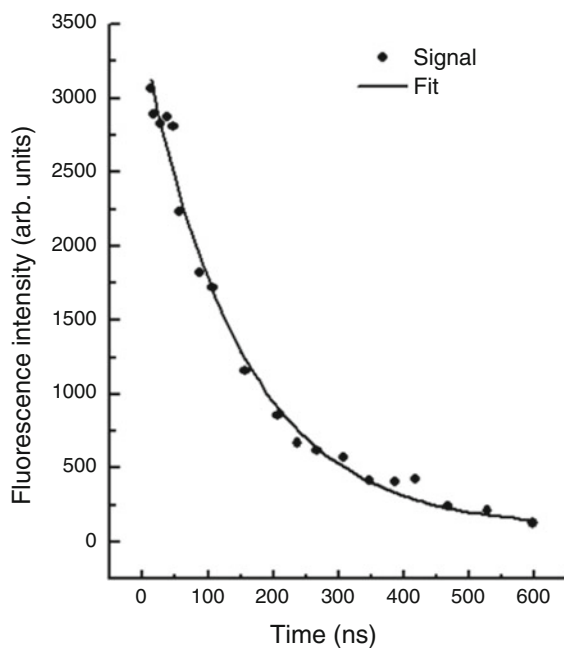




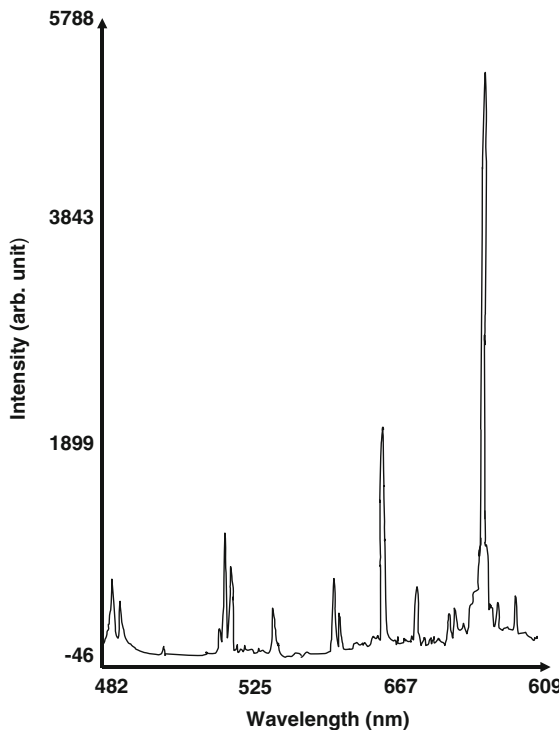
**Fig. 11.25** Laser-induced fluorescence decay channels (resonant and nonresonant) at 541.1, 549.8, and 566.0 nm for the atomic transition excited by laser at 565.99 nm  $811.92 \rightarrow 18,475.28 \text{ cm}^{-1}$

Figure 11.27 shows the spectrally resolved LIF from the second excited level. This way, large number of radiative lifetimes, branching ratios, and excitation cross sections can be measured. We have demonstrated its utility by measuring radiative lifetimes, branching ratios, and consequently absolute transition probabilities – both of first and second excited levels of samarium [14]. It must be mentioned that conventional methods of measuring branching ratios are quite complex and error prone. Thus, two-color LIF offers a very simple technique, and this has been demonstrated to have good accuracy as well.

**Fig. 11.26** Radiative lifetime measurement using single-color in samarium for energy level  $(18,225.13 \text{ cm}^{-1})$



**Fig. 11.27** Two-color LIF for branching ratio and transition probability measurement. Spectrally resolved fluorescence from second excited level  $35,935.5 \text{ cm}^{-1}$



## 11.15 Conclusion

Laser spectroscopy has given a new dimension to the observation and understanding of all complex spectra. It has opened up possibilities of new techniques. Orders of magnitude improvement in sensitivity, selectivity, and new dimension of temporal resolution of high order have enabled new physics of atoms and molecules to be explored. Even though the highest resolution is attained with CW tunable lasers and pulsed tunable lasers are normally restricted in resolution because of Fourier transform limit, still plenty of high-resolution spectroscopies aimed at eliciting new spectroscopic data, both of interest to basic and applied sciences, are possible. This is well demonstrated by our work described. The techniques of multicolor optogalvanic, resonance ionization, and laser-induced fluorescence have been employed for the study of highly excited energy levels of lanthanides and actinides. These techniques are universal and applicable to wherever complex spectra occur. In this context, it was pointed out that pulsed tunable lasers can cover much wider spectral range and thus resonance excitation/ionization of much larger number of elements/isotopes can be covered.

## References

1. B. Barbieri, N. Beverini, A. Sasso, Optogalvanic spectroscopy. *Rev. Mod. Phys.* **62**(3), 603 (1990)
2. B.M. Suri, R. Kapoor, G.D. Saksena, Systematic trends in optogalvanic signals of some transitions in a uranium hollow cathode discharge. *Opt. Commun.* **52**, 315 (1985)
3. M.L. Shah, P.K. Mandal, V. Dev, B.M. Suri, Study of even-parity autoionization states of atomic uranium. *J. Opt. Soc. Am. B* **29**(7), 1625–1630 (2012)
4. V. Dev, M.L. Shah, A.K. Pulhani, B.M. Suri, Two-color photoionization spectroscopy of Uranium in U-Ne hollow cathode discharge tube. *Appl. Phys. B* **200**, 1–8 (2005)
5. B.M. Suri, K. Dasgupta, K.G. Manohar, P.N. Bajaj, R. Talukdar, P.K. Chakraborti, P.R.K. Rao, Observation of new high-lying odd levels of U I in a two-color multiphoton ionization spectrum. *J. Opt. Soc. Am. B* **4**, 1835 (1987)
6. P.N. Bajaj, K.G. Manohar, B.M. Suri, K. Dasgupta, R. Talukdar, P.K. Chakraborti, P.R.K. Rao, Two color multiphoton ionization spectroscopy of uranium from a meta stable state. *Appl. Phys. B* **47**, 55 (1988)
7. K.G. Manohar, P.N. Bajaj, B.M. Suri, R. Talukdar, K. Dasgupta, P.K. Chakraborti, P.R.K. Rao, Observation of auto- ionization resonances in uranium by stepwise laser photoionization. *Appl. Phys. B* **48**, 525 (1989)
8. K.G. Manohar, P.N. Bajaj, V. Dev, P.K. Chakraborti, P.R.K. Rao, Isotope shift measurement of high-lying atomic levels by multi-step photoionization. *Pramana J. Phys.* **37**(6), 539–544 (1991)
9. R.C. Das, P.K. Mandal, M.L. Shah, A.U. Seema, D.R. Rathod, V. Dev, K.G. Manohar, B.M. Suri, Measurements of radiative lifetimes of high-lying odd parity energy levels of U I. *J. Quant. Spectrosc. Radiat. Transf.* **113**, 382–386 (2012)
10. E. Miron, R. David, G. Erez, S. Lavi, L.A. Levin, Laser spectroscopy of U I using stepwise excitation and fluorescence detection. *J. Opt. Soc. Am.* **69**, 256 (1979)

11. L.R. Carlson, J.A. Paisner, E.F. Worden, S.A. Johnson, C.A. May, R.W. Solarz, Radiative lifetimes, absorption cross-sections and observation of new high lying odd levels of U using multi-step laser photoionization. *J. Opt. Soc. Am.* **66**, 846 (1976)
12. T. Jayasekharan, M.A.N. Razvi, G.L. Bhale, Investigation of new high lying even parity energy levels of the Samarium atom below its first ionization limit. *J. Opt. Soc. Am. B* **17**(9), 1607 (2000)
13. A.K. Pulhani, M.L. Shah, V. Dev, B.M. Suri, High-lying even parity excited levels of atomic samarium. *J. Opt. Soc. Am. B* **22**(5), 1117–1122 (2005)
14. M.L. Shah, A.K. Pulhani, G.P. Gupta, M. Suri, Measurement of radiative lifetimes, branching fractions, and absolute transition probabilities in atomic samarium using laser induced fluorescence. *J. Opt. Soc. Am. B* **27**(3), 423–431 (2010)

# **Chapter 12**

## **Lasers in Materials Processing**

**L.M. Kukreja, C.P. Paul, Atul Kumar, R. Kaul, P. Ganesh, and B.T. Rao**

**Abstract** Laser is undoubtedly one of the most important inventions of the twentieth century. Today, it is widely deployed for a cornucopia of applications including materials processing. Different lasers such as CO<sub>2</sub>, Nd:YAG, excimer, copper vapor, diode, fiber lasers, etc., are being used extensively for various materials processing applications like cutting, welding, brazing, surface treatment, peening, and rapid manufacturing by adopting conventional and unconventional routes with unprecedented precision. In view of its potential for providing solution to the emerging problems of the industrial materials processing and manufacturing technologies, a comprehensive program on laser materials processing and allied technologies was initiated at our laboratory. A novel feature-based design and additive manufacturing technologies facilitated the laser rapid manufacturing of complex engineering components with superior performance. This technology is being extended for the fabrication of anatomically shaped prosthetics with internal heterogeneous architectures. Laser peening of spring steels brought significant improvement in its fatigue life. Laser surface treatments resulted in enhanced intergranular corrosion resistance of AISI 316(N) and 304 stainless steel. Parametric dependence of laser welding of dissimilar materials, AISI 316M stainless steel with alloy D9, was established for avoiding cracks under optimum processing conditions. In the domain of laser cutting and piercing, the development of a power ramped pulsed mode with high pulse repetition frequency and low duty cycle scheme could produce highly circular, narrow holes with minimum spattered pierced holes. A review of these experimental and some theoretical studies is presented and discussed in this chapter. These studies have provided deeper insight of fascinating laser-based materials processing application for industrial manufacturing technologies.

**Keywords** Materials processing • Rapid manufacturing • Peening • Cutting • Brazing

---

L.M. Kukreja (✉) • C.P. Paul • A. Kumar • R. Kaul • P. Ganesh • B.T. Rao  
Laser Materials Processing Division, Raja Ramanna Centre for Advanced Technology,  
Indore, MP, India  
e-mail: [kukreja@rrcat.gov.in](mailto:kukreja@rrcat.gov.in)

## 12.1 Introduction

As it is well known, lasers deliver one of the cleanest forms of energy onto the materials and hence are some of the most effective and invaluable tools for processing materials. Some of the properties of lasers that make those suitable for materials processing under different specialized conditions include coherence, both spatial and temporal; high intensities and fluence capabilities; short to ultrashort pulse durations; no need of vacuum for its propagation; and feasibility of transportation through flexible optical fibers. One of the first applications of lasers after its invention in 1960 was in fact to demonstrate its potential for materials processing with drilling and welding of stainless steel blades and foils during 1963 and 1964 [1]. As the time progressed newer lasers, their technological systems and methodologies to control their parameters emerged which made their application in materials processing a vast industrial utilization and a continued research area. A glimpse of different materials processing-related applications of different lasers is presented in Table 12.1. Today, laser materials processing is not only a well-established area from utilitarian point of view but also a vibrant research area to seek solutions for the emerging future requirements of manufacturing technologies. With emphasis on this aspect, we have presented a review of the current research in emerging areas of laser materials processing in this chapter. At our laboratory, we are currently pursuing

**Table 12.1** Different types of lasers and their potential applications

Laser (wavelength)	Applications
CO <sub>2</sub> laser (10.6 μm)	Light to heavy duty industrial cutting, welding, and rapid manufacturing
	Laser surface modification for wear/corrosion resistance and dimensional restoration
	Laser ablation, surface of steels, and laser glazing
Nd:YAG laser (1.06 μm)	Light to heavy duty job shops in drilling, welding, cutting, marking, and rapid manufacturing
Fiber laser (1.08 μm)	Laser cleaning in conservation of artifact, paint stripping
Excimer laser	Optical stereolithography
KrF (0.248 μm)	Marking, scribing, and precision micromachining involving drilling, cutting, and etching of profile
XeCl (0.309 μm)	High-speed photography
Copper vapor laser (0.51 and 0.58 μm)	Detection of fingerprints for forensic applications
	Excitation source for tunable dye laser for isotope separation
	Precision micro-hole drilling and cutting
Semiconductor laser/diode laser (0.8–1.0 μm)	Optical computers, CD drivers, laser printers, scanners, and photocopiers
	Optical communication
	Industrial alignment
	Holography, spectroscopy, biodetectors, ozone layer detector, pollution detection, bar-code scanners, 3D image scanners

research on laser rapid manufacturing on porous structures and graded composition of different prosthetic and engineering materials, laser cladding of vertical surfaces, welding and brazing of advanced engineering components, and newer techniques of piercing and cutting of different engineering materials. The detailed results of our research in these areas are presented and discussed in this chapter.

## 12.2 Laser Rapid Manufacturing

The field of rapid manufacturing has recently encountered new directions upon advancements in high-speed computers, computer-aided design (CAD), and laser technologies. This layered additive manufacturing technique led to the evolution of next-generation “feature-based design and manufacturing” and also deployed for the repair of existing prime components at lower cost with improved functionality. This fabrication procedure is known as **Laser Rapid Manufacturing (LRM)**. This process utilizes the laser energy as a heat source to melt a thin layer of the substrate together with the blown metal powder to form a layer in a predetermined shape. A number of such layers are formed one on another to fabricate three-dimensional (3D) objects with novel properties directly from their CAD models. Thus, LRM eliminates many production steps such as assembly, man-machine interaction process planning, intermittent quality checks, and consequently related human errors. It also offers many advantages due to its inherent manufacturing features over the conventional subtractive techniques such as reduction of production time and fabrication of functionally graded parts (complex heterogeneous/porous structures). Laser rapid manufacturing is now put to commercial use for the fabrication of functional metal parts. Conventional operations show obvious advantages for fabrication of parts in large volume. But when the production volume is small and the part has some irregular shape or has fine internal features, the turnaround and cost increase multifold in most of the cases. Moreover, it is impossible to realize the parts in some cases. For high-value prime parts involving aeronautical, military, aerospace, marine, and biomedical applications, price is secondary to function and LRM is potentially most appropriate process due to many intrinsic advantages. Because of the process flexibility (in terms of raw material selection and feeding), it is possible to make components with compositional grading across length/width to meet the multifunctional requirements. Thus, fabrication of functionally graded materials is one of the important capabilities of rapid manufacturing which finds applications in both the engineering and prosthetic components.

Features that can be attributed to a part include the geometry of the part, the material composition, and the microstructure. The material composition is governed by the efficiency of the material delivery method, whereas the microstructure is governed by the specific energy input. As laser-based additive manufacturing techniques can address these complex issues, manufacturing techniques, similar to LRM, are being developed with different names at various laboratories around the world. At Sandia National Laboratories, USA, Laser Engineered Net Shaping

(LENS<sup>TM</sup>) is being developed with prime focus on creating complex metal parts in a single day [2]. National Research Council, Canada, is developing Freeform Laser Consolidation for manufacturing of structural components for advanced robotic mechatronic systems [3]. Automated Laser Fabrication (ALFa) is being developed to produce low-cost tungsten carbide components at the University of Waterloo, Canada [4]. Selective Laser Cladding (SLC) at the University of Liverpool, UK, and Direct Metal Deposition at the University of Michigan, USA, are being used for depositing critical surfaces on prime components [5, 6]. Laser Powder Deposition (LPD) at the University of Manchester, UK, and Direct Metal Deposition/Laser Additive Manufacturing at Fraunhofer Institute, Germany, are being augmented for the fabrication of high-performance materials [7]. The researchers at Tsinghua University, China, are working on diverse areas and evaluating the potential of technology for the development of graded Ti alloys for aeronautics, Ni alloys for power plants, and various in situ repair applications [8]. Thus, the ongoing global research is spearheading toward the deployment of fabrication technology for improving qualities of the products integrated with multi-material and multi-functional components, enhancing a step benefit in economics.

### **12.2.1 Lasers in LRM**

In LRM, high-power laser system is used as heat source to melt thin layer of substrate/Previously deposited layer and fed material. CO<sub>2</sub>, Nd:YAG, and diode lasers are most widely used for the application. The availability of high-power fiber lasers made it a new entrant in this application domain [9]. Since the wavelength of Nd:YAG, diode, and fiber lasers is near 1 μm, the absorption is better for laser materials processing involving metals as compared to that of CO<sub>2</sub> lasers. Still CO<sub>2</sub> lasers are being used due to established systems and procedures. As against the common notion, both pulsed and CW lasers have been successfully used for LRM. The laser energy intensity of 20–60 kW/cm<sup>2</sup> is used for CO<sub>2</sub> lasers, while it is 150–200 kW/cm<sup>2</sup> for pulsed Nd:YAG lasers [10, 11]. The basic prerequisite for laser beam energy intensity distribution is symmetry along the axis of laser beam propagation. It allows uniform material deposition independent of direction of processing. Therefore, multimode laser beam with flattop distribution is most widely used. Gedda et al. studied the energy distribution during LRM process using CO<sub>2</sub> laser and Nd:YAG laser [12]. The observations are summarized in Table 12.2.

**Table 12.2** Redistribution of laser power during laser cladding

Use of laser power\laser type	CO <sub>2</sub> laser (%)	Nd:YAG laser (%)
Reflected off the cladding melt	50	40
Reflected off the powder cloud	10	10
Heat the substrate	30	30
Melt the substrate/Previously deposited layer	10	20

As indicated in Table 12.2, about 10 % laser energy is utilized to melt substrate layer/Previously deposited layer in case of CO<sub>2</sub> laser. The value is 20 % in case of Nd:YAG laser due to increased absorption. The laser energy utilization for Nd:YAG laser is more by a factor 1.3 for processing metals (such as SS316L) in solid state. This factor reduces as the temperature rises and is same for both the lasers in molten/liquid states. Thus, about 769 W of continuous wave Nd:YAG laser replaces 1 kW of continuous wave CO<sub>2</sub> laser of same beam product parameter for almost same results during LRM. Since the wavelengths of other commonly used lasers (diode and fiber) are close to that of Nd:YAG laser, similar results as compared to CO<sub>2</sub> laser are pertinent.

### 12.2.2 System Description

Figure 12.1 presents the schematic arrangement of a typical laser rapid manufacturing (LRM) setup. An LRM system consists of the following three primary subsystems:

(A) High-power laser system:

1. CO<sub>2</sub> laser
2. Nd:YAG laser
3. Diode laser
4. Fiber laser

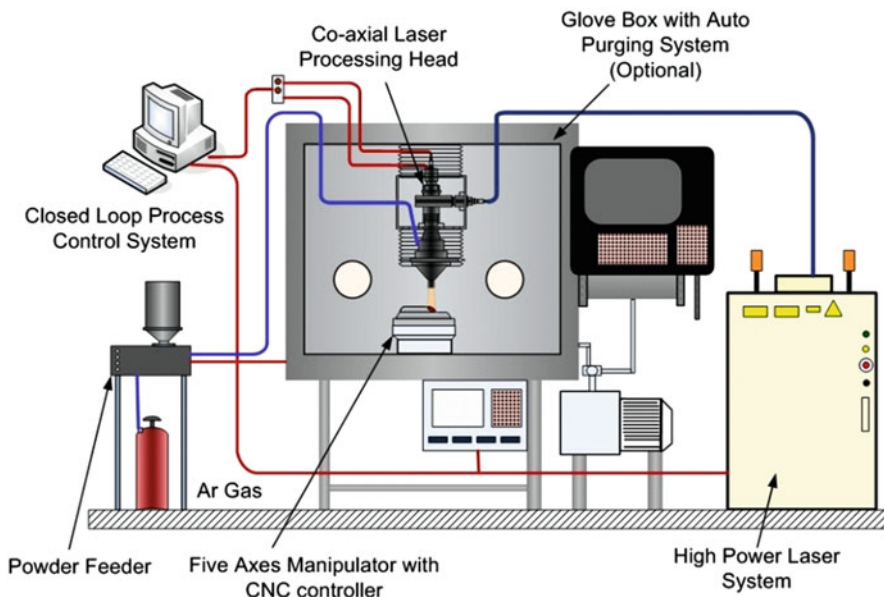


**Fig. 12.1** Schematic arrangement of LRM setup

**(B) Material feeding system:**

1. Wire feeder
2. Preplaced powder bed
3. Dynamic powder blowing

**(C) Computer numerical controlled (CNC) workstation:**

1. 3-axis workstation
2. 5-axis workstation

Among the material feeding systems, wire feeders are directly adopted from Metal Inert Gas (MIG) welding process. Wire feeding is preferred for the fabrication of components involving continuous deposition [13, 14], as intermittent start/stop results in discontinuity in deposited material. This method is not adopted as universal method, because of poor wire/laser coupling leading to poor energy efficiency, unavailability of various materials in wire forms, and their cost. In preplaced powder bed, a predefined thickness of the powder is laid on the substrate and the powder is melted using laser to form the solidified layer. The method is preferred to fabricate fine features and overhang structures. The method has limitation in achieving cent-percent density in the deposits. Dynamic powder blowing is convenient and most widely used approach for material feeding in LRM systems. It allows online variation in feed rate and multi-material feeding. Moreover, laser energy utilization is also more in dynamic powder blowing, as the laser beam passes through the powder cloud to the substrate/Previously deposited layer, resulting in preheating of powder particles by multiple reflections. Since the powder is fed into the molten pool for melting and forming layer, some powder particles are ricocheted from the pool. The ratio of the powder deposited to powder fed is termed as powder catchment efficiency. The typical achieved powder catchment efficiency is 35–80 %. In CNC workstations, three-axis interpolation ( $X$ ,  $Y$ , and  $Z$ ) is sufficient to reach to any point in the space, but two more axes ( $A$  and  $C$ ) are required to orient particular direction to reach. Therefore, three-axis configuration is minimum system requirement and 5-axis is universal requirement without redundancy. Apart from axis movement, laser workstation needs some more features, like laser on/off, gas on/off, powder feeder on/off, etc., for laser rapid manufacturing.

Figure 12.2 schematically illustrates the LRM setup depicting an integrated LRM station with scope for glove box operation to fabricate components in a controlled atmosphere developed at authors' laboratory. Research is underway to incorporate the feedback-based, closed-loop control to precisely manage the temperature, cooling rate, size of the melt pool, and shape of the parts being manufactured.

### **12.2.3 Recent Developments**

At authors' laboratory, a comprehensive program was undertaken to address various industrial and in-house applications. The fabrication of Colmonoy 6 bushes, solid

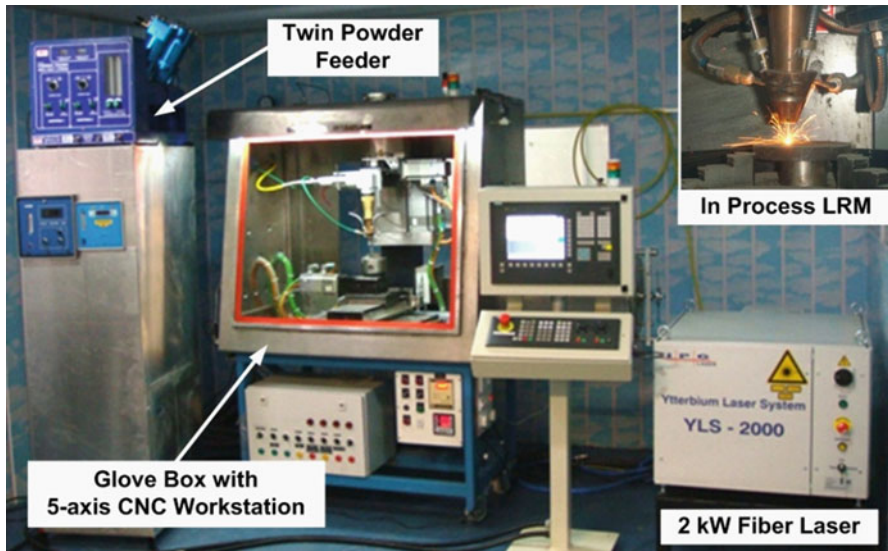


**Fig. 12.2** Laser rapid manufacturing facility at author's laboratory

and porous structures of Inconel 625, and low-cost WC-Co tools are important among them [15–19]. The properties and performance of laser rapid manufactured components/structures were found to be at par with that of conventionally processing component.

#### 12.2.3.1 Development of High-Performance Surface on SS316L for Improved Wear Resistance

Recently, the studies are extended to the development of high-performance surfaces by depositing tungsten carbide (WC)-reinforced nickel matrix on SS316L. In the study, Inconel 625 alloy (particle size, 45–105  $\mu\text{m}$ ) was used to provide nickel matrix for reinforcing WC particles (particle size, 45–75  $\mu\text{m}$ ). A number of test trails were made to optimize the processing parameters for laser rapid manufacturing of continuous multilayered overlapped deposition at various powder compositions. It was observed that the deposit got delaminated during the laser rapid manufacturing of second layer for 5 % weight Inconel 625 due to insufficient wetting material. This problem was not observed for higher compositions. Figure 12.3 presents a typical laser rapid manufactured WC-reinforced nickel matrix on 316L stainless steel.

The microscopic examination revealed the dendritic microstructure of Ni matrix originating from WC particles due to directional quenching (Fig. 12.4). The erosion wear performance of the laser rapid manufactured samples was evaluated using  $\text{Al}_2\text{O}_3$  air jet erosion test rig for Inconel 625 in deposit ranging 5–25 % weight,

**Fig. 12.3** Typical laser rapid manufactured WC-reinforced nickel matrix on 316L SS substrate

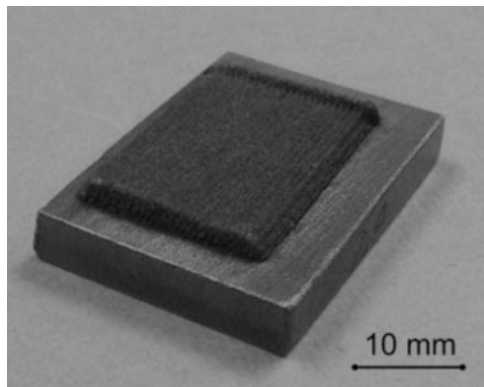
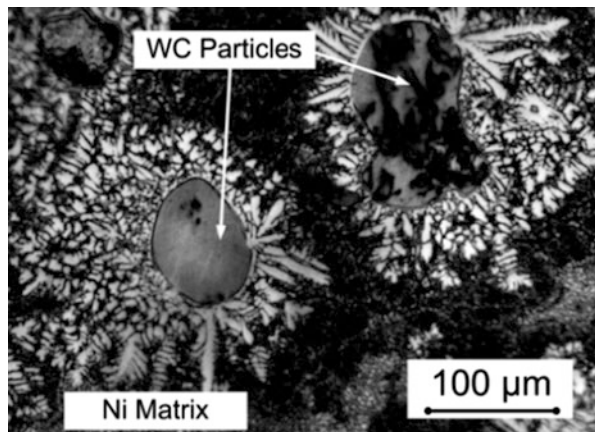


**Fig. 12.4** Micrograph depicting the WC particles in Ni matrix with dendrites



erodent jet velocity ranging 10–50 m/s, jet impinging angle ranging 0–68°, and substrate temperature ranging 50–250 °C. Figure 12.5 presents contours depicting erosion wear rate (EWR) for various compositions and impinging angle at erodent velocity 30 m/s and substrate temperature 150 °C. The study demonstrated that WC-reinforced Ni matrix laser rapidly manufactured with 18 wt% of Inconel 625 has least erosion wear rate (EWR) for the range of parameters under investigation and it was found to be nine times lower than that of bare SS316L surface.

In another study, high-performance layers of cobalt-free materials were developed, and their cavitation and slurry erosion behaviors were studied. The preference to the cobalt-free materials for nuclear applications to avoid induced radioactivity was the main motivation to develop laser cladding of Colmonoy 5 (a nickel base alloy) and Metco 41C (an iron base alloy) on AISI type 316L stainless steel substrate. The process parameters were optimized for developing continuous and defect-free laser cladding of Colmonoy 5 and Metco 41C on AISI type 316L stainless steel substrate using dynamic powder blowing methodology (powder

**Fig. 12.5** Contours depicting EWR for various compositions and impinging angle at erodent velocity 30 m/s and substrate temperature 150 °C

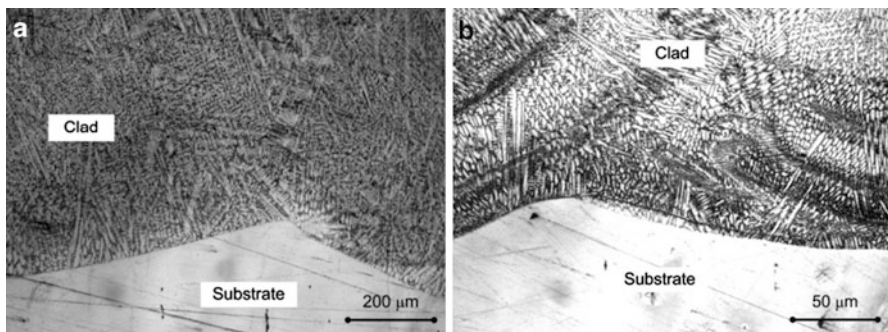
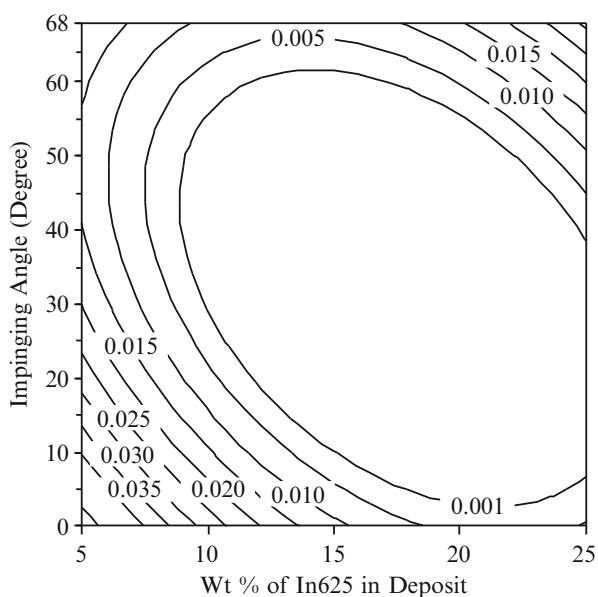


**Fig. 12.6** Typical microstructure at clad-substrate interface for (a) Colmonoy 5 and (b) Metco 41C

particle size used, 45–105  $\mu\text{m}$ ). The observed optimum parameters were as follows: laser power, 1.6 kW; scan speed, 0.6 m/min; and powder feed rate, 8 g/min with 60 % overlap index.

Figure 12.6 presents the typical microstructure at substrate-clad interface for Colmonoy 5 and Metco 41C. X-ray diffraction studies showed the presence of carbides, borides, and silicides of Cr and Ni for Colmonoy 5, whereas Metco 41C cladding exhibited the presence of the work hardening microconstituent, i.e., austenite. The microstructural studies showed that the clad layers of Colmonoy 5, Metco 41C, and Stellite 6 primarily contain very fine columnar dendritic structure, while clad-substrate interface exhibited planar and non-epitaxial mode of solidification due

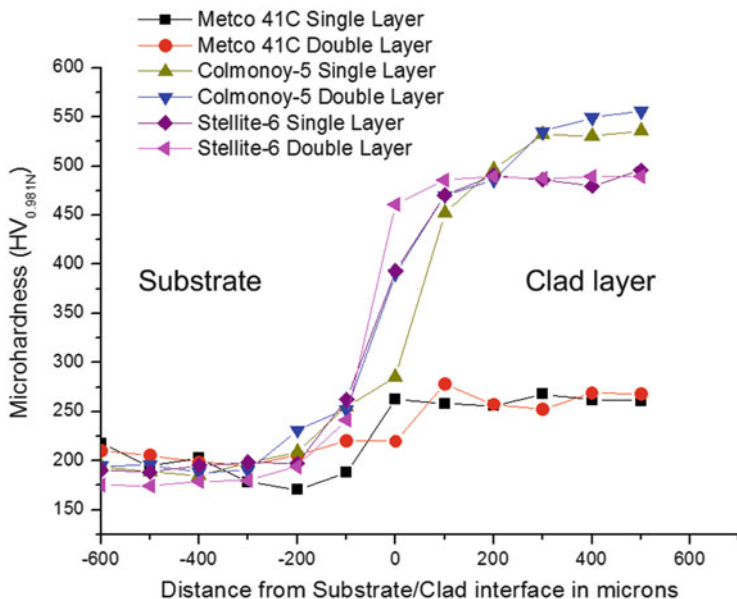


**Fig. 12.7** Microhardness profiles across clad-substrate interface for various laser clad specimens

**Table 12.3** Improvement in wear behavior with respect to bare AISI type 316L stainless steel

Description	Colmonoy 5	Stellite 6	Metco 41C
Cavitation erosion	1.6	4.1	4.6
Slurry erosion at $30^\circ$	1.5	1.75	4.9
Slurry erosion at $90^\circ$	2.2	3.5	2.9

to high cooling rates. Multi-pass cladding showed refined zone at interface due to remelting and solidification. Figure 12.7 presents the microhardness profile for these cladding.

The improvement in cavitation and slurry erosion resistance of laser cladding with respect to AISI type 316L is summarized in Table 12.1. Metco 41C showed better cavitation and slurry erosion resistance (especially at  $30^\circ$ ) than other clads used in this work. The improvement in erosion resistance of developed clad layers (Table 12.3) was primarily attributed to arrest of craters formed by the metal matrix due to high toughness and reasonably good hardness.

### 12.2.3.2 Laser Suppresses Dilution in Ni-Based Colmonoy 6 Deposits on Austenitic SS

Laser cladding, because of its low heat input characteristics, is a suitable choice for controlling dilution in clad deposits. This characteristic of laser cladding

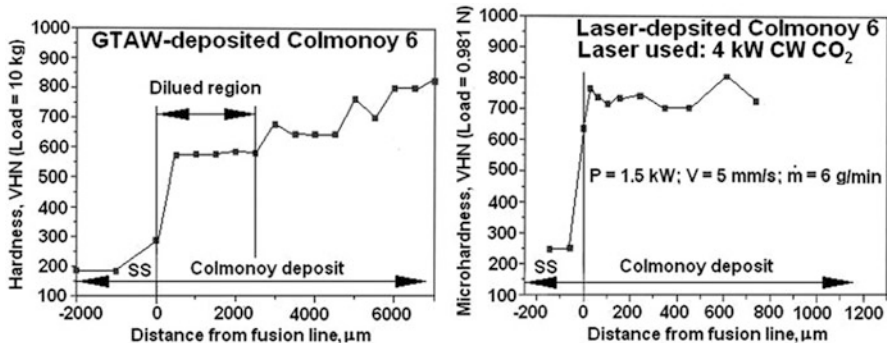


**Fig. 12.8** Comparison of hardness profiles across the cross section of Colmonoy 6-deposited specimens of austenitic SS

was effectively exploited to suppress dilution from the austenitic SS substrate in hardfaced deposits of Colmonoy 6 (nickel base superalloy) [20]. Colmonoy 6 has been selected as a hardfacing material for austenitic SS components of 500 MWe Prototype Fast Breeder Reactor, which is still under-construction. In the hardfaced deposits made with conventional gas tungsten arc welding (GTAW), hardness is influenced by the dilution from the substrate up to a deposit thickness as high as 2.5 mm. In contrast, Colmonoy 6 cladding with CW CO<sub>2</sub> laser effectively suppressed dilution from the substrate and produced thin Colmonoy deposits with low level of dilution. Cracking of the deposit was minimized by controlling the heating and cooling rates by adopting substrate preheating. Figure 12.8 compares hardness profiles across the cross section of Colmonoy 6-hardfaced type 316L SS specimen.

### 12.2.3.3 Laser-Based Graded Cladding of Co-Based Alloy Stellite 6 on Austenitic SS

Laser cladding, due to relatively smaller width of laser clad track, provides the capability to spatially control chemical composition in the multilayered clad deposits. This feature of laser cladding has been effectively employed to generate engineered structure with controlled heterogeneity in terms of chemical composition and associated microstructural, mechanical, and thermophysical properties [15, 21–23]. Figure 12.9 compares concentration profiles across 3 and 4 layer graded deposits of Stellite 6 on austenitic SS substrate, whereas corresponding microhardness profile across substrate and 3/4 layer graded clad interface is presented in Fig. 12.10.

Compositional grading across austenitic SS/Stellite boundary significantly influenced the mode of crack propagation across the boundary. In contrast to initiation-controlled brittle crack propagation across sharp type 316L SS/Stellite boundary (under high strain rate impact loading condition), crack propagation across compositionally graded boundary was marked with significant plastic deformation,

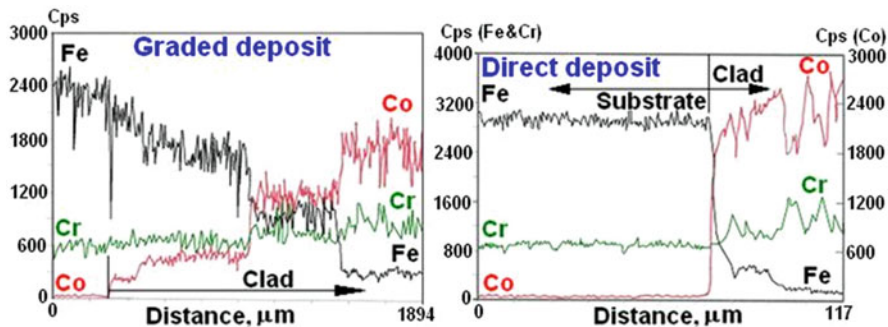
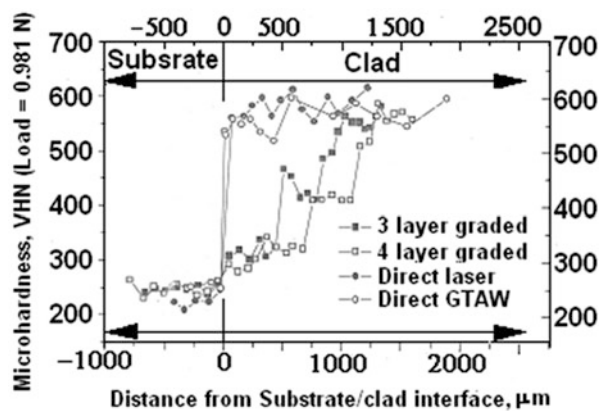


**Fig. 12.9** Concentration profiles of Fe, Cr, and Co across graded and direct deposits of Stellite 6 on austenitic SS substrate

**Fig. 12.10** Comparison of hardness profiles across graded and direct deposits of Stellite 6 on austenitic SS substrate

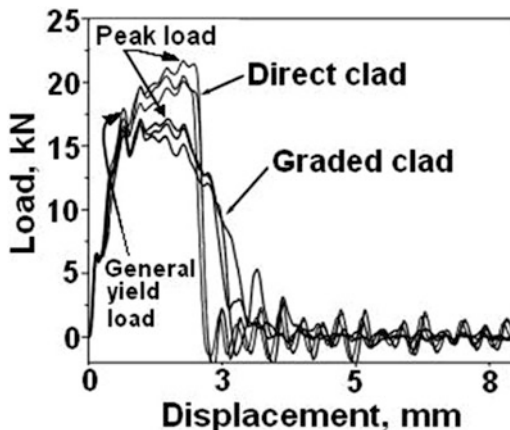


which is translated into slower crack propagation [15]. Figure 12.11 compares load-displacement traces of instrumented impact test of “direct” and “graded” Stellite 21 clad type 316L SS specimens. It should be noted that for graded clad specimens, gradual drop in load after the peak load reflects crack growth associated with plastic deformation. These graded structures are technologically important materials for suppressing cracking in dissimilar joints with abrupt transition in thermophysical properties.

#### 12.2.4 Process Modeling

Understanding the physical phenomena involved in the LRM process is very complex and extremely difficult. This requires significant analytical and numerical modeling works to investigate/understand various aspects of LRM. In the forgoing

**Fig. 12.11** Load-displacement traces of instrumented Charpy impact test of “direct” and “graded” specimens of type 316L SS/Stellite 21. Crack growth is from SS to Stellite



section, the basic theory, equations, and the effect of various processing parameters on LRM process are discussed. A numerical model, using a finite element method (FEM)-based 2D modeling approach, is also developed to simulate the temperature distributions and geometries of single layer deposition as well as multilayered thin wall during laser rapid manufacturing (LRM). This involved an algorithm for computation of local track height at every node along the track width on the substrate/previosuly deposited layer. This was estimated by calculating the excessive enthalpies above melting point for all nodal points in the process domain to simulate multilayered thin wall. The approach takes laser power, laser beam size with its spatial profile, scan speed, powder feed rate, and powder stream diameter with its flow distribution as user-defined input and computes the temperature profiles across the process domain and the geometries of the deposited layers in a dynamic fashion. Some of the process constants, such as laser absorption coefficient, powder catchment efficiency, etc., used in the model are either from the reported literature or experimentally obtained at authors' lab to enhance the accuracy of the results. The algorithm was assessed for laser rapid manufacturing of single-layered as well as five-layered thin wall of SS 316L on a workpiece of same material with corresponding experimental results.

The basic governing equation of LRM process is given by the generalized heat equation

$$\frac{\partial(\rho C_p T)}{\partial t} - \nabla \cdot (K \nabla T) = 0 \quad (12.1)$$

where  $K$  ( $\text{W m}^{-1} \text{ K}^{-1}$ ) is the thermal conductivity,  $C_p$  ( $\text{J kg}^{-1} \text{ K}^{-1}$ ) is the specific heat capacity,  $\rho$  ( $\text{kg m}^{-3}$ ) is the density,  $T$  (K) is the temperature, and  $t$  (s) is the time.

The effect of the various processes is modeled using Eulerian approach, the material properties are considered to be temperature dependent, and the associated boundary condition is expressed as

$$\begin{aligned} -K(\nabla T \cdot n)|_{\Omega} &= [\beta_e I(x, z, u) - h_c(T - T_0)]_{\Omega} && \text{if } \Omega \in \Gamma \\ &= [-h_c(T - T_0)]_{\Omega} && \text{if } \Omega \notin \Gamma \end{aligned} \quad (12.2)$$

where  $n$  is the normal vector of the surface,  $\beta_e$  is the effective absorption factor,  $I$  ( $\text{Wm}^{-2}$ ) is the laser energy distribution on the unit length,  $u$  ( $\text{m/s}$ ) is the velocity of the laser beam normal to the cross section of workpiece,  $h_c$  is the heat convection coefficient ( $\text{Wm}^{-2} \text{ K}$ ),  $\Omega$  ( $\text{m}^2$ ) and  $\Gamma$  ( $\text{m}^2$ ) is the area of unit length workpiece surface under laser beam irradiation, and  $T_0$  ( $\text{K}$ ) is the ambient temperature. The initial boundary conditions are

$$T(x, z, t) = T_0, \quad \text{when } t = 0 \text{ and } t = \infty \quad (12.3)$$

The laser beam is assumed to be mixture of the first two fundamental modes with mixing factor of 40 % of TEM00 and 60 % of TEM01, which gives a near flattop beam profile (Fig. 12.12). The combined intensity profile for a mixed mode laser beam is given by Kumar et al. [24].

The laser beam passes through the powder cloud and falls on the workpiece. During this travel, only a part of the laser power is absorbed by the powder particles. This is incorporated by introducing an absorption factor to the laser energy. A combined radiative and convective heat transfer coefficient ( $h_c^*$ ) is considered in order to reduce computational time:

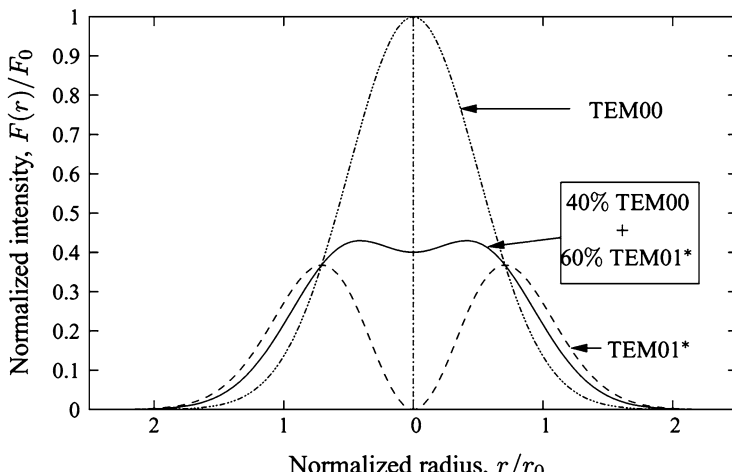


**Fig. 12.12** Laser beam profiles: fundamental modes and their mixture

$$h_c^* = 24.1 \times 10^{-4} \varepsilon_t T^{1.61} \quad (12.4)$$

where  $\varepsilon_t$  is the emissivity of the body surface.

The algorithm uses “thermal analysis” and “incorporation of additive material” recursively for small time steps to model the track geometry during LRM. To simulate the melt pool dimensions, ELMER multi-physics open-source code [25] was used to solve the governing equations and their associated initial and boundary conditions in discrete time steps. Once the melt pool boundary is obtained from the thermal analysis, material is added on the workpiece. The local height  $h_e(x)$  of the track for each discrete location  $i$  is computed by considering energy balance of the molten pool beneath it. Mathematically, it can be represented as

$$Z_{\text{new},e}|_{\Omega} = z + h_e(x)|_{\Omega} \quad \text{at } (x, z) \in W_{\text{jet}}^{\text{melt}} \quad (12.5)$$

$$W_{\text{jet}}^{\text{melt}} = \left\{ \left[ (x, z) \mid T_{(x)} \geq T_m \in W_{\text{melt}} \right] \cap \left[ (x, z) \in W_{\text{jet}} \right] \right\} \quad (12.6)$$

$$h_e(x) = \frac{h_{\text{melt}}(x)\rho_w \{C_p(T(x) - T_m) + L_f\}_w}{\rho_{\text{jet}} \{C_{pp}(T_{mp} - T_i(x)) + L_{fp}\}_{\text{jet}}} \quad (12.7)$$

where  $T_m$ ,  $T_i(x)$ , and  $T(x)$  are the melting temperature of workpiece and powder jet, local preheating temperature of powder material, and local temperature of molten pool, respectively.

The effect of powder flow rate and its local distribution is incorporated in the model by calculating local track height  $h_m(x)$  and using the conservation of mass, as represented by the following mathematical expressions:

$$h_m(x) = \frac{\eta m_p}{W_{\text{jet}} \rho_{\text{jet}} u} \quad (12.7)$$

Finally,

$$h_{\text{new}} = h_e \cap h_m \quad (12.8)$$

It may be noted that the proposed methodology carries out the mass and energy balance at the end of each time step and calculates the geometry of deposited material during that time step. This deposited geometry is meshed and used for the subsequent computational steps. A complementary code was also developed using FORTRAN to incorporate the above additive material into the process domain in between the steps. More details regarding the modeling process and its verification are provided by Kumar et al. [26]. To discretize the substrate, three-node triangular elements were used. All required element quality checks of the FE model were also performed including a convergence test. Prior to implementing the proposed model, the mesh size independency was checked using standard technique. The result of mesh independency test shows that the “near to exact solution index” becomes

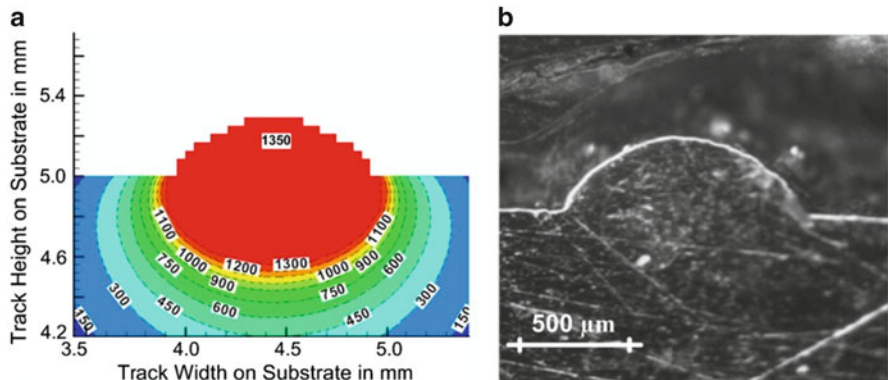


**Fig. 12.13** (a) Simulated and (b) optical micrograph of track geometry

almost steady with temperature difference less than  $10^{-3}$  K in successive runs for  $D_L/e > 30$ , where  $D_L$  is laser width and  $e$  is the width of square element.

For comparison of simulated and experimentally obtained single track geometries, a number of track geometries were simulated using developed model at different sets of processing parameters. For a set of processing parameters (laser power ( $P_1$ ) = 800 W, powder feed rate ( $m_p$ ) = 5 g/min, scan speed ( $u$ ) = 600 mm/min), the results obtained for simulation of single track geometry along with the isotherms are presented in Fig. 12.13a. Simulated results are shown in Fig. 12.13a, while for experimental results, the tracks were laid and cut normal to scanning direction. The track geometries were examined under the optical microscope. The obtained results are presented in Fig. 12.13b. It is observed that the track width governed by laser beam diameter is also a weak function of scan speed, while the track height is basically governed by the powder feed per unit length. This is in concurrence with the earlier reported work.

The above studies were also extended to multilayered deposition. Various simulated results of five-layered thin wall were obtained using the present modeling approach. For the processing parameters,  $P_1 = 1 \text{ kW}$ , laser width ( $D_L$ ) = 2 mm,  $u = 1,000 \text{ mm/min}$ , interaction time = 0.12 s, and each layer was deposited after 20 s of interval. After 4 s of fifth layer deposition, the 2D temperature distribution is given in Fig. 12.14.

Tables 12.4 and 12.5 present the maximum height of various layers after different cooling times for two sets of processing parameters. It was observed that the deposition height increased initially in successive layer deposition for same set of processing parameters. However, it saturates at a particular layer depending on the processing parameter. This is due to preheating of the substrate and deposits in successive layers. However, after few layer depositions, the top of the thin wall cools at a faster rate. Therefore, saturation occurs. For laser power of 1 kW, fourth layer deposition was found to be the largest. Further, for lower scan speeds

**Fig. 12.14** Geometry and temperature profile after five-layer deposition

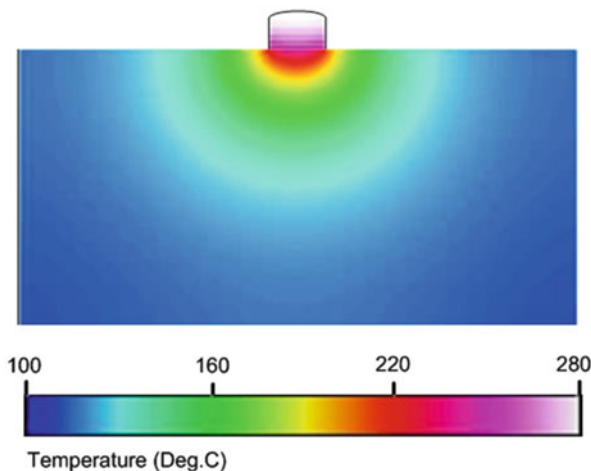


**Table 12.4** Maximum height (in mm) of various layers after different cooling times for power = 1,000 W, scan speed = 1,000 mm/min

Cooling time	Layer 1	Layer 2	Layer 3	Layer 4	Layer 5
After 5 s	0.167	0.171	0.264	0.386	0.351
After 10 s	0.167	0.171	0.261	0.271	0.366
After 20 s	0.167	0.169	0.262	0.272	0.364
After 40 s	0.167	0.169	0.261	0.270	0.362

**Table 12.5** Maximum height of various layers after different cooling times for power = 1,000 W, scan speed = 700 mm/min

Cooling time	Layer 1	Layer 2	Layer 3	Layer 4	Layer 5
After 5 s	0.278	0.339	0.602	0.773	0.720
After 10 s	0.278	0.335	0.601	0.767	0.711
After 20 s	0.278	0.335	0.599	0.768	0.716
After 40 s	0.278	0.334	0.597	0.764	0.707

(keeping other process parameters same), the deposition is more in each successive layer (Table 12.5) due to higher interaction time.

The study showed that a thin wall could be fabricated if the laser power, scanning velocity, powder feed rate, and other process parameters were matched suitably. The accuracy and capability of the developed algorithm was experimentally verified for LRM using SS316L powder on the same workpieces. It was found that the wall thickness decreased with density and increased in specific heat. Thus, for the same set of processing parameters, the thickness of the wall varied with the change of material. Wall thickness increased with increasing laser power. An increase in laser spot diameter or a decrease in scanning speed resulted in an increase in wall thickness, but an over large laser spot made the pool rather cool so that melted powder decreased, resulting in a decrease in wall width. Powder feed rate had

influence on laser absorptivity. Laser absorptivity decreased with increasing powder feed rate, resulting in a decrease in wall thickness. The developed model is capable of dynamically predicting the temperatures and multilayered thin wall geometry at various process parameters.

### ***12.2.5 Ratiocination***

Laser rapid manufacturing is an extremely flexible technique with application in multiple areas from repair of large-scale components to manufacturing of component with specific end application. It is now crossing the barriers of conventional component fabrication and entering into new era of “feature-based design and manufacturing.” The scope of this technology is being extended to more complex multi-material and multifunctional components with high degree of control on fabrication. The availability of compact high-power lasers, advanced CAD/CAM systems with faster computing speeds, and advanced diagnostic and control systems has provided a new dimension to manufacturing, and laser rapid manufacturing is one of such development. Technical factors, such as advancement in subsystems, and economic factors, such as falling price of lasers and other subsystems, will further alleviate the deployment of LRM technology to manufacturing.

## **12.3 Laser Peening**

Laser shock peening (LSP) is a surface engineering process that imparts a layer with beneficial residual compressive stress on metallic components to help them better resist the detrimental effects of fatigue and corrosion. In this process, a high peak power density ( $\text{GW}/\text{cm}^2$ ) and short duration (10–25 ns) laser pulse is fired at the surface of a metal part to generate high-pressure plasma, which sends shock waves into the part resulting in consistent and deeper compressive stresses in the material near surface. It is similar to shot peening but imparts compressive stresses much deeper into components with minimal surface deformation. The process replaces the stream of tiny metal or ceramic balls and exhibits substantial advantages over conventional shot peening relative to fatigue strength improvement, depth of compression layer, and process control. Each laser pulse creates an intense shock wave over a surface area of few  $\text{mm}^2$  that drives a residual compressive stress up to 2 mm deep into the base metal. In conventional peening, this compressed layer is approximately 0.25 mm deep. The added depth is key to laser peening’s superior ability to prevent cracks from initiating and propagating, which extends the life of parts 3–10 times over that provided by conventional treatments.

Only in the past two decades, there has been an increased interest in this technology for applications ranging from aeronautic to automotive fields. Recently, major gas-turbine manufacturers brought in laser shock peening to improve fatigue

performance of fatigue critical parts of engine components (e.g., engine blades). The residual stresses introduced by laser shock peening can also be used to generate curvatures in metallic plates. This area is currently under investigation by major aircraft manufacturers. Current LSP-related R&D activities encompass a broad spectrum of areas including biomedical implants, aeroengine and aerospace structural materials, and nuclear materials [27].

### ***12.3.1 Lasers in Peening***

Laser peening technology and processes have been refined for practical use; commercial applications range from large aircraft components, to power generation system parts, to knee replacements. All these critical, high-cost components require greater depths of compressive stress [28]. Mobile systems are also advancing the widespread acceptance and use of laser peening. Transportable laser peening systems, currently in routine operation, facilitate reaching components of arbitrarily large size, such as naval vessels in a shipyard. Commercial laser peening system relies on high-pulse-energy (20–50 J) flash-lamp-pumped glass laser systems that can place high-quality square or rectangular spots onto the treatment surface at a pulse repetition frequency of up to 5 Hz [[www.metalimprovement.com](http://www.metalimprovement.com)]. Nd:YAG laser with output energy in the range of 1–5 J is also being widely used in applications where laser beam transmission through fiber optics is essential from application point of view. Painless underwater laser peening, using Nd:YAG ( $\lambda = 1064$  nm) and 2nd harmonic Nd:YAG laser ( $\lambda = 532$  nm) with a maximum pulse energy in the range of 1.5–3 J, has been studied particularly for nuclear applications.

Since the last one decade, efforts are underway at RRCAT, Indore, India, to develop a laser system suitable for pursuing laser peening. A 2.5 J flash-lamp-pumped electro-optically (E-O) Q-switched Nd:YAG laser system has been indigenously developed and being extensively used for laser peening studies for various applications including automotive, power, and nuclear applications [29–31].

### ***12.3.2 Experimental Setup***

The experimental LSP setup comprises of (1) Nd:YAG laser system, (2) beam delivery system consisting of a 45° plane mirror and a focusing lens of 400 mm focal length, (3) a 2-axis computer numerically controlled (CNC) workstation, and (4) a water recirculation system. The raw laser beam, emanating out of the laser system, is folded with a 45° plane mirror and focused with the help of a convex lens of 400 mm focal length. For avoiding laser-induced air breakdown at the focal

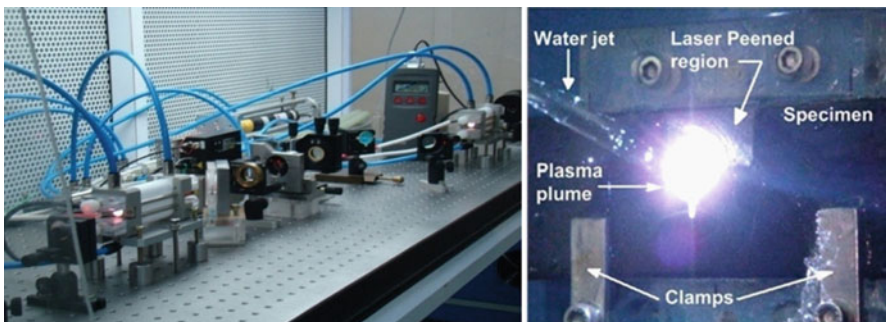


**Fig. 12.15** Experimental setup for laser shock peening at Solid State Laser Division of RRCAT

**Table 12.6** Important features of laser peening system

Parameters	Value
Wavelength	1,064 nm
Configuration	Oscillator and amplifier
Output energy	2.5 J
Pulse width	7 ns
Spatial profile	Super Gaussian
$M^2$	$\sim 4$
Rep. rate	5 Hz

spot, the specimen was placed before the focal plane. The experimental setup and the laser peening process are depicted in Fig. 12.15, and important features of the system are listed in Table 12.6.

### 12.3.3 Recent Developments

Comprehensive studies about parametric dependence are reported in the literature. The effects of various processing parameters on resultant compressive residual stresses during laser peening are summarized in Table 12.7.

Laser shock peening (LSP) study, performed on 6 mm thick SAE 9260 spring steel specimens with 2.5 J/7 ns Nd:YAG laser, demonstrated how residual compressive surface stress generated by LSP brought about large increase in the fatigue life [29]. Laser peening successfully introduced about 370  $\mu\text{m}$  thick compressed layer with surface stress ranging from  $-300$  to  $-450$  MPa, without causing noticeable effect on surface roughness or morphology of the treated surface. Laser shock-peened specimens exhibited significant increase in fatigue life over untreated as well as shot-peened specimens (Fig. 12.16), treated as per the existing shot peening practice adopted for leaf springs. Improved fatigue performance of laser

**Table 12.7** Effects of processing parameters on resultant compressive residual stresses

Processing parameter	Effect on compressive residual stresses
Laser power density	Increases with increase in laser power until saturation due to possible air breakdown
Number of shots per unit area	Increasing the number of shots increases the magnitude of compressive residual stress and depth of compressed zone until saturation
Spot size	Large spot size generates deep compressed zone, whereas small spot size can produce higher surface compressive stress as compared to large spot at the same laser power density
Pulse duration	Reducing the pulse duration reduces the depth of compressive residual stresses through the thickness

**Fig. 12.16** Comparison of fatigue lives of untreated, shot-peened, and laser-peened specimens of SAE 9260 spring steel

shock-peened specimens is attributed to compressive surface residual stress field and largely unaltered surface finish without peening-induced surface defects, which are potential fatigue crack nucleation sites in shot-peened specimens.

### 12.3.4 Ratiocination

Since laser peening is based on widespread science and technology ranging from plasma physics to automated robotic system, interdisciplinary cooperation and information exchange are highly effective to accelerate research and development on laser peening. Persistence and stability of peening-induced residual stress fields, under cyclic loading and thermal exposure, are active research areas being pursued extensively. Other research areas of laser peening include femtosecond laser shock hardening and laser peening-based controlled forming of metal sheets.

## 12.4 Emerging Trends in Conventional Laser Processing

### 12.4.1 Novel Laser Power Modulation for Improved Quality of Laser Cut Profiles

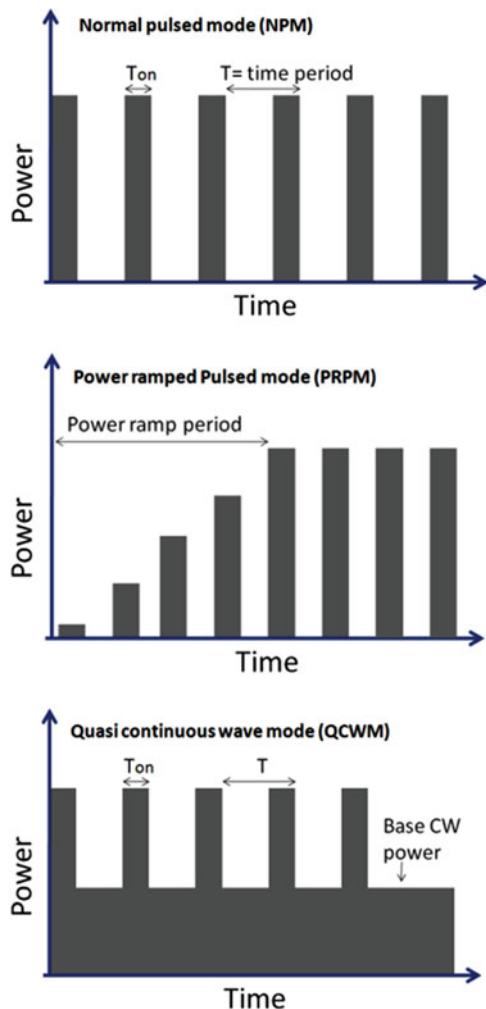
High average power infrared lasers are being extensively used worldwide to meet the expanding productivity requirements in industrial cutting. Laser cutting as a noncontact process offers unparalleled match in terms of accuracy and quality. Today, laser cutting is extensively deployed in different industries for 2D and 3D profile cutting of metal sheets and plates. In spite of successful applications, fundamental research with aid of improved laser technology and understanding the dynamics of laser cutting process still have a lot of potential to realize very fine featured cut profiles that cannot be produced with other conventional cutting methods [32–35]. Till date, high-power CO<sub>2</sub> and Nd:YAG lasers are primary workhorses for industrial metal sheet cutting.

Recently developed high-power fiber laser is also an upcoming candidate for laser cutting due to its compact system design and ease of beam portability [36, 37]. Developments in laser systems in terms of power, beam quality, and different novel power modulation schemes have aided in addressing many complex problems in more productive way. To produce high-quality laser cut profiles of steel, it is important to obtain fine and spatter-free pierced holes at the site of cut initiation along with dross-free cut edges of minimum roughness and microstructural changes. The following section presents the innovation with laser processing parameters by employing laser power modulations for producing narrow featured laser cut profiles. In the comprehensive study, various power modulations are employed to study oxygen-assisted laser piercing process and edge quality of laser cut mild steel (MS) samples. The various power modulations under investigation include power ramped pulsed mode (PRPM), quasi-continuous wave mode (QCWM), and normal pulsed mode (NPM) as presented schematically in Fig. 12.17.

#### 12.4.1.1 Oxygen-Assisted Laser Piercing Process and Effect of Power Modulations

Laser piercing is one of the inevitable requirements of laser profile cutting process, and it has a direct bearing on the quality of the cut profiles. The pierced hole at the incipient location of a cut profile helps in establishing a uniform melt ejection from lower side of the kerf. To produce intricate and closely spaced laser cut profiles, clean and fine pierced holes of dimensions close to kerf width are essential. In oxygen-assisted laser piercing of steel if the piercing is performed with the same laser power as used for the cutting, it results into large size irregular pierced holes as shown in Fig. 12.18a. The formation of large pierced hole can be understood from laser and oxygen jet interaction with the workpiece during the piercing which is shown in Fig. 12.19. When the laser-assisted combustion initiates the melting of

**Fig. 12.17** Schematic representation of laser power variations in different modes



the metal, the combustion front propagates radially outward. The thrust provided by the pressurized oxygen jet on the formed molten material causes its explosive ejection toward the cutting nozzle. Because of explosive melt ejection, this kind of piercing is termed as blast piercing. Since the diameter of interacting laser beam is much smaller (typically about 0.1–0.3 mm) than that of the reacting oxygen jet (more than 2 mm), the combustion front can easily propagate much away from the laser interaction zone which leads to the formation of large size pierced holes. If the workpiece is thicker, the laser interaction time is longer and so the length of heat diffusion. Therefore, in blast mode piercing, the pierced hole diameter scales with the workpiece thickness. Though blast piercing is a relatively faster process, it obstructs in producing finer or closely spaced cut profiles. Further, the irregular,

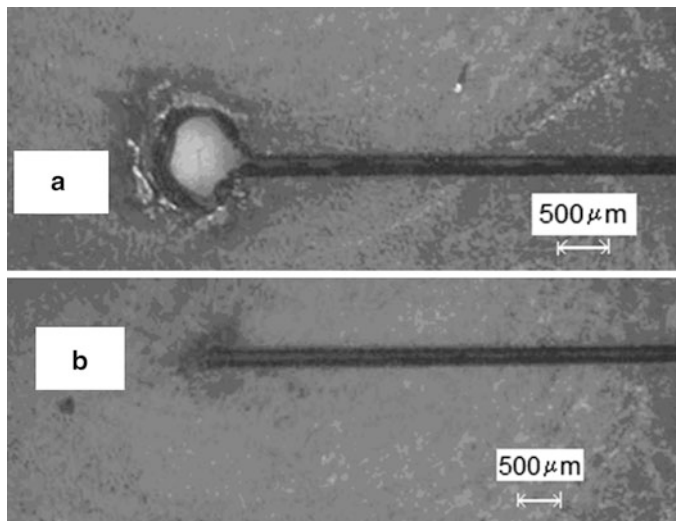
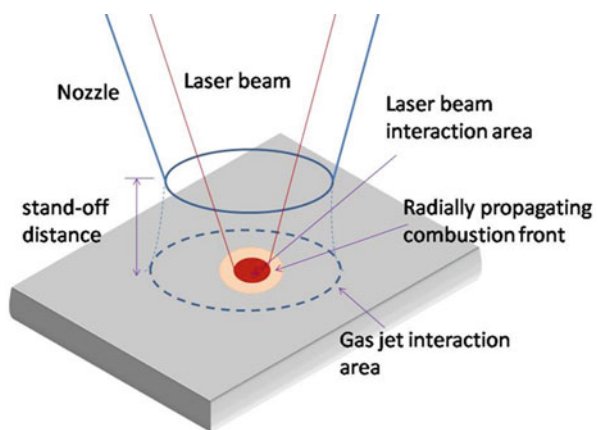


**Fig. 12.18** Laser cut initiation with (a) blast piercing and (b) PRPM piercing

**Fig. 12.19** Schematic representation of laser and gas jet interaction during laser piercing



nonparallel, and large size pierced holes enforce to avoid their remnant marks in the required cut profile. Moreover, the involved explosive molten material ejection causes frequent damage of the cutting nozzle, and sometimes its adhesion at the tip of the nozzle perturbs the standoff distance control and oxygen flow.

To produce smaller size pierced holes, control of radially propagating combustion by limiting the temperature of surrounding area of the laser interaction zone is very essential. The rise in temperature at a given point mainly depends upon the laser intensity (power) and interaction time. Normal pulsed mode (NPM) is capable of controlling the laser interaction time. As a result, it decreases the severances of some of the above-mentioned problems associated with continuous wave (CW) mode produced blast piercing [38]. In contrast to this, the authors have developed

a power ramped pulsed mode (PRPM) as shown in Fig. 12.17 which is found to be an effective solution to oxygen-assisted laser piercing [39]. Figure 12.18b presents the laser cut kerf initiated with controlled pierced hole produced with the PRPM laser piercing. The PRPM mode controls the laser peak power and interaction time simultaneously; thus, it eliminates the undesirable effects of blast piercing. In PRPM, very low power at the beginning of the process restricts the radially spreading combustion front which allows the formation of narrow pierced hole at the top side. As the piercing progresses, the increasing peak power helps in efficient melt ejection from deeper part of the formed hole. Therefore, PRPM method produces finer pierced holes compared to NPM piercing. By implementing NPM and PRPM techniques in an indigenously developed CO<sub>2</sub> laser, laser piercing was studied in both the modes and process parameters; mainly pulse repetition frequency (PRF) and duty cycle ( $T_{on}/T$ , Fig. 12.17) were optimized to produce finer pierced holes [39].

Figure 12.20 presents micrographs of the pierced holes produced with NPM at 300 and 500 Hz PRF. From this figure, it can be observed that as the pulse duty cycle was increased, the size of the pierced hole increased along with large amount of spatter adhesion around the hole. Since an increase in duty cycle increases the average power and decreases the cooling effect, both the factors favor the laser-assisted combustion process. Consequently, duty cycle has shown a strong influence on pierced hole's size, shape, and spatter.

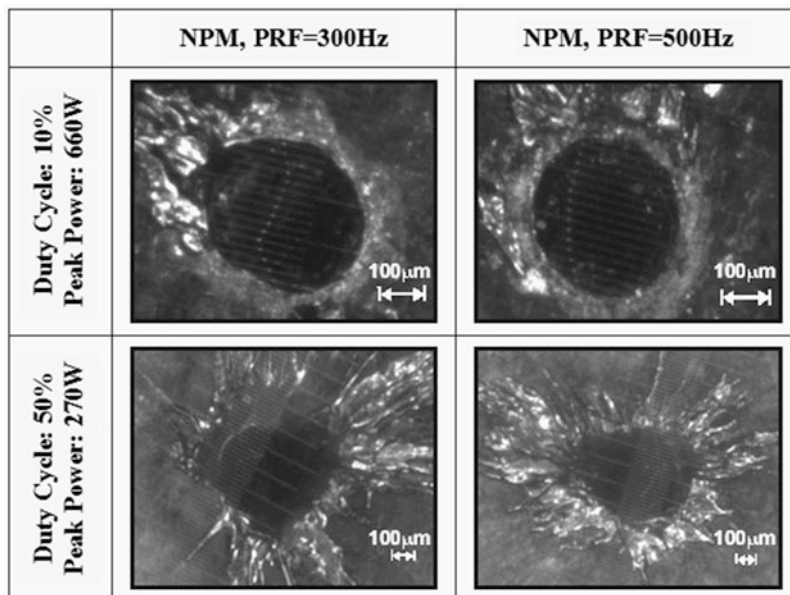


**Fig. 12.20** Micrographs of the laser pierced holes in 1.5 mm thick mild steel sheet with NPM at 300 and 500 Hz frequency and 10 % and 50 % duty cycles

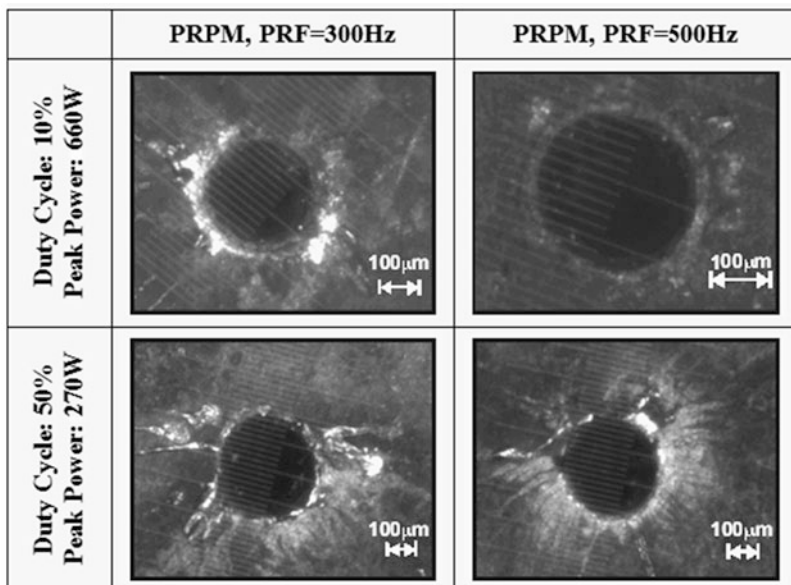


**Fig. 12.21** Micrographs of the laser pierced holes in 1.5 mm thick mild steel sheet with PRPM at 300 and 500 Hz frequency and 10 % and 50 % duty cycles

Figure 12.21 presents the micrographs of the pierced holes produced with PRPM under the same process parameters of NPM. It was observed that the pierced holes produced in PRPM are more circular along with lesser amount of spatter. From this figure, it can be seen that at low duty cycle even though the peak power is higher, the pierced holes are more circular and associated with low spatter. The use of higher pulse frequency with lower duty cycles is found to be more suitable for producing circular, narrow, and minimum spattered holes. Also, the process parameter zone for producing the narrow size pierced holes was found to be large in PRPM as compared to NPM. This study demonstrated that controlled laser power modulations using PRPM significantly affect the dynamics of oxygen-assisted piercing process in mild steel.

#### 12.4.1.2 Effect of Different Laser Power Modulations on Cut Edge Quality of Mild Steel

The quality of laser cut profiles and their suitability for subsequent component fabrication (without any intermediate machining) is governed by cut edge morphological features: mainly roughness and dross adhesion. Roughness on laser cut edges is a consequence of periodic striations formed on the cut edges. The formation of periodic striations on laser cut edges even with constant CW power reveals that interaction between incident laser beam and the workpiece as well as the melt

ejected during the cutting behaves in cyclic manner. Therefore, modulations in laser power at certain PRF, duty cycle, and power levels can influence the basic cyclic processes of laser-assisted combustion and melt ejection. By using optimum power modulations, cut edge can be produced with finer striations having low roughness.

Laser cutting in NPM, at a given duty cycle with change in PRF, maintains a constant average power, but it alters the laser interaction period. In contrast to this, change in duty cycle alters the average laser power in addition to change in interaction period. Furthermore, a quasi-continuous wave mode (QCWM) schematically shown in Fig. 12.17 is a hybrid mode of NPM and CW mode. Laser cutting in this mode with systematic variation of PRF and duty cycle is helpful in detailed understanding of changes in striation morphology produced with CW mode and NPM. Therefore, with the help of a suitably configured switched mode power supply (SMPS), NPM and QCWM laser power modulations were implemented in an indigenously developed CO<sub>2</sub> laser and the effect of these modes on oxygen-assisted laser cutting of 1.5 mm thick mild steel was studied [40]. For laser cutting in both modes, the peak power of about 500 W was used, and for QCWM, the base power of 250 W was employed (Fig. 12.17).

For oxygen-assisted CO<sub>2</sub> laser cutting of mild steel with NPM and QCWM, cutting speed range was experimentally determined for 30 and 60 % duty cycles and presented in Fig. 12.22. The important requirements governing the lower and upper limits of the cutting speed are as follows: (1) avoiding uncontrolled burning (determines lower limit) and (2) acquiring full penetration cutting (determines the upper limit). In the figure, the values presented within the brackets at both limits of speed correspond to severance energy, defined as the average laser energy consumed in producing unit surface area of the cut edge. As compared to the optimum severance energy range of 4–13 J/mm<sup>2</sup> using CW mode [41], in NPM, the cut

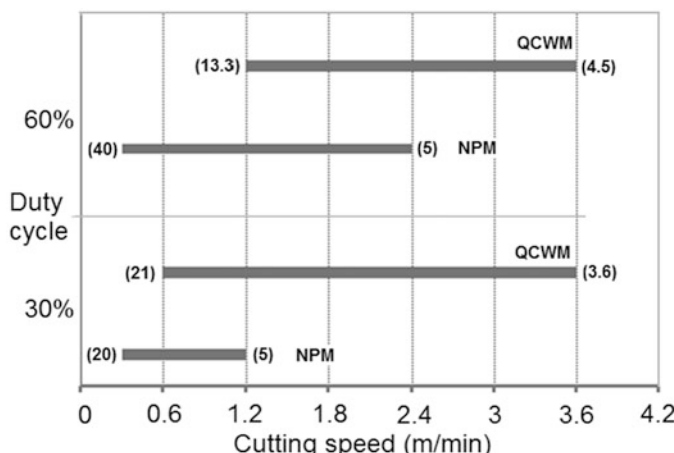


**Fig. 12.22** Cutting speed variation under different laser power modulations along with severance energy (J/mm<sup>2</sup>, shown in the *brackets*)

edges produced with severance energy up to  $20 \text{ J/mm}^2$  were found to be of high quality without any gouging. The observed higher range of severance energy in NPM is due to completely different dynamics of laser interaction with respect to that prevalent in CW mode cutting. In NPM laser cutting, intermittent cooling between successive laser pulses suppresses the uncontrolled combustion which is responsible for gouging. In contrast to this, laser cutting in QCWM at 60 % duty cycle as the severance energy approaches to  $13 \text{ J/mm}^2$ , gouging on cut edges was observed. This range is in agreement with that of reported values for CW mode cutting [38, 41] which is as expected since in QCWM, as the duty cycle increases, it approaches to CW mode.

Figure 12.23 presents the micrographs of laser cut edges produced in NPM with 30 and 60 % duty cycles and 100 and 500 Hz PRFs. From this figure, it can be seen that at 30 % duty cycle, for low PRF, the striations were distinctly visible, but their visibility faded out at higher PRF. This is because at higher PRF, pulse interaction length and pulse energy in pulse are lesser which in turn causes a decrease in melt

$V (\text{m/min})$ (S.E.)	NPM, DC-30%, Peak power =500W	
	100Hz	500Hz
0.3 (20)		
1.2 (5)		
NPM, DC-60%, Peak power =500 W		
0.6 (20)	100 Hz	500 Hz
1.8 (6.6)		

**Fig. 12.23** Micrographs of laser cut edges produced with NPM at different pulse parameters. In the *left column*, values written in *brackets* represent severance energy ( $\text{J/mm}^2$ )

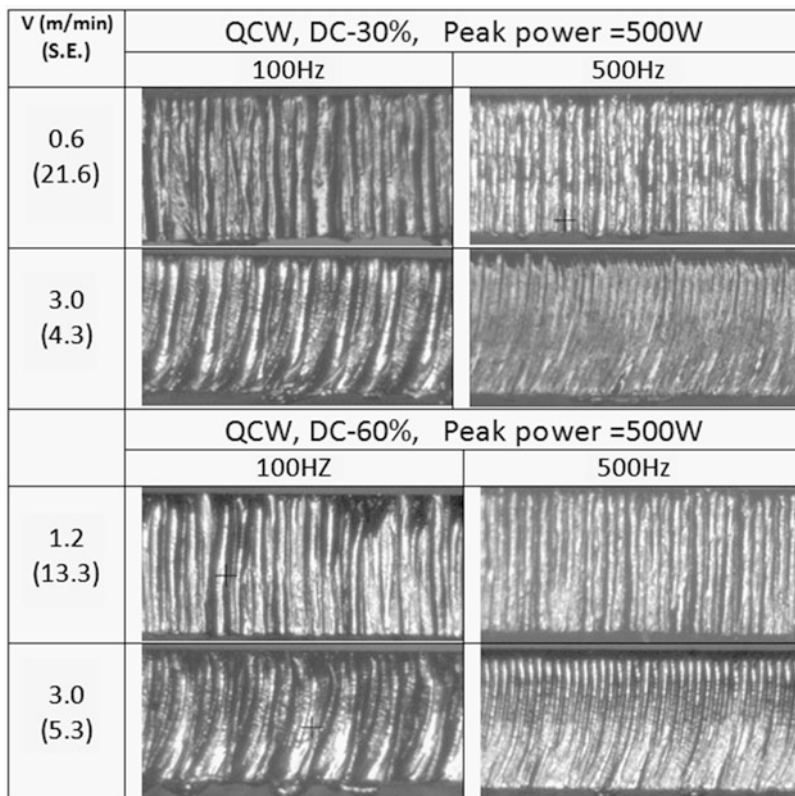


**Fig. 12.24** Micrographs of laser cut edges produced with QCWM at different pulse parameters. In the *left column*, values written in *brackets* represent severance energy in  $J/mm^2$

front propagation ahead of the laser spot. An increase in duty cycle from 30 to 60 % resulted in an increase of maximum cutting speed from 1.2 to 2.4 m/min, indicating conservation of severance energy. It was observed that the cut edges produced at lower and higher cutting speeds were accompanied with adhered dross.

Figure 12.24 presents micrographs of laser cut edges produced in QCWM with different PRFs and cutting speeds at 30 and 60 % duty cycles. In this case, the maximum cutting speed (3.6 m/min) obtained with 30 % duty cycle is same as that obtained with 60 % duty cycle, in spite of an increase in average laser power from 325 to 400 W. At 30 % duty cycle in QCWM, the average power is about twice of that in NPM, but the obtained maximum cutting speed was three times (3.6 m/min in QCWM) of that in NPM (1.2 m/min). This shows that the threshold severance energy required for obtaining full penetration cutting in NPM is higher than that of QCWM. This is attributed to the associated intermittent cooling between successive laser pulses in NPM, whereas the presence of base power between successive pulses in QCWM sustains combustion even at higher cutting speeds.

This study shows that the range of severance energy is extended toward higher values as compared to that of QCWM cutting for optimum laser cutting in NPM. Therefore, a suitable closed-loop control of duty cycle in proportion to cutting speed in NPM (involving progressive change in pulse duty cycle in proportion to cutting speed) will effectively suppress unwanted heating effects at sharp corners of laser cut profiles. In NPM particularly at 30 % duty cycle with low PRF, distinct striations are formed on the cut edges. But as the PRF increased to 500 Hz, obtained cut edges were almost free of striations. In NPM, the maximum cutting speed increases proportionately with the duty cycle, but in QCWM, the maximum cutting speed is mainly governed by the base CW power between the pulses rather than duty cycle.

#### ***12.4.2 Vertical Surface Cladding***

Laser cladding is one of the established alternative techniques for improving surface properties of the engineering components [42]. Laser cladding utilizes a high-power laser as energy source to melt and deposit a layer of the desired material (in the form of powder or wire) onto the substrate forming a sound metallurgical bond with minimal dilution [16]. A wide variety of the clad materials and substrates are reported in the literature for various applications in automotive, aerospace, machinery, petrochemical, power generation, and shipbuilding industries [1, 43]. Laser cladding on vertical surface is important for many engineering applications, such as surface cladding of turbine blade shroud and interlock, offshore drilling heads, cylinder body, sleeve and mold side walls, etc. At our laboratory, a newly designed laser processing head is augmented to existing laser workstation and successfully used for laser vertical surface cladding experiments. In vertical configurations, the gravity plays an important role to decide the clad geometry, surface finish, and waviness. The effective viscosity of solidifying molten metal clad that counteracts the effect of gravity changes with the interaction time. Hence, it is important to understand the effect of gravity on molten clad and its subsequent downward flow before solidification for prediction of clad geometry in vertical configuration. Therefore, an analytical model incorporating gravitational effect during laser vertical surface cladding was developed and experimentally verified. The processing window for various values of laser energy per unit length, powder fed per unit length, and overlapping index for laser vertical surface cladding of Inconel 625 was experimentally identified. The effect of powder catchment efficiency for various standoff distances was also evaluated. The effect of overlapping parameter on the waviness of the overlapped clad was experimentally determined.

The schematic arrangement of laser cladding head is shown in Fig. 12.25. The overall dimension of the nozzle is 63 mm × 63 mm × 60 mm. The laser cladding head has two subassemblies: (a) laser processing head and (b) side-blown powder feeding tube. The laser processing head has a Quartz lens of 200 mm focal length to focus the laser beam. The focusing laser beam is reflected normal to the vertical plane by an Au-coated plane mirror (diameter, 25 mm and 6 mm thick) mounted 45°

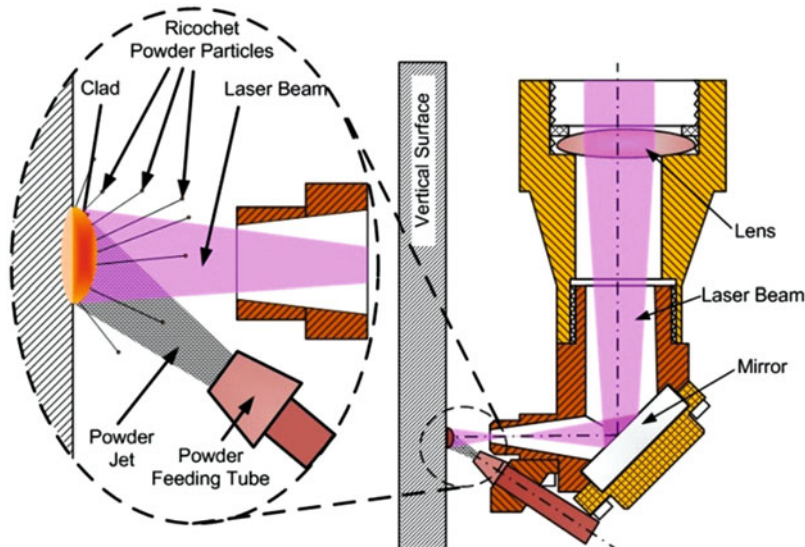


**Fig. 12.25** Schematic arrangement of laser cladding head for processing vertical surfaces

to the incoming laser beam axis. There is a provision of moving beam bender up and down with respect to focusing lens to match the laser beam size to the powder stream size to facilitate the maximum powder catchment efficiency. A port for inert gas is provided at the upper part of laser processing head to protect the Au-coated mirror from ricocheted powder particles which may enter the beam bender and damage the mirror. This gas also assists the shielding of molten metal from oxidation. The laser has suitable water cooling arrangement to control the temperature of processing head during the processing. The side-blown powder feeding tube has inside diameter of 2 mm and is mounted at the bottom of the laser head making an inclination angle of 35° with laser beam axis. It may be noted that the cooling of the tip of the powder feeding nozzle and the laser processing head also reduces the tendency of clogging of the nozzle with ricocheted powder. It is because the nozzle tip at lower temperature does not allow the wetting of bounced metal particles on the nozzle surface due to higher cooling rate resulting in lower contact area. The material of the construction is copper because of its lower laser absorption and higher thermal conductivity.

It was observed that a minimum threshold laser power, sufficient interaction time, and optimal powder flow rate were required for successful deposition of material in vertical configuration. However, we find the effect of these three parameters can be accounted with the following two parameters:

$$\text{Laser Energy per unit traverse length } (E_l) = \frac{\text{Laser Power } (P_L)}{\text{Scan Speed } (v)} \quad (12.9)$$

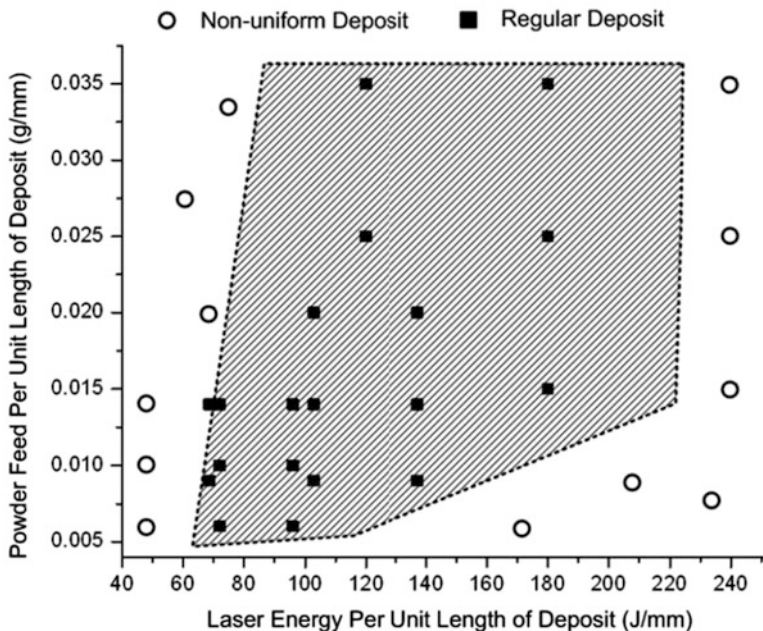


**Fig. 12.26** Processing window for laser vertical surface cladding of Inconel 625

$$\text{Powder fed per unit traverse length } (m_{p/l}) = \frac{\text{Powder feed rate } (m_p)}{\text{Scan Speed } (v)} \quad (12.10)$$

The parameters “laser energy per unit traverse length” and “powder fed per unit traverse length” govern the laser energy and the material available for the single clad deposition, respectively. Figure 12.26 presents the processing window for laser cladding on the vertical surface for the experimental range of parameters under investigation. At extremely high laser energy per unit traverse length and lower powder fed per unit traverse length, there may be vaporization of the feed material. As a result, there may be very thin or no clad formation. On the contrary, at extremely low laser energy per unit traverse length and higher powder fed per unit traverse length, the feed material may not fuse and form a discontinuous irregular clad. Hence, there is a processing window, where a balance of both the parameters results in fused continuous clad.

The powder catchment efficiency is one of the important processing parameters for high-quality deposit geometry and economical viability of the process. It is the ratio of the powder deposited to the powder fed for the deposition during the laser cladding process. Mathematically,

$$\eta = \frac{\text{Powder deposited per unit length } (m_d)}{\text{Powder fed per unit length } (m_p)} \quad (12.11)$$

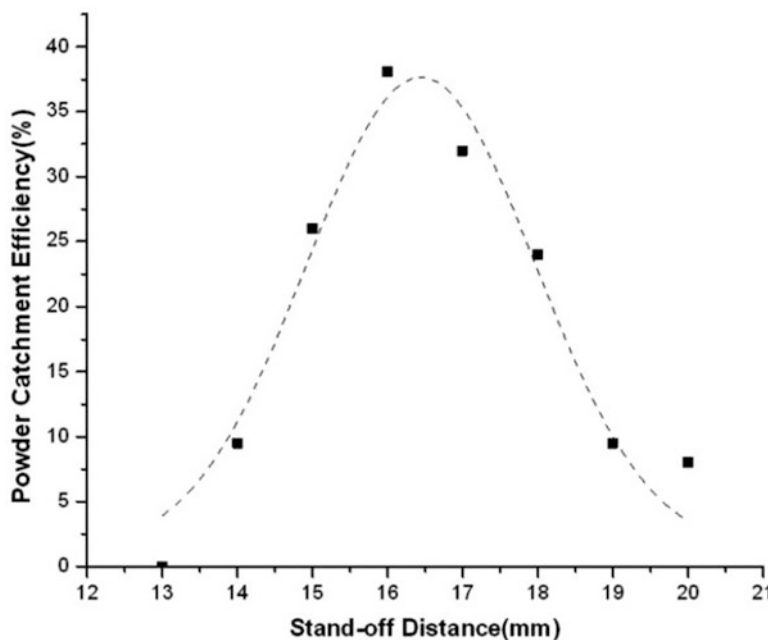


**Fig. 12.27** Powder catchment efficiency as a function of standoff distance between the nozzle tip and substrate during laser vertical surface cladding on Inconel 625

Maximum powder catchment efficiency is obtained when there is cent-percent overlap of powder stream diameter and laser beam diameter at the substrate. In the side-blown powder delivery configuration, it is not possible to achieve the cent-percent overlap of the diameters due to geometrical constraints [44]. The maximum powder catchment efficiency derived from ray diagram at maximum overlap region of powder stream and laser beam on the substrate for our present configuration is 65 %. Since various nozzle standoff distances between the nozzle tip and substrate resulted in different powder and laser beam diameters, the catchment efficiency varies accordingly. Figure 12.27 shows the variation of powder catchment efficiency at different nozzle standoff distances between the nozzle tip and substrate during laser vertical surface cladding on Inconel 625. It is observed that catchment efficiency increases as the standoff distance is increased up to a certain value and then it falls. The maximum catchment efficiency is obtained where there is maximum overlapping region of powder stream and laser beam. For our configuration, the maximum catchment efficiency is obtained at the standoff distance between 15 and 17 mm.

The surface characteristics of the deposited geometry on vertical substrate play an important role as it defines the manufacturing tolerance and post-processing of the deposits. Generally, multilayered overlapped clad is used for the fabrication of any engineering components or cladding on the surfaces. Higher waviness and poor

surface roughness mean less effective deposition to achieve on the plane surface. The laser cladding surfaces have two distinct characteristics: surface roughness and surface waviness. The surface roughness is primarily due to semi-molten powder particles adhered on the deposit, while overlapping parameter governs the surface waviness to a great extent.

As shown in Fig. 12.28, “overlap index” is defined as the ratio of the center distance between the two successive overlap clads to the overall clad width, while “waviness factor” is defined as the ratio of the height to be removed to get the flat surface to the total height deposited. Mathematically,

$$\text{overlap index } (i) = \frac{s}{W} \times 100 \quad (12.12)$$

$$\text{waviness factor } (j) = \frac{H_{\max} - H_{\min}}{H_{\max}} \quad (12.13)$$

A number of overlapped clad samples were made at various overlap indices. Figure 12.29 presents the variation in waviness factor at different overlap indices.

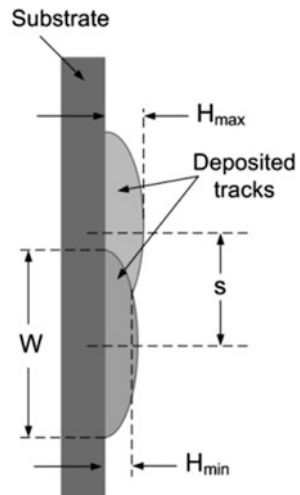


**Fig. 12.28** Schematic diagram for various parameters for overlapped deposition

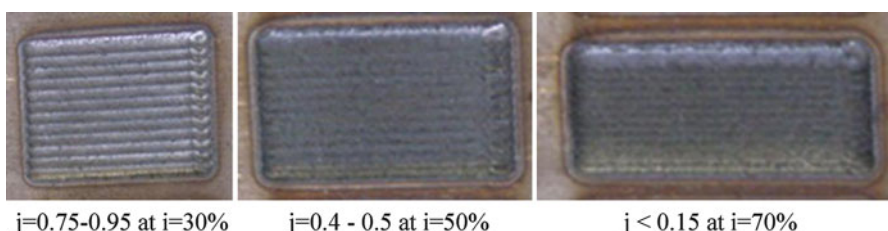


**Fig. 12.29** Variation in waviness factor at different overlap indices

It can be seen that the waviness factor decreases as the overlap index is increased. For overlap index greater than 70 %, layer height goes on increasing in subsequent overlapping clads and it leads to inter-run porosity due to a lack of fusion zone along the clad. The surface finish was also measured in the samples across and along the clad. The surface finish was found to be 12–14  $\mu\text{m}$   $R_a$  and 9–12  $\mu\text{m}$   $R_a$  across and along the clad, respectively. A similar trend is observed for surface finish along and across the clads for laser cladding on horizontal surfaces [44–46]. The surface finish during laser cladding on horizontal surfaces was in the range of 12–25  $\mu\text{m}$   $R_a$  [45]. Thus, the surface finish in vertical surface cladding was found to be better than that of horizontal surfaces. It is because the semi-molten particles sprayed toward molten pool fall down due to gravity, and it leads to reduced tendency of the semi-molten powder particles adhering to the surface.

The laser cladding on the vertical surface depends on a number of processing parameters, and proper combination of these parameters results in the uniform and sound deposition of the material. It has been observed that the surface roughness during laser cladding in vertical configuration is better than that of horizontal configuration. It is because the powder particles do not adhere to the vertical surface in partial melting condition and slide down due to gravity. Figure 12.30a, b presents the laser cladding carried out on the internal and external surfaces, respectively, of tubular geometry in vertical configuration at authors' laboratory.

### 12.4.3 *Laser Welding*

Laser welding is a technique used to join multiple pieces of metal through laser melting. Laser beam provides a concentrated heat source, allowing for narrow, deep welds and high welding rates. The process is a well-established industrial process due to key advantages in terms of automation and high productivity. The following section presents some of the recent innovations at authors' laboratory. The innovation involves a systematic control of the laser processing parameters to achieve the desired results.

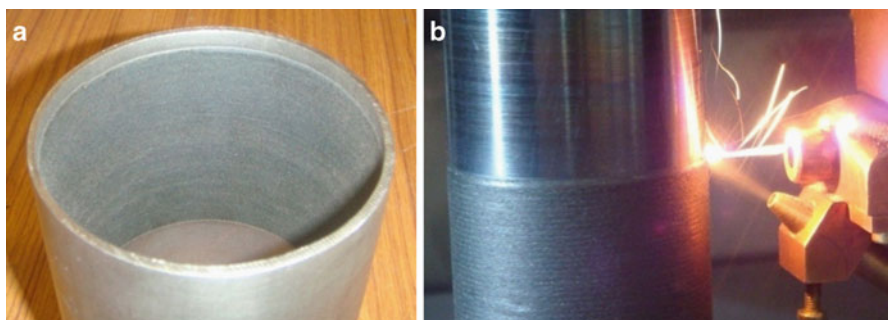


**Fig. 12.30** Laser vertical surface cladding on (a) internal and (b) external surface of tubular geometry

In one of the studies, precise focusability of laser beam was exploited to control weld metal chemistry for suppressing weld solidification cracking in dissimilar weld. Dissimilar weld of a clad tube (alloy D9) and an end plug made of AISI 316M forms a part of the fuel pin of 500 MWe Indian Prototype Fast Breeder Reactor (Fig. 12.31a). Alloy D9, because of its low  $\text{Cr}_{\text{eq}}/\text{Ni}_{\text{eq}}$  ratio (close to 1), solidifies with primary austenite mode which makes its welds particularly susceptible to solidification cracking. A defect-free weld, with predominantly primary ferrite mode of solidification, was obtained by preferential displacement of focused CW  $\text{CO}_2$  laser beam toward the end plug side to obtain greater dilution of weld metal from end plug [47]. Figure 12.31b presents the cross section of one of the sound end plug laser welds.

Termination site of a CW laser weld is usually marked with an unfilled crater, formed as a result of abrupt drop in incident laser power. The craters are usually associated with cracks. Figure 12.32 shows crater and associated crack at termination site of end plug weld, made with CW  $\text{CO}_2$  laser, as described above. An optimized laser power ramping scheme (laser power, 2 kW; welding speed, 8.3 mm/s; ramp up time, 0.5 s; time for welding at 2 kW power, 6 s; ramp down time, 1 s) toward the end of laser welding eliminated crater formation [47]. In the resultant weld, termination site was not identifiable.

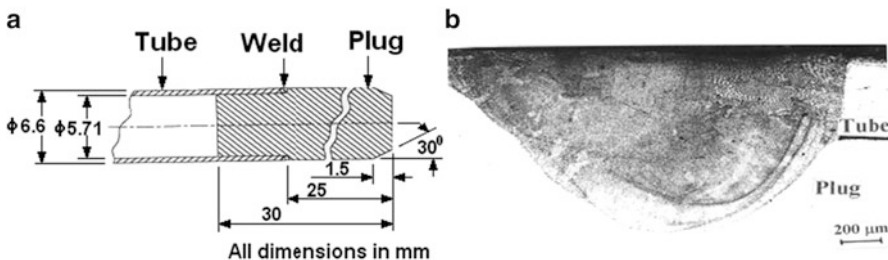


**Fig. 12.31** (a) Dimensional details of nuclear fuel element and (b) cross section of one of the sound laser welds

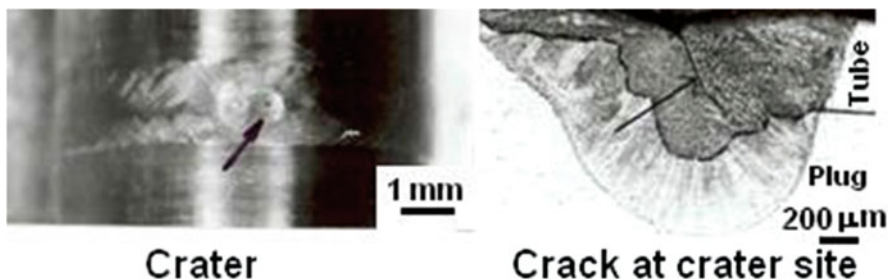


**Fig. 12.32** Crater and associated crack at the site of laser weld termination

#### 12.4.4 *Laser Brazing*

Dissimilar metals are preferred due to better material utilization with improved functionality in many engineering applications. It has encouraged the research thrust on various brazing processes including laser brazing. Among the various combinations of materials, Cu-SS combination is important as Cu has higher thermal conductivity while SS has higher strength. This joint finds application in many advanced engineering applications, like particle accelerators and power plants where efficient removal of heat is mandatory along with material strength. Joining of AISI 304L stainless steel with copper using conventional processing portrays multifold problems due to the difference in thermophysical properties, while it is challenging for laser processing due to high reflectivity of Cu [48, 49]. Various brazing techniques are used to join two dissimilar materials [50–52]. In this process, the closely fitted materials/parts with filler metal are heated above 450 °C, facilitating molten filler metal to flow into fine gaps by capillary action to form material joint. Conventionally, the brazing is performed in a controlled atmosphere furnace or in vacuum chamber [53] for the joining of Cu with SS. Furnace brazing is a very slow process with the unnecessary heating of whole job at high temperature. This heating may produce high thermal stresses in the parts and can change the surface properties of base materials. Laser is widely used as heat source in many materials processing applications, including cutting, welding, cladding, surface treatment, and rapid manufacturing [54–56]. When this is used for the brazing process, it is called as laser brazing [57–59]. By using laser brazing, very thin and miniature parts can be joined with well-controlled heat-affected zone.

In the present study, a 2 kW ytterbium fiber laser integrated with 5-axis workstation was used for laser brazing. A number of samples were brazed using active brazing filler foil (Ag-63 Cu-35.25 Ti-1.75) of thickness 50 μm in butt joint configuration. The brazed joints were subjected to various nondestructive (visual and dye-penetrant test) and destructive (microscopic examination, energy-dispersive spectroscopy, and four-point bend testing) characterization techniques.

Two basic parameters, laser power (P) and scan speed (v), were varied and their effect on the brazed joint was studied. At laser power below 350 W and moderate scan speed (4 mm/min), the proper melting of brazing foil was not occurred. As we increased the laser power, keeping the scan speed constant, the melting of filler foil observed and the brazing of Cu-SS was witnessed having relatively good strength. Experiments were also carried out to evaluate the effect of scan speed at laser power constant (450 W) on laser brazing; it was observed that when scan speed was 6 mm/min, the proper melting of filler foil was not occurred. As the scan speed decreased from 6 mm/min, the melting of foil was observed, but still the joint was not good by appearance. As the scan speed is reduced to 2 mm/min, the melting of foil occurred and a better brazed joint was observed. The optimum processing parameters for laser brazing of 3 mm SS-Cu joint were found to be 450 W and 2 mm/min.

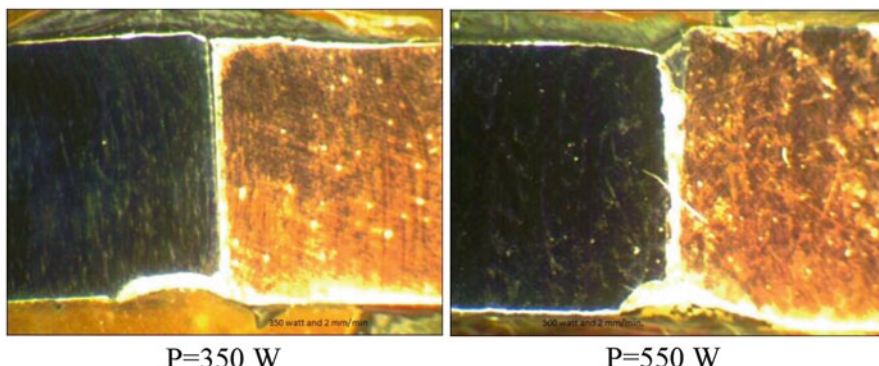


**Fig. 12.33** Pictographs of transverse cross section of laser brazed samples of 3 mm thick sheets for constant scan speed of 2 mm/min at two laser powers

A number of nondestructive and destructive tests were carried out to characterize the brazed joints. Visual examination is the preliminary examination carried out after laser brazing to detect surface defects, distortion, bead appearance, lack of penetration, spattering, etc. The visual examination for the various brazed joints was carried out, and the defect-free joints were taken for further examinations. Dye-penetrant test is also carried out for the selected samples and found with no leak. This constitutes one of the most important tests, capable of providing insight into modifications taking place in the material as results of laser processing. The feedbacks received from microstructural analysis are often used for optimizing laser processing parameters. The test can provide wide-ranging information, e.g., microstructural changes, development of deleterious phases, if any (especially during dissimilar metal welding), extent of laser-affected zone, and nature and extent of defects developed in the laser processed. Figure 12.33 presents microscopic examination of typical laser brazed samples at various laser power and constant scan speed (2 mm/min).

The brazed samples are polished by various metallurgical techniques and prepared for energy-dispersive X-ray spectroscopy. Elemental distribution across the brazed joint was studied through point and line scanning. Cu substrate that is used for the brazing experiments had 99.9 % purity. Figure 12.34 presents the elemental distribution across the laser brazed joint of SS-Cu. It is evidently clear that Fe signal falls as we move from the SS to Cu. There is rise in Cu signal. There is peak of Ag in the middle of SS and Cu. The gradient at the interface is sharp; it reconfirms that the dilution of the SS and Cu substrate was not significant during the brazing process. The line scan of Ag is displaced toward the Cu, as the solubility of Ag is more on Cu as compared to SS. Prior to testing of brazed joints, four-point bending test specimen was machined from as-received material for evaluating the flexure strength of the material in as-received condition. Table 12.8 summarizes the results of four-point bending test of material in as-received condition.

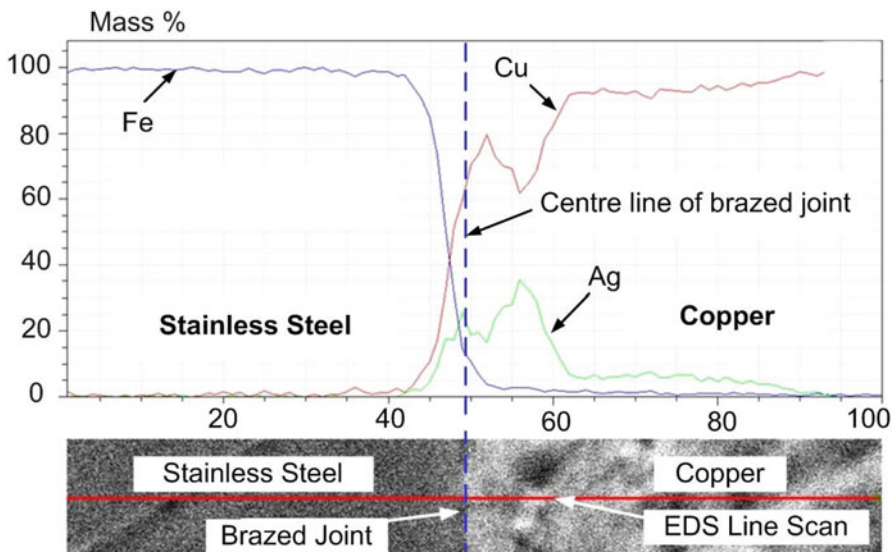


**Fig. 12.34** Typical elemental distribution across the laser brazed joint of SS-Cu

**Table 12.8** Results of four-point bending test of material in as-received condition

Sample	Flexural strength [MPa]	Average flexural strength [MPa]
Copper	579.07	506.82
Copper	434.57	
SS 316L	838.83	748.97
SS 316L	659.11	
Brazing foil		450 <sup>a</sup>

<sup>a</sup>As per manufacturer's material test report

Figure 12.35 summarizes the effect of laser power on flexural strength at various scan speeds. Figure 12.34b clearly indicates that the flexural strength is high at lower scan speed and higher laser power. The experimental trials were limited up to 600 W of the laser power, as further increase in laser power resulted in undesirable melting and partial welding of brazing coupons. At lower laser power and higher scan speed, there was not sufficient energy available for sound laser brazing to take place. Thus, laser energy per unit length plays a critical role in the flexural strength of laser brazed joint. The laser energy per unit length is defined as the ratio of laser power to scan speed. It is estimated that a laser energy per unit length of 100 J/mm is minimum requirement to achieve flexural strength of 50 MPa in the brazed joint of 3 mm thick copper stainless steel. As the laser energy per unit length is increased, the flexural strength of brazed joint increases. It is because the availability of more energy per unit length will result in proper melting and wetting of the brazed material across the joint. As the thermal conductivity of copper is more

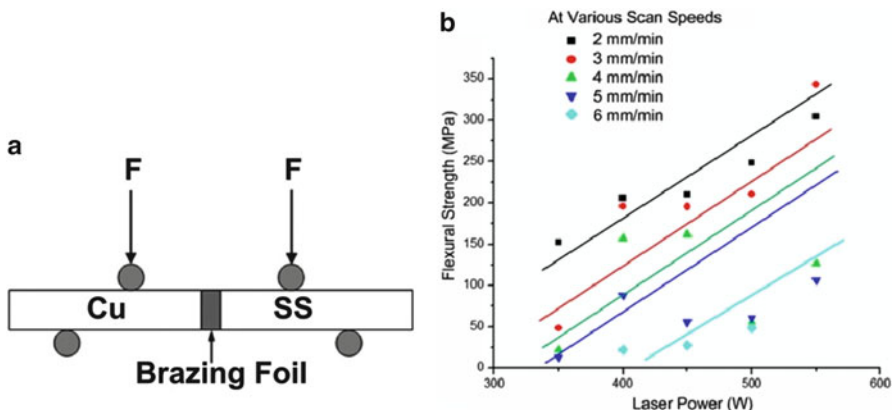


**Fig. 12.35** (a) Schematics depicting four-point bend testing setup. (b) Effect of laser power, scan speed, and beam offset on flexure strength of brazed joint of 3 mm SS-Cu sheets

and melting point is lower as compared to corresponding values of stainless steel, the effect of laser focal spot offset in transverse plane is also investigated. The laser beam was offset by 0.5 mm toward SS and Cu and brazing was carried out. When we offset the laser beam toward the Cu side by 0.5 mm, the flexural strength decreases for the laser brazed joint at various combination of laser power and scan speed. This is due to the availability of lower laser energy (because of high reflectivity at Cu surface and higher thermal conductivity of Cu material) yielding to insufficient wetting of to-be brazed surfaces. When the laser beam was offset toward the SS side by 0.5 mm, the flexural strength of brazed joint was decreased as compared to that of with zero offset, but the flexural strength was increased as compared to that of with laser beam offset toward the Cu side. This is due to the less reflection of laser beam and less thermal conductivity of SS as compared to Cu yielding to relatively higher wetting. Further, the flexural strength is low as compared to zero offset beam brazing joint because the offset of laser beam affects the melting of brazing foil and the heating of contacted surfaces. Results also indicate that the offset of laser beam is very sensitive as it affects the strength of the joint. So the alignment and laser beam positioning should be done very carefully. Laser brazing is an attractive technique of joining the material when heat input and subsequent distortion is one of the major criteria for the fabrication of engineering component.

In our present study, the laser brazing of Cu and SS was done and the results were compiled. The visual inspection and dye-penetrant testing were done and found that the joints are good. The optical microscopy for the various joints was done. Further, the flexural testing using four-point bending using UTM (universal testing machine) was carried out, and the flexural stresses for different brazed joints were determined

and compared with base materials. The scanning electron microscopy is done for the various joints, and an analysis of the element distribution was performed for material characterization. Maximum flexural stress observed was 343 MPa at the laser power of 550 W and the scan speed of 3 mm/min. If we further increase the laser power, the samples are observed with more heat-affected zone (HAZ) and some melting of base metal copper is observed at 600 W power with 2 and 3 mm/min scan speed. At low laser power (less than 350 W), the brazing foil was not melted fully even the scan speed was as low as 2 mm/min. The scanning electron microscopic analysis shows that the diffusion of Ag component of brazing foil is greater in the copper side than SS side.

#### 12.4.5 *Laser Surface Melting Reduces End-Grain Corrosion of Austenitic Stainless Steels (SS)*

Laser surface melting treatment serves to effect breakdown and redistribution of inclusions, which are potential sites for localized corrosion. A related study performed on type 304L SS has demonstrated that laser surface melting treatment brought about significant improvement in end-grain corrosion resistance [60], which is a problem with bar, wire, and tubular products of austenitic SS operating in nitric acid environment. The improvement in resistance against end-grain corrosion is attributed to refinement and uniform distribution of otherwise elongated MnS inclusions, in addition to the elimination of segregation of Cr, S, and P along the flow lines. Figure 12.36 presents the cross section of laser surface-melted type 304L SS showing modification in the morphology of MnS inclusions as a result of laser melting.

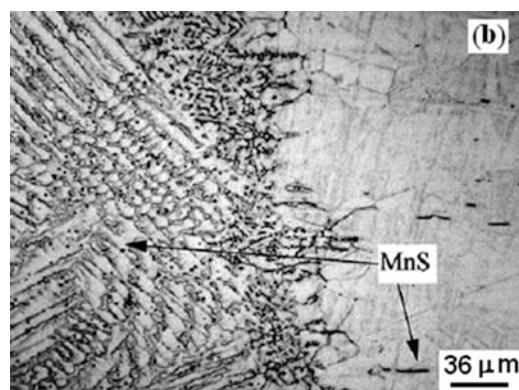


**Fig. 12.36** Cross section of laser surface-melted specimen of type 316L SS. Note the change in the morphology of MnS inclusions in laser-melted zone

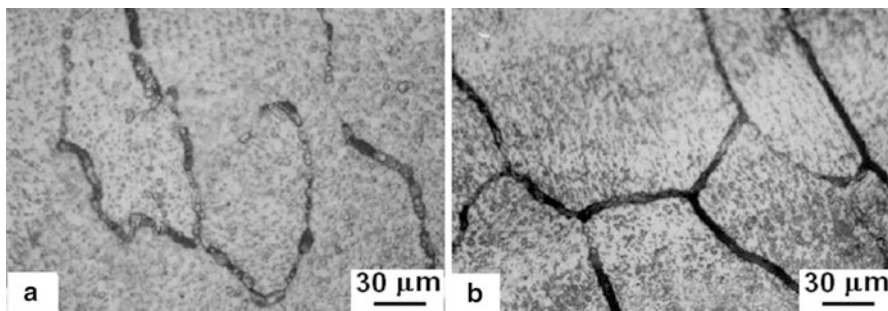


**Fig. 12.37** Comparison of microstructures of (a) laser-melted WM and (b) WM after solution annealing treatment. Note the disrupted intergranular carbide network in laser-melted specimen

#### 12.4.6 *Laser Surface Melting Treatment for Reducing Susceptibility of 316(N) Weld Metal and Type 304 SS Against Intergranular Corrosion (IGC)*

Laser surface melting treatment, besides causing modification in the distribution and morphology of inclusions (as shown in the previous case study), also introduces new set of grains which should influence its resistance against sensitization and susceptibility to intergranular corrosion (IGC). A research study performed on type 316(N) weld metal (WM) demonstrated that surface melting with high repetition rate pulse-modulated CO<sub>2</sub> laser beam generated significant increase in material's resistance against sensitization [61]. Figure 12.37 compares microstructures of untreated and laser-melted 316(N) WMs after same solution annealing treatment at 1323 K, followed by slow cooling at the rate of 65 K/h. Note the disruption in continuous grain boundary network of carbides in laser-melted and solution-annealed WM. ASTM A262 practice E test established lower susceptibility of laser-melted and solution-annealed WM (with respect to solution-annealed WM) to IGC. Direct implication of these results is that laser surface-treated type 316 LN SS weldments can be cooled at a slower rate during post-weld solution annealing treatment (for stress relieving), without the risk of sensitization, thereby minimizing distortion and reintroduction of thermal stresses.

A related study, performed on type 304 SS, demonstrated that surface melting treatment, performed with pulse-modulated CO<sub>2</sub> laser, brought about significant reduction in its susceptibility to sensitization during subsequent exposure to a susceptible temperature region and to IGC during service [62]. The laser-melted surface, even after being subjected to severe sensitization heat treatment, developed comparable or even a lower degree of sensitization than the base metal in the as-received condition. Figure 12.38 presents the cross section of untreated and laser surface-melted specimens of type 304 SS, after undergoing ASTM A262 practice B test. Enhanced resistance of laser-treated surface against sensitization is attributed to its higher fraction of low-angle grain boundaries.

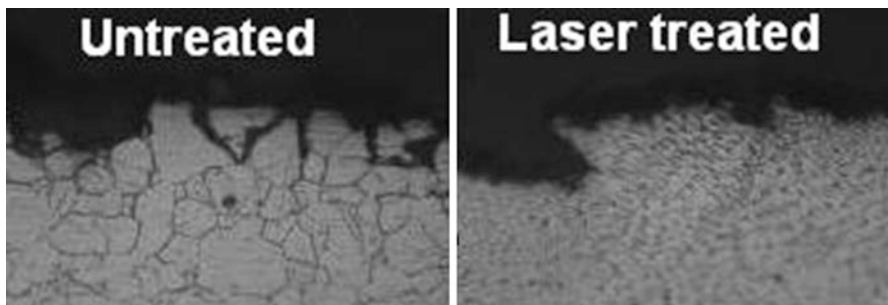


**Fig. 12.38** Cross section of untreated and laser-treated specimens of type 304 SS, after undergoing ASTM A262 practice E test

#### **12.4.7 *Laser Melting-Based Pre-weld Surface Treatment of Gas Tungsten Arc Weld of Type 304 SS for Reducing IGC Susceptibility of the Weldment***

The approach of laser surface melting for enhancing resistance against IGC was extended to develop a pre-weld laser surface treatment scheme to suppress sensitization in the heat-affected zone (HAZ) of gas tungsten arc weldment of type 304 SS. The study, performed with pulse-modulated CO<sub>2</sub> laser, demonstrated that pre-weld laser-treated HAZ of gas tungsten arc weldment developed significantly lower degree of sensitization and susceptibility to IGC than those of untreated HAZ [63]. Enhanced sensitization resistance and lower susceptibility to IGC of laser-melted surface are attributed to higher fraction of  $\Sigma 1$  sub-grain boundaries introduced by laser-assisted melting and resolidification.

### **12.5 Conclusions**

In the area of laser rapid manufacturing (LRM), we have demonstrated that compositionally graded and porous structures with controlled properties can be effectively grown using a fiber laser. It has been found that LRM fabricated WC-reinforced Ni matrix specimens with 18 wt% of Inconel 625 have the least erosion wear rate (EWR), and it was about nine times lower than that of the bare SS316L surface. The numerical modeling of multilayered thin wall geometry adopted for LRM was successfully carried out and used to gain a deeper insight into the experimental observation. In laser cladding, the controlled heat input from a CW CO<sub>2</sub> laser was effectively used to suppress dilution in Colmonoy 6 deposit on austenitic stainless steel substrate to a thickness less than about 100  $\mu\text{m}$ . Laser shock peening of SAE 9260 spring steel, due to unaltered surface finish of the treated surface, brought about improvement in its fatigue life over shot-peened specimens by more than about 5 times. By fine spatial positioning of the laser beam toward the plug material of AISI 316M stainless steel for welding with a tube of

dissimilar material of alloy D9, we could cleverly avoid cracking of the weld metal, which would normally occur had there been no control on the weld metal chemistry effected by the positioning of the laser beam. Significant improvement in end-grain corrosion resistance of AISI 304 stainless steel was achieved by refinement and uniform distribution of MnS inclusions through laser surface melting. Laser surface melting was used to enhance intergranular corrosion resistance of AISI 316(N) and 304 stainless steel through the mechanism of altering the grain boundary character distribution by increasing the fraction of low-angle grain boundaries. This process was developed as a pre-weld surface treatment to suppress heat-affected zone sensitization and enhance intergranular corrosion resistance of gas tungsten arc weldment of AISI 304 stainless steel. For oxygen-assisted laser piercing of mild steel, a power ramped pulsed mode with high pulse repetition frequency and low duty cycle scheme has been developed by us, which is found to be more effective for producing highly circular, narrow holes with minimum spattered pierced holes. In laser cutting of mild steel, an increase in pulse repetition frequency is shown to result in finer striations and low roughness of the cut edges. It was found that for normal pulsed mode (NPM) laser cutting, the maximum cutting speed was determined by the pulse duty cycle, whereas in the quasi-continuous wave mode (QCWM) of laser cutting developed by us, it was mainly governed by CW base power between the pulses. With respect to NPM, QCWM laser cutting was found to be associated with lower value of severance energy for the onset of uncontrolled combustion. In conclusion, lasers are shown to offer solutions to many intriguing problems of laser materials processing and hence will continue to support the requirements of future manufacturing technologies.

**Acknowledgments** The authors express their sincere gratitude to Dr. P.D. Gupta, Director RRCAT, for his constant support and encouragement. Thanks are due to our collaborators: Prof A.K. Nath of Indian Institute of Technology, Kharagpur, India, and Prof B.K. Gandhi of Indian Institute of Technology, Roorkee, India. The authors are also thankful to our collaborators and colleagues: Dr. S M Oak, Mr. K Ranganathan, Mr. R Sundar, and Mr. P. Hedao of Solid State Laser Division RRCAT for laser peening work. During the experimental work presented above, the technical supports of Mr. S.K. Mishra, Mr. C.H. Prem Singh, Mr. M.O. Ittoop, Mr. Abrat Varma, Mr. Anil Adbol, Mr. Ram Nihal Ram, and Mr. S.K. Perkar are thankfully acknowledged. One of the authors, Dr. C.P. Paul, acknowledges the enthusiastic collaboration and fruitful discussions with Prof. A. Khajepour, Prof. E. Toyserkani, Prof. S. Corbin, and Dr. M. Alimardani at the University of Waterloo, Canada.

## References

1. J.C. Ion, *Laser Processing of Engineering Materials: Principles, Procedure and Industrial Application* (Elsevier/Butterworth-Heinemann, Amsterdam/Oxford, 2005)
2. <http://www.sandia.gov/mst/pdf/LENS.pdf>, visited on June 29, 2010
3. L. Xue, M.U. Islam, A. Theriault, Laser consolidation process for the manufacturing of structural components for advanced robotic mechatronic system – a state of art review, in *Proceedings of 6th International Symposium on Artificial Intelligence and Robotics & Automation in Space (i-SAIRAS 2001)*, Canadian Space Agency, St-Hubert, Quebec, Canada, 18–22 June 2001

4. C.P. Paul, A. Khajepour, Automated laser fabrication of cemented carbide components. *Opt. Laser Technol.* **40**, 735–741 (2008)
5. S.J. Davis, K.G. Watkins, G. Dearden, E. Fearon, J. Zeng, Optimum deposition parameters for the direct laser fabrication (DLF) of quasi-hollow structures, in *Proceedings of Photon Conference Manchester, Institute of Physics*. Bristol, UK (2006)
6. X. He, G. Yu, J. Mazumder, Temperature and composition profile during double-track laser cladding of H13 tool steel. *J. Phys. D Appl. Phys.* **43**, 015502 (2010)
7. R.J. Moat, A. Pinkerton, L. Li, P.J. Withers, M. Preuss, Crystallographic texture and microstructure of pulsed diode laser-deposited Waspaloy. *Acta Mater.* **5**, 1220–1229 (2009)
8. M. Zhong, W. Liu, Laser surface cladding: the state of the art and challenges. *Proc. Inst. Mech. Eng. Part C J. Mech. Eng. Sci.* **224**, 1041–1060 (2010)
9. B. Valsecchi, B. Previtali, M. Vedani, G. Vimercati, Fiber laser cladding with high content of Wc-Co based powder. *Int. J. Mater. Form.* **3**(Suppl 1), 1127–1130 (2010)
10. E. Kreutz, G. Backes, A. Gasser, K. Wissenbach, Rapid prototyping with CO<sub>2</sub> laser radiation. *Appl. Surf. Sci.* **86**, 310–316 (1995)
11. S. Sun, Y. Durandet, M. Brandt, Parametric investigation of pulsed Nd:YAG laser cladding of Stellite 6 on stainless steel. *Surf. Coat. Technol.* **194**, 225–231 (2005)
12. H. Gedda, J. Powell, G. Wahstrom, W.B. Li, H. Engstrom, C. Magnusson, Energy redistribution during CO<sub>2</sub> laser cladding. *J. Laser Appl.* **14**, 78–82 (2002)
13. U. Draugelates et al., Corrosion and wear protection by CO<sub>2</sub> laser beam cladding combined with the hot wire technology, in *Proceedings ECLAT '94*, DGM Informationsgesellschaft Verlag, Oberursel, Germany (1994), pp. 344–354
14. F. Hensel, C. Binroth, G. Sepold, A comparison of powder and wire-fed laser beam cladding, in *Proceedings ECLAT '92*, DGM Informationsgesellschaft Verlag, Oberursel, Germany (1992), pp. 39–44
15. P. Ganesh, A. Moitra, P. Tiwari, S. Sathyaranayanan, H. Kumar, S.K. Rai, R. Kaul, C.P. Paul, R.C. Prasad, L.M. Kukreja, Fracture behavior of laser-clad joint of Stellite 21 on AISI 316L stainless steel. *Mater. Sci. Eng. A* **527**, 3748–3756 (2010)
16. C.P. Paul, H. Alemohammad, E. Toyserkani, A. Khajepour, S. Corbin, Cladding of WC-12Co on low carbon steel using a pulsed Nd:YAG laser. *Mater. Sci. Eng. A* **464**, 170–176 (2007)
17. C.P. Paul, P. Ganesh, S.K. Mishra, P. Bhargava, J. Negi, A.K. Nath, Investigating laser rapid manufacturing for Inconel-625 components. *Opt. Laser Technol.* **39**, 800–805 (2007)
18. C.P. Paul, A. Jain, P. Ganesh, J. Negi, A.K. Nath, Laser rapid manufacturing of colmonoy components. *Laser Opt. Eng.* **44**, 1096–1109 (2006)
19. C.P. Paul, S.K. Mishra, C.H. Prem Singh, P. Bhargava, P. Tiwari, L.M. Kukreja, Studies on laser rapid manufacturing of cross-thin-walled porous structures of Inconel 625. *Int. J. Adv. Manuf. Technol.* **61**, 757–770 (2012)
20. R. Kaul, P. Ganesh, S.K. Albert, A. Jaiswal, N.P. Lalla, A. Gupta, C.P. Paul, A.K. Nath, Laser cladding of austenitic stainless steel with nickel base hardfacing alloy. *Surf. Eng.* **19**, 269–273 (2003)
21. P. Ganesh, R. Kaul, S. Mishra, P. Bhargava, C.P. Paul, C.P. Singh, P. Tiwari, S.M. Oak, R.C. Prasad, Laser rapid manufacturing of Bi-metallic tube with Stellite-21 and austenitic stainless steel. *Trans. IIM* **62**, 169–174 (2009)
22. R. Kaul, P. Ganesh, C.P. Paul, S.K. Albert, U.K. Mudali, A.K. Nath, Some recent studies on laser cladding and dissimilar welding, in *Proceedings of International Conference – Laser Applications and Technologies (LAT 2005)*, St. Petersburg, SPIE vol. 6053, pp. 60530O1–60530O10.
23. R. Kaul, P. Ganesh, M.K. Tiwari, A.K. Singh, P. Tripathi, A. Gupta, A.K. Nath, Laser-assisted deposition of graded overlay of Stellite 6 on austenitic stainless steel. *Lasers Eng.* **12**, 207–225 (2002)
24. S. Kumar, S. Roy, C.P. Paul, *Numer. Heat Transf. Part B* **53**, 271 (2008)
25. [www.csc.fi/english/pages/elmer](http://www.csc.fi/english/pages/elmer)
26. A. Kumar, C.P. Paul, A.K. Pathak, P. Bhargava, L.M. Kukreja, *Opt. Laser Technol.* **44**, 555–565 (2012)

27. Y. Sano, O. Hatamleh, Conf. Chairs, Technical Digest, The 3rd International Conference on Laser Peening and Related Phenomena, October 11–14, 2011, Osaka, Japan, pp 1–99
28. [www.nmc.ctc.com](http://www.nmc.ctc.com), visited on 18th August 2012
29. P. Ganesh, R. Sundar, H. Kumar, R. Kaul, K. Ranagnathan, P. Hedao, P. Tiwari, L.M. Kukreja, S.M. Oak, S. Dasari, G. Raghavendra, Studies on laser peening of spring steel for automotive applications. Opt. Lasers Eng. **50**, 678–686 (2012)
30. R. Sundar, K. Ranganathan, J. George, S.M. Oak, Experimental analysis of the effects of orientation and location of the Pockels cell in an Nd:YAG laser resonator. Opt. Laser Technol. **41**, 705–709 (2009)
31. R. Sundar, K. Ranganathan, S.M. Oak, Generation of flattened Gaussian beam profiles in a Nd:YAG laser with a Gaussian mirror resonator. Appl. Opt. **47**, 147–152 (2008)
32. S.L. Chen, W. O'Niel, The effects of power rippling on CO<sub>2</sub> laser cutting. Opt. Laser Technol. **29**, 125–134 (1997)
33. J. Powell, D. Petring, R.V. Kumar, S.O. Al-Mashikhi, A.F.H. Kaplan, K.T. Voisey, J. Phys. D. Appl. Phys. **42**, 015504 (2009)
34. B.S. Yilbas, B. Abdul Aleem, J. Phys. D. Appl. Phys. **39**, 1451–1461 (2006)
35. P. Yudin, K. Oleg, J. Laser Appl. **21**, 39–45 (2009)
36. A. Mahrle, E. Beyer, J. Phys. D. Appl. Phys. **42**, 175507 (2009)
37. M. Sobih, P.L. Crouse, L. Li, J. Phys. D. Appl. Phys. **40**, 6908–6916 (2007)
38. J. Powell, *CO<sub>2</sub>Laser Cutting*, 1st edn. (Springer, New York, 1993)
39. B.T. Rao, M.O. Ittoop, L.M. Kukreja, Opt. Lasers Eng. **47**, 1108–1116 (2009)
40. B.T. Rao, B. Verma, R. Kaul, L.M. Kukreja, in *Proceeding of DAE-BRNS National Laser Symposium*, Raja Ramanna Center for Advanced Technology, Indore, Contributed Paper No. 7.14, 1–4 Dec. 2010
41. W.M. Steen, *Laser Material Processing*, 3rd edn. (Springer, London/Berlin/Heidelberg, 2003)
42. E. Toyserkani, A. Khajepour, S.F. Corbin, *Laser Cladding* (CRC Press, 2004). ISBN: 0-8493-2172-7
43. C.P. Paul, P. Bhargava, A. Kumar, A.K. Pathak, L.M. Kukreja, in *Lasers in Manufacturing*, ed. by J.P. Davim, John Wiley & Sons, Inc. Hoboken, NJ, USA (2013)
44. C.P. Paul, Parametric studies of Laser Metal Deposition for fabrication engineering components. PhD Thesis, 2005, Devi Ahilya University, Indore, India
45. Y. Li, J. Ma, Surf. Coat. Technol. **90**, 1 (1997)
46. J. Zeng, Y.-H. Kim, Y. Chen, Adv. Mater. Res. **399–401**, 1802 (2012)
47. R. Kaul, P. Ganesh, M.O. Ittoop, A.K. Nath, A. Kumar, R.B. Bhatt, A. Kumar, Microstructural characterization of a dissimilar weld of alloy D9 and 316M stainless steel produced using a 2.5 kW CW CO<sub>2</sub> laser. Lasers Eng. **12**, 17–33 (2002)
48. E.M. Anawa, A.G. Olabi, Optimization of tensile strength of ferritic/austenitic laser welded components. Opt. Laser Technol. **46**, 571–577 (2008)
49. M.J. Torkamany, S. Tahamtan, J. Sabbaghzadeh, Dissimilar welding of carbon steel to 5754 aluminum alloy by Nd:YAG pulsed laser. Mater. Des. **31**, 458–465 (2010)
50. C. Dharmendra, K.P. Rao, J. Wilden, S. Reich, Study on laser welding–brazing of zinc coated steel to aluminum alloy with a Zinc based filler. Mater. Sci. Eng. A **528**, 1497–1503 (2011)
51. T.A. Mai, A.C. Spowage, Characterization of dissimilar joints in laser welding of steel–kovar, copper–steel and copper–aluminium. Mater. Sci. Eng. A **374**, 224–233 (2004)
52. Y. Sechi, T. Tsumura, K. Nakata, Dissimilar laser brazing of boron nitride and tungsten carbide. Mater. Des. **31**, 2071–2077 (2010)
53. W. Lippmann, J. Knorr, R. Wolf, R. Rasper, H. Exner, A.-M. Reinecke, M. Nieher, R. Schreiber, Laser joining of silicon carbide – a new technology for ultra-high temperature resistant joints. Nucl. Eng. Des. **231**, 151–161 (2004)
54. J.P. Davim, *Lasers in Manufacturing*, John Wiley & Sons, Inc. Hoboken, NJ, USA (2013)
55. M. Kimura, *Fiber Lasers: Research, Technology and Applications* (Nova Science Publishers Inc., New York, 2009)
56. W.M. Steen, J. Mazumder, *Laser Materials Processing*, 4th edn. (Springer-verlag London Limited, London, 2010)

57. S. Huang, H. Tsai, S. Lin, Effects of brazing route and brazing alloy on the interfacial structure between diamond and bonding matrix. *Mater. Chem. Phys.* **84**, 251–258 (2004)
58. L.-q. Li, X.-s. Feng, Y.-b. Chen, Influence of laser energy input mode on joint interface characteristics in laser brazing with Cu-base filler metal. *Trans. Nonferr. Met. Soc. China* **18**, 1065–1070 (2008)
59. P. Peyre, G. Sierra, F. Deschaux-Beaume, D. Stuart, G. Fras, Generation of aluminium–steel joints with laser-induced reactive wetting. *Mater. Sci. Eng. A* **444**, 327–338 (2007)
60. K. Chandra, V. Kain, P. Ganesh, Controlling end-grain corrosion of austenitic stainless steels. *J. Mater. Eng. Perform.* **17**, 115–122 (2008)
61. N. Parvathavarthini, R.K. Dayal, R. Kaul, P. Ganesh, J. Khare, A.K. Nath, S.K. Mishra, I. Samajdar, Novel laser surface treatment approach to suppress sensitization in modified Type 316(N) stainless steel weld metal. *Sci. Technol. Weld. Join.* **13**, 335–343 (2008)
62. R. Kaul, S. Mahajan, V. Kain, P. Ganesh, K. Chandra, I. Samajdar, A.K. Nath, R.C. Prasad, Laser surface treatment for enhancing intergranular corrosion resistance of AISI 304 stainless steel. *Corrosion* **64**, 755–762 (2008)
63. R. Kaul, N. Parvathavarthini, P. Ganesh, S.V. Mulki, I. Samajdar, R.K. Dayal, L.M. Kukreja, A novel pre-weld laser surface treatment for enhanced inter-granular corrosion resistance of austenitic stainless steel weldment. *Weld. J.* **88**, 233s–242s (2009)

# **Chapter 13**

## **Biomedical Applications of Lasers**

**Pradeep Kumar Gupta and H.S. Patel**

**Abstract** Lasers are being increasingly used for biomedical imaging, diagnosis, and therapy. In this chapter we first provide a brief overview of light propagation in tissue. Next we discuss the techniques developed for a more comprehensive utilization of the information content of the light scattered from tissue and how this is helping high-resolution biomedical imaging of tissue microstructure and quantitative, sensitive, and noninvasive diagnosis. The use of lasers for ultraprecise surgery in a minimally invasive manner and also the use of photoactivated drugs for therapy with high selectivity are discussed next. By using illustrations from the work carried out at RRCAT, the chapter also provides a brief overview of the activities at RRCAT in these areas.

**Keywords** Laser tissue interaction • Biomedical optics • Optical techniques for biomedical imaging and diagnosis • Mechanistic and spectroscopic studies on optically trapped cell • Phototherapy

### **13.1 Introduction**

Improving the quality of health care has been an eternal pursuit of mankind. Quality health care has two prime objectives: first to detect disease at an early stage before it becomes difficult to manage and second to treat it with high selectivity and precision without any adverse effect on uninvolved tissues. Therefore, the utilization of the continued technological advances toward these objectives has always been a priority research area. Last century has witnessed the development of computerized X-ray tomography (CT scan), magnetic resonance imaging (MRI), ultrasonography, etc., which have made it possible to noninvasively peep inside the body and thus help detect disease at an early stage. Several new therapeutic modalities and drugs have also been developed to improve the selectivity of the treatment. The technological developments have also led to improved understanding of the cause of disease

---

P.K. Gupta (✉) • H.S. Patel

Laser Biomedical Applications & Instrumentation Division, Raja Ramanna Centre for Advanced Technology, Indore, Madhya Pradesh 452013, India  
e-mail: [pkgupta@rrcat.gov.in](mailto:pkgupta@rrcat.gov.in)

and the ways it can be treated. Lasers, one of the major inventions of the last century, are also playing a very important role in the pursuit of both the objectives. Although light has been used for diagnosis and therapy from time immemorial, the availability of lasers as light source with remarkable control on its properties, the advances in optics and instrumentation, and the large image processing capability of the computers are making possible a much more comprehensive use of the information content of the light coming from the tissue for high-resolution imaging and quantitative, sensitive, noninvasive diagnosis. Optical techniques are helping image microstructures in living tissue with resolution down to a few micrometers, whereas with current frontline biomedical imaging techniques like MRI, CT scan, ultrasonography, etc., it is difficult to achieve resolution better than  $100\text{ }\mu\text{m}$ . Optical spectroscopy of elastically and inelastically scattered light from tissue is also facilitating *in situ* noninvasive diagnosis with no potential adverse effects associated with the use of ionizing radiation. Photoactivated drugs that are inert until photoexcited by radiation with the right wavelength are being used to target the tissue selectively by exercising the control on light exposure (only the tissue exposed to both drug and light will be affected). A good example is the fast developing photodynamic therapy of cancer. There are indications that selective photoexcitation of native chromophores in the tissue may also lead to therapeutic effects.

In this chapter we first provide a brief overview of the propagation of light through tissue and then discuss the use of light for biomedical imaging, diagnosis, and therapeutic applications. The use of light to manipulate single cells/subcellular objects and the role it can play in biomedical diagnosis at single cell level are also addressed.

## 13.2 Laser Tissue Interaction

Light passing through the biological tissue gets attenuated both because of absorption by its constituents and scattering due to the presence of microscopic inhomogeneities (macromolecules, cell organelles, organized cell structure, interstitial layers, etc.). Since the tissue is an inhomogeneous and multicomponent system, its absorption at a given wavelength is a weighted average of the absorption by its constituents. The major contributors of absorption in tissue in the ultraviolet spectral range are DNA and proteins. In the visible and near-infrared (NIR) wavelength range, the absorption in tissue is dominated by hemoglobin and melanin. Absorption by water, the main constituent of all tissues, becomes significant beyond  $\sim 1\text{ }\mu\text{m}$  and becomes dominant beyond about  $2\text{ }\mu\text{m}$  wavelength [1]. For biomedical imaging applications, one uses wavelengths in the so-called diagnostic window ( $650\text{ nm}$  to  $1.3\text{ }\mu\text{m}$ ) where tissue absorption is weakest. This is desirable for two reasons. First, it allows probing larger depths of the tissue, and, second, it avoids unnecessary deposition of energy in the tissue which might lead to adverse effects.

Attenuation of light propagating in a non-scattering medium is completely described by the Beer-Lambert's law;  $I = I_0 \exp(-\mu_a z)$ , where  $\mu_a$  is the absorption

coefficient. While scattering may remove photons from the beam path and thus contribute to its attenuation, multiple scattering events might also bring photons back into the beam path. These photons although not part of the collimated beam also add to the irradiance at a given point along the direction of propagation of the beam, making prediction of depth profile of the propagating beam a bit more complicated. It should also be noted that the degree of attenuation arising due to scattering depends on the angular distribution of the scattered photons which in turn has a strong dependence on the size of the scatterer. For scatterers with size  $\ll$  wavelength, referred to as Rayleigh scatterers, the phase of the electromagnetic field across the scatterer can be treated as constant. Therefore, the light scattered by all the induced dipoles in the scatterer adds up in phase resulting in dipole-like scattering. Here the angular distribution of the scattered light often referred to as “phase function” shows no dependence on the angle of scattering in the plane transverse to the electric field of the incident light, but in the plane containing the electric field, it shows a cosine square intensity pattern with minima along the dipole axis due to the transverse nature of the electromagnetic wave. Further, as first shown by Rayleigh, for such small scatterers, the scattered intensity is inversely proportional to the fourth power of wavelength. For larger size scatterers ( $>\lambda$ ), light scattered by all the induced dipoles in the scatterer does not add up in phase except only in the forward direction making the angular distribution of the scattered light peak in the forward direction.

An exact mathematical description of scattering from spherical particles of size  $>$  wavelength was provided by Ludwig Valentine Lorenz and Gustav Mie [2]. This is therefore referred to as Lorenz-Mie scattering or often just Mie scattering. In Mie regime the wavelength dependence of scattering coefficients for different tissue is given as  $\lambda^{-k}$  where  $k$  typically varies from 1 to 2 [3]. The first moment of the phase function is the average cosine of the scattering angle, denoted by “ $g$ .” It is also referred to as the anisotropy parameter. The value of “ $g$ ” ranges from  $-1$  to  $+1$ , where  $g = 0$  corresponds to isotropic scattering (Rayleigh scattering),  $g = +1$  corresponds to ideal forward scattering, and  $g = -1$  corresponds to ideal backward scattering. A photon acquires random direction after about  $1/(1-g)$  scattering events, which is only five for  $g = 0.8$ . Typical values of  $g$  for biological tissues vary from 0.7 to 0.99. The parameter used to describe the scattering properties of the tissue are the scattering coefficient  $\mu_s$  and the reduced scattering coefficient  $\mu_s' (= \mu_s(1-g))$ . The reduced scattering coefficient defines the path length over which the incident light loses its directional information, that is, the angular distribution of the scattered light becomes isotropic. In Table 13.1 we show the value of these optical parameters for some biological tissue [4].

### 13.3 Optical Imaging

A major difficulty in the use of light for biomedical imaging arises because in contrast to X-ray, visible light photons undergo multiple scattering in the tissue leading to a blurring of image. Therefore, for histopathology one makes use of

**Table 13.1** The typical values for absorption coefficient ( $\mu_a$ ), scattering coefficient ( $\mu_s$ ), and anisotropy parameter ( $g$ ) for some human tissues at different wavelengths (Adapted from Ref. [3])

Tissue type	$\lambda(\text{nm})$	$\mu_a(\text{mm}^{-1})$	$\mu_s(\text{mm}^{-1})$	$g$
Breast	530	0.05–0.10	22.5–35	~0.92
Bladder	633	0.14	8.8	0.96
Lung	633	0.3	25	0.94
Myocardium	1,064	0.3	17	0.96
Skin (dermis)	630	0.18	20	0.82

transverse sections of tissue whose thickness is smaller than the mean free path for scattering. In order to comprehend how light can be used for *in situ* optical imaging of objects embedded in a turbid medium, let us consider the propagation of a short-duration laser pulse through the turbid medium. The un-scattered (ballistic) photons will emerge first followed by the predominantly forward scattered (snakelike) component and the multiple scattered diffuse component. To have a perspective of the relative magnitude of these components, let us take the value for the scattering coefficient to be  $\sim 100 \text{ cm}^{-1}$ . Therefore, the number of ballistic photons on propagation through a 1 cm thick tissue will be of the order of  $e^{-100}$  of the incident number of photons, that of snakelike component  $e^{-10}$  assuming  $g \sim 0.9$  for the tissue, and the major fraction will be diffuse component. Since coherence of light is lost in a few scattering events, coherence gating can be used to filter out the ballistic photons which being un-scattered or minimally scattered have the highest image information and hence can provide images with the best resolution (down to a few  $\mu\text{m}$ ). However, imaging depth will be limited to at best a few mm. Therefore, coherence gating can only be used for imaging of transparent objects (like ocular structure) or thin turbid tissue like the mucosal layers of hollow organs. Optical coherence tomography (OCT), the approach that exploits coherence gating for optical imaging, has emerged as a rapid, noncontact, and noninvasive high-resolution imaging technique and is already being used for clinical applications in ophthalmology, dermatology, etc. [5].

Another approach to filter out the multiple scattered light is to make use of the depolarization of the multiple scattered light or the fact that multiple scattered light travels longer and hence will take longer time to reach the detector [6–9]. Since in these approaches both the snakelike and ballistic photons are collected, the sum total of which is orders of magnitude larger than the ballistic component, these can provide image through larger depths. Further, with the use of nonlinear optical techniques like stimulated Raman scattering, the image-bearing component of light can be selectively amplified to further enhance the depth of imaging [10]. However, due to the use of predominantly forward scattered photons, which might have undergone several scattering events, the resolution is poorer (of the order of 100  $\mu\text{m}$ ).

For imaging through larger depths as, for example, for imaging human brain or female breast, one has to necessarily work with diffuse photons. Although the spatial resolution possible in imaging using diffuse photons is rather limited (at best few

mms), there is considerable interest in this approach referred to as diffuse optical tomography because it allows imaging through the largest depths of the turbid medium.

### 13.3.1 Optical Coherence Tomography (OCT)

A schematic of an OCT setup is shown in Fig. 13.1. It comprises of a low temporal coherence light source and a fiber-optic Michelson interferometer, one arm of which has the sample and the other arm a reference mirror. Light reflected from a layer of the sample and the reference mirror will interfere when the two path lengths are within the coherence length of the source. Axial scanning of the reference mirror helps record interferograms from different depths of the sample. Two-dimensional cross-sectional images and three-dimensional tomograms of the backscattered intensity distribution within the sample can be obtained by recording the interference signals from various axial (A scan) and transverse positions (B scan) on the sample [11–13]. High spatial coherence (i.e., single transverse mode) is needed since superposition of interferences corresponding to multiple spatial modes leads to washout of information. Considering the electric fields in the reference and sample arm to be  $E_R$  and  $E_S$ , respectively, the intensity at the detector can be described as

$$I_D \propto |E_R + E_S|^2 \quad (13.1)$$

$$I_D \propto |E_R|^2 + |E_S|^2 + 2|E_R||E_S|\operatorname{Re}[\gamma(\tau)]\cos\left(\frac{2\pi}{\lambda_0}2z\right) \quad (13.2)$$

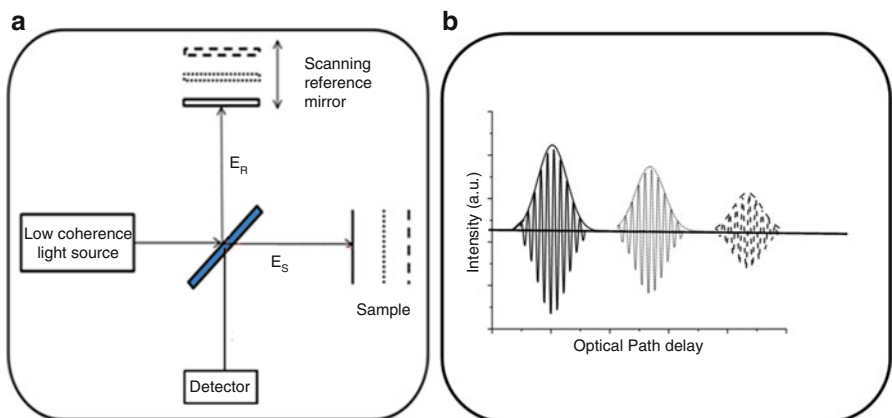


**Fig. 13.1** (a) Schematic of a low coherence interferometry setup. The sample is assumed to comprise of three layers as shown by solid, dotted, and dashed line. The path-matched locations of reference mirror (a) as well as the interference pattern and its envelope (b) for the three layers in the sample are shown in solid, dotted, and dashed line, respectively

where  $2z$  is the round trip optical path difference between reference and sample arms,  $\lambda_0$  is the central wavelength of the source, and  $\gamma(\tau)$  is the complex degree of coherence of the electric fields. A scan of the optical path in the reference arm with uniform velocity  $v$  allows probing of different layers in the sample and generates amplitude modulated signal  $I_D(t)$  at a carrier frequency determined by the velocity of scanning. This can be expressed as

$$I_D(t) \propto |E_R|^2 + |E_S|^2 + 2|E_R||E_S|\operatorname{Re}[\gamma(\tau)]\cos\left(\frac{2\pi}{\lambda_0}2vt\right) \quad (13.3)$$

Unlike microscopy, axial and lateral resolutions are decoupled in OCT. The axial resolution is one half of the coherence length ( $l_c$ ) of the source which is directly proportional to the square of its central wavelength ( $\lambda_0$ ) and inversely proportional to its spectral bandwidth ( $\Delta\lambda$ ). For a source with Gaussian spectral distribution, axial resolution is given by  $\Delta z = l_c/2 = \frac{2 \ln 2}{\pi} \left( \frac{\lambda_0^2}{\Delta\lambda} \right)$ . The transverse (lateral) resolution is governed by the spot size formed by the focusing optics used in the sample arm and can be expressed as  $\Delta x = 4\lambda_0 f/\pi d$  where  $d$  is the spot size on the objective lens and  $f$  is its focal length. Although the use of a higher NA objective lens can provide better lateral resolution, it comes with a reduced imaging depth arising due to the reduced depth of focus for high NA objective. Therefore, to achieve imaging depth larger than the depth of focus of the objective lens, it becomes necessary to focus the light beam at different depths and stitch the different images together [14, 15]. Other approaches investigated for ensuring large depth of focus with good lateral resolution are the use of an axicon lens [16] and tapered fiber tip probe to illuminate the sample [17].

In time-domain OCT setups, the reference arm path length is changed either by moving the reference mirror or by using a Fourier optic delay line [18]. Though all depths in the sample are illuminated, data is collected sequentially only from one depth at a time. While this makes time-domain OCT setup less sensitive to vibrations or the movement of scatterers, it also leads to the drawback of slow image acquisition speed.

In Fourier domain OCT (FDOCT), the Fourier transform (FT) of the interference spectrum is used to retrieve the axial (depth) information from all depths without the need for scanning the reference arm [19]. This enhances image acquisition speed. There are two variants of Fourier domain approach: the one referred to as spectral domain OCT (SDOCT) utilizes broadband source (SLD) and a spectrometer in detection arm, and the other referred to as swept source OCT (SSOCT) makes use of a swept source (source whose wavelength is tuned as a function of time) and a single photodetector in the detection arm [20].

A schematic of SDOCT is shown in Fig. 13.2. Here the reflected light from reference mirror and sample layers is spatially dispersed with the help of grating on linear photodiode array or CCD. Because each pixel of the detector sees only a narrow spectral band ( $\delta\lambda$ ), the resulting coherence length is large and allows interference of reference light and the light reflected from different depths of the

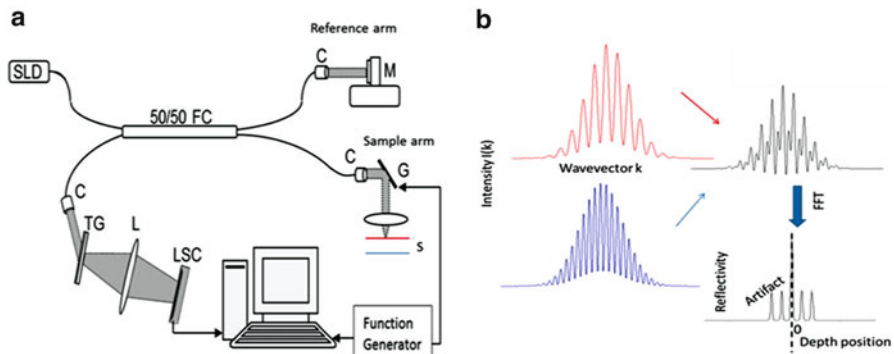


**Fig. 13.2** (a) Schematic of a SDOCT system. *C* collimator lens, *FC* fiber coupler, *G* galvo-scanner, *L* imaging lens, *LSC* line scan camera, *M* reference mirror, *S* sample, *SLD* superluminescent diode, *TG* transmission grating. (b) Relation between depth and frequency. Interference patterns shown in the red and blue colour are from the corresponding layers of sample. The measured interference spectrum is shown in black colour. Fourier transform of this provides peaks at the depth location corresponding to the two layers of the sample

sample. This leads to fringes in  $k$  space with the frequency of fringes increasing for signal arising from deeper layers. The highest resolvable spatial frequency is determined by the number of sampling points  $N$ , which corresponds to the number of the illuminated pixels. Because as per the Nyquist theorem, the sampling frequency should be at least twice that of maximum detectable frequency of the spectrum, the maximum imaging depth is given by

$$Z_{\max} = \frac{\lambda_0^2}{2n \Delta \lambda} N \quad (13.4)$$

where  $N$  is the number of pixels,  $\Delta \lambda$  is the width of the spectrum recorded on the detector, and  $n$  is the refractive index of the medium. Since Fourier transform of the real-value spectrum is Hermitian symmetric, only half of this range can be used effectively for positive and negative distances. Therefore, the maximum imaging depth is given by  $Z_{\max} = \pm \lambda_0^2 / 4n\delta\lambda$  [21].

It should be noted that the data collected by spectrometer is sampled with equal wavelength increments and hence is unequally spaced in  $k$  domain. FT of unevenly spaced data points in  $k$  space results in broadening of the point spread function with increase in optical path delay. Hence, the axial resolution degrades with increasing depth inside the sample. A proper depth profile can be obtained only after the interference pattern is converted from evenly spaced  $\lambda$  to evenly spaced  $k$  domain. This is done by resampling the interference pattern  $I(\lambda)$  to generate equi-spaced data  $I(k)$  in  $k$  domain [22]. Another point to be noted is that the Fourier transform of a real-valued function like  $I(k)$  produces complex conjugate artifact. Therefore, FT of  $I(k)$  leads to two mirror images about the zero delay plane, the plane in the sample for which the path difference between the sample and the reference arm is zero. To

avoid overlapping of images from different layers, the reference arm path length is kept such that the plane in the sample arm corresponding to zero path difference is on the outermost surface of the sample or preferably outside the sample by a distance of a few coherence length of the source. The complex conjugate artifact can be removed by generating a complex spectral intensity pattern from the measured real-valued function  $I(k)$ . One approach used for this purpose is to impart a constant modulation frequency to the interferograms by moving the reference mirror with a uniform velocity during the B scan [23]. This not only doubles the imaging range of the FDOCT setup but also provides a way to place the highest sensitivity region, which is at zero delay plane, inside the sample.

At longer wavelengths (greater than 1,100 nm) where larger imaging depth can be achieved due to reduced scattering, the cheaper silicon-based area detectors cannot be used. Since SSOCT requires only a single point detector, its use at these longer wavelengths becomes even more attractive. A better SNR and dynamic range is generally achieved in SSOCT because it avoids the use of a spectrometer and the resulting losses. Further, here, balanced detection mode can be used to cancel the common mode noise, whereas this is not possible in SDOCT.

Although the Fourier domain approach facilitates rapid imaging, the trade-off between the lateral resolution and the depth of imaging is a major bottleneck limiting its applicability for *in situ* cytological analysis. Several approaches like the use of an axicon lens and binary phase filter, the use of computational methods to digitally focus the probe beam, or the use of multiple probe beams focused at different depths of the sample are being investigated to enhance the depth of focus without compromising the lateral resolution [16, 24, 25]. FDOCT systems are commercially available from several companies, like Carl Zeiss Meditec (Germany), Optovue (USA), Heidelberg Engineering (USA), and Topcon (USA), with scanning speeds of few tens of kHz that are adequate to provide low definition 3D images of tissues like human retina.

Full-field OCT (FFOCT) is another variant of OCT [26]. FFOCT uses wide-field illumination of the sample and a CCD or CMOS camera with a phase stepping technique for acquiring an en face or C scan image. Full-field imaging avoids the requirement of transverse scanning, thereby allowing capturing a 2D en face image just like in microscopy. Most often FFOCT employ a Linnik interferometer with a spatially incoherent light source to reduce speckles and inter-pixel cross talk. Since FFOCT acquires en face images, high NA (0.3–0.5) objectives can be used to obtain high transverse resolution. The high ( $\sim 1 \mu\text{m}$ ) axial and transverse resolution offered by FFOCT makes it a useful tool for noninvasive histology and real-time cellular imaging as in embryology and developmental biology.

Apart from high-resolution structural information, OCT, with suitable adaptations, can also provide functional information about the sample. For example, by taking OCT images for the two orthogonal linear polarizations of the scattered light using polarization-sensitive OCT (PSOCT), we can get information about the birefringent properties of the tissue [27]. Since the morphology and even the magnitude of the connective tissue protein like collagen change during healing of the wounds or even during the progression of cancer, the measurement of tissue

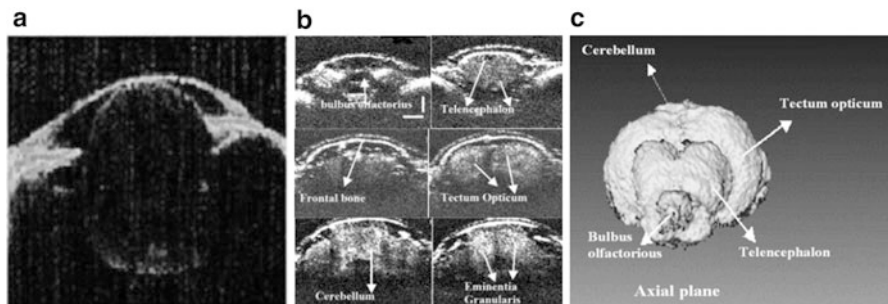


**Fig. 13.3** (a) In vivo OCT image of a zebra fish eye, (b) 2D cross-sectional image of zebra fish brain, and (c) 3D isosurface model of the zebra fish brain constructed using cross-sectional images

birefringence can provide valuable diagnostic information. Doppler OCT system can allow measurement of vascular blood flow in the sample and thus significantly add to the diagnostic potential for noninvasive monitoring of wounds.

At RRCAT, OCT setups of varying sophistication have been developed and used for noninvasive, high-resolution ( $\sim 10\text{--}20 \mu\text{m}$ ) biomedical imaging applications. A typical OCT image of a zebra fish eye recorded *in vivo* is shown in Fig. 13.3a.

From the image we could estimate important ocular parameters like corneal and retinal thickness, the anterior angle of cornea with iris [28]. Further, exploiting the fact that OCT measures the optical path length, we measured the gradient refractive index profile of the lens without excising the lens by fitting the measured path length at different lateral positions to the known parabolic gradient profile [29]. The images of zebra fish brain sections recorded *in vivo* [30] using a real-time OCT setup are shown in Fig. 13.3b. About 90 cross-sectional images (XZ plane) of the brain were taken by moving the sample in the Y direction in a step of 0.05 mm. Internal structures such as bulbus olfactorius, telencephalon, tectum opticum, cerebellum, frontal bone, and eminentia granularis were clearly distinguishable in these images. The raw images were thresholded for minimizing the speckle noise. Using these images, a three-dimensional isosurface model of the zebra fish brain was constructed in the axial plane (Fig. 13.3c). The ability to record images of internal organs noninvasively has also been used to study abnormalities in the development of zebra fish embryos subjected to different toxins like alcohol. The zebra fish embryos were exposed to ethanol at varying concentrations in the range 150–350 mM for 48 h postfertilization, and OCT imaging was performed at regular intervals both on unexposed (controls) and ethanol-treated samples. The study showed that as compared to control, the ethanol-exposed embryos show shrinkage in the size of their eyes and the internal structures of the eye in the ethanol-exposed embryos were also less featured. Further, it was observed that while there was no change in the mean retinal thickness of the control larvae from 6 days postfertilization (dpf) to 10 dpf, the retinal thickness of the exposed larvae decreased during 6–10 dpf. The ethanol-exposed larvae also showed malformations in the spinal cord as evidenced by the distortions in the notochord and bending of tails [31].

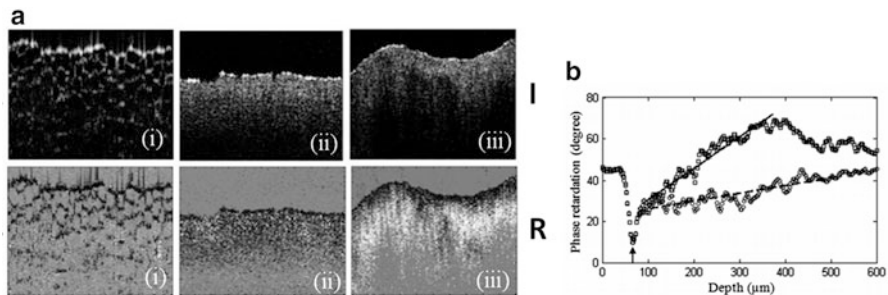


**Fig. 13.4** (a) The intensity (*I*) and retardance (*R*) images of normal (1st column), malignant (2nd column), and benign (3rd column) human breast tissue samples. (B) Phase retardation depth profile of benign (top) and malignant tumor (bottom). Polarization-sensitive OCT images of (i) normal, (ii) malignant, and (iii) benign human breast tissues. (b) Retardance estimated from the PSOCT image

The intensity and the retardance images of malignant (invasive ductal carcinoma), benign (fibroadenoma), and normal breast tissue samples obtained using a PSOCT system are shown in Fig. 13.4. The resolution of the OCT system used for these measurements was limited to  $\sim 10\text{--}15 \mu\text{m}$  due to the limited bandwidth of the source and was not sufficient to discriminate cytological differences between the normal and the abnormal tissues. However, significant structural differences can be seen between the normal and the abnormal tissues. While the normal breast tissue is composed of large lipid-filled cells and hence has low attenuation, the abnormal tissues exhibit dense scattering effects. These differences lead to characteristic texture in their OCT images, which can be discriminated using statistical analysis of the OCT images. We have made use of spectral techniques involving Fourier-based classification method as well as statistical techniques involving texture analysis (TA) for the identification of three different histological tissue types, normal, fibroadenoma (FA), and invasive ductal carcinoma (IDC). Excellent classification results with specificity and sensitivity of 100 % could be achieved for binary (normal-abnormal) classification by the use of an algorithm that used Fourier domain analysis (FDA) of the OCT image data set to carry out the feature extraction and TA for classification. The method yielded specificity and sensitivity of 90 and 85 %, respectively, for the discrimination of FA and IDC [32]. The retardation images also show considerable difference for different pathologies of the breast tissue samples. The birefringence value ( $4 \times 10^{-4}$ ) for benign tumor (fibroadenoma) was significantly higher than that of malignant tumor ( $8 \times 10^{-5}$ ) and could be used to differentiate these [33].

Polarization-sensitive OCT images and the corresponding histological measurements on the morphology of the tissues resected at different time points from the bacteria (*Staphylococcus aureus*) infected and uninfected wounds in mice are shown in Fig. 13.5. These measurements showed that compared to the uninfected wounds, the infected wounds had prominent edematous regions. Further, a significant delay was seen in re-epithelialization and collagen remodeling phases of wound healing

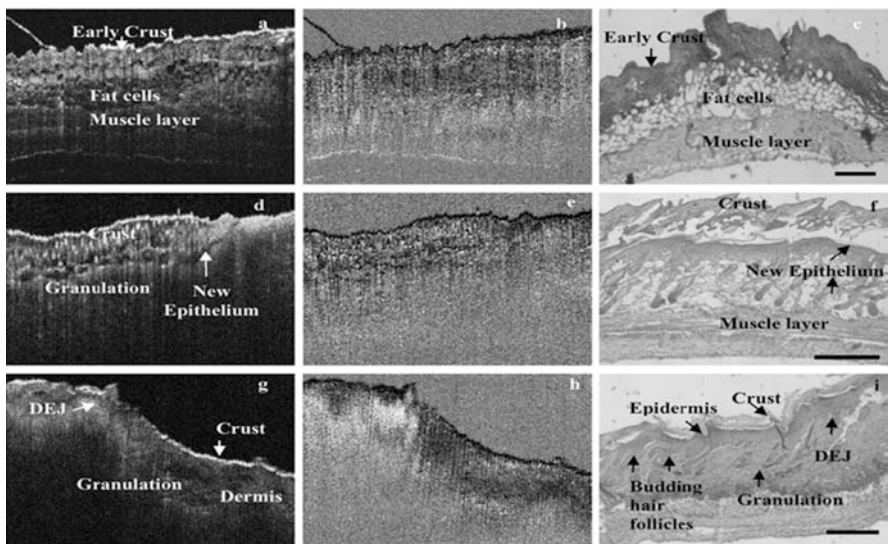


**Fig. 13.5** Time-dependent structural changes in uninjected wound skin of mice. *Left* (a, d, g), *middle* (b, e, h), and *right* (c, f, i) panels represent backscattered intensity OCT images, PSOCT images, and histological images, respectively. *Top* (a–c), *middle* (d–f) and *lowermost* (g–i) rows represent images of resected wounded skin sample imaged on days 2, 4, and 10 of wounding, respectively. OCT images, image size: 1.5 mm × 3 mm. Histology images, scale bar: 100 μm

in infected wounds. The OCT measurements were found to be consistent with the corresponding histological measurements demonstrating the potential of OCT for monitoring the signatures of microbial infection in wounds as well as the progression of wound healing [34]. The results of a recent study by us further show that phase retardance of wound tissue increases with the healing of wound as is the case for wound tensile strength [35]. This indicates that retardance measured by PSOCT can be a good indicator of tissue tensile strength and wound repair. In contrast hydroxyproline estimation, which gives an idea of collagen synthesis, does not increase along with wound tensile strength beyond a certain time point. Therefore, a significant difference in wound tensile strength following a therapeutic intervention, compared to untreated wounds, might also be observed sometimes even without a difference in hydroxyproline content. This will necessitate repeated histological and biochemical measurements to assess a therapeutic outcome. By using PSOCT, these aspects may be addressed.

### 13.3.2 Diffuse Optical Tomography (DOT)

For imaging through larger depths as, for example, for imaging human brain or female breast, one has to necessarily work with diffuse photons [36]. The basic

idea here is to measure the light emerging from the biological object for different source and detector positions around it and finding a three-dimensional distribution of the optical properties of the sample that is able to reproduce the measurements. This distribution corresponds to the image of the sample. This approach referred to as diffuse optical tomography (DOT) can be used in three modes: continuous wave (CW), time domain (TD), and frequency domain (FD) [37–42]. In continuous wave DOT, a constant intensity light is used to illuminate the object, and measured intensity for various combinations of source-detector positions is used to reconstruct the image. The technique though relatively inexpensive and simple in nature suffers from the drawback that it is not possible to discriminate between the absorbing and scattering inhomogeneities which often provides useful clinical information. This is because the intensity of light which is the only measurable parameter in CW DOT can be affected by change in both absorption and scattering. Further it lacks the temporal information which is necessary for imaging fast spatiotemporal changes such that occur in hemodynamics during the brain activity. Time-domain DOT technique measures the delay and spread of an ultrafast (ps-fs) pulse and provides the most complete information about the optical properties on the medium and embedded heterogeneities through the diffuse photons reaching the detectors. Frequency-domain methods on the other hand measure the phase shift and demodulation of the intensity-modulated (MHz-GHz) waves propagating through tissue. Although frequency-domain DOT setup has a limitation in that measurements are made at only few discrete frequencies, it is still more widely used because of being less expensive and portable compared to time-domain setups [43]. By exploiting the differences in the absorption spectra of oxy- and deoxy-hemoglobin, DOT can provide useful functional information about the blood dynamics and oxygenation level.

In DOT large depth of imaging comes at the cost of resolution which is typically a few mm. Ultrasound-assisted DOT has been investigated as a means to improve the resolution [44]. In this method ultrasound waves focused in a tissue volume are used to cause localized modulation of the phase of the light scattered from this volume, thereby allowing the measurement of the optical properties of the scattering medium with ultrasound-limited resolution. Because only a small fraction of light traversing through the ultrasound focal region is modulated, a highly efficient photon collection and sensitive phase detectors are required [45]. Photoacoustic tomography (PAT) is another approach that makes simultaneous use of optical and ultrasound methods to achieve large depth of imaging with good resolution [46–48]. Here, acoustic waves generated by absorption of a short laser pulse focused in a small tissue volume are detected by an ultrasonic transducer placed on the surface. By measuring the amplitude and time taken by the photoacoustic waves to reach the receiver and knowing the distribution of light inside the tissue volume using a suitable light propagation algorithm, one can determine the optical properties of the imaged region. The PAT imaging offers greater tissue specificity and differentiation than ultrasound because the difference in optical absorption between different tissue components is usually much larger than their acoustic impedance. Hence, features that are not visible with ultrasound can be observed with ease using PAT. Further,

because the resolution of PAT imaging system is determined solely by the transducer geometry and the parameters of photoacoustic signal which depend on the energy deposited and thermal properties of the medium, the diffuse nature of the light does not hamper the resolution.

## 13.4 Optical Spectroscopic Diagnosis

While for imaging one exploits the intensity, coherence, or polarization of the scattered light, other parameters of the scattered light like its angular distribution and the spectral content also contain significant diagnostic information. As noted earlier the angular distribution of the scattered light can provide information about the density and the size distribution of scatterers. By making use of polarized fraction of the scattered light, one can selectively probe epithelial tissue and use the information on size distribution and the density of the nuclei for diagnosis of cancer in early stage [49]. Changes in the polarization parameters of the tissue (retardance, diattenuation, and depolarization) arising due to its birefringent (collagen, tendon, etc.) and chiral (glucose) constituents can also be exploited for diagnostics [50, 51].

It is important to note here that the scattered light also has a very weak component which is scattered inelastically, i.e., with a change in frequency via processes like fluorescence, Raman scattering, etc. The inelastically scattered light is the characteristic of the chemical composition and morphology of the tissue and thus can help in monitoring metabolic parameters of the tissue and also in discriminating diseased tissue from normal. Since the inelastically scattered light is a very small fraction of incident light, practical applications require use of high-brightness source like lasers and appropriate light delivery and collection systems. Both fluorescence and Raman spectroscopic approaches are being widely investigated for their diagnostic potential. These offer several important advantages for biomedical diagnosis like very high intrinsic sensitivity and the use of nonionizing radiation, which makes it particularly suited for mass screening and repeated use without any adverse effects. Further, the diagnosis can be made near-real time and *in situ* whereby no tissue needs to be removed. Also tissue diagnosis by this technique can be easily automated facilitating its use by less skilled medical personnel also. Here we shall restrict ourselves to the use of optical spectroscopy for noninvasive diagnosis of cancer.

### 13.4.1 *Optical Spectroscopy for Cancer Diagnosis*

Laser-induced fluorescence (LIF) has been used for diagnosing cancer in two ways. One approach involves systemic administration of a drug like hematoporphyrin derivative (HpD) which is selectively retained by the tumor. When photoexcited with light of appropriate wavelength, the drug localized in the tumor fluoresces. This fluorescence is used for detection and imaging of the tumor. Photoexcitation

also leads to populating the triplet state via intersystem crossing. The molecule in excited triplet state can directly react with biomolecules or lead to the generation of singlet oxygen, which is toxic to the host tissue. The resulting destruction of the host tissue is exploited for photodynamic therapy of tumor. From the point of view of use in diagnosis, this approach has two drawbacks: a possible dark toxicity of the drug and the possibility of drug-induced photosensitization. There is therefore interest in developing tumor markers where the triplet state is rapidly quenched and thereby photosensitization is avoided. The other approach, the one that has received more attention, does not use any exogenous tumor markers. Instead it exploits for diagnosis the subtle changes in the parameters of fluorescence (spectra, yield, decay time, and depolarization) from native tissues as it transforms from normal to the malignant state.

The fluorescence of native tissue originates from a number of endogenous fluorophores that are present in tissue. Table 13.2 lists the prominent fluorophores, along with their excitation and emission bands.

Extensive studies carried out on laser-induced fluorescence (LIF) from native tissues resected at surgery or biopsy from patients with cancer of different organs – uterus [52], breast [53–56], and oral cavity [57] – have shown a significant variation in the concentration of the fluorophores in the different tissue types. In particular, it was inferred from these studies that while the concentration of NADH (reduced nicotinamide adenine dinucleotide) should be higher in malignant breast tissues compared to benign tumor and normal breast tissues [53], the reverse should be the case for tissues from oral cavity where NADH concentration was inferred to be higher in normal oral tissues [57]. The differences in fluorophore concentration, inferred from spectroscopic studies, were able to qualitatively account for the observed differences in the yield and spectrum of autofluorescence from the normal and diseased oral and breast tissues. Significant differences in the depolarization of fluorescence were also observed in malignant tissues compared to normal. Whereas for thin tissue sections of breast tissue (thickness < optical transport length), the depolarization of fluorescence was observed to be smaller in malignant sites compared to normal (due to the changes in biochemical environment of the fluorophores), the reverse was observed for thicker tissue sections because

**Table 13.2** Excitation and emission spectra of the some endogenous tissue fluorophores

Endogenous fluorophores	Excitation maxima (nm)	Emission maxima (nm)
<i>Amino acids</i>		
Tryptophan	280	340
<i>Structural proteins</i>		
Collagen/elastin	335	400
<i>Coenzymes</i>		
NADH/NADPH	340	460
FAD/flavins	430	550
<i>Porphyrins</i>	400	630,690

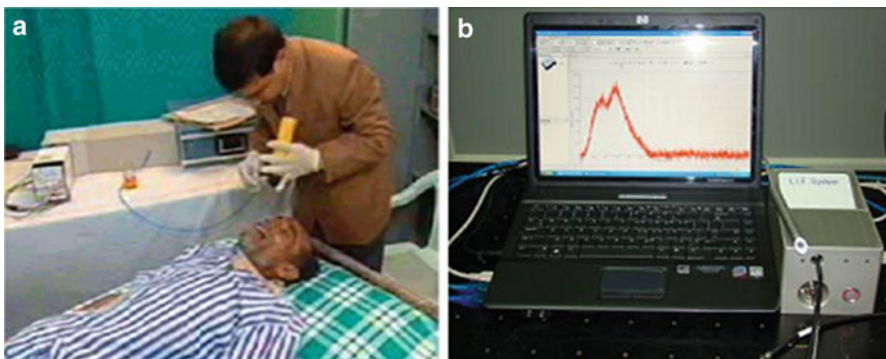


**Fig. 13.6** (a) The first prototype nitrogen laser-based fluorescence spectroscopy system for cancer diagnosis (b) a more compact version of the fluorescence spectroscopy system

of the larger scattering coefficient of malignant sites. Because the fluorescence from superficial layer of tissue is the least depolarized and that originating from deeper layers becomes increasingly more depolarized, the depth dependence of depolarization could also be exploited to make a depth-resolved measurement of the concentration of fluorophores in tissue phantoms as well as in tissues [59].

A photograph of the first system developed at RRCAT for the evaluation of the LIF technique for in vivo diagnosis of cancer is shown in Fig. 13.6a. The system comprised of a sealed-off N<sub>2</sub> laser (pulse duration, 7 ns; pulse energy, 80 µJ; and pulse repetition rate, 10 Hz), an optical fiber probe, and a gateable intensified CCD (ICCD) detector. The diagnostic probe was a bifurcated fiber bundle with a central fiber surrounded by an array of six fibers. The central fiber delivers the excitation light to the tissue surface and the tissue fluorescence is collected by the six surrounding fibers.

An additional fiber was put in the diagnostic probe to monitor the energy of each pulse of nitrogen laser output by monitoring luminescence of a phosphor coated on the tip of this fiber. The light coming from the distal ends of the six collection fibers and the reference fiber is imaged on the entrance slit of a spectrograph coupled to the ICCD. One such unit was used at the Government Cancer Hospital, Indore, for a detailed clinical evaluation of the technique after satisfactory results were obtained in a pilot study on 25 patients with histopathologically confirmed squamous cell carcinoma of oral cavity [58]. The spectral database of in vivo autofluorescence spectra recorded from more than 150 patients enrolled at outpatient department of the Government Cancer Hospital, Indore, for screening of neoplasm of oral cavity and ~50 healthy volunteers was used to develop algorithms that could efficiently discriminate between the spectral features of the malignant and nonmalignant tissue sites. Both linear and nonlinear statistical techniques have been investigated to explore their discrimination efficacy. The diagnostic algorithms developed to quantify the spectral differences in the nitrogen laser-excited fluorescence from malignant, benign tumor, and normal tissue sites provided good discrimination

with sensitivity and specificity toward cancer of ~90 % in general and up to 100 % in favorable cases [60–62]. Multiclass diagnostic algorithms capable of simultaneously classifying spectral data into several different classes have also been developed using the theory of total principal component regression [63] and also by making use of nonlinear maximum representation and discrimination feature (MRDF) for feature extraction and sparse multinomial logistic regression (SMLR) for classification [64].

Figure 13.6b shows a photograph of the more compact version of the fluorescence spectroscopy system incorporating the nitrogen laser, a chip-based miniaturized ocean optics spectrograph and CMOS detector in one single box. The Raman spectroscopy-based system developed for *in vivo* screening of the cancer of oral cavity is shown in Fig. 13.7. The Raman setup was housed in a 32" suitcase for ease in portability. The system incorporates a 785 nm diode laser and a fiber-optic Raman probe to excite and collect the Raman-scattered light.

A notch filter placed at the distal end of the probe was used to remove the excitation light, and the filtered Raman output was imaged onto a spectrograph equipped with a thermoelectrically cooled, back-illuminated, deep-depletion CCD camera. Good quality tissue Raman spectra could be acquired from oral cavity tissue with an integration time of less than 5 s. Although the use of near-infrared excitation leads to significant reduction in the background, fluorescence extracting the weak Raman signal from the broad and much stronger background still remains a challenge. We have developed a method that makes use of iterative smoothening of the raw Raman spectrum to extract the Raman spectra. Compared to the widely used iterative modified polynomial fitting method, our method offers the advantage that the extracted Raman features are not sensitive to the spectral range over which the raw spectrum is fitted [65]. The central idea of this new approach is to iteratively

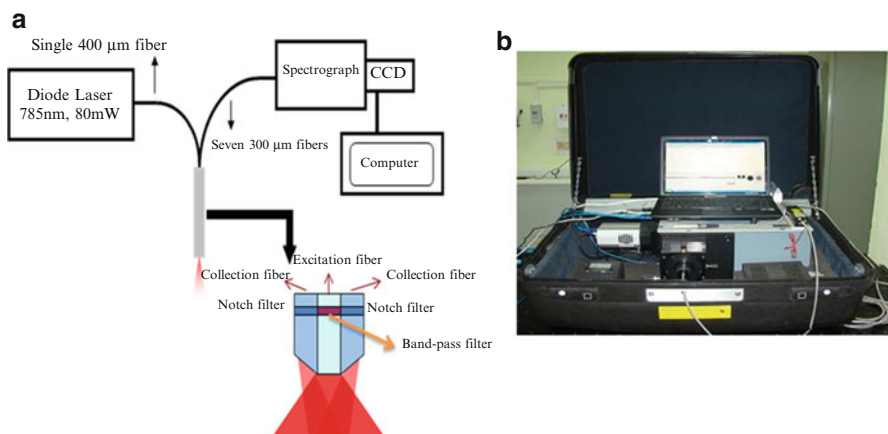


**Fig. 13.7** A compact Raman spectroscopy system for cancer diagnosis. (a) A schematic of the system and (b) a photograph of the portable unit

smooth the raw Raman spectrum, by using moving average of the spectral data, such that Raman peaks are automatically eliminated, leaving only the baseline fluorescence, to be subtracted from the raw spectrum. The scheme allows retrieval of all Raman peaks and shows good range independence.

Both the Raman spectroscopy system and the compact version of the fluorescence spectroscopy system have been used at Tata Memorial Hospital (TMH), Mumbai, for the screening of the neoplasm of oral cavity. The study involved 28 healthy volunteers and 199 patients undergoing routine medical examination of the oral cavity. The different tissue sites investigated belonged to either of the four histopathological categories: (1) squamous cell carcinoma (SCC), (2) oral submucosal fibrosis (OSMF), (3) leukoplakia (LP), or (4) normal. Probability-based multivariate statistical algorithms capable of direct multiclass classification were used to analyze the diagnostic content of the measured *in vivo* fluorescence and Raman spectra of oral tissues [66]. Of the 227 subjects involved in this study, both fluorescence and Raman spectral data was available from the tissue sites of 138 patients and 26 healthy volunteers. The results of a comparative analysis of the diagnostic performance of two approaches using direct multiclass classification algorithms are shown in Table 13.3. While, over this population, an overall classification accuracy of ~76 % was achieved using the fluorescence spectra, with Raman data the overall classification accuracy was found to be ~91 %. For binary classification (normal vs. abnormal), the corresponding classification accuracy was 94 % and 98 %, respectively.

The use of Raman spectroscopy for differential diagnosis over a database of 28 healthy volunteers and 171 patients enrolled for medical examination of lesions of oral cavity at TMH yielded an accuracy of ~86 % in classifying the oral tissue spectra into the four histopathological categories. For binary classification, a sensitivity of 94.2 % and a specificity of 94.4 % were achieved in discriminating the normal from all the abnormal oral tissue spectra belonging to SCC, OSMF, and LP [67]. It may be noted that because of its higher molecular specificity, the Raman spectra of the different anatomical sites of oral cavity were found to exhibit significant differences and based on the similarity of spectral patterns, the normal oral tissue sites, could be grouped into four major anatomical clusters: (1) outer lip and lip vermillion border, (2) buccal mucosa, (3) hard palate, and (4) dorsal, lateral,

**Table 13.3** Classification results for the use of fluorescence and Raman spectroscopy for *in vivo* diagnosis of cancer of oral cavity

Pathology diagnosis	Fluorescence diagnosis				Raman diagnosis			
	Normal	SCC	SMF	LP	Normal	SCC	SMF	LP
Normal	76.1 %	19 %	3.4 %	1.5 %	89.1 %	7.1 %	1.9 %	1.9 %
SCC	21.1 %	76.1 %	2.8 %	0 %	8 %	90 %	0 %	2 %
SMF	8.2 %	1.4 %	86.3 %	4.1 %	4.1 %	0 %	93.2 %	2.7 %
LP	9.8 %	12.4 %	14.6 %	73.2 %	1.2 %	0 %	4.9 %	93.9 %

and ventral tongue and soft palate. When the anatomy-matched data sets were used for classification, the overall classification accuracy was found to improve to 95 % with the algorithm correctly discriminating the corresponding tissue sites with 94 %, 99 %, and 91 % accuracy, respectively [68]. Another interesting observation made during this work was that if the spectra acquired from healthy volunteers with no clinical symptoms but having tobacco consumption history were removed from the “normal” database, a significant improvement in classification accuracy was observed for both fluorescence and Raman spectroscopy-based diagnosis.

A drawback of nitrogen laser-based fluorescence spectroscopy system is the need for periodic maintenance, cleaning of spark gap, and refilling of the sealed nitrogen laser tube. Therefore, with the availability of high-power white and near-UV (365 nm) LEDs, an LED-based combined fluorescence and diffuse reflectance spectroscopic system has been developed (Fig. 13.8). The LED-based system is even more compact, cheaper, and rugged compared to the nitrogen laser-based system. Further, incorporation of diffuse reflectance measurements helps monitoring the blood parameters of the tissue which is expected to further improve the diagnostic efficacy.

The present point spectroscopy-based systems are better suited for screening of areas suspected to be abnormal by the doctor. Since qualified doctors may not be available in remote areas, to make a system better suited for use by rural health workers, a wide-area imaging system capable of delineating suspect areas has also been developed and is being integrated with the point spectroscopy setup. This wide-area imaging system will make use of differences in fluorescence intensities of certain bands between normal and abnormal tissue to demarcate abnormal areas which can be further investigated by the point spectroscopy system for screening of the cancer of oral cavity.

Apart from cancer diagnosis, Raman spectroscopy is being explored for several other diagnostic applications like measurement of the different analytes in whole blood (like glucose, cholesterol, urea, albumin, triglycerides, hemoglobin, and bilirubin) [69]. Raman spectroscopy is also being used for monitoring of the adulterations in food products and quality of drugs [70, 71].



**Fig. 13.8** A compact LED-based fluorescence spectroscopy system for cancer diagnosis

### 13.4.2 Diagnostic Studies on Single Optically Trapped Cells

Lasers because of their ability to be focused to a diffraction-limited spot are also being used as a tweezers to hold and manipulate individual microscopic objects, like a single cell or even intracellular objects [72]. Since light carries momentum, its absorption, scattering, or refraction by an object will result in a transfer of momentum and thus a force on the object. While usually this force is in the direction of light propagation, it can be shown that for a tightly focused beam, there also exists a gradient force in the direction of the spatial gradient of the light intensity. A simple ray optics description [73], which is valid when the dimensions of the object is much larger than the wavelength of the laser beam, can be used to explain the existence of the gradient force and its role in stable three-dimensional trapping of the object. Referring to Fig. 13.9, consider two light rays ("a" and "b") situated at equal radial distance from the beam axis. Due to the refraction of rays  $a$  and  $b$  from the sphere, assumed to have a refractive index higher than the surroundings, there will be forces  $F_a$  and  $F_b$ , respectively, on it. The net force denoted as  $F$  will try to pull the sphere to

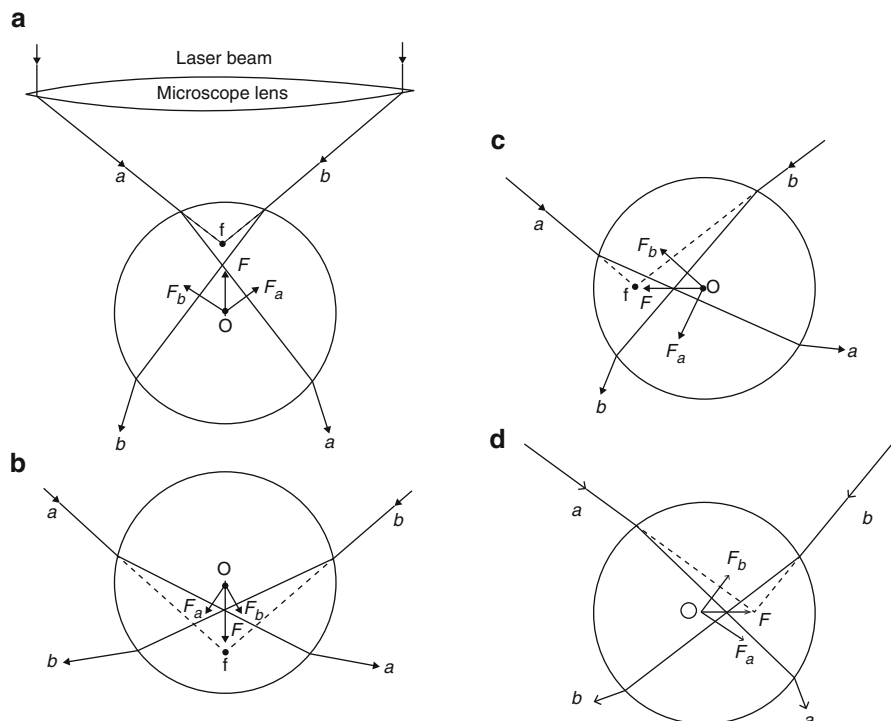


**Fig. 13.9** Ray diagram explanation of the trapping of a dielectric spherical particle in a focused laser beam.  $F$  is the net gradient force on particle with geometric centre (a) below, (b) above, (c) left, and (d) right to the focus position of trapping beam. (Adapted from Ashkin [73])

the focal point. When at the focal point, there is no refraction and hence no force on the sphere. It can be verified from Fig. 13.9 that in all the cases where the sphere is positioned away from the focal point, the resultant force acts to pull the sphere onto the beam focus (the equilibrium position).

For stable trapping in all three dimensions, the axial gradient component of the force that pulls the particle toward the focal region must exceed the scattering component of the force pushing it away from that region. To achieve this, trap beam needs to be focused to a diffraction-limited spot using a high numerical aperture (NA) objective lens. Generally for the manipulation of biological objects, we use laser in near-infrared wavelengths where the absorption in the object is minimal. This is to avoid photo-induced damage to the object.

The trapping efficiency ( $Q$ ) of an optical tweezers is usually described as the fraction of the trap beam's momentum being transferred to the particle. A value of 1 for  $Q$  corresponds to all the momentum of the beam being transferred to the particle. In conventional optical tweezers, the trapping efficiency and hence the trapping force in the lateral direction are usually an order of magnitude larger than the axial direction. Typical lateral trapping efficiency varies in the range of 0.001–0.5 depending on the difference in the refractive index of the object and the surrounding medium. This leads to trapping forces in the range of few pico-Newton (pN) to hundreds of pN [74].

Optical tweezers are finding widespread applications in biological research and technology [72, 75] because unlike mechanical microtools, the optical trap is gentle and absolutely sterile and can be used to capture, move, and position single cells or subcellular particles without direct contact. Since optical tweezers can work as a precise pressure transducer in pico-Newton (pN) to several hundreds of pN range [72, 75, 76], these have been used to apply mechanical forces on single optically trapped cells and thus measure viscoelastic parameters of the cells and how these are altered under some disease conditions. In particular there has been considerable work on the use of optical tweezers for the measurement of the viscoelastic parameters of red blood cells (RBCs) which get altered in certain disease conditions. While silica beads attached to the RBC membrane have been used as handles to stretch RBC [77, 78], the RBC, optically trapped in aqueous buffer suspension, can also be stretched by moving the stage and thus the fluid around the cell (Fig. 13.10). Measurements are often made on RBCs suspended in hypotonic buffer (osmolarity of  $\sim$ 150 mOsm/kg), since higher salt concentration inside the cell leads to flow of fluid into the cell causing it to get swollen and become spherical, the shape which is easier to model.

In Fig. 13.10a we show a trapped normal RBC when the stage was stationary and in Fig. 13.10b when it was moved at  $\sim$ 100  $\mu\text{m/s}$ . By varying the speed of stage, the viscous force on the cell was varied, and elongation along the direction of stretching and compression of the cell in orthogonal directions was measured, and from these the elastic properties were determined. These measurements showed a significant increase in the shear modulus for aged RBCs and cells infected with *Plasmodium falciparum* in comparison to that for normal [79]. An interesting consequence of the difference in membrane rigidity of normal and infected RBCs is that in hypertonic

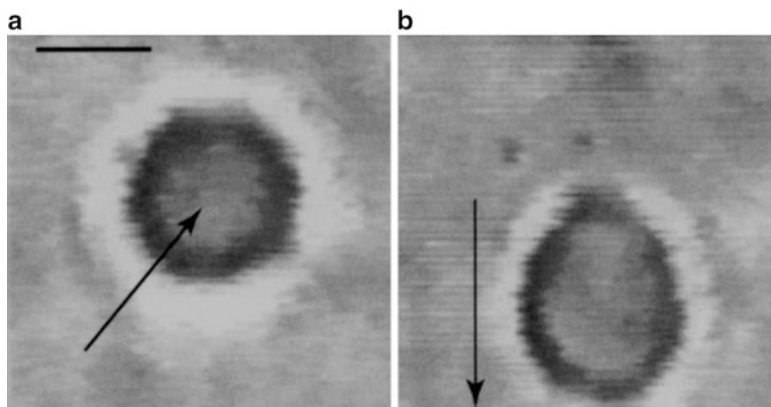


**Fig. 13.10** Stretching of an optically trapped RBC by the use of viscous drag. RBC (marked by arrow) on a stationary stage (a); stretched RBC on moving the stage at 10  $\mu\text{m/s}$  (b). Scale bar: 5  $\mu\text{m}$

buffer medium (osmolarity  $>800 \text{ mOsm/kg}$ ), while the shape of normal RBC gets distorted to a peculiar asymmetric shape, the shape of infected RBC does not change because of the larger rigidity of its membrane. Therefore, while the asymmetric shaped normal RBC rotates by itself when placed in laser trap, at the same trap beam power, RBCs having malaria parasite, due to their larger membrane rigidity, do not rotate [80].

Optical tweezers can trap and immobilize a motile cell in a suspension away from a substrate and thus help acquire even weak Raman signals with good signal to noise ratio by allowing an increased time for spectral acquisition. Compared to the use of physical or chemical methods for immobilization of cells on a substrate, as is practiced in micro-Raman spectroscopy, optical trapping, being noncontact, helps minimize substrate effects and also the effect of the immobilization method used [81, 82]. Setups facilitating acquisition of Raman spectra from an optically trapped cell, referred to as Raman optical tweezers, are being used to monitor changes induced in isolated single cells by a change in their environment, for example, monitoring the real-time heat denaturation of yeast cells [83]. Since the binding or the dissociation of oxygen with heme leads to significant conformational changes of hemoglobin, Raman optical tweezers are particularly suited as a sensitive probe for monitoring the oxygen carrying capacity of RBCs under different physiological or disease conditions [84, 85].

Two- or three-dimensional trap arrays can be conveniently created using a holographic optical tweezers (HOT) setup, which makes use of a spatial light modulator (SLM) on which a computer-generated hologram is imprinted to phase modulate the wave front of the incident 1,064 nm laser beam. This results into a fan out of beams with suitable angular separation which, when coupled to the microscope objective lens, creates multiple traps at the focal plane. The dynamically reconfigurable trap arrays generated in two or three dimensions using HOT can be

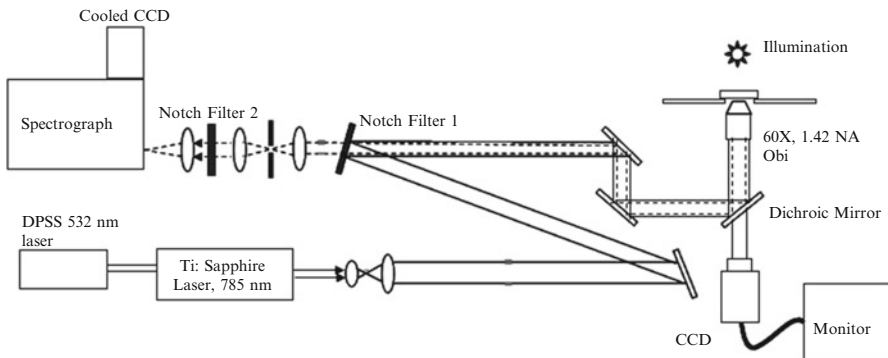


**Fig. 13.11** A schematic of Raman optical tweezers setup. The *solid* and *dashed lines* indicate beam path for trapping laser beam from 785 nm Ti:sapphire laser and backscattered Raman signal from sample, respectively

used to sort colloidal particles/cells of different size or composition by exploiting the difference in optical forces experienced by these when moving through a periodic array of optical traps [86–88]. Multiple traps can also be used for controlled orientation or translation of the trapped cell with respect to a fixed excitation beam. This helps Raman spectroscopic measurements from different areas of the cell with spatial resolution of  $\sim 1 \mu\text{m}$ .

A schematic of the first Raman tweezers setup developed at RRCAT is shown in Fig. 13.11. The setup used the same 785 nm laser beam from a Ti:sapphire laser for trapping as well as Raman excitation. One interesting study carried out using this setup was the Raman spectroscopy of optically trapped RBCs obtained from blood sample from malaria patients suffering from *P. vivax* infection (iRBCs) and healthy volunteers (hRBCs). As compared to hRBCs, significant changes were observed in the oxygenation/deoxygenation marker bands at  $\sim 1,210$ ,  $1,223$ ,  $1,544$ , and  $1,636 \text{ cm}^{-1}$  in the spectra of a significant fraction ( $\sim 30\%$ ) of iRBCs. The observed changes suggest a reduced oxygen affinity of iRBCs as compared to hRBCs [89].

Integration of Raman tweezers with holographic optical tweezers allows translating the trapped cell across a fixed Raman excitation beam to generate spatially resolved (resolution  $\sim 1 \mu\text{m}$ ) Raman spectrum. Investigations made with this setup on the oxygenation status of optically trapped red blood cells show that the cellular site where the trap beam is localized is more deoxygenated compared to the rest of the cell and the level of deoxygenation increases with an increase in trap beam power. Our studies have shown that this deoxygenation arises due to the photodissociation of oxygen from hemoglobin at increased trapping power [90]. The use of surface plasmon resonances of metallic nanoparticles to enhance the Raman spectra from optically trapped cells offers the possibility of selectively acquiring spectra from cell membrane and may help understand the changes occurring in the membrane under some disease conditions.

### 13.5 Therapeutic Applications

Surgical and therapeutic applications of lasers make use of the energy deposited in the tissue by the absorption of laser light [91, 92]. The absorbed energy can broadly lead to three effects. Most common effect is a rise in tissue temperature (photothermal effect). At high intensities associated with lasers operating in short pulse duration (nanosecond to femtoseconds), absorption of laser radiation may lead to the generation of pressure waves or shock waves (photomechanical effects). Short wavelength lasers can cause electronic excitation of chromophores in the tissue and thus initiate a photochemical reaction (photochemical effect). The relative role played by the three depends primarily on the laser wavelength, irradiance, and pulse duration.

Majority of the surgical applications of light exploit the biological effect arising due to the rise in tissue temperature following the absorption of light. The biological effect depends on the level of rise in tissue temperature, which is determined by two factors: first, the depth of penetration of the laser beam which determines the volume of the tissue in which a given energy is deposited and, second, the time in which the energy is deposited vis-à-vis the thermal relaxation time (the inverse of which determines the rate of flow of heat from heated tissue to the surrounding cold tissue). A small rise in temperature (5–10 °C) can influence the vessel permeability and the blood flow. Tissues heated to a temperature of 45–80 °C may get denatured as a result of breakage of van der Waal bonds, which stabilize the conformation of proteins and other macromolecules. Thermal denaturation is exploited for therapy in several ways. For example, hemostasis occurs because of increased blood viscosity caused by denaturation of plasma proteins, hemoglobin, and perivascular tissue. When the temperature exceeds 100 °C, water, the main constituent of tissue, boils. Because of the large latent heat of water, energy added to tissue at 100 °C leads to conversion of water from liquid to steam without further increase in temperature. A volume expansion by ~1,670-fold occurs when water is vaporized isobarically. When this large and rapid expansion occurs within tissue, physical separation or “cutting” occurs. Tissue surrounding the region being vaporized will also be heated, resulting in coagulation of the tissue at the wound edges and thus preventing blood loss. If the rate of deposition of energy is faster than that required for the boiling of water, the tissue is superheated and can be thermally ablated. Thermal ablation or explosive boiling is similar to what happens when cold water is sprinkled on a very hot iron. In ablation, practically all the energy deposited in the tissue is converted into the kinetic energy of the ablation products leading to minimal thermal damage to the adjoining tissues. It is pertinent to emphasize that by exploiting the wavelength dependence of the absorption by different tissue constituents, it is possible to selectively deposit energy in a target site. Further, by use of laser pulses of duration shorter than the thermal relaxation time, heat can be confined within the target tissue so that it can be vaporized without significant effect on surrounding tissue. Such selective photothermolysis has been exploited for several therapeutic applications, such as laser treatment of port-wine stains. Another approach that is

receiving attention for controlled localized heating involves the use of near-infrared light tuned to surface plasmon resonance of metallic nanoparticles. Such heating of metallic nanoparticles that have been selectively deposited in target cells can be used for applications such as hyperthermia for cancer treatment.

At high intensities, typical of short-duration ( $10^{-9}$ – $10^{-14}$  s) laser pulses, localized absorption of laser radiation can lead to very large temperature gradients which in turn result in enormous pressure waves causing localized photomechanical disruption. Such disruption is useful, for example, in the laser removal of tattoo marks. Tattoo ink has pigmented molecular particles too large for the body's immune system to eliminate. Photodisruption of these into smaller particles enables the body's lymphatic system to dispose them, resulting in removal of the tattoo mark. At high intensities, the electric field strength of radiation is also very large (about  $3 \times 10^7$  V/cm at an intensity of  $10^{12}$  W/cm<sup>2</sup>) and can cause dielectric breakdown in the tissue. The resulting plasma absorbs energy and expands, creating shock waves, which can shear off the tissue. Since the plasma generation can occur not only in the pigmented tissue but also in transparent tissues, the plasma-mediated absorption and disruption is applicable to all tissues. The plasma-mediated shock waves are used for breaking stones in the kidney or urethra (lithotripsy) and in posterior capsulotomy for the removal of an opacified posterior capsule of the eye lens. Localized deposition of energy by an intense focused laser pulse can also lead to cavitation. The shock waves generated as a consequence of the collapse of the low-pressure cavitation bubble are also used for photomechanical disruption.

The photothermal and photomechanical effects depend on the intensity of irradiation and will not be significant if the rate of deposition of energy is so low that there is no significant rise in temperature of the tissue. In such a situation, only photochemical effects can take place provided the energy of the laser photon is adequate to cause electronic excitation of biomolecules, which can be either endogenous or externally injected. The photoexcitation of molecules and the resulting biochemical reactions can lead to either bioactivation, exploited in various phototherapies [93, 94], or generation of some free radicals or toxins, which are harmful for the host tissue. The latter process is used for photodynamic therapy (PDT) of cancer [92, 95]. PDT involves the administration of a photosensitizing agent which over a period of time (typically 48–72 h) is excreted by normal tissue and preferentially retained by tumor. The photosensitizer when excited with light of the appropriate wavelength leads to the generation of singlet oxygen or other reactive oxygen species (ROS) (like superoxides, hydroxyl radicals, hydrogen peroxides) which are toxic to the host tumor tissue, thereby leading to tumor destruction [92]. Because of the preferential localization of the photosensitizer in tumor and the fact that the generation of toxins occurs only in the region exposed to light, photodynamic therapy provides much better selectivity compared to the more established treatment modalities, such as radiation therapy and chemotherapy.

An ideal photosensitizer for PDT should simultaneously satisfy several parameters like suitable photophysical/photochemical characteristics to result in selective and large uptake in tumor, a large quantum yield for ROS generation, low dark toxicity, minimal photo-transformation when subjected to photo irradiation and

strong absorption in the 650–900 nm spectral region where tissues are relatively transparent. Further, the excited state of the photosensitiser should have sufficient energy to excite molecular oxygen present in the tissue from the ground triplet state to the singlet state. Since it is difficult to find photosensitizers that satisfy all the parameters well, the quest for better photosensitizers continues. At RRCAT we have focused our attention on the use of chlorophyll derivatives as PDT agents because of their strong absorbance peak in the red region and the economics of synthesis. Chlorin *p*<sub>6</sub> (*Cp*<sub>6</sub>), one of the water soluble derivatives of chlorophyll, which has shown good tumor selectivity and localization, has been used for treating tumors induced in hamster cheek pouch animal models by the application of a carcinogen (7,12-dimethyl-benz(a) anthracene). Studies showed that for small tumors (size <5 mm), a complete tumor necrosis was achieved following PDT at 4 h after intraperitoneal injection of *Cp*<sub>6</sub>. Treated tumor became edematous at 24 h after PDT, and then a reduction in tumor size was observed in the next 48 h. In the animal kept for follow-up a week after PDT, the tumor regressed completely and only scar tissue was observed (Fig. 13.12). However, for bigger tumors the accumulation of *Cp*<sub>6</sub> was inadequate which compromised the effectiveness of PDT [96]. To address this issue, chlorin *p*<sub>6</sub>-histamine conjugate was prepared, and enhanced histamine receptor-mediated cellular uptake in oral cancer cell lines was confirmed [97]. With the use of chlorin *p*<sub>6</sub>-histamine conjugate, tumors with volumes of up to ~1,000 mm<sup>3</sup> have been successfully treated [98]. Studies are also being carried out on the interaction of potential photosensitizers with nanoparticles to evaluate and comprehend the photodynamic effects of the photosensitizer-nanoparticle complex since the use of nanoparticles can provide a valuable approach for targeted delivery of drugs [99, 100].

The use of PDT for antimicrobial applications [101] and for the management of wounds infected with antibiotic-resistant bacteria [102] is also being investigated at RRCAT with some promising results. The advantage of PDT over conventional antimicrobials is that the treatment is localized to light-irradiated regions of the

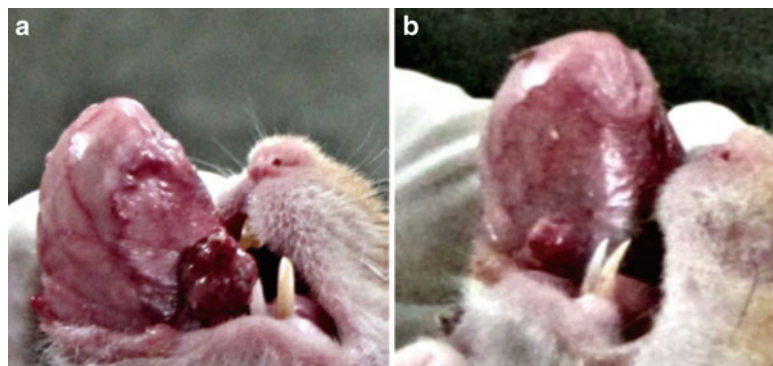


**Fig. 13.12** Photodynamic treatment of the tumor in animal model, (a) before treatment, (b) one week after treatment

drug-treated area, thereby avoiding adverse systemic effects. Further, the reactive oxygen species generated in PDT react with almost every cellular component, and therefore it is highly unlikely that bacteria can develop resistance to PDT [103].

## 13.6 Summary

The remarkable properties of lasers as a light source and the significant advancement in the photonic and information processing technology have led to an upsurge of interest in the utilization of optical techniques for noninvasive, near-real-time biomedical imaging and diagnosis and also for therapeutic modalities providing higher precision and selectivity than offered by the current frontline modalities. Rapid advancements being made in the ability to structure materials at nanoscale and tailor their optical properties to suit specific applications are expected to further enhance the efficacy and the range of these applications. Therefore, the use of optical techniques in advancing the quality of health care is expected to grow even more rapidly in the coming decades.

**Acknowledgment** The authors would like to thank Drs. Y. Verma, R. Dasgupta, S. K. Majumder, Mr. M. K. Swami, and Ms. P. Sharma for their help in the preparation of the manuscript and all the members of Laser Biomedical Applications and Instrumentation Division, RRCAT, for their contributions to the work described in this chapter.

## References

1. S.L. Jacques, Optical properties of biological tissues: a review. *Phys. Med. Biol.* **58**, R37–R61 (2013)
2. C.F. Bohren, D. Huffman, *Absorption and Scattering of Light by Small Particles* (Wiley, New York, 1983)
3. V.V. Tuchin, *Tissue Optics: Light Scattering Methods and Instruments for Medical Diagnosis*, 2nd edn. (SPIE Press, Bellingham, 2007)
4. J. Mobley, T. Vo-Dinh, Optical properties of tissues, in *Biomedical Photonics Handbook*, ed. by T. Vo-Dinh (CRC Press, Boca Raton, 2003)
5. A.M. Zysk, F. Nguyen, A.L. Oldenburg, D.L. Marks, S.A. Boppart, Optical coherence tomography: a review of clinical development from bench to bedside. *J. Biomed. Opt.* **12**, 051403 (2007)
6. J.M. Schmitt, A.H. Gandjbakhche, R.F. Bonner, Use of polarized light to discriminate short-path photons in a multiply scattering medium. *Appl. Opt.* **31**, 6535–6546 (1992)
7. H. Horinaka, K. Hashimoto, K. Wada, Y. Cho, M. Osawa, Extraction of quasi-straightforward-propagating photons from diffused light transmitting through a scattering medium by polarization modulation. *Opt. Lett.* **20**, 1501–1503 (1995)
8. S. Andersson-Engels, R. Berg, S. Svanberg, O. Jarlman, Time-resolved transillumination for medical diagnostics. *Opt. Lett.* **15**, 1179–1181 (1990)
9. B.B. Das, K.M. Yoo, R.R. Alfano, Ultrafast time-gated imaging in thick tissues: a step toward optical mammography. *Opt. Lett.* **18**, 1092–1094 (1993)
10. D. Rao, H.S. Patel, B. Jain, P.K. Gupta, Time-gated optical imaging through turbid media using stimulated Raman scattering: Studies on image contrast. *Pramana. J. Phys.* **64**, 229–238 (2005)

11. B. Bouma, G. Tearney (eds.), *Handbook of Optical Coherence Tomography* (Marcel Dekker, New York, 2002)
12. J.M. Schmitt, Optical Coherence Tomography (OCT): a review. *IEEE J. Sel. Top. Quantum Electron.* **5**, 1205–1215 (1999)
13. A.F. Fercher, W. Drexler, C.K. Hitzenberger, T. Lasser, Optical coherence tomography principles and applications. *Rep. Prog. Phys.* **66**, 239–303 (2003)
14. W. Drexler, U. Morgner, F.X. Kaertner, C. Pitris, S.A. Boppart, X.D. Li, E.P. Ippen, J.G. Fujimoto, In vivo ultra high resolution optical coherence tomography. *Opt. Lett.* **24**, 1221–1223 (1999)
15. B. Povazay, K. Bizheva, A. Unterhuber et al., Sub-micrometer axial resolution optical coherence tomography. *Opt. Lett.* **27**, 1800–1802 (2002)
16. K.-S. Lee, J.P. Rolland, Bessel beam spectral-domain high-resolution optical coherence tomography with micro-optic axicon providing extended focusing range. *Opt. Lett.* **33**, 1696–1698 (2008)
17. Y. Verma, K.D. Rao, S.K. Mohanty, P.K. Gupta, Optical coherence tomography using a tapered single mode fiber tip. *Lasers Phys. Lett.* **4**, 686–689 (2007)
18. A.M. Rollins, M.D. Kulkarni, S. Yazdanfar, R. Ung-arunyawee, J.A. Izatt, In vivo video rate optical coherence tomography. *Opt. Express* **3**, 219–229 (1998)
19. R. Leitgeb, C.K. Hitzenberger, A.F. Fercher, Performance of Fourier domain vs. time domain optical coherence tomography. *Opt. Express* **11**, 889–894 (2003)
20. M.A. Choma, M.V. Sarunic, C. Uang, J.A. Izatt, Sensitivity advantage of swept source and Fourier domain optical coherence tomography. *Opt. Express* **11**, 2183–2189 (2003)
21. M. Wojtkowski, R. Leitgeb, A. Kowalczyk, T. Bajraszewski, A.F. Fercher, In vivo human retinal imaging by Fourier domain optical coherence tomography. *J. Biomed. Opt.* **7**, 457–463 (2002)
22. Y. Yasuno, V.D. Madjarova, S. Makita, Three-dimensional and high-speed swept-source optical coherence tomography for in vivo investigation of human anterior eye segments. *Opt. Express* **13**, 10652 (2005)
23. R.K. Wang, In vivo full range complex Fourier domain optical coherence tomography. *Appl. Phys. Lett.* **90**, 054103 (2007)
24. L. Yu, B. Rao, J. Zhang, J. Su, Q. Wang, S. Guo, Z. Chen, As improved lateral resolution in optical coherence tomography by digital focusing using two dimensional numerical diffraction methods. *Opt. Express* **15**, 7634–7641 (2007)
25. B.A. Standish, K.K.C. Lee, A. Mariampillai, N.R. Munce, M.K.K. Leung, V.X.D. Yang, I.A. Vitkin, In vivo endoscopic multi-beam optical coherence tomography. *Phys. Med. Biol.* **55**, 615–622 (2010)
26. E. Dalimier, D. Salomon, Full-field optical coherence tomography: a new technology for 3D high-resolution skin imaging. *Dermatology* **224**, 84–92 (2012)
27. J.F. de Boer, T.E. Milner, Review of polarization sensitive optical coherence tomography and stokes vector determination. *J. Biomed. Opt.* **7**, 359–371 (2002)
28. K.D. Rao, Y. Verma, H.S. Patel, P.K. Gupta, Non-invasive ophthalmic imaging of adult Zebrafish eye using optical coherence tomography. *Curr. Sci.* **90**, 1506 (2006)
29. Y. Verma, K.D. Rao, M.K. Suresh, H.S. Patel, P.K. Gupta, Measurement of gradient refractive index profile of crystalline lens of fisheye in-vivo using optical coherence tomography. *Appl. Phys. B* **87**, 607–610 (2007)
30. K.D. Rao, A. Alex, Y. Verma, S. Thampi, P.K. Gupta, Real-time in-vivo imaging of adult Zebrafish brain using optical coherence tomography. *J. Biophotonics* **2**, 288–291 (2009)
31. K.D. Rao, P. Upadhyaya, M. Sharma, P.K. Gupta, Noninvasive imaging of ethanol-induced developmental defects in Zebrafish embryos using optical coherence tomography. *Birth Defects Res. B* **95**, 7–11 (2012)
32. M. Bhattachrjee, P.C. Ashok, K.D. Rao, S.K. Majumder, Y. Verma, P.K. Gupta, Binary tissue classification studies on resected human breast tissues using optical coherence tomography images. *J. Innov. Opt. Health Sci.* **4**, 59–66 (2011)

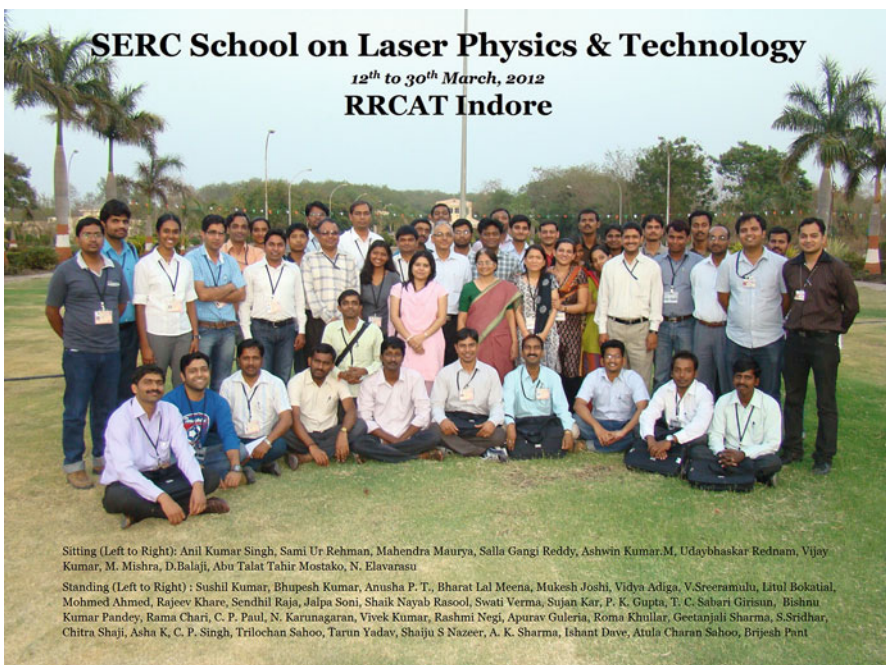
33. Y. Verma, M.K. Suresh, K.D. Rao, M.K. Swami, P.K. Gupta, Imaging of human breast tissue samples using polarization sensitive optical coherence tomography. *Lasers Phys.* **21**, 2143–2148 (2011)
34. K. Sahu, Y. Verma, M. Sharma, K.D. Rao, P.K. Gupta, Non-invasive assessment of healing of bacteria infected and uninjected wounds using optical coherence tomography. *Skin Res. Tech.* **16**, 428 (2010)
35. K. Sahu, M. Sharma, P. Sharma, Y. Verma, K.D. Rao, H. Bansal, A. Dube, P.K. Gupta, Effect of poly-L-lysine-chlorin P6-mediated antimicrobial photodynamic treatment on collagen restoration in bacteria-infected wounds. *Photomed. Laser Surg.* **32**, 23–29 (2014)
36. J.C. Hebden, S.R. Arridge, D.T. Delpy, Optical imaging in medicine I: experimental techniques. *Phys. Med. Biol.* **42**, 825–840 (1997)
37. A.M. Siegel, J.J.A. Marota, D.A. Boas, Design and evaluation of a continuous-wave diffuse optical tomography system. *Opt. Express* **4**, 287–298 (1999)
38. J.C. Schotland, Continuous-wave diffusion imaging. *J. Opt. Soc. Am. A* **14**, 275–279 (1997)
39. J.C. Hebden, Imaging through scattering media using characteristics of the temporal distribution of transmitted laser pulses. *Opt. Lasers Tech.* **27**, 263–268 (1995)
40. E. Hideo et al., Multichannel time-resolved optical tomographic imaging system. *Rev. Sci. Instrum.* **70**, 3595–3602 (1999)
41. J.B. Fishkin, O. Coquoz, E.R. Anderson, M. Brenner, B.J. Tromberg, Frequency-domain photon migration measurements of normal and malignant tissue optical properties in a human subject. *Appl. Opt.* **36**, 10–20 (1997)
42. B.W. Pogue, M. Testorf, T. McBride, U. Osterberg, K. Paulsen, Instrumentation and design of a frequency-domain diffuse optical tomography imager for breast cancer detection. *Opt. Express* **1**, 391–403 (1997)
43. A. Gibson, H. Dehghani, Diffuse optical imaging. *Philos. Trans. R Soc. A* **367**, 3055–3072 (2009)
44. M. Kempe, M. Larionov, D. Zaslavsky, A.Z. Genack, Acousto-optic tomography with multiply scattered light. *J. Opt. Soc. Am. A* **14**, 1151–1158 (1997)
45. M.-X. Tang, D.S. Elson, R. Li, C. Dunsby, R.J. Eckersley, Photoacoustics, thermoacoustics, and acousto-optics for biomedical imaging. *Proc. IMechE H J. Eng. Med.* **224**, 291–306 (2010)
46. P. Lai, X. Xu, L.V. Wang, Ultrasound-modulated optical tomography at new depth. *J. Biomed. Opt.* **17**, 066006 (2012)
47. L.V. Wang, Prospects of photoacoustic tomography. *Med. Phys.* **35**, 5758–5767 (2008)
48. H. Nathel, Laser Opto-acoustic imaging: let there be light that sounds! *Opt. Photonics News* **10**, 27–32 (1999)
49. R.S. Gurjar, V. Backman, L.T. Perelman et al., Imaging human epithelial properties with polarized light-scattering spectroscopy. *Nat. Med.* **7**, 1245–1248 (2001)
50. S. Manhas, M.K. Swami, H.S. Patel, A. Uppal, N. Ghosh, P.K. Gupta, Polarized diffuse reflectance measurements on cancerous and noncancerous tissues. *J. Biophotonics.* **2**, 581–587 (2009)
51. S. Manhas, M.K. Swami, P. Buddhiwant, N. Ghosh, P.K. Gupta, K. Singh, Mueller matrix approach for determination of optical rotation in chiral turbid media in backscattering geometry. *Opt. Express* **14**, 190–202 (2006)
52. S.K. Majumder, A. Uppal, P.K. Gupta, In-vitro diagnosis of human uterine malignancy using N<sub>2</sub> laser induced autofluorescence spectroscopy. *Curr. Sci.* **70**, 833–836 (1996)
53. P.K. Gupta, S.K. Majumder, A. Uppal, Breast cancer diagnosis using N<sub>2</sub> laser excited autofluorescence spectroscopy. *Lasers Surg. Med.* **21**, 417–422 (1997)
54. S.K. Majumder, P.K. Gupta, Synchronous luminescence spectroscopy for cancer diagnosis. *Lasers Life Sci.* **9**, 143–152 (2000)
55. B. Jain, S.K. Majumder, P.K. Gupta, Time resolved and steady state autofluorescence spectroscopy of normal and malignant human breast tissue. *Lasers Life Sci.* **8**, 163–173 (1998)

56. S.K. Majumder, P.K. Gupta, B. Jain, A. Uppal, UV excited autofluorescence spectroscopy of human breast tissue for discriminating cancerous tissue from benign tumor and normal tissue. *Lasers Life Sci.* **8**, 249–264 (1999)
57. S.K. Majumder, P.K. Gupta, A. Uppal, Autofluorescence spectroscopy of tissues from human oral cavity for discriminating cancerous from normal oral tissue. *Lasers Life Sci.* **8**, 211–227 (1999); S.K. Majumder, P.K. Gupta, Synchronous luminescence spectroscopy for oral cancer diagnosis. *Lasers Life Sci.* **9**, 143–152 (2000).
58. S.K. Majumder, S.K. Mohanty, N. Ghosh, P.K. Gupta, D.K. Jain, F. Khan, A pilot study on the use of autofluorescence spectroscopy for diagnosis of the cancer of human oral cavity. *Curr. Sci.* **79**, 1089–1094 (2000)
59. N. Ghosh, S.K. Majumder, H.S. Patel, P.K. Gupta, Depth resolved fluorescence measurement in layered turbid medium by polarized fluorescence spectroscopy. *Opt. Lett.* **30**, 162–164 (2005)
60. S.K. Majumder, N. Ghosh, S. Kataria, P.K. Gupta, Nonlinear pattern recognition for laser induced fluorescence diagnosis of cancer. *Lasers Surg. Med.* **33**, 48–56 (2003)
61. S.K. Majumder, N. Ghosh, P.K. Gupta, Relevance vector machine for optical diagnosis of cancer. *Lasers Surg. Med.* **36**, 323–333 (2005)
62. S.K. Majumder, N. Ghosh, P.K. Gupta, Support vector machine for optical diagnosis of cancer. *J. Biomed. Opt.* **10**, 024034 (2005)
63. S.K. Majumder, A. Gupta, S. Gupta, N. Ghosh, P.K. Gupta, Multi-class classification algorithm for optical diagnosis of oral cancer. *J. Photochem. Photobiol. B* **85**, 109–117 (2006)
64. S.K. Majumder, S.C. Gebhart, M.D. Johnson, R. Thompson, W.C. Lin, A. Mahadevan-Jansen, A probability-based spectroscopic diagnostic algorithm for simultaneous discrimination of brain tumor and tumor margins from normal brain tissue. *Appl. Spectrosc.* **61**, 548–557 (2007)
65. H. Krishna, S.K. Majumder, P.K. Gupta, Range-independent background subtraction algorithm for recovery of Raman spectra of biological tissue. *J. Raman Spectrosc.* **43**, 1884–1894 (2012)
66. S.K. Majumder, H. Krishna, M. Sidramesh, P. Chaturvedi, P.K. Gupta, A comparative evaluation of Raman and fluorescence spectroscopy for optical diagnosis of oral neoplasia. *Proc. SPIE* **8173**, 817306 (2010)
67. H. Krishna, S.K. Majumder, P. Chaturvedi, M. Sidramesh, P.K. Gupta, In vivo Raman spectroscopy for detection of oral neoplasia: a pilot clinical study. *J. Biophotonics* (2014). doi:[10.1002/jbio.201300030](https://doi.org/10.1002/jbio.201300030)
68. H. Krishna, S.K. Majumder, P. Chaturvedi, P.K. Gupta, Anatomical variability of in vivo Raman spectra of normal oral cavity and its effect on oral tissue classification. *Biomed. Spectrosc. Imaging* **2**, 199–217 (2013)
69. A.M.K. Enejder, T. Koo, J. Oh et al., Blood analysis by Raman spectroscopy. *Opt. Lett.* **27**, 2004–2006 (2002)
70. D.I. Ellis, V.L. Brewster, W.B. Dunn, J.W. Allwood, A.P. Golovanov, R. Goodacre, Finger-printing food: current technologies for the detection of food adulteration and contamination. *Chem. Soc. Rev.* **41**, 5706–5727 (2012)
71. J.O. William, E. Jaatinen, P. Fredericks, B. Cletus, H. Panayiotou, E.L. Izake, Spatially offset Raman spectroscopy (SORS) for the analysis and detection of packaged pharmaceuticals and concealed drugs. *Forensic Sci. Int.* **212**, 69–77 (2011)
72. M.W. Berns, K.O. Greulich (eds.), *Laser Manipulation of Cells and Tissues* (Academic, San Diego, 2007)
73. A. Ashkin, Forces of a single-beam gradient laser trap on a dielectric sphere in the ray optics regime. *Biophys. J.* **61**, 569–582 (1992)
74. N. Malagnino, G. Pesce, A. Sasso, E. Arimondo, Measurements of trapping efficiency and stiffness in optical tweezers. *Opt. Commun.* **214**, 15–24 (2002)
75. K.O. Greulich, *Micromanipulation by Light in Biology and Medicine: The Laser Microbeam and Optical Tweezers* (Birkhäuser Verlag, Basel, 1999)
76. R. Dasgupta, P.K. Gupta, Optical tweezers and cytometry, in *Advanced Optical Flow Cytometry*, ed. by V.V. Tuchin (Wiley, Weinheim, 2011), pp. 363–386

77. S. Henon, G. Lenormand, A. Richert, F. Gallet, A new determination of the shear modulus of the human erythrocyte membrane using optical tweezers. *Biophys. J.* **76**, 1145–1151 (1999)
78. G. Lenormand, S. Hénon, A. Richert, J. Siméon, F. Gallet, Direct measurement of the area expansion and shear moduli of the human red blood cell membrane skeleton. *Biophys. J.* **81**, 43–56 (2001)
79. S.K. Mohanty, A. Uppal, P.K. Gupta, Optofluidic stretching of RBCs using single optical tweezers. *J. Biophotonics* **1**, 522–525 (2008)
80. S.K. Mohanty, A. Uppal, P.K. Gupta, Self-rotation of red blood cells in optical tweezers: prospects for high throughput malaria diagnosis. *Biotech. Lett.* **26**, 971–974 (2004)
81. D.V. Petrov, Raman spectroscopy of optically trapped particles. *J. Opt. A Pure Appl. Opt.* **9**, S139–S156 (2007)
82. A. Min, L. Jun-Xian, H. Shu-Shi, W. Gui-Wen, C. Xiu-Li, C. Zhi-Cheng, Y. Hui-Lu, Application and progress of Raman tweezers in single cells. *Chin. J. Anal. Chem.* **37**, 758–763 (2009)
83. C. Xie, Y. Li, W. Tang, R.J. Newton, Study of dynamical process of heat denaturation in optically trapped single microorganisms by near-infrared Raman spectroscopy. *J. Appl. Phys.* **94**, 6138–6142 (2003)
84. S. Rao, S. Balint, B. Cossins, V. Guallar, D. Petrov, Raman study of mechanically induced oxygenation state transition of red blood cells using optical tweezers. *Biophys. J.* **96**, 209–216 (2009)
85. A.C. De Luca, G. Rusciano, R. Ciancia, V. Martinelli, G. Pesce, B. Rotoli, L. Selvaggi, A. Sasso, Spectroscopical and mechanical characterization of normal and thalassemic red blood cells by Raman Tweezers. *Opt. Expr.* **16**, 7943–7957 (2008)
86. R. Dasgupta, S. Ahlawat, P.K. Gupta, Microfluidic sorting with a moving array of optical traps. *Appl. Opt.* **51**, 4377–4387 (2012)
87. R. Dasgupta, R.S. Verma, P.K. Gupta, Microfluidic sorting with blinking optical traps. *Opt. Lett.* **37**, 1739–1741 (2012)
88. S. Ahlawat, R. Dasgupta, R.S. Verma, N.V. Kumar, P.K. Gupta, Optical sorting in holographic trap arrays by tuning inter trap separation. *J. Opt.* **14**, 125501–125512 (2012)
89. R. Dasgupta, R.S. Verma, S. Ahlawat, A. Uppal, P.K. Gupta, Studies on erythrocytes in malaria infected blood sample with Raman optical tweezer. *J. Biomed. Opt.* **16**, 077009 (2011)
90. S. Ahlawat, N. Kumar, R. Dasgupta, R.S. Verma, A. Uppal, P.K. Gupta, Raman spectroscopic investigations on optical trap induced deoxygenation of red blood cells. *Appl. Phys. Lett.* **103**, 183704 (2013)
91. P.K. Gupta, N. Ghosh, H.S. Patel, Lasers and laser tissue interaction. in *Fundamentals and Applications of Biophotonics in Dentistry*, ed. by A. Kishen, A. Asundi (Imperial College Press, London, 2007), pp. 123–148; P.K. Gupta, M.K. Swami, H.S. Patel, History and fundamentals of light tissue interactions. in *Handbook of Photomedicine*, ed. by M.R. Hamblin, Y. Huang (CRC Press/Taylor & Francis, New York, 2013), pp. 25–34.
92. M.R. Hamblin, Y. Huang (eds.), *Handbook of Photomedicine* (CRC Press/Taylor & Francis, New York, 2013), pp. 25–34
93. G.D. Baxter, *Therapeutic Lasers, Theory and Practice* (Churchill Livingstone, Edinburgh, 1994)
94. T. Karu, Cellular and molecular mechanisms of photobiomodulation (low-power laser therapy). *IEEE J. Select. Top. Quant. Electron.* **20**(6603355) (2014)
95. P. Agostinis, K. Berg, K.A. Cengel, T.H. Foster et al., Photodynamic therapy of cancer: an update. *CA Cancer J. Clin.* **61**, 250–281 (2011)
96. A. Dube, S. Sharma, P.K. Gupta, Evaluation of chlorin p6 for photodynamic treatment of squamous cell carcinoma in hamster cheek pouch model. *Oral Oncol.* **42**, 76–81 (2006)
97. A. Parihar, A. Dube, P.K. Gupta, Conjugation of chlorin p6 to histamine enhances its cellular uptake and phototoxicity in oral cancer cells. *Cancer Chemother. Pharmacol.* **68**, 359–369 (2011)

98. A. Parihar, A. Dube, P.K. Gupta, Photodynamic treatment of oral squamous cell carcinoma in hamster cheek pouch model using chlorin p6-histamine conjugate. *Photodiag. Photodyn. Ther.* **10**, 79–86 (2013)
99. K. Das, A. Uppal, B. Jain, B. Bose, P.K. Gupta, Light induced toxicity of merocyanine 540–silica. *J. Nanosci. Nanotech.* **9**, 5642–5645 (2009)
100. A. Uppal, B. Jain, P.K. Gupta, K. Das, Photodynamic action of Rose Bengal Silica nanoparticle complex on breast and oral cancer cell lines. *Photochem. Photobiol.* **87**, 1146–1151 (2011)
101. M. Sharma, L. Visai, F. Bragheri, I. Cristiani, P.K. Gupta, Toluidine blue-mediated photodynamic effects on staphylococcal biofilms. *Antimicrob. Agents Chemother.* **52**, 299–305 (2008)
102. K. Sahu, M. Sharma, H. Bansal, A. Dube, P.K. Gupta, Topical photodynamic treatment with poly-L-lysine chlorin p6 conjugate improves wound healing by reducing hyper inflammatory response in *Pseudomonas aeruginosa* infected wounds of mice. *Lasers Med. Sci.* **28**, 465–471 (2013)
103. T. Maisch, Anti-microbial photodynamic therapy: useful in the future? *Lasers Med. Sci.* **22**, 83–91 (2007)

# Group Photograph



# Index

## A

Abdul Aleem, B., 346  
Abhinandan, L., 69  
Agarwal, G.P., 116, 119, 120, 122, 127, 128  
Agarwal, P.K., 69  
Agostinis, P., 397  
Agrawal, G.P., 28, 63  
Agrawal, P.K., 69  
Ahlawat, S., 394, 395  
Ai, C., 282  
Aizpurua, J., 191  
Akiyama, A., 86  
Albert, S.K., 335  
Alemohammad, H., 331, 354  
Alex, A., 381  
Alfano, R.R., 60, 376  
Alferov, Z.I., 123  
Alharbi, M., 82  
Allwood, J.W., 391  
Al-Mashikhi, S.O., 346  
Ambartsumyan, R.V., 170  
Anawa, E.M., 361  
Anderson, E.R., 384  
Anderson, P.W., 168  
Andersson-Engels, A., 376  
Arima, T., 192, 203  
Arimondo, E., 392  
Ariyoshi, S., 191  
Arnone, D.D., 182  
Arridge, S.R., 384  
Arthur, J.R., 126  
Ashkin, A., 391, 392  
Ashok, P.C., 382  
Aspect, A., 175  
Attfield, J.P., 192, 203

## Auzel, F., 171

Averitt, R.D., 182, 191–193, 203  
Awari, N., 192, 203  
Azuma, M., 192, 203

## B

Bachmann, F., 122, 129, 131  
Backes, G., 328  
Backman, V., 385  
Baguer, N., 240  
Bajaj, P.N., 314  
Bajraszewski, T., 379  
Balachandran, R.M., 171  
Balbashov, A.M., 192, 203  
Balint, S., 394  
Banerjee, N.S., 74  
Bansal, H., 383, 384, 398  
Barber, J., 182  
Barbieri, B., 310, 312  
Bardou, F., 175  
Bartal, B., 182, 187  
Bartolini, P., 168  
Basov, N.G., 74, 116, 117, 170  
Bastiaans, G.J., 182, 191  
Bauer, T., 191  
Baumgart, B., 82  
Baxter, G.D., 396  
Beach, R.J., 80  
Beard, T.M.C., 182–184  
Beaurepaire, E., 182  
Beenakker, C.W.J., 171  
Beiser, A., 3  
Belan, V.R., 171  
Benabid, F., 82

- Benard, D.J., 77  
 Bennett, W.R., 66  
 Berg, K., 397  
 Berg, R., 376  
 Berger, G.A., 171  
 Berns, M.W., 391, 392  
 Berry, E., 182  
 Bethea, C.G., 108  
 Bevacqua, S.F., 86  
 Beverini, N., 310, 312  
 Beyer, E., 346  
 Bhadani, P.K., 69  
 Bhaduri, B., 282, 285, 286, 293  
 Bhale, G.L., 317  
 Bhargava, B., 339  
 Bhargava, P., 331, 335, 339, 354  
 Bhatnagar, P., 74  
 Bhatnagar, R., 69  
 Bhatt, R.B., 360  
 Bhattachjee, M., 382  
 Binroth, C., 330  
 Biswal, R., 69  
 Biswas, B., 163  
 Biswas, D.J., 72  
 Bizheva, K., 378  
 Bloembergen, N., 28, 33, 52, 59, 63  
 Boas, D.A., 384  
 Bobrow, L., 182  
 Bohren, C.F., 375  
 Boldyrev, S., 175  
 Bonner, R.F., 376  
 Boppert, S.A., 376, 378  
 Borak, A., 182–184  
 Bose, B., 398  
 Botez, D., 122  
 Bouchaud, F., 175  
 Bouchaud, J.P., 175  
 Bouma, B., 377  
 Bouske, R.R., 77  
 Bowen, J.W., 182  
 Boyd, R.W., 28, 33, 52, 59, 63  
 Bradley, T., 82  
 Bragheri, F., 398  
 Brandt, M., 328  
 Brau, C.A., 156  
 Brenner, M., 384  
 Brewster, V.L., 391  
 Bridges, T.J., 79  
 Bridges, W.B., 68  
 Briskina, C.M., 171  
 Brunner, F., 111  
 Buddhiwant, P., 385  
 Burns, G., 86  
 Butcher, P.N., 28, 33  
 Butler, J.K., 116, 127  
 Byer, R.L., 95, 96, 98
- C**  
 Callebaut, H., 182, 188, 189  
 Calvani, P., 192, 195, 203  
 Campbell, N., 82  
 Cao, C.Q., 172  
 Cao, H., 172  
 Cao, Y., 192  
 Capasso, F., 127, 131  
 Carlson, L.R., 317  
 Carlson, R.O., 86  
 Casey, H.C., 116, 118, 119, 121–124, 127–130  
 Caulfield, H.J., 171  
 Cengel, K.A., 397  
 Chainani, A., 192, 203  
 Chakraborti, P.K., 314  
 Chakraborty, A., 69  
 Chamberlain, J.M., 182–184  
 Chan, W.L., 183, 192  
 Chandra, K., 365, 366  
 Chang, R.P.H., 172  
 Chang, S.-H., 172  
 Chang, T.Y., 79  
 Chang, Y.M., 21, 148  
 Chatterjee, S., 281–294  
 Chaturvedi, P., 389, 390  
 Chen, H.-T., 191  
 Chen, S.L., 346  
 Chen, S.Y., 108  
 Chen, Y.-B., 182, 191, 359, 361  
 Chen, Z.Q., 108, 380  
 Cheong, S.-W., 192, 203  
 Chiang, A.C., 108  
 Chinn, S.R., 86  
 Cho, A.Y., 126  
 Cho, G., 191  
 Cho, Y., 376  
 Choi, Y.J., 192, 203  
 Choma, M.A., 379  
 Choube, R., 69  
 Choudhary, P., 72  
 Chouksey, S., 163  
 Christov, I.P., 29  
 Chu, C.W., 192  
 Ciancia, R., 394  
 Clarkson, W.A., 134  
 Clery, D., 182  
 Cletus, B., 391  
 Cohen-Tannoudji, C., 175  
 Cole, B.E., 182  
 Colson, W.B., 162

- Coquoz, O., 384  
Corbin, S.F., 331, 354  
Corson, J., 182, 191, 201, 202  
Corwin, K.L., 82  
Cossins, B., 394  
Cotter, D., 28, 33, 57, 58  
Couny, F., 82  
Cox, S., 192, 203  
Crawley, D., 182  
Creath, K., 282  
Cristiani, I., 398  
Crouse, P.L., 346  
Cryst, J., 240  
Czasch, S., 191  
Dingle, R., 125  
Dixit, S.K., 65–83  
Dobroiu, A., 191  
Draugelates, U., 330  
Drew, H.D., 192, 203  
Drexler, W., 377, 378  
Dube, A., 383, 384, 398  
Dumke, W.P., 86  
Dunn, M.H., 2  
Dunn, W.B., 391  
Dunsby, C., 384  
Durandet, Y., 328  
Dussardier, B., 149  
Dutta, N.K., 116, 119, 120, 122, 127, 128

**D**

- Dadashzadeh, N., 82  
Dagotto, E., 192, 200, 203  
Dalimier, E., 380  
D'Amore, F., 192, 195, 203  
Danilychev, V.A., 74  
Das, B.B., 376  
Das, K., 398  
Das, R.C., 314  
Dasgupta, K., 314  
Dasgupta, R., 392, 394, 395  
Daultabad, S.R., 69  
David, R., 317  
Davies, A.G., 182  
Davim, J.P., 361  
Davis, S.J., 328  
Davison, B., 170  
Dawber, M., 192, 203  
Day, G.M., 182  
Dayal, R.K., 366, 367  
de Boer, J.F., 381  
De Dore, P., 192, 195, 203  
De Luca, A.C., 394  
Dearden, G., 328  
Degiorgio, V., 28  
Dehghani, H., 384  
Delpy, D.T., 384  
Derwent, R.G., 77  
Deschaux-Beaume, F., 361  
Dessau, D.S., 192, 230  
Dev, V., 312–314, 318  
Dexheimer, S.L., 182–184  
Dharmendra, C., 361  
Dianov, E.M., 134  
Diehl, R., 122, 127, 129, 130  
Dill, F.H., 86  
Dimitrova, O.V., 171

**E**

- Eberly, J.H., 2  
Eckersley, R.J., 384  
Eckstein, J.N., 182, 191, 201, 202  
Egarievwe, S.U., 171  
Einstein, A., 5  
Ellis, D.I., 391  
Elson, D.S., 384  
Emile, O., 175  
Enejder, A.M.K., 391  
Engstrom, H., 328  
Erenstein, W., 192, 203  
Erez, G., 317  
Exner, H., 361

**F**

- Fan, T.Y., 95, 96, 98  
Fattinger, C., 182, 193  
Fearon, E., 328  
Feller, W., 174  
Feng, X.-S., 361  
Fenner, G.E., 86  
Ferch, A.F., 378  
Fercher, A.F., 377, 379  
Ferguson, B., 182, 191  
Ferrari, A.C., 149  
Fiebig, M., 192, 200, 203  
Fiedler, T., 82  
Finlayson, D.M., 39, 52, 54, 59  
Fischer, B.M., 182  
Fishkin, J.B., 384  
Fitzgerald, A.J., 182  
Flytzanis, C., 28  
Foster, T.H., 397  
Foulds, A.P., 182  
Fourcade-Dutin, C., 82

- Fras, G., 361  
 Fredericks, P., 391  
 Frisch, U., 175  
 Fröhlich, D., 192, 203  
 Fujimoto, G., 378  
 Fukasawa, R., 182, 191
- G**  
 Gagliardi, S., 192, 195, 203  
 Gallet, F., 392  
 Gallot, G., 182  
 Galvao, R.K.H., 182  
 Gandjbakhche, A.H., 376  
 Ganesh, P., 325–368  
 García, J., 192, 203  
 Garcia, N., 168  
 Gasser, A., 328  
 Gebhart, S.C., 388  
 Gedda, H., 328  
 Genack, A.Z., 168, 171, 384  
 George, J., 89, 95, 343  
 Gerecht, E., 191  
 Ghatak, A.K., 2, 6, 131, 134, 137, 142,  
     144, 149  
 Ghodke, D.V., 74  
 Ghosh, N., 385, 387, 388, 395  
 Gibson, A., 384  
 Goldner, P., 171  
 Golovanov, A.P., 391  
 Goltsev, A.V., 192, 203  
 Gomes, A.S.L., 171  
 Gooch, C.H., 116  
 Goodacre, R., 391  
 Goto, T., 192, 203  
 Gouedard, C., 171  
 Gould, G., 69  
 Greivenk, J.E., 282, 293  
 Greulich, K.O., 391, 392  
 Grischkowsky, D., 182, 193  
 Gruener, G., 192, 195, 203  
 Grüner, G., 192, 198, 203  
 Gu, D., 191  
 Guallar, V., 394  
 Guidi, M.C., 192, 195, 203  
 Gui-Wen, W., 393  
 Guo, S., 380  
 Gupta, A., 335, 388  
 Gupta, G.P., 318, 320  
 Gupta, P.K., 1–25, 74, 80, 373–398  
 Gupta, S.K., 163, 388  
 Gurjar, R.S., 385  
 Gwinn, C.R., 175

- H**  
 Hadjiloucas, S., 182  
 Hall, R.N., 86  
 Hamada, N., 192, 230  
 Hamblin, M.R., 395, 397  
 Han, J., 182  
 Hanna, D.C., 2, 28, 57, 58  
 Hasan, T., 149  
 Hashimoto, K., 376  
 Hatamleh, O., 343  
 He, G.S., 61–63  
 He, X., 328  
 Heard, H., 74  
 Hebden, J.C., 384  
 Hebling, J., 182, 187  
 Hedaoo, P., 343  
 Helm, H., 182  
 Hemberger, J., 192, 203  
 Hennrech, F., 149  
 Henon, S., 392  
 Hensel, F., 330  
 Herriott, D.R., 66  
 Herrmann, M., 191  
 Hideo, E., 384  
 Highstrete, C., 182  
 Hillenbrand, R., 191  
 Hilton, D.J., 182, 191  
 Hitzenberger, C.K., 377, 378  
 Ho, S.T., 172  
 Hoffmann, M.C., 182, 187  
 Holonyak, N., 86  
 Horinaka, H., 376  
 Hu, Q., 182, 188, 189, 191  
 Huang, C.H., 108  
 Huang, L.X., 108  
 Huang, S., 361  
 Huang, Y., 395, 397  
 Huang, Y.C., 108  
 Huang, Z.J., 192  
 Huber, A.J., 191  
 Huffman, D., 375  
 Hui-Lu, Y., 393  
 Husson, D., 171

- I**  
 Iga, K., 122, 129  
 Imai, T., 182, 191  
 Innerhofer, E., 111  
 Inoue, H., 182, 191  
 Ioffe, A.F., 168  
 Ion, J.C., 326, 354

- Ipeen, E.P., 378  
Ishizaka, K., 192, 203  
Ittoop, M.O., 349, 360  
Ivanov, V.Y., 192, 203  
Izake, E.L., 391  
Izatt, J.A., 378, 379
- J**  
Jaatinen, E., 391  
Jacobsen, R.H., 191  
Jacques, S.L., 374  
Jain, A., 115–131, 331  
Jain, B., 376, 386, 398  
Jain, D., 115–131  
Jain, D.K., 387  
Jain, K.K., 163  
Jaiswal, A., 335  
Jarlman, O., 376  
Javan, A., 66  
Jayasekharan, T., 317  
Jepsen, P.U., 182  
Jha, S.S., 28, 52  
Jhon, Y.M., 21, 148  
Jiang, M.H., 108  
Jimenez, J., 129  
Jiminez-Linan, M., 182  
John, S., 168, 171  
Johnson, M.D., 388  
Johnson, S.A., 317  
Jones, A.M., 82  
Jones, W., 182  
Jonnalagadda, P.N., 72  
Joo-Hiuk Son, J., 182, 183  
Joshi, M.P., 27–64  
Jun-Xian, L., 393
- K**  
Kadel, R., 82  
Kaertner, F.X., 378  
Kain, V., 365, 366  
Kakkar, C., 149  
Kale, U., 163  
Kanz, V.K., 80  
Kaplan, A.F.H., 346  
Kapon, E., 116, 127, 128  
Kapoor, R., 312  
Kapteyn, H.C., 29  
Karsai, S., 131  
Karu, T., 396  
Kasper, J.V.V., 76, 77  
Kataria, S., 388  
Kato, K., 182, 191
- Kaul, R., 325–368  
Kawai, T., 182, 193  
Kawamoto, S., 192, 203  
Kawase, K., 182, 183, 191, 203  
Kawayama, I., 182, 191–193, 200, 203  
Kearns, D.R., 77  
Keiding, S., 182, 193  
Keilmann, F., 191  
Keller, U., 111  
Kemp, M.C., 182  
Kempe, M., 171, 384  
Kersting, R., 191  
Keyes, R.J., 86  
Khajepour, A., 328, 331, 354  
Khan, F., 387  
Khare, J., 366  
Khare, R., 1–25  
Khodkevich, D.D., 74  
Khursheed, M., 163  
Kida, N., 182–184, 191, 192, 200  
Kim, S.M., 191  
Kim, Y.-H., 359  
Kimura, M., 361  
Kimura, T., 192, 203, 230  
Kinder, L.R., 175  
Kingsley, J.D., 86  
Kitaeva, G.K., 182–184, 190, 200  
Kittle, C., 117  
Kiwa, T., 183, 203  
Klafter, J., 175  
Knorr, J., 361  
Koechner, W., 2, 53, 57, 59, 62, 63, 95,  
    103, 105  
Kohler, R., 182, 188, 189, 192  
Komashko, A., 81  
Koo, T., 391  
Kotani, K., 182, 191, 200  
Kowalczyk, A., 379  
Krag, W.E., 86  
Kressel, H., 116, 127  
Kreutz, E., 328  
Krishna, H., 389, 390  
Krishnagopal, S., 163  
Krishnan, K.M., 74  
Kroemer, H., 123  
Krupke, W.F., 80, 81  
Kryukov, P.G., 170  
Kukreja, L.M., 325–368  
Kulkarni, M.D., 378  
Kumar, A., 163, 325–368  
Kumar, H., 331, 335, 336, 343  
Kumar, M., 72  
Kumar, N., 171, 176, 395  
Kumar, R.V., 346

Kumar, S., 182, 188, 189, 338  
 Kumar, V., 156, 160, 163  
 Kumazawa, R., 182, 191  
 Kumigashira, H., 192, 203  
 Kuratev, L.I., 86  
 Kuruvilla, S.M., 147  
 Kuwahara, H., 192, 203  
 Kwon, C., 192, 193, 203

**L**

Lagendijk, A., 168, 171  
 Lai, P., 385  
 Lal, S., 163  
 Lala, A., 72  
 Lalla, N.P., 335  
 Langevin, D., 175  
 Larionov, M., 384  
 Lasers, S., 116, 127, 128  
 Lasher, G.J., 86  
 Lasser, T., 377  
 Lavi, S., 317  
 Lavrov, A.V., 171  
 Lawandy, N.M., 171  
 Lax, B., 86  
 Lee, A.W.M., 191  
 Lee, J., 21, 148  
 Lee, J.H., 21, 148  
 Lee, K.K.C., 380  
 Lee, K.-S., 378, 380  
 Lee, M., 182  
 Lee, Y.-S., 182, 184, 189, 200  
 Leitgeb, R., 378, 379  
 Lenormand, G., 392  
 Leonhardt, R., 191  
 Letokhov, V.S., 170  
 Leung, M.K.K., 380  
 Levin, L.A., 317  
 Li, A.H., 108  
 Li, H., 122, 129  
 Li, L., 328, 346  
 Li, L.-Q., 361  
 Li, R., 384  
 Li, W., 182  
 Li, W.B., 328  
 Li, X.D., 378  
 Li, Y., 359, 394  
 Lin, S., 361  
 Lin, W.C., 388  
 Lin, Y.Y., 108  
 Linfield, E.H., 182  
 Ling, Y., 172  
 Lippmann, W., 361

Liu, B., 192, 203  
 Liu, H.-B., 182, 191  
 Liu, H.C., 127, 131  
 Liu, K., 182, 192, 193  
 Liu, S.H., 61–63  
 Liu, W., 328  
 Lo, T., 182  
 Lobad, A.I., 192, 193, 203  
 Loffler, T., 191  
 Loidl, A., 192, 203  
 Longbottom, C., 182  
 Loosen, P., 122, 129, 131  
 Lottermoser, T., 192, 203  
 Loudon, J.C., 192, 203  
 Lund, D.N., 182  
 Lunkenheimer, P., 192, 203  
 Lupi, S., 192, 195, 203

**M**

Ma, J., 359  
 Macleod, H.A., 211, 212, 216, 218, 220, 240  
 Madjarova, V.D., 380  
 Magnusson, C., 328  
 Mahadevan-Jansen, A., 388  
 Mahajan, S., 366  
 Mahdi, M., 171  
 Mahrle, A., 346  
 Mai, T.A., 361  
 Maisch, T., 398  
 Maitland, A., 2  
 Majumder, S.K., 382, 386–390  
 Makita, S., 380  
 Malacara, D., 282  
 Malagnino, N., 392  
 Malik, S.K., 192, 203  
 Mandal, P.K., 312–314  
 Manhas, S., 385  
 Manohar, K.G., 314  
 Mantravadi, M.V., 282  
 Mao, C., 82  
 Marchese, S.V., 111  
 Marcuse, D., 136  
 Mariampillai, A., 380  
 Marks, D.L., 376  
 Markushev, V.M., 171  
 Marota, J.J.A., 384  
 Marshall, T.C., 156, 160  
 Martinelli, V., 394  
 Marzi, G., 192, 195, 203  
 Masahiko, T., 182, 185  
 Maselli, P., 192, 195, 203  
 Masson, J.-B., 182

Masson, M.-P., 182

Mathur, N.D., 192, 203

Matveets, Y.A., 170

Mavani, K.R., 182, 183, 192, 193, 200, 203

May, C.A., 317

Mazumder, J., 328, 361

McBride, T., 384

McDermott, W.E., 77

McLean, T.P., 28

McWhorter, A.L., 86

Mehta, S.K., 115–131

Meservey, R., 175

Midgley, P.A., 192, 203

Migus, A., 171

Miles, R.E., 182

Miller, A., 39, 52, 54, 59

Milne, W.I., 149

Milner, T.E., 381

Milonni, P.W., 2

Min, A., 393

Miron, E., 317

Mishra, G.K., 69

Mishra, S.K., 331, 335, 366

Misra, M., 182, 191, 200

Mittal, J.K., 69

Mittleman, D.M., 21, 182–184

Mittleman, D.M., 191

Miyazaki, T., 175

Moat, R.J., 328

Mobley, J., 375

Modjesch, G., 182

Mohanty, S.K., 378, 387, 393

Moitra, A., 331, 335, 336

Monnom, G., 149

Montroll, E.W., 175

Moodera, J., 175

Moreo, A., 192, 203

Morgner, U., 378

Morita, Y., 191

Moritomo, Y., 192, 230

Mott, N.F., 168

Mudali, U.K., 335

Mujumdar, S., 172, 173

Mukherjee, C., 209–279

Mukherjee, S., 146

Mukhin, A.A., 192, 203

Mukhopadhyay, P.K., 85–112

Mulki, S.V., 367

Munce, N.R., 380

Murakami, H., 182, 191–193, 200, 203

Murakmai, H., 183

Murnane, M.M., 29

## N

Nagai, M., 182

Nagai, N., 182, 191

Nagarajan, V., 192, 203

Nakata, K., 361

Nakhe, S.V., 69

Nampoothiri, A.V.V., 82

Nanophoton, J., 172

Nath, A.K., 72, 331, 335, 360, 366

Nathan, M.I., 86

Nathan, T.P.S., 89, 95

Nathel, H., 385

Neaton, J.B., 192, 203

Negi, J., 331

Nelson, K.A., 182, 187

Nerpagar, P., 163

Newmann, R., 86

Newton, R.J., 394

Nguyen, F., 376

Nguyen, K.L., 191

Nicholson, J.J., 191

Nieher, M., 361

Nilaya, J.P., 72

Nilsson, J., 134

Nirmala, R., 192, 203

Nishida, N., 86

Noginov, M.A., 171

Noginova, N.E., 171

Nucara, P., 192, 195, 203

Nundy, U., 72, 74, 80

Nuss, M.C., 191

## O

Oak, M.R.S., 147

Oak, S.M., 102, 103, 335, 343

Ogale, S.B., 192, 203

Ogawa, Y., 182, 191

Oh, J., 391

Oh, S., 182, 191, 201, 202

Ohshima, Y.N., 191

Olabi, A.G., 361

Oldenburg, A.L., 376

Oleg, K., 346

O’Niel, W., 346

Orenstein, J., 182, 191, 201, 202

Ortolani, M., 192, 195, 203

Osawa, M., 376

Osterberg, U., 384

Ostroumov, V., 171

Otani, C., 191

Ott, A., 175

**P**

- Padilla, W.J., 182  
 Paisner, J.A., 317  
 Panayiotou, H., 391  
 Pandey, P., 192, 203  
 Pang, G., 171  
 Panish, M.B., 116, 118, 119, 121–124,  
     127–130  
 Pant, K.K., 151–163  
 Parihar, A., 398  
 Parker, E.H.C., 124  
 Parvathavarthini, N., 366, 367  
 Paschotta, R., 111  
 Patel, A., 163  
 Patel, C.K.N., 71  
 Patel, H.S., 373–398  
 Pathak, A.K., 339, 354  
 Patil, G.C., 72  
 Paul, C.P., 325–368  
 Paulsen, K., 384  
 Pavan Kumar, Y., 282, 285, 286, 288, 293  
 Payne, D.N., 134  
 Payne, S.A., 80  
 Pchelkin, D., 77  
 Pendry, J.B., 182  
 Pepper, M.J., 182  
 Perelman, L.T., 385  
 Pesce, G., 392, 394  
 Petring, D., 346  
 Petrov, D.V., 393, 394  
 Peyre, P., 361  
 Pfister, G., 175  
 Pickwell, E., 182  
 Piltch, M., 69  
 Pimenov, A., 192, 203  
 Pimentel, G.C., 76, 77  
 Ping, G., 182, 185  
 Pinkerton, A., 328  
 Pisarevet, R.V., 192, 203  
 Pitris, C., 378  
 Pogue, B.W., 384  
 Polanyi, J.C., 76  
 Popa, D., 149  
 Popov, Y.M., 74  
 Poprave, R., 122, 129, 131  
 Povazay, B., 378  
 Powell, J., 328, 346, 348, 352  
 Prabhu, S.S., 192, 203  
 Pramana, J., 95  
 Prasad, B.R., 171  
 Prasad, M.B.S., 72  
 Prasad, R.C., 331, 335, 336, 366  
 Prasantkumar, R.P., 182, 191  
 Premsingh, C.H., 331

**P**

- Preuss, M., 328  
 Previtali, B., 328  
 Pulhani, A.K., 312, 313, 318, 320  
 Purushotham, A.D., 182  
 Pye, R.J., 182

**Q**

- Quast, H., 191  
 Quist, T.M., 86

**R**

- Rabe, K.M., 192, 203  
 Rades, T., 182  
 Rai, S.K., 331, 335, 336  
 Ramachandran, H., 165–178  
 Ramesh, R., 192, 203  
 Rana, D.S., 181–206  
 Rana, R., 192, 203  
 Ranganathan, K., 89, 95, 102, 343  
 Rao, B.T., 325–368, 380  
 Rao, C.N.R., 192, 200, 203  
 Rao, D., 376  
 Rao, K.D., 378, 381–384  
 Rao, K.P., 361  
 Rao, P.R.K., 314  
 Rao, S., 394  
 Raote, P., 72  
 Rasper, R., 361  
 Ratanavis, A., 82  
 Rathod, D.R., 314  
 Raulis, C., 131  
 Raveau, B., 192, 200, 203  
 Ravi Kumar, A.V., 163  
 Razvi, M.A.N., 317  
 Rediker, R.H., 86  
 Redo-Sanchez, A., 182  
 Regel, A.R., 168  
 Reich, S., 361  
 Reinecke, A.-M., 361  
 Reintjes, J.F., 28, 36  
 Ren, L., 191  
 Reno, J.L., 182, 188, 189  
 Rghini, R., 168  
 Richardson, D.J., 134  
 Richert, A., 392  
 Rodriguez-Morales, F., 191  
 Rolland, J.P., 378, 380  
 Rollins, A.M., 378  
 Roskos, H.G., 191  
 Ross, M., 86  
 Rotoli, B., 394  
 Roy, S., 338

- Rozhini, A.G., 149  
Rudolph, W., 82  
Rusciano, G., 394
- S**  
Sabbaghzadeh, J., 361  
Sahoo, N.K., 209–279  
Sahoo, S., 146  
Sahu, K., 383, 384, 398  
Saitoh, T., 192, 230  
Sakai, K., 182–184, 186, 191, 192, 200  
Saksena, G.D., 312  
Salomon, D., 380  
Samajdar, I., 366  
Samajdar, R.K., 367  
Sano, Y., 343  
Sarkar, A.K., 163  
Sarunic, M.V., 379  
Sasikumar, S., 80  
Sasso, A., 310, 312, 392, 394  
Sathyanarayanan, S., 331, 335, 336  
Sautert, C., 171  
Sauviat, G., 182  
Saxena, P., 69  
Scardaci, V., 149  
Schade, U., 192, 203  
Scher, H., 175  
Schlom, D.G., 192, 203  
Schmidt, R., 192, 195, 203  
Schmitt, J.M., 376, 377  
Schmuttenmaer, C.A., 182–184  
Schotland, J.C., 384  
Schreiber, S., 361  
Schrette, F., 192, 203  
Schurig, D., 182  
Schwider, J., 282  
Scifres, D.R., 122  
Scott, J.F., 192, 203  
Sechi, Y., 361  
Seelig, E.W., 172  
Seema, A.U., 314  
Selvaggi, L., 394  
Sendhil, R.S., 74  
Sepold, G., 330  
Shah, M.L., 312–314, 318, 320  
Sharma, D., 176  
Sharma, M., 382–384, 398  
Sharma, P., 383, 384  
Sharma, S., 398  
Sharma, S.K., 89, 95, 102, 103  
Shen, H.Y., 108  
Shen, Y.C., 182  
Shen, Y.R., 28, 44, 52, 58, 59
- Shi, Z.B., 108  
Shikarkhane, N.S., 80  
Shintani, H., 192, 203  
Shlesinger, M.F., 175  
Shu-Shi, H., 393  
Sidramesh, M., 389, 390  
Siebert, K.J., 191  
Siegel, A.M., 384  
Siegman, A.E., 2, 10  
Sierra, G., 361  
Silfvast, W.T., 2, 10  
Siméon, J., 392  
Singh, A.J., 102, 103, 192, 203  
Singh, A.K., 335  
Singh, B., 69, 74  
Singh, C.P., 335  
Singh, K., 385  
Singhal, V.P., 80  
Singleton, J., 192, 203  
Smith, D.R., 182  
Sobih, M., 346  
Solarz, R.W., 317  
Solimene, N., 69  
Solomon, T.H., 175  
Soltis, T.J., 86  
Sood, A.K., 171  
Sopracase, R., 192, 195, 203  
Souvain, E., 171  
Spaldin, N.A., 192, 200, 203  
Spowage, A.C., 361  
Standish, B.A., 380  
Steen, W.M., 351, 352, 361  
Strachan, C.J., 182  
Streetman, B.G., 118, 119  
Stringer, M.R., 182  
Stringfellow, G., 126  
Stuart, D., 361  
Su, J., 380  
Subramaniam, V.V., 69  
Subramanian, C.K., 171  
Sun, S., 328  
Sun, Y.Y., 192  
Sun, Z., 149  
Sundar, R., 343  
Suresh, M.K., 381, 383  
Suri, B.M., 295–322  
Sushkov, A.B., 192, 203  
Sutherland, R.L., 28, 59, 61, 62  
Svanberg, S., 376  
Swami, M.K., 383, 385  
Swelto, O., 2  
Swinney, H.L., 175  
Sykes, J.B., 170  
Sze, S.M., 116, 117, 119

**T**

- Taday, P.F., 182  
 Tahamtan, S., 361  
 Takada, H., 86  
 Takahashi, K., 182, 183, 191–193, 200, 203  
 Takahashi, T., 192, 203  
 Takano, M., 192, 203  
 Talukdar, R., 314  
 Tanaka, H., 182, 193  
 Tanaka, K., 182  
 Tang, M.-X., 384  
 Tang, W., 394  
 Tani, M., 191  
 Taylor, A.J., 182, 191  
 Tayloret, A.J., 192, 193, 203  
 Tearney, G., 377  
 Ter-Gabriélyan, N.É., 171  
 Testorf, M., 384  
 Tezuka, N., 175  
 Thampi, S., 381  
 Theriault, A., 328  
 Thompson, R., 388  
 Thompson, T., 171  
 Thomson, M., 191  
 Thorsmølle, V.K., 192, 193, 203  
 Thrush, B.A., 77  
 Thyagarajan, K., 2, 6, 131, 133–149  
 Tilborg, J., 182  
 Tiwari, M.K., 335  
 Tiwari, P., 331, 335, 336, 343  
 Tokura, Y., 192, 200, 203, 230  
 Tomioka, Y., 192, 203  
 Tomm, J.W., 129  
 Tonouchi, M., 182–184, 186, 191–193, 200, 203  
 Torkamany, M.J., 361  
 Torre, R., 172  
 Torrisi, F., 149  
 Toyserkani, E., 331, 354  
 Tribe, W.R., 182  
 Tripathi, P., 335  
 Tromberg, B.J., 384  
 Trugman, S.A., 182, 191–193, 203  
 Tsai, H., 361  
 Tsallis, C., 175  
 Tsang, W.T., 116, 124  
 Tsumura, T., 361  
 Tu, R.Y., 108  
 Tuchin, V.V., 375, 376  
 Turner, G.M., 182–184

**U**

- Uang, C., 379  
 Uddin, A., 182

Ung-arunyawee, R., 378

- Unterhuber, A., 378  
 Upadhyaya, B.N., 147  
 Upadhyaya, P., 382  
 Uppal, A., 385, 386, 393–395, 398  
 Urbach, W., 175  
 Usha Chakravarty, A., 147

**V**

- Vaithyanathan, V., 192, 203  
 Valdas Aguilar, R., 192, 203  
 Valsecchi, B., 328  
 van Exter, M., 182, 193  
 Varshnay, N.K., 74  
 Vedani, M., 328  
 Venkateswarlu, P., 171  
 Verdeyen, J.T., 2, 10  
 Verma, B., 351  
 Verma, R.S., 394, 395  
 Verma, Y., 378, 381–384  
 Viehland, D., 192, 203  
 Vimercati, G., 328  
 Vinit Kumar, 163  
 Visai, L., 398  
 Vitkin, A., 380  
 Vo-Dinh, T., 375  
 Voisey, K.T., 346

**W**

- Wada, K., 376  
 Wade Falk, N., 191  
 Waghmare, U.V., 192, 203  
 Wahstrom, G., 328  
 Wallace, V.P., 182  
 Walter, W.T., 69  
 Wang, F., 149  
 Wang, J., 192, 203  
 Wang, J.Y., 108  
 Wang, K., 182  
 Wang, L.V., 385  
 Wang, Q., 380  
 Wang, Q.H., 172  
 Wang, R.K., 380  
 Wang, Y.Y., 82  
 Wang, Z.P., 108  
 Washburn, B.R., 82  
 Watanabe, Y., 182, 191  
 Watkins, K.G., 328  
 Weeks, E.R., 175  
 Wegener, M., 29  
 Wei, Y., 108  
 Wheeler, N.V., 82

- White, I.H., 149  
Wiersma, D.S., 168, 171, 172  
Wilden, J., 361  
William, J.O., 391  
Williams, A.J., 192, 203  
Williams, B.S., 182, 188, 189  
Wissenbach, K., 328  
Withers, P.J., 328  
Wittborn, J., 191  
Wojtkowski, M., 379  
Wolf, R., 361  
Wong, T.M., 175  
Woodward, R.M., 182  
Worden, E.F., 317  
Wuttig, M., 192, 203  
Wyant, J.C., 282
- X**  
Xi-Cheng, Z., 182, 191  
Xie, C., 394  
Xiu-Li, C., 393  
Xu, H., 182  
Xu, J., 182, 192, 193  
Xu, J.Y., 172  
Xu, X., 385  
Xue, L., 328  
Xue, Y.Y., 192
- Y**  
Yada, H., 182  
Yamada, I., 192, 203  
Yamashita, M., 183, 191, 203  
Yamauchi, K., 182, 191  
Yanagida, T., 182, 193  
Yang, V.X.D., 380  
Yariv, A., 2, 10, 28, 49, 52  
Yasuno, Y., 380  
Yazdanfar, S., 378  
Ye, Q.J., 108  
Yeh, P., 28, 49  
Yen, T.J., 182  
Yilbas, B.S., 346  
Yngesson, K.S., 191
- Yoo, K.M., 376  
Yu, G., 328  
Yu, G.F., 108  
Yu, H.H., 108  
Yu, L., 380  
Yu, X., 182  
Yu, Y.G., 108  
Yuan, T., 182, 192, 193  
Yuasa, H., 86  
Yudin, B., 346  
Yunoki, S., 192, 203  
Yuratich, M.A., 28, 57, 58
- Z**  
Zannoni, R., 191  
Zaslavsky, D., 384  
Zaslavsky, G.M., 175  
Zeiger, H.J., 86  
Zeitler, J.A., 182  
Zeng, J., 328, 359  
Zeng, R.R., 108  
Zeng, Z.D., 108  
Zhang, C.L., 192, 203  
Zhang, G., 108  
Zhang, H.J., 108  
Zhang, J., 380  
Zhang, S., 182  
Zhang, W.J., 108  
Zhang, X.-C., 182, 191–193  
Zhang, X.Y., 108  
Zhao, X., 191  
Zhao, Y.G., 172  
Zheng, H., 192, 203  
Zhi-Cheng, C., 393  
Zhong, H., 182  
Zhong, M., 328  
Zhou, Y.P., 108  
Zhu, H.Y., 108  
Zhu, Z., 182  
Zolin, V.F., 171  
Zory, P., 125, 126  
Zweiback, J., 81  
Zysk, A.M., 376  
Zyuzin, A.Y., 171